Ming-ko Woo

Cold Region Atmospheric and Hydrologic Studies

The Mackenzie GEWEX Experience

Volume 1: Atmospheric Dynamics

Springer

Ming-ko Woo

Editor

Cold Region Atmospheric and Hydrologic Studies

The Mackenzie GEWEX Experience

Volume 1: Atmospheric Dynamics

Ming-ko Woo
Editor

Cold Region Atmospheric and Hydrologic Studies

The Mackenzie GEWEX Experience

Volume 1: Atmospheric Dynamics

with 136 Figures

Springer

Mr. Ming-ko Woo
McMaster University
School of Geography
and Earth Sciences
1280 Main Street West
Hamilton ON L8S 4K1
Canada

Email: woo@mcmaster.ca

Cover photograph: Mackenzie River flowing across the Interior Plains near Norman Wells, as seen from Franklin Range

Library of Congress Control Number: 2007931626

ISBN 978-3-540-73935-7 Springer Berlin Heidelberg New York

Springer is a part of Springer Science+Business Media
springer.com

Cover design: deblik, Berlin
Production: Almas Schimmel
Typesetting: Camera-ready by the editor

Printed on acid-free paper 32/3180/as 5 4 3 2 1

Preface

The geography of Canada makes it one of the best locations in the world for cold region atmospheric and hydrologic studies: its high latitude and high mountains, proximity to oceans in the Arctic and cold temperate zones, a broad assemblage of landscape and vegetation, and numerous lakes and rivers. For years, Canadians have conducted research on cold regions, either individually or in small groups, thus accumulating rich experience and ample expertise in the far North. Creation of the Global Energy and Water Cycle Experiment (GEWEX), under the auspices of the World Climate Research Program, provided an external impetus for large-scale collaborative research. Canada responded to this initiative by creating the Mackenzie GEWEX Study or MAGS that focused on the cold region. It was recognized at the early stage of MAGS that the atmosphere and the hydrosphere are strongly linked. A concerted effort of atmospheric and hydrologic scientists is beneficial, if not essential, to a successful large research program. In this regards, investigation conducted by a group of scientists and engineers of MAGS was entirely relevant and timely. This study, carried out between 1994 and 2005, had the research objectives of (1) understanding and modeling the high-latitude energy and water cycles that play roles in the climate system, and (2) improving our ability to assess the changes to Canada's water resources that arise from climate variability and anthropogenic climate change.

So vast a world region that is under the influence of intense and persistent coldness cannot be covered by a contingent of Canadian researchers over a decadal time horizon. The Mackenzie River Basin and its vicinity in northwestern Canada, occupying an area of about two million square kilometers, was adopted as the preferred research location. It offers a wide assemblage of environments, including mountains and plains, tundra and forests, lakes and wetlands, and winters landscapes of snow, ice and frost. Its climatic continentality is accompanied by pronounced external influences, notably from the Pacific Ocean. The Mackenzie area presents a diversity of atmospheric and hydrologic conditions with their attendant research problems to challenge the MAGS investigators.

With increasing pressure of development, the previously neglected northern areas in many circumpolar nations have come to the fore. The cold region with its permafrost, snow and ice that are sensitive to climate

warming, and with its ecosystem that is vulnerable to disturbances, must be developed in a considered fashion to enable environmental sustainability. Information needs to be gathered and sound knowledge should be available for proper planning and operational purposes. Furthermore, the cold region is acknowledged to be highly sensitive to variations and changes in the climate. The effects of its atmospheric and hydrologic feedback extend well beyond the confines of the high latitudes to influence the global movements of water and energy. There are large uncertainties regarding how the cold region responds to the impetus of changes imposed by nature and human. Progress in cold climate research would contribute to improved understanding of how the system behaves, hence enabling better preparation for and appropriate adaptation to these changes.

MAGS attempted to increase our knowledge of the North. All its projects placed an explicit or implicit emphasis on improving the current understanding of the cold region atmospheric and hydrologic processes. Results from process studies were incorporated into atmospheric, land surface and hydrologic models so as to better represent and predict the cold region phenomena. Importantly, knowledge of the processes can be used to explain the occurrence of physical features or events in other world cold areas. Many algorithms developed are applicable universally. Considered this way, MAGS contribution appeals to a much broader audience than the title Mackenzie implies.

Water and energy budgets are one major means to characterize the hydroclimatology of a world region. MAGS undertook detailed analyses and mapping of components of the energy and water cycle to quantify the fluxes and stores in the atmosphere and in the hydrosphere. Closely associated with the water and energy balance studies was research on the mechanisms that convey heat and moisture, leading to improved understanding of large scale airflows, clouds and precipitation, snow and ice regimes, runoff generation, and lake dynamics. The instruments of scientific enquiry included field observations, remote sensing, modeling and statistical analyses, capitalizing on the cross-disciplinary collaborative opportunities and the asset of Canadian expertise on cold region research.

Research is useful if, in the end, the results are broadly disseminated. While it is satisfying for MAGS investigators to see their research efforts unified into a single publication, it is far more important that the results are made available to and used by a community of environmental scientists, resource managers, policy makers, instructors and students of the cold regions. Such is the goal of this book.

This collaborative research venture could not have been realized without the necessary organizational structure, financial support and institutional

partnership. To coordinate the MAGS Program, a Management Board was in place, chaired by John Stone. A Science Committee with a rotating Chair and membership set the overall research agenda, facilitated and monitored research projects. An International Advisory Panel offered critical annual reviews of MAGS progress. At various times, the Panel members included Alan Betts, Denis Lettenmaier, Tetsuo Ohata, Eherhardt Rashke, John Roads and Brian Wilkinson. Ming-ko Woo, Wayne Rouse, Ronald Stewart, Kent Moore and Han Ru Cho served as the Principal Investigator at different periods and phases of MAGS. We were fortunate to have able Managers to assist in the program, information, and finance aspects: Peter diCenzo, Geoff Strong, Terry Krause, Bob Crawford and Joan Parker.

Funding from the Natural Sciences and Engineering Research Council of Canada (NSERC) has enabled all the university investigators and their students to carry out multiple years of research, and an expression of gratitude to NSERC is provided here on behalf of every one of the MAGS investigators and their trainees. We acknowledge the unwavering support, both financial and institutional, of Environment Canada through the former Atmospheric Environment Service, the National Water Research Institute and the Prairie and Northern Region. The Departments of Indian and Northern Affairs, and Natural Resources of Canada, and several Canadian universities (Alberta, McGill, McMaster, Quebec, Saskatchewan, Toronto, Waterloo and York) gave their endorsement of the program. Other sources of support are acknowledged in individual chapters.

The production of this book was facilitated by an editorial advisory team consisting of Wayne Rouse, Kit Szeto, Lawrence Martz and Ron Stewart. We are grateful to the many reviewers who provided valuable comments to ensure that all the chapters are of a high standard. The coherent appearance of this book is a result of the dedication and efficiency of the team that brought its materials into the final format. In this regard, Michael and Laurine Mollinga, Robin Thorne and Laura Brown deserve much credit and my gratitude.

Ming-ko Woo

May 2007

Table of contents

List of Contributors

Paul Bartlett
Science and Technology Branch, Environment Canada
4905 Dufferin Street, Downsview, ON
Canada M3H 5T4

Jacqueline Binyamin
School of Geography and Earth Sciences
McMaster University, Hamilton, ON
Canada L8S 4K1

Peter Blanken
Department of Geography, 260 UCB
University of Colorado
Boulder, Colorado
USA 80309-0260

Julian C. Brimelow
Department of Earth and Atmospheric Sciences
University of Alberta, Edmonton, AB
Canada T6G 2E3

Ross Brown
Environment Canada at OURANOS Inc.
550 Sherbrooke Ouest, 19e étage, Montréal, QC
Canada H3A 1B9

William R. Burrows
Environment Canada, Prairie and Northern Science Section
Hydrometeorology and Arctic Lab
Room 200, 4999 98–Ave. NW, Edmonton, AB
Canada T6B 2X3

Normand Bussières
Science and Technology Branch, Environment Canada
4905 Dufferin Street, Downsview, ON
Canada M3H 5T4

Zuohao Cao
Meteorological Service of Canada, Environment Canada
National Research Lab for Nowcasting and Remote Sensing
4905 Dufferin Street, Downsview, ON
Canada M3H 5T4

Ed Chan
Science and Technology Branch, Environment Canada
4905 Dufferin Street, Downsview, ON
Canada M3H 5T4

Robert Crawford
Science and Technology Branch, Environment Canada
4905 Dufferin Street, Downsview, ON
Canada M3H 5T4

Yves Delage
Recherche en prevision numerique, Environment Canada
Dorval, QC, Canada H9P 1J3
[Deceased]

Chris Derksen
Science and Technology Branch, Environment Canada
4905 Dufferin Street, Downsview, ON
Canada M3H 5T4

Stephen J. Déry
Environmental Science and Engineering Program
University of Northern British Columbia, Prince George, BC
Canada V2N 4Z9

Claude R. Duguay
Department of Geography
University of Waterloo, Waterloo, ON
Canada N2L 3G1

Max L. Dupilka
Department of Earth and Atmospheric Sciences
University of Alberta, Edmonton, AB
Canada T6G 2E3

Jian Feng
Meteorological Service of Canada, CMC, Environment Canada
2121 Rte TransCanadienne, Doval, QC
Canada H9P 1J3
[Formerly at McGill University]

Michael D. Flannigan
Canadian Forest Service, Great Lakes Forestry Centre
Sault Ste Marie, ON
Canada P6A 2E5

Mark Gordon
Centre for Research in Earth and Space Science
York University, Toronto, ON
Canada M3J 1P3

Song Guo
Canada Centre for Remote Sensing, Natural Resources Canada
4th floor, 588 Booth St., Ottawa, ON
Canada K1A 0Y7
[Formerly at McGill University]

John Gyakum
Department of Atmospheric and Oceanic Sciences
McGill University, Montreal, QC
Canada H3A 2K6

William D. Hogg
Reach Consulting
45 Applewood Cove, RR#1, Bath ON
Canada K0H 1G0

David Hudak
Science and Technology Branch, Environment Canada
King City Radar, King City, ON
Canada L7B 1A3

Lily Ioannidou
Department of Atmospheric and Oceanic Sciences
McGill University, Montreal, QC
Canada H3A 2K6

Konstantin V. Khlopenkov
Canada Centre for Remote Sensing
Natural Resources Canada, Ottawa, ON
Canada K1A 0Y7

Bohdan Kochtubajda
Environment Canada, Prairie and Northern Science Section
Hydrometeorology and Arctic Lab
Room 200, 4999 98–Ave. NW, Edmonton, AB
Canada T6B 2X3.

Rasim Latifovic
Canada Centre for Remote Sensing, Natural Resources Canada
588 Booth St., Ottawa, ON
Canada K1A 0Y7

Henry G. Leighton
Department of Atmospheric and Oceanic Sciences
McGill University, Montreal, QC
Canada H3A 2K6

Jinliang Liu
Environmental Monitoring and Reporting Branch
Ontario Ministry of the Environment
125 Resources Road, East Wing, Toronto, ON
Canada M9P 3V6

Kimberley A. Logan
Canadian Forest Service, Great Lakes Forestry Centre
Sault Ste Marie, ON
Canada P6A 2E5

Yi Luo
Noetix Research Inc., Ottawa, ON, Canada
[Under contract with Canada Centre for Remote Sensing]

Murray MacKay
Science and Technology Branch, Environment Canada
4905 Dufferin Street, Downsview, ON
Canada M3H 5T4

Claire J. Oswald
Department of Geography
University of Toronto, Toronto, ON
Canada M5S 3G3

William B. Park
Canada Centre for Remote Sensing, Natural Resources Canada
588 Booth St., Ottawa, ON
Canada K1A 0Y7

Gerhard W. Reuter
Department of Earth and Atmospheric Sciences
University of Alberta, Edmonton, AB
Canada T6G 2E3

Evan Richardson
Canadian Wildlife Service, Environment Canada
5320 122 St., Edmonton, AB
Canada T6H 3S5

Harold Ritchie
Science and Technology Branch, Environment Canada
45 Alderney Drive, Dartmouth, NS
Canada B2Y 2N6

Peter Rodriguez
Science and Technology Branch, Environment Canada
King City Radar, King City, ON
Canada L7B 1A3

Wayne Rouse
School of Geography and Earth Sciences
McMaster University, Hamilton, ON
Canada L8S 4K1

William M. Schertzer
National Water Research Institute
867 Lakeshore Road, Burlington, ON
Canada L7R 4A6

Mark Schuster
Science and Technology Branch, Environment Canada
4905 Dufferin Street, Downsview, ON
Canada M3H 5T4
[Formerly at York University]

Frank R. Seglenieks
Department of Civil and Environmental Engineering
University of Waterloo, 200 University Avenue West, Waterloo, ON
Canada N2L 3G1

Craig D. Smith
Climate Research Division, Environment Canada
11 Innovation Blvd, Saskatoon, SK
Canada S7N 3H5

E.D. (Ric) Soulis
Department of Civil and Environmental Engineering
University of Waterloo, 200 University Avenue West, Waterloo, ON
Canada N2L 3G1

Christopher Spence
National Water Research Institute at NHRC
11 Innovation Blvd., Saskatoon, SK
Canada S7N 3H5

Ronald E. Stewart
Department of Atmospheric and Oceanic Sciences
McGill University, Montreal, QC
Canada H3A 2K6

Ian Stirling
Canadian Wildlife Service, Environment Canada
5320 122 St., Edmonton, AB
Canada T6H 3S5

John M.R. Stone
3411 Paul Anka Drive, Unit 32
Ottawa, ON
Canada K1V 9R8
[Formerly with Meteorological Service of Canada]

Kit K. Szeto
Science and Technology Branch, Environment Canada
4905 Dufferin Street, Downsview, ON
Canada M3H 5T4

Peter A. Taylor
Centre for Research in Earth and Space Science
York University, Toronto, ON
Canada M3J 1P3

Peter Toose
Department of Geography
University of Waterloo,Waterloo, ON
Canada N2L 3C1

Hang Tran
[Formerly at Climate Research Division, Environment Canada]

Alexander P. Trishchenko
Canada Centre for Remote Sensing, Natural Resources Canada
588 Booth St., Ottawa, ON
Canada K1A 0Y7

Calin Ungureanu
Noetix Research Inc., Ottawa, ON, Canada
[Under contract with Canada Centre for Remote Sensing]

Diana Verseghy
Science and Technology Branch, Environment Canada
4905 Dufferin Street, Downsview, ON
Canada M3H 5T4

Anne Walker
Science and Technology Branch, Environment Canada
4905 Dufferin Street, Downsview, ON
Canada M3H 5T4

Andrew M. Way
Department of Atmospheric and Oceanic Sciences
McGill University, Montreal, QC
Canada H3A 2K6

Alexander Wong
[Formerly at Climate Research Division, Environment Canada]

Ming-ko Woo
School of Geography and Earth Sciences
McMaster University, Hamilton, ON
Canada L8S 4K1

M.K. Yau
Department of Atmospheric and Oceanic Sciences
McGill University, Montreal, QC
Canada H3A 2K6

List of Acronyms

AL	Aleutian Low
AMSR	Advanced Microwave Scanning Radiometer
AO	Arctic Oscillation
AVHRR	Advanced Very High Resolution Radiometer
BALTEX	Baltic Sea (GEWEX) Experiment
BERMS	Boreal Ecosystem Research and Monitoring Sites
BOREAS	Boreal Ecosystem-Atmosphere Study
CAGES	Canadian GEWEX Enhanced Study (Sept. 1998 to July 1999)
CANGRID	Environment Canada's gridded monthly surface climate dataset
CCCma	Canadian Centre for Climate modelling and analysis
CCRS	Canadian Centre for Remote Sensing
CERES	Clouds and Earth's Radiant Energy System
CLASS	Canadian Land Surface Scheme
CMC	Canadian Meteorological Centre (of Environment Canada)
CRCM	Canadian Regional Climate Model
CRYSYS	Cryosphere System in Canada
CSE	Continental Scale Experiment (of GEWEX)
DEM	Digital Elevation Model
DIAND	Department of Indian Affairs and Northern Development
DYRESM	A 1-D Dynamic Reservoir Model
EC	Environment Canada
ECMWF	European Centre for Medium-range Weather Forecasts
ELCOM	A 3-D hydrodynamic model
ENSO	El Niño and Southern Oscillation
ERA	European Reanalysis of Global Atmospheric data (from ECMWF)
ERA-40	40-year Global Reanalysis data from ECMWF
GAME	GEWEX Asian Monsoon Experiment
GAPP	GEWEX Americas Prediction Project (formerly GCIP)
GCIP	GEWEX Continental-scale International Project
GCM	Global Climate Model; or General Circulation Model
GEM	Global Environmental Multi-scale Model
GEWEX	Global Energy and Water Cycle Experiment
GFDL	Geophysical Fluid Dynamics Laboratory
GHP	GEWEX Hydrometeorology Panel
GRACE	Gravity Recovery and Climate Experiment

GPCP	Global Precipitation Climatology Project
GRDC	Global Runoff Data Center
GSC	Geological Survey of Canada
GTOPO-30	Global 30 Arc-Second Elevation Data Set
HYDAT	Hydrometric Data from Environment Canada
ISBA	Interactions Soil-Biosphere-Atmosphere (land surface scheme)
ISCCP	International Satellite Cloud Climatology Project
LiDAR	Light Detection And Ranging
MAGS	Mackenzie GEWEX Study
MBIS	Mackenzie Basin Impact Study
MC2	Mesoscale Compressible Community Model
MEC	Modèle Environnemental Communautaire (of CMC)
MODIS	Moderate-Resolution Imaging Spectroradiometer
MRB	Mackenzie River Basin
MSC	Meteorological Service of Canada
NARR	North American Regional Reanalysis (from NCEP)
NAO	North Atlantic Oscillation
NASA	National Aeronautics and Space Administration
NCAR	National Center for Atmospheric Research
NCEP	National Center for Environmental Prediction
NESDIS	National Environmental Satellite, Data and Information Service (NOAA)
NOAA	National Oceanographic and Atmospheric Administration
NRC	National Research Council of Canada
NRCan	Natural Resources Canada
NSIDC	National Snow and Ice Data Center
NSERC	Natural Sciences and Engineering Research Council
NWP	Numerical Weather Prediction
NWRI	National Water Research Institute
NWT	Northwest Territory, Canada
PBSM	Prairie Blowing Snow Model
PDO	Pacific Decadal Oscillation
PIEKTUK	York University blowing snow model
PNA	Pacific North American Oscillation
RadarSat	Canadian Space Agency satellite designed to study polar regions
RCM	Regional Climate Model
RFE	Regional Finite Element model
RIVJAM	River ice jam model
SAR	Synthetic Aperture Radar
ScaRaB	Scanner for Earth Radiation Budget

SPOT	Satellite Probatoire d'Observation de la Terre
SEF	Canadian Global Spectral Forecast model
SLURP	Semi-distributed Land Use-Based Runoff Processes (hydrological model)
SMMR	Scanning Multichannel Microwave Radiometer
SRES	Special Report on Emissions Scenarios
SSM/I	Special Sensor Microwave Imager
TOPAZ	TOPgraphic PArameterZation
WATCLASS	A coupled model of WATFLOOD and CLASS
WATFLOOD	University of Waterloo river basin model
WCRP	World Climate Research Program
WEBS	Water and Energy Budget Study
WSC	Water Survey of Canada

Chapter 1

The Mackenzie GEWEX Study: A Contribution to Cold Region Atmospheric and Hydrologic Sciences

Ming-ko Woo, Wayne R. Rouse, Ronald E. Stewart
and John M.R. Stone

Abstract The Mackenzie GEWEX Study (MAGS) is a collaborative study with the goals of understanding and modeling the high-latitude energy and water cycles, and improving our ability to assess the changes to the water resources of northern Canada that arise from climate variability and anthropogenic climate change. The Mackenzie River Basin (MRB) was selected for a comprehensive study as it possesses many of the environmental attributes of the northern circumpolar region, offers an excellent natural laboratory for studying cold region processes, and experiences significant climate warming and large climate variability. The Basin exhibits an annual negative heat balance, low annual mean temperature and a large positive water balance that promotes large river flow, notably during the spring snowmelt period. High topography of the Western Cordillera and low relief of the central and eastern Basin exert a strong influence on the pattern of atmospheric circulation, and on the advective heat and moisture fluxes. Numerous lakes and extensive wetlands affect surface energy and water balances through evaporation enhancement. Snow, ice (river and lake), and frost are major land surface features molded by the cold climate, and they in turn have strong feedbacks to the atmospheric and hydrologic processes. One major research challenge was to piece together the energy and water budgets given limited data of reliable quality. Through the decade-long MAGS research, this challenge was met in part by intensive studies in select regions within the MRB, the use of remote sensing information and ground observations, and the development and employment of models at various scales. This book is a compilation of the knowledge gained which is equally applicable to other cold regions in the world.

1 Introduction

Cold regions are a major research frontier for atmospheric and hydrologic sciences. They are defined as areas where air temperature stays below 0^{o}C for over half of a year so that snow, ice and frost are common occurrences.

Circumpolar cold regions are considered to be highly sensitive to global warming which can lead to significant changes in the environment (ACIA 2005). This sensitivity promotes alteration of the weather patterns, increased melting of snow, ice and permafrost, and shifts in the river flow regime. Such changes are especially relevant to the climate and water resources of the high latitudes. There is a clear need to enlarge the information base and to improve understanding on the atmospheric and hydrologic processes. To participate in the international Global Energy and Water Cycle Experiment (GEWEX), the Mackenzie GEWEX Study (MAGS) was created in Canada. It was designed specifically to increase our understanding of the atmospheric dynamics and the hydrologic processes of cold regions as coupled systems and to enhance our ability to model them.

Harsh climate, isolation and high cost of research have often discouraged field investigations, and most research to date has been limited in scope, focusing on particular aspects of the environment such as the climate, hydrology, vegetation or landforms (Nuttall and Callaghan 2000). However, many aspects of the natural environment are inter-connected. Atmospheric and hydrologic processes, for example, are strongly coupled. There is a need to understand the climate–hydrologic system on various spatial scales, from the local to the regional level. Recognizing this need, a concerted effort was made to study the water and energy cycles of a large cold-climate domain represented by the Mackenzie River Basin (MRB) in northern Canada, and to apply the collective Canadian expertise to address issues of climate variation and climate change in cold regions.

A primary purpose of this book is to share knowledge gained through our studies, with other researchers and students of the cold environment. It is a compilation of research achievements obtained through a decade of collaborative study. While the Mackenzie drainage basin provides the focal point for the study, the information on cold region processes, and the research methodologies developed, can be applied to other circumpolar regions. This chapter offers background information on the MRB and its relation to world cold regions in terms of physical setting, climate, and water resources.

2 The Circumpolar Cold Region

The circumpolar region has extreme seasonal radiation regimes, with negative radiation balances in the dark winter months and positive balances in the long daylight months of the summer. Atmospheric processes and air

mass dynamics are strongly influenced by these seasonal radiation balance extremes. Annually, the surface heating is restricted by large winter heat loss to the atmosphere, high reflectance of solar radiation by the snow cover in the spring, and low sun angles even in the summer season. Snowfall is an important part of annual precipitation and the snow cover often lasts over half a year. Rivers and lakes have an ice cover for much of the year, and below ground, seasonal frost and permafrost are prevalent (Fig. 1). At high elevations and on a number of Arctic islands, vestiges of Pleis-

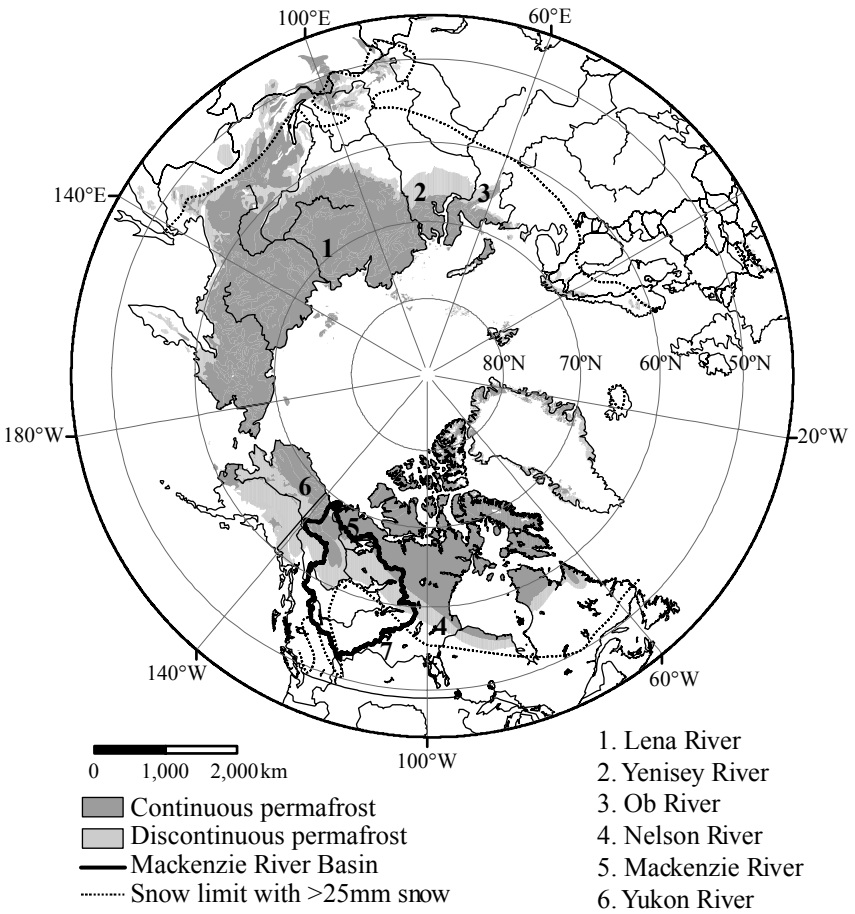

Fig. 1. The circumpolar region of the Northern Hemisphere showing major rivers and lakes and areas with snow on the ground for at least 180 days. Also shown is the distribution of continuous and discontinuous permafrost and the boundary of the Mackenzie River Basin

tocene glaciation are preserved as remnant glaciers, the largest being the Greenland Ice Cap.

The cold region in the Northern Hemisphere includes both areas of high latitude and of high elevation. Two vast land masses in the circumpolar area, Eurasia and North America, surround the Arctic Ocean. Many Arctic islands occupy the perimeter of the central Arctic Basin, including Greenland which is the largest island in the world. On the continents, several major mountain chains that run approximately north-south were created at different geological times along the former edges of the Precambrian platforms. These mountains include the Western Cordillera in North America, the Scandinavian mountains in Europe, the Ural and other mountains in Siberia.

Topography focuses the major drainage into the Arctic Ocean. The northwestward flowing Yukon River is an exception. Among the five largest rivers, the Ob, Yenisey and Lena (basin areas of 2.5×10^6, 2.6×10^6 and 2.5×10^6 km^2, respectively) are in Asia; the Mackenzie and theYukon (basin areas of 1.8×10^6 and 0.9×10^6 km^2) are in North America. In terms of flows from these pan-Arctic rivers, the North American contribution at 281 and 203 km^3 per year for the Mackenzie and the Yukon respectively, is large, but it is moderate compared with 580, 538 and 402 km^3 per year for the Yenisey, Lena, and the Ob (ACIA 2005).

Most of these large basins include a range of climatic and vegetation zones, from temperate grassland (steppes in Asia, prairies in North America) in the south, through boreal forests and subarctic woodlands in the central regions, to tundra in the north. Altitudinal zonation is also conspicuous in mountainous areas, with diminished vegetation diversity and coverage at high elevations. Lakes and wetlands are common on the plains and on the Precambrian bedrock topography (National Wetland Working Group 1988; Zhulidov et al. 1997).

3 The Mackenzie River Basin

The Mackenzie River Basin (or MRB) was selected for a comprehensive study of its climate and hydrology for a number of reasons that are listed as follows. It possesses many of the environmental attributes of the northern circumpolar region, thus offering an excellent natural laboratory for studying cold region processes. It is experiencing significant climate warming, making it a good candidate to examine climatic change and variability, and their attendant effects. The MRB has a moderately dense net-

work of weather stations and streamflow gauging sites that offer 30 or more years of records. The Mackenzie is the largest river in North America flowing into the polar seas. For the MRB, there have been several studies on aspects of the physical and human dimensions that provide useful background information (e.g., Cohen 1997; Mackenzie River Basin Board 2004; Marsh and Ommanney 1991).

3.1 Physical Setting and Vegetation

The MRB extends from 52° to 69°N, with a total area of 1.8 million km^2. This represents about 20% of the Canadian land mass (Fig. 2). From west to east, it straddles three major physiographic provinces: the Cordillera, the Interior Plains and the Precambrian Canadian Shield (French and Slaymaker 1993). At the northern extremity, the Mackenzie Delta forms part of the Arctic Coastal Plain (Fig. 3a). The Western Cordillera is a mountainous region with sub-parallel ridges that trend northwest-southeastward on the western flank of the Basin (Fig. 3b). The high peaks reach from 4000 to over 5000 m. There is a large elevation range of about 1000 m between the valley floors and the mountain tops. In contrast, the Interior Plains (Fig. 3c) are flat-lying and underlain by thick glacial, fluvial, and lacustrine deposits. The Plains drop very gradually from over 800 m in the south to the Mackenzie Delta near sea level. Large parts of the Plains are occupied by wetlands and lakes, as is the Delta which also includes a maze of levee-lined distributary channels. The eastern part of the MRB is dominated by the Precambrian Shield which has an undulating topography (Fig. 3d), with bedrock outcrops sculpted by Laurentide glaciation into rounded hills, and valleys that contain wetlands and lakes.

There is a diversity of surface cover conditions in the basin (Fig. 1 in Trischenko et al. 2007). Farmlands are restricted to the lowlands in the south and the plateau and valleys of the Peace River basin. Forests cover most of the Basin. The boreal forest has a diversity of tree species, including black and white spruce (*Picea mariana, Picea glauca*), mixed with aspen and poplar (*Populus tremuloides, Populus balsamifera*), pines (*Pinus banksiana, Pinus contorta*), birch (*Betula papyrifera*), balsam fir (*Abies balsamea*) and with larch (*Larix laricina*) in poorly drained areas. There is often a rich ground cover of shrubs. The subarctic open woodland is dominated by black or white spruce, with a ground cover of lichen and low shrubs. Wetlands including bogs, fens and marshes are a common feature in the forest zones, as are ponds and lakes. Alpine tundra and barren ground are found at high elevations and Arctic tundra follows a strip of

about 50 km in width along the Beaufort Sea coast. These zones lie beyond the tree-line and the surfaces range from bare soil to coverage by herbaceous plant communities and/or shrubs.

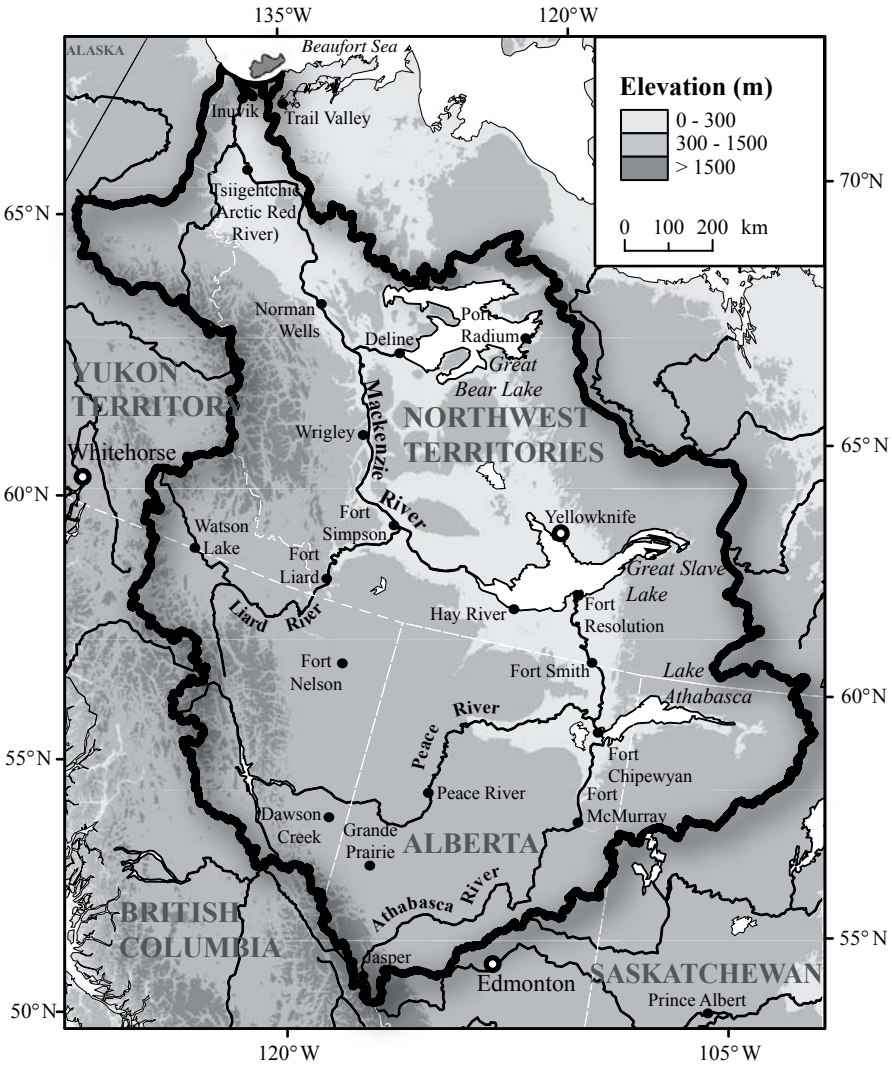

Fig. 2. The Mackenzie River Basin: its topography, major rivers and lakes

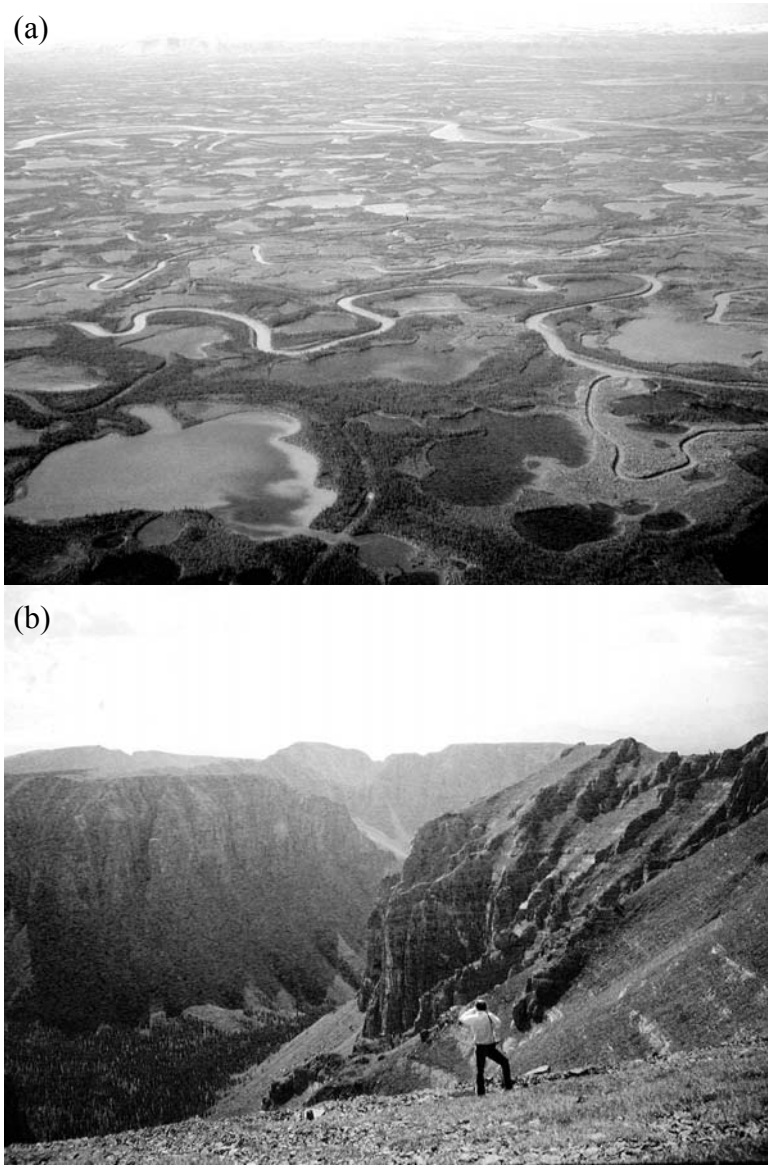

Fig. 3. Major regional landforms of the Mackenzie River Basin: (a) labyrinth of distributaries, ponds and wetlands in the Mackenzie Delta, (b) Western Cordillera with South Nahanni River deeply incised into a high plateau, (c) Fort Simpson situated on an island of the Mackenzie River that flows through the Interior Plain with low relief, and (d) undulating bedrock upland and lake in the Canadian Shield near Yellowknife. (Photos: M.K. Woo)

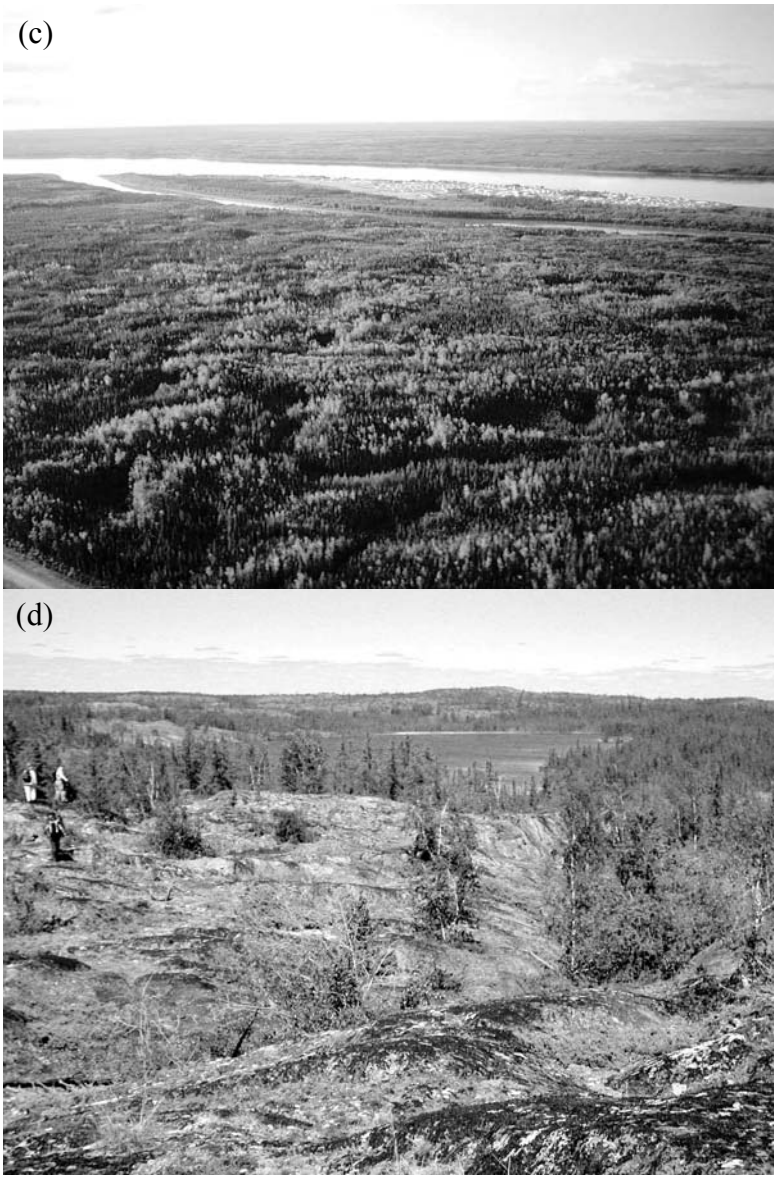

Fig. 3. (cont.)

3.2 Climate and Climate Variability

The MRB lies athwart the circum-global westerly wind circulation. Within this circulation, moisture transport to the northwestern coastal region of North America is accomplished by the cyclones initiated over the west Pacific, while secondary cyclones spawned from these primary cyclones are responsible for bringing precipitation to the Basin. Topography exerts a major influence on atmospheric circulation in the MRB. This is especially pronounced in the cold season when the interaction of the low-level onshore flow with the lofty Western Cordillera induces significant disturbances along the mean westerly flow to incite a stationary long wave pattern. Associated with this wave are a mean westerly transport of warm moist air into the region from the Pacific, and a mean northerly transport of cold dry air to the Basin from the Arctic (Cao et al. 2007; Szeto 2007). In the warm season, the Basin receives moisture flux from the Pacific and the Arctic Oceans, and sometimes from the Gulf of Mexico also (Liu et al. 2007); the latter can bring extreme rainfall to the Basin (Brimelow and Reuter 2007). Moisture recycling is also pronounced (Szeto et al. 2007a) as the large areas of wetlands and lakes facilitate evaporation and the mountain slopes enhance precipitation of the atmospheric moisture. Within the Basin, there is a strong precipitation gradient, with annual precipitation exceeding 1000 mm in the mountains to the southwest and decreasing to less than 300 mm in the northeast. Snowfall constitutes about 30% of total precipitation in the southern Interior Plains but over 60% in the far north and at high altitudes in the west.

As a high-latitude continental basin, the MRB is an important source region of cold continental polar air during the winter when monthly mean air temperatures range from -25 to -35^{o}C, but daily temperature can fall below -50^{o}C. In contrast, summer heating of the large land mass brings about high temperatures, with monthly averages ranging from 15^{o}C in the northern to 20^{o}C in the southern sector of the MRB. Daily high temperature can occasionally reach 30^{o}C. One consequence of persistent coldness is the formation and maintenance of permafrost, or ground with temperatures at or below 0^{o}C for at least two consecutive summers. Over 75% of the Basin is underlain by permafrost which is continuous north of the tree-line and discontinuous in the subarctic regions south of tree-line and in the alpine zone (Fig. 1). The entire MRB, including the non-permafrost zones, experiences seasonal ground freezing.

Temperature variations in circumpolar regions have been larger than those in the temperate and tropical areas. Records show that over the period 1950–98 the annual temperature in the Arctic region has generally in-

creased by 1 to 1.5°C, except in Eastern Canada and Greenland which experienced cooling (ACIA 2005). Reanalysis data indicate that winter temperature variability has been particularly large for the Yenisey and the Mackenzie areas (Kistler et al 2001; Szeto 2007). Mean annual temperature at Fort Simpson, located near the middle of the basin, indicates a rise of about 1°C after 1975 (Fig. 4). Simulation of temperature tendencies by several Global Climate Models confirms that the Arctic is a sensitive indicator of climate change. A scenario of a moderate future global emission of greenhouse gases, known as a B2 scenario, is expected to warm the zone 60–90°N by 3.5–5.5°C by 2100, depending on which model result is consulted (ACIA 2005).

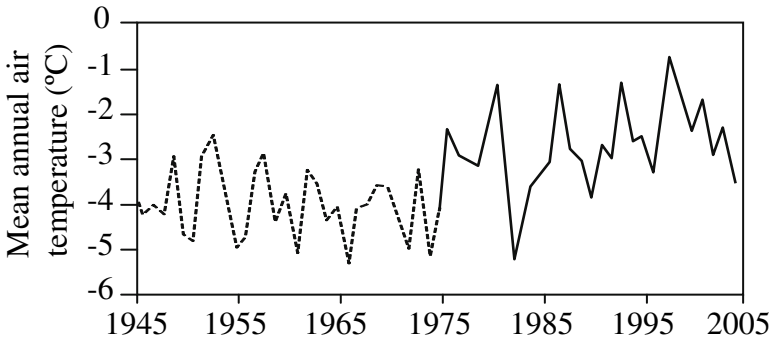

Fig. 4. Annual temperature of Fort Simpson in Mackenzie Basin showing a sharp increase after the mid-1970s

A change in the snow cover conditions has accompanied recent climate warming (Derksen et al. 2007). Compared with the 1915–55 snow cover extent, the snow cover of the Northern Hemisphere for the period 1956–97 indicates a statistically significant decrease in March and April but an increase in November (Brown 2000). This is possibly related to cooling in November and warming in April, with a resulting shift in the snow season towards earlier dates of maximum snow depth and earlier disappearance of snow.

3.3 Energy and Water Budgets

A fundamental way to characterize the climate of a region is through its energy and water balances. The mean annual water and energy budgets for three large river basins along a north-south transect in the Americas are presented (Table 1) for comparison, using the results for 1988–99 produc-

Table 1. The water and energy budgets for a northern (Mackenzie), a temperate (Mississippi) and a tropical (Amazon) river basin compared with data for the global terrestrial environment for the 1988-99 period. All energy units are in K/d where K is an energy normalization unit used for presentation purposes. Calculations are based on data from the National Centers for Environmental Prediction Reanalysis II (adapted from Roads et al 2002)

	Mackenzie	Mississippi	Amazon	Global land
Water budget				
Precipitable water [mm]	9.90	16.68	40.22	18.71
Moisture convergence [mm d^{-1}]	0.67	0.55	1.72	0.69
Precipitation [mm d^{-1}]	1.79	2.30	5.28	2.28
Evaporation [mm d^{-1}]	1.76	2.34	3.91	1.80
Runoff [mm d^{-1}]	0.72	0.53	2.08	0.94
Storage (2 m soil moisture, and snow) [mm]	643.8	424.3	588.7	5376.0
Residual, atmospheric water balance [mm d^{-1}]	-0.64	-0.58	-0.35	-0.21
Residual, surface water balance [mm d^{-1}]	0.69	0.57	0.71	0.46
Moisture recycling ratio	0.18	0.14	0.13	0.12
Energy budget				
Net atmospheric radiation budget [K d^{-1}]	-0.83	-0.81	-0.91	-0.77
Condensation heat of the atmosphere [K d^{-1}]	0.45	0.57	1.31	0.57
Heat convergence in the Atmosphere [K d^{-1}]	0.51	0.18	-0.90	0.04
Net surface radiation Balance [K d^{-1}]	0.33	0.73	1.12	0.61
Sensible heat flux from the surface [K d^{-1}]	-0.22	0.10	0.14	0.11
Evaporative heat flux from the surface [K d^{-1}]	0.44	0.58	0.97	0.45
Heat flux from the ground [K d^{-1}]	-0.11	-0.05	-0.02	-0.05

ed by Roads et al. (2002). These basins are the Mackenzie in the far north, the Mississippi in the temperate zone, and the Amazon in the tropics. Although the residual errors can be as large as the magnitudes of some of the energy and water balance components, the relative magnitude differences between regions are qualitatively meaningful. Roads et al.'s (2002) work was based on NCEP-R2 re-analysis data and the results for the MRB exhibit some bias in the surface fluxes compared with the findings of a detail study by Szeto et al. (2007b).

The energy balance indicates that all three basins experience negative atmospheric radiation balances of comparable magnitudes. They gain heat through the condensation of water vapor in the atmosphere. Annually the Amazon advects sensible heat out of its basin, but the Mississippi and the Mackenzie basins gain sensible heat. For the Mackenzie Basin, most of the advective heat comes from the Pacific Ocean. The Amazon and Mississippi both gain sensible heat from the terrestrial surface and lose it to the atmosphere, whereas the atmosphere of the MRB loses heat to the surface. All three basins have a net heat flux into the ground but it is substantially larger for the Mackenzie. The annual energy balance of the Mackenzie is distinguished from its temperate and tropical counterparts by a substantially smaller positive surface radiation balance and by a larger advective heat input.

The water balance comparison indicates that there is a global moisture convergence from the oceans to the land in all three basins. Both precipitation and evaporation decrease from the tropical Amazon to the temperate Mississippi, with the least occurring in the Mackenzie basin. Runoff is largest from the Amazon, but the Mackenzie yields more flow than the Mississippi due to a lower evaporation/precipitation ratio and to a concentration of most flow into the snowmelt season. Low evaporation and high snow accumulation also produce a large seasonal storage term for the Mackenzie Basin.

3.4 Hydrology

The Mackenzie River has six major, and many lesser, tributaries. The major tributaries in the south are the Athabasca River and the Peace River (which is regulated), both of which rise from the Rocky Mountains. Also rising in the Rockies and draining to the Interior Plains is the Liard River and other smaller rivers in the northwest. The Great Bear River in the northeast collects runoff from the Canadian Shield while Great Slave Lake captures the flows of the Athabasca, the Hay and other minor rivers in the northeast collects runoff from the Canadian Shield while Great Slave Lake captures the flows of the Athabasca, the Hay and other minor rivers in the southern parts of the Shield and from the Interior Plains. Within the Basin, mountainous areas with high precipitation produces about 60% of the Mackenzie flow (Fig. 5) of which most (50%) is contributed by the Peace and the Liard rivers. The Interior Plains and the eastern Shield, covering 40% of the total basin area, provide only about 25% of the Mackenzie discharge (Woo and Thorne 2003). Annual flow of the river at the village of

Arctic Red River (before the Mackenzie enters its delta) averages 8994 m^3 s^{-1} based on the 1973–2003 record, with a standard deviation of 954 m^3 s^{-1}.

Snow plays a major role in cold region hydrology. Sublimation loss can account for 10–50% of the snowfall (Pomeroy et al. 2007). The patterns of snow accumulation, redistribution and melt control the temporal and spatial distribution of spring runoff. Melting is accelerated when patchy conditions prevail in the open areas (Marsh et al. 2007); and synchronous melting of snow across a range of elevations in mountainous terrain can release large meltwater volumes. The presence of frozen soils, rendered impervious by frozen pore water, hinders infiltration and enhances surface runoff that generates high flows in most streams. The flow of Mackenzie River and many of its tributaries experience a nival streamflow regime in which the snowmelt contribution dominates (Woo and Rouse 2007). Spring floods are exacerbated by the damming effect of breaking up of the river ice that develops over the intensely cold and long winter (Hicks and Beltaos 2007). Ice jams and their associated flood problems are a recurrent concern for the riparian zones in most parts of the MRB.

Myriad lakes of different dimensions occupy the Basin (see Fig. 1 in Oswald et al. 2007), including the very large lakes Great Bear, Great Slave, and Athabasca (with surface areas of 31.3×10^3, 28.6×10^3, and 7.9×10^3 km^2, respectively). These all rank among the ten largest fresh water lakes in the world. The presence of lakes as well as wetlands enhances evaporation but at high latitude locations, all lakes acquire a winter ice cover that inhibits evaporation loss for a period of four months in the south to eight months in the north (Rouse et al. 2007). Large lakes also modify streamflow by dampening and retarding high flows and by raising the low flows to produce a pro-lacustrine regime of flow (Woo 2000). In a semi-arid environment, rivers that drain through a chain of lakes can experience flow interruption if lake storage falls below the outflow threshold. Unlike large Siberian rivers that are impounded to create a series of reservoirs, the Mackenzie has only one major reservoir that regulates the flow of its tributary, the Peace River, for hydroelectric power generation.

Besides human interference that affects the flow of the large Siberian rivers, large natural variations in the recent decades have been reported. The Ob and the Lena show a shift in their hydrologic regime towards earlier snow melt and increased summer discharge, due to warmer melt seasons and higher summer precipitation (Yang et al. 2004a; Ye et al. 2003). For the Yenisey, however, snowmelt runoff has been delayed due to a cooling trend in the melt season for central Siberia (Yang et al. 2004b). The Mackenzie River has undergone a recent volume increase in winter low flow and the date of spring runoff arrival has been earlier (Burn and

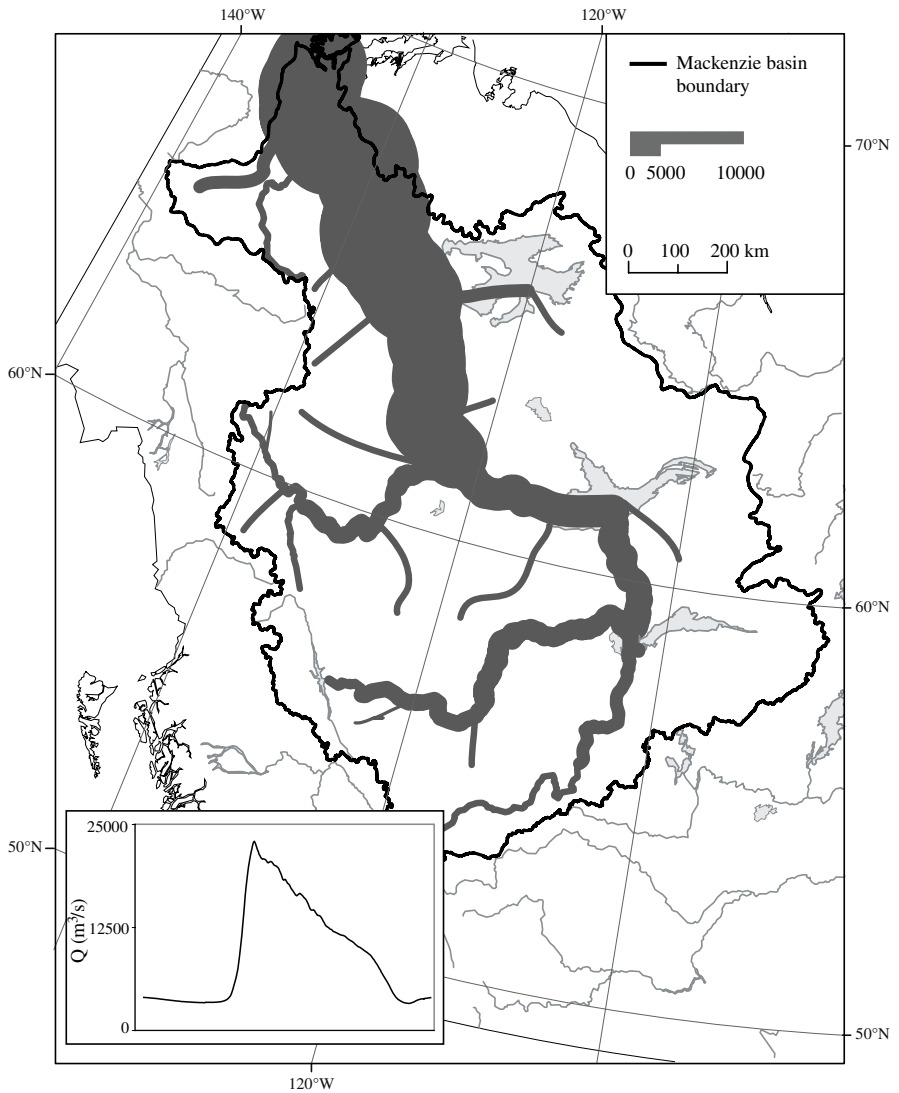

Fig. 5. Downstream change in annual flow as Mackenzie River receives contributions from its major tributaries. Inset is mean daily discharge of Mackenzie River

Hesch 2007). The change occurred in the mid-1970s and represents a step change rather than as a steady trend. Such a shift is also apparent in the temperature (e.g., Fort Simpson temperature shown in Fig. 5). These shifts can be related to the Pacific Decadal Oscillation (cf., Woo et al. 2006, who

noted that streamflow response to large-scale climate forcing is complicated by topographic modification of local climate and by basin storage).

4 The Role of MAGS in International GEWEX Program

In 1988, the World Climate Research Program initiated the Global Energy and Water Cycle Experiment (GEWEX) to improve our understanding and prediction of the role played by the hydrologic cycle in the climate system. Several regional research programs covering a wide range of climatic conditions have been undertaken. Each program is charged to quantify the energy and water vapor fluxes into and out of their particular region, characterize the precipitation and evapotranspiration fields, and document runoff and discharge (Lawford et al. 2004). In 1994 Canada began its participation by undertaking the Mackenzie GEWEX Study (MAGS), emphasizing a cold climate system. The Mackenzie Basin was a suitable candidate for regional energy and water balance study because in a global context it is representative of the low temperature and low precipitation environment. Other Continental Scale Experiments cover a range of conditions, but the closest to MAGS was the GAME (GEWEX Asian Monsoon Experiment) program, part of which was carried out in Siberia (Fig. 6).

Canada is, in general, richly endowed with water. Nevertheless, a proper understanding of the atmospheric and hydrologic processes is paramount to the inventory and prediction, management and sustainable usage of water resources. A suite of models is needed to improve climatic and hydrologic numerical prediction. The models have significant applications at various scales, including, for example, the operation of small hydroelectric power schemes, the prediction of Mackenzie River discharge to the Arctic Ocean, the analysis of local forest fire events, and weather forecasting on a regional scale. Towards these ends, the goals of MAGS were (1) to understand and model the high-latitude energy and water cycles that play roles in the climate system, and (2) to improve our ability to assess the changes to Canada's water resources that arise from climate variability and anthropogenic climate change.

Canada is, in general, richly endowed with water. Nevertheless, a proper understanding of the atmospheric and hydrologic processes is paramount to the inventory and prediction, management and sustainable usage of water resources. A suite of models is needed to improve climatic and hydrologic numerical prediction. The models have significant applications at various scales, including, for example, the operation of small hydroelectric

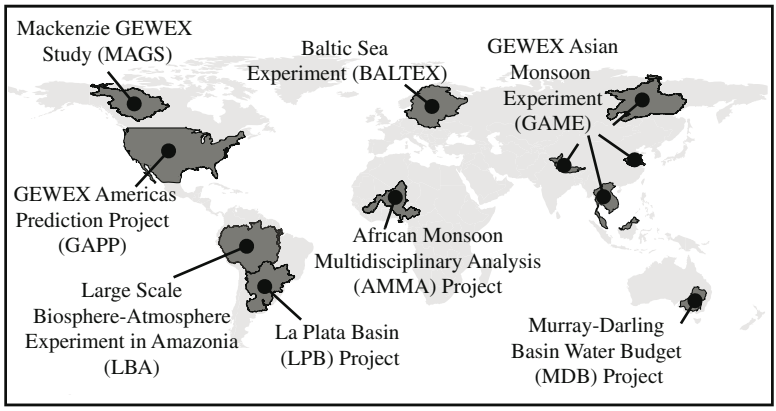

Fig. 6. Location of GEWEX Continental Scale Experiments

power schemes, the prediction of Mackenzie River discharge to the Arctic Ocean, the analysis of local forest fire events, and weather forecasting on a regional scale. Towards these ends, the goals of MAGS were (1) to understand and model the high-latitude energy and water cycles that play roles in the climate system, and (2) to improve our ability to assess the changes to Canada's water resources that arise from climate variability and anthropogenic climate change.

4.1 Research Challenges

4.1.1 Data Availability and Accuracy

Circumpolar regions are remote and have a small human population, with the consequence that there are few climatic and hydrometric stations. Since the 1990s, there has been a significant attrition of the already sparse Arctic data collection network (Shiklomanov et al. 2002). Ground measurements are also known to suffer inaccuracies under a cold climate. Snow gauges have long been known to undercatch snowfall, particularly under windy conditions (Goodison 1978). Radiation and temperature sensors may be covered by frost or snow in the winter and wind sensors may be coated by rime. Stream gauging in winter is under a river ice cover which affects the accuracy of measurement. It is extremely dangerous to measure discharge manually during river ice breakup or freeze-up. Additionally, the former event is usually accompanied by very large flows. Model results and reanalysis products offer a possibility to augment in situ measurements. Furthermore, they provide spatial coverage not available from point

observations made on the ground. Remote sensing permits the mapping of snow cover extent, ice coverage, soil wetness, surface temperature, and several radiation fields. These spatial data are especially helpful to climatic and hydrologic investigation of the cold regions.

As for other cold regions, study of the MRB is hampered by data shortage. Still, this Basin has the highest concentration of climatic and hydrometric stations among the cold areas of Canada. During the MAGS research period, an additional collection of data was obtained and archived. It is available on website
http://www.usask.ca/geography/MAGS/lo_Data_e.htm.

4.1.2 Cross-disciplinary Collaboration

Atmospheric and hydrologic investigations have traditionally been treated as separate research pursuits. MAGS, however, was cross-disciplinary, being a collaborative study that involved scientists and engineers from ten universities and five government research institutions. The research program brought together investigators with divergent background training and experiences in atmospheric and hydrologic fields, in earth sciences and remote sensing, as well as in data processing and modeling. Initial difficulties had to be surmounted as various disciplinary approaches had to be reconciled, uninhibited scientific and technical dialogues had to be fostered and even language barriers due to unfamiliar usage of terms had to be overcome. The lists of acronyms and symbols provided in this book are testament to the divergent vocabulary. The investigators soon worked as a team and the membership expanded as research directions evolved continuously throughout the span of MAGS. Between 1994 and 2005, there were regular annual meetings and many thematic workshops. The papers presented were recorded in the Annual Proceedings and can be found in MAGS website: www.usask.ca/geography/MAGS/.

Several hundred publications in refereed journals have enabled the worldwide dissemination of MAGS research results. Research progress was also synthesized and reported in review articles (Rouse 2000; Rouse et al. 2003; Stewart et al.1998) and journal special issues (Marsh and Gyakum 2003; Stewart 2002).

4.1.3 Application of Scientific Results

MAGS successfully attained all its scientific objectives and the findings constitute the subjects of this book. It was further recognized that the research results should be applied. To do so, MAGS undertook joint ven-

tures among its investigators to target specific problems related to the region. Meetings were held with the aboriginal and scientific communities in the MRB, particularly to address climate change and climate variability impacts (e.g., Woo et al. 2007). Individual investigators of MAGS collaborated with government and industrial partners in a number of projects, some of which are alluded to in this book. The themes of this collaboration include river ice and floods, hydrologic modeling and hydropower production, lightning and forest fire occurrence and frequency, snow and aviation weather forecasting.

5 Presentation of the Book

This book is a synthesis of a benchmark effort by Canadian researchers to study the cold region. The coverage of topics is too extensive to be consolidated into a single book, hence the division into two volumes. Volumes I and II can be treated as a stand-alone contribution to atmospheric and hydrologic sciences respectively. Together, these volumes reflect the spirit of MAGS in describing, understanding, and modeling the atmospheric–hydrologic system in its entirety.

Both volumes similarly emphasize the physical processes, because knowledge of these processes is universally transferable to promote a general advancement of cold region sciences. A range of research methods and tools is extensively employed, including field work, remote sensing, modeling, and statistical analyses. Both volumes provide examples of application for predictive, planning or management purposes. Effects of climatic variability and change in the region are considered in a number of chapters.

Thematically, Volume I concentrates on the atmospheric component of MAGS research. Investigations were oriented towards large areas that usually cover the entire Basin or large parts thereof. This volume introduces an overview of atmospheric research conducted under MAGS, followed by presentations on the atmospheric processes occurring in and influencing the cold region of northwestern North America, particularly the MRB. Topics include anticyclone generation and impacts, cold season temperature behavior, water vapor fluxes and moisture source for precipitation, cloud development and frequency and precipitation mechanisms and patterns. Research focusing on rainfall, snowfall, blowing snow sublimation, and regional-scale snow distribution is presented. The studies of moisture and energy fluxes provide a strong basis for the investigation of large scale

energy and water cycle. One chapter reviews the water and energy budgets of the MRB. This is followed by examination of the role of lakes in regional climate, the radiation balance as affected by clouds and wildfire aerosols, and the moisture flux convergence. Thunderstorms and related wildfire are common in the warm season, and they have been studied using ground observation and models. Satellite data have been used for the mapping land surface attributes, including snow cover, surface albedo and radiation. In terms of modeling, the coupling of the Canadian Land Surface Scheme (CLASS) with the Canadian global spectral forecast model (SEF) and with the Canadian Regional Climate Model of MAGS is described. A concluding chapter provides a synopsis of hydrologic results presented in Volume II.

Volume II opens with a summary of the materials presented in Volume I, and a survey of the hydrologic research carried out under MAGS. This is followed by chapters on the near-surface temperature and wetness that provide background information of the MRB region. Subsequent chapters are presented on processes uniquely important in a cold region context, including topics on snow, frost and ice. The predictive aspect of river ice is emphasized because ice jams and associated floods pose a recurring problem to the riverine environment and the river-side communities. Several chapters focus on lakes which are a common feature throughout the central and eastern Mackenzie Basin. MAGS has significantly advanced knowledge on their hydroclimate and hydrology, a knowledge that is transferable to lakes of different dimensions in other cold climates. The investigations of Shield and wetland hydrology are documented. Results from these studies have relevance to the Fennoscandia area with conditions similar to the Canadian Shield, and to the wetlands that abound on the northern plains of the Russian rivers and in much of Alaska. A section is devoted to the macro-scale analysis and modeling of northern river flows. Streamflow trends of the Mackenzie system are examined. Several chapters develop and apply techniques of aggregating drainage patterns to larger spatial units, of using land surface schemes CLASS and ISBA, and the SLURP hydrologic model, and promoting the coupled WATCLASS model as a step towards linking hydrologic with atmospheric models. A concluding chapter draws together the MAGS research on the atmospheric and hydrologic environments of the MRB.

By fostering an integration of atmospheric and hydrologic sciences, MAGS has improved our understanding of the fundamental processes pertinent to the MRB, and has also developed knowledge that can be applied broadly to cold regions of the globe. Not all aspects of MAGS research can be presented as separate chapters within the space of the two volumes.

Some topics such as the build-up and dissipation of available potential energy, and the hydrologic processes of mountainous catchments, are given summary presentations in the overview chapters. It is recognized that MAGS is a pioneering endeavor to overcome inadequacies in current knowledge of cold region processes; and so, the directions of future research are identified in many chapters.

References

ACIA (2005) Arctic climate impact assessment. Cambridge University Press, Cambridge.

Brown RD (2000) Northern Hemisphere snow cover variability and change. J Hydrol 13:2339–2355

Brimelow JC, Reuter GW (2007) Moisture sources for extreme rainfall events over the Mackenzie River Basin. (Vol. I, this book)

Burn DH, Hesch N (2007) Trends in Mackenzie River Basin streamflows. (Vol. II, this book)

Cao Z, Stewart RE, Hogg WD (2007) Extreme winter warming over the Mackenzie Basin: observations and causes. (Vol. I, this book)

Cohen SJ (1997) Mackenzie Basin Impact Study (MBIS) Final Report. Environment Canada, Downsview, Ontario

Derksen C, Brown R, MacKay M (2007) Mackenzie Basin snow cover: variability and trends from conventional data, satellite remote sensing, and Canadian Regional Climate Model simulations. (Vol. I, this book)

French HM, Slaymaker HO (1993) Canada's cold environments. McGill-Queen's University Press, Montreal & Kingston

Goodison BE (1978) Accuracy of Canadian snow gauge measurements. J Appl Meteorol 17:1541–1548

Hicks F, Beltaos S (2007) River ice. (Vol. II, this book)

Kistler R, Kalnay E, Collins W, Saha S, White G, Woollen J, Chelliah M, Ebisuzaki W, Kanamitsu M, Kousky V, van den Dool H, Jenne R, Fiorino M (2001) The NCEP-NCAR 50-year reanalysis: monthly means CD-ROM and documentation. B Am Meteorol Soc 82:247–267

Lawford RG, Stewart R, Roads J, Isemer H-J, Manton M, Marengo J, Yasunari T, Benedict S, Koike T, Williams S (2004) Advancing global- and continental-scale hydrometeorology. B Am Meteorol Soc 85:1917–1920

Liu J, Stewart RE, Szeto KK (2007) Water vapor fluxes over the Canadian prairies and the Mackenzie River Basin. (Vol. I, this book)

Mackenzie River Basin Board (2004) Mackenzie River Basin: state of the aquatic ecosystem report 2003. Mackenzie River Basin Board Secretariat, Fort Smith, NT.

Marsh P, Gyakum JR (2003) The hydrometeorology of the Mackenzie River Basin during the 1998–99 Water Year. J Hydrometeorol 4:645–648

Marsh P, Ommanney CSL (1991) Mackenzie Delta: environmental interactions and implications of development. NHRI Symposium No. 4, Environment Canada, Ministry of Supply and Services, Canada

Marsh P, Pomeroy JW, Pohl S, Quinton W, Onclin C, Russell M, Neumann N, Pietroniro A, Davison B, McCartney S (2007) Snowmelt processes and runoff at the Arctic treeline: ten years of MAGS research. (Vol. II, this book)

National Wetlands Working Group, Canada Committee on Ecological Land Classification (1988) Wetlands of Canada. Ecological land classification series no. 24, Environment Canada, Ottawa

Nuttall M, Callaghan TV (2000) The Arctic: environment, people, policy. Harwood Academic Publishers, Amsterdam, the Netherlands

Oswald CJ, Rouse WR, Binyamin J (2007) Modeling lake energy fluxes in the Mackenzie River Basin using bulk aerodynamic mass transfer theory. (Vol. II, this book)

Pomeroy JW, Gray DM, Marsh P (2007) Studies on snow redistribution by wind and forest, snow-covered area depletion and frozen soil infiltration in Northern and Western Canada. (Vol. II, this book)

Roads J, Kanamitsu M, Stewart RE (2002) CSE water and energy budgets in the NCEP-DOE Reanalysis II. J Hydrometeorol 3:227–248

Rouse WR (2000) Progress in hydrological research in the Mackenzie GEWEX Study. Hydrol Process 14:1667–1685

Rouse WR, Blyth EM, Crawford RW, Gyakum JR, Janowicz JR, Kochtubajda B, Leighton HG, Marsh P, Martz L, Pietroniro A, Ritchie H, Schertzer WM, Soulis ED, Stewart RE, Strong GS, Woo MK (2003) Energy and Water Cycles in a High Latitude, North-Flowing River System: summary of results from the Mackenzie GEWEX Study – Phase 1. B Am Meteorol Soc 84:73–87

Rouse WR, Blanken PD, Duguay CR, Oswald CJ, Schertzer WM (2007) Climate–lake interactions. (Vol. II, this book)

Shiklomanov AI, Lammers RB, Vörösmarty CJ (2002) Widespread decline in hydrological monitoring threatens pan-Arctic research. EOS 83(2):13–17

Stewart RE (2002) Towards understanding water and energy processes within the Mackenzie River Basin. Atmos Ocean 40:91–94

Stewart RE, Leighton HG, Marsh P, Moore GWK, Ritchie H, Rouse WR, Soulis ED, Strong GS, Crawford RW, Kochtubajda B (1998) The Mackenzie GEWEX Study: the water and energy cycles of a major North American River basin**.** B Am Meteorol Soc 79:2665–683

Strong GS, Proctor B, Wang M, Soulis ED, Smith CD, Seglenieks F, Snelgrove K (2002) Closing the Mackenzie Basin water budget, Water Years 1994/95 to 1996/97. Atmos Ocean 40:113–124

Szeto KK (2007) Cold-season temperature variability in the Mackenzie Basin. (Vol. I, this book)

Szeto KK, Liu J, Wong A (2007a) Precipitation recycling in the Mackenzie and three other major river basins. (Vol. 1, this book)

Szeto KK, Tran H, MacKay MD, Crawford R, Stewart RE (2007b) Assessing water and energy budget for the Mackenzie River Basin. (Vol. I, this book)

Trischenko AP, Khlopenkov KV, Ungureanu C, Latifovic R, Luo Y, Park WB (2007) Mapping of surface albedo over Mackenzie River Basin from satellite observations. (Vol. I, this book)

Woo MK (2000) Permafrost and hydrology. In: Nuttall M, Callaghan TV (eds) The Arctic: environment, people, policy. Harwood Academic Publishers, Amsterdam, the Netherlands, pp 57–96

Woo MK, Modeste P, Martz L, Blondin J, Kochtubajda B, Tutcho D, Gyakum J, Takazo A, Spence C, Tutcho J, diCenzo P, Kenny G, Stone J, Neyelle I, Baptiste G, Modeste M, Kenny B, Modeste M (2007) Science meets traditional knowledge: water and climate in the Sahtu (Great Bear Lake) Region, Northwest Territories, Canada. Arctic 60:37–46

Woo MK, Rouse WR (2007) MAGS contribution to hydrologic and surface process research. (Vol. II, this book)

Woo MK, Thorne R (2003) Streamflow in the Mackenzie Basin, Canada. Arctic 56:328–340

Woo MK, Thorne R, Szeto KK (2006) Reinterpretation of streamflow trends based on shifts in large-scale atmospheric circulation. Hydrol Process 20:3995–4003

Yang D, Ye B, Shiklomanov A (2004a) Discharge characteristics and changes over the Ob River watershed in Siberia. J Hydrometeorol 5:595–610

Yang D, Ye B, Kane DL (2004b) Streamflow changes over Siberian Yenisei River basin. J Hydrol 296:59–80

Ye B, Yang D, Kane DL (2003) Changes in Lena River streamflow hydrology: human impacts versus natural variations. Water Resour Res 39:1200, doi:10.1029/2003WR001991

Zhulidov AV, Headley JV, Robarts RD, Nikanorov AM, Ischenko AA (1997) Atlas of Russian wetlands: biogeography and metal concentrations. Environment Canada, Saskatoon

Chapter 2

The Mackenzie Climate System: A Synthesis of MAGS Atmospheric Research

Kit K. Szeto, Ronald E. Stewart, M.K. Yau and John Gyakum

Abstract This chapter presents a synthesis of the atmospheric research achievements of the Mackenzie GEWEX Study (MAGS) that has advanced our understanding of the Mackenzie River Basin (MRB) climate system. It highlights our knowledge on key aspects of the system, and discusses the significance of MAGS contribution to cold region hydroclimate. Attention is focused on (1) the large-scale atmospheric processes that control the transport of water and energy into the Basin, (2) interactions of the large-scale atmospheric flows with physical environment of the Basin and their effect on its weather and climate, and (3) application of research results to climate issues in the Basin and beyond.

1 Introduction

As a large continental region located between the Pacific Ocean and the interior continent of North America, and from the cold temperate to the Low Arctic latitudes, the hydrometeorological processes that occur in the Mackenzie River Basin (MRB) (Fig. 1) have significant and far-reaching consequences on the large-scale weather and climate. In addition, some of the strongest climate variability and change signals have been found in the region (Serreze et al. 2000; Szeto 2007b) (Figs. 2 and 3), suggesting that climate of the MRB is extremely sensitive to changes in large-scale conditions, making it an excellent area for studying regional responses to climate change. Indeed, the Mackenzie GEWEX Study (MAGS) is one of the Continental Scale Experiments (CSEs) selected by the Global Energy and Water Cycle Experiment (GEWEX) to understand and model water and energy cycling at high-latitudes (Stewart et al. 1988; Woo et al. 2007).

Because of its mobile, dynamic and omnipresent nature, the atmosphere is the agent that couples and integrates the various water and energy cycling processes that affect or comprise the MRB climate system. Our goal is to make use of this special trait of the atmosphere to weave a picture that presents a macro-perspective of the intrinsic and complex linkages among the myriad climate processes that occur within and outside the Basin, in

different seasons and on vastly diverse spatio-temporal scales. In so doing, we position individual MAGS research efforts and contributions in this complex multi-dimensional web of water and energy flows in the Earth's climate system.

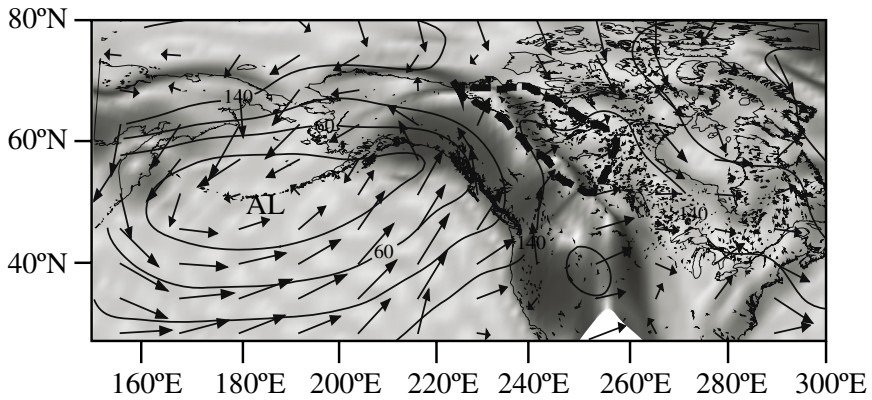

Fig. 1. Large-scale environment characterizing the Mackenzie River Basin, overlain with mean DJF geopotential height contours at 1000 hPa and associated wind vectors at 925 hPa (data from NCEP/NCAR reanalysis). Basin boundary is marked by thick dashed line and AL denotes the Aleutian Low

Rather than compiling a compendium of the atmospheric work performed under MAGS, we provide an integrative description of the MRB climate system and highlight MAGS atmospheric and hydrometeorological research results that have enhanced our understanding of key aspects of the system. (See Rouse et al. (2003) for an overview of earlier MAGS results and Woo and Rouse (2007) for a synthesis of MAGS hydrologic research). The significance of MAGS research in advancing our knowledge on the Basin's hydroclimate will be discussed, with particular attention given to (1) large-scale atmospheric processes that control the transport of water and energy into the Basin, (2) interactions of the atmospheric circulations with the Basin's physical environment and their effects on its weather and climate, and (3) the application of research results to climate issues in the Basin and beyond.

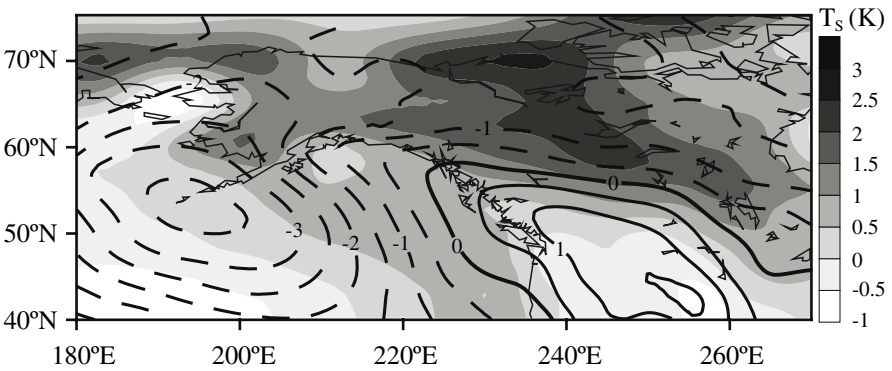

Fig. 2. Differences of mean DJF mean sea level pressure (in hPa) and surface air temperatures (shaded) between the 1980–99 and 1960–79 periods (data from NCEP/NCAR reanalysis)

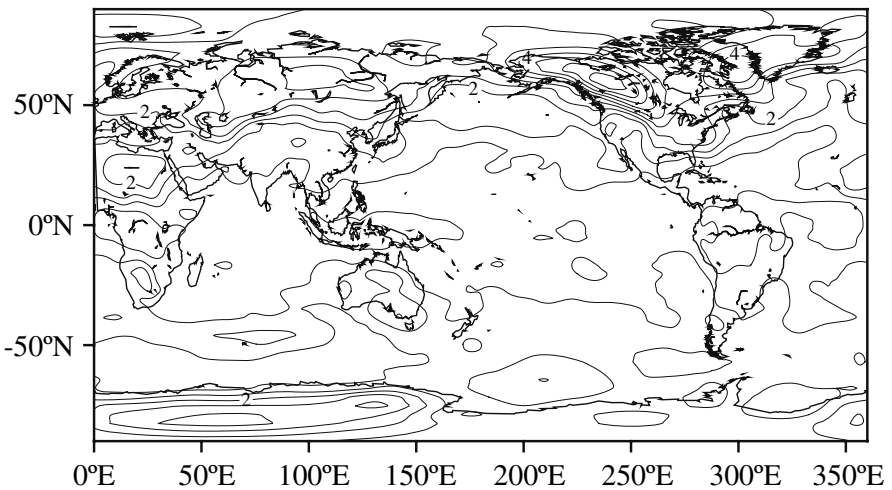

Fig. 3. Interannual standard-deviation of mean January air temperatures at 850 hPa for the 1948–2003 period (data from NCEP/NCAR reanalysis)

2 Upstream and Large-scale Atmospheric Processes

Atmospheric general circulation is driven ultimately by the pole-to-equator temperature gradient produced by differential solar radiation input. The circulation acts to reduce this gradient to below thermal-radiative equilibrium values by transporting the equatorial warm and moist air to high lati-

tudes where the air is cooled by diabatic processes before being transported back to lower latitudes. It is well known that this net poleward transport of water and energy in the atmosphere is accomplished by the Hadley circulation in the tropics and by transient and stationary eddies associated with cyclones and meandering planetary waves in the mid- and high latitudes. As a vast continental region that spans from mid- to high-latitudes, the MRB thus acts as one of the major heat and moisture sink regions in the global circulation system, and the atmospheric transport of water and energy into and through the Basin is determined by both extra-tropical cyclone activities and planetary wave motions.

As the MRB is located just downwind of the Pacific storm track, cyclonic systems over the North Pacific naturally have the greatest influence on the transport of water and energy into the Basin. MAGS research has elucidated the dynamics and structure of these systems as well as the mechanisms by which the storms transport water and energy into the MRB. For example, Danielson et al. (2006a, b) documented the energetics of these North Pacific synoptic systems and Carrera et al. (1999) examined secondary cyclogenesis from these systems. The prominent role these systems play in the transport of water vapor into the Basin was discussed in Lackmann and Gyakum (1996), Lackmann et al. (1998) and Smirnov and Moore (2001). Results in Carrera et al. (1999) showed that the climatological southwesterly moisture transport into the northwest coastal region of North America is accomplished by cyclones initiated over the west Pacific, and secondary cyclones spawned from the primary cyclones are responsible for transporting water into the Basin. The importance of surface evaporation in the development of both the primary and secondary oceanic cyclones was also identified.

Collectively, these synoptic systems aggregate into large-scale circulation features, such as the North Pacific stormtrack and the Aleutian low pressure system (AL) (Fig.1), on the seasonal and longer timescales. Most studies of linkages between the low-frequency variability of these large-scale features and the climate of MRB have focused on the cool and cold seasons when the atmosphere is dynamically active and teleconnection signals are strong. Most North Pacific variability modes, and in particular the Pacific-North American pattern (PNA) (Wallace and Gutzler 1981), are found to have strong and statistically significant correlations with the interannual climate variability in the MRB (Derksen et al. 2007; Ioannidou and Yau 2007; Szeto 2007a). Szeto (2007a), for example, shows that warm and dry conditions in the MRB occur typically during the positive phase of PNA with the associated strengthening of the AL and increased storm frequency over the North Pacific; while anomalously cold conditions in the

Basin are commonly found during the negative phase when the AL weakens and the blocking highs are more frequent over the Gulf of Alaska. While the study of such low-frequency variability patterns is outside the scope of MAGS, an important research question for MAGS was to understand the physical mechanisms by which the hydroclimate of the Basin responds to the varying large-scale atmospheric circulations.

3 Topographic Influence and MRB Climate Variability

The MRB is known to exhibit the largest intra- and interannual variability of winter temperatures in the world (Fig. 3) (Szeto 2007b; see also Fig. 19 of Kistler et al. 2001), suggesting that the physical environment of the Basin might amplify its thermal response to large-scale forcings. As winter transport of water and energy into the MRB is accomplished by the synoptic storms and the mean southwesterly flow over the North Pacific, strong horizontal flow convergence occurs when the onshore flow encounters abrupt changes in surface roughness and elevation at the coastal zone (Fig. 1) which results in enhanced updraft and precipitation at the mountainous coastal region. The release of latent heat over the western slopes and the subsequent sinking and adiabatic warming over the lee side of the mountains, effectively enhance the transport of dry static energy (DSE) into the Basin. In fact, the DSE convergence into the MRB during the cold season is the strongest among all the high-latitude CSE basins (see Table 1 and Fig. 11 of Roads et al. 2002). Through examining the large-scale circulations that characterize the anomalously warm and cold winters for the Basin, Szeto (2007a) found that the anomalous warming and cooling are largely accounted for by the enhanced (reduced) precipitation at the coastal regions as the circulation regime changes over the North Pacific (Fig. 4).

Cao et al. (2007) and Szeto (2007a) examined the feedback processes that occur over the Basin during periods of extreme warming and cooling. Cao et al. (2007) showed that warming events are linked to warm air advection as well as to adiabatic heating induced by both the topography and the controlling low and/or high pressure system, particularly when low-level temperature inversion occurs. They also noted that cold periods are associated with the occurrence of high pressure systems that advect polar air into the region. Sections 4 will elaborate on interactions of the anticyclonic airflows with the regional topography in accelerating airmass cooling during such events, as well as the effects of cloud fields in accentuating these large-scale induced warming and cooling patterns.

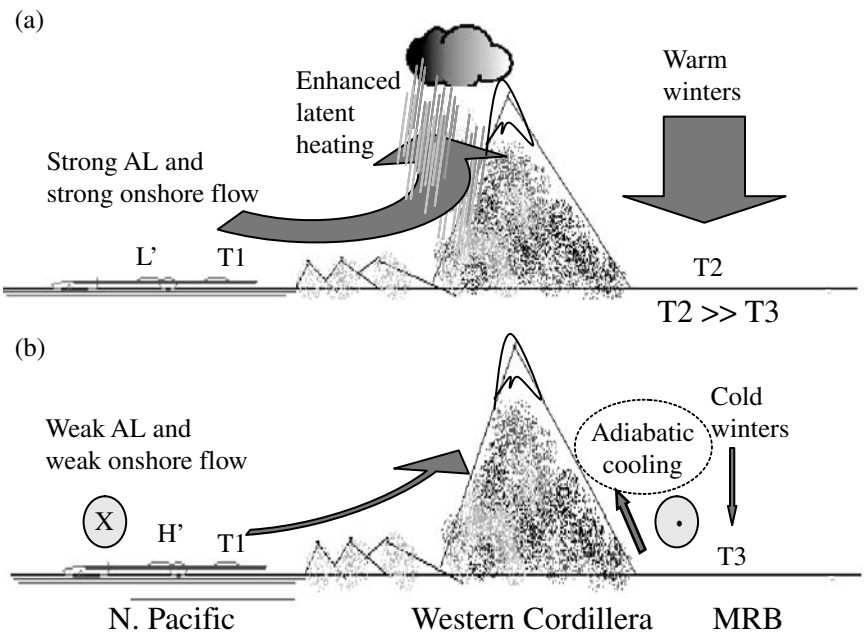

Fig. 4. Schematics illustrating how basin topography enhances the sensitivity of the MRB winter temperature (T) response to variations in the large-scale circulation over the North Pacific. (a) When Aleutian Low (AL) is stronger than normal, mean southwesterly onshore flow is strengthened, resulting in increased precipitation and latent heat release on the windward slopes, enhanced subsidence and compressional warming over the MRB. (b) When large-scale circulation over North Pacific is characterized by a weakened AL, low-level onshore flow is weak, resulting in substantially reduced precipitation over the coastal mountains and weakened subsidence on the lee side. The cold northerly anticyclonic flow could be further chilled through adiabatic ascent over the east slopes.

These results show that the western Cordillera and processes that occur within MRB magnify the thermal response to changes in the upstream large-scale circulation, and such findings provide the theoretical basis to explain the extreme interannual variability and the enhanced warming observed in the winter temperature of the Basin.

4 Regional Processes and Interactions

The MRB climate system is the combined result of complex interactions between the large-scale airflow with the Basin's physical environment. Apart from the orographic effects on the onshore flow, the impingement of the circumpolar air stream on the western Cordillera excites a planetary wave with a wave crest situated over the west coast and creates a climatological high pressure ridge that dominates the climate and weather of the region, especially during the cold season when the mean westerly is strong. With its lee-side location, the Basin is under the influence of a mean subsidence throughout most of the year. These large-scale processes, together with the cold region setting, provide the backdrop for myriad synoptic features of the MRB.

4.1 Anticyclogenesis and Development of Cold Airmass

Similar to other major heat sink regions in the global climate system (e.g., Siberia), the MRB is long known to be an important source region of cold airmass and anticyclones (Harman 1987; Zishka and Smith 1980) though no detailed study has been conducted previously to elucidate the characteristics and nature of these features. Ioannidou and Yau (2007) compiled a climatology of winter anticyclones for the Northern Hemisphere over the 1957–2002 period by using the ERA-40 reanalysis (Simmons and Gibson 2000) and confirmed that the MRB is one of the preferred regions of anticyclonic development in northern latitudes, and noted that the MRB anticyclones exhibit significant interannual variability in their intensity and distribution. Quite unexpectedly for a cold region, they found that many of the MRB anticyclones start as deep warm-core structures and that warm air advection from the Gulf of Alaska eastwards amplifies the upper level ridge and builds the anticyclone at the surface over the MRB. The surface highs typically follow a southward or southeastward trajectory toward the Canadian prairies.

The distinct local maximum of anticyclonic activities over the MRB suggests the presence of additional regional factors that act to localize anticyclonic development in the Basin. Some of the MRB warm core anticyclones transform into cold core low level structures. (Szeto 2007) suggests that when a high pressure ridge builds in from Alaska, the cold anticyclonic flow into the basin could be further chilled by adiabatic ascent over the eastern slopes of the foothills (i.e., cold air damming). The resultant dense cold air over the MRB effectively reduces or eliminates the

sloping effects of the mountains and thereby restraining the sinking and warming of the airflow that passes over the Cordillera (Fig. 4). Curry (1983) hypothesized that the loss of IR radiation at the top of thin low-level clouds in cold-core anticyclones could induce cooling at the lower troposphere. The eventual gravitation sedimentation of the condensates (e.g., ice crystals) would dry out the air and enhance radiational loss at the surface to accelerate the airmass cooling. Interaction of the anticyclonic flow with the Western Cordillera provides a lifting mechanism to initiate and accelerate the processes theorized by Curry to occur over the Basin. The reduced cloudiness during cold episodes over the MRB was observed by Stewart and Burford (2002) and enhanced radiational loss during these events was shown in Szeto (2007a). It is found in some studies (e.g., Tanaka and Milkovich 1990) that classical idealized theories of anticyclone and cold airmass (e.g., Wexler 1936; Curry 1983) could not satisfactorily account for the observed development of these events. The regional processes might complement the theories of Wexler and Curry to better account for the frequent development of these features in the region.

4.2 Lee-cyclones

Although the Basin is under the influence of a mean high pressure ridge all year round, being located on the lee side of the Cordillera, it is also one of the two major source areas of continental cyclones in North America, especially during the autumn when moisture is still abundant, the polar front is located near the region, and the climatological high pressure ridge is not as strong as it is in the winter. The general development of MRB lee cyclones and their importance in affecting the weather of the Basin and its downstream areas have long been known (Chung et al. 1976). When a cyclone from the Gulf of Alaska approaches the west coast of Canada, the onshore flow strengthens and augments precipitation on the west slopes. A quasi-stationary surface trough is formed as a result of tropospheric warming when the flow descends on the lee-side. If coupled to a mid-to-upper level feature such as a shortwave trough, a jet-streak, or the decaying parent cyclonic system, this lee-trough may become mobile and develop into a lee-cyclone. Detailed mechanisms that govern the development of these systems are, however, still not fully understood.

Lackmann and Gyakum (1996) examined mechanisms that affect the lee-side regeneration of Gulf of Alaska cyclones. They found that a thermally-indirect “topographic tilting” mechanism, involving downslope warming over the southern MRB and upslope cooling to the north, could

increase the warm-frontal baroclinicity and thus lee-cyclogenesis over the Basin. The lee-trough is a direct consequence of the adiabatic warming of the downslope flow which in turn is affected by the orographic precipitation from the flow that crosses the Cordillera. Hence, accurate prediction of lee-cyclogenesis over the Basin could depend critically on the accurate simulation of orographic precipitation over the western slopes (Mati 2006).

Since the Gulf of Alaska cyclones are instrumental in the transport of energy into the Basin, the lee-regeneration of these systems often occurs during warm episodes. Cao et al. (2007) and Szeto (2007a) found that the lower-level warm air advection by the perturbation cyclonic airflow in these systems could further contribute to the warming. Szeto (2007a) also suggested that the warm air advection could destabilize the lower troposphere (e.g., weaken or destroy the low-level inversion) to facilitate lee-cyclogenesis and intensify lee-side subsidence over the Basin.

Lee-cyclones have considerable effects on the water and energy budgets of MRB through storm cloud and precipitation developments and moisture transports (Brimelow and Reuter 2007; Lackmann et al. 1998; Misra et al. 2000). Misra et al. (2000) investigated numerically the detailed water budget during the genesis and passage of three autumn lee-cyclones over the Basin. They found that the Basin might be moistened or dried during these cyclonic events depending on the lateral moisture flux convergence. However, in all cases, surface evaporation was found to play a vital role in frontal convection within the system.

4.3 Clouds

The importance of clouds in modulating the earth's radiation and water budgets is well known but poorly understood, especially for remote northern regions. Stewart and Burford (2002) found that clouds are ubiquitous in the MRB and their characteristics are highly variable. Although the Basin is located in the rain shadow of the Rockies and is under the influence of the climatological high pressure ridge all year round, it has an annual cloud cover of over 60% (Stewart and Burford 2002; Szeto et al. 2007a). Summer and autumn are typically more cloudy, with maximum cloud coverage occurring between September and November when many cyclones visit the west coast of Canada, lee-cyclogenesis is frequent, and the Basin is still relatively moist. Maximum cloud cover is found over the western mountains throughout the year (Szeto and Crawford 2006). The relatively cloud-free conditions over the Interior Plains may be a consequence of the mean subsiding motion over the region.

Clouds in the MRB affect the basin water budget mainly through their roles in the development of precipitation. Cloud radar measurements during MAGS revealed the detailed characteristics of these high-latitude cloud features (Hudak et al. 2007). The cloud systems are often multi-layered (with up to 5 layers). Much of the precipitation occurs within narrow banded features that sometimes move upslope, and much of the precipitation is in the form of individual ice crystals with little riming. Because of their common layered structure, it is not surprising that clouds in the Basin are generally inefficient in the production of precipitation (Stewart and Burford 2002). Particularly, the precipitation efficiency (PE which is the ratio of precipitation to net moisture influx) of systems that occur over the ice-covered Beaufort Sea and which affect the northern Basin, where surface evaporation is presumably insignificant during the cold season, was found to be extremely low; and most precipitation in those systems was sublimated in the sub-cloud region (Burford and Stewart 1998; Hanesiak et al. 1997). On the other hand, PE of the autumn systems studied in Misra et al. (2000), which occur over the southern Basin and are strongly affected by surface evaporation, was found to be in the 70–80% range. These contrary results offer support to the hypothesis put forward by Szeto et al. (1997) that the PE of high-latitude frontal cloud systems might exhibit a bi-modal characteristic (either very low or very high), depending on the humidity of the storm environment.

4.4 Radiation

Radiative transfers play a critical role in affecting the water and energy balance of the MRB because of the strong coupling between radiative transfers and other hydrometeorological processes (Table 1a). Owing to the northern location of the Basin, there is strong seasonal contrasts in its incoming solar radiation which in turn leads to different modes of cloud-radiation interactions. During summer when strong and extended duration of insolation is experienced, shortwave (SW) transfers dominate the cloud-radiative interactions and net surface radiative forcing (QRS). This is evident from the strong (relatively weak) correlations between QRS and SW (longwave, LW) radiation at the surface during the summer (Table 1b). Hence, the cloud-albedo effect dominates the combined cloud-water vapor greenhouse effects, and clouds in general exert a negative surface radiative forcing during the warm season (i.e., there is negative correlation between cloudiness and QRS). The resultant strong positive QRS warms, and enhances sensible and latent heat fluxes at the surface (i.e., there are positive

correlations between QRS and T, SH and E), creating an environment that is conducive to moist convection over the Basin. Although the ample amount of tropospheric water vapor in the Basin enhances atmospheric IR cooling (i.e., the net atmospheric radiative forcing QR, and Q are negatively correlated) during the warm season, the convective clouds typically have relatively high cloud tops (i.e., low temperature at cloud-top), and they generally exert a net radiative warming effect for the atmosphere (i.e., net atmospheric radiative forcing, QR and cloudiness are positively correlated, as shown in Table 1b). The importance of cloud radiative forcing is noted by Guo et al. (2007a) who found that cloud effects can account for 30–50% of the surface and TOA radiative budgets in the summer.

Table 1. Contemporaneous correlation coefficients between monthly basin-average net radiative forcing at the surface (*QRS*) and top-of-the-atmosphere (*QR*) and various water and energy budget parameters derived from the ERA-40 reanalysis for July and December, 1979-2001: (a) *T* (surface temperature); *P* (precipitation); *SH* (surface sensible heat flux); *MC* (tropospheric moisture flux convergence); *E* (evapotranspiration), and *Q* (precipitable water); (b) surface-observed cloud amount and various shortwave (*SW*) and longwave (*LW*) radiative flux components at the surface (BOA) and top-of-the-atmosphere (TOA). Correlations that are significant at the 95% are given in italics

(a)	*T*	*P*	*SH*	*MC*	*E*	*Q*
Jul. *QRS*	0.57	*-0.75*	0.52	*-0.63*	0.48	-0.01
Dec.*QRS*	0.25	0.39	0.41	0.52	-0.18	0.50
Jul. *QR*	*-0.72*	0.04	0.21	0.03	-0.56	-0.57
Dec. *QR*	*-0.87*	0.02	0.27	-0.05	-0.34	*-0.83*

(b)	*SWU* TOA	*SWU* BOA	*SWD* BOA	*LWU* TOA	*LWU* BOA	*LWD* BOA	*Cloud amount*
Jul. *QRS*	*-0.98*	*0.98*	*0.99*	*0.89*	*0.62*	*-0.12*	*-0.60*
Dec.*QRS*	0.16	*-0.68*	*-0.78*	0.17	0.23	0.47	*0.66*
Jul. *QR*	0.43	-0.34	-0.32	*-0.72*	-0.57	-0.49	0.56
Dec. *QR*	-0.25	*0.67*	*0.70*	*-0.88*	*-0.86*	*-0.94*	*-0.86*

Cloud-radiation interactions are vastly different in the winter when large parts of the MRB experiences little or no solar radiation and LW processes dominate the radiative balance (Tables 1a and 1b). Although the atmospheric greenhouse forcing (the difference in outgoing LW fluxes at BOA and TOA) is much weaker, it plays a major role in affecting the net surface radiative forcing (i.e., the correlations between QRS and Q and downward LW radiation at the surface become much stronger in the winter). The net radiation deficit at the surface cools the surface and produces deep and en-

during surface-based temperature inversion layers that characterize much of the Basin during the winter. Under the influence of the broad climatological high pressure ridge and mean subsidence, winter clouds are typically shallow, have low cloud tops and have cloud bases that are above but close to the top of the inversion layer (Hudak et al. 2007). As such, cloud base temperatures are often higher than surface temperatures, thus exerting a positive surface radiative forcing (Table 1b). On the other hand, the shallow clouds with their low tops would work in tandem with the atmospheric water vapor to enhance atmospheric IR cooling (i.e., QR correlates strongly and negatively with Q and cloudiness).

The elucidation of these different feedback processes is important to the improved understanding of climate variability and change in the Basin, as well as to the attribution of biases in the modeled radiative budgets (Guo et al. 2007b; Szeto et al. 2007a). For example, increasing trends have been found for cloud coverage in the Basin during summer and autumn but no significant trend can be identified for winter and spring (Milewska 2004). As clouds tend to exert a negative surface radiative forcing on the Basin during the summer, an increased cloudiness produces a cooling effect that offsets any warming that might have otherwise occurred. On the other hand, Stewart and Burford (2002) found that clouds are more (less) widespread with lower (higher) bases during warm (cool) winter periods. Since clouds exert a positive surface radiative forcing during the winter, such linkages between clouds and temperature would act in concert with the large-scale processes to amplify winter temperature perturbations in the Basin, as discussed in Section 3.

4.5 Precipitation

Precipitation in the MRB exhibits strong seasonal variability and is typically light during winter (Szeto et al. 2007a) due to the low temperatures and to the topographic blockage of moisture influx from the Pacific. Much of the precipitation comes from a relatively small number of events. Stewart et al. (2004), for example, found that 10–15 events typically account for 50% of the annual precipitation at several locations.

The Western Cordillera strongly affects the distribution of precipitation in the MRB. Precipitation decreases in general from the mountainous region towards the eastern Basin during all seasons (Szeto and Crawford 2006). In the cold season, the highest precipitation accumulation is found over the southwestern boundary at the top of the Rocky Mountain chain, suggesting that the precipitation there is a “spillover” from the topographic

precipitation associated with the coastal cyclones (Hobbs et al. 1973) rather than from synoptic systems that develop within the Basin. A secondary precipitation maximum is commonly observed over the northwestern Basin near the mountains (Szeto and Crawford 2006) during the autumn. This second maximum can be explained by the enhanced moisture transport towards the mountainous northwest by the cyclonic storm flows during the autumn when both evaporation from the northern great lakes of the Canadian Shield (Rouse et al. 2007a, b) and lee-cyclone activities reach their peaks. Since these lakes are not represented in most current models, it is not surprising that none of the models or assimilation systems considered in Szeto et al. (2007a) can reproduce this observed autumn precipitation maximum. The study of the northern great lakes was a major research initiative of MAGS (Woo and Rouse 2007); results from these studies will enhance our understanding and modeling of water cycling in the Basin.

Away from the mountainous region, winter precipitation comes largely from the lee cyclones that develop over the southern Basin or central Alberta (Sect. 4.2). These systems (Alberta Clippers) often move quickly from their source region along a NW-SE track (Zishka and Smith 1980). They typically produce relatively small amounts of precipitation over a narrow path because of their characteristic lack of moisture and fast movements, with moderate snow generally occurring in areas up to a few hundred kilometers along their tracks (Thomas and Martin 2007). Over a season, these storms produce a band of thick snow accumulation over the boreal zone as identified by Derksen et al. (2007).

4.6 Cold-region Boundary-layer and Surface Processes

Cold region surface and hydrologic processes as well as their interactions with the atmosphere play an important role in shaping the climate of MRB. For example, although precipitation is typically light during winter, the snow can accumulate on the surface for several months due to extremely low temperatures. In fact, much of the Basin is snow-covered for 6–8 months of the year (see Fig. 1 in Woo and Rouse 2007). The snow storage provides a link between winter and summer hydroclimate and strongly influences the seasonal water and energy cycling in the Basin.

One research activity of MAGS concerns the atmospheric effects on snow sublimation. Blowing snow is common over the tundra, especially when intensifying anticyclones bring strong northerly wind into the region (Déry and Yau 2007; Gordon and Taylor 2007). There, blowing snow sublimation loss can account for up to 30% of the snow mass (Pomeroy and Li

2000). Blowing snow is rare in the boreal forest because the winds are relatively weak due to the enhanced surface roughness (Stewart et al. 1995). However, boreal forest canopies can intercept up to 60% of cumulative snowfall by midwinter and sublimation, notably of the intercepted snow, can remove 30–45% of the annual snowfall (Pomeroy et al. 1999). For the MRB, Déry and Yau (2007) applied the PIEKTUK model with ERA-15 reanalysis data to show that surface and blowing snow sublimation deplete 29 mm of the annual precipitation. For comparison, the mean observed basin-average precipitation (Szeto et al. 2007a) for the snow season from November to March is about 115 mm while mean sublimation estimates for the corresponding period from the ERA-40 reanalysis is about 20 mm. Hence, despite the large interannual variability of surface snow observed in the region (Derksen et al. 2007) and large uncertainties in our estimates of sublimation, one can safely conclude that by the end of winter, there is much snow left on the surface of the Basin.

With abundant snow available in the spring, snowmelt contribution dominates the annual Basin runoff (Woo and Rouse. 2007) and the latent heat consumed by snowmelt is a major process that affects the surface energy budget during the spring and early summer. Marsh et al. (2007) and MacKay et al. (2002) respectively demonstrated the importance of local and mesoscale circulations in affecting snowmelt in the region. The prevalence of frozen ground during this period limits meltwater infiltration (Pomeroy et al. 2007). In addition, the Basin is widely covered with organic soil with high water retention capacity. For these reasons, grounds are often saturated during and soon after the snowmelt period.

Nagarajan et al. (2004) investigated the effects of the many small water bodies on the surface sensible and latent heat fluxes and the transport of heat and water vapor in the atmospheric boundary-layer over northern MRB. Their results show that the presence of myriad lakes reduces the domain-averaged surface sensible heat flux by 7–9% but raises the surface latent heat flux by 18–80%, depending on the synoptic situations. Low-level heat advection and cold lake surfaces affect the air–land/lake temperature contrast, which in turn controls the sensible heat flux. In the absence of lakes the surface wind speed impacts the latent heat flux, but in the presence of lakes the moisture availability and the atmospheric surface layer stability control the latent heat flux.

In summary, although evaporation from the large lakes in eastern Basin does not become significant until the autumn, the abundance of surface water and saturated soils following snowmelt allow for strong and sustained surface evaporation to occur and thus set the stage for active air–land interactions in the warm season.

4.7 Summer Processes

Warm-season atmospheric processes also constitute a significant component of the MRB climate system. Evaporation is stronger in the summer than in the winter, and much of the annual precipitation occurs during summer. While the bulk of annual runoff is discharged in the spring, summer precipitation is also an important contributor to the flow of the Mackenzie River and its tributaries (Woo and Thorne 2003).

During summer, the large-scale atmospheric forcing is generally weak and the North Pacific circulation plays a more subdued role than it does in winter in the transport of water and energy into the Basin (Smirnov and Moore 2001). On the other hand, being the northern extension of the Great Plains, the MRB could receive substantial moisture from the southern Plains and even from the Atlantic Ocean through its southeastern boundary (Brimelow and Reuter 2007; Liu et al. 2007). Although the large-scale atmospheric forcing is weak, synoptic activities such as lee-cyclogenesis are still frequent. The extended period of solar heating and the abundance of surface moisture create conditions favorable to active evapotranspiration and moist convection.

Important research issues for MAGS were to clarify how these large-scale settings influence summer precipitation in the Basin. In particular, it is important to identify the mechanisms by which diurnal forcing, local evapotranspiration and external moisture fluxes interact to produce summer precipitation, and the organization of these interactions by Basin-scale processes and synoptic activities to account for its spatial and temporal variability.

As in many other continental regions, a low-level nocturnal temperature inversion that limits the development of convective activities often forms over the MRB when the surface cools at night. During the day, the extended solar heating induces strong evapotranspiration, especially in south-central Basin where strong mean subsidence (and associated clear sky conditions), high temperatures and dense surface vegetation are found. On the other hand, the strongest upward sensible heat fluxes (SH) occur over the relatively dry eastern slopes of the mountains where they intercept large amounts of solar radiation. The strong SH warms the air over the slope and induces a local circulation (the mountain–plains circulation, MPC) (Smith and Yau 1993) that brings the air, along with the moisture evaporated from the Interior Plains, towards and up the foothills of the Cordillera. Strong moisture convergence develops over the western Basin as the circulation strengthens in the afternoon (Figs. 5a and b). The upslope flow would eventually destroy the capping inversion to trigger con-

vection over the western Basin (Figs. 5c and d). Some of the convective cells will move eastward with the steering level westerly wind and affect the interior Basin.

The MPC organizes summer precipitation in the Basin and accounts for the characteristic out-of-phase spatial distributions of precipitation and evaporation (Figs. 5e and f). The results also suggest that evaporation, and hence moisture recycling and air–land interactions are important for the warm-season precipitation in the MRB. Szeto (2002) and Szeto et al. (2007b) showed that, depending on the datasets used for the diagnostics, 40–50% of the summer precipitation is derived from local evaporation. However, due to the Basin-scale organization of the convective activities, a substantial amount is deposited on the mountainous region where runoff is large, and this reduces the potential for further recycling of moisture.

Summer precipitation in the MRB exhibits strong inter-annual variability (Stewart et al. 2002). Szeto (2002) analyzed the large-scale atmospheric conditions that characterize anomalous wet and dry summers and found that different large-scale flow patterns can strengthen (dampen) moisture transport and the MPC to produce anomalously wet (dry) summers (Fig. 6), thereby enhancing the precipitation response to variations in large-scale conditions and increasing its interannual variability. Brimelow and Reuter (2007) also found that low pressure systems over the Basin can act in concert with the Great Plains low-level jet to increase moisture influx from the southern Plains into the region, and subsequently contribute to the development of extreme precipitation events in Basin.

5 Water and Energy Budget Synthesis

The regional climate system operates through the exchange of water and energy between the region and its environment, and through the internal cycling of these quantities within the region. The ultimate test of our knowledge and understanding of the climate of a region is thus measured by our capability to quantify, and to predict its water and energy cycle. One major objective for all the CSEs is to assess the water and energy budgets for their respective study basins in the so-called Water and Energy Budget Studies (WEBS) (Lawford et al. 2004), and WEBS is a topic for

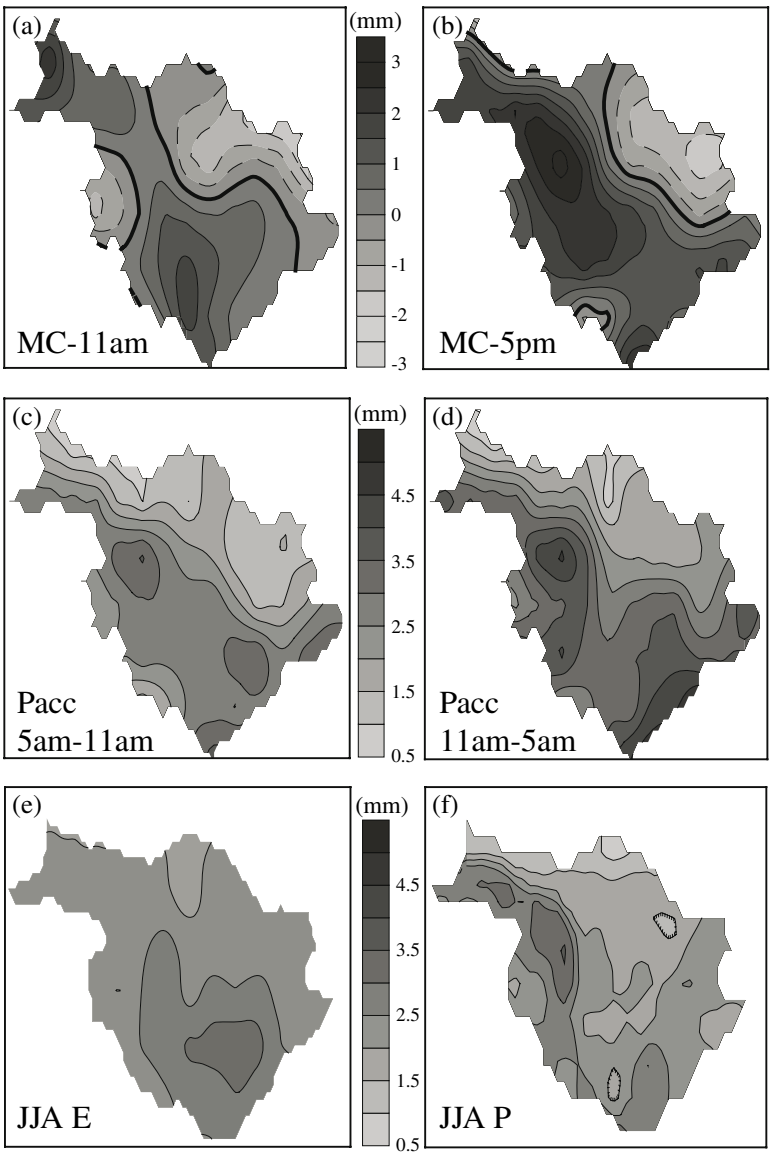

Fig. 5. Diurnal variations of several mean July water cycling variables in the MRB: vertically-integrated moisture flux convergence (MC) at (a) 11AM and (b) 5 PM local time; accumulated precipitation (Pacc) (c) between 5 AM – 11 AM and (d) between 11 AM – 5 PM. Also shown are (e) mean JJA evapotranspiration (E) and (f) precipitation (P). Results in (a)–(e) are calculated from ERA-40 analysis and precipitation in (f) is derived from CANGRID gridded data. Units for all panels are in mm d^{-1}

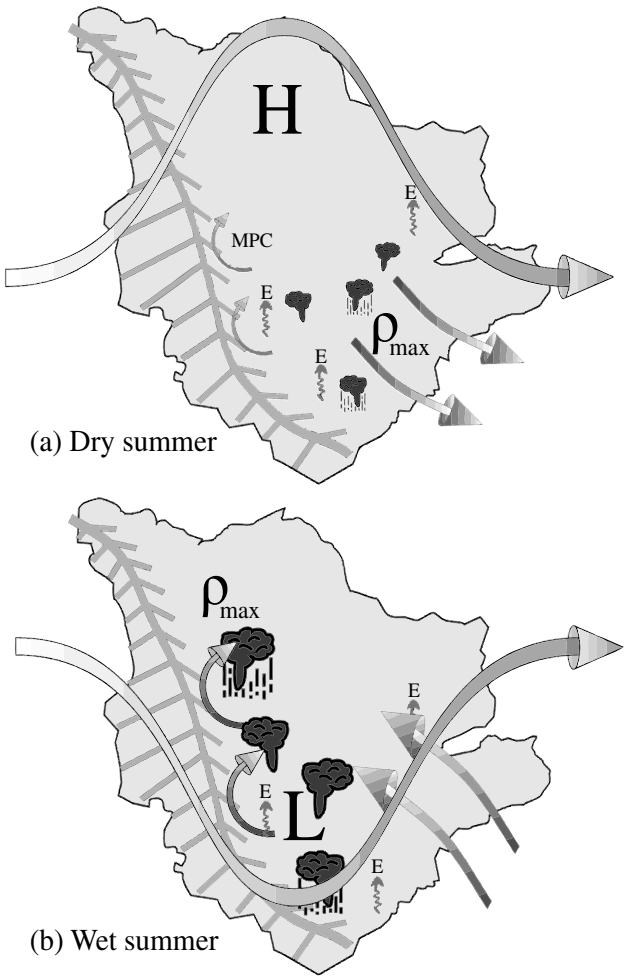

Fig. 6. Schematics illustrating the response of summer precipitation over the MRB to variations in large-scale circulations. (a) When the region is under the influence of a persistent large-scale high pressure system, the anomalous subsiding northwesterly flow would suppress the mountain-plains circulation (MPC), enhance evapotranspiration under the clear-sky conditions and advect moisture out of the Basin, and thus exerts a detrimental effect on both the precipitation and its recycling over the Basin. (b) When the Basin is under the influence of a low-pressure system, the anomalous southeasterly boundary layer flows would enhance the influx of external moisture and advect both the external and locally evaporated moisture towards the western Cordillera, resulting in enhanced precipitation and recycling over the Basin. Also shown are regions where maximum precipitation recycling ratios (ρmax) are found in the corresponding situations.

several MAGS research endeavors (e.g., Liu et al. 2007; Schuster 2007; Strong et al. 2002), with the most comprehensive effort provided by Szeto and Crawford (2006) and Szeto et al. (2007a).

MAGS WEBS utilizes data from global and regional analyses and climate model simulations along with various in situ and remotely-sensed measurements to arrive at quasi-independent evaluations of water and energy budgets for the MRB. Our capability to close the water budget for a region is traditionally gauged by comparing the measured runoff with estimated atmospheric moisture convergence (Strong et al. 2002). Using this approach, the regional water budget for the MRB was closed at 6, 8, and 10 % of the observed runoff using the moisture convergence from ERA-40, NARR (Mesinger et al. 2006), CMC (Côté et al. 1998), and CRCM (MacKay et al. 2007), respectively. While these are noted improvements over some previous water closure assessments for the region (Strong et al. 2002), there are substantial spreads in the budget estimates. Magnitudes of the residuals in balancing the budgets are often comparable to the budget terms themselves in all the model and analysis datasets (Szeto et al. 2007a), suggesting that improvements to the models and observations are still to obtain better assessments of water and energy budgets for this northern region.

However, a good understanding of the energy and water cycling processes provides a powerful theoretical basis to explain and to suggest remedies for some of the biases in the budget estimates. For example, the Canadian Regional Climate Model exhibits a cold season bias (MacKay et al. 2007) and there is a large moisture surplus and energy deficit in the NCEP-R2 reanalysis (Kanamitsu et al. 2002) budgets. Both features can now be attributed to the model under-prediction of orographic precipitation and associated latent heat release on the western slopes of the Cordillera (Szeto 2007a; also see Sect. 3). An over-predicted warm-season water cycle of the MRB in the NCEP-R2 (Szeto et al. 2007a) can be explained by the inability of the model to accurately simulate the Basin-scale water cycling and the associated removal of surface moisture (see Sect. 4.7), giving rise to excessive surface moisture and consequent over-prediction of local recycling in the model. Proper representation of these and other processes in the models will certainly improve the simulation of the cold region climate system, and the comprehensive results from MAGS WEBS will provide a benchmark to gauge the performance of future models in regard to budget assessment.

6 Applications to Climate Issues

Water and energy processes in the MRB have great impacts on larger-scale circulation and on many climate-sensitive issues in the region and beyond. Several MAGS studies have applied the basic research results to address these issues.

6.1 Regional Impacts – Wildfires

Wildfires, a common feature in the MRB, have major impacts on the ecosystem. Most wildfires are started by lightning and fire occurrence is predicted to increase under a warmer climate (Flannigan et al. 2007). In agreement with precipitation climatology compiled for the region (e.g. Szeto et al. 2007a), the convective storm season and resultant lightning activities is characterized as short but intense, with high occurrences in June and July. A variety of datasets have been used to improve understanding of these processes and to develop applications of lightning information (Kochtubajda et al. 2007). In particular, the synoptic situations that are commonly associated with enhanced lightning and fire activities have been identified. A statistical forecast models that has been shown to successfully predict the probability of lightning out to 4 days was also developed. In addition, Guo et al. (2007b) investigated the radiative impact of aerosols from the wildfire on energy budgets in the Basin. They found that the aerosols can significantly modify the shortwave radiative budgets with up to ~100 W m-2 of incoming radiation being absorbed by aerosols in the atmosphere.

6.2 Downstream Influence

The downstream influence of lee-cyclones and cold airmass originated in the MRB is extended to the nearby regions and in turn, MRB is affected by processes occurring over these neighboring areas. An example is the interaction between processes occurring over the MRB and its adjacent Saskatchewan River Basin (SRB) to its south (Liu et al. 2007; Szeto 2007a). The SRB normally gains moisture from the MRB in all months except April, May and June, but the MRB receives moisture from the SRB during these three months. From an inter-annual variation perspective, the MRB gains much more moisture from its environment (Liu et al. 2002, 2007) than does the SRB. Szeto (2007b) noted that the MRB remains as a mois-

ture sink all year long while the SRB becomes a moisture source for the atmosphere during summer. The Prairies is a drought-prone region. A major research program that builds upon the sciences and success of MAGS is studying droughts and related water resource issues in the region.

6.3 Upscale Influences and Feedbacks

The climate processes that occur in the MRB have far-reaching influence on the global atmospheric and ocean circulations. Freshwater discharge of Mackenzie River to the Arctic Ocean has a strong impact on the thermohaline circulation of the distant Atlantic Ocean and associated long-term global climate responses (Milliman and Meade 1983). The developments of synoptic features in the MRB also have profound upscale influences. Carrera and Gyakum (2003), for example, noted the importance of mass build-up during anticyclogenesis over the MRB in initiating large-scale cold surge events and cross-equatorial mass exchange. Wintels and Gyakum (2000) examined the build up and collapse of semi-hemispheric atmospheric available potential energy. They found that the development of cold airmass in the MRB enhances the N–S temperature gradient near the airmass boundary (frontogenesis). Results from these studies elucidate some of the feedback effects of the MRB on the large-scale circulation.

6.4 Climate Change in MRB

Previous studies have documented recent increasing trends of winter temperatures (e.g., Serreze et al. 2000; see also Fig. 2) and decreasing trends of winter precipitation and annual runoff (Burn et al. 2004; Déry and Wood 2005) in Arctic regions, including the MRB. Szeto (2007a) found that recent warming in the MRB largely reflect a “jump” in the climatic state as the Basin responded to the well-documented shift in the Pacific Decadal Oscillation during the mid-1970s (e.g., Mantua et al. 1997). In particular, changes in the mean pressure pattern over the North Pacific after the regime shift resulted in enhanced mean southwesterly onshore flow into the northwest coast of the continent (Fig. 2). The winter warming, and associated reduction in winter precipitation and spring runoff can thus be understood as the amplified response of the Basin to these changes in the North Pacific circulation, as discussed in Sect. 3. One example that illustrates some of these sequences of hydroclimatic events is the 1994/95 water year when the discharge of Mackenzie River and many of its tributaries reached their lowest recorded values (Stewart et al. 2002). According to

the nonlinear perspective of climate change put forward by Palmer (1998) and others, anthropogenic climate change might manifest itself as changes in the occurrence frequency of natural circulation regimes. Hence, though the observed warming can be attributed to changes in natural climate variability modes, we cannot simply conclude that it is not a result of anthropogenic forcing.

Szeto (2007a) argued that the same orographic processes that amplify the thermal response of MRB to variations in upstream flow configurations can also reduce the difference in moisture influx into the Basin. This is achieved through the effective orographic depletion of moisture from the onshore flows, consequently muting the precipitation and the hydrologic responses in the Basin to these large-scale forcings. Although there are many competing factors that complicate the problem, observed evidences that support such inferences are given in Woo et al. (2006). In addition, Woo et al. (2006) cautioned with examples the difficulties and subtleties that researchers should be aware of in the identification and interpretation of long-term streamflow trends.

These studies lead to the larger question of whether the water cycle has been accelerating in the MRB. Stewart et al. (2000) utilized available data products covering the last several decades to examine this issue. Their analysis suggested that there is no clear answer to this question, at least over the time period for which data are available. Water vapor showed a systematic increase with temperature but not so for many other variables such as the recycling ratio.

7 Concluding Remarks

Important advances have been made in our understanding of the MRB climate system though MAGS research. We have improved our quantitative knowledge of its water and energy cycle, and on atmospheric features such as clouds and storms. Mechanisms responsible for the atmospheric transport of water and energy into and through the Basin, as well as the effects of these processes on the weather and climate have been elucidated. In addition, we gain an appreciation of how the atmosphere interacts with the Basin's physical environment, especially the topographic barriers, in shaping the Basin's hydroclimate. Results from these MAGS large-scale process studies are being applied to understand the nature of climate variability and change in the Basin.

Professor Han-Ru Cho, one of the pioneers of MAGS, once told the lead author that a good research is one that is open-ended, in the sense that its results should reveal new issues and foster new research areas and opportunities. In this regard, MAGS has been highly successful since a number of hypotheses, including those presented in this chapter, has been developed through MAGS research to better understand the MRB climate system. The implications and significance of these hypotheses continue to be explored, and these hypotheses need to be further validated, refined or corrected with future research. In addition, MAGS research has identified specific aspects in which current models need to be improved to better simulate the water and energy cycle of the region. The improved understanding of climate processes through MAGS and the eventual incorporation of the knowledge into numerical models will enhance our predictive capability for the Basin, and results from MAGS will collectively form a firm foundation for pursuing future cold-region research in the MRB and other mid- and high-latitude regions.

Acknowledgements

Billy Szeto is acknowledged for his help in the figure preparations. We would also like to thank Environment Canada and the Natural Sciences and Engineering Research Council of Canada (NSERC) for their support. This chapter is based on a paper by Szeto et al. entitled “Northern tales: a synthesis of MAGS atmospheric and hydrometeorological research” that is to appear in the Bulletin of the American Meteorological Society.

References

Burford JE, Stewart RE (1998) The sublimation of falling snow over the Mackenzie River Basin. Atmos Res 49:289–313

Brimelow JC, Reuter GW (2007) Moisture sources for extreme rainfall events over the Mackenzie River Basin. (Vol. I, this book)

Burn DH, Cunderlik JM, Pietroniro A (2004) Hydrological trends and variability in the Liard River Basin. Hydrol Sci J 49:53–67

Cao Z, Stewart RE, Hogg WD (2007) Extreme winter warming over the Mackenzie Basin: observations and causes. (Vol. I, this book)

Carrera ML, Gyakum JR (2003) Significant events of interhemispheric atmospheric mass exchange: composite structure and evolution. J Climate 16:4061–4078

Carrera ML, Gyakum JR, Zhang DL (1999) A numerical case study of secondary marine cyclogenesis sensitivity to initial error and varying physical processes. Mon Weather Rev 127:641–660

Chung KD, Hage KD, Reinelt ER (1976) On lee cyclogenesis and airflow in the Canadian Rocky Mountains and East Asian mountains. Mon Weather Rev 104:897–891

Côté J, Gravel S, Méthot A, Patoine A, Roch M, Staniforth A (1998) The operational CMC-MRB Global Environmental Multiscale (GEM) model. Part I: design considerations and formulation. Mon Weather Rev 126:1373–1395

Curry J (1983) On the formation of continental polar air. J Atmos Sci 40:2278–2292

Danielson RE, Gyakum JR, Straub DN (2006a) A case study of downstream baroclinic development over the North Pacific Ocean. Part I: dynamical sensitivity. Mon Weather Rev 134:1534–1548

Danielson RE, Gyakum JR, Straub DN (2006b) A case study of downstream baroclinic development over the North Pacific Ocean. Part II: diagnosis of eddy energy and wave activity. Mon Weather Rev 134:1549–1567

Derksen C, Brown R, MacKay M (2007) Mackenzie Basin snow cover: variability and trends from conventional data, satellite remote sensing, and Canadian regional climate model simulations. (Vol. I, this book)

Déry SJ, Wood EF (2005) Decreasing river discharge in northern Canada. Geophys Res Lett 31, L10401, doi:10.1029/2005GL022845

Déry SJ, Yau MK (2007) Recent studies on the climatology and modeling of blowing snow in the Mackenzie River Basin. (Vol. I, this book)

Flannigan MD, Kochtubadjda B, Logan KA (2007) Forest fires and climate change in the Northwest Territories. (Vol. I, this book)

Gordon M, Taylor PA (2007) On blowing snow and sublimation in the Mackenzie River Basin. (Vol. I, this book)

Guo S, Leighton HG, Feng J, MacKay M (2007a) Comparison of solar radiation budgets in the Mackenzie River Basin from satellite observations and a regional climate model. (Vol. I, this book)

Guo S, Leighton HG, Feng J, Trishchenko A (2007b) Wildfire aerosol and cloud radiative forcing in the Mackenzie River Basin from satellite observations. (Vol. I, this book)

Hanesiak JM, Stewart RE, Szeto KK, Hudak DR, Leighton HG (1997) The structure, water budget and radiational features of a high latitude warm front. J Atmos Sci 54:1553–1573

Harman JR (1987) Mean monthly North American anticyclone frequencies. Mon Weather Rev 115:2840–2848

Hobbs P, Easter R, Fraser A (1973) A theoretical study of the flow of air and fallout of solid precipitation over mountainous terrain: Part II. Microphysics. J Atmos Sci 30:813–823

Hudak D, Stewart R, Rodriguez P, Kochtubajda B (2007) On the cloud and precipitating systems over the Mackenzie Basin. (Vol. I, this book)

Ioannidou L, Yau MK (2007) Climatological analysis of the Mackenzie River Basin anticyclones: structure, evolution and interannual variability. (Vol. I, this book)

Kanamitsu M, Ebisuzaki W, Woollen J, Yang S-K, Hnilo JJ, Fiorino M, Potter GL (2002) NCEP–DOE AMIP-II Reanalysis (R-2). B Am Meteorol Soc 83:1631–1643

Kistler R, Kalnay E, Collins W, Saha S, White G, Woollen J, Chelliah M, Ebisuzaki W, Kanamitsu M, Kousky V, Van Den Dool H, Jenne R, Fiorino M (2001) The NCEP–NCAR 50-year reanalysis: monthly means CD-ROM doc. B Am Meteorol Soc 82:247–267

Kochtubajda B, Flannigan MD, Gyakum JR, Stewart RE, Burrows WR, Way A, Richardson E, Stirling I (2007) The nature and impacts of thunderstorms in a northern climate. (Vol. I, this book)

Lackmann GM, Gyakum JR (1996) The synoptic and planetary-scale signatures of precipitating systems over the Mackenzie River Basin. Atmos Ocean 34:647–674

Lackmann GM, Gyakum JR, Benoit R (1998) Moisture transport diagnosis of a wintertime precipitation event in the Mackenzie River Basin. Mon Weather Rev 126:668–691

Lawford R, Stewart R, Roads J, Isemer H-J, Manton M, Marengo J, Yasunari T, Benedict S, Koike T, Williams S (2004) Advancing global-and continental-scale hydrometeorology: contributions of GEWEX Hydrometeorology Panel. B Am Meteorol Soc 85:1917–1930

Liu J, Cho H-R, Stewart RE (2002) Characteristics of water vapor transport over the Mackenzie River Basin during the 1994–95 water year. Atmos Ocean 40:101–111

Liu J, Stewart RE, Szeto KK (2007) Water vapor fluxes over the Canadian Prairies and the Mackenzie River Basin. (Vol. I, this book)

MacKay M, Bartlett P, Chan E, Verseghy D Soulis R, Seglenieks F (2007) The MAGS regional climate modeling system: CRCM-MAGS. (Vol. I, this book)

MacKay MD, Szeto K, Verseghy D, Chan E, Bussières N (2002) Mesoscale circulations and surface energy balance during snowmelt in high resolution simulations of a regional climate model. Nord Hydrol 34:91–106

Mantua NJ, Hare SR, Wallace JM, Francis RC (1997) A Pacific decadal climate oscillation with impacts on salmon production. B Am Meteorol Soc 78:1069–1079

Marsh P, Pomeroy J, Pohl S, Quinton W, Onclin C, Russell M, Neumann N, Pietroniro A, Davison B, McCartney S (2007) Snowmelt processes and runoff at the Arctic treeline: ten years of MAGS research. (Vol. II, this book)

Mati I (2006) A comparison study of two regional atmospheric models over the Mackenzie Basin. M.Sc. thesis, Dept. Atmos. Oceanic Sci, McGill University

Mesinger F, DiMego G, Kalnay E, Mitchell K, Shafran PC, Ebisuzaki W, Jovic D, Woollen J, Rogers E, Berbery EH, Ek MB, Fan Y, Grumbine R, Higgins W,

Li H, Lin G, Manikin G, Parrish D, Shi W (2006) North American regional reanalysis. B Am Meteorol Soc 87:343–360

Milewska E (2004) Baseline cloudiness trends in Canada 1953–2002. Atmos Ocean 42(4):267–280

Milliman JD, Meade RH (1983) World-wide delivery of river sediment to the oceans. J Geol 91:1–21

Misra V, Yau MK, Badrinath N (2000) Atmospheric water species budget in mesoscale simulations of lee cyclones over the Mackenzie River Basin. Tellus 52A:140–161

Nagarajan B, Yau MK, Schuepp PH (2004) The effects of small water bodies on the atmospheric heat and water budgets over the Mackenzie River Basin. Hydrol Process 18(5):913–938

Palmer TN (1998) Nonlinear dynamics and climate change: Rossby's legacy. B Am Meteorol Soc 79:1411–1423

Pomeroy JW, Essery R, Gray DM, Shook KR, Toth B, Marsh P (1999) Modelling snow–atmosphere interactions in cold continental environments. In: Tranter et al. (eds) Interactions between the cryosphere, climate and greenhouse gases. IAHS Publ no 256, IAHS Press, Wallingford, UK., pp 91–102

Pomeroy JW, Gray DM, Marsh P (2007) Studies on snow redistribution by wind and forest, snow-covered area depletion and frozen soil infiltration in Northern and Western Canada. (Vol. II, this book)

Pomeroy JW, Li L (2000) Prairie and arctic areal snow cover mass balance using a blowing snow model. J Geophys Res 105(D21):26619–26634

Roads J, Kanamitsu M, Stewart RE (2002) Continental-scale experiment water and energy budgets in the NCEP-DOE reanalysis II. J Hydrometeorol 3:227–248

Rouse WR, Binyamin J, Blanken PD, Bussières N, Duguay CR, Oswald CJ, Schertzer WM, Spence C (2007a) The influence of lakes on the regional energy and water balance of the central Mackenzie River Basin. (Vol. I, this book)

Rouse WR, Blanken PD, Duguay CR, Oswald CJ, Schertzer WM (2007b) Climate–lake interactions. (Vol. II, this book)

Rouse WR, Blyth EM, Crawford RW, Gyakum JR, Janowicz JR, Kochtubajda B, Leighton HG, Marsh P, Martz L, Pietroniro A, Ritchie H, Schertzer WM, Soulis ED, Stewart RE, Strong GS, Woo MK (2003) Energy and water cycles in a high latitude, north-flowing river system: summary of results from the Mackenzie GEWEX Study – Phase 1. B Am Meteorol Soc 84:73–87

Schuster M (2007) Characteristics of the moisture flux convergence over the Mackenzie River Basin for the Water-Years 1990–2000. (Vol. I, this book)

Serreze MC, Walsh JE, Chapin III FS, Osterkamp T, Dyurgerov M, Romanovsky V, Oechel WC, Morison J, Zhang T, Barry RG (2000) Observational evidence of recent change in the northern high-latitude environment. Climatic Change 46:159–207

Simmons AJ, Gibson JK (2000) The ERA-40 project plan. ECMWF ERA-40 project report series no 1

Smirnov V, Moore GWK (2001) Short-term and seasonal variability of the atmospheric water vapor transport through the Mackenzie River Basin. J Hydrometeorol 2:441–452

Smith SB, Yau MK (1993) The causes of severe convective outbreaks in Alberta. Part I: a comparison of a severe outbreak with two nonsevere events. Mon Weather Rev 121:1099–1125

Stewart RE, Bachand D, Dunkley RR, Giles AC, Lawson B, Legal L, Miller ST, Murphy BP, Parker MN, Paruk BJ, Yau MK (1995) Winter storms over Canada. Atmos Ocean 33:223–248

Stewart RE, Burford JE (2002) On the features of clouds occurring over the Mackenzie River Basin. J Geophys Res AAC18:1–13

Stewart RE, Burford JE, Crawford RW (2000) On the water cycle of the Mackenzie River Basin. Contrib Atmos Phys 9:103–110

Stewart RE, Burford JE, Hudak DR, Currie B, Kochtubajda B, Rodriguez P, Liu J (2004) Weather systems occurring over Fort Simpson, Northwest Territories, Canada during three seasons of 1998/99. Part 2: precipitation features. J Geophys Res 109:D22109, doi:10.1029/2004JD004929

Stewart RE, Bussières N, Cao Z, Cho HR, Hudak DR, Kochtubajda B, Leighton H, Louie PYT, MacKay MD, Marsh P, Strong GS, Szeto KK, Burford JE (2002) Hydrometeorological features of the Mackenzie Basin climate system during the 1994/1995 water year: a period of record low discharge. Atmos Ocean 40:257–278

Stewart RE, Leighton HG, Marsh P, Moore GWK, Ritchie H, Rouse WR, Soulis ED, Strong GS, Crawford RW, Kochtubajda B (1998) The Mackenzie GEWEX Study: the water and energy cycles of a major North American river basin. B Am Meteorol Soc 79:2665–2684

Strong GS, Proctor B, Wang M, Soulis ED, Smith CD, Seglenieks F, Snelgrove K (2002) Closing the Mackenzie Basin water balance budget, water-years 1994–95 through 1996–97. Atmos Ocean 40:113–124

Szeto KK (2002) Moisture recycling over the Mackenzie Basin. Atmos Ocean 40:181–197

Szeto KK (2007a) Cold-season temperature variability in the Mackenzie Basin. (Vol. I, this book)

Szeto KK (2007b) Assessing water and energy budgets for the Saskatchewan River Basin. J Meteorol Soc Jpn CEOP special issue (in press)

Szeto KK, Crawford R (2006) The MAGS Water and Energy Budget Study (WEBS) CD-ROM. Available online and through request at the MAGS website at http://www.usask.ca/geography/MAGS/index_e.htm.

Szeto KK, Liu J, Wong A (2007b) Precipitation recycling in the Mackenzie and three other major river basins. (Vol. I, this book)

Szeto KK, Stewart RE, Hanesiak JM (1997) High latitude cold season frontal cloud systems and their precipitation efficiency. Tellus 49:439–454

Szeto KK, Tran H, MacKay M, Crawford R, Stewart RE (2007a) Assessing water and energy budgets for the Mackenzie River Basin. (Vol. I, this book)

Tanaka HL, Milkovich MF (1990) A heat budget analysis of the polar troposphere in and around Alaska during abnormal winter of 1998/89. Mon Weather Rev 118:1628–1639

Thomas BC, Martin JE (2007) A synoptic climatology and composite analysis of the Alberta Clipper. Weather Forecast 22:315-333

Wallace JM, Gutzler DS (1981) Teleconnections in the geopotential height field during the Northern Hemisphere winter. Mon Weather Rev 109:784–812

Wexler H (1936) Cooling in the lower atmosphere and the structure of polar continental air. Mon Weather Rev 64:122–136

Wintels W, Gyakum JR (2000) Synoptic climatology of Northern Hemisphere available potential energy collapses. Tellus 52A:347–364

Woo MK, Rouse WR (2007) MAGS contribution to hydrologic and surface process research. (Vol. II, this book)

Woo MK, Rouse WR, Stewart RE, Stone JMR (2007) The Mackenzie GEWEX Study: a contribution to cold region atmospheric and hydrologic sciences. (Vol. I, this book)

Woo MK, Thorne R (2003) Streamflow in the Mackenzie Basin, Canada. Arctic 56:328–340

Woo MK, Thorne R, Szeto KK (2006) Reinterpretation of streamflow trends based on shifts in large-scale atmospheric circulation. Hydrol Process 20:3995-4003

Zishka KM, Smith PJ (1980) The climatology of cyclones and anticyclcones over North America and surrounding ocean environs for January and July, 1950–77. Mon Weather Rev 108:387–401

Chapter 3

Climatological Analysis of the Mackenzie River Basin Anticyclones: Structure, Evolution and Interannual Variability

Lily Ioannidou and Peter M.K. Yau

Abstract A compilation of a climatology of anticyclones allows identification of the structural and dynamic features that characterize anticyclonic development in the Mackenzie River Basin (MRB) during the winter period. A sophisticated tracking algorithm is applied to the analysis of the ERA-40 dataset that spans the 1957-2002 period. The MRB anticyclones are monitored at consecutive times to obtain statistical estimates of their characteristics and density distributions. The results indicate that the MRB anticyclones are deep, warm-core structures whose development is caused by the amplification of the climatological semi-permanent ridge that dominates over western North America in winter. The warm anomalies that lead to the ridge amplification are, at low levels, generated locally in response to the orographic effect of the Rockies and, at upper levels, advected from other high latitude regions. Sensitivity to the interannual variations of the Pacific-North-American and the Arctic Oscillation was identified. This is mainly manifested in the weaker or stronger meridional/zonal orientation of the anticyclonic activity for opposite phases. The transformation of the MRB anticyclones to cold core structures as they move away from the Basin toward the eastern Provinces of Canada and the remote origin of the upper tropospheric warm anomalies that sustain them point to strong dynamical links with atmospheric developments over other Canadian regions.

1 Introduction

This study was motivated by earlier reports (Harman 1987; Zishka and Smith 1980) that western North America, including the Mackenzie River Basin (MRB) is among the preferred regions of winter anticyclonic activity in the Northern Hemisphere. The region is also noted for events of rapid anticyclogenesis (Alberta et al. 1991). The predominance of anticyclonic conditions affects precipitation and the regional hydrologic cycle, the sublimation and redistribution of accumulated snow by blowing snow events (Déry and Yau 1999, 2007) and the regional radiation budget. The

latter is associated with an increase in outgoing longwave radiation under clear sky conditions induced by anticyclones.

The geographical position of the MRB in the lee of the Rockies subjects it to several orography related effects. The westerly flow impinging on the mountain range leads to the formation of a semi-permanent ridge over the broader region of western North America in winter. The orography also affects the thermal characteristics of the air masses as the air warms adiabatically upon its descent down the mountain barrier (Szeto 2007). In addition, there is the influence of the Alaskan region to the west and the western Arctic Ocean to the north both of which are known to be regions of anticyclonic activity (Serreze and Barry 1988). The Alaskan anticyclones have received particular attention in the literature because of their intensity and persistence (Tan and Curry 1993).

There has been limited success by operational models in accurately predicting the occurrence of anticyclones in the MRB. The implication is that the MRB anticyclones may differ from the neighboring anticyclones of Alaska and the Arctic and that the factors underlying their development may not be fully understood. In view of their complex character and their importance to the water and radiative budgets a detailed study of anticyclones over the MRB is warranted. Thus the first objective of this study was to compile a climatology of the activity of the winter time anticyclones over the MRB, focusing on the structural and dynamic features that characterize their generation and evolution. A second objective was to investigate their interannual variability, especially in relation to the Pacific-North American pattern (PNA) and the Arctic Oscillation (AO), two of the most prominent patterns of low frequency variability in the extratropics of the Northern Hemisphere.

2 Data and Method

Two datasets were used in our climatological analysis, the ERA-15 and the ERA-40. The former covers the 1979–94 period, and the latter spans from 1957 to 2002. The ERA-40 is the most up-to-date atmospheric reanalysis dataset because (a) a three dimensional variational technique for data assimilation was employed and (b) measurements from satellites and past field experiments were incorporated. The assimilation of satellite observations began in 1973 with radiance measurements, and progressed in 1979 to include more advanced observations such as altimeter wave heights, cloud track winds, ozone profile data, scatterometer winds, and TOVS measurements. Fifty three atmospheric fields are available but in our

analysis we only made use of the fields of mean sea level pressure (MSLP), geopotential height, temperature, and vorticity.

The algorithm used in our analysis was designed by Hodges (1994, 1995, 1999). It identifies anticyclones as maxima in MSLP, tracks their centers at consecutive timesteps and monitors the evolution of their properties along their paths. The track data were processed to obtain statistical measures of (a) the frequencies of occurrence of anticyclonic events, (b) numbers of generated or decaying anticyclones per unit area per unit time, and (c) anticyclonic intensities and growth rates on a regular latitude-longitude grid.

The fields on which the tracking analysis was initially performed contain all scales and will be referred to as the 'total' fields. They were then decomposed spectrally to identify the contribution of different scales to anticyclonic development in the MRB. Three bands were analyzed: the large scale band (LL) that includes scales 6670 to 2850 km, the intermediate (IS) band with scales between 2900 and 1700 km, and the small scale band (SS) representing scales of 1700 to 900 km. The physical processes operating in each band are different. Large scale processes are associated with planetary waves generated by intense thermal forcing in the equatorial Pacific and radiating into the extratropics along a waveguide passing over western North America (Horel and Wallace 1981). Processes at the intermediate scales are associated with traveling baroclinic waves. For the small scales, they are related to regional processes like intense surface cooling that can locally generate anticyclonic vorticity at low levels. In the MRB and other high latitude regions, surface cooling is often attributed to blowing snow sublimation or longwave radiative emission to space from the snow covered surfaces.

3 Structure and Evolution of MRB Anticyclones

Figure 1a shows the distribution of anticyclogenesis events at sea level per 3 month winter period per 1000×1000 km^2 area. The MRB is one of four regions of North America where anticyclonic activity is identified. The second region is located over Oregon and northern Nevada in the lee of the Rockies. The third region extends from the Great lakes eastward towards Labrador. The fourth region stretches from Texas into the subtropical North Atlantic. On average, 10–15 anticyclones with a characteristic lifetime of 4.0 days (not shown) are generated over the MRB every winter.

The main region for the lysis of the MRB anticyclones (Fig. 1b) lies in northern Saskatchewan, about 600–700 km southeast of their genesis region. The lysis density distribution indicates that approximately half of the

MRB anticyclones dissipate in this location while the remaining 50% continue into eastern Canada.

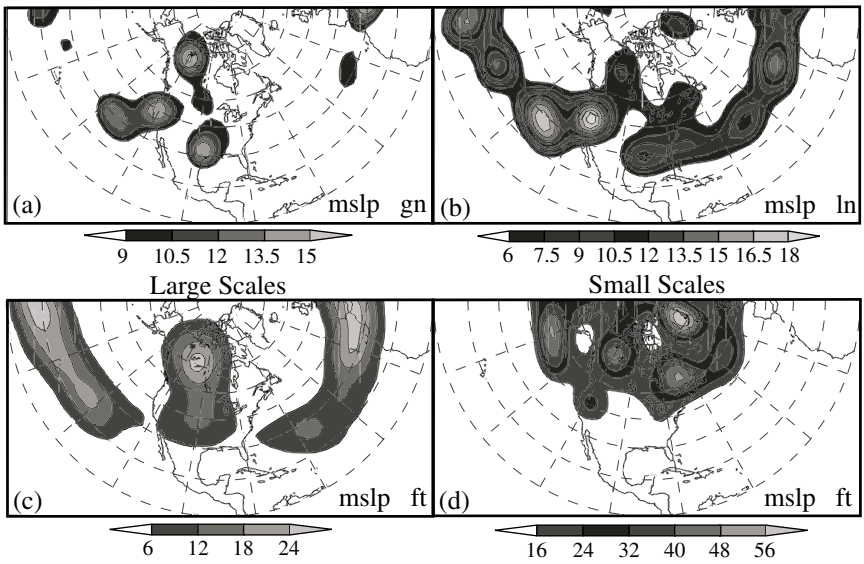

Fig. 1. Distribution of events of (a) genesis and (b) lysis of anticyclones over North America and the surrounding oceans as they appear at mean sea level pressure (MSLP). Units correspond to numbers of events per 1000x1000 km^2 area per winter period. Note the maxima over the MRB. In (c) and (d) frequency distributions are shown at MSLP for the large scale and the small scale bands respectively. Units represent the amount of time that an anticyclone is identified over the MRB, expressed as percentage of the 3 month winter period. Symbols gn, ln and ft stand for genesis, lysis and anticyclonic frequency

Spectral decomposition points to the prominence of the large scales and the small scales contribution to the anticyclonic activity of the MRB. The large scales (Fig. 1c) show an extensive maximum over western North America that represents an amplification of the climatological semi-permanent North American ridge due to distant, planetary scale influences like the increase in sea surface temperatures in the eastern Pacific. The distinct local maximum over the MRB in the small scales (Fig. 1d) suggests the presence of additional regional factors that act to localize anticyclonic development in the Basin.

Theoretical studies have identified a number of mechanisms that can trigger anticyclonic development. These include orographic forcing, heating below a mid-tropospheric geopotential height ridge in association with warm air advection or diabatic effects, and intense low-level cooling. De-

pending on the forcing mechanism, anticyclones can possess a warm or a cold core, and accordingly, a deep or a shallow vertical structure. The thermal signal of the MRB anticyclones was examined in the lower and upper tropospheric levels in relation to the aforementioned forcing mechanisms. At low levels (850 hPa), the frequency distributions of warm and cold temperature anomalies (Figs. 2a, 2b) suggest a transition from a warm zone that dominates the Gulf of Alaska and the western part of North America to a cold zone that dominates eastern North America. The transition is centered in the MRB. The tongue of warm temperatures that penetrates from Alaska into the continent has a southeastward orientation, following closely the direction of motion of the MRB anticyclones from their

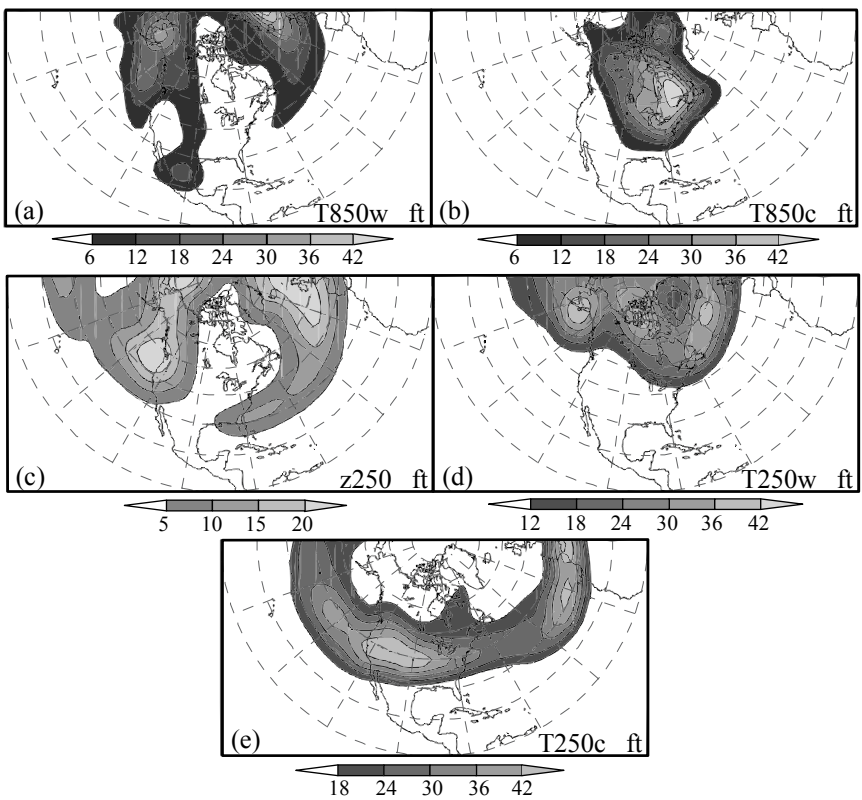

Fig. 2. Frequency (ft) of (a) warm and (b) cold temperature anomalies at 850 hPa (T850w, T850c), of (c) positive geopotential height anomalies at 250 hPa, and of (d) warm and (e) cold temperature anomalies (T250w, T250c) at 250 hPa. Units as in Fig. 1

genesis to their lysis positions. Such a thermal configuration implies that the MRB anticyclones start their life as warm core structures and remain so until they reach the lysis region in Saskatchewan. Those that continue into the eastern provinces transform into cold-core structures.

It was also found that the MRB anticyclones have the characteristic deep structure of warm-core anticyclones. Figures 2c and 2d show the frequency distributions of geopotential height anomalies and positive temperature anomalies at 250 hPa. The height distribution (Fig. 2c) displays two centers of activity: one lying north of Alaska over the Beaufort Sea, the other situated off the U.S coast in the eastern Pacific. Both centers have a semi-stationary character. The MRB lies to the east of the ridge that connects these two centers. As the MRB anticyclones follow their trajectories southeastward they move away from the influence of the ridge and the upper level forcing. This results in their progressive weakening and dissipation over northern Saskatchewan.

An examination of the upper level distribution of the thermal fields sheds further light on the lifecycle of the MRB anticyclones. Comparison of the frequency distributions of warm and cold temperature anomalies at 250 hPa (Figs. 2d and 2e) points to a strong contrast in the thermal characteristics between northern Canada (including the region where the MRB anticyclones originate) and the regions of southern Alberta, Saskatchewan and Manitoba. The rise in the upper level geopotential height that supports the deep structure of the MRB anticyclones is linked to the two centers of warm temperatures that dominate the areas north of the MRB. One center is located over the Arctic coast of Alaska and the other over the Canadian Archipelago (Fig. 2d). The collapse of the deep, warm-core structure leading to the decay of the MRB anticyclones over Saskatchewan is associated with the wavy pattern of cold anomalies that characterize southwestern Canada and its adjacent areas in the United States (Fig. 2e).

4 Interannual Variability of MRB Anticyclones

4.1 Pacific-North American pattern (PNA)

The interannual variability of MRB anticyclones was first examined with respect to the PNA pattern (Wallace and Gutzler 1981) identified as the most significant low frequency oscillation in the Pacific–North American sector. The pattern comprises four centers of action: two centers of similar sign, one located over the North Pacific Ocean and one over the southeastern U.S., and two centers of the opposite sign, located in the subtropical North Pacific and over western Canada. The positive phase of the PNA

corresponds to a deeper than normal Aleutian low, a deeper than normal trough over the southeastern U.S. and an extensive ridge over western Canada; whereas during the negative PNA phase the anomalies over these locations are reversed. The geographical location of one of the centers over western Canada suggests a direct impact of the PNA oscillation on the MRB anticyclones.

To investigate the sensitivity of the MRB anticyclonic activity to the phase of the PNA, the tracking algorithm was applied separately to two subsets of years, one consisting of years in which the PNA phase is positive, the other of years in which it is negative. For the positive PNA years, the MRB anticyclones were more frequent, their tracks were shorter and had a stronger eastward component than for the years of negative PNA. Decomposition into different bands of scales showed that for the large scale band or a transition from a positive to a negative PNA phase there is a change in the orientation of the growth-decay axis of the anticyclonic anomalies – the axis shifts from a north-south orientation for positive PNA to an east-west orientation for negative PNA. For the small scale band, the difference between the two phases is manifested in the direction of anticyclonic displacement that has a more zonal (meridional) component for positive (negative) PNA phase.

4.2 Arctic Oscillation (AO)

The AO represents the most prominent mode of low frequency variability for the sector of the Northern hemisphere lying north of 20^{o}N (Thompson and Wallace 1998). There is growing evidence in the last decade (Baldwin and Dunkerton 1999) that the AO is a robust mode identifiable throughout the tropospheric and lower stratospheric levels. It is considered to be a barotropic, zonally symmetric oscillation of mass between the polar cap and the middle latitudes with the positive (negative) phase representing a surplus (deficiency) of mass over the pole. The AO is particularly important for high latitude regions like the MRB due to their proximity to the pole. Sensitivity of the MRB anticyclones to the AO phase is manifested mainly in the retraction (extension) of the anticyclonic activity to the northern (southern) sector of the Basin for positive (negative) AO. The frequency distribution of anticyclonic activity for positive and negative AO at sea level (Figs. 3a, b) clearly shows that during negative AO, the activity extends southwards across Saskatchewan to southern Manitoba.

Changes over the MRB associated with the AO phase are also evident in the upper levels. The 250 hPa geopotential height field depicted in Figs. 3c and 3d indicates that the ‘Alaskan’ center of anticyclonic development is stronger during the negative phase of the AO. The ridge connecting that

center to the geopotential height center off the Pacific coast of the U.S. is also stronger relative to the positive AO phase and its position is displaced east, toward the Gulf of Alaska. As a result, for negative AO, the upper level support for MRB anticyclones is sustained as they move southeastwards away from their genesis region. This explains the longer trajectories of the anticyclones and the extension of the anticyclonic activity to the south of the Basin.

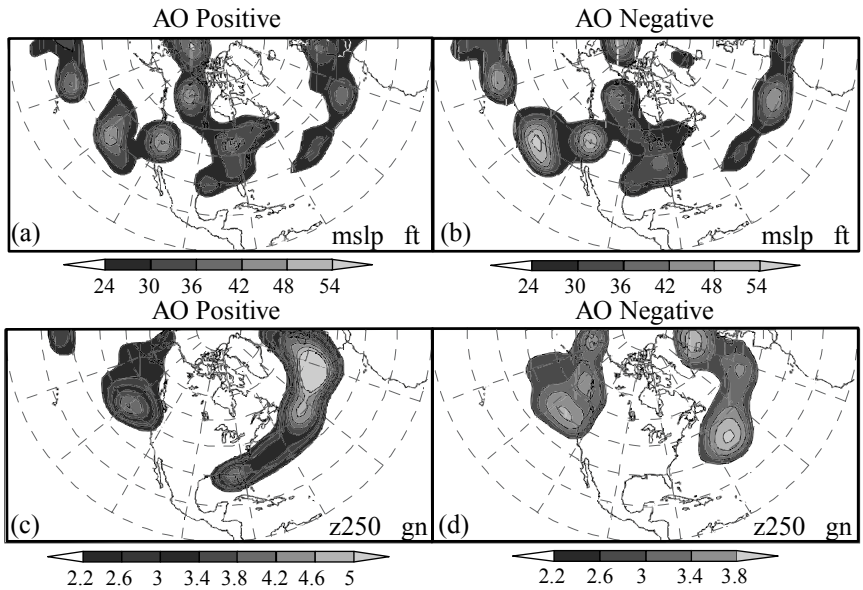

Fig. 3. Frequency (ft) of anticyclonic activity at mean sea level pressure (MSLP) for years of (a) positive and (b) negative AO index. Similarly, distribution of genesis events (gn) of positive geopotential height anomalies at 250 hPa (z250) for (c) positive and (d) negative AO

5 Discussion and Conclusions

A tracking algorithm was applied to generate a three-dimensional picture of the structure and evolution of winter anticyclones in the MRB. The results suggest that MRB anticyclones belong to the warm-core type, the development of which is forced by warming below the climatological semi-permanent ridge that dominates western North America in winter. Warming is identified at all levels over the MRB. In the low levels it is caused by adiabatic compression of the air mass as it descends the lee of the

Rockies. In the upper levels, the warming results from the advection of warm anomalies from distant locations like the Canadian Archipelago and the Gulf of Alaska. The warming is concentrated in the western and northern sectors of the MRB while the eastern and southern sectors are dominated by cold anomalies.

The MRB anticyclones share certain features with their Alaskan neighbors. Their deep warm-core structure is also a feature of the 'Alaskan' anticyclones. However, the 'Alaskan' anticyclones typically belong to the blocking type characterized by long persistence and stationarity while the MRB anticyclones have a relatively short life span of 4.0 days and southeastward mobility. The band of warm anomalies at 850 hPa lies in the lee and in parallel to the Rocky mountain chain. This suggests that orography is essential in generating the warm band and in creating conditions favorable to anticyclonic development in the MRB. In this respect the MRB anticyclones are similar to the anticyclones that develop further south in the lee of the U.S Rockies whose forcing is purely of orographic nature.

The anticyclonic structure is sensitive to interannual variations related to the PNA and the AO modes. For both oscillations, the strongest effect lies in the orientation of the anticyclonic activity which exhibits a stronger or a weaker meridional component depending on the oscillations' phase, leading to longer or shorter trajectories for the MRB anticyclones. During the positive PNA phase, a more wavelike 500 hPa geopotential height field enhances the meridional flow over North America and drives the MRB anticyclones towards a more southward direction than during negative PNA. For positive AO, there is an increase in the distance between the 'Alaskan' upper-level center of activity and the center located further south off the Pacific coast of the U.S., resulting in the withdrawal of anticyclonic activity into the northern MRB. During negative AO the MRB anticyclonic activity extends further south.

Our analysis reveals the regional features of the MRB anticyclones: their generation and characteristics are linked to the geography of the MRB and its position relative to the Alaskan peninsula and the Cordilleran mountain chain. They also have dynamic linkages and implications for other Canadian regions as half of the anticyclones that originate in the MRB continue over eastern Canada after their transformation into cold structures over the Prairies. In addition, a large portion of the upper level warm anomalies identified over the northern MRB originate at different points along the Canadian Arctic Circle between northern Labrador and the Beaufort Sea. The connection between the atmospheric developments in these regions of Canada merits further investigation.

Within the MRB, there is considerable intra-basin variability of the anticyclonic activity associated with the relatively sharp transition from warm to cold temperatures from west to east and the spatially varying effect of the two modes of low frequency variability. A corresponding signal should be identifiable in the distribution of winter precipitation in the Basin. An investigation relating the distribution of precipitation to the spatial variations of the MRB anticyclonic activity could improve the accuracy of the precipitation input to hydrologic models.

References

Alberta TL, Colucci SJ, Davenport JC (1991) Rapid 500 mb cyclogenesis and anticyclogenesis. Mon Weather Rev 119:1186–1204

Baldwin MP, Dunkerton TJ (1999) Propagation of the Arctic oscillation from the stratosphere to the troposphere. J Geophys Res 104:30937–30946

Déry SJ, Yau MK (1999) A climatology of adverse winter-type weather events. J Geophys Res 104:16657–16672

Déry SJ, Yau MK (2007) Recent studies on the climatology and modeling of blowing snow in the Mackenzie River Basin. (Vol. I, this book)

Harman JR (1987) Mean monthly North American anticyclone frequencies. Mon Weather Rev 115:2840–2848

Hodges KI (1994) A general method for tracking analysis and its applications to meteorological data. Mon Weather Rev 122:2573–2586

Hodges KI (1995) Feature tracking on the unit sphere. Mon Weather Rev 123:3458–3465

Hodges KI (1999) Adaptive constraints for feature tracking. Mon Weather Rev 127:1362–1373

Horel JD, Wallace JM (1981) Planetary scale atmospheric phenomena associated with the Southern Oscillation. Mon Weather Rev 109:813–829

Tan Y-C, Curry JA (1993) A diagnostic study of the evolution of an intense North American anticyclone during winter 1989. Mon Weather Rev 121:961–975

Serreze MC, Barry RG (1988) Synoptic activity in the Arctic basin. J Climate 1:1276–1295

Szeto KK (2007) Cold-season temperature variability in the Mackenzie Basin. (Vol. I, this book)

Thompson WJ, Wallace JM (1998) The Arctic oscillation signature in the wintertime geopotential height and temperature fields. Geophys Res Lett 25:1297–1300

Wallace JM, Gutzler DD (1981) Teleconnections in the geopotential height field during the Northern Hemisphere winter. Mon Weather Rev 109:784–812

Zishka KM, Smith PJ (1980) The climatology of cyclones and anticyclones over North America and surrounding oceans for January and July, 1950–77. Mon Weather Rev 108:387–401

Chapter 4

Variability of Cold-Season Temperatures in the Mackenzie Basin

Kit K. Szeto

Abstract The Mackenzie River Basin exhibits extremely large interannual variability in its cold-season atmospheric temperatures while some of the strongest warming signals in the Northern Hemisphere have also been observed over the Basin. To understand these observed thermal characteristics and behavior of the region, the atmospheric enthalpy budget for the Basin during 1970–99 was studied using the NCEP reanalysis dataset. Adiabatic warming associated with mean subsidence was found to be more important than net horizontal temperature advection in governing the heat budget during the cold-season. Processes responsible for the development of extreme warm/cold winters were investigated in conjunction with the composite atmospheric heat budget and large-scale atmospheric conditions that prevailed during the anomalous winters. The large temperature variability is linked to the interactions between the North Pacific airflow and the regional environment, notably the Western Cordillera. Understanding the mechanisms responsible for winter temperature variability facilitates the interpretation of temperature trends and offers an explanation of the cold-season temperature bias found in some climate modeling results.

1 Introduction

The Mackenzie River Basin (MRB) has an extremely variable climate (Stewart et al. 2002). In particular, it has the largest intra- and inter-annual variability of winter temperatures in the world (Fig. 19 in Kistler et al. 2001; Fig. 3 in Szeto et al. 2007a), suggesting that its cold-season climate is highly sensitive to variations in the large-scale circulation on both intra-seasonal and interannual time scales. These characteristics make predicting the climate for the region a particularly challenging task. For example, simulating the hydroclimate for the MRB is particularly problematic among the several major arctic basins considered in a study by Finnis (2005). Recent climate simulations for the MRB have also produced a persistent cold bias with attendant negative effects (MacKay et al. 2007, Szeto et al. 2007b). Improving our physical understanding and modeling capabil-

ity of climate variability for this northern region is a pressing issue because most Global Climate Models have predicted an amplified polar response to the increase in atmospheric greenhouse gas content (Houghton et al. 2001). Indeed, some of the strongest warming signals have been observed in high-latitude continental regions, including the MRB (e.g., Zhang et al. 2000).

A first step in improving climate predictions is to examine the underlying mechanisms that cause extreme winter temperature variability in this region. The purpose of the present study is to better understand these mechanisms through an assessment of the mean and anomalous atmospheric enthalpy budgets, and relate the temperature response of the MRB to variations in the large-scale circulation over the North Pacific. Implications of the results for the understanding and prediction of climate change in the region will also be discussed.

2 Methodology and Datasets

Consider the atmospheric energy budgets for the MRB. Neglecting the kinetic energy which accounts for only a small faction of total energy in the atmosphere, energy conservation in a hydrostatic vertical air column is given by the temperature equation:

$$\frac{1}{g}\int \frac{\partial H}{\partial t}\,dp = \frac{1}{g}\int \left(-u\frac{\partial H}{\partial x} - v\frac{\partial H}{\partial y} - \omega\frac{\partial H}{\partial p} + \alpha\omega + \dot{Q} \right) dp \qquad (1)$$

where the atmospheric specific enthalpy H is defined by $H = Cp\ T$, with Cp and T representing the specific heat capacity for dry air and atmospheric temperature, respectively; u, v, ω are x-, y-, and pressure velocities, α is specific volume, and p is atmospheric pressure. The advective form of the temperature equation is used to illustrate the relative importance of the atmospheric transport terms in affecting the H-budgets. The first two terms within the integral on the RHS represent horizontal temperature advection, the third term is vertical advection, the fourth term gives the heating/cooling effects associated with adiabatic compression/expansion in descending/ascending air, and the fifth term represents net diabatic effects such as radiative and latent heating in the atmosphere. The vertical advection and adiabatic heating terms are combined into a single term, called the "vertical" term in the following discussion.

The 3-D wind velocities and air temperatures from the 6-hourly and 2.5° resolution NCEP/NCAR reanalysis dataset (Kalnay et al. 1996; Kistler et

al. 2001) were used to calculate the basin- and vertically-integrated *H*-budget terms in Eq. (1) for a 30-year period (1970–99). The diabatic term is calculated as a residue in balancing the budget. The rectangular domain used to approximate the MRB in the calculation of spatial averages for the variables spans from 52.5°N to 67.5°N and from 235°E to 255°E. Since only the variability of tropospheric and surface temperatures is of interest, the vertical integrals in Eq. (1) are carried out from the surface to 250 hPa.

Physical processes responsible for the occurrence of extreme warm and cold winters during the study period were investigated, focusing on the five warmest and the five coldest winters (based on the domain-averaged surface air temperatures for December, January, and February, DJF). These were also the winters with basin-average temperature anomalies exceeding the interannual standard deviation value of 2.3 K. Anomalous *H*-budgets and atmospheric parameters representative of the extreme warm/cold winters (Table 1) were obtained by compositing these variables over the five corresponding cases. The results were then inter-compared to gain insight into the processes that produce the large interannual variability of winter temperatures.

Table 1. Five coldest and five warmest winters in the Mackenzie River Basin and their corresponding surface air temperature anomalies (*T*, in K) for the 1970–1999 period

Rank	Coldest DJF	*T* (coldest)	Warmest DJF	*T* (warmest)
1	1971/72	-4.7	1986/87	5.6
2	1981/82	-3.4	1980/81	3.1
3	1993/94	-3.2	1979/80	2.8
4	1970/71	-2.7	1976/77	2.7
5	1978/79	-2.4	1991/92	2.3

3 Results

3.1 Mean H-budgets and Governing Processes

The seasonal variations of the 30-year mean component enthalpy budget terms are shown in Fig. 1a. Except for the summer, energy gained through net atmospheric transport of dry static energy or DSE (i.e., the combined net horizontal advection and "vertical" terms are positive in Fig. 1) is balanced by loss through atmospheric diabatic processes that occur within the Basin. Since much of the region receives little solar radiation and relative-

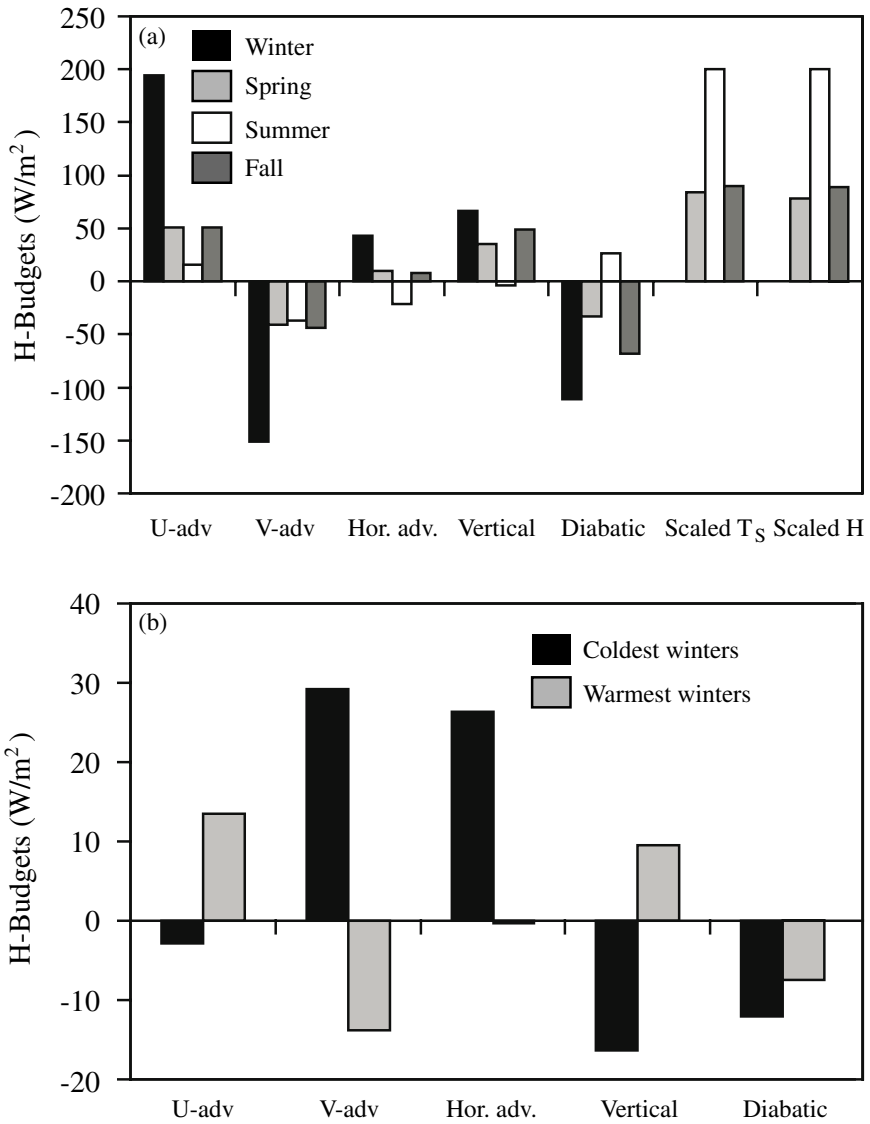

Fig. 1. (a) Seasonal variability of 30-year (1970-1999) mean H-budget, and (b) composite anomalous DJF H-budget components for the 5 warmest and 5 coldest winters, over the MRB

ly low precipitation during the cold season, the diabatic term is largely accounted for by thermal radiation to space through the top of the atmosphere, and to a lesser extent by the downward heat flux into the surface

(Szeto et al. 2007b). In the summer (JJA), the Basin experiences long daylight hours and receives ample precipitation (Szeto et al. 2007b) and the region becomes a heat source for the large-scale flow (Fig. 1a).

Located just downwind of the Pacific Ocean, climate in the MRB is strongly affected by large-scale atmospheric circulation features over the North Pacific, such as the prominent Aleutian Low pressure system (AL, Fig. 2a). While the transport of energy into the continent during the cold season is largely accomplished by such circulation features, the atmospheric thermal response of the Basin to the transport is a collective result of the interactions of the circulation with the environmental features that characterize the region. This is particularly true for the MRB due to its location directly to the lee of the Western Cordillera and its relative proximity to the Pacific Ocean. The combined land/sea contrast and mountain blocking effects induce significant disturbance to the mean westerly flow to produce a stationary long wave with an upper-level ridge over the west coast of North America (Fig. 2a). Consequently, the MRB is under the influence of a mean westerly flow that brings in warm and moist air from the North Pacific, and a mean northerly flow that imports cold air from the High Arctic, as reflected in the mean positive zonal and negative meridional heat transports shown in Fig. 1a. Although magnitudes of the individual transports are considerable, they largely cancel each other over the domain to produce a relatively weak net horizontal transport.

In addition, strong horizontal flow convergence occurs as the onshore flow encounters abrupt changes in surface roughness and elevation (Fig. 2a) to produce enhanced updraft and precipitation (hence latent heat release) on the western slopes of the coastal mountains (Figs. 3a and 4a). As the air flow from the warm ocean surface is loaded with moisture, winter precipitation at the coastal region of western Canada is comparable to that over either the equatorial or the storm track regions (Fig. 4a). The maritime polar air mass thus undergoes strong modification by precipitating out a substantial portion of its moisture content as it ascends to cross the continental divide. Thus, the mountain barriers effectively strengthen the transport of dry static energy (DSE) into the Basin by forcing the release of latent heat over the western slopes, and the air that descends over the MRB is relatively warm and dry. In fact, the *H*-budget in the cold season (Fig. 1a) shows that when integrated over the vertical column, the adiabatic warming effect is far more important than the net horizontal heat transport in affecting the Basin's atmospheric enthalpy budgets.

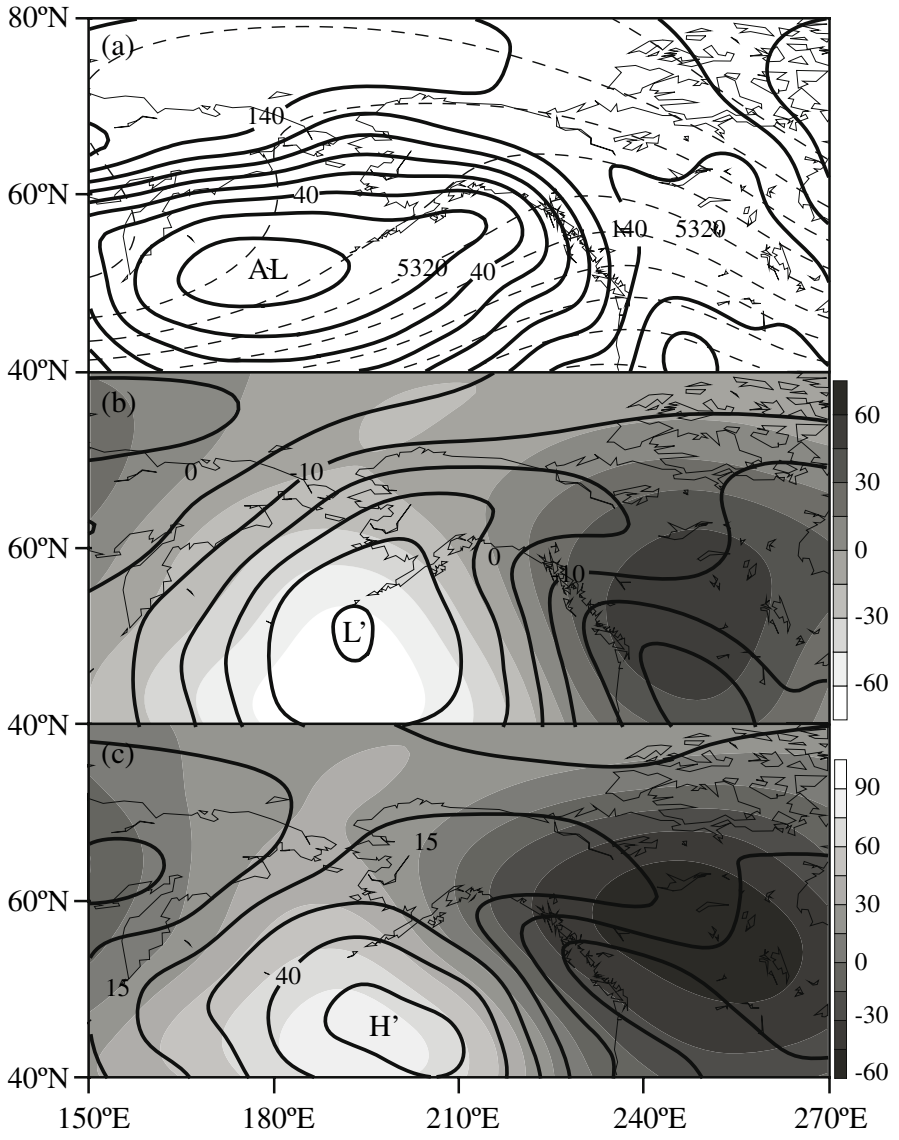

Fig. 2. Mean and anomalous DJF atmospheric conditions: (a) 30-year mean geopotential height (m) at 1000 hPa (solid) and 500 hPa (dashed); composite anomalous geopotential height (m) at 1000 hPa (contours) and 500 hPa (shaded) for the 5 warmest (b) and 5 coldest (c) winters

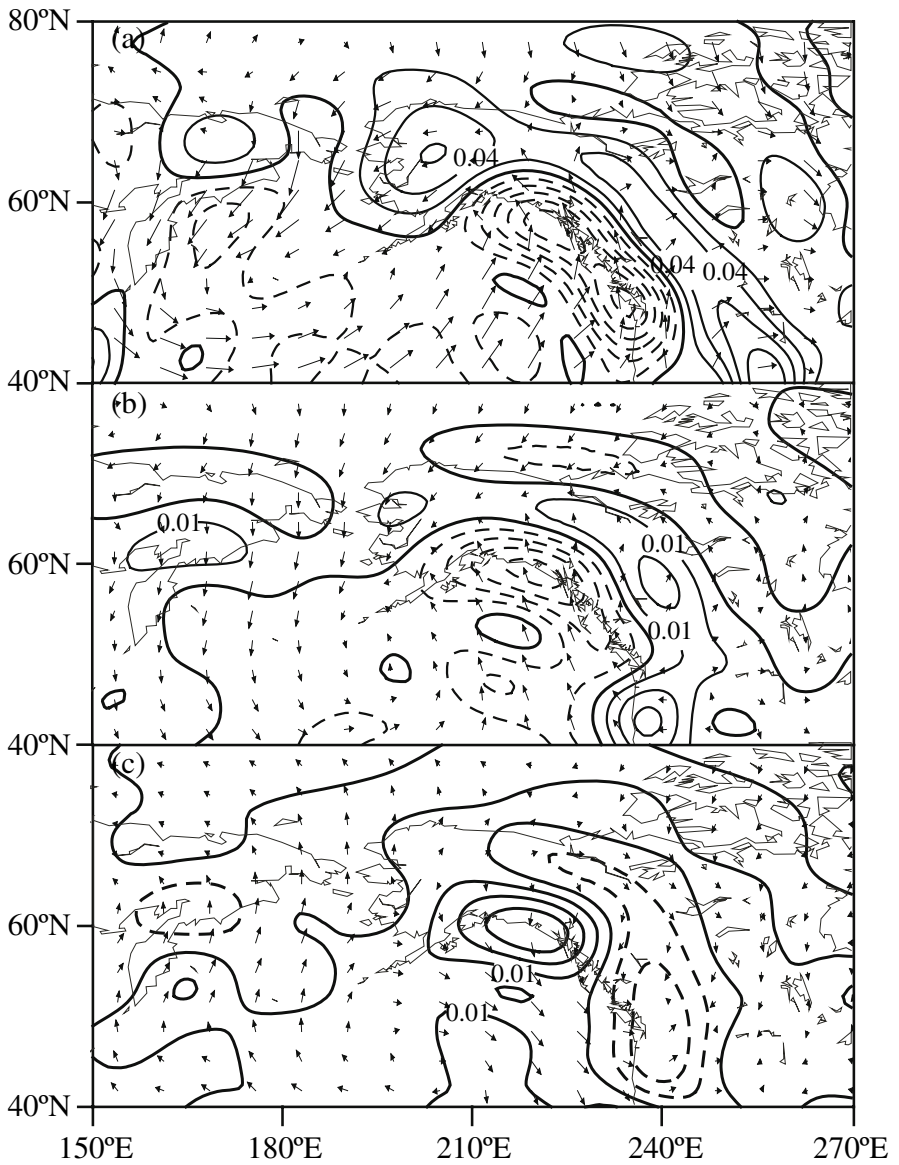

Fig. 3. Mean and anomalous DJF atmospheric conditions: (a) 30-year mean wind vectors at 1000 hPa and ω at 850 hPa (Pa s^{-1}); composite anomalous wind vectors at 1000 hPa and ω at 850 hPa (Pa s^{-1}) for the 5 warmest (b) and 5 coldest (c) winters. Maximum magnitude of wind vectors equals 6.5 m s^{-1}. Contour interval is 0.02 Pa s^{-1} for (a) and 0.01 Pa s^{-1} for (b) and (c)

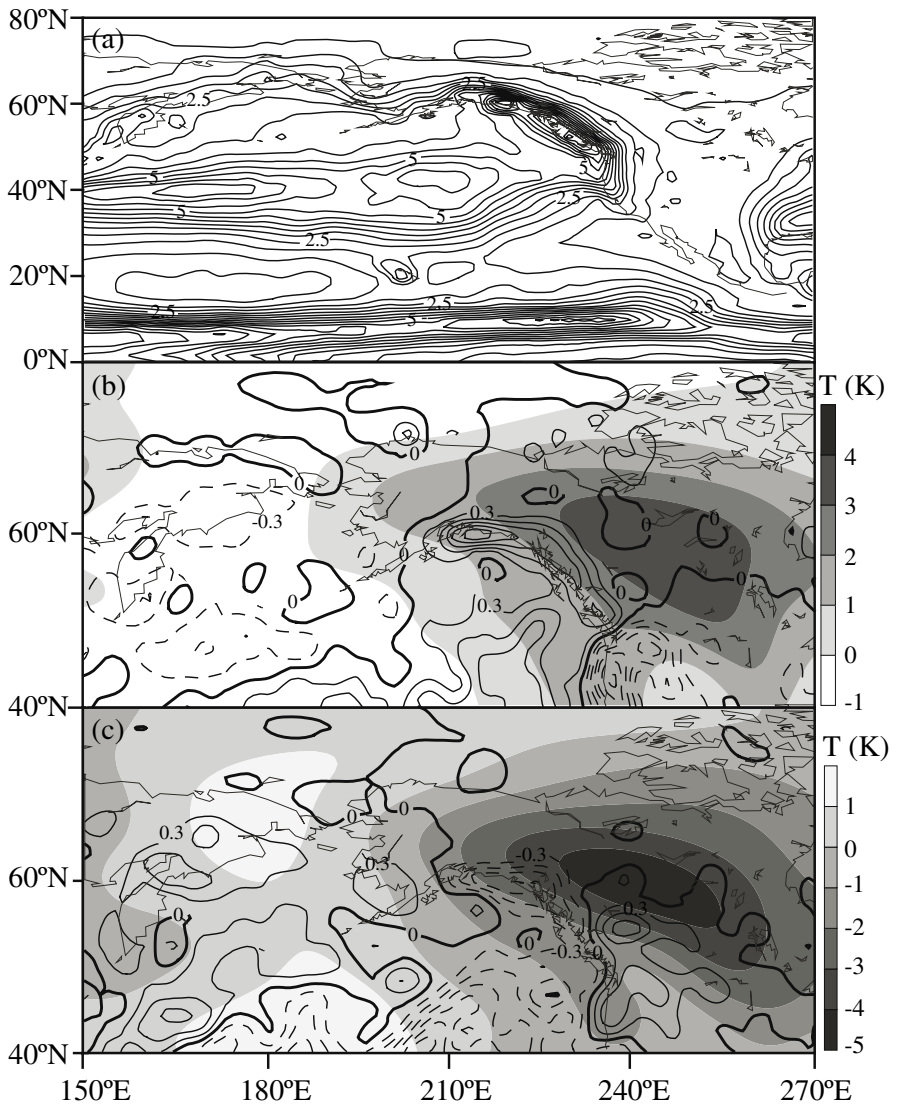

Fig. 4. Mean and anomalous DJF atmospheric conditions: (a) Global Precipitation Climatology Project (GPCP) 1979–2000 mean precipitation rate (mm d^{-1}); composite anomalous precipitation rate (mm d^{-1}) and temperature (K, shaded) at 850 hPa for (b) the five warmest, and (c) the five coldest winters. Precipitation isohyetal interval is 0.5 mm d^{-1} for (a) and 0.3 mm d^{-1} for (b) and (c)

1.2 H-budgets and Processes for Extreme Warm/Cold Winters

The composite enthalpy budget anomalies for the five warmest and five coldest winters for the Basin are given in Fig. 1b and the corresponding composite anomalous atmospheric conditions are shown in Figs. 2-4. Exceptionally warm winters in the 30-year period were characterized by both enhanced warm and cold air advections into the Basin by the mean westerly and northerly winds, respectively, which together produced extremely weak net cooling conditions (Fig. 1b). There was, however, significantly enhanced sinking and adiabatic warming which were balanced by an increased radiational loss from the Basin. These warm winters were associated with strong large-scale onshore/upslope flows into the continent due to a strengthened AL (Figs. 2b and 3b). The strengthened onshore flow induced powerful upward motions and condensation at the coastal regions (Figs. 3b and 4b) accompanied by enhanced subsidence and adiabatic warming over the MRB (Figs. 1b, 3b, and 4b). The southwesterly flow over the mountains also developed an upper-level high pressure ridge which in turn led to warm air advection into the western basin and enhanced cold air advection over the eastern basin (Figs. 1b and 2b). The "vertical" term dominated the budget to produce pronounced warming (Fig. 4b); the enhanced atmospheric radiative cooling (Fig. 1b) was largely a response to this warming.

Extreme cold winters were characterized by a slight decrease in the mean westerly warm air advection and a large reduction in the mean northerly cold air advection, with the combined result being a large net influx of warm air to the MRB (Fig. 1b). The mean subsidence and associated adiabatic warming decreased substantially but somewhat surprisingly, radiational loss increased. These anomalously cold winters were associated with weakened mean onshore/upslope flows into the continent that could be attributed to a weakened Aleutian Low over the North Pacific (Figs. 2c and 3c). Such conditions are often caused by an increased occurrence of blocking high pressure systems over the North Pacific (Renwick and Wallace 1996) which split the zonal flow. One component of the flow is diverted northward into western Alaska but it subsequently turns anticyclonically to bring cold air into the MRB through its northern boundary (Fig. 3c). This flow splitting also diminished the onshore wind (Fig. 3c) and weakened the long wave ridge over the coastal region (Fig. 2c), thus reducing both the upper-level warm air advection into the western basin and the upper-level cold air advection to the eastern basin (Figs. 1b, 2c, and 3c). At the same time, the weakened onshore flow greatly reduced the updraft and precipitation in the coastal region (Figs. 3c and 4c) as well as

diminishing the associated sinking and adiabatic warming on the lee side (Figs. 1b and 3c).

4 Discussions

The causes for the extreme interannual variability of cold season temperatures in the MRB will be further analyzed in this Section to gain insight into the problem. The dynamic North Pacific clearly is a major source of temperature variations in the MRB, but the myriad North Pacific atmospheric flow features alone are not sufficient to account for the extreme temperature variability of the Basin. For instance, such extreme variability does not occur over Western Europe, which is also located just downstream of the equally dynamically active North Atlantic Ocean. Continentality, which promotes large regional temperature fluctuations, also does not explain the extreme variability in the MRB. For example, Siberia which is farther from the ocean than is the MRB, does not exhibit the same degree of extreme conditions. Based on these arguments, we hypothesize that the extreme variability in the MRB is the collective result of vigorous upstream dynamic forcings and their interactions with the physical environment that characterizes, and feedback processes that occur within, the MRB. Since these processes take place over the whole Northeast Pacific/Northwest North America sector that spans almost a third of the circumpolar region, to facilitate the analysis of the complex problem, we will take the reductionistic approach and break down the vast domain of interest into three key component regions: (1) the North Pacific which is a source region for the large-scale atmospheric circulation features that ultimately force temperature variations in the MRB; (2) the mountainous region between the west coast and the continental divide where the onshore airflow undergoes strong modifications before entering the Basin, and (3) the MRB itself. Fundamental processes that play significant roles in affecting the energy transport and temperature response in the Basin will be identified and discussed in sequence for the three regions. The aggregated effects of these processes are then related to the observed longer-term features that were presented in Section 3 while a synthesis of these elements to account for the extreme temperature variability in the MRB along with applications of the results to climate change studies for the region will be given in Section 5.

4.1 North Pacific Atmospheric Circulations and Teleconnections with MRB Temperatures

The fundamental role played by synoptic scale eddies in the energy transport at mid- and high latitudes is well known (Peixoto and Oort 1992). Located just downwind of the Pacific storm track, the transport of water and energy into the MRB is naturally affected most strongly by cyclonic activities over the North Pacific (Lackman et al. 1998; Smirnov and Moore 2001), especially during the cold season when the baroclinic systems are active and frequent. Aggregated over the seasonal time-scale, these synoptic disturbances manifest themselves as the Aleutian Low pressure system (Fig. 2a) that, as discussed in the last Section, affects critically the mean transport of energy into the MRB.

The variability of large-scale atmospheric circulation features over the North Pacific such as the AL is characterized by patterns or modes of oscillations that occur over a wide range of temporal scales (e.g., Mantua et al. 1997; Overland et al. 1999; Wallace and Gutzler 1981). Physical linkages between the North Pacific atmospheric circulation regimes and temperature response in the MRB are reflected in the statistically significant correlations between winter temperatures in the Basin and teleconnection indices commonly used to characterize the variability of these circulation patterns (Table 2). Note that the stronger correlations are with the vertically-integrated enthalpy (i.e., the mid- and upper level temperatures) than with the surface temperatures. Not surprisingly, very weak correlations are found for climate modes with weak links to the Pacific circulation such as the Arctic Oscillation/North Atlantic Oscillation (AO/NAO).

Table 2. Contemporaneous correlations between DJF surface air temperature in the MRB, vertically-integrated enthalpy and various teleconnection indexes over the 1970–99 period

Teleconnection index	Surface temperature	Enthalpy
Aleutian low index (ALI)	0.59	0.74
Pacific-circulation index (PCI)	0.33	0.42
North Atlantic oscillation (NAO)	0.18	0.07
Pacific/North American pattern (PNA)	0.65	0.76
DJF Southern oscillation index (SOI)	-0.33	-0.48
SON SOI	-0.33	-0.61
ΔZ at 1000 hPa	0.80	0.78
ΔZ at 925 hPa	0.82	0.71
ΔZ at 850 hPa	0.76	0.54

There is evidence that the longer-period climate modes often force or create large-scale conditions that modulate the frequency and phase of shorter-period variability patterns (e.g., Palmer 1998; Straus and Shukla 2002). For example, the positive (negative) phase of the Pacific/North American pattern or PNA is known to be associated with increased frequency of cyclones (blocking events) (Renwick and Wallace 1996) while increased frequency of positive (negative) PNA phase periods are in turn found to be associated with warm (cold) phases of ENSO (Mo et al. 1998) and Pacific Decadal Oscillation PDO (Mantua et al. 1997). Since the wave cyclones are fundamental features responsible for transporting energy into the region, temperature response in the MRB to variations in the North Pacific circulation is best understood through the ways by which the low frequency modes modulate the occurrence frequency of shorter-period circulation features in the region. For example, the warming (cooling) response of the MRB to a shift into a positive (negative) PNA period can be related to the increased frequency of cyclonic (blocking) activities over the North Pacific, while the enhanced warming (cooling) over the region during the warms (cold) phases of ENSO and PDO in turn be linked with the associated increase in frequency of positive (negative) PNA events, and so on.

Regardless of the nature and detailed structure of the circulation features over the North Pacific, the transport of water and energy into the continent is ultimately accomplished by the shore-normal (onshore) flow component, particularly by the ocean surface-conditioned lower-level flow which is high in moist static energy content. In addition, orographic lifting and associated heating of the onshore flow through condensation, which will be shown to exert great impact on the lower-level temperatures over the MRB, also depend critically on the low-level onshore flow strength. Hence, lower-level temperatures in the MRB respond to variations in the North Pacific atmospheric circulation primarily through changes in the low-level onshore flow strength. To quantify this inference, we computed the contemporaneous correlations between basin DJF temperature and a new index ΔZ which is the difference of geopotential height at [110^{o}W, 50^{o}N] and [135^{o}W, 65^{o}N] (it thus gives a measure of the mean geostrophic onshore flow strength) at various pressure levels near the surface (Table 2). The results confirm that correlations associated with ΔZ at the lowest levels of 1000 and 925 hPa, are somewhat stronger than those established with ΔZ at the 850 hPa level or with other indices, thereby lending support to the arguments. Potential applications of the new index to improve seasonal temperature forecasts in the region are discussed in Szeto (2007).

4.2 Coastal and Orographic Influences

In addition to the excitation of a stationary long wave from the impingement of the mean westerly into the Western Cordillera, the mountainous terrain that separates the MRB from the Pacific Ocean also exerts significant influences on the cyclonic systems that approach the northwest coast of North America. While there is recent progress in the theoretical investigation of orographic influences on the landfall of cyclones and their potential regenerations on the lee side (e.g., Banon 1992; Davies 1997), many aspects of such events as summarized in Palmen and Newton (1969) remain valid. In their conceptual model, the cyclonic onshore flow strengthens as a Pacific cyclone approaches the coast of western Canada, and results in enhanced precipitation over the west slopes as the flow crosses the Rocky Mountains. A quasi-stationary surface trough would form due to tropospheric warming by the enhanced descent over the lee-side. If coupled to a mid-to-upper level feature such as a shortwave trough, a jet-streak or the decaying parent cyclonic system, this lee-trough may become mobile and develop into a lee-cyclone.

The interaction of moist flow with orography and its consequences on precipitation enhancement is a complicated phenomenon governed by the interplay of such factors as the velocity, static stability, and shear structure that characterize the ambient flow, synoptic conditions, and the geometry of the orographic features (Lin 2005). Despite extensive research, many aspects of orographic precipitation remain poorly understood. For the present discussion, it suffices to note that due to the release of potential instability in the forced ascent, the orographic precipitation and associated latent heat release depend non-linearly on the onshore flow configuration, such that latent heating at the coastal region could be significantly enhanced (significantly reduced or totally halted) during strong (weak) onshore flow situations. Through its amplifying and gating effects on latent heat release, the mountainous coastal region enlarges the difference of DSE transports into the MRB for various flow configurations over the North Pacific. For example, using the precipitation anomalies presented in Fig. 4 for the warm and cold winters, differences in mean latent heating over the coastal region between warm and cold winters could exceed 60 W m^{-2} (~0.5 K d^{-1}), which in turn contributed to the difference of over 25 W m^{-2} in basin-average combined vertical advection/adiabatic heating over the MRB on the seasonal time scale (Fig. 1b).

A corollary that follows from the above discussion is that warm (cold) bias in model simulations of cold season temperatures over the MRB might result when the orographic precipitation over the mountainous

coastal region is over- (under-)predicted. Simulations of water and energy processes in the MRB using the Canadian Regional Climate Model (CRCM) were troubled by a cold bias in the modeled lower troposphere (MacKay et al. 2003; Szeto et al. 2007b). This bias causes an over-prediction of snowcover, which affects the surface energy balance, the timing and magnitude of spring runoff and soil recharge, and subsequently the warm-season water cycling. Insight gained from the present study allows us to diagnose the cold bias as a consequence of the under-prediction of orographic precipitation at the coastal region. In agreement with the theoretical prediction, the cold bias is the strongest during the cold season (Fig. 5a) when synoptic activities are frequent and the zonal flow is strong, and it occurs mainly over the areas immediately downstream of coastal precipitation maximum and to the lee of the Cordillera (Fig. 5b). Further diagnostics of the model results (not shown) confirmed that the CRCM precipitation over the coastal region was indeed substantially lower than either the analyzed or observed amounts.

It follows that accurate predictions of the lee-side trough, and hence lee-cyclogenesis over the MRB which is one of the two source regions of lee-cyclones in North America, may also depend critically on the accurate simulation of the coastal orographic precipitation. Preliminary results from Mati (2006) show that, compared with other models that have better resolved the coastal precipitation, some lee-cyclogenesis cases were poorly simulated with the CRCM, therefore lending support to this inference.

The same orographic processes that enlarge the difference of DSE transports into the MRB for various upstream flow configurations would also reduce the difference in moisture influx into the Basin through the orographic depletion of moisture from strong onshore flows, hence muting the precipitation and subsequent hydrologic responses in the Basin to the same large-scale forcings. Although there are many competing factors that complicate the problem, evidences that support such inferences are given in Woo et al. (2006).

4.3 Feedback Processes within the MRB

While the processes that occur over the North Pacific and the coastal region play a dominant role in affecting the transport of energy into the MRB, feedback processes that take place within the Basin can influence how the temperature of the Basin responds to these forcings. For instance, latent heating in the ascending onshore flow over the coastal region can only be “felt” over the MRB when the energy used to do work against the

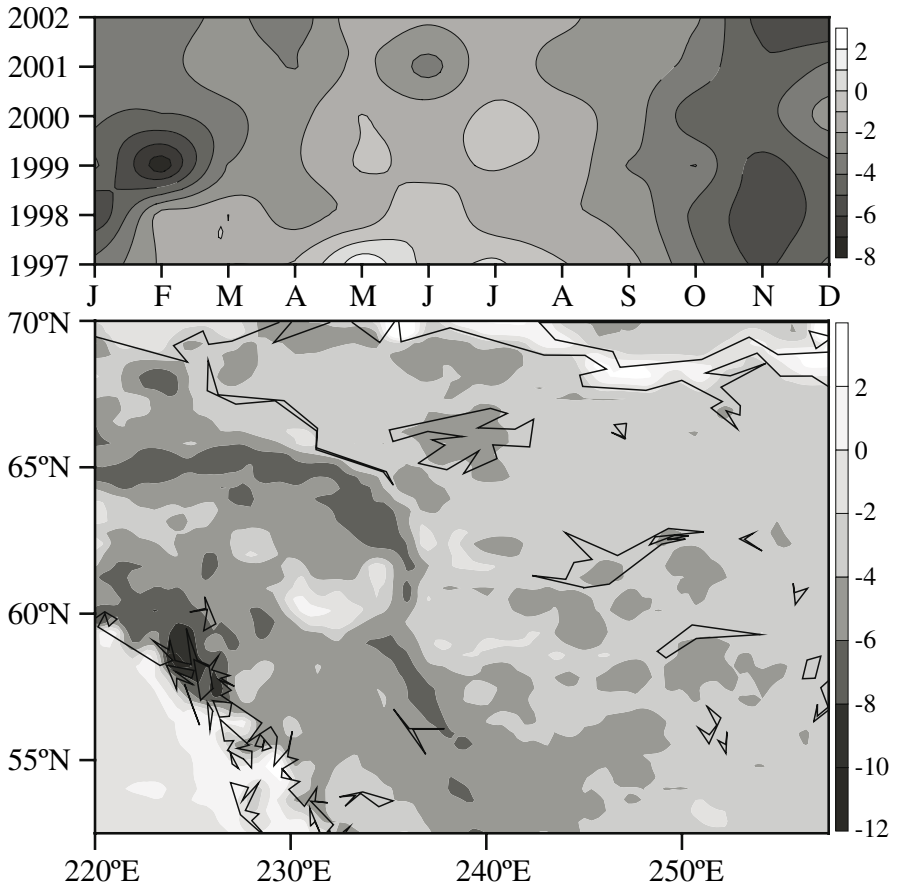

Fig. 5. Surface air temperature bias (K) in the CRCM obtained by using the Canadian Meteorological Centre (CMC) analysis data as reference: (top) interannual variability of monthly basin-average bias and (bottom) spatial variability of 5-year (1998–2002) mean January bias

ambient air pressure and gravity are converted back into sensible heat as the air parcels descend and are compressed adiabatically over the lee side. Hence, any processes that affect the lee-side subsidence can greatly influence the temperature over the Basin. In addition, temperature advection by perturbation airflows and modifications to local radiative transfers by synoptic scale processes can also significantly affect the temperature response.

As discussed earlier, a quasi-stationary surface trough would form on the lee-side of the mountains during a warm episode over the Basin. The low-level cyclonic perturbation flow induced by the surface trough could

advect warm air into the Basin from the south as well as enhancing the downslope descent at locations southwest of the trough (see also Cao et al. 2007). This warm air advection could in turn destabilize the lower troposphere (i.e., weaken or destroy the surface-based low-level temperature inversions commonly observed over the Basin in the winter), creating an environment that facilitates further low-level descent and associated warming. In addition, clouds in the lee-cyclones that are spawned from the lee-troughs could reduce infrared radiative loss from the surface, thus contributing to warming of the lower troposphere and the basin surface.

Further examination of the processes that affect the atmospheric thermodynamics of the Basin during the development of extreme cold episodes (Szeto 2007) shows that many of these events started as a ridge of high pressure that extends from Alaska. The enhanced low-level anticyclonic flow into the Basin could be forced to rise up the eastern slopes of the foothills to induce adiabatic cooling and subsequent condensation and light precipitation (e.g., ice crystal) that dries out the cold air. Curry (1983) theorized that longwave radiation loss from the thin clouds formed near the top of the inversion layer and the enhanced surface radiational loss under the dry and clear-sky conditions following the dissipation of the cloud through light precipitation could play an important role in the development of cold continental polar air mass and anticyclones. The interaction of northeasterly anticyclonic flows with the Western Cordillera provides a lifting mechanism that can initiate the sequence of events hypothesized in Curry (1983). The resulting cold air could expand both horizontally and vertically, effectively eliminating the sloping effects of the mountains such that the westerly flow that passes over the Rockies cannot descend through the dense low-level cold air. Such cold air damming phenomena and their associated impacts on the regional weather have been investigated extensively for southern regions (e.g., Bell and Bosart 1988). The geographic and synoptic environments that characterize the Basin suggest that these phenomena should occur frequently during the winter and they can significantly influence the cold-season energy cycling in the MRB.

The MRB is a major source region of anticyclones and of the polar continental air mass during the winter (Ioannidou and Yau 2007). It is found in previous studies (e.g., Tanaka and Milkovich 1990) that classical theories of anticyclogenesis and cold airmass development (e.g., Curry 1983; Wexler 1936) cannot accurately account for the observed development of these events in the nearby region of Alaska. We hypothesize that regional factors such as the topographic influences and the cold air damming effects could complement the idealized static theories of Wexler and Curry to better account for the development of these features.

Szeto (2007) showed that anomalous warm (cold) winters in the MRB are characterized by higher than normal number of days that were affected by anomalous low (high) surface pressure conditions. When aggregated over a season, the frequent lee-troughs and lee-cyclones manifest themselves as a low-level pressure perturbation trough during anomalous warm winters over the MRB (Fig. 2b). On the other hand, the high pressure systems and the associated perturbation flows that affect the temperatures of the Basin during cold episodes are manifested on the seasonal time scale as the anomalous low-level high pressure ridge over the region and the associated perturbation upslope flow and much reduced mean subsidence over the Basin during extreme cold winters (Figs. 2c and 3c). The associations of stationary low- and high- pressure features with warm and cold periods on the monthly time scale were also identified and discussed in Cao et al. (2007). In addition, Stewart and Burford (2002) showed that, in agreement with the above discussions, clouds were more (less) widespread during warm (cool) winter periods when compared to average conditions.

5 Synthesis and Applications to Climate Change Research

Extensive studies have been conducted on the atmospheric circulation features over the North Pacific and their interactions with the mountainous terrain of northwestern North America. This study provides fresh insight into the causes of temperature variability in the MRB when these processes were examined in tandem with a detailed analysis of the atmospheric enthalpy budgets of the Basin. In particular, the results show that interactions of synoptic disturbances (that are of either Pacific or MRB origin) with the Western Cordillera can enlarge the differences in thermal response of the Basin to changes in synoptic situations over the North Pacific, thereby increasing the sensitivity of its winter temperatures to changing large-scale conditions. The observed extreme intra-seasonal variability of winter temperatures in the Basin can thus be understood as a consequence of the amplified sensitivity of the region's temperatures to the highly variable synoptic conditions over the North Pacific. As discussed in Section 4.1, longer-period climate variability can be described in terms of changes in occurrence frequency of shorter period circulation patterns all the way down to the synoptic time scale. The extreme interannual temperature variability of the MRB can then be understood as a result of the enhanced sensitivity of the region's seasonal temperatures to the low fre-

quency variability of atmospheric circulations through their modulating effects on weather regimes over the North Pacific. A conceptual model that summarizes these processes is given in Szeto et al. (2007a).

There have been suggestions that due to the nonlinear nature of the climate system, anthropogenic climate change will manifest primarily in terms of changes to the occurrence frequency of natural climate variability patterns (Palmer 1998). When combined with this hypothesis, the sensitivity of cold-season temperatures of the MRB to variability in the large-scale circulation would predict an amplified long-term winter temperature response to anthropogenic climate forcing. Several studies have reported significant recent winter warming of the MRB (e.g., Serreze et al. 2000; Zhang et al. 2000). It is evident from Fig. 6a, however, that the linear trends noted in some of the previous studies are largely statistical artifacts of the "jump" in the climatic state of the MRB as the Basin responded to the well-documented shift in the PDO during the mid-1970s (e.g., Mantua et al. 1997). Using the argument put forward in this paper, the significant recent warming can be interpreted as an amplified temperature response to the increased frequency of positive PNA patterns after the regime shift (Fig. 6b). Although the observed warming can be attributed to changes in natural climate variability modes, according to the nonlinear perspective of climate change put forward by Palmer and others, one cannot simply conclude that the warming was not due to anthropogenic forcing. In addition, due to the sensitivity of its winter temperature to climate change, the Basin can serve as an effective "thermometer" for gauging anthropogenic climate change. On the other hand, the sensitivity of the Basin temperature to synoptic scale processes poses particular challenge to model prediction of its future temperature changes. Our results suggest that accurate model representation of the interactions of synoptic features with the Western Cordillera is critical to the prediction of long-term climate variability and change in the interior continent.

Although warming due to anthropogenic causes is currently the most pressing climate issue, feedback processes in the MRB could have amplified regional climate change in the geologic past. For example, while cold air damming provides a feedback process to accentuate cooling over the Basin on synoptic time scales, one can extrapolate the argument to infer processes that could have affected climate conditions in the region over much longer timescales. In particular, much of North America was covered with thick glaciers (up to 1.5 km over southern Canada and deeper near the mountains and in northern regions, Peltier 1994) during the Pleistocene. Similar to the cold air damming effect, the development and merging of the Cordilleran and Laurentide Ice Sheets would progressively

eliminate the sloping effects of the mountains and the westerly flow that crossed the Cordillera would not be able to descend and warm the continental interior. All else being equal (this of course is not a good assumption because the general circulation during the Ice Age differed radically from its present configuration), the resulting cold conditions could have contributed to a further buildup of the glacier which in turn limited the lee-side subsidence and associated warming. Unlike Eurasia without a high mountain range to separate it from the Atlantic Ocean, the presence of the Cordillera with its feedback mechanisms might have been one factor that contributed to the development of a more extensive Pleistocene ice sheet over North America than over Eurasia.

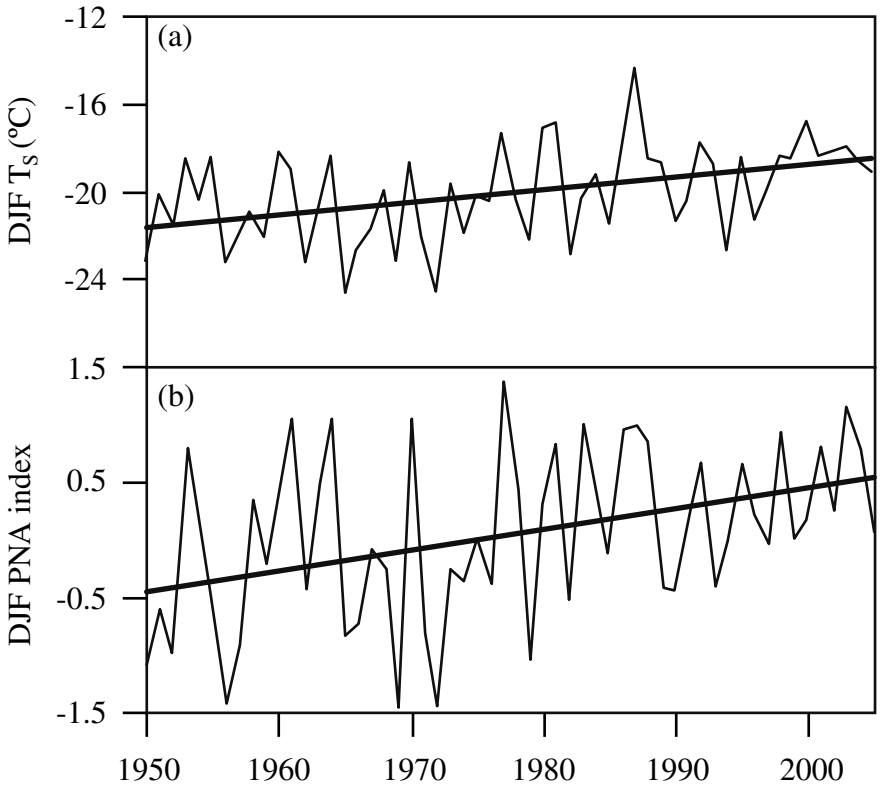

Fig. 6. Inter-annual time series of (a) DJF basin-average surface air temperature (K) and (b) DJF PNA index. Also shown are the linear trend lines (dashed)

In summary, the knowledge acquired through the *H*-budget analysis provides a powerful theoretical basis for understanding the extreme cold-

season temperature variability and change in the Mackenzie Basin. The reductionistic approach adopted to analyze the problem allows its results to be easily applied to identify the causes of certain deficiencies, and to suggest appropriate remedies, in climate model simulations, as well as to improve understanding of various synoptic scale features and climatic processes that affect the region. The study also illustrates how results from traditional synoptic-climatological analyses can be used in conjunction with concepts derived from modern nonlinear dynamical approaches to climate studies to offer fresh insights into the problem of regional climate response to anthropogenic forcing, which is generally regarded as a most pressing, relevant, and difficult issue in climate change research.

Acknowledgments

This work was financially supported by Environment Canada, the Panel on Energy Research and Development (PERD) and MAGS. Ms. Hang Tran is acknowledged for her assistance in data processing and calculations. The CRCM simulations were conducted by Dr. Murray MacKay. The NCEP Reanalysis data was provided by the NOAA-CIRES Climate Diagnostics Center, Boulder, Colorado, from their website at http://www.cdc.noaa.gov/

References

Bannon PR (1992) A model of Rocky Mountain lee cyclogenesis. J Atmos Sci 49:1510–1522

Bell BD, Bosart LF (1988) Appalachian cold-air damming. Mon Weather Rev 116:137-161

Cao Z, Stewart RE, Hogg WD (2007) Extreme winter warming over the Mackenzie Basin: observations and causes. (Vol. I, this book)

Curry J (1983) On the formation of continental polar air. J Atmos Sci 40:2278–2292

Davis CA (1997) The modification of baroclinic waves by the Rocky Mountains. J Atmos Sci 54:848–868

Finnis J (2005) Representation of the atmospheric hydrologic cycle over the Arctic in CCSM3. 8th Conf on Polar Meteorology and Oceanography, Jan. 10–14, 2005, San Diego, CA, USA

Houghton JT, Ding Y, Griggs DJ, Noguer M, van der Linden PJ, Xiaosu D (2001) Climate change: the scientific basis. Cambridge University Press, Cambridge

Ioannidou L, Yau MK (2007) Climatological analysis of the Mackenzie River Basin anticyclones: structure, evolution, and interannual variability. (Vol. I, this book)

Kalnay E, Kanamitsu M, Kistler R, Collins W, Deaven D, Gandin L, Iredell M, Saha S, White G, Woollen J, Zhu Y, Chelliah M, Ebisuzaki W, Higgins W, Janowiak J, Mo KC, Ropelewski C, Wang J, Leetmaa A, Reynolds R, Jenne R, Joseph D (1996) The NCEP/NCAR 40-year reanalysis project. B Am Meteorol Soc 77**:**437–471

Kistler, R, Kalnay E, Collins W, Saha S, White G, Woollen J, Chelliah M, Ebisuzaki W, Kanamitsu M, Kousky V, Van Den Dool H, Jenne R, Fiorino M (2001) The NCEP–NCAR 50-year reanalysis: monthly means CD-ROM documentation. B Am Meteorol Soc 82:247–267

Lackmann GM, Gyakum JR, Benoit R (1998) Moisture transport diagnosis of a wintertime precipitation event in the Mackenzie River Basin. Mon Weather Rev 126:668–691

Lin Y-L (2005) Dynamics of orographic precipitation. 2005 Yearbook of science and technology, McGraw Hill, pp 248–250

MacKay MD, Seglenieks F, Verseghy D, Soulis ED, Snelgrove KR, Walker A, Szeto K (2003) Modeling Mackenzie Basin surface water balance during CAGES with the Canadian Regional Climate Model. J Hydrometeorol 4:748–767

MacKay MD, Bartlett PA, Chan E, Verseghy D, Soulis ED, Seglenieks FR (2007) The MAGS regional climate modeling system: CRCM-MAGS. (Vol. I, this book)

Mati I (2006) A comparison study of two regional atmospheric models over the Mackenzie Basin. M.Sc. thesis, McGill University

Mantua NJ, Hare SR, Wallace JM, Francis RC (1997) A Pacific decadal climate oscillation with impacts on salmon production. B Am Meteorol Soc 78:1069–1079

Mo R, Fyfe J, Derome J (1998) Phase-locked and asymmetric correlations of the wintertime atmospheric patterns with the ENSO. Atmos Ocean 36:213–239

Overland JE, Adams JM, Bond NA (1999) Decadal variability of the Aleutian Low and its relation to high latitude circulation. J Climate 12:1542–1548

Palmen E, Newton CW (1969) Atmospheric circulation systems. Academic Press

Palmer TN (1998) Nonlinear dynamics and climate change: Rossby's legacy. B Am Meteorol Soc 79:1411–1423

Peixoto JP, Oort AH (1992) Physics of climate. American Institute of Physics

Peltier W (1994) Ice age paleotopography. Science 265:195–201

Renwick JA, Wallace JM (1996) Relationship between North Pacific wintertime blocking El Nino, and the PNA Pattern. Mon Weather Rev 124:2071–2076

Serreze MC, Walsh JE, Chapin III FS, Osterkamp T, Dyurgerov M, Romanovsky V, Oechel WC, Morison J, Zhang T, Barry RG (2000) Observational evidence of recent change in the northern high-latitude environment. Climatic Change 46:159–207

Smirnov VV, Moore WK (2001) Short-term and seasonal variability of the atmospheric water vapor transport through the Mackenzie River Basin. J Hydrometeorol 2:441–452

Stewart RE, Bussières N, Cao Z, Cho HR, Hudak DR, Kochtubajda B, Leighton H, Louie PYT, MacKay MD, Marsh P, Strong GS, Szeto KK, Burford JE (2002) Hydrometeorological features of the Mackenzie Basin climate system during the 1994/1995 water year: a period of record low discharge. Atmos Ocean 40:257-278

Stewart RE, Burford JE (2002) On the features of clouds occurring over the Mackenzie River Basin. J Geophys Res AAC18:1–13

Stewart RE, Burford JE (2002) On the features of clouds occurring over the Mackenzie River basin. J Geophys Res AAC18:1–13

Straus DM, Shukla J (2002) Does ENSO force PNA? J Climate 15:2340–2358

Szeto KK, (2007) On the variability and change of cold-season temperatures in Northwest Canada. J Climate (in press)

Szeto KK, Stewart RE, Yau MK, Gyakum J (2007a) The Mackenzie climate system: a synthesis of MAGS atmospheric research. (Vol. I, this book)

Szeto KK, Tran H, MacKay M, Crawford R, Stewart RE (2007b) Assessing water and energy budgets for the Mackenzie Basin. (Vol. I, this book)

Tanaka HL, Milkovich MF (1990) A heat budget analysis of the polar troposphere in and around Alaska during abnormal winter of 1998/89. Mon Weather Rev 118:1628–1639

Wallace JM, Gutzler DS (1981) Teleconnections in the geopotential height field during the northern hemisphere winter. Mon Weather Rev 109:784-812

Wexler H (1936) Cooling in the lower atmosphere and the structure of polar continental air. Mon Weather Rev 64:122-136

Woo MK, Thorne R, Szeto KK (2006) Reinterpretation of streamflow trends based on shifts in large-scale atmospheric circulation. Hydrol Process 20:3995–4003

Zhang X, Vincent LA, Hogg WD, Niitsoo A (2000) Temperature and precipitation trends in Canada during the 20th Century. Atmos Ocean 38:395–429

Chapter 5

Extreme Winter Warming over the Mackenzie Basin: Observations and Causes

Zuohao Cao, Ronald E. Stewart and William D. Hogg

Abstract Over the last few decades, the Mackenzie River Basin (MRB) has experienced a pronounced winter warming trend. In this study, a number of extreme basin warming events and related processes during the winter are investigated using surface (1950–94) and rawinsonde (1946–94) data. We found that the basin warming is associated mainly with low pressure systems within and near the Basin, with extratropical and subpolar high pressure systems in the vicinity of the Basin.

The dynamic and thermodynamic contributions (due to atmospheric circulations, topography, low-level temperature inversion, and the interactions among these factors) to the basin warming are examined. It is shown that the warming events occur through the horizontal advection of warm air from west and south of MRB, and through adiabatic descent induced by both the topography and the low and/or high pressure system, particularly when the low-level temperature inversion occurs. The impacts of the warming on the MRB climate are also discussed.

1 Introduction

Observations over the last few decades indicate that a warming trend of surface air temperature is significant during the winter over the Northern Hemisphere (e.g., ACIA 2004; IPCC 2001; Wallace et al. 1995, 1996). Numerical studies using different climate models also show that atmospheric warming is expected to be pronounced in the winter (e.g., Ingram et al. 1989; IPCC 1990, 1992, 2001; Manabe and Stouffer 1980). Although various forcings are generally expected to raise global temperatures, there are uncertainties about how the entire climate system will change, especially at regional levels (Pilifosova et al. 1997) to cause an increasing concern regarding the impacts of global climate changes on regional-scale water resources.

Several studies have documented climate changes at the regional level, such as climate changes in Switzerland (Beniston et al. 1994; Beniston and Rebetez 1996) and in Kazakhstan (Pilifosova et al. 1997), anomalous warming in the Canadian Prairie provinces (Majorowicz and Skinner 1997) and spatial and temporal changes in extreme air temperatures in the Arctic (Przybylak 1997). In this study, we investigate regional-scale climate changes over the Mackenzie River Basin (MRB), paying particular attention to a number of extreme warming events that have occurred during the last few decades (Cao et al. 2001).

The Mackenzie River is the fifteenth largest in the world in terms of mean annual discharge and the twelfth largest in sediment discharge (Milliman and Meade 1983). Within its basin, there occur many cold-region phenomena (such as snow and ice processes, permafrost, Arctic water vapor, and clouds and radiation interactions) that must be properly handled within a global climate system model. The MRB has highly varied terrain (Woo et al. 2007) that strongly influences its climate. In the winter, this region is commonly associated with a low-level temperature inversion. In addition, the MRB is experiencing pronounced winter warming with temperature increases of up to 1.3 K decade^{-1} for the period 1961 to 1990 (Fig. 4 of Stewart et al. 1998). Furthermore, substantial anomalies of monthly mean surface air temperature have been observed during the last few decades. These anomalies refer to the departure from the 30-year (1961–90) average. The term "positive anomalies" is hereafter used interchangeably with "warming events". As shown in Fig. 1a, warming events have become increasingly frequent in recent years. On the other hand, the anomaly of the 1000-hPa geopotential height over the Basin (Fig. 1b) shows a recent increase in interannual variability. In particular, the variability of geopotential height anomalies is larger in the winter than in other seasons. Thus, the increasing interannual variability of circulation systems may be closely associated with the recent frequent occurrence of winter warming events. Szeto (2007) also noted that this large temperature variability in the cold season is linked to the interactions between the North Pacific airflow and the regional environment, particularly the mountains west of MRB.

The objectives of this study are to investigate the monthly-scale warming events over the MRB in relation to atmospheric circulations, topography, and the low-level temperature inversion, and to understand some of the dynamic and the thermodynamic processes operating in these situations. The monthly time scale was chosen because there are strong signals of positive anomalies in the monthly average fields of surface air temperature and consistent patterns of anomalies in both the temperature and the

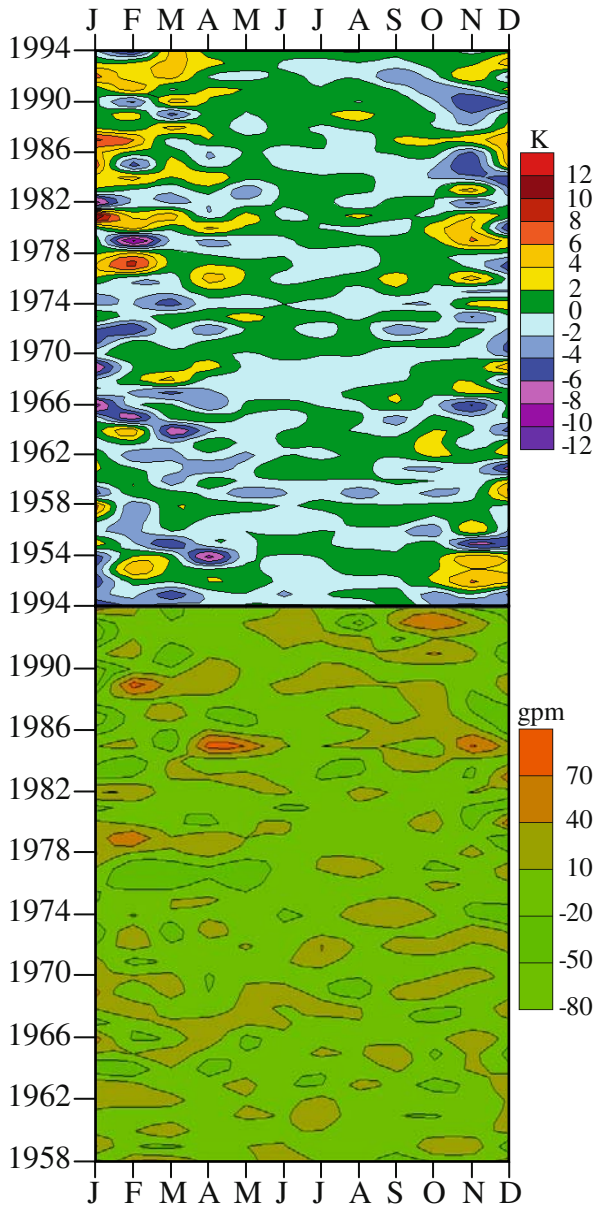

Fig. 1. Monthly-scale anomoalies of (top) surface air temperature, and (bottom) the 1000-hPa geopotential height over the Mackenzie Basin, calculated by subtracting the normal (1961–1990 average) from the actual monthly average

pressure fields. The signals of the temperature anomalies over seasonal or annual scales are weaker than those over the monthly scale simply because positive and negative anomalies are averaged out over these longer periods. On the other hand, within a month, there is some variability in the temperature and pressure fields on daily or weekly scales, and those fluctuations are filtered out in this study. The monthly time scale is considered generally to be appropriate for climatic change research (Robeson 1993). Monthly scale temperature is one of the most important elements for representing a regional climate, especially for the investigation of extremes as unusual weather conditions at such a scale can have considerable impacts on the society (Murata 1993).

This study has two main components: (1) identification of the relationships between each of the monthly-scale warming events and the corresponding circulations, with (2) special attention paid to the effects of the local topography and to the commonly-occurring low-level temperature inversions in the Basin.

2 Data

2.1 Surface Data

Two sets of data are used in this study. Set 1 contains 45-year (1950–94) monthly mean surface climate parameters derived from Environment Canada climate stations. Temperature measurements recorded with at least daily frequency at about 150 locations in and near the MRB, are used to generate values on a grid with 50 km spacing by employing statistical optimal interpolation (Alaka and Elvander 1972) and by following a strategy of using a first guess field and interpolating residuals to this field. A similar method was used by Yamamoto and Hoshiai (1980) to interpolate Northern Hemisphere mean surface air temperature fields. If the first guess field is chosen well, residuals are homogeneous and isotropic (essential for proper statistical optimal interpolation), the expected patterns of the parameters are preserved, and interpolation errors over the data-sparse MRB are minimized. For monthly mean maps of surface climate parameters, gridded estimates of 30-year normals (1961–90) are used as the first guess field in this study.

2.2 Upper-air Data

Set 2 contains all regular daily reports (00 and 12 UTC) from the North American rawinsonde network over the period 1946 to 1994 (49 years). The rawinsonde observations are interpolated using a method called bivariate interpolation and smooth surface fitting, developed by Akima (1978). This method has been widely tested and implemented (IMSL 1989; NCAR graphics 1995). The rawinsonde data include geopotential height, zonal and meridional components of velocities, temperature, and dew point temperature. Observations are interpolated on the mandatory levels: 1000, 850, 700, 500, 400, 300, 250, 200, 150, and 100 hPa pressure surfaces. The horizontal domain of all interpolated fields is within the rectangle of 28–70^{o}N and 68–130^{o}W where higher density rawinsonde observations are available (Fig. 2). The horizontal resolution of the interpolated data is 1.55° latitude × 1.05° longitude.

2.3 Quality of Surface and Upper-air Data and their Interpolations

2.3.1 Topographic Variability

Topography has substantial influence on surface air temperature fields if a spatial interpolation is applied to raw data of surface air temperature. The topographic effect on spatial variability of anomalous fields, however, can be dramatically reduced by removing the mean from the raw data and interpolating the anomaly only (Robeson 1993). This operation is part of the procedure for statistical optimal interpolation (Alaka and Elvander 1972) used in this study. In addition, the effect of topography on the mean of these temperature fields is corrected using the formula of Soulis et al. (1994) which takes account of the effect of station elevation.

2.3.2 Station Inhomogeneities

Station inhomogeneity (Hansen and Lebedeff 1987; Jones et al. 1986; Legates and Willmott 1990; Mitchell 1953) is due mainly to changes in instrumentation, station location, observation time and the methods used to calculate monthly means, and environmental factors such as urbanization (Karl and Jones 1989). Jones et al. (1986) noted that there is no simple way to quantify the magnitude of changes in instrumentation, and it is also rare to have a sufficient number of overlapping readings available to derive correction factors between different locations. Jones et al. (1986)

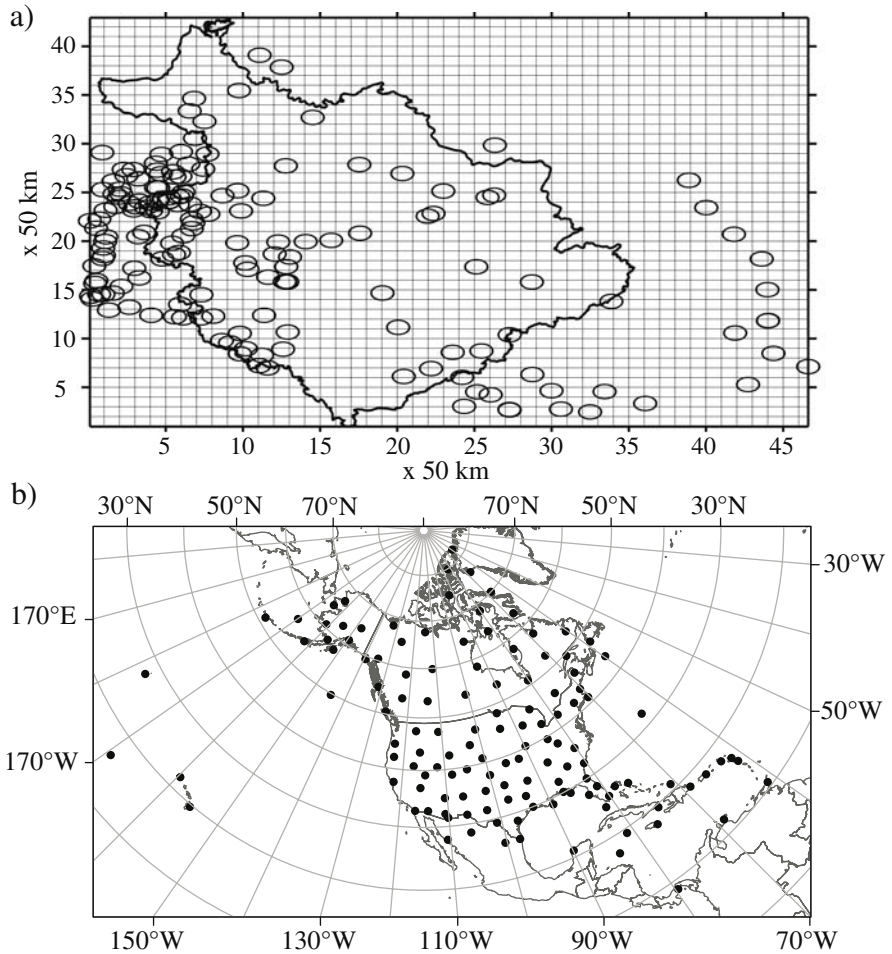

Fig. 2. (a) Distribution of surface meteorological stations (circles) in 1988 in and near the Mackenzie River Basin (boundary shown by solid lines). The rows and columns are represented by grid lines 50 km apart. The numbers labeled along the abscissa and the ordinate are grid points from the origin (at the bottom and left corner). (b) Distribution of 130 rawinsonde stations (solid circles) in January 1969, with solid lines marking the boundary of the Mackenzie Basin

further suggested that the errors resulting from different observation times and from different methods used to calculate monthly means, can be considerably reduced if all fields are transformed to anomaly values from a common reference period. Since we focus on anomalies of surface air temperature field, the corresponding errors should be small. Jones et al.'s

(1986) homogeneity analysis also shows that urbanization effects are very small for most Arctic locations, at least for annual mean data.

Although corrections can be made with respect to the biases mentioned above, the correction procedure involves many subjective judgments in deciding which station's data are in error, which data to correct, and whether or not to correct (Jones et al. 1986). Therefore, no corrections were made in Legates and Willmott (1990) and in other studies because there are no viable means to correct these biases. Likewise, the data used in this study are not systematically corrected with respect to station inhomogeneities though these biases can be much reduced by using anomalous fields.

2.3.3 Network Bias

Another central issue regarding data and their interpolation is whether samples are spatially uneven. Methods for examining network variability have been developed but questions regarding air temperature network adequacy may never be answered fully due to insufficient data (Robeson 1993). Cross validation is one method widely used for determining network adequacy (Diaconis and Efron 1983; Efron 1982; Elsner and Tsonis 1991; Robeson 1993). Network bias due to spatial variations of station number and location occurs when the calculation is made for an area-averaged quantity or area-averaged-related time series. However, in this study, we investigate the spatial distribution of surface air temperature anomalies and relate them to spatial patterns of atmospheric circulation.

3 Surface Air Temperature Anomalies and their Relation to Circulation Systems

Surface air temperature anomalies over the MRB are examined for the winter months (November through March) in the last few decades (from 1958 to 1994). Based on 40-month surface air temperature analyses, it was found that 50% of the warming events are related to low pressure systems in the Basin. As well, 50% and 20% of the warming events are associated with, respectively, extratropical and subpolar high pressure systems adjacent to the Basin. Because of overlapping, one warming event may be related to two different pressure systems, and so the total percentage is greater than 100%. Here, the term "subpolar high pressure systems" refers to high pressure systems centered (to the east of the Basin) between 60.0^{o}

and 66.5°N, and "extratropical high pressure systems" refer to those centered (to the southeast/south of MRB) south of 60.0°N.

This paper presents six *extreme* warming events, each satisfying the criterion that all parts of the Basin had a positive monthly mean temperature anomaly. These events are also representative of the various types of circulation systems that are dominant during the warming periods. For each event, Table 1 shows the time periods, magnitudes of the surface air temperature anomalies, (i.e., maximum anomalies over the basin), and the dominant pressure systems and their origins. The warming events and associated pressure systems presented in the following subsections are organized by pressure systems and their locations with respect to the Basin.

Table 1. Extreme winter warming events presented in this study. The magnitude shows the maximum departure from the normal (1961–1990 average). The anomaly is calculated using surface air temperatures derived from Environment Canada climate stations.

Period [month/year]	Magnitude [K]	System	Origin
12/87	10	L	MRB
2/77	17	L	MRB
12/86	11	L	MRB
2/78	12	H	EX
2/87	12	H	SP
11/68	3	L, H	MRB, EX

L low pressure system, *H* high pressure system, *MRB* Mackenzie River Basin, *SP* subpolar, *EX* extratropical regions, of the dominant large scale pressure systems described in the text

3.1 Low Pressure Systems in the Mackenzie Basin

Low pressure systems typically develop on the lee side of the Rocky Mountains, leading to a horizontal advection of warm air into the Basin. Topography also significantly modifies their vertical motion (Hobbs et al. 1996). The topographically-induced vertical velocity can affect the surface temperature field through vertical advection and adiabatic heating, as is illustrated by some typical events documented in this subsection.

December of 1987

The MRB experienced a large positive anomaly of surface air temperature in December 1987 (Fig. 3a). For most parts of the Basin, the anomaly ex-

ceeded 5 K, with a maximum value of about 10 K. Comparisons of Fig. 3a and Figs. 3b–c indicate that the warming was closely related to the low pressure system and to a negative anomaly of the 1000-hPa geopotential height over the Basin. The well-organized low pressure system (Fig. 3b) was associated with the horizontal advection of warm air both from the west and from the south. If the low pressure system interacted with the Rocky and Mackenzie Mountains located in the western part of MRB, the vertical velocity induced by the mountains may be important for the development of surface air temperature anomaly.

In contrast to the adiabatic warming induced by the downslope winds, adiabatic cooling related to upward motions in the region of the low pressure system may also impact the surface temperature field. To understand if this adiabatic cooling is important, we examine the vertical structure of the low pressure system. Figure 4a shows the monthly-averaged temperature difference between the 850 and 1000-hPa pressure surfaces. Positive values mean that temperature increases with height; negative values indicate the opposite. As shown in Fig. 4a, the low-level temperature increased with height over the area where the low pressure system developed.

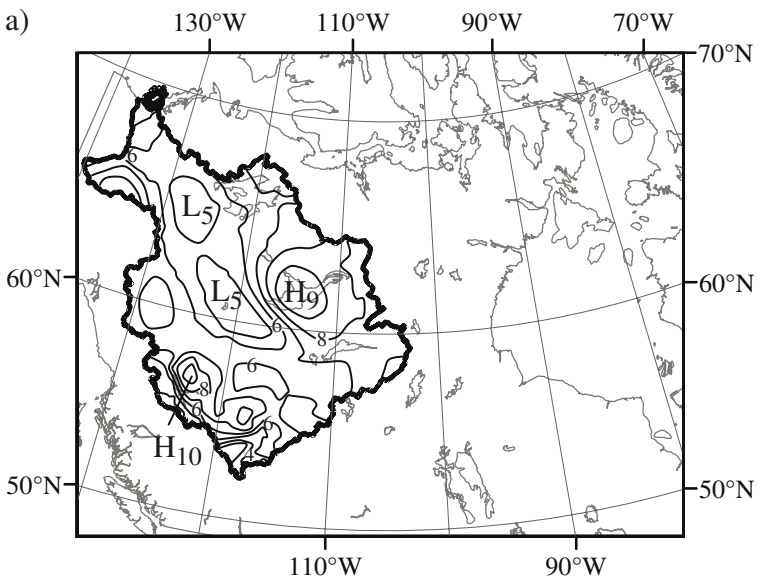

Fig. 3. Spatial distribution in December 1987 of (a) the anomaly of surface air temperature at an interval of 1 K, (b) the monthly average of the 1000-hPa geopotential height at an interval of 5 gpm, and (c) the anomaly of the 1000-hPa geopotential height at an interval of 5 gpm. Dashed lines denote negative values; solid lines are the boundary of the Mackenzie River Basin

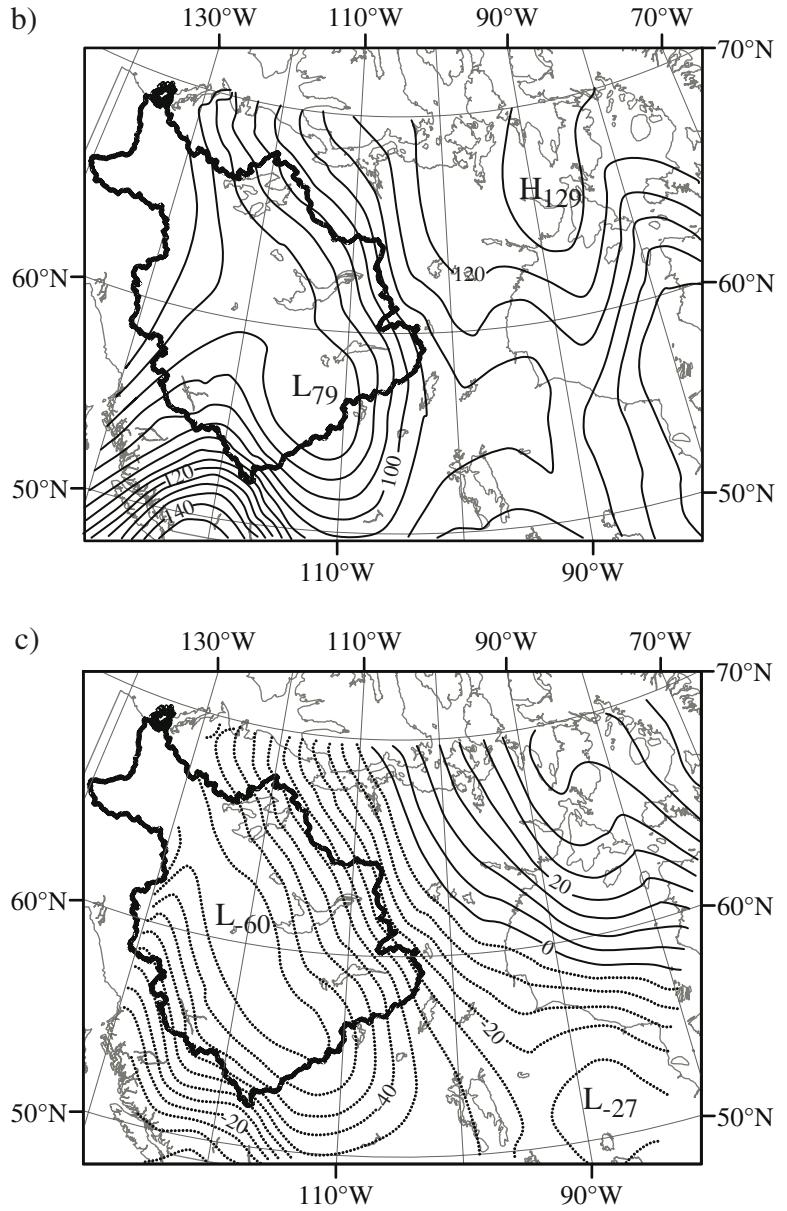
b)
130°W
110°W
90°W
70°W
70°N
60°N
50°N
H129
120
L79
100
20
40
c)
L-60
20
0
-20
40
L-27

Fig. 3. (cont.)

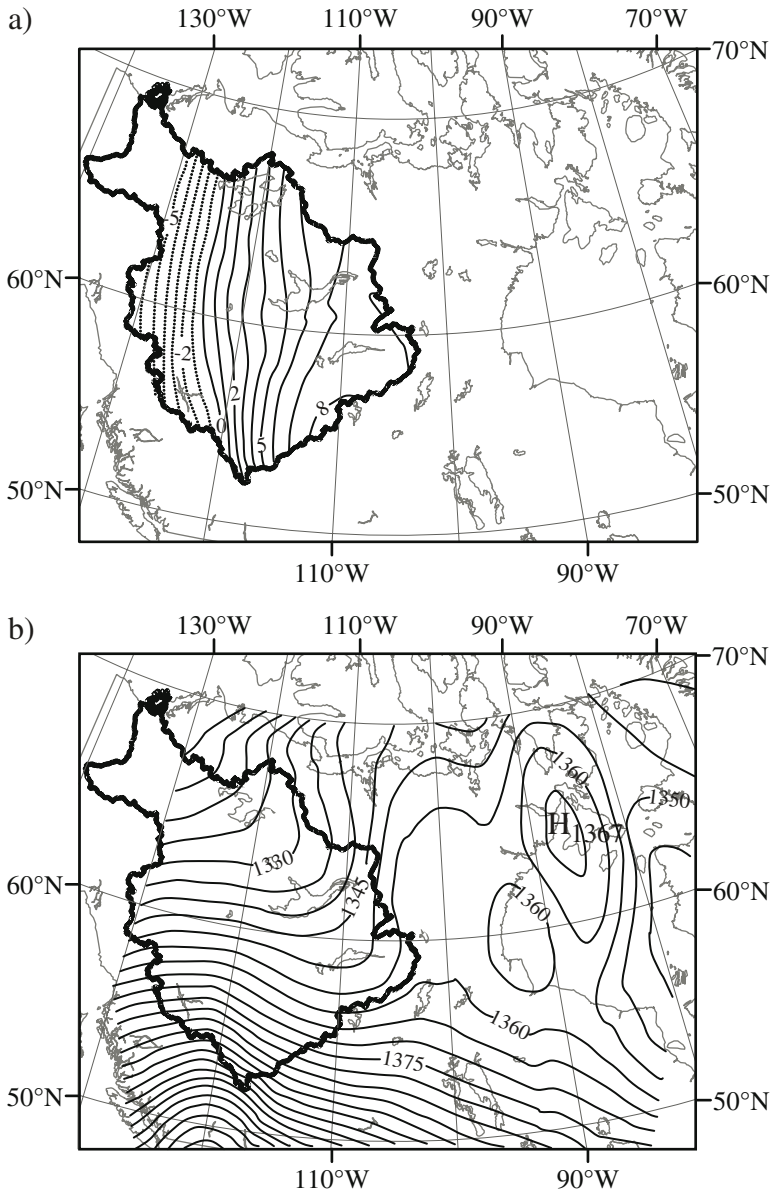

Fig. 4. Spatial distribution in December 1987 of (a) the difference of the monthly-averaged air temperature between the 850-hPa and 1000-hPa at an interval of 1 K, and (b) the monthly average of the 850-hPa geopotential height at an interval of 5 gpm. Dashed lines indicate negative values; solid lines are the boundary of the Mackenzie River Basin

The maximum temperature difference was 8 K. Due to this low-level temperature inversion, the atmosphere was very stable and the vertical motion directly induced by the low pressure system was probably small and so was adiabatic cooling. In addition, the low pressure system developed in the region of the low-level temperature inversion was very shallow. This shallow system was also evident from Fig. 4b where the 850-hPa trough was positioned ahead of the 1000-hPa low (compare Fig. 4b with Fig. 3b).

February of 1977

The difference between this event and the one of December 1987 is that the negative anomaly of the 1000-hPa geopotential height in this case was more intense (compare Fig. 5c with Fig. 3c), and positive anomalies of the surface air temperature were correspondingly more significant (compare Fig. 5a with Fig. 3a). The maximum anomaly of surface air temperature in the present case reached 17 K within the Basin, about 1.7 times warmer than that in December 1987. There was a good relationship between the low pressure system and the temperature anomalies (Fig. 5). Although physical processes contributing to this warming event were probably similar to those in December 1987, the horizontal advection of warm air from

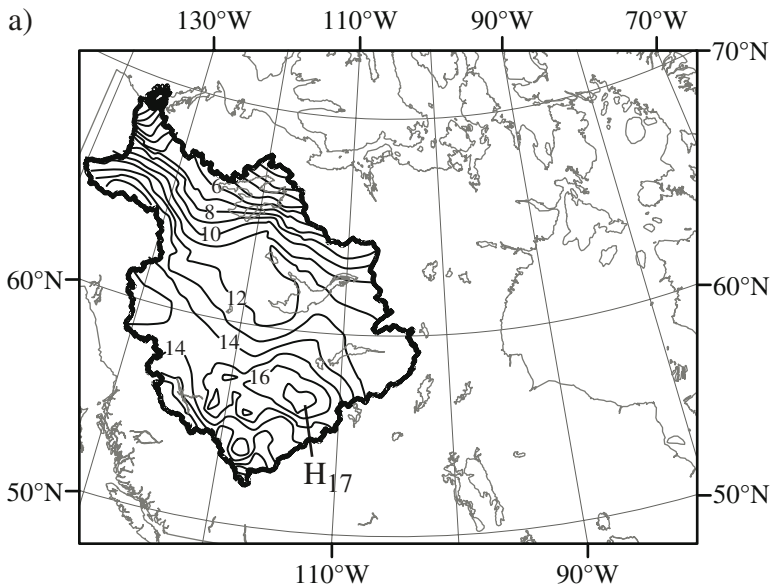

Fig. 5. Same as Fig. 4 except in February 1977

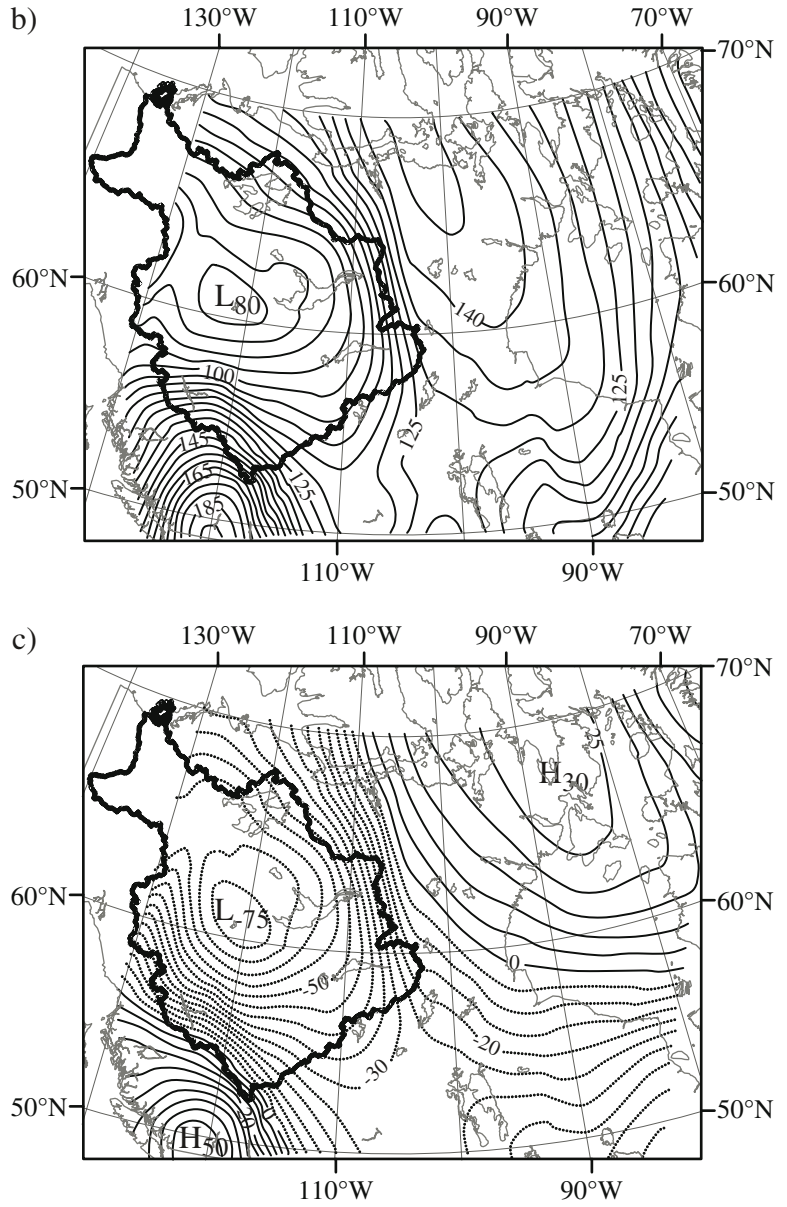

Fig. 5. (cont.)

the west and the south was likely to be stronger in this case since the gradients of 1000-hPa geopotential height (Fig. 5b) were larger (Fig. 3b). In

both cases, a ridge to the southwest played an important role in the horizontal transport of warm air into the Basin.

December of 1986

This example also shows a strong link of the warming signal with a low pressure system in the MRB (Figs. 6a–b). Since horizontal winds are, as a first order approximation, determined by gradients of geopotential heights on a constant pressure surface, in a region of the intersection between the low pressure system and the ridge, the gradients are larger and so are the horizontal winds. Hence, the combination of the low pressure system in the Basin and the ridge to the southwest favored warm air advection into the Basin. The entire MRB experienced positive anomalies of surface air temperature with a maximum value of about 11 K, which occurred at the intersection between the low pressure system and the ridge (compare Fig. 6a with Fig. 6b).

3.2 Extratropical and Subpolar High Pressure Systems in the Vicinity of the MRB

Other types of circulation patterns, also associated with positive anomalies of surface air temperature, that occur near the MRB during the winter are extratropical and subpolar high pressure systems. Two cases are presented.

February of 1978

The positive anomalies (maximum of 12 K) of surface air temperature (Fig. 7a) were distributed in a symmetric manner across the MRB in that they mainly increased from the boundary of the Basin toward its center. Circulation over the MRB was dominated by an extratropical high pressure system (Fig. 7b) centered to the southeast of the Basin.

February of 1987

The entire Basin experienced substantial positive anomalies (3–12 K) of surface air temperature (Fig. 8a) which were likely influenced by at least two different pressure systems. In eastern MRB, temperature anomalies were associated with a high pressure system centered over the east of the Basin, whereas in the western sector, they were associated with a high pressure system located over the southern part of the Basin.

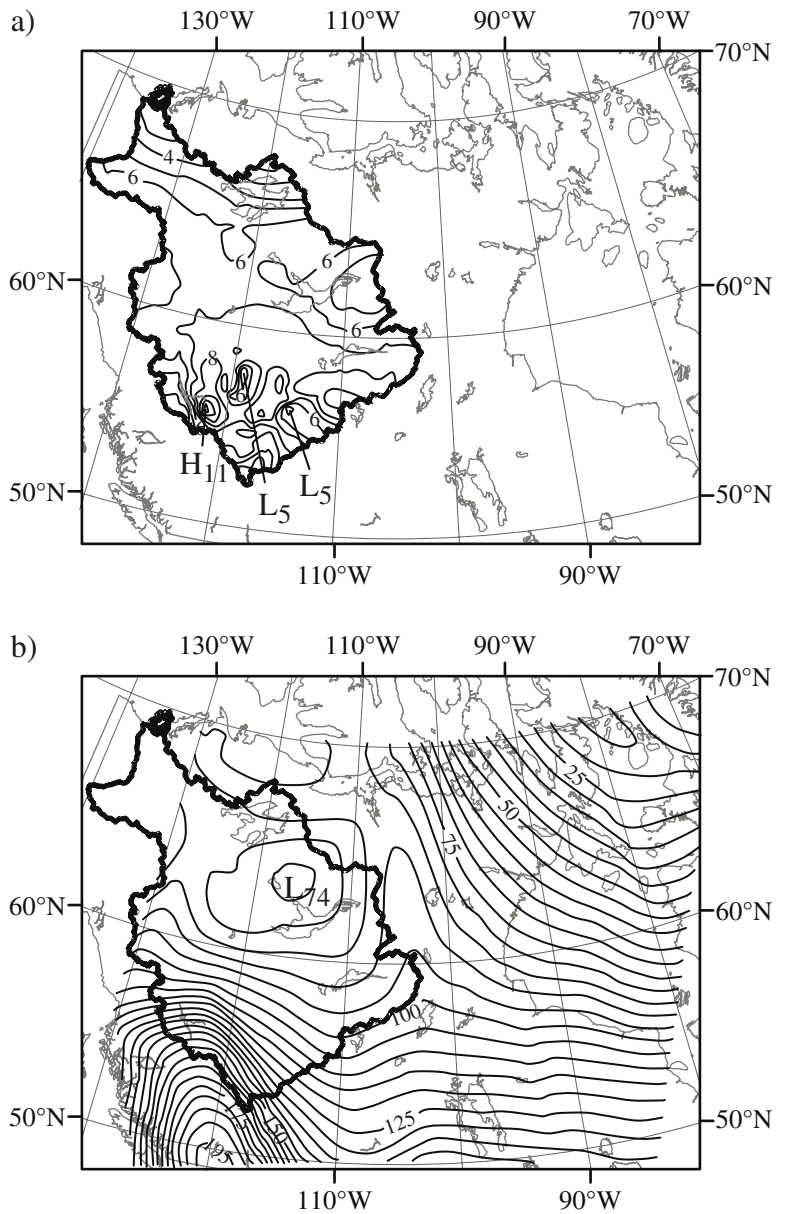

Fig. 6. Spatial distribution in December 1986 of (a) the anomaly of surface air temperature at an interval of 1 K, and (b) the monthly average of the 1000-hPa geopotential height at an interval of 5 gpm. Solid lines are the boundary of the Mackenzie River Basin

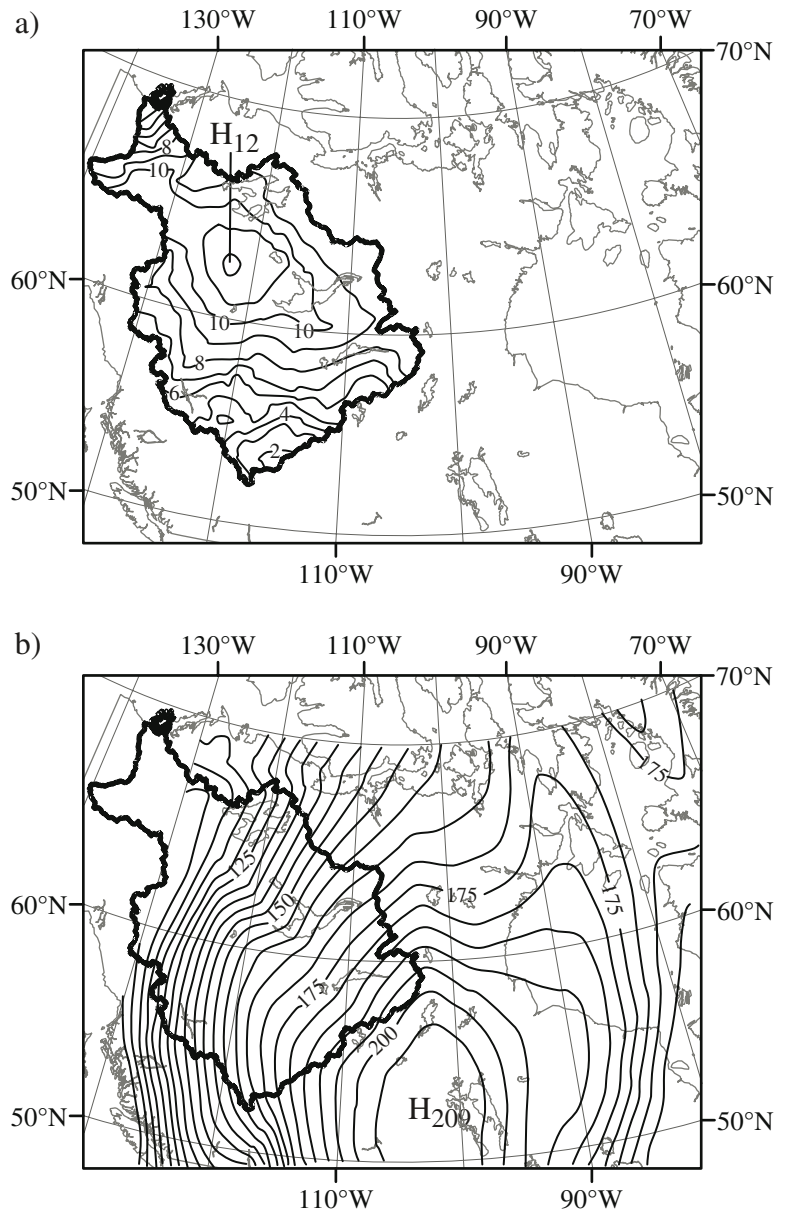

Fig. 7. Same as Fig. 6 except in February 1978

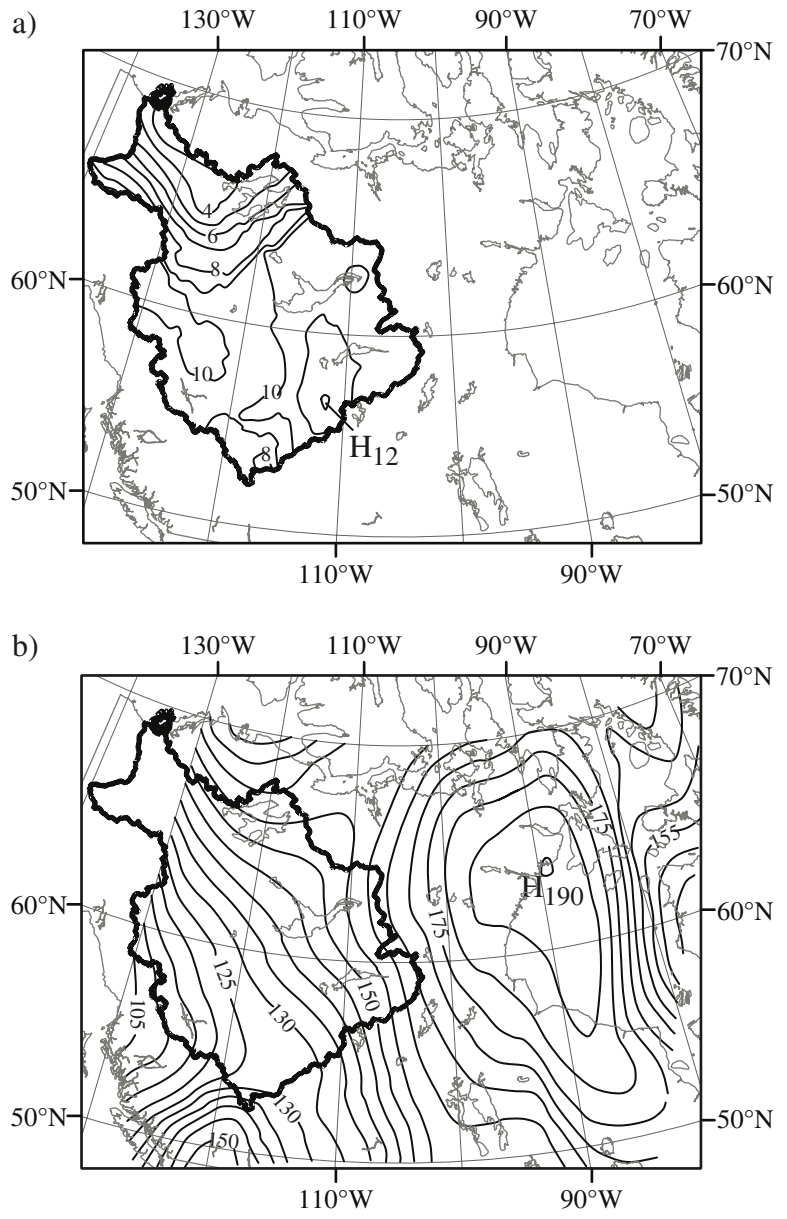

Fig. 8. Same as Fig.6 except in February 1987

3.3 Combined Systems of 3.1 and 3.2 Types

Anomalies of surface air temperature over the MRB basin in the winter are sensitive not only to the presence of different low/high pressure systems, but also to combinations of these systems. For example, in November 1968, a low pressure system developed in the Basin together with the occurrence of a high pressure system in the extratropical region (Fig. 9b). A deformation flow associated with these two systems was favorable for warm air advection. Consequently, the whole MRB experienced positive surface air temperature anomalies, with a maximum value of 3 K (Fig. 9a).

4 Discussions

Positive anomalies of surface air temperature over the MRB in the winter are closely linked to the occurrence of quasi-stationary cyclones and anticyclones. Changes of circulation (Fig. 1b) associated with these quasi-stationary flows lead to substantial changes in temperature through heat advection into high latitudes of Northern America, particularly over the MRB. The changes of these quasi-stationary cyclones and anticyclones are well simulated by the Geophysical Fluid Dynamics Laboratory coupled ocean-atmosphere GCM in a global warming scenario with gradually increasing CO_2 amount (Stephenson and Held 1993). They found that a large part of the change is associated with an equivalent-barotropic stationary wave with a high over eastern Canada and a low over southern Alaska.

Circulation over the MRB is frequently modified by two important elements: the topography and the low-level temperature inversion. As a forcing, the topography is usually considered to provide upward or downward motion over the Basin, which has a significant impact on the surface air temperature anomaly through vertical advection and adiabatic cooling or heating. The topographically-induced vertical velocity ω is highly dependent on the gradient of the terrain height along the horizontal wind direction as well as on the magnitude of the horizontal velocity v_h:

$$\omega = -\rho g \vec{v}_h \cdot \nabla h \tag{1}$$

where the data of terrain height h are obtained from the Canadian Regional Finite Element (RFE) model output fields archived for the Mackenzie GEWEX Study.

During the winter, the MRB often experiences a temperature inversion in the lower troposphere up to about 700 hPa, and the circulation systems

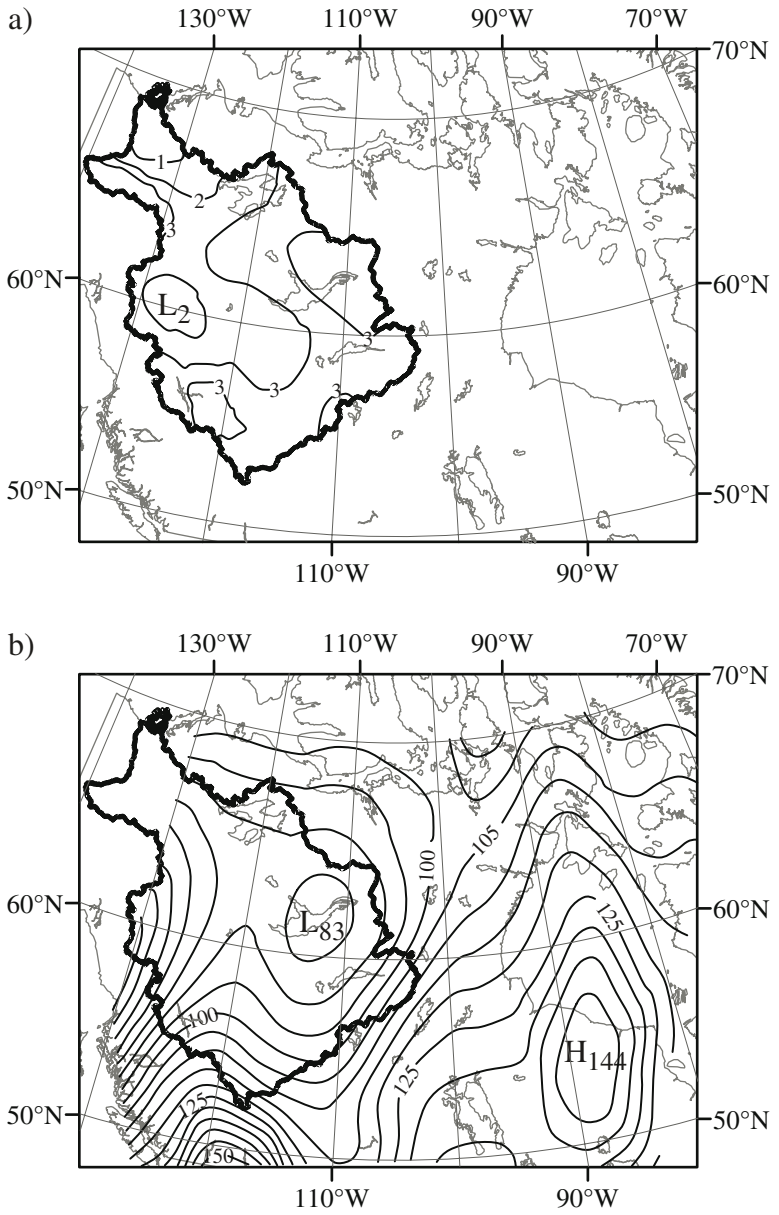

Fig. 9. Same as Fig. 6 except in November 1968

are consequently very shallow under the constraint of this temperature structure. The anomalies of surface air temperature are then influenced by the combined effects of the circulation systems, the topography, and the temperature inversion. The topography and the temperature inversion modify the circulations while the modified circulations in turn affect the surface air temperature anomalies.

Figure 10 shows vertical cross sections along 57^{o}N in December 1987 of the monthly-averaged temperature, vertical velocity, velocity vectors and their anomalies with zonal and vertical wind components. The vertical motion is computed from the horizontal divergence by vertically integrating the continuity equation, except the topographically-induced vertical velocity is calculated using Eq. (1). It is evident that there was a low-level temperature inversion, with maximum strength at 850 hPa, over most areas of the MRB (Fig. 10a). The low pressure system was very shallow and the updraft associated with it was, to a large extent, confined below 700 hPa (Fig. 10b). The effect of adiabatic cooling was therefore less important than the other factors such as horizontal advection. Downward motion occurred in a very shallow layer (Figs. 10b–c) with significant values (-1.0 to -2.5 cm s^{-1}) mainly between 850 hPa and 700 hPa. This descending motion was induced through interactions among the low pressure system, the topography, and the low-level temperature inversion.

One factor contributing to the vertical motion is the interaction between the low-level temperature inversion and the topography. Klemp and Lilly (1975) showed that lee waves can be trapped and amplified by a strong elevated inversion to generate severe wind storms. Carruthers and Choularton (1982) noted that a much thicker and more intense inversion layer can lead to more rapid descent down the lee side. This situation frequently occurs over the MRB since the inversion layer is typically well positioned in the region of the downward motion (compare Fig. 10a with Fig. 10c).

In addition, vertical motion is enhanced when the low pressure system and the inversion simultaneously occur over the mountainous basin. To understand this, we have calculated the total velocity anomalies for the warming event of December 1987. Fig. 10d shows anomalies of velocity with zonal and vertical components. An interesting feature is a return flow. Due to the inversion, the anomalous easterly flow associated with the low pressure system is enhanced near the top of the inversion. As the anomalous easterly wind was bounded by the mountains, an anomalous return flow was formed at a lower level. This return flow also made a positive contribution to the descending motion on the lee side of the mountains.

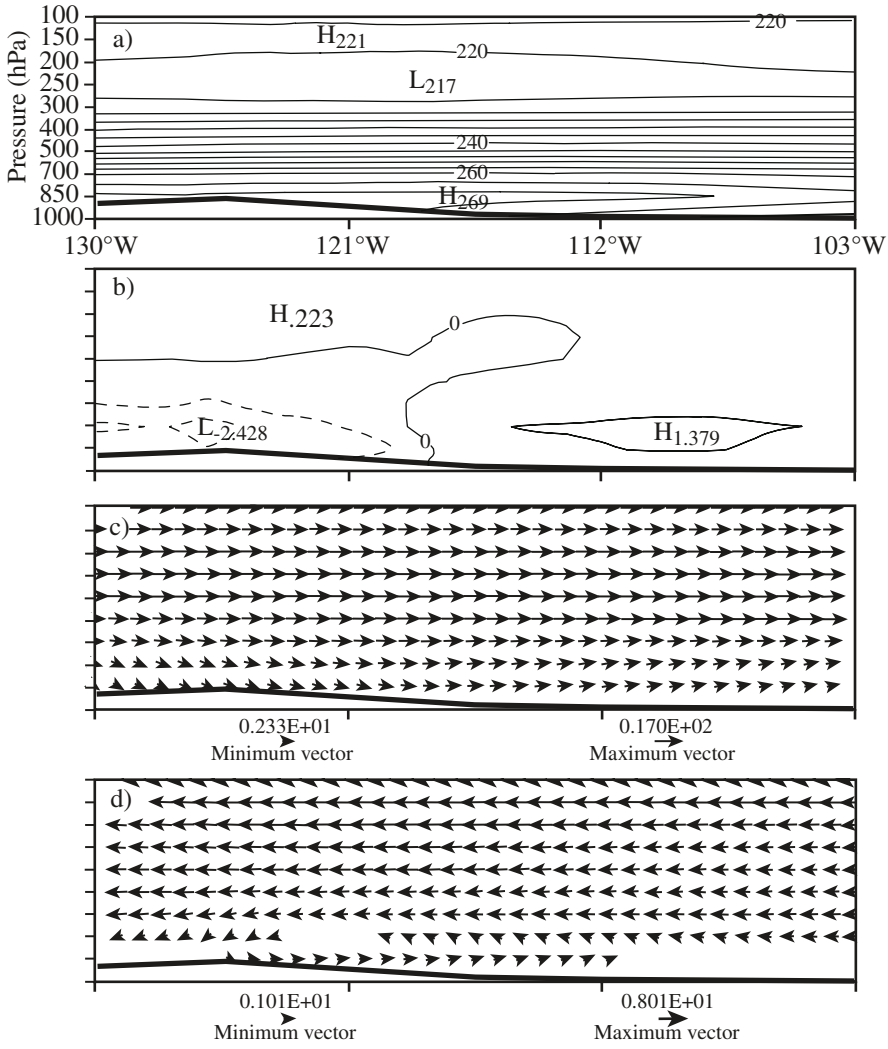

Fig. 10. Vertical cross sections along 57ºN in December 1987 of (a) monthly-averaged temperature with isoline interval of 4 K, (b) monthly-averaged vertical velocity with the isoline interval of 1 cm s^{-1} (solid and dashed lines denote upward and downward motions, respectively), (c) monthly-averaged velocity vectors with zonal and vertical components, and (d) anomalies of velocity vectors with zonal and vertical components. To show vectors in (c) and (d) clearly, the vertical components of velocity vectors are multiplied by a factor of 100 (i.e., vertical components of velocity vectors are in cm s^{-1} whereas zonal components are in m s^{-1}). The darker solid lines are outlines of the mountains

5 Concluding Remarks

Extreme warming events during the winter over the MRB are examined using surface and rawinsonde observations, with particular attention given to their relation with atmospheric circulations in and near the Basin. Basin warming is mainly associated with low pressure systems in the MRB, and high pressure systems adjacent to extratropical and subpolar regions. As summarized in Fig. 11, the warming is mainly attributed to horizontal advection of warm air from west and south of the Basin, and to the adiabatic heating induced by topography and the circulation systems. Further examination of the warming events suggests that interactions among the circulation systems, the topography, and the low-level temperature inversion are also critical. It was found that the surface-level descending motion induced by the topography leads to significant warming over the Basin.

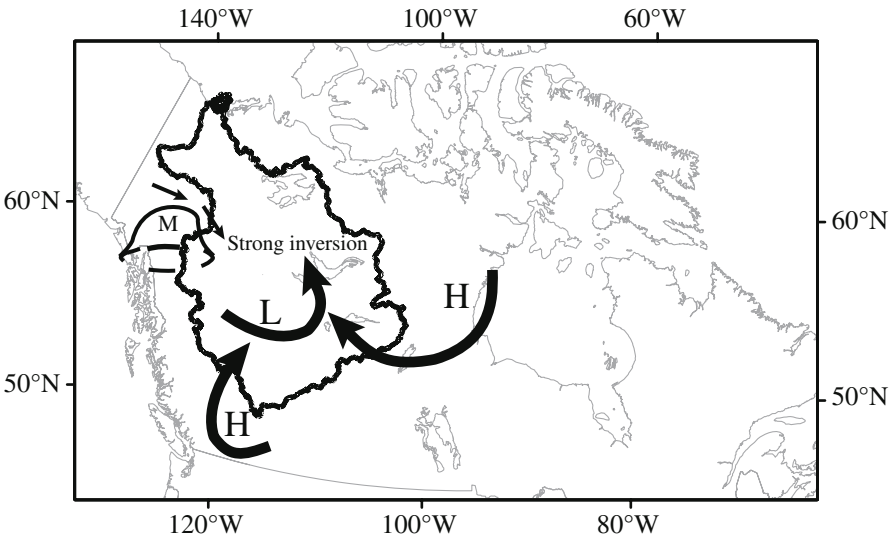

Fig. 11. Schematic diagram showing physical processes responsible for extreme winter warming events over the Mackenzie River Basin. H and L represent high and low pressure systems, respectively, and large arrows indicate the flows associated with these systems. Small arrows indicate descending motion associated with the mountains (labeled M)

As a complement to the present study, all winter cooling events over the MBR in the last few decades were examined though the results are not presented here. The main finding is that almost all of the cooling events were related to high pressure systems that originated in the polar regions,

and these systems advected cold polar air into the region where there was either a weak or no low-level temperature inversion. It is interesting to note that the warming and the cooling events are linked with different circulation systems, and they are also linked with different intensities of low-level temperature inversion.

The cloud fields over the MRB should also contribute somewhat to the observed temperature anomalies. For example, a climatological study by Stewart and Burford (2002) indicated that extreme winter warming events were often associated with more extensive cloud and lower cloud base than average. Such cloud characteristics would act to trap more radiation and therefore to increase temperatures in tandem with the dynamic and thermodynamic considerations discussed in this chapter. In contrast, Hudak et al. (2004) and Stewart et al. (2004) observed an extreme winter warming event (December 1998) with a cloud radar (Hudak et al. 2007). They found that the cloud fraction was less than normal and concluded, for this case, that dynamical factors such as discussed by Cao et al. (2001) must have been the dominant factors that led to the observed warming.

In summary, this study has shown that extreme winter warming events over the MRB are associated with distinct patterns in regional scale circulations that are modified by regional topography and the low-level temperature inversion. The modified circulations in turn influence the surface air temperature anomalies.

Acknowledgments

This research was supported by the Mackenzie GEWEX Study (MAGS) and the Panel on Energy Research and Development (PERD). We thank Paul Louie for generously providing us with Fig. 1a. Thanks are also extended to Walter Skinner for his valuable discussions, and to Robert Crawford for assisting with topographic information.

References

ACIA (2004) Scientific Report, Cambridge University Press

Akima H (1978) A method of bivariate interpolation and smooth surface fitting for irregularly distributed data points. ACM TOMS 4:148–159

Alaka MA, Elvander RC (1972) Optimum interpolation from observations of mixed quality. Mon Weather Rev 100:612–624

Beniston M, Rebetez M (1996) Regional behavior of minimum temperature in Switzerland for the period 1979–1993. Theor Appl Climatol 53:231–243
Beniston M, Rebetez M, Giorgi F, Marinucci MR (1994) An analysis of regional climate change in Switzerland. Theor Appl Climatol 49:35–159
Cao Z, Stewart RE, Hogg W (2001) Extreme winter warming events over the Mackenzie Basin: dynamic and thermodynamic contributions. J Meteorol Soc Jpn 79:785–804
Carruthers DJ, Choularton TW (1982) Airflow over hills of moderate slope. Q J Roy Meteor Soc 108:603–624
Diaconis P, Efron B (1983) Computer-intensive methods in statistics. Sci Am 248:116–130
Efron B (1982) The jackknife, the bootstrap and other resampling plans. SIAM
Elsner JB, Tsonis AA (1991) Comparisons of observed Northern Hemisphere surface air temperature records. Geophys Res Lett 18(7):1229–1232
Hansen J, Lebedeff S (1987) Global trends of measured surface air temperature. J Geophys Res 20:13345–13372
Hobbs PV, Locatelli JD, Martin JE (1996) A new conceptual model for cyclones generated in the lee of the Rocky Mountains. B Am Meteorol Soc 73:1962–1970
Hudak D, Currie B, Stewart RE, Rodriguez P, Burford J, Bussieres N, Kochtubajda B (2004) Weather systems occurring over Fort Simpson, Northwest Territories, Canada during three seasons of 1998/99. Part 1: cloud features. J Geophys Res 109, D22108, doi:10.1029/2004JD004876
Hudak D, Stewart R, Rodriguez P, Kochtubajda B (2007) On the cloud and precipitating systems over the Mackenzie Basin. (Vol. I, this book)
IMSL (1989) User's Manual, IMSL Math Library, Houston, Texas
Ingram WJ, Wilson CA, Mitchell JFB (1989) Modeling climate change: an assessment of sea ice and surface albedo feedbacks. J Geophys Res 94:8609–8622
IPCC (1990) Climate change, IPCC Scientific Assessment, Cambridge University Press, Cambridge
IPCC (1992) Climate change 1992, The Supplementary Report to the IPCC Scientific Assessment, Cambridge University Press, Cambridge
IPCC (2001) Climate change 2001: the scientific basis. Cambridge University Press, Cambridge
Jones PD, Raper SCB, Bradley RS, Diaz HF, Kelly PM, Wigley TML (1986) Northern hemisphere surface air temperature variations: 1851–1984. J Clim Appl Meteorol 23:1520–1530
Karl TR, Jones PD (1989) Urban bias in area-averaged surface air temperature trends. B Am Meteorol Soc 67:1370–1377
Klemp JB, Lilly DK (1975) The dynamics of wave-induced downslope winds. J Atmos Sci 32:320–339
Legates DR, Willmott CJ (1990) Mean seasonal and spatial variability in global surface. Theor Appl Climatol 41:11–21

Majorowicz JA, Skinner WR (1997) Anomalous ground warming versus surface air warming in the Canadian prairie provinces. Climatic Change 35:485–500

Manabe S, Stouffer RJ (1980) Sensitivity of a global climate model to an increase of CO_2 concentration in the atmosphere. J Geophys Res 85:5529–5554

Milliman JD, Meade RH (1983) World-wide delivery of river sediment to the oceans. J Geol 91:1–21

Mitchell JM Jr (1953) On the causes of instrumentally observed secular temperature trends. J Meteorol 10:244–261

Murata A (1993) Monthly-mean temperature anomalies in relation to spatial scale in Japan. Int J Climatol 13:329–341

NCAR Graphics (1995) User's guide for NCAR GKS-0A graphics. NCAR Scientific Computing Division, 80307–3000

Pilifosova OV, Eserkepova IB, Dolgih SA (1997) Regional climate change scenarios under global warming in Kazakhstan. Climatic Change 36:23–40

Przybylak R (1997) Spatial and temporal changes in extreme air temperatures in the Arctic over the period 1951–1990. Int J Climatol 17:615–634

Robeson S (1993) Spatial interpolation, network bias, and terrestrial air temperature variability. C. W. Thornthwaite Associates, New Jersey

Soulis ED, Solomon SI, Lee M, Kouwen N (1994) Changes to the distribution of monthly and annual runoff in the Mackenzie Basin under climate change using a modified square grid approach. Proc 6th Biennial AES/DIAND meeting on northern climate and mid study workshop of the Mackenzie Basin impact study, Yellowknife, NWT, Canada, pp 197–209

Stephenson DB, Held IM (1993) GCM response of northern winter stationary waves and storm tracks to increasing amounts of carbon dioxide. J Climate 6:1859–1870

Stewart RE, Burford JE (2002) On the features of clouds occurring over the Mackenzie River Basin. J Geophys Res 107(D23):4720, doi:10.1029/2001JD001559

Stewart RE, Burford JE, Hudak DR, Currie B, Kochtubajda B, Rodriguez P, Liu J (2004) Weather systems occurring over Fort Simpson, Northwest Territories, Canada during three seasons of 1998/99. Part 2: precipitation features. J Geophys Res 109, D22109, doi: 10.1029/2004JD004929

Stewart RE, Leighton HG, Marsh P, Moore GWK, Rouse WR, Soulis ED, Strong GS, Crawford RW, Kochtubajda B (1998) The Mackenzie GEWEX Study: the water and energy cycles of a major North American river basin. B Am Meteorol Soc 79:2665–2683

Szeto KK (2007) Variability of cold-season temperatures in the Mackenzie Basin. (Vol. I, this book)

Wallace JM, Zhang Y, Bajuk L (1996) Interpretation of interdecadal trends in northern hemisphere surface air temperature. J Climate 9:249–259

Wallace JM, Zhang Y, Renwick JA (1995) Dynamic contribution to hemispheric mean temperature trends. Science 270:780–783

Woo MK, Rouse WR, Stewart RE, Stone JMR (2007) The Mackenzie GEWEX Study: a contribution to cold region atmospheric and hydrologic sciences. (Vol. I, this book)

Yamamoto R, Hoshiai M (1980) Fluctuations of the northern hemisphere mean surface air temperature during recent 100 years estimated by optimum interpolation. J Meteorol Soc Jpn 58:187–193

Chapter 6

Water Vapor Fluxes over the Canadian Prairies and the Mackenzie River Basin

Jinliang Liu, Ronald E. Stewart and Kit K. Szeto

Abstract This paper examines water vapor flux features over the Mackenzie River Basin (MRB) and the Canadian Prairies, primarily the Saskatchewan River Basin (SRB). The long-term (1948–2001) climatology of the atmospheric moisture fluxes of the SRB is investigated and then compared with that of the MRB. In addition, moisture transport and associated hydrometeorological features during an extreme climate event, the 2000–01 severe drought over the Prairies, are discussed.

While the Pacific and Arctic Oceans are two main moisture sources for the MRB, these oceans as well as the Gulf of Mexico, the Gulf of California, and Hudson Bay are moisture sources for the SRB. Significant differences between the two regions are also found in the detailed vertical profiles of moisture transport. Topography and surface properties are key factors causing such differences. However, there are connections between them through seasonal moisture exchange across the shared boundary.

1 Introduction

Water vapor transport into and out of a region significantly influences its climate. Extensive water budget analyses have been carried out over several regions around the world, including the Arctic (Cullather et al. 2000; Serreze et al. 1995; Walsh et al. 1994), the Mississippi River basin (Betts et al. 1999; Roads 2002; Roads and Betts 2000; Roads et al. 1998, 2002; and many others), and the Mackenzie River Basin (MRB) (Betts and Viterbo 2000; Cao et al. 2002; Liu et al. 2002; Proctor et al. 1999; Roads 2002; Roads et al. 2002; Smirnov and Moore 1998; Stewart et al. 1998, 2002; Strong and Proctor 1998; Walsh et al. 1994). Many of these studies are parts of the Global Energy and Water Cycle Experiment (GEWEX) (Lawford et al. 2004).

While the MRB has a common boundary with the Saskatchewan River Basin (SRB) of western Canada, little research has been carried out over the SRB which is one of the most ecologically diverse areas in North

America (http://www.saskriverbasin.ca/STORY/index.htm). The Saskatchewan River is Canada's fourth longest river and its basin is an international watershed that spans more than 420 000 km^2, encompassing parts of three Canadian Prairie provinces and parts of Montana. This basin is bounded by the Rocky Mountains to the west, the boreal forest to the north and east, and grassland and agricultural land to the south. To the north, the SRB shares a boundary with the MRB, and it is natural to compare these two basins in terms of their water vapor fluxes.

The SRB is situated mostly in a dry region (Bullas 2001; Hare and Thomas 1979; Kendrew and Currie 1955; Longley 1972; Phillips 1990), but only a limited number of studies have approached the aridity problem from the water vapor budget perspective. There were case studies at hourly and daily scales (Barr and Strong 1996; Strong 1996) based on data obtained during the Regional Evapotranspiration Study (RES), focusing on diurnal features of local water vapor fluxes. Raddatz (2000) investigated rainfall recycling in the Canadian Prairies for three summers (1997–99) and concluded that these were dry periods according to both recycling model results and water budget estimates from the gridded data of the Canadian Global Environment Multiscale model (GEM) (Côté et al. 1998).

The present study addresses two aspects of the atmospheric moisture transport that affect the Canadian Prairies: their long-term (1948–2001) climatology and their anomalous features and characteristics during an extreme hydroclimate event in 2000–01 when a severe drought occurred. Drought is a chronic concern in Canada but rarely has it been as serious or extensive as in 2001. According to Phillips (2002), for the western and central Canadian Prairies, "… it was the worst of times. Even in the dust bowl of the 1930s, no single year between Medicine Hat, Kindersley and Saskatoon was drier than in 2001. Astonishingly, Saskatoon was 30% drier this year than any other over the last 110 years". The 2000–01 drought inflicted agricultural and economic losses – for Saskatchewan alone the damage was in the range of $4–5 billion, if a multiplier effect is applied (Garnett 2002).

This study examines three aspects in relation to water vapor transport in western Canada: (1) long-term pattern over the SRB, (2) comparison with conditions over the MRB, and (3) transport features during the severe 2000–01 drought over the western and central Canadian Prairies.

2 Data and Methodology

The National Center for Environmental Prediction (NCEP) and the National Centre for Atmospheric Research (NCAR) have produced reanalysis datasets for many years using a frozen state-of-the-art global data assimilation system (Kalnay et al. 1996; Kistler et al. 2001). This study uses four atmospheric variables (four times daily, or six-hourly data) from the NCEP T62/28-level global spectral model: the specific humidity, q; the west-east wind, u; the south-north wind, v; and the surface pressure, Ps. Variables u, v, and q are located on a 144×73 horizontal grid with a resolution of 2.5×2.5 degrees of latitude by longitude, and on 8 levels in the vertical, 1000, 925, 850, 700, 600, 500, 400, 300 hPa because above 300 hPa, the air is very dry and contributes little to water vapor transport.

On a specific pressure level, moisture flux is the product of the specific humidity q and the horizontal wind vector V defined as

$$\vec{Q} = q\vec{V} = qu\,\vec{i} + qv\,\vec{j} \tag{1}$$

where u and v are respectively the zonal and meridional wind components of the horizontal wind field. Consequently, qu and qv are usually called, respectively, zonal and meridional moisture transport.

Vertical integration of moisture fluxes across the four main boundaries is calculated by integrating qu and qv with respect to pressure along corresponding boundaries:

$$\vec{Q}_{\varphi} = -\frac{1}{g}\int_{1000}^{300}(qu)dp \quad \text{along the western and eastern boundaries} \tag{2}$$

and

$$\vec{Q}_{\lambda} = -\frac{1}{g}\int_{1000}^{300}(qv)dp \quad \text{along the southern and northern boundaries.} \tag{3}$$

Note that surface pressure (P_s) is used to recognize whether the lower levels are below ground and if so, the underground levels do not contribute to these integrations.

3 Results

3.1 Long-term Moisture Fluxes Features over the Saskatchewan River Basin

There have been no previous investigations on moisture fluxes and transports over the SRB. This section focuses on such an analysis, including moisture sources and the horizontal and vertical variations of the fluxes and their annual cycles.

3.1.1 Vertically-integrated Moisture Fluxes

The vertically integrated water vapor fluxes into (negative) or out of (positive) the basin across the four main boundaries were analyzed. It is found that there are always moisture influxes to the basin from the west, and moisture effluxes across the eastern boundary, with the overall magnitude of the effluxes exceeding that of the influxes.

In the south-north direction, moisture transport is much more complex, and the nature of moisture fluxes changes from month to month across the northern and southern boundaries of SRB. Across the southern boundary, influxes occur only in early summer and effluxes occur in other months. In contrast, across the northern boundary, effluxes occur only in early summer with influxes during all other months. These features are clearly seen in the annual cycles. The net moisture gain or loss in the south-north direction is determined by the balance of the moisture transport across the southern and northern boundaries.

The 54-year normals of the summer zonal and meridional moisture transport show that the zonal transport increases from west to east (i.e., the magnitude of the effluxes at the eastern boundary of the basin exceeds that of the influxes at the western boundary from the Pacific Ocean). The meridional moisture transport shows a pronounced belt originating over the Gulf of Mexico and another relatively strong transport belt originating over the Gulf of California. This latter source is in agreement with the conclusion of Schmitz and Mullen (1996) that moisture at lower levels over this core region of the North American monsoon system is mainly derived from the Gulf of California. It is also found that the Gulf of California appears to be a more significant moisture source to the SRB during summer than the Gulf of Mexico, even though one would intuitively expect the opposite.

The long-term averaged monthly horizontal pattern of moisture transport reveals that the zonal transport has an almost uniform distribution

over the basin from November to May. This results in symmetry between the annual cycles of the moisture fluxes across the western and the eastern boundaries. A similar case occurs in the meridional moisture transport, in which the strong moisture transport belt from the Gulf of Mexico is also far away from the basin for the months mentioned above in the zonal transport. As well, the meridional moisture transport has an almost uniform distribution over the basin, leading to the symmetry between the moisture fluxes across the southern and the northern boundaries. These uniform horizontal distributions of the zonal and meridional moisture transport over SRB are not favorable for the basin to exhibit a significant moisture flux convergence.

Beginning in June, the strong zonal moisture transport belt extends further to the west and begins to influence the basin. With the horizontal distribution pattern in June, July, and August, substantial moisture convergence does not occur over the basin because it experiences small moisture inflows from the west but much larger outflows at the eastern boundary. This could in part be associated with the impact of the Western Cordilleras that block or slow down the zonal air flows, allowing only a limited amount of moisture to enter the basin. In most cases, much of the moisture is already lost to precipitation on the western side of the Cordillera and after passing over the mountains, the air flow in the lee is speeded up (Fig. 6 in Liu and Stewart 2003). Other dynamic or thermodynamic factors associated with gradients in pressure (or height) and temperature may also play a role. Of course, the influxes from the meridional direction must also affect this process in accordance with mass conservation.

As the strong zonal moisture transport belt extends to the west, the strong meridional transport belt expands northward and begins to affect SRB in May. Again, the Gulf of California is shown to be a more significant moisture source than the Gulf of Mexico during June, July, and August, though the contributions from these two gulfs cannot be easily and quantitatively separated because moisture influxes from the south are usually a combination from these two regions. From May to August, the basin gains moisture in the south-north direction because it experiences large moisture influxes across its southern boundary and smaller moisture effluxes across its northern boundary. In July and August, the intersection of the southward and northward meridional moisture transport results in net moisture gains over the basin in the south-north direction. Beginning in September, the strong meridional moisture transport belt initiated in the Gulf of Mexico changes its axis from south-north to southwest-northeast. This allows the southward meridional moisture transport band to move into the basin from the north. During this movement, the basin has a weak

net moisture gain in the south-north direction in September, but negligible gain in October and November.

3.1.2 Moisture Sources

The SRB has four moisture sources (Fig. 1):

1. The basin receives moisture from the Pacific Ocean in all seasons, though the amount varies with the season. Strong moisture transport occurs in summer and late autumn with the maximum attained in October. Relatively weak fluxes occur during other seasons, especially in late spring and early summer (February to May) when the zonal wind is usually weak over this region.
2. The Gulf of California and the Gulf of Mexico have a combined contribution from the south, especially in summer. The interannual variability of this moisture source is determined largely by the strength of the Great Plains low-level jet during the development of the North American monsoon system and the dynamic circulation pattern over this region. However, moisture influxes do not always occur across the thern boundary during summer, as happened in 1950 and 1992. In fact, there are a wide variety of situations. In some years, such influxes occur each month throughout the summer.
3. Hudson Bay becomes a moisture source for the basin when the synoptic pattern is such that the Bay is at the north of a deep low pressure system or at the south of a high pressure system. The strong northeasterly flow at the northwestern portion of the low pressure system or at the southeastern portion of the high pressure system brings moisture to the SRB (e.g., on June 4, 1998). Such instances are usually observed during late spring and early summer according to the 50+ years of analysis data (Liu and Stewart 2003).
4. The Arctic Ocean is a moisture source for the SRB during most months except the early summer. Moisture from the Arctic Ocean can reach the basin after passing over the MRB, as will be discussed in a later section.

3.1.3 Vertical Variation

Analysis of the vertical structure provides additional insights into moisture transport (Fig. 2). The shapes of the vertical profiles indicate that the magnitudes of the fluxes at the southern and northern boundaries do not change

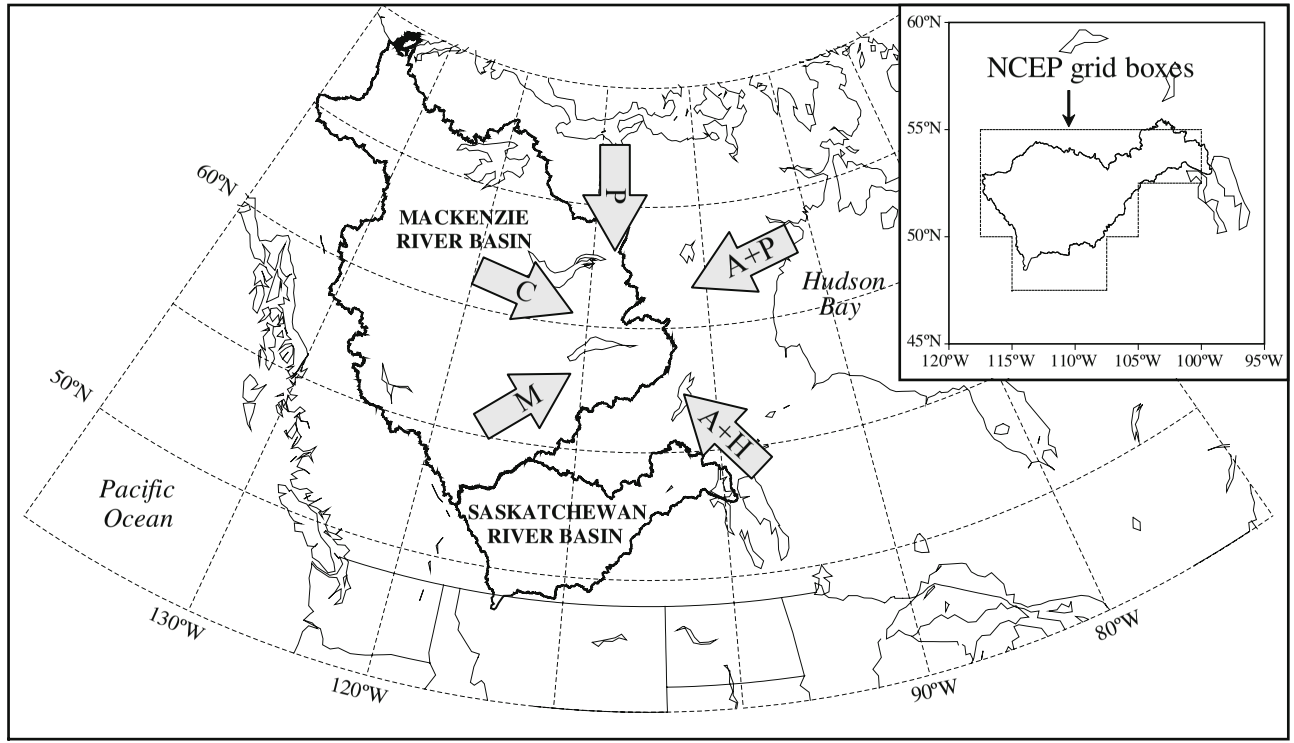

Fig. 1. Location of Saskatchewan River Basin (SRB) and its neighboring Mackenzie River Basin. Arrows show the moisture sources of the SRB; A, C, M, H, and P represent the moisture sources from the Arctic, Gulf of California, Gulf of Mexico, Hudson Bay, and Pacific Ocean, respectively. Also shown at the upper-right corner is a close-up of the SRB with the NCEP grid boxes used for calculation

much from month to month. However, the magnitudes of the western and eastern ones have substantial seasonal variations. Beginning in January, the profiles are being squeezed towards zero and the envelope becomes thinner and thinner until April and May when the profiles are most "compact". Then the envelope grows wider and becomes widest in July and August. After that, the envelope begins to become thinner again. This evolution is controlled more by the changes in zonal moisture transport than those in meridional transport. The net moisture flux for the basin shows an important feature. It indicates that moisture influxes occur above 700 hPa and moisture effluxes below this level.

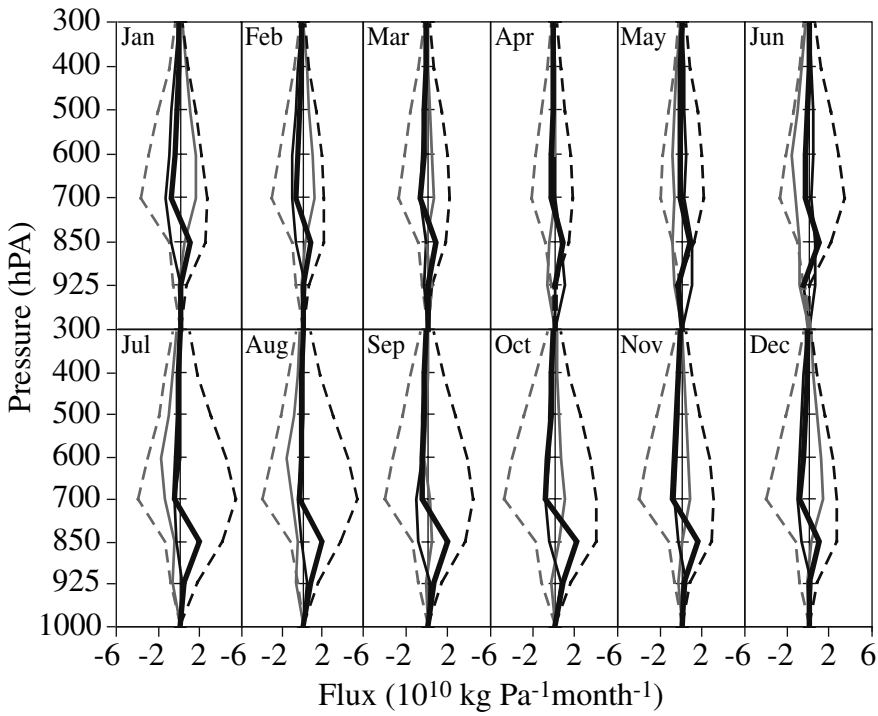

Fig. 2. Vertical profiles of the 40-year averaged (1962-2001) monthly mean moisture fluxes ($\times 10^{10}$ kg Pa^{-1} $month^{-1}$) at the four main boundaries of the Saskatchewan River Basin: west (grey dash), east (black dash), south (grey), north (black), and the net moisture flux (thick line). The vertical axis is pressure (hPa)

3.1.4 Comparison with the Mackenzie River Basin

While the Pacific Ocean is a moisture source for both MRB and the SRB (the P arrow in Fig. 1), other sources vary between these basins. The combination of the Gulf of California and the Gulf of Mexico is another major moisture source (the C and M arrows in Fig. 1) for the SRB in summer, though not always. As well, Hudson Bay is a moisture source for the SRB when the Bay is at the north of a low pressure system or at the south of a high pressure system (the A+H arrow in Fig. 1). However, no counter situations of Hudson Bay as a moisture source for the MRB have been found. During most seasons, the Arctic Ocean is also a source of moisture that reaches the SRB after passing over the MRB. The MRB has the Arctic Ocean as its other primary moisture source, and it sometimes also receives moisture from the Gulf of Mexico during summer.

Given a larger number of moisture sources, it appears that it is easier for the SRB to acquire moisture than the MRB. However, topography plays a major role in this regard. For example, the relatively flat topography of the Great Plains allows easy passage of the moisture from the Gulf of Mexico to reach the SRB without significant loss. Furthermore, the sloping topography (>2000 m at the west dropping to 300–500 m at the east) does not offer any topographic forcing on its easterly flank to initiate precipitation. In contrast, the topography of the MRB is much more complicated, especially in the wide upland area on its western flank. The west-east topographic profile of MRB is more concave and saucer-like (>2000 m at the west, <100 m in the middle and rising again to 300–500 m in the east) than that of the SRB, a shape that is more favorable for moisture convergence since, though small in concavity, it focuses onto a location for precipitation initiation.

Stewart (2000) and Cao et al. (2002) pointed out other effects of topographic features on the water cycle of the MRB. The blocking effect of the western mountainous topography is considered to contribute to the major differences between the two basins in low-level moisture advection (Fig. 3). The MRB experiences moisture influx at these levels, whereas the SRB basin experiences moisture efflux. Compared with the SRB, the western boundary of the MRB is much longer and therefore provides a greater potential to benefit from the Pacific Ocean moisture. As well, there are many mountain passes and valleys across the western boundary of the MRB through which moisture can be efficiently brought into the basin at relatively low levels (Cao et al. 2002). In contrast, the higher “wall-like” topographic barrier at the western border of the SRB does not possess such avenues for moisture flow, significantly reducing the amount of moisture

influx at low levels from the Pacific Ocean. These considerations cause contrasts between the two basins, determining whether moisture may be available and how much of it can reach the basins from the sources.

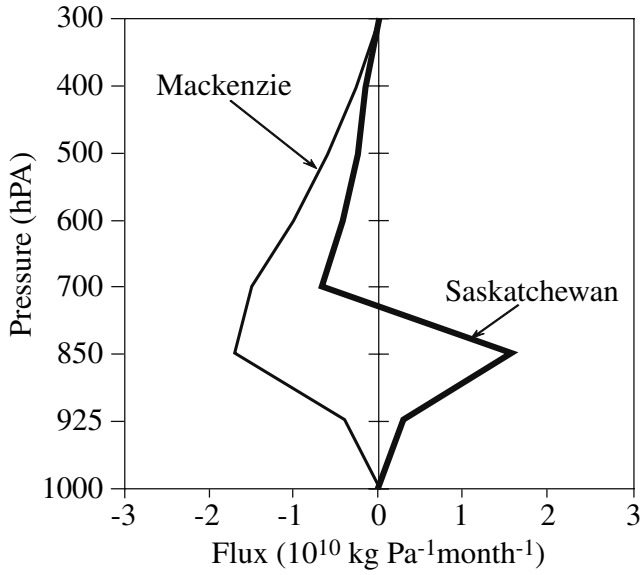

Fig. 3. Comparison of vertical profiles of annual mean net moisture fluxes ($\times 10^{11}$ kg Pa^{-1} $month^{-1}$) for the Mackenzie River Basin (thin line) and the Saskatchewan River Basin (thick line)

The two basins have a common boundary, with sections of the southern boundary of the MRB being the northern boundary of the SRB. There is naturally an excellent match between the calculated outflow from one basin with the calculated inflow to the other across the shared boundary (Fig. 4.) In particular, the SRB gains moisture from the MRB in all months except April, May, and June, and the MRB receives moisture from the SRB in these three months. Proctor et al.'s (1999) study of 1994–99 noted that the MRB usually loses moisture across its southeastern or southern boundary in all months except June. The absence of influxes in April and May in their result is likely due to different sample lengths for the calculations.

In terms of interannual variation, the MRB gains much more moisture from its environment (Liu et al. 2002) than does the SRB. Assuming that long-term averaged moisture convergence is equal to long-term averaged discharge, long-term annual average of convergence is 176 mm over the MRB, but only 50 mm over the SRB.

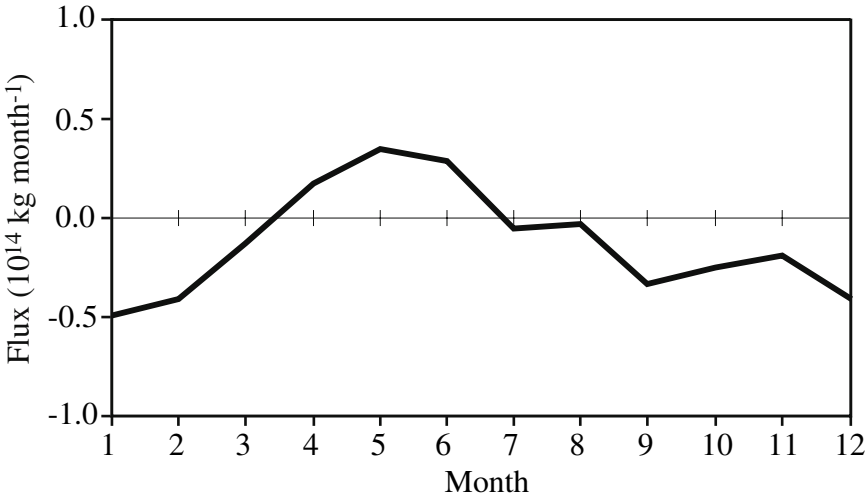

Fig. 4. Annual cycle of moisture flux ($\times 10^{14}$ kg month^{-1}) across the shared boundary between Saskatchewan River Basin in the south and Mackenzie River Basin in the north

3.2 Moisture Fluxes Features during the 2000–01 Severe Drought over the Prairies

Precipitation anomalies for the 2000–01 agriculture year (AY) showed the prevalence of dry conditions over the western and central Canadian Prairies whereas wetter conditions occurred in the eastern region (Fig. 4). This section analyses the moisture transport and associated hydrometeorological features during this drought (see Liu et al. 2004 for additional information).

3.2.1 Relative Importance of Different Moisture Sources

Correlation between monthly precipitation amounts and moisture influxes from different sources shows that moisture from the Pacific Ocean is more important to the winter precipitation over the western and central Prairies; whereas moisture from the Gulf of Mexico is more important than that from the Pacific Ocean during other seasons, especially summer when convection is common. A similar conclusion is reached when correlating seasonally averaged precipitation with moisture transport. This implies that most of the moisture for precipitation over the western and central Ca-

nadian Prairies is from the Pacific Ocean in winter and from the Gulf of Mexico in summer. The likelihood of a severe drought over the western and central Prairies becomes much higher when there is significantly reduced zonal moisture transport into the continent during the winter followed by greatly reduced meridional moisture transport during spring and summer. These conditions occurred with the severe drought of 2000–01.

Within the 54 year period from 1954 to 2001, the winter of 2000–01 AY experienced the most significantly reduced moisture transport from the Pacific Ocean. The moisture transport from the Gulf of Mexico during this period was not much enhanced and therefore did not compensate for the deficiency in the zonal transport. In the following summer the moisture transport from the Pacific Ocean was slightly higher than normal whereas the moisture transport from the Gulf of Mexico was below normal. However, this slightly enhanced moisture transport from the Pacific Ocean did not offset the adverse effect of the reduced meridional influxes on summer precipitation over the region.

3.2.2 Spatial Variation of Moisture Transport

The averaged zonal moisture transport anomalies clearly show that, during the winter, a reduced zonal moisture transport band extended across the middle and southern portions of the North American continent from coast to coast (Fig. 5a). The north-south extension of this band at the West Coast was from the Gulf of California to 55°N. Furthermore, these reduced anomalies were above the 90% significance level for the winter (Fig. 5b). In other words, the zonal moisture transport from the Pacific to the continent and the western and central Canadian Prairies was significantly less than normal during the winter of the 2000–01 AY. During the summer of 2001 there was enhanced zonal moisture transport from the Pacific Ocean (Fig. 5c) but this enhanced band extended only from 42.5°N to approximately 49°N (Fig. 5d). No significantly enhanced zonal moisture transport was observed over the Canadian Prairies.

A similar analysis of meridional moisture transport showed that the transport was significantly reduced during the 2000–01 winter over the areas at the southwest of, and a small portion of, the Canadian Prairies (Figs. 5e and 5f). There was enhanced moisture transport from the Gulf of Mexico and the Gulf of California but only the transport from the latter was notably enhanced. Moisture from the Gulf of Mexico, instead of being transported directly to the north, was diverted to the northeast and bypassed the Canadian Prairies (Fig. 5e). Moisture transport from the Gulf of Mexico into the continent was greatly reduced during the summer of 2001 (Figs.

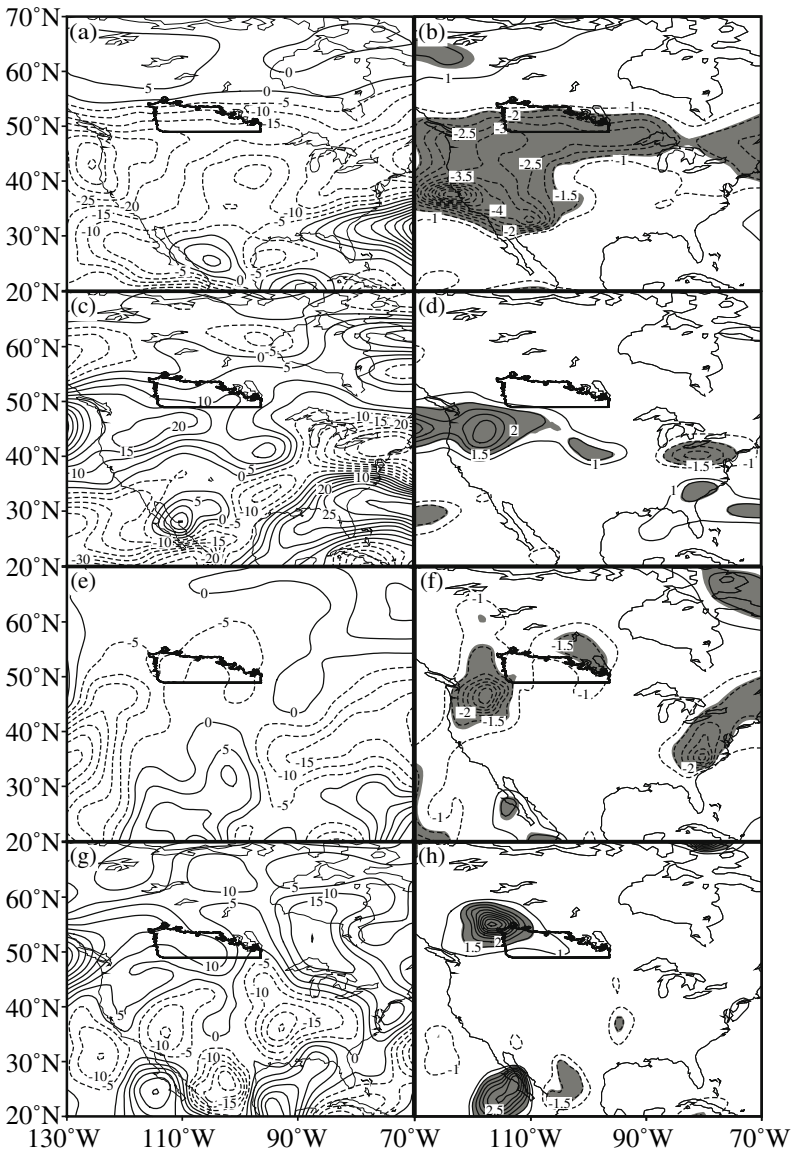

Fig. 5. Averaged zonal moisture transport anomalies (kg m^{-1} s^{-1}) during (a) the winter and (c) the summer of the 2000/01 AY; and the corresponding t-test scores, (b) for (a) and (d) for (c). Averaged meridional moisture transport anomalies (kg m^{-1} s^{-1}) during (e) the winter and (g) the summer of the 2000/01 AY; and the corresponding t-test scores, (f) for (e) and (h) for (g). The shaded areas in (b), (d), (f), and (h) are those with over 90% significance level. The location of the Canadian Prairies is also shown

5g and 5h). Moisture transport from the Gulf of California, though enhanced, did not extend far into the continent.

These features occurred in part due to extraordinarily strong high pressures which began in the winter of 2000 and persisted over much of the AY 2000–01. These high pressures blocked the zonal moisture influx into the western and central Prairies in the winter, and they were responsible for the extraordinarily strong subsidence that led to extremely warm summer conditions over the region. Collectively, these exceptional, interrelated atmospheric conditions contributed to the initiation and maintenance of the severe drought.

4 Conclusions and Discussion

Using reanalysis data from NCEP/NCAR, long-term (1948–2001) atmospheric moisture fluxes over the SRB were analyzed. The direction of the meridional moisture fluxes over this basin changes with seasons, but that of the zonal moisture fluxes does not. Moisture flows into the basin from the west (the Pacific Ocean) during all seasons. Moisture influxes from the south in early summer are usually related to the long-range meridional transport of water vapor from the Gulf of California and the Gulf of Mexico. Moisture flows into the basin from the north in all seasons except for late spring and early summer. The moisture outflow to the east mainly arises from the extensive zonal transport across the basin in all seasons, though this is most pronounced in late summer and autumn. The net moisture gain is determined by the balances among the influxes/effluxes at these boundaries which are controlled by dynamic circulation features.

Significant differences are found between the SRB and its adjacent MRB in terms of temporal and vertical variations of water vapor fluxes. Moisture influx occurs at all levels for the MRB but only above 700 hPa for the SRB. Topographic shape may play a major role in defining this feature. Moisture sources for these basins are somewhat different. The MRB has the Pacific Ocean and the Arctic Ocean as its primary sources, and it benefits from the Gulf of Mexico during early summer but our study has not found Hudson Bay as a moisture source. As two connected basins, the SRB receives moisture from the MRB over most of the year, but the MRB receives moisture from the SRB only in late spring and early summer when the meridional moisture transport from the Gulf of Mexico is strong.

The case study of the severe 2000–01 drought over the western and central Canadian Prairies revealed that most of the moisture for precipitation

over the region is from the Pacific Ocean in winter (November–March) and from the Gulf of Mexico in summer (May–August). The zonal moisture transport from the Pacific Ocean into the North American continent, including the Canadian Prairies, during the winter of the 2000–01agricultural year was the lowest over a 54-year period, and the low winter precipitation was not compensated by the summer moisture influx from the Gulf of Mexico. These moisture transport features were mainly associated with prolonged and extraordinarily strong anomalously high pressures over western North America and their related stronger-than-normal air mass sinking over the western and central Prairies and adjacent regions. Low winter moisture transport left the region with dry surface conditions for the growing season. The stronger-than-normal subsidence produced hot and dry surface air during the summer. These dynamic factors collectively caused the severe drought.

This study revealed that the semi-arid Saskatchewan Basin receives water vapor from several sources but it is subject to large swings in its water vapor fluxes that can sometimes lead to catastrophic droughts. Although contiguous with the Mackenzie Basin, differences between the Saskatchewan and the Mackenzie basins highlight some of the issues that need to be addressed when transferring results between large drainage basins.

Acknowledgments

This study was financially supported by Environment Canada and the Panel on Energy Research and Development (PERD).

References

Barr AG, Strong GS (1996) Estimating regional surface heat and moisture fluxes above prairie cropland from surface and upper-air measurements. J Appl Meteorol 35:1716–1735

Betts A, Ball JH, Viterbo P (1999) Basin-scale surface water and energy budgets for the Mississippi from the ECMWF reanalysis. J Geophys Res 104:19293–19306

Betts A, Viterbo P (2000) Hydrological budgets and surface energy balance of seven subbasins of the Mackenzie River from the ECMWF model. J Hydrometeorol 1:47–60

Bullas JM (2001) The climate of the Prairie Provinces (1961–1990): A review. Report AHSD-S2000-01, Environment Canada, Prairie and North Region

Cao Z, Wang M, Proctor BA, Strong GS, Stewart RE, Ritche H, Burford JE (2002) On the physical processes associated with the water budget and discharge of the Mackenzie Basin during 1994/1995 water year. Atmos Ocean 40:125–143

Côté J, Gravel S, Méthot A, Patoine A, Roch M, Staniforth A (1998) The operational CMC-MRB global environmental multiscale (GEM) model. Part I: design considerations and formulation. Mon Weather Rev 126:1373–1395

Cullather RI, Bromwich DH, Serreze MC (2000) The atmospheric hydrologic cycle over the Arctic basin from reanalysis. Part I: comparison with observations and previous studies. J Climate 13:923–947

Garnett R (2002) The Canadian Prairie drought of 2001: a four billion dollar shortfall. CMOS B 30:37–39

Hare FK, Thomas MK (1979) Climate Canada (2nd ed). John Wiley.

Kalnay E, Kanamitsu M, Kistler R, Collins W, Deaven D, Gandin L, Iredell M, Saha S, White G, Woollen J, Zhu Y, Chelliah M, Ebisuzaki W, Higgins W, Janowiak J, Mo KC, Ropelewski C, Wang J, Leetmaa A, Reynolds R, Jenne R, Dennis J (1996) The NCEP/NCAR 40-year reanalysis project. B Am Meteorol Soc 77:437–478

Kendrew WG, Currie BW (1955) The climate of central Canada. Queen's Printer, Ottawa

Kistler R, Kalnay E, Collins W, Saha S, White G, Woollen J, Chelliah M, Ebisuzaki W, Kanamitsu M, Kousky V, Van Den Dool H, Jenne R, Fiorino M (2001) The NCEP/NCAR 50-year reanalysis: monthly means CD-ROM and documentation. B Am Meteorol Soc 82:247–267

Lawford RG, Stewart RE, Yasunari T, Isemer HJ, Manton M, Marengo J, Koike T, Benedict S, Kabat P, Lebel T, Roads J, Try P (2004) Advancing global and continental scale hydrometeorology: a summary of the contributions of the GEWEX Hydrometeorology Panel (GHP). B Am Meteorol Soc 85:1917–1930

Liu J, Cho HR, Stewart RE (2002) Characteristics of the water vapour transport over the Mackenzie River Basin during the 1994-95 water year. Atmos Ocean 40:101–111

Liu J, Stewart RE (2003) Water vapor features over the Saskatchewan River Basin. J Hydrometeorol 4:944–959

Liu J, Stewart RE, Szeto KK (2004) Moisture transport and other hydrometeorological features associated with the severe 2000/01drought over the western and central Canadian. J Climate 17:305–319

Longley RW (1972) The climate of the Prairie Provinces. Climatological Studies, No. 13, Environment Canada

Phillips DW (1990) The climates of Canada. Environment Canada

Phillips DW (2002) The top ten Canadian weather stories for 2001. CMOS B 30:19–23

Proctor BA, Wang M, Strong GS, Smith CD (1999) Atmospheric moisture budgets for MAGS. Proc 5th Scientific workshop for the Mackenzie GEWEX Study, November 21–23, 1999. Edmonton, Alberta, pp 117–124

Raddatz RL (2000) Summer rainfall recycling for an agricultural region of the Canadian Prairies. Can J Soil Sci 80:367–373

Roads J (2002) Closing the water cycle. GEWEX Newsletter 12, pp 6–8

Roads J, Betts A (2000) NCEP-NCAR and ECMWF reanalysis surface water and energy budgets for the Mississippi River Basin. J Hydrometeorol 1:88–94

Roads J, Chen S-C, Kanamitsu M, Juang H (1998) Vertical structure of humidity and temperature budgets over the Mississippi River Basin. J Geophys Res 103(D4):3741–3759

Roads, J, Kanamitsu M, Stewart RE (2002) CSE water and energy budgets in the NCEP-DOE reanalysis II. J Hydrometeorol 3:227–248

Schmitz JT, Mullen S (1996) Water vapor transport associated with summertime North America Monsoon as depicted by ECMWF analyses. J Climate 9:1621–1634

Serreze MC, Barry RG, Walsh JE (1995) Atmospheric water vapor characteristics at 70°N. J Climate 8:719–731

Smirnov V, Moore GWK (1998) Spatial and temporal structure of atmospheric water transport in the Mackenzie River Basin. J Climate 12:681–696

Stewart RE (2000) The variable climate of the Mackenzie River Basin: its water cycle and fresh water discharge. In: Lewis et al. (eds) The freshwater budget of the Arctic Ocean. Kluwer Academic Publishers, the Netherlands, pp 367–381

Stewart RE, Bussières N, Cao Z, Cho HR, Kochtubajda B, Leighton HG, Louie PYT, Mackay MD, Marsh P, Szeto KK, Walker AE, Burford JE (2002) Hydrometeorological features influencing the Mackenzie Basin climate system during the 1994/1995 water year: a period of record low discharge. Atmos Ocean 40:257–278

Stewart RE, Leighton HG, Marsh P, Moore GWK, Ritchie H, Rouse WR, Soulis ED, Strong GS, Crawford RW, Kochtubajda B (1998) The Mackenzie GEWEX Study: the water and energy cycles of a major North American river basin. B Am Meteorol Soc 79:2665–2683

Strong GS (1996) Atmospheric moisture budget estimates of regional evapotranspiration from RES-91. Atmos Ocean 34:29–63

Strong GS, Proctor BA (1998) Diurnal variation in atmospheric moisture during GEWEX/MAGS. Proc 32nd CMOS congress, June 1–5, 1998, Halifax, Canada, pp 52–53

Walsh JE, Zhou X, Portisi D, Serreze MC (1994) Atmospheric contribution to hydrologic variations in the Arctic. Atmos Ocean 32:733–755

Chapter 7

Moisture Sources for Extreme Rainfall Events over the Mackenzie River Basin

Julian C. Brimelow and Gerhard W. Reuter

Abstract Extreme summer rainfall events (rainfall exceeding 100 mm) have a marked impact on the hydrologic budget over the Mackenzie River Basin (MRB). In this study we test the hypothesis that the atmospheric moisture feeding these rainstorms can be traced back to the Gulf of Mexico. Three-dimensional parcel trajectories were identified that originated near the Gulf of Mexico and terminated over the southern MRB. The transport time ranged from 6 to 10 days. Our study indicates that rapid lee cyclogenesis over Alberta (associated with a 500-hPa cut-off low) and the Great Plains Low Level Jet can act in unison to produce this moisture transport.

1 Introduction

Smirnov and Moore (2001) stressed the importance of understanding the atmospheric processes that transport water vapor into the Mackenzie River Basin (MRB) because changes in the hydrologic processes within the Basin can have important consequences for the regional climate. Lackmann and Gyakum (1998) demonstrated that mid-level moisture from the Gulf of Alaska is crucial for wintertime precipitation in the MRB. Subsequent research by Smirnov and Moore (2001) found that during the autumn, winter, and spring months, extratropical cyclones are responsible for transporting mid-level moisture from the subtropical and mid-latitude Pacific Ocean across the western boundary of the MRB.

This study provides the first quantitative investigation into the source of moisture for summertime extreme rainfall events over the southern MRB. Our investigation focused on three extreme events that occurred on 22–23 June 1993, 19 June 1996, and 28–29 July 2001. During these rainfall events, portions of the southern MRB received between 100 and 150 mm of rain. Our objective was to determine whether the Gulf of Mexico (GOM) could act as a source of low-level moisture during extreme meso-α scale (200–2000 km) summertime rainfall events over the southern MRB

and if so, to identify the mechanism(s) responsible for transporting the moisture-laden air.

2 Study Area

Our study area is the southern MRB that encompasses the Peace River and Athabasca River basins, and covers an area of approximately 450 000 km^2 (Fig. 1). The mean annual precipitation over the southern MRB is approximately 500 mm, with 50% falling in the summer (Louie et al. 2002). A single heavy rainfall event producing 125 mm of rain can account for up to 25% of the annual rainfall over portions of this region.Extreme meso-α scale rainfall events are almost exclusively associated with the passage of a 500-hPa cutoff low and rapid lee cyclogenesis over south-central Alberta (Reuter and Nguyen 1993). During early summer, the southern MRB is a climatologically preferred region for 500-hPa cutoff lows (Bell and Bosart 1989) and rapid lee cyclogenesis (Whittaker and Horn 1981). The rapidly intensifying surface low produces strong synoptic-scale lift and, when this lift is coupled with a moist air mass and a sustained upslope flow, widespread and heavy rainfall ensues.

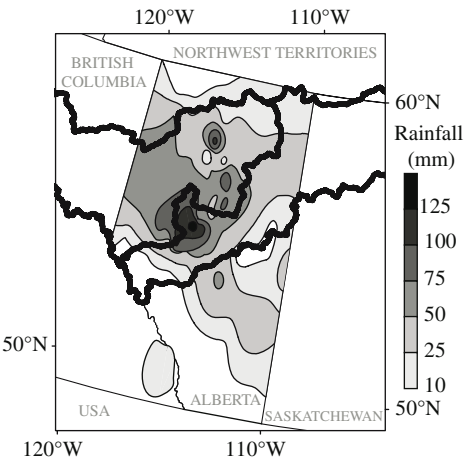

Fig. 1. 48-h accumulated rainfall (mm) for the 22–23 June 1993 extreme rainfall event over northern Alberta. The two polygons enclosed by the solid dark lines over northern Alberta approximate the boundaries of the Peace River and Athabasca River basins

3 Method

Lagrangian trajectories were computed using the HYSPLIT model. HYSPLIT is capable of computing forward or backward Lagrangian trajectories for an air parcel from any user-specified height and location

(Draxler and Hess 1998). Hourly values of specified meteorological variables including the pressure, height, temperature, potential temperature, and relative humidity are provided along each trajectory. The input data for HYSPLIT consist of the four-dimensional wind field. The case study presented here is based on archived data from NCEP Regional Analysis and Forecast System (RAFS), which use the Nested Grid Model (NGM) for the forecasts. These data are archived every 2 h on a 33 by 28 polar stereographic grid (horizontal grid spacing of 180 km) with 10 data levels in the vertical. The HYSPLIT model allows the user to simultaneously release parcels from all points within a user-specified matrix for a given time and height. Forward trajectories from the Gulf of Mexico to the southern MRB were identified by placing matrices along the entire United States Gulf coast and releasing the parcels at hourly intervals between 5 and 10 days prior to the heavy rainfall events (given the distances involved this was deemed to be a reasonable time frame). A similar approach was adopted for identifying backward trajectories starting over the MRB that ultimately could be traced back to the Gulf of Mexico. Brimelow and Reuter (2005) discussed the limitations of the trajectory calculations and the sensitivity of trajectories to changes in temporal and spatial density of meteorological data during a wide range of synoptic conditions.

The exact path of a trajectory is sensitive to the initial conditions, uncertainties contained in the wind fields, and interpolation errors. Rolph and Draxler (1990) investigated the sensitivity of trajectories to changes in temporal and spatial density of meteorological data during a wide range of synoptic conditions. Specifically, using a grid resolution of 90 km and a temporal resolution of 2 h, mean relative horizontal transport deviations of approximately 5% of the trajectory length were observed after 96 h. Using a temporal resolution of 6 h, the mean relative horizontal error increased to 15%. Stohl (1998) concluded that position errors of close to 20% of the travel distance are typical for trajectories calculated using analysis fields in data-rich areas (e.g., North America), with errors of up to 30% or more expected for trajectories calculated using forecast data. In contrast, Reiff et al. (1986) verified trajectory calculations for an African dust plume using wind analyses produced at the European Centre for Medium Range Weather Forecasts and found that the errors were at most 200 km (~7%) for a 3000 km trajectory. Stohl (1998) provided a comprehensive review of error sources in trajectory calculations.

It is also important to note that the “parcels” referred to in this study do not represent the hypothetical parcels used in buoyancy theory. In other words, mixing with the surrounding air does occur and some of the moisture is removed by precipitation. Consequently, the mixing ratios specified

along the trajectory represent the moisture content at a particular point and time along the trajectory, and do not suggest that all the moisture present in the air at that time originated from the GOM.

We thus refer to "modified" moisture content because, as shown in Fig. 2d, there is a decrease in the mixing ratio with time as the parcel moves northwards. Data points along the trajectories suggest that the diurnal fluctuation in the low-level mixing ratio might be attributed to turbulent mixing with dry elevated mixed-layer air (Lanicci and Warner 1991) that is often present over the High Plains during the warm season, and/or rainfall associated with vertical ascent. Nevertheless, the mean precipitable water (PW) over the southern MRB for the duration of this event, calculated from 12-hourly soundings released from Stony Plain (53.53°N, 114.10°W), was about 20 mm. This is 40% higher than the long-term mean PW observed at this time of the year and reflects the influx of unusually moist air into the region.

4 Results

For a complete analysis of three extreme rainfall events, the reader is referred to Brimelow and Reuter (2005). Here, we summarize the results for one of the cases, namely the rainstorm of 22–23 June 1993. This rainstorm produced 50 mm or more of precipitation over an area of approximately 136 000 km^2 (~30% of the southern MRB) in less than 48 h. The number of rainfall stations in Alberta that were used to create the rainfall maps for the 1993 event was 106, compared to 209 for the 1996 event and 258 for the 2001 event. The mean spacing between stations varied markedly but was typically between 50 and 75 km.

The highest rainfall amounts (up to 140 mm) were recorded over the Swan Hills, located about 150 km northwest of Edmonton (Fig. 1). The high rainfall amounts observed between 22 and 23 June 1993 were produced by a classic synoptic-scale setting for heavy summer rainfall events over central Alberta. Specifically, Fig. 2a shows that a 500-hPa cutoff low (5460 gpm) was located just off the coast of British Columbia on the morning of 22 June 1993, and over the next 36 h the cutoff low slowly migrated northeastward. As the system approached the continental divide, rapid lee cyclogenesis occurred over south-central Alberta (Fig. 2b), with the central pressure of the surface low decreasing from 1006 hPa at 12 UTC 21 June to 988 hPa at 00 UTC 23 June.

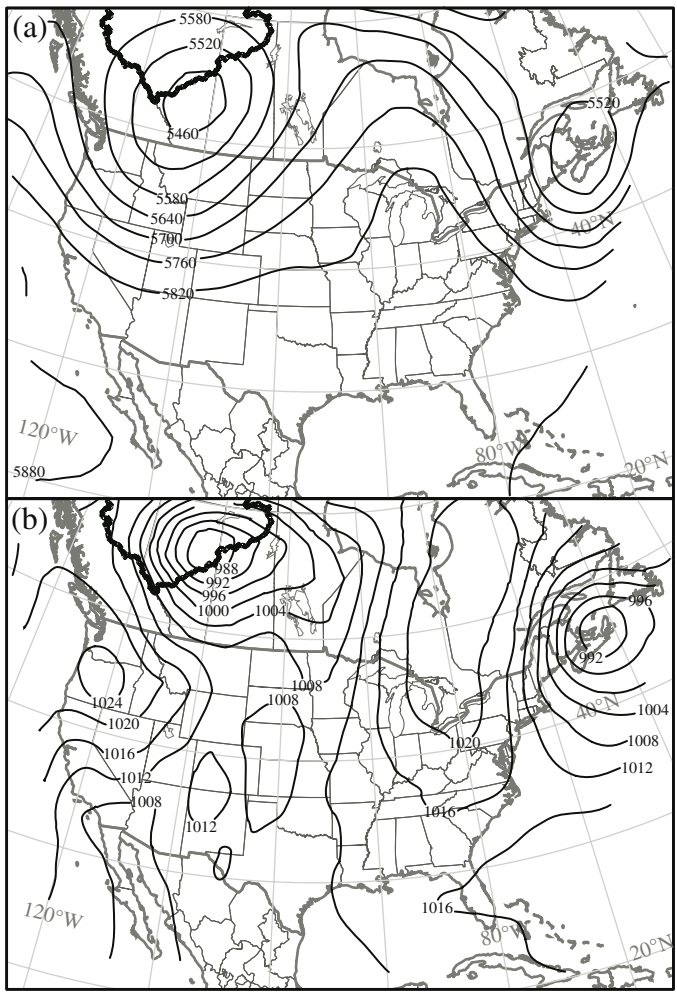

Fig. 2. (a) 500-hPa and (b) mean sea-level pressure maps for the 22–23 June 1993 extreme rainfall event. Contour interval for the 500-hPa heights is 60 gpm and for the mean sea-level pressure 4 hPa (after NOAA-CIRES Climate Diagnostics Center Web site at www.cdc.noaa.gov); (c) continuous trajectory from the Gulf of Mexico to the southern MRB for the 22–23 June 1993 extreme rainfall event. Solid triangles are shown every 24 hours. Also depicted are locations of the 500 hPa cutoff low (COL), surface low (L) and the Great Plains low-level jet (GPLLJ). The shaded area denotes the location of the mesoscale convective complexes over the Dakotas. The star indicates where the heavy rain occurs. (d) pressure (light line) and water vapor mixing ratio (dark line) along each trajectory. Dates are shown along the abscissa

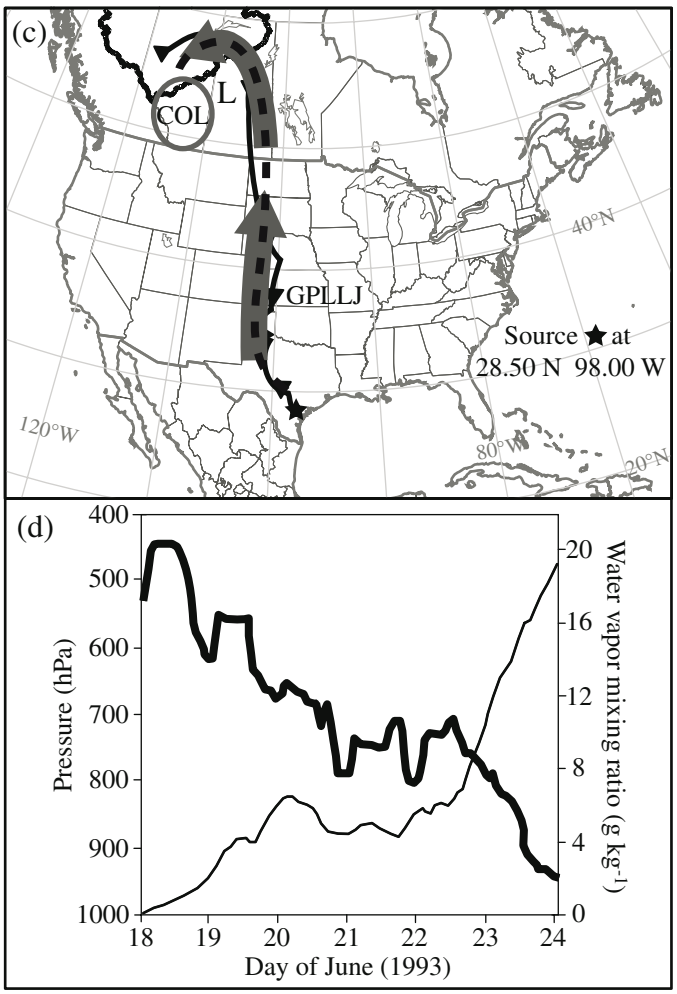

Fig. 2. (cont.)

An example of a forward trajectory for the 1993 extreme rainfall event is shown in Figs. 2c and 2d. We refer to this type of trajectory as "quasi-continuous" to indicate that the trajectories are not strictly continuous in space and time. This is evidenced by the tight loops that are sometimes found along the trajectories. Inspection of the trajectory data indicates that these loops coincide with times when the winds were light and/or precipitation events were occurring. Over a period of about four days, very moist boundary layer air (initially 20 g kg^{-1}) from the Gulf of Mexico was advected in the boundary layer from the Texas coast northwards through the

Texas Panhandle area to the midwestern United States. In a study of warm-season moisture transport over the United States, Schubert et al. (1998) referred to this region of preferred moisture transport as the "Texas corridor". The arrival of the modified GOM moisture over Nebraska coincided with the formation of a strong southerly flow over the northern Great Plains and Saskatchewan in response to rapid lee cyclogenesis over south-central Alberta.

Comparison of six-hourly surface analyses and coincident trajectory locations indicated that over a period of about 48 h, the strong cyclonic flow around the deep surface low drew the modified GOM moisture (>11g kg^{-1}) from the northern Great Plains northwards to central Saskatchewan and finally westwards over the southern MRB. The total time required to transport the modified GOM moisture to the southern MRB, a distance of approximately 3500 km, was six days. It is clear from the short time taken to transport the moisture from the GOM to the northern Plains that the Great Plains low-level jet (LLJ) played a key role in the northerly transport of GOM moisture during this event. The Great Plains LLJ is frequently observed over the midwestern United States during spring and summer (Helfand and Schubert 1995). Consequently, the Great Plains LLJ has a pronounced effect on moisture transport and precipitation over the central United States. Specifically, moisture budget analyses for the continental United States indicate that strong poleward transport of GOM moisture exists in the vicinity of the Great Plains LLJ (Liu et al. 2007; Schubert et al. 1998). The northerly transport of GOM moisture over the Great Plains typically peaks in June and July, and at this time also extends as far north as the Dakotas and Wisconsin (Liu and Stewart 2003). Higgins et al. (1997) showed that the frequent northward transport of GOM moisture to the midwestern United States by the Great Plains LLJ accounts for a significant portion (up to 45%) of the regional moisture transport in that region. Likewise, Helfand and Schubert (1995) showed that the Great Plains LLJ is responsible for transporting almost one-third of all the moisture that enters the continental United States annually.

A noteworthy observation from the trajectory analysis is the ascent of moist low-level air over Saskatchewan and the southern MRB as it was lifted into the cutoff low during the last 36 h of its journey. The water vapor mixing ratio of the air prior to this rapid ascent was 11 g kg^{-1}. The combination of sustained moderate vertical ascent and a continuous supply of moist air over the southern MRB favored significant rainfall over the basin. Indeed, continuous rainfall was observed to last up to 48 h at many locations, while the average rainfall for all stations in the southern MRB that reported precipitation was approximately 54 mm.

5 Discussion

Brimelow and Reuter (2005) present two other cases of large-scale transport of low-level moisture for extreme rainfall events over the southern MRB. They found that there was a striking similarity between the synoptic-scale circulation patterns (both at the surface and at 500 hPa) that were observed over North America during these events. All three events were associated with a 500-hPa cutoff low and a deep surface low over central Alberta. While June and July are favored months for cutoff lows over the southern MRB, rarely do these systems produce over 100 mm of rain as they traverse the Basin. We are, therefore, dealing with a special subset of rainstorms that make a significant contribution (25%) to the annual moisture budget for a small portion (10–30 %) of the southern MRB in less than 48 h. The similarities between the synoptic-scale circulation patterns were reflected in the trajectory analyses computed for each case study. The modified GOM moisture followed similar trajectories and required about the same amount of time (6 to 10 days) to reach the southern MRB. This represents a 3500 km poleward transport of moist, sub-tropical air in 10 days or less. It is remarkable that moist air originating over sub-tropical waters can feed rainstorms in the high latitudes and ultimately move to the Arctic Ocean.

The trajectory of air flow for the 22–23 June 1993 event enables a conceptual model to be proposed for the transport of Gulf of Mexico moisture for extreme rainfall events over the southern MRB (Fig. 2c). A critical component of the moisture trajectories analyzed in this study was the Great Plains low level jet (LLJ), which plays a key role in the summer precipitation and hydrology of the central United States. The high frequency of LLJ events over the Great Plains of the United States accounts for a significant portion of the regional moisture transport in this region during the warm season. What is very uncommon, however, is for the arrival of modified GOM moisture over the central and northern Great Plains to coincide with lee cyclogenesis over Alberta that is associated with a deep 500-hPa cutoff low. Under these circumstances, the low-level moisture that was advected over the Northern Plains by the Great Plains LLJ was caught up in the strong southerly flow developing ahead of the deep low over central Alberta. For example, during the 1993 event the Great Plains LLJ and associated moisture transport extended farther north than is typically observed at this time of the year. The anomalously strong southerly low-level flow (>5 m s^{-1}) over Saskatchewan was related to the formation of a deep surface low (<1000 hPa) over Alberta. The low-level, subtropical

moisture from the GOM was then transported northwards over Saskatchewan and finally westwards over the southern MRB by the cyclonic flow around the surface low. For the three cases studied, the quasi-continuous transport of modified GOM moisture to the southern MRB typically took a week to 10 days.

6. Conclusion

We have shown that rapid lee cyclogenesis over Alberta (associated with a 500-hPa cutoff low) and the Great Plains Low Level Jet can act in unison to transport moisture from the Gulf of Mexico to the southern MRB. Given the importance of meso-α scale extreme rainfall events on the hydrologic cycle of the MRB, future work should focus on conducting a detailed study of the dynamics responsible for producing the heavy rainfall, as well as developing analog techniques to assist forecasters in identifying cases when the antecedent large-scale flow has the potential to produce extreme rainfall over the southern MRB. Also of interest would be to investigate the moisture sources on occasions when the synoptic pattern was similar to the events presented in this chapter but the rainfall amounts were less than 100 mm.

Acknowledgements

The authors acknowledge the NOAA Air Resources Laboratory (ARL) for providing the HYSPLIT transport and dispersion model.

References

Bell GD, Bosart LF (1989) A 15-year climatology of Northern Hemisphere 500 mb closed cyclone and anticyclone centers. Mon Weather Rev 117:2142–2164

Brimelow JC, Reuter GW (2005) Transport of atmospheric moisture during three extreme rainfall events over the Mackenzie River Basin. J Hydrometeorol 6:423–440

Draxler RR, Hess GD (1998) An overview of the HYSPLIT_4 modelling system for trajectories, dispersion, and deposition. Aust Meteorol Mag 47:295–308

Helfand HM, Schubert SD (1995) Climatology of the simulated Great Plains low-level jet and its contribution to the continental moisture budget of the United States. J Climate 8:784–806

Higgins RW, Yao Y, Yarosh ES, Janowiak JE, Mo KC (1997) Influence of the Great Plains low-level jet on summertime precipitation and moisture transport over the central United States. J Climate 10:481–507

Lackmann GM, Gyakum JR, Benoit R (1998) Moisture transport diagnosis of a wintertime precipitation event in the Mackenzie River Basin. Mon Weather Rev 126:668–692

Lanicci JM, Warner TT (1991) A synoptic climatology of the elevated mixed-layer inversion over the southern Great Plains in spring. Part I: structure, dynamics, and seasonal evolution. Wea Forecast 6:181–197

Liu J, Stewart RE (2003) Water vapor fluxes over the Saskatchewan River Basin. J Hydrometeorol 4:944–959

Liu J, Stewart RE, Szeto K (2007) Water vapor fluxes over the Canadian prairies and the Mackenzie River Basin. (Vol. I, this book)

Louie PYT, Hogg WD , MacKay MD, Zhang X, Hopkinson RF (2002) The water balance climatology of the Mackenzie River Basin with reference to the 1994/1995 water year. Atmos Ocean 49:159–180

Reiff J, Forbes GS, Spieksma FTM, Reynders JJ (1986) African dust reaching northwestern Europe: a case study to verify trajectory calculations. J. Clim Appl Meteorol 25:1543–1567

Reuter GW, Nguyen CD (1993) Organization of cloud and precipitation in an Alberta storm. Atmos Res 30:127–141

Rolph GD, Draxler RR (1990) Sensitivity of three-dimensional trajectories to the spatial and temporal densities of the wind field. J Appl Meteorol 29:1043–1054

Schubert SD, Helfand HM, Wu C, Min W (1998) Subseasonal variations in warm-season moisture transport and precipitation over the central and eastern United States. J Climate 11:2530–2555

Smirnov VV, Moore GWK (2001) Short-term and seasonal variability of the atmospheric water vapor transport through the Mackenzie River Basin. J Hydrometeorol 2:441–452

Stohl A (1998) Computation, accuracy and applications of trajectories – a review and bibliography. Atmos Environ 32:947–966

Whittaker LM, Horn LH (1981) Geographical and seasonal distribution of North American cyclogenesis, 1958–1977. Mon Weather Rev 109:2312–2322

Chapter 8

Precipitation Recycling in the Mackenzie and Three Other Major River Basins

Kit K. Szeto, Jinliang Liu and Alexander Wong

Abstract Local evaporation is an important source of moisture for precipitation in many continental regions. The precipitation recycling ratio (ρ = fraction of total precipitation derived from local evaporation) for four major river basins (the Mackenzie, Mississippi, Amazon and Lena) are evaluated by applying the ECMWF ERA-40 reanalysis data to the bulk recycling estimation method of Eltahir and Bras (1994). On an annual basis, recycling is strongest in the Amazon at 30%, and ρ for the other three regions are within 2% of each other with values between 23 and 25%. Apart from the Amazon, the estimated precipitation recycling ratios for all basins exhibit strong seasonal variability, with very low values during the cold season and typically high values during the warm season. The results indicate that close to or more than half of the summer precipitation in the downstream regions of all the test basins is derived from local evaporation. The role of moisture recycling in governing the warm season precipitation variability in the regions is also discussed.

1 Introduction

Precipitation, P, over a region can be partitioned according to the source of the moisture that contributes to the precipitation: (1) P_a, precipitation derived from water vapor advected into the region by atmospheric circulations, and (2) P_m, precipitation derived from water vapor supplied by evapotranspiration within the region. The latter is attributed to the mechanism of land–atmosphere moisture recycling, or precipitation recycling, over the region, quantified by the precipitation recycling ratio ρ, defined as P_m/P (Eltahir and Bras 1996). As the atmospheric and surface portions of the hydrologic cycle are coupled through precipitation and evapotranspiration, the recycling ratio gives a diagnostic measure of the degree by which land surface processes and land–atmosphere interactions affect the water budget of the region. In addition, recycling can effectively redistribute the surface water content over long distances within a large area. Depending on the spatial variability of the land surface characteristics, this spatial re-

distribution can critically affect both the local and regional-scale hydrologic responses to large-scale atmospheric forcing (Szeto 2002).

Because of the important roles it could play in influencing the regional water cycle of continental regions, precipitation recycling has been studied extensively in hydrometeorology (e.g., Budyko 1974; Lettau et al. 1979) and recycling ratios for major river basins of the world have been estimated in a number of studies (e.g., Brubaker et al. 1993 for several basins; Eltahir and Bras 1994 for the Amazon Basin; Bosilovich and Schubert 2001 for the Mississippi Basin; Szeto 2002 for the Mackenzie Basin). This study extends the work of Szeto (2002) to include ρ estimates for four major river basins (the Mackenzie, Mississippi, Amazon and Lena) using the new and improved ERA-40 reanalysis data from the European Centre for Medium-Range Forecasts (ECMWF). The use of a single dataset and ρ estimation method allows meaningful inter-comparison of recycling in different continental regions. Results of the analysis provide insights into the operation of the regional water cycle, particularly the role that moisture recycling plays in governing the warm season precipitation variability. Although discussion centers on the Mackenzie River Basin (MRB), comparison with the Mississippi River Basin, the Amazon River Basin (ARB) and the Lena River Basin (LRB) will lead to a better overall understanding of water cycling through examination of different factors and features that affect water cycling on a continental scale.

2 Methodology and Datasets

2.1 Bulk Estimation of the Precipitation Recycling Ratio

Despite recent development of complex and sophisticated methods to quantify sources of water vapor for precipitation (e.g., the use of isotope or water vapor tracers in GCMs such as described in Bosilovich and Schubert 2002), the simple bulk methods such as those developed by Brubaker (1993) and Eltahir and Bras (1994, 1996) remain a viable, well-tested and economical approach for estimating the recycling ratio in a region. Similar assumptions are typically adopted in the development of these bulk estimation methods: (1) the planetary boundary layer (PBL) is well-mixed; and (2) the change in atmospheric water vapor storage over long time scales is small compared to the atmospheric vapor fluxes (including the evaporative flux). With these assumptions, the following equation can be derived by

considering the conservation of water mass for a control volume within the region of interest (Eltahir and Bras 1994, 1996):

$$\rho = (I_i + E)/(I_i + E + I_e) \tag{1}$$

where E and I represent the evaporation and water vapor influx for the control volume, respectively. The indices i and e denote respectively the variables corresponding to the internal (i.e., from evapotranspiration within the domain) and external (i.e., advected by airflow into the domain) sources of water vapor. By dividing the domain of interest into a grid of control volumes, one can apply Eq. (1) to estimate the spatial distribution of the recycling ratio at monthly time scales through an iterative procedure. Spatially lumped or annual estimates can be obtained by aggregating the spatially distributed values using precipitation as the weighting factor in the averaging process. More detail can be found in Eltahir and Bras (1994) and Szeto (2002).

Owing to the inherent limitations of the bulk method, these semi-empirical estimates should be best treated as an index for comparing the temporal (e.g., seasonal or annual) variability of recycling for a region or for comparing different regions of the globe, rather than as absolute measures of moisture recycling over a region.

2.2 ECMWF 40-yr Global Reanalysis (ERA-40)

The main dataset used in this study is the new ERA-40 reanalysis from the ECMWF (Simmons and Gibson 2000; Kållberg et al. 2004), covering the period 1957–2002. The 3D-Var technique was applied using the T159L60 version of the Integrated Forecasting System to produce the analyses every six hours. A comprehensive study of water and energy budgets for the MRB assessed by using different source datasets (Szeto et al. 2007a) found that the ERA-40 data yielded budget estimates that compare most favorably with available observations. For this reason, as well as the global coverage and long time span of the ERA-40 dataset, this dataset was selected for use in the present study. The ERA-40 evapotranspiration (E), precipitation (P) and water vapor fluxes (from the 3-D wind field and specific humidity) were applied to Eq. (1) to estimate ρ for the various study basins during the 20-year period of 1979–98. Table 1 gives the rectangular latitude–longitude domains for the study basins.

Table 1. Physical and annual and domain-average water cycling parameters for the study basins: longitude range, latitude range, domain area, domain length scale (L), recycling ratio (ρ), (values in parentheses are calculated using NCEP-R2 data), rainy season-average recycling ratio (ρ_r), evaporation (E), precipitation (P), moisture flux (F), coefficient of variation for rainy season P (CV_p) (i.e., ratio of interannual standard deviation of P to average P over the 1979–1998 study period)

Parameters	Mackenzie	Lena	Mississippi	Amazon
Long. range [°E]	235–257.5	102.5–140	247.5–277.5	280–310
Lat. range [°N]	55–67.5	52.5–70	30–50	-16.25–3.75
Area [x10^6 km^2]	1.67	3.89	5.66	8.24
L [km]	1292	1972	2378	2871
ρ [%]	23 (27)	25 (42)	24 (29)	30 (33)
ρ_r [%]	33(JJA)	37(JJA)	31(MJJA)	31(NDJFMA)
E [mm d^{-1}]	0.96	0.81	1.76	3.32
P [mm d^{-1}]	1.10	1.16	1.74	5.46
F [kg m^{-1} s^{-1}]	39.1	24.3	84.6	143.8
CV_p [%]	13.8 (JJA)	12.2(JJA)	8.3(MJJA)	4.4(NDJFMA)

3 Results and Discussions

3.1 Annual Cycles of Water Cycling Variables

The mean annual cycles of various domain-average water cycling variables for the four basins are given in Fig. 1. The effects of continentality and latitudinality on the mean moisture flux magnitudes F are evident (Fig. 1a). The LRB, located in a northern cold region and being the most remote from oceanic moisture source, has weak moisture flux throughout the year, particularly during the winter. Although the MRB is somewhat closer to the ocean than is the LRB, the mountains that separate it from the North Pacific Ocean block out a large portion of the moisture flow to the continent. Consequently, the net moisture flux over the MRB is also weak but slightly larger than over the LRB. Lying to the lee of the Rocky Mountains, the Mississippi basin has a substantially larger F than the MRB due to the relatively higher temperatures and exposure to the influx of moisture from the Gulf of Mexico. The ARB, located in the tropical region and without any topographic barrier to the moisture flux from the Atlantic Ocean, has the highest F values among the four basins, with an annual value six times larger than that for the LRB (Table 1). Its net basin-average flux is the highest during the austral winter.

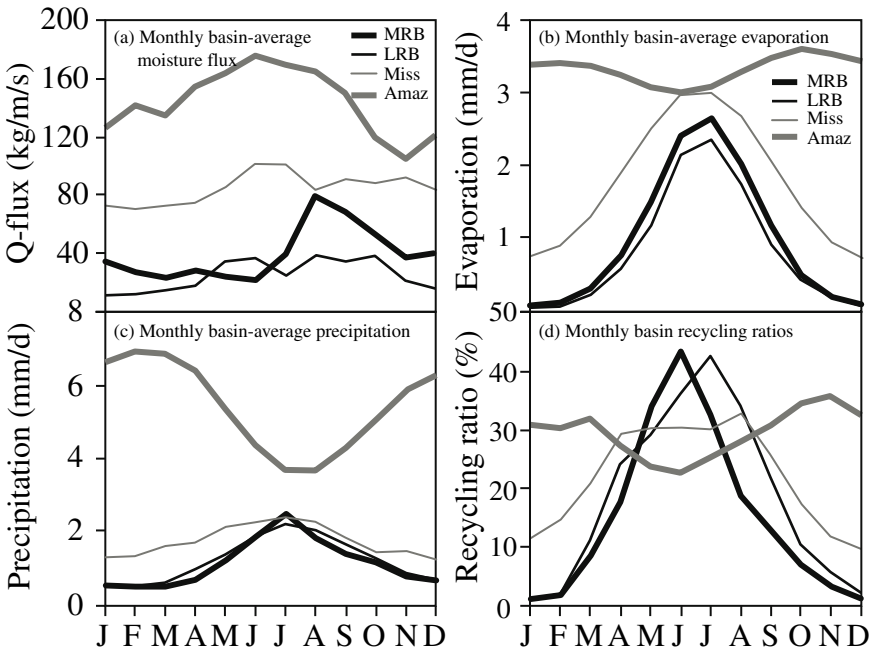

Fig. 1. Annual cycles of basin-average water cycle variables for the study basins: (a) moisture flux, (b) evaporation, (c) precipitation, and (d) recycling ratio

Since evapotranspiration *E* is strongly controlled by surface solar radiation, it exhibits the largest seasonality among the water cycling variables for the extra-tropical basins (Fig. 1b). As seasonal variation of solar radiative input is low for the Amazon, so is its seasonal variation in evapotranspiration. For the Mississippi basin located in the temperate latitudes, basin-average *E* varies from low values of about 0.7 mm d^{-1} during the winter to larger than 3 mm d^{-1} during the summer. Both of the northern basins (MRB and LRB) receive little or no solar input during the boreal winter, *E* is extremely low from December to February. On the other hand, with long hours of solar insolation during the summer, their warm season *E* is only slightly lower than those for the southern basins.

The four basins exhibit varying degrees of seasonality in their precipitation, *P* (Fig. 1c). In response to the South American monsoon system that affects the region, the ARB has summer *P* values that are about twice that of the winter values. The Mississippi basin with substantially lower mean annual precipitation than the ARB, also has a summer *P* that is about twice as high as its winter *P*. With large seasonal temperature (and hence precipitable water) contrasts that characterize the two northern basins, their

seasonal variability of P is also the highest among the four regions. Their maximum summer P is 4 to 5 times higher than their winter counterparts, and the summer P in these northern basins can be close to (LRB) or even exceed (MRB) that for the southern Mississippi basin.

Since the recycling ratio ρ for a region is directly (inversely) related to its E (F), the seasonal variability of ρ can be diagnostically related to the seasonal variations of these two other variables. For example, the relatively low seasonal variation of ρ for the ARB can be diagnostically related to the relatively low seasonal variability of F and E for the region. The relative low (high) ρ for the region in June (November) is a result of the low E–high F (high E–low F) conditions that characterize the region during the period (Fig. 1d). On the other hand, the strong seasonal variability of ρ (from negligibly small during the winter to >40% during the summer) for the northern basins is largely a result of their strong seasonal E variations (Figs. 1b and c). Indeed, recycling during the summer is strongest in the northern basins, which can be diagnostically related to the relatively low F–high E conditions that prevail in these regions. Table 1 shows that 33 and 37% of the rainy season precipitation in the MRB and LRB are respectively derived from evapotranspiration within the regions. The sharp drop of ρ during July and August for the MRB can be diagnostically related to a sharp increase in F (Figs. 1a and d). The Mississippi basin, however, has low variation in ρ (stable at ~ 30%) throughout the warm season.

On an annual timescale, recycling is the strongest in the Amazon at 30%; and ρ for the other three regions are within 2% of each others with values between 23 and 25% (Table 1). Since ρ scales with the length scale L of the study region (i.e., ρ approaches 0 for a small area and approaches 1 when the entire globe is considered as one region), it is of interest to note that ρ estimates for the MRB, LRB and Mississippi regions are close to each other despite their substantial differences in L.

3.2 Rainy-season Regional Water Cycling

The spatial and temporal variability of precipitation in different terrestrial regions are a result of complex interactions among the large-scale circulation, principal precipitation-producing mechanisms, air-land interaction processes, and soil moisture dynamics. We analyze the interplay of these factors that affect the warm-season precipitation in the four continental basins. Interpretation of our recycling results is facilitated by the use of con-

temporaneous and time-lagged correlations which provide measures of statistical linkage between the basin-average water cycling variables (Tables 2 and 3).

Table 2. Correlation coefficients between basin and rainy-season-average water cycle variables for the study basins computed over the 20-y study period. Correlations exceeding the 95% significance level are in italics

	Mackenzie (JJA)				Lena (JJA)			
Parameter	*P*	*E*	*Fx*	*Fy*	*P*	*E*	*Fx*	*Fy*
E	*0.34*	*1.00*			-0.58	*1.00*		
Fx	*-0.26*	*0.17*	*1.00*		*0.06*	*0.20*	*1.00*	
Fy	0.58	0.44	*-0.06*	*1.00*	0.41	*0.20*	*0.28*	*1.00*
ρ	*0.17*	*0.20*	-0.74	*0.27*	-0.55	*0.19*	*-0.33*	-0.06
	Mississippi (MJJA)				Amazon (NDJFMA)			
Parameter	*P*	*E*	*Fx*	*Fy*	*P*	*E*	*Fx*	*Fy*
E	0.61	*1.00*			*-0.28*	*1.00*		
Fx	*-0.10*	*0.16*	*1.00*		*0.25*	*0.07*	*1.00*	
Fy	0.44	*0.37*	*-0.26*	*1.00*	*0.09*	*0.10*	*-0.04*	*1.00*
ρ	*-0.19*	*0.14*	*-0.36*	*-0.30*	*0.17*	0.50	0.41	0.58

P precipitation, *E* evaporation, *Fx* zonal moisture flux, *Fy* meridional moisture flux, ρ recycling ratio.

Table 3. One-month lagged correlation coefficients between monthly basin-average *P* and *E* during the rainy season. Correlations exceeding the 95% significance level are in italics

	Mackenzie (M=August)			Lena (M=August)			Mississippi (M=August)			Amazon (M=March)		
Months	*P*, *E*	*E*, *E*	*P*, *P*	*P*, *E*	*E*, *E*	*P*, *P*	*P*, *E*	*E*, *E*	*P*, *P*	*P*, *E*	*E*, *E*	*P*, *P*
M–3, M–2	*-0.37*	0.45	*0.28*	*-0.07*	*0.29*	*0.20*	0.65	0.97	*0.15*	*-0.01*	0.97	*0.17*
M–2, M–1	*0.36*	*0.04*	0.58	*-0.09*	0.49	0.44	0.54	0.98	0.44	*-0.30*	0.68	0.70
M–1, M	0.52	0.53	*0.08*	*-0.29*	0.57	*0.38*	*0.20*	0.74	*0.27*	-0.51	0.62	0.60

3.2.1 The Mackenzie Basin

Although precipitation is typically light in this northern basin during winter, the snow can accumulate on the surface for months due to the extremely low temperatures (Woo et al. 2007). The recharge of soil moisture from the spring snowmelt is restricted by the widespread occurrence of seasonally frozen soil and permafrost which often inhibit infiltration (Pomeroy et al. 2007). As a result, top soil layers are often saturated after snowmelt. In addition, many parts of the MRB (other than the mountains

and the Canadian Shield) are extensively covered with organic soil with large water retention capacity (Quinton and Hayashi 2007). For these reasons, soil water recharge and its associated influence on summer water cycling in the MRB might not be sensitive to the interannual variation of winter precipitation. This hypothesis is supported by the weak time-lagged correlation ($r<0.2$) between summer precipitation and the precipitation of the previous winter.

The large-scale atmospheric forcing is generally weak and the mean moisture transport into the Basin is accomplished largely in the warm season by the weak westerly flow (Fig. 2b). Although the large-scale atmospheric forcing is weak in the summer, being located on the lee side of the Cordillera and with the climatological summer arctic front lying within the Basin near the forest-tundra treeline (Serreze et al. 2001), synoptic activities such as lee-cyclogenesis are still frequent. On the other hand, the mean lee-side subsidence suppresses cloud formation and allows strong and extended solar insolation to reach the land surface. The extended period of solar heating and the abundance of surface moisture promote active evapotranspiration over the interior basin (Fig. 2a) and enable the build up of convective available potential energy (CAPE) during the day in the PBL. Surface heating and surface sensible heat flux are particularly strong over the eastern slopes of the Cordillera where they intercept larger amount of solar radiation. The enhanced sensible heat flux over the mountain slopes acts as an elevated heat source that induces a local circulation (the mountain–plains circulation, MPC) which advects the moisture evaporated from the interior plains towards and up the Cordilleran foothills. Strong moisture convergence develops over the western basin as the circulation strengthens and triggers convective activities during the afternoon (see also Fig. 5 in Szeto et al 2007b). Once convection has started, latent heating in the updraft maintains or further enhances the circulation, while some of the convective cells that move with the steering level westerly wind into the interior basin wet the surface and maintain the surface moisture, and so on. The MPC offers an explanation for the enhanced summer precipitation over the mountainous western basin while the sinking branch of the MPC could reinforce the background subsiding motion to suppresses precipitation (and enhance evaporation) over the interior basin (Fig. 2a).

The above discussion of precipitation-producing mechanisms in the MRB also provides a means to interpret the interannual and intra-seasonal correlations between the water cycling variables. For example, the enhanced precipitation over the mountainous western basin is largely derived from the evaporated moisture advected by the MPC to the foothills, lead-

ing to a net transport of surface water from the interior basin to western basin that is characterized by high runoff ratios. As such, *E* contributes to, and is linked positively to summer *P* in the Basin (Table 2). On the other hand, the strong subsidence associated with the stronger westerly moisture flux (*Fx*) over the basin would inhibit precipitation in the region and hence a negative association between *Fx* and *P*. With ample surface water in early summer to sustain evaporation, *P* plays a minor role in affecting *E* during this season (Table 3). However, as the summer progresses and surface water is depleted through evapotranspiration (and subsequently transport out of the basin either through the unhindered southeastern boundary

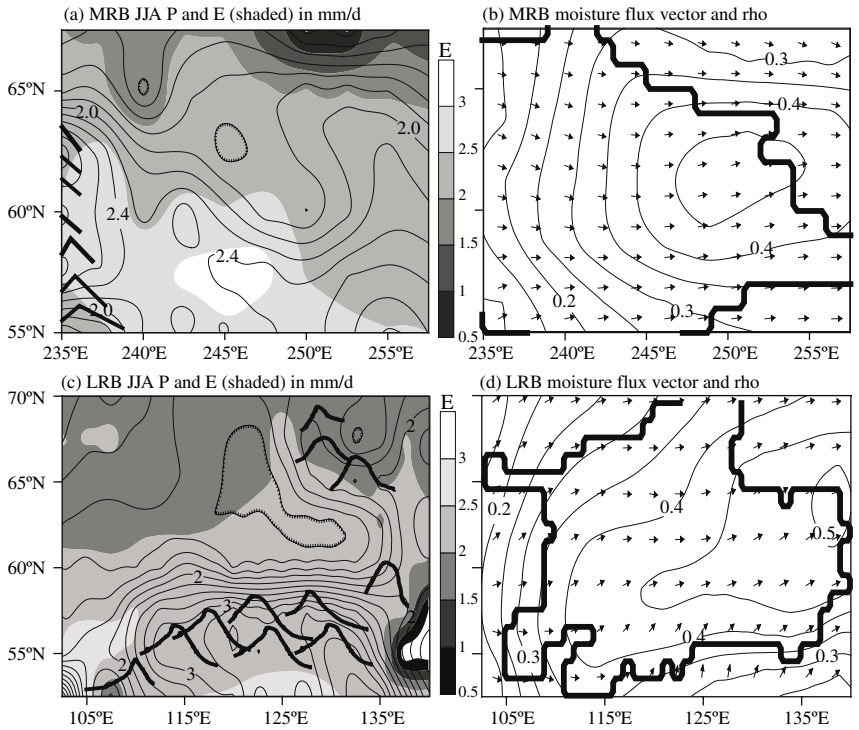

Fig. 2. Spatial variability of rainy-season-average water cycle variables for the study basins: (a), (c), (e) and (g) shows precipitation and evaporation for the Mackenzie, Lena, Mississippi and Amazon basins, respectively. Also shown schematically in the left panels are the locations of the mountain ranges in the domains. Corresponding moisture flux vectors, recycling ratios and basin boundary (thick line) are show in (b), (d), (f) and (h). Maximum vector length represents moisture flux of 360 kg m^{-1} s^{-1}

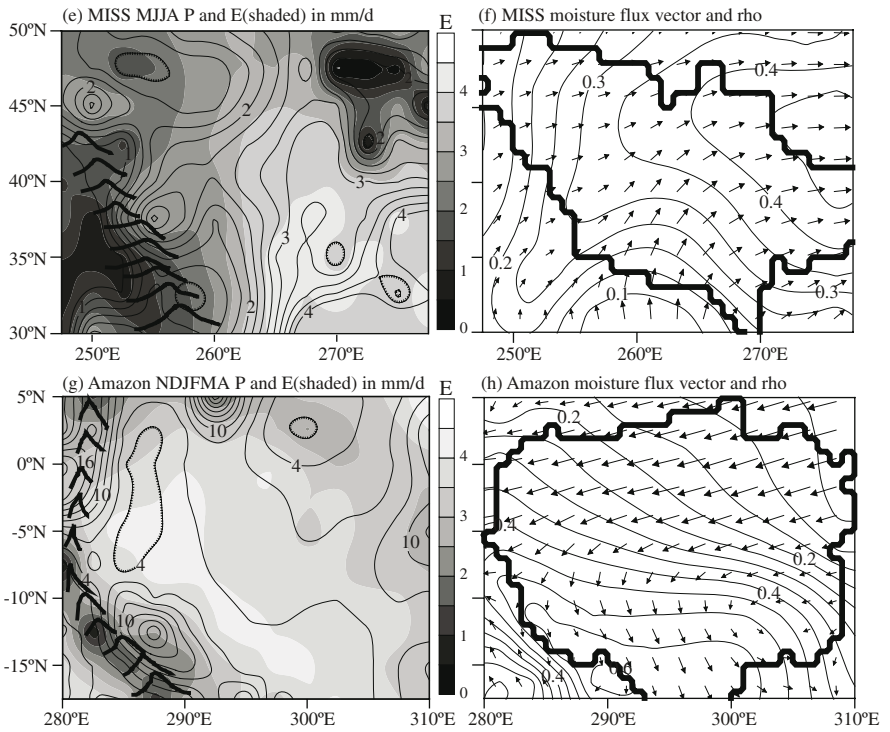

Fig. 2. (cont.)

or as runoff from the western basin), P starts to exert increasing influence on subsequent E over the basin.

In addition to moist convections, synoptic systems also contribute significantly to P. Szeto (2002) noted that different large-scale conditions that favor the development of different synoptic system can enhance (dampen) "normal" convective activities over the basin to produce anomalously wet (dry) summers in the basin. In particular, under the influence of a persistent large-scale high pressure system, the anomalous northwesterly surface flow would advect the evaporated water vapor out of the basin through the unobstructed eastern and southeastern boundaries, and would thus be detrimental to both the precipitation and its recycling within the basin. Hence, enhanced surface evaporation during dry periods would not have regulating effects on the precipitation in the region, i.e., recycling (ρ) does not increase when P is anomalously low (Table 2). On the other hand, when the basin is under the influence of large-scale conditions that favor the development of low-pressure systems, the anomalous southeasterly cyclonic boundary layer flow would enhance the influx of external moisture and

advect both the external and locally-evaporated moisture towards the mountains to promote orographic precipitation over the western basin (Fig. 3). These feedback processes are reflected in the significant positive correlations of E and P to the meridional moisture flux (Fy) over the basin and they also partially account for the large interannual variability of summer rainfall (note that CVp for the MRB is the highest among the four basins in Table 1). Case studies of synoptic enhancements of southerly moisture influx into the basin are also reported in Brimelow and Reuter (2007) and a schematic illustration of the discussed feedback processes can be found in Fig. 6 of Szeto et al. (2007b).

Fig. 3. Summer (July 1976) precipitation (top left of photograph) on Ram Mountain west of Fort Simpson resulting from recycling of moisture in the Mackenzie River Basin. (Photo: M.K. Woo)

3.2.2 The Lena Basin

As in the MRB, there is abundant surface water after snowmelt in the LRB to support active evapotranspiration. The LRB is bounded to the east by the Verhayanski Range and to the south by the Sayan Mountains and

Yablonovy Ranges (Fig. 2c). While these mountains are a barrier to moisture loss, their location on the downwind side of the LRB renders them ineffective in producing cyclonic system in the basin. The mean westerly moisture flux over the LRB is the weakest among the four study basins because of its remoteness from the ocean. Hence, despite the extended topographic barriers located downstream of the region, moisture convergence at the barriers is weak and the mean westerly moisture flux contributes little to the regional precipitation (hence a lack of linkage between P and Fx as shown in Table 2, and the absence of local precipitation maximum at the eastern mountains, shown in Fig. 2c). Furthermore, with most slopes in the basin facing west and north, the magnitude and timing of insolation on the mountain slopes are ineffective in generating the MPC that plays a major role in producing summer precipitation for such basins as the Mackenzie.

Synoptic activities, particularly cyclonic systems developed along the polar front just south of the region, are the main contributors to basin precipitation during the summer. Hence, the highest precipitation is over the mountainous southernmost region where the moisture-laden southerly flows (induced either by the synoptic systems or the thermal Mongolia low pressure system) encounter the mountain slopes (Figs. 2c and d; see also the strong correlation between Fy and P, in Table 2). Without effective convective organization mechanisms, precipitation in the interior basin comes largely from scattered convective showers, as evident from the lack of structure in the distribution of P over the area.

Due to the absence of a basin-scale mechanism (such as the MPC in the MRB) that redistributes surface moisture from the interior basin to feed the precipitation and runoff in the mountainous region, spatial distributions of P and E are largely in phase with each other over the LRB (Fig. 2c). Local moisture recycling is effective (warm-season ρ for the LRB is the highest among the basins) and the drying of the basin surface would be slower than in the MRB. Consequently, surface moisture supply for evapotranspiration exhibits little dependence on precipitation, and P exerts little effect on subsequent surface evaporation even during late summer (Table 3). As such, E is largely controlled by solar radiation at the surface throughout the summer, as evident from the strong negative correlations between E and P (Table 2), i.e., lower (higher) E would occur as a result of cloudy (clear sky) conditions during high (low) precipitation periods. These results suggest that, unlike the MRB, E and recycling can effectively regulate precipitation variability within the LRB, as indicated by the strong negative correlation between its P and ρ (Table 2). The results also can partially account for the slightly weaker interannual variability of warm-season P when compared to the MRB; but Fukutomi et al. (2003) sug-

gested that the interannual variability of *P* in the LRB is instead controlled by the modulation of synoptic activities by large-scale low-frequency variability modes.

3.2.3 The Mississippi Basin

Unlike the northern basins, the Mississippi Basin is largely free of snow in the spring, apart from the high elevations and some of its northernmost areas. Thus, pre- or early season precipitation can significantly control its soil water state, and precipitation variation can give rise to large interannual and spatial variability of the soil moisture in the basin at the beginning of summer. Consequently, *E* in the basin is influenced by both solar input and surface water supply and is strongly linked to previous precipitation in the basin, as suggested by the strong time-lagged correlation between *P* and *E* during early and mid-summer (Table 3).

The main influx of moisture into the basin is from the south (Fig. 2f) and is associated with the anticyclonic flow forced by the Bermuda High located over the central North Atlantic. Diurnal variations of enhanced heating/cooling over the arid high plains can induce dynamic conditions that enhance a poleward flow to create the diurnal Great Plains low-level jet system (LLJS) important to the heat and moisture influx from the Gulf of Mexico. Since the climatological polar front (and the associated jet system) is located north of the basin during summer, lee cyclones are uncommon and play little role in producing summer precipitation. As in the MRB, enhanced heating over the eastern slopes of the Rockies induces a MPC that produces areas of enhanced precipitation over the western basin (Fig. 2e). Such orographic precipitation maximizes in the afternoon and some of the precipitating convective cells might propagate into the interior plains. However, the major precipitation-producing systems for the region are mesoscale convective systems (MCSs) that develop at night when the nocturnal moisture-bearing LLJS encounters either the convective storms that propagate into the plains from the west or the W–E aligned stationary front frequently found over the northern plains. This stationary front marks the boundary between the cool air from the MRB and the warm, moist air from the Gulf (Higgins et al. 1997). When the MCSs develop into a mature state, they propagate southeastward towards the region where ample low-level moisture is available to fuel moist convections in the systems. A large area of maximum *P* over the central eastern basin is mainly the result of the precipitation from these MCS. The significant correlation between its *Fy* and *P* (Table 2) underscores the importance of the southerly moisture flux from the Gulf in producing summer precipitation in the basin.

Solar radiation at the surface exerts a strong control on *E* in the Mississippi Basin, especially over the southeastern moist and vegetated area. Unlike the LRB, the Mississippi yields a strong positive correlation between *E* and *P* (Table 2), though maximum *E* and *P* are temporally out of phase, i.e., *E* maximizes during the day when solar insolation is intense and helps to build up the CAPE while the MCS-produced precipitation reaches its maximum during the night. In addition, *P* exerts a strong control on soil water, and subsequently on *E*, so that *P* and *E* are strongly coupled. Indeed, among the four study basins, the Mississippi yields the strongest positive contemporaneous and time-lagged correlations between *P* and *E* (Tables 2 and 3). The strong air–land coupling also accounts for the extremely large auto-correlation in the monthly E (Table 3), with the Mississippi exhibiting the highest spatial coherence between *E* and *P* (Fig. 2e) among the study basins. These results lend support to Koster et al. (2004) who found that some of the regions that exhibit the strongest sensitivity of its summer rainfall to air–land interactions ("hot spots") are located in the Mississippi and not in the other basins studied here.

3.2.4 The Amazon Basin

Compared to the mid- and high latitude basins, water cycling in the tropical ARB is relatively simple, due to the weak seasonal variations in solar input and the lack of seasonal storage and release of surface snow water. In spite of large seasonal variation in *P* (Fig. 1c), the evapotranspiration from the extensive, dense rainforests shows little seasonal variation (Fig. 1b), suggesting that *E* in the basin is largely controlled by solar radiation rather than surface water supply. Consequently, *P* and *E* have weak or even negative time-lagged correlations (Table 3).

Although the large-scale conditions and dynamical features that organize convection in the basin can be complicated (Fu et al. 1999), the influence of recycling on *P* can be easily summarized. During the rainy season, there is strong moisture influx associated with the northeast trade winds that prevail over the northern basin in the austral summer (Fig. 2h). The regional precipitation maximum in the northeast is produced mainly from convective systems that develop over the Inter-Tropical Convergence Zone and/or from sea-breeze fronts that form near the coast. The depleted atmospheric moisture in the coastal precipitation is replenished by moisture from active evapotranspiration, which in turn returns to the surface as convective rainfall when air parcels travel westward towards the Andean Cordillera in the western basin. The northeasterly flow turns southward under the influence of the continental thermal low pressure system (and the asso-

ciated "Bolivian High" at the upper levels) located south of the basin and converges towards the Andes to produce significant orographic precipitation (Figs. 2g and h). Lettau et al. (1979) showed that almost 88% of the precipitation over the southwestern basin has recycled at least once over the ARB, although we obtained slightly lower values (Fig. 2h).

Enhanced heating on the east slopes of the Andes also induces a MPC that further intensifies the large-scale moisture convergence, giving rise to the pronounced precipitation maximum along the mountains in the southwest (Fig. 2g). Some moisture from the enhanced surface evaporation is recycled to produce the topographic precipitation at the Andes before it drains out of the basin as surface runoff, while some of it is transported out of the basin through its southern boundary. Evapotranspiration is largely controlled by surface radiation rather than surface water supply and convective activities are more intense in the late afternoon (Fig. 4) than at night (Nesbitt et al. 2000), such as those MCSs that occur over the Mississippi. Thus, E in the ARB is negatively correlated with precipitation (arguments that explain the negative E-P relationship in LRB apply similarly here). It is of interest to note that auto-correlations of monthly-E (and to a lesser extent monthly-P) are also strong for the ARB (Table 3), likely a result of the coherent seasonal response of E and P to interannual variations in large-scale circulations. This is different from the Mississippi Basin where the strong auto-correlations in E and P are attributed to the internal feedback mechanisms.

4 Concluding Remarks

Moisture recycling over four selected continental scale basins was investigated by estimating their precipitation recycling ratios with the ERA-40 reanalysis dataset. On the annual timescale, recycling is strongest in the Amazon at 30%, and the ratios for the Mackenzie, Lena and Amazon basins are within values between 23 and 25%. Apart from the Amazon, the estimated ratios exhibit strong seasonal variability with very low values during the cold season and typically high during the warm season. Close to or more than half of the summer precipitation in the downwind regions of all the test basins is derived from local evaporation.

The recycling results were analyzed in relation to the environmental and meteorological conditions of the four basins. In view of the northern location of the Mackenzie Basin, snowmelt recharges the soil moisture in the spring to provide ample soil water in support of evapotranspiration in the

Fig. 4. Late-afternoon (December 12, 2006, 4 p.m.) convective rainfall over Rio Negro in central Amazon Basin. (Photo: M.K. Woo)

summer. Much of the evaporated moisture is advected towards the Cordillera by local circulations to feed the orographic precipitation, but is subsequently lost to runoff; or the moisture is advected out of the Basin through the unobstructed southeastern boundary. Hence despite active summer evapotranspiration and recycling, these processes exert little effect in regulating the interannual variability of warm-season precipitation. In the Lena Basin, without corresponding local circulations to redistribute the evaporated moisture and being bounded by mountain ranges only at its downwind boundaries, surface drying in the summer is considerably slower than in the MRB. Consequently, E is largely controlled by solar insolation, and recycling processes exert a regulating effect on warm-season P variability in the region. The Mississippi Basin does not have much snow meltwater to recharge its soils, and the soil water status and hence its evaporation rate is strongly dependent on the pre- and early season precipitation. Both P and E have strong spatial and temporal coherencies, suggesting the governing role of air–land coupling processes with regard to its warm-season hydrologic cycle. The Amazon Basin is characterized by relatively small variation in solar insolation, extensive rainforest, predominant convective precipitation and a lofty downwind boundary marked by the Andean Cordillera. These factors make the Amazon the most effective region for pre-

cipitation recycling and, despite a large external moisture influx, its annual basin-average recycling ratio is the highest among the four study basins.

Findings of this study on warm-season large-scale water cycling enable a better understanding of the roles played by regional feedback processes in affecting the hydrometeorological response of continental basins to climate variability and change. Further assessment of recycling activities over land regions using alternative approaches (e.g., observational or numerical isotope tracing methods) for the purposes of cross-validation will provide additional insight into the subject.

Acknowledgments

This study was financially supported by Environment Canada and the Panel on Energy Research and Development (PERD).

References

Bosilovich MG, Schubert SD (2001) Precipitation recycling over the central United States diagnosed from the GEOS-1 data assimilation system. J Hydrometeorol 2:26–35

Bosilovich MG, Schubert SD (2002) Water vapor tracers as diagnostics of the regional hydrologic cycle. J Hydrometeorol 3:149–165

Brimelow JC, Reuter GW (2007) Moisture sources for extreme rainfall events over the Mackenzie River Basin (Vol. I, this book)

Brubaker KL, Entehabi D, Eagleson PS (1993) Estimation of continental precipitation recycling. J Climate 6:1077–1089

Budyko MI (1974) Climate and life. Academic Press, New York

Eltahir EAB, Bras RL (1996) Precipitation recycling. Rev Geophys 34:367–378

Eltahir EAB, Bras RL (1994) Precipitation recycling in the Amazon Basin. Q J Roy Meteor Soc 120:861–880

Fu R, Zhu B, Dickinson RE (1999) How do atmosphere and land surface influence seasonal changes of convection in the tropical Amazon? J Climate 12:1306–1321

Fukutomi Y, Igarashi H, Masuda K, Yasunari Y (2003) Interannual variability of summer water balance components in three major river basins of northern Eurasia. J Hydrometeorol 4:283–296

Higgins RW, Yao Y, Yarosh ES, Janowiak JE, Mo KC (1997) Influence of the Great Plains low-level jet on summertime precipitation and moisture transport over the central United States. J Climate 10:481–507

Kalnay E and coauthors (1996) The NCEP/NCAR 40-year reanalysis project. B Am Meteorol Soc 77:437–471

Kistler R and coauthors (2001) The NCEP–NCAR 50-year reanalysis: monthly means CD-ROM documentation. B Am Meteorol Soc 82:247–267

Kållberg P, Simmons A, Uppala S, Fuentes M (2004) The ERA-40 archive. ERA-40 project report series no 17

Koster RD and coauthors (2004) Regions of strong coupling between soil moisture and precipitation. Science 305:1138–1140

Lettau H, Lettau K, Molion LCB (1979) Amazonia's hydrologic cycle and the role of atmospheric recycling in assessing deforestation effects. Mon Weather Rev 107:227–238

Nesbitt SW, Zipser EJ, Cecil DJ (2000) A census of precipitation features in the tropics using TRMM: radar, ice scattering, and lightning observations. J Climate 13:4087–4106

Pomeroy JW, Gray DM, Marsh P (2007) Studies on snow redistribution by wind and forest, snow-covered area depletion and frozen soil infiltration in northern and western Canada. (Vol. II, this book)

Quinton WL, Hayashi M (2007) Recent advances toward physically-based runoff modeling of the wetland-dominated central Mackenzie River Basin. (Vol. II, this book)

Simmons AJ, Gibson JK (2000) The ERA-40 project plan. ECMWF ERA-40 project report series no 1

Serreze MC, Lynch AH, Clark MP (2001) The Arctic frontal zone as seen in NCEP-NCAR reanalysis. J Climate 14:1550–1567

Szeto KK (2002) Moisture recycling over Mackenzie Basin. Atmos Ocean 40:181–197

Szeto KK, Stewart RE, Yau MK, Gyakum J (2007b) The Mackenzie climate system: a synthesis of MAGS atmospheric research. (Vol. I, this book)

Szeto KK, Tran H, MacKay MD, Crawford R, Stewart RE (2007a) Assessing water and energy budgets for the Mackenzie River Basin. (Vol. I, this book)

Woo MK, Rouse WR, Stewart RE, Stone JMR (2007) The Mackenzie GEWEX Study: a contribution to cold region atmospheric and hydrologic research. (Vol. I, this book)

Chapter 9

On the Cloud and Precipitating Systems over the Mackenzie Basin

David Hudak, Ronald Stewart, Peter Rodriguez
and Bohdan Kochtubajda

Abstract Cloud systems and their associated precipitation are fundamental aspects of the Mackenzie Basin climate system. Special measurements of these systems, including cloud radar sampling, were carried out in three intense observing periods between autumn 1998 and spring 1999 at Fort Simpson near the center of the basin. Cloud and precipitation features were closely linked to synoptic forcing conditions. Multi-layering of clouds was common and precipitation was typically reduced through sublimation beneath or between cloud layers. Proposed satellite missions such as CloudSat will detect many of the clouds but will lead to biases in inferred cloud thickness and multi-layering. State-of-the-art operational models tend to produce too much high cloud but too little surface precipitation due to sublimation and evaporation rates being too high.

1 Introduction

Clouds are a key aspect of the water cycle over the Mackenzie Basin since they convert water vapor into precipitation, and they have a major impact on radiative processes through their reflective and absorptive properties (Stewart et al. 1998). The actual impact of the clouds furthermore depends upon their vertical distribution, extent, internal microphysical characteristics, and the nature of the ensuing precipitation.

Previous studies have shown that there is a large annual cloud cover (approximately 65%) in the basin (e.g., Stewart and Burford 2002). However, there is a large seasonal and interannual variability. Some of this variability arises from the different types of cloud systems that affect the basin. For much of the year, cyclonic storms with relatively little convection pass over the region. These systems undergo considerable evolution as well since they are affected by the orographic barrier and their access to moisture is consequently altered. The occurrence of lee cyclogenesis on

the eastern flank of the orographic barrier is one key phenomenon associated with this evolution. At least during the summer, a substantial amount of convection also occurs.

The annual precipitation produced over the basin is estimated to be about 410 mm. Maximum precipitation rates occur in the summer in association with convective systems, yielding almost 50% of the total annual precipitation (Stewart et al. 1998). However, snowfall dominates 6–8 months of the year.

Several studies have been conducted on the nature of the cloud systems producing this precipitation. For example, Asuma et al. (1998, 2000) examined some of the features of storms that produced snow on the ground over the northern portion of the Mackenzie Basin; such storms entered the region from the Arctic Ocean or from the Pacific. Hanesiak et al. (1997) examined a storm over the southern Beaufort Sea that entered the region from the Arctic and which produced very light snowfall. Hudak and Young (2002) showed that over the Beaufort Sea, storms with a Pacific origin have become more frequent in recent years.

It was also found that much of the snow produced aloft does not reach the surface. This is evident on the global scale in that the zonal averages of integrated water and ice paths at latitudes near 60º are large, whereas the associated precipitation is not (Stephens et al. 2002). Burford and Stewart (1998) estimated that over the Mackenzie Basin half of the snow produced aloft is sublimated below cloud before reaching the surface.

To study the detailed nature of clouds and precipitation over the Basin, an observational effort lasting 14 months was carried out at Fort Simpson (61°54'N; 121°24'W), near the center of the basin, in 1998–99. It encompassed three intensive operating periods (IOPs) of 2–3 weeks duration were conducted: one in the fall of 1998, one in early winter of 1998–99, and one in the spring of 1999 (Hudak et al. 2004). The objectives of this study were (1) to describe the cloud fields occurring over Mackenzie Basin; (2) to examine the relationship between the large scale and time averaged vertical properties of coherent cloud structures; (3) to relate precipitation to these cloud features; and (4) to identify implications of this information to modeling studies and satellite observations.

2 Data and Methodology

The McMaster University IPIX portable X-band radar was deployed at the Fort Simpson weather station located at the airport during the 1998–1999

field experiment. The local topography is relatively flat though the mountainous region to the west stretches all to the way to the Pacific Ocean. The radar is capable of making reflectivity, Doppler and dual polarization measurements, and it was operated in different scanning modes, including various vertical stare and horizontal sweep scans in either "cloud" mode or "precipitation" mode, depending on the particular nature of the cloud system being observed (Hudak et al. 2004). Details of the experimentation at Fort Simpson are provided in Hudak et al. (2004) and Stewart et al. (2004).

Additional information was also obtained. (1) Special sounding releases were made from the site. Canadian Global Environmental Multiscale (GEM) model (Côté et al. 1998) analyses were utilized as well as a special archive of its vertical profile analysis over Fort Simpson that spanned all the IOP periods. (2) A cloud mask for the greater part of each IOP from which macroscopic cloud properties were derived. (3) Vertical profiles of reflectivity (Z), specific differential phase shift (k_{dp}), and horizontal wind for selected periods within the IOPs from which vertically resolved microphysical cloud and precipitation properties were derived. An example of the derivation of the cloud mask using various data sources and radar collection modes is given in Fig. 1. This figure demonstrates the data mining that was necessary to produce a continuous cloud mask, which in this case showed the merging of two cloud layers into a single thick layer.

Much of the information was synthesized in order to extract critical cloud and precipitation features. This included a synoptic and cloud classification of events as summarized in Table 1. Other derived features included cloud occurrence, cloud top height and temperature, cloud thickness, precipitation occurrence and type, precipitable water estimate, vertical profiles of ice water content (IWC), precipitation content, and winds.

3 Results and Discussion

3.1 IOPs Clouds and Precipitation Summary

The meteorological conditions experienced during the observing periods showed similarities to 'long-term' values. For example, the wide distribution in synoptic types is typical for the western Arctic (Asuma et al. 2000) and the total amount of precipitation and its daily distribution were both close to 'long term' averages. Therefore, the examination of clouds and precipitation during these three IOPs should provide insights applicable to 'long term' conditions.

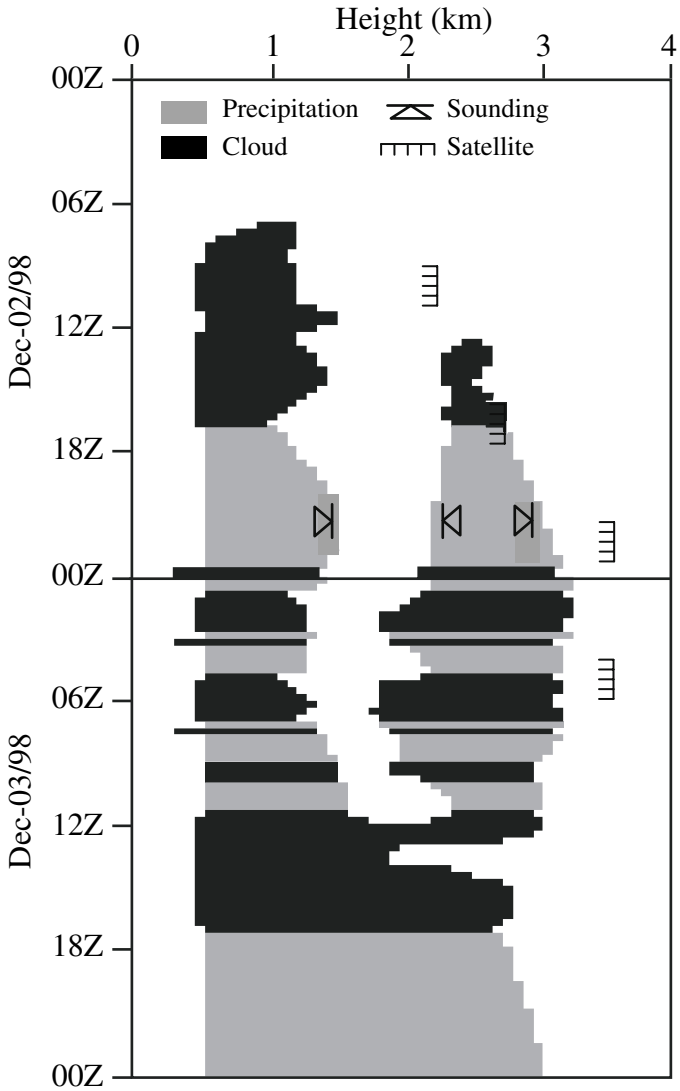

Fig. 1. The time history of the cloud mask for an event in Intense Observation Period 2 (winter). The top information bar describes the radar operating mode – black for cloud mode, gray for precipitation mode, white for no radar data. The cloud mask in the body of the figure is shaded black during radar cloud mode data collection and gray during either radar precipitation mode or when no radar data were available and supplementary data were used. For supplementary data, cloud boundaries using upper air sounding data is indicated by triangles and cloud top deduced from satellite measurements is indicated by vertical hatching

Table 1. Definitions of cloud and synoptic types used in the analysis

Cloud Type		Description
DCS	Deep cloud system	Cloud present from the low levels through most of the troposphere
MLS	Multi-layer system	Persistent layers of low, middle, and perhaps high cloudiness during the event
LOW	Low cloud	Self-evident
MID	Middle cloud	Self-evident
CNV	Convective cloud	Self-evident

Synoptic Type		Description
MLO	Major low	Identifiable systems crossing the coast usually spawned by a Gulf of Alaska upper vortex
CYC	Cyclogenesis	An approaching trough aloft with positive vorticity advection providing support for the development of a surface closed circulation to the lee of the mountains
UTR	Upper trough	As above but with a less intense vorticity center and no surface manifestation
WAA	Warm air advection	Significant warm air advection aloft in association with a cyclone well to the west. May or may not include a warm frontal passage at the surface
AMS	Airmass	Usually unstable airmass after the passage of a cyclone, but also could include significant low-level inversions due to an approaching ridge

General features of the IOPs are summarized in Table 2. Cloudy conditions prevailed during all IOPs. Cloudiness was above normal during IOPs 1 (fall) and 3 (spring) and below normal during IOP 2 (winter). Stratiform clouds dominated, though somewhat less so during IOP 3. There was a pronounced positive temperature anomaly in IOP 2 and an above average precipitation in all three IOPs (Table 2). Above average precipitation occurred during all three IOPs. IOP 1 had more days with precipitation but fewer intense events than normal. IOP 2 had fewer precipitation days, but the events were dynamically more intense and longer in duration than normal. IOP 3 had both above normal precipitation days and more intense events including the one day record snowfall for Fort Simpson, plus a rare hail event.

Table 2. Cloud and precipitation properties for each IOP

Cloud / Precipitation properties	IOP 1 (Fall)	IOP 2 (Winter)	IOP 3 (Spring)
Number of days	19	14	21
Precipitation [mm]	52	20	73
Days with precipitation	17	6	17
Cloud occurrence [%]	77	48	79
Average cloud thickness [km]	3.0	2.3	2.8
Cloud thickness < 3.0 km [%]	56	83	66
Cloud distribution skewness	0.48	0.53	0.32
Average ice water path [g m^{-2}]	70	81	99

3.2 Large Scale Forcing

The clouds were linked with a wide variety of large-scale forcing conditions that ranged from local convection to major storm systems from the Gulf of Alaska. There was no single dominating mechanism for the production of cloud. A synoptic classification was developed and shown to be important in explaining the variability of cloud properties. For example, the cyclogenesis category was the most efficient at producing ice aloft. The individual synoptic scenarios encompass the spread in cloud properties seen among the various numerical models. This demonstrates the importance of considering specific synoptic systems in assessing model capabilities. A consistent picture emerges of the upslope component and wind shear aloft contributing to the cloud structure in five synoptic classes.

Precipitation was most commonly associated with particular synoptic types. During the autumn and winter, the occurrence and long duration of precipitation were frequently associated with the deep low and cyclogenesis types with their thick, persistent clouds. In contrast, no precipitation was produced from warm air advection cases. When present, the actual precipitation was often organized into banded features that sometimes moved upslope within the low-level winds fields induced by the parent synoptic system.

3.3 Cloud Properties

Analysis of the cloud mask revealed that during the three IOPs clouds were present 70% of the time, subdivided as 77, 48, and 79% for IOPs 1, 2, and 3 respectively (Table 2). The cloud thickness distribution was simi-

lar in IOPs 1 and 3 but significantly different in IOP 2 when the clouds were less thick (Table 2) and the distribution being bimodal (Fig. 2).

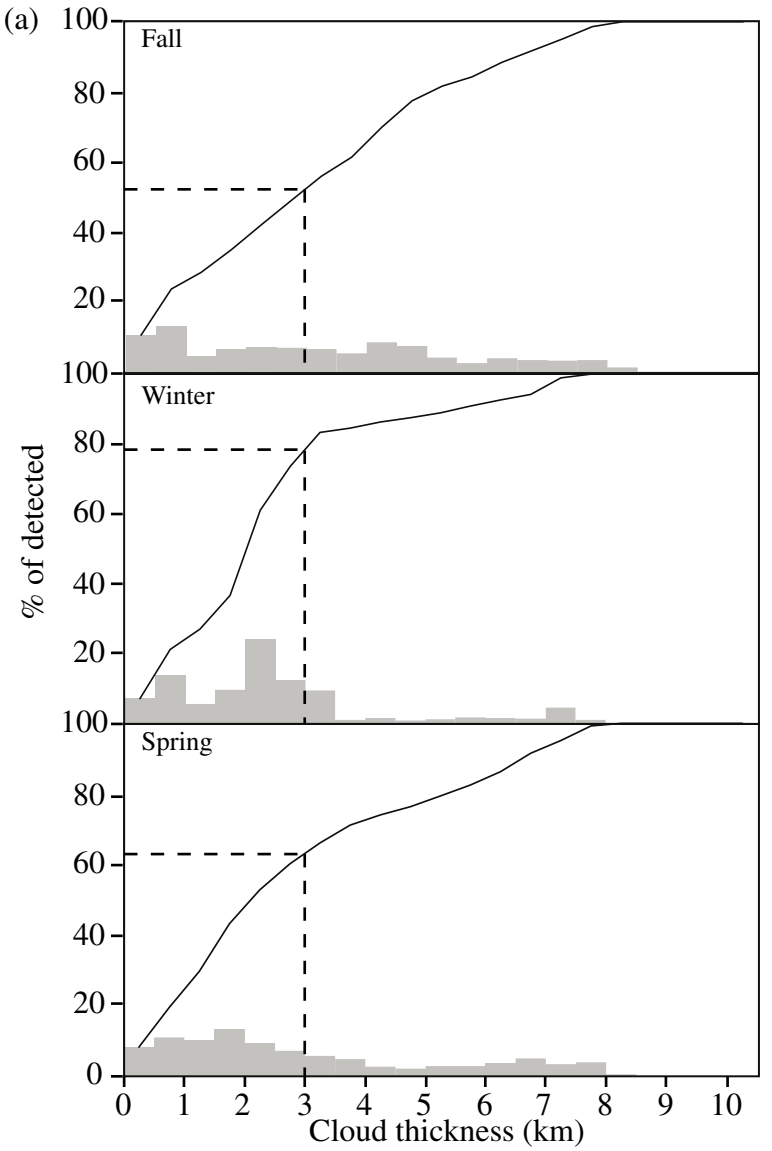

Fig. 2. Cloud mask statistics for the three Intense Observation Periods of (a) the distribution of cloud thickness and its cumulative distribution; and (b) the vertical distribution of cloud occurrence

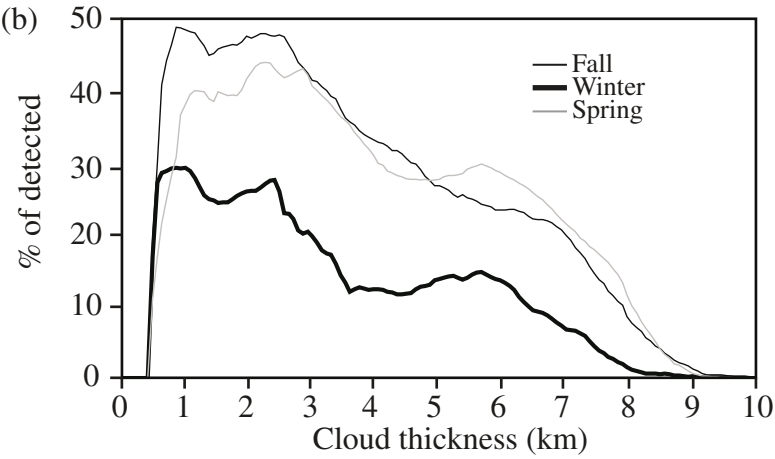

Fig. 2. (cont.)

Other cloud properties described in detail in Hudak et al. (2004) are summarized as follows. Given cloudy conditions, there was a significant prevalence of multi-layered systems (23%) that were associated with the widest variety of synoptic types. The cloud thicknesses in these multilayered situations were also most poorly correlated with surface incoming short wave solar radiation, an indication that these systems are the most complex to characterize. Other unique features of the clouds compared to those in mid-latitudes were the low temperatures of the low clouds and the absence of very thick cloud systems. Overall, the most frequent temperature at which the radar detected clouds was -12°C. The temperature corresponding to the largest radar reflectivity values was -15°C. The radar measurements when converted to ice water content showed large values throughout the period, especially in IOP 3. These observations are a clear, though not surprising, confirmation of the central role played by ice processes in these cloud systems.

A significant diurnal trend in cloud properties that had cloud thickness 18% or greater overnight was deduced for the winter period. These results are consistent with radiatively induced circulations due to an IR cloud top cooling mechanism (Lazarus et al. 2000). However, no diurnal trend in precipitation was detected.

3.4 Precipitation Properties

Precipitation events were typically associated either with the merging of cloud layers or with the division of one layer into many. Multi-layering was present during 36% of the instances of cloud across all three IOPs, while it was present only 15% of the time during precipitation events.

A number of critical features are linked with the production of precipitation at Fort Simpson. The presence of cloud layers and sub-saturated conditions below cloud impede the production of high precipitation amounts so that, for example, light snow can be generated from deep clouds as well as from low clouds. In the cold season, the limited available information indicated that a significant portion of the precipitation is also in the form of single ice crystals as opposed to aggregates. However, conditions are sometimes ideal for the production of quickly growing dendritic crystals.

4 Satellite and Model Application

4.1 Satellite Application

The determination of cloud top based on a passive technique using Advanced Very High Resolution Radiometer (AVHRR) satellite data was compared to cloud top based on direct IPIX radar measurements.

There was clearly a tendency for the AVHRR-based technique to underestimate cloud top height when cloud top is above 4 km. The correlation between ice water path (IWP) and difference between radar and AVHRR estimates for cloud with tops higher than 5 km was -0.84. In other words, the greater the ice content in the upper parts of the cloud, the better the AVHRR algorithms perform. The transparent nature of the uppermost cloud layers in low-IWP conditions was suggested as the cause of the high negative correlation of the AVHRR and radar techniques.

One way to overcome this problem is envisioned in the NASA/CSA CloudSat mission to place a 94 GHz active radar, with a minimum detectable signal (MDS) of -28 dBZ, onboard a polar orbiting satellite. The extensive presence of ice in clouds in the Fort Simpson area would make detection of these clouds by the radar onboard CloudSat reliable. Simulations with the IPIX radar data indicated that CloudSat would detect about 94% of the clouds, but the relatively coarse vertical resolution (500 m) of the CloudSat instrument would bias cloud thickness estimates. Cloud thickness simulated using the CloudSat had an average thickness of 3.0 km,

compared to 2.4 km measured by IPIX. This overestimate could in turn cause biases in other derived products such as ice and liquid water content.

It also remains a challenge to quantify precipitation from space. Precipitation statistics from Fort Simpson suggest that detectable precipitation will be present for approximately 17% of the overpasses for CloudSat. In contrast to CloudSat, the relatively high radar thresholds (MDS of approximately 11 dBZ) of the proposed Global Precipitation Measurement (GPM) mission will lead to many of the precipitation events being undetected or under-detected. Even when precipitation is detected with either satellite, there are other issues to be considered including, for example, the representativeness of derived instantaneous values within a precipitating event that often has banded features, and the inference of rate information within different types and combinations of precipitation.

4.2 Model Application

To evaluate the capability of the data set to identify significant model shortcomings and provide important cloud statistics to promote model parameterization development, the overall performance of cloud occurrence of the GEM model was examined. There was a distinct bias in placing too much cloud in the upper atmosphere (above 6 km) and too little in the lower atmosphere (below 3 km). The model cloud systems had more layers than were observed in all seasons, but especially in winter. Model cloud thicknesses were slightly greater in IOPs 1 and 3 but much less than observed in IOP 2. In particular, model thicknesses correlated most poorly with observed values when clouds were in the middle of the troposphere.

GEM also generally under-predicts surface precipitation. This is consistent with shortcomings of the model in its parameterization of the loss of precipitation mass through sublimation/evaporation between cloud layers and near the surface.

5 Concluding Remarks

A study of clouds and precipitation conducted at Fort Simpson during the autumn and winter of 1998 and the spring of 1999 yielded several conclusions. Cloud systems and their associated precipitation varied with the seasons. Clouds occurring in autumn and spring were generally deeper and more multi-layered than those occurring in mid-winter. Precipitation was produced under a variety of cloud conditions. In general, precipitation was

less likely to occur when clouds are multi-layered. Also, the low precipitation rates characteristic of this semi-arid region prevailed either when clouds were low, or when high thick clouds allowed precipitation to sublimate before reaching the surface.

Quantifying key aspects of these clouds, such as thickness and degree of layering, and the associated precipitation, will be a challenge even with the measurements obtained using proposed satellites such as CloudSat and GMP. The clouds and their precipitation are also very difficult to model successfully with current models such as GEM. Models tend to produce too much upper level cloud and moisture and they also generate too much multi-layering. Through enhanced sublimation they generate too little precipitation.

It should be noted that these results are from Fort Simpson, a location having no pronounced local source of moisture and in an area of generally descending large-scale motion in the lee of the mountains. Such factors certainly impact the nature of the clouds and precipitation production mechanisms. Similar studies are consequently needed in other regions having different background conditions if there is to be a comprehensive understanding of cold region clouds and precipitation. The highly variable clouds and precipitation are fundamental aspects of the water and energy cycle that need to be well understood if predictions of future conditions over this region are to be credible.

Acknowledgements

This research was supported by the Natural Sciences and Engineering Research Council of Canada, Environment Canada, and the Canadian Foundation for Climate and Atmospheric Sciences.

References

Asuma Y, Inoue Y, Kikuchi K, Kajikawa M, Sato N, Hayasaka T (2000) Wintertime precipitation behavior in the western Canadian Arctic region. J Geophys Res 105(D11):14,927–14,939

Asuma Y, Iwata S, Kikuchi K, Moore GWK, Kimura R, Tsuboki K (1998) Precipitation features observed by Doppler radar at Tuktoyaktuk, Northwest Territories, Canada, during the Beaufort and Arctic Storms Experiment. Mon Weather Rev 126:2384–2405

Burford JE, Stewart RE (1998) The sublimation of falling snow over the Mackenzie River Basin. Atmos Res 49:289–314

Côté J, Gravel S, Méthot A, Patoine A, Roch M, Staniforth A (1998) The operational CMC-MRB Global Environmental Multiscale (GEM) model, Part I: design considerations and formulation. Mon Weather Rev 126:1373–1395

Hanesiak JM, Stewart RE, Szeto KK, Hudak DR, Leighton HG (1997) The structure, water budget and radiational features of a high latitude warm front. J Atmos Sci 54:1553–1573

Hudak DR, Currie B, Stewart RE, Rodriguez P, Burford JE, Bussières N, Kochtubajda B (2004) Weather systems occurring over Fort Simpson, Northwest Territories, Canada during three seasons of 1998–1999. Part 1: cloud features. J Geophys Res 109: D22108, doi:10.1029/2004JD004876

Hudak DR, Young JMC (2002) A storm climatology of the southern Beaufort Sea. Atmos Ocean 40:145–158

Lazarus SM, Krueger SK, Mace GG (2000) A cloud climatology of the southern Great Plains ARM CART. J Climate 13:1762–1775

Stephens G, Vane D, Boain R, Mace G, Sassen K, Wang Z, Illingsworth A, O'Connor E, Rossow W, Durden S, Miller S, Austin R, Beneditti A, Mitrescu C and the CloudSat Science Team (2002) The CloudSat mission and the EOS constellation: a new dimension of space-based observations of clouds and precipitation. B Am Meteorol Soc 83:1771–1790

Stewart RE, Burford JE (2002) On the features of clouds occurring over the Mackenzie River Basin. J Geophys Res 107: D23,4720, doi:10.1029/2001JD001559

Stewart RE, Burford JE, Hudak DR, Currie B, Kochtubajda B, Rodriguez P, Liu J (2004) Weather systems occurring over Fort Simpson, Northwest Territories, Canada, during three seasons of 1998–1999: 2. Precipitation features. J Geophys Res 109: D22109, doi:10.1029/2004JD004929

Stewart RE, Leighton HG, Marsh P, Moore GWK, Ritchie H, Rouse WR, Soulis ED, Strong GS, Crawford RW, Kochtubajda B (1998) The Mackenzie GEWEX Study: the water and energy cycles of a major North American river basin. B Am Meteorol Soc 79:2665–2683

Chapter 10

The Relationship between Monthly Precipitation and Elevation in the Alberta Foothills during the Foothills Orographic Precipitation Experiment

Craig D. Smith

Abstract To better monitor and understand precipitation processes in the Alberta foothills, the Foothills Orographic Precipitation Experiment (FOPEX) was initiated in August 2001, consisting of six meteorological sites installed in a 40 km east-west transect in west-central Alberta to measure precipitation between 1070 and 2120 m above sea level. There are significant linear correlations between monthly accumulated precipitation and elevation when precipitation exceeds 70% of the long term average, but these relationships break down when monthly precipitation drops below the 70% threshold. During the cold season and when precipitation is greater than 70% of the long term mean, the altitudinal increase of monthly precipitation shows a linear dependency on the total amount of precipitation observed. Between October and April inclusive (cold season), accumulated precipitation increases by 74% for every 1000 m rise in elevation. However, for the cold months when precipitation is under the 70% threshold, this scaling factor is reduced to 46%. Spatial and topographic variability in precipitation during the warm season (May to September) makes it difficult to develop such a scaling factor. Based on these precipitation–elevation relationships, a simple but effective model is presented to extrapolate precipitation to various elevations along the transect using precipitation measured at a single location.

1 Introduction

Precipitation and precipitation processes in mountainous areas (Barry 1981) are relatively well understood on the windward side of the Western Cordillera but less so on the leeward side of the front-range due to the sparseness of climate observations, most of which are limited to areas east of the foothills or confined to lower elevations. Since the mountain region is a significant source region for early spring runoff to both the prairies and the north, proper assessment of winter snow accumulation on the foothills is important to water resource management and flood forecasters in Alberta, Northwest Territories, and other locations farther downstream.

Research into precipitation in the Rocky Mountain foothills and eastern front-range of Alberta is relatively sparse. Reinelt (1970) divided Alberta into regions based on topography and assessed the orographic component of precipitation in each region. The author estimated that conservatively, 37% of the precipitation in the area immediately east of the Rocky Mountain barrier is due to orographic influence. It was also noted that upslope flow over the Alberta foothills produces light but prolonged precipitation during winter arctic anticyclones and heavy prolonged precipitation during frequent cold low events in spring and summer. Both synoptic features, combined with orographic influence, lead to higher precipitation in the foothills than farther east in the Alberta prairies.

In the absence of direct measurements in regions of complex terrain, modeling methods were used to estimate precipitation. Raddatz and Khandekar (1977, 1979) simulated upslope airflow over the foothills and discussed mechanisms and influences on precipitation on a large scale with limited quantification and validation. Other examples of physically based precipitation–elevation models can be found in Colton (1976) and Sinclair (1994). Numerical weather prediction models, such as the Global Environmental Multiscale (GEM) (Côté et al. 1998) have been used to spatially distribute precipitation for initializing hydrologic models (Kite and Haberlandt 1999; Soulis and Seglenieks 2007; Voisin et al. 2002). Statistical models such as PRISM (Precipitation–elevation Regressions on Independent Slopes Model) apply regression analysis to develop precipitation–elevation relationships employing station observations and a digital elevation model to spatially distribute precipitation in complex terrain (Daly et al. 1994). PRISM is highly dependent on reliable observations made within an observation network over a large range of elevations, but this prerequisite cannot be met in areas of variable topography in Alberta and British Columbia. Long-term measurements of precipitation at various elevations remain important for climate monitoring, model development, and verification.

The Foothills Orographic Precipitation Experiment (FOPEX) was initiated to quantify precipitation in the Alberta foothills, establish precipitation–elevation relationships in foothills topography, and to employ this information to better understand the climatology and atmospheric processes related to precipitation in this area. In so doing, the ultimate goal is to improve the ability to quantify and distribute precipitation in this region. This chapter examines the relationships between monthly accumulated precipitation and elevation in the foothills and presents a simple model to estimate monthly precipitation at all elevations using observed precipitation from a single site.

2 Study Area

2.1 Site Description

The FOPEX study area is located in west-central Alberta, a topographic transition zone between the Rocky Mountains and the prairies (Fig. 1). The area is a genesis zone for severe convective weather in the summer (Strong 2003) and it is also subjected to heavy spring and fall snowfall events. Snowfall accumulations typically begin in mid- to late October and often persist until late April or mid-May, depending on elevation. At higher elevations (>2000 m above sea level), it is common to find sizeable snow packs remaining in June. As a transitional zone in elevation, the foothills have snowmelt occurring later than on the prairies but earlier than at the higher elevations. It is therefore a major source region for mid- to late-spring runoff to the Mackenzie and Saskatchewan River basins.

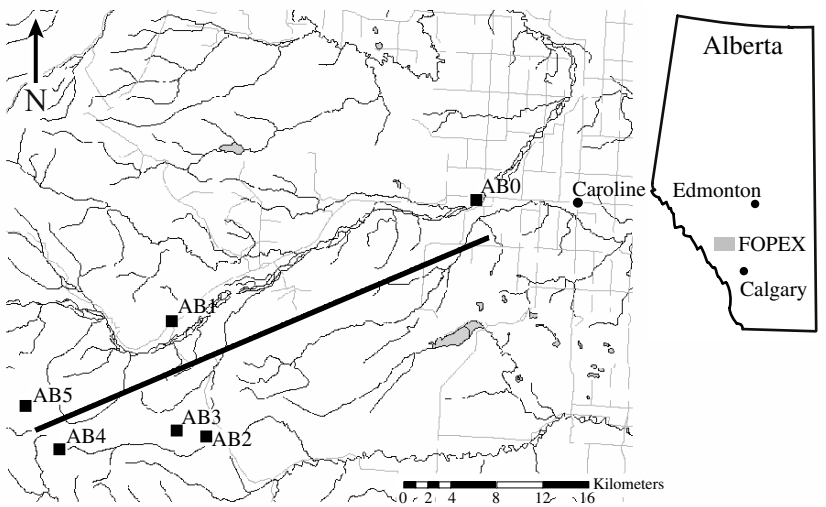

Fig. 1. The FOPEX study area in west-central Alberta

Six stations were set up along a 40-km transect in the Alberta foothills to measure precipitation and other meteorologic variables at elevations between approximately 1000 and 2000 meters above sea level (masl). The transect runs in a south-westerly direction (from lowest to highest elevation) between Caroline and Limestone Mountain (Fig. 1). The average slope of the transect is approximately 25 m km^{-1} with topography becom-

ing steeper towards the higher elevations as shown by a topographic profile, drawn approximately between Limestone Mountain and Caroline (Fig. 2). Limestone Mountain represents the final foothill peak before reaching the front range of the Rocky Mountains, approximately 8–10 km to the west. Thus, the study region lies within the rain shadow of the Rocky Mountains but is frequently subjected to upslope flow from the east and northeast, often resulting in enhanced precipitation (Szeto 2007). This provides the opportunity for some unique case studies. Also, the Limestone Mountain region has a history of meteorological research (Honch and Strong 1990; Smith and Yau 1993a, 1993b; Strong 2003; Strong and Smith 2001) that offers much climatological background information for this locale. More importantly, relatively long term climate data were available for a location in the transect to provide a climatology for the current research.

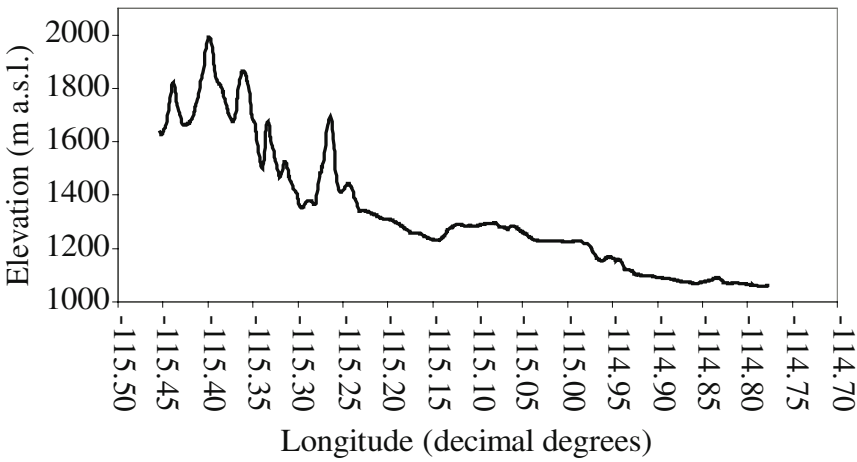

Fig. 2. Topographical profile of the FOPEX transect drawn approximately between Limestone Mountain (115.42° W) and Caroline (114.87° W), Alberta

Individual site selection was based on the criteria of elevation, exposure, and accessibility. Resource was available to install six sites at 200 m elevation intervals between Caroline and Limestone Mountains (Table 1). These sites were named according to their relative elevation, with AB0 at the lowest elevation and AB5 at the highest elevation. Each site was located to gain maximum exposure, especially to the east (the direction of up-slope airflow). To minimize installation and service costs as well as safety concerns, all sites were accessible by snowmobile, motor vehicle, all terrain vehicle, or a relatively short hike. In some instances, compro-

mises were required where exposure or elevation was sacrificed to ensure accessibility. With good accessibility, in turn, instrument serviceability and data quality were enhanced.

Table 1. FOPEX site locations and elevations

Site Name	Site Identifier	Latitude [Dec. degrees]	Longitude [Dec. degrees]	Elevation [masl]
Caroline	AB0[a]	52.09°	-114.87°	1070
Clearwater Ranger Station	AB1	51.99°	-115.24°	1280
Marble Mountain East	AB2[b]	51.90°	-115.19°	1440
Marble Mountain West	AB3	51.91°	-115.23°	1640
Limestone Ridge East	AB4	51.89°	-115.37°	1950
Limestone Ridge	AB5[b]	51.92°	-115.42°	2120

[a]Site out of service in May, 2005. [b]Sites decommissioned in June, 2004.

2.2 Climatology

Between 1962 and 1987, observations of temperature and precipitation were made at the Clearwater Ranger Station (same geographical location as AB1) at an elevation of 1280 masl. These data were used to calculate a monthly climatology (to approximate the 1961–90 30-year normal period) for temperature and precipitation (Fig. 3).

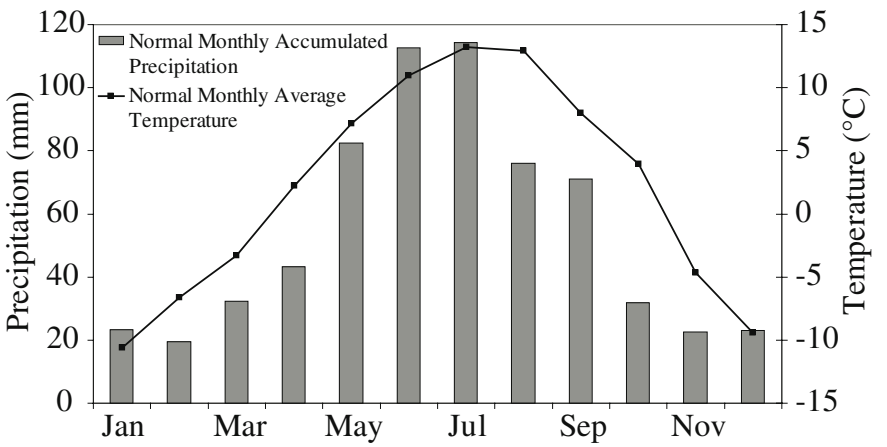

Fig. 3. Long-term monthly averages of precipitation and temperature as measured at the Clearwater Ranger Station

The average annual precipitation in this region, as measured at the Clearwater Ranger Station, is 652 mm with approximately 50% occurring from June to August. The average annual temperature is approximately 2ºC with the average monthly temperature below 0ºC from November through March.

By co-locating a FOPEX site at the Clearwater Ranger Station, the recent FOPEX observations can be put into context with the long term average. Figure 4 provides a summary of the differences between observations of monthly precipitation and temperature at AB1 (from October 2001 through September 2005) and the long term averages. Differences in precipitation are expressed as a percentage of the long term average and temperature is expressed as the absolute deviation from the long term mean (AB1 minus normal). The FOPEX observation period was characterized by drier than normal winters and summers and wetter than normal springs and autumns, but the average annual precipitation during this period was nearly normal at 649 mm. Temperatures were typically higher than the long term average throughout the FOPEX period with an annual mean of 3.5 ºC.

3 Methods

3.1 Instrumentation and Observation Period

The instruments at each site were selected based on Meteorological Service of Canada standards for automatic stations at the time of installation. Each site measured accumulated precipitation, temperature, humidity, wind speed and direction (at the height of the precipitation gauge of approximately 2 m), snow depth, and rainfall rate. Several sites also measured surface pressure. The instruments, with the exception of the tipping-bucket rain gauge and snow depth sensor, were installed inside a 3 x 3 m (2.5 m high) chain link enclosure designed to minimize vandalism and interference from animals. The accumulating precipitation gauge was raised so that the orifice was higher than the fence to minimize the fence interference with the flow of air around the gauge orifice. The open chain link fencing material permitted relatively unobstructed air flow around the instrumentation, offering neither an advantage nor disadvantage to the catch of precipitation in the gauge. Accumulated precipitation was measured using a Geonor T-200B precipitation gauge installed with an Alter wind shield (Alter 1937) to minimize the bias in precipitation measurements caused by wind. An exception was the deployment at AB0 of a Belfort

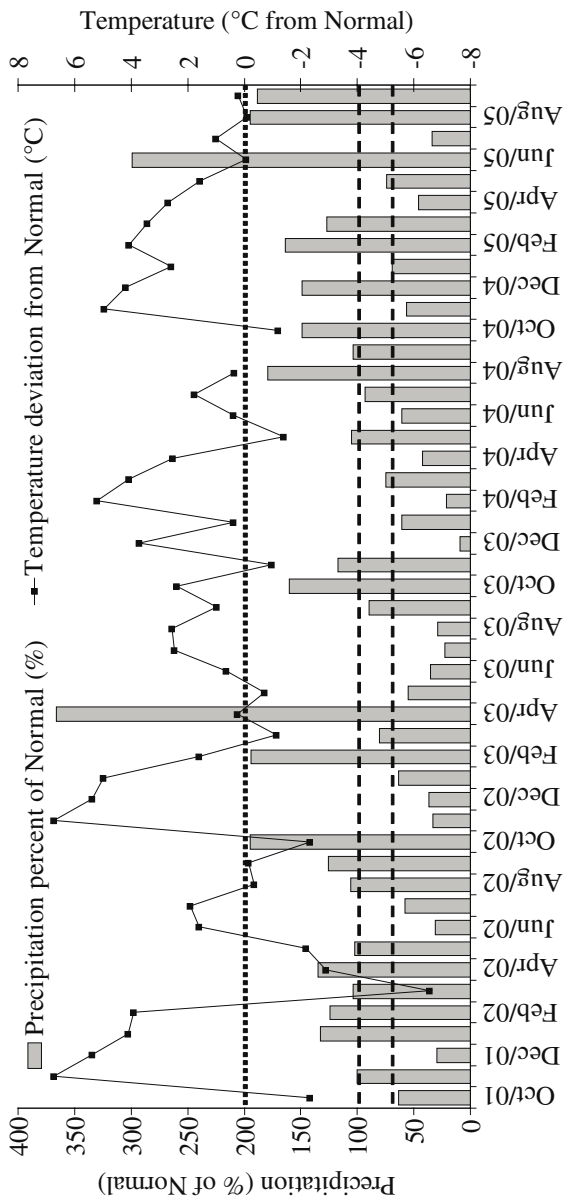

Fig. 4. Differences between FOPEX (AB1) observed precipitation and temperature from the long term average at Clearwater Ranger Station. Precipitation expressed as percent of normal and temperature expressed as absolute deviation (°C) from normal (AB1 minus normal). The 0°C line is marked with a dotted line while 70% and 100% of normal precipitation lines are marked with dashed lines

high-capacity gauge, from October 2001 to June 2003 and from June 2004 to May 2005 (also installed with an Alter wind shield). A glycol mixture was used in the collector to induce the melting of solid precipitation as it was collected. A layer of oil was floated on top of the collector to prevent evaporation. Snow depth was measured using Campbell Scientific SR50 and UDG01 (prior to 2002) sonic depth sensors. All data were averaged or accumulated at 30-minute intervals.

Neither the climate station precipitation data nor the FOPEX precipitation data were adjusted for wind induced bias as described in Goodison et al. (1998). Analysis of wind speeds at AB5 (the highest and most exposed site) for 2003 suggests that when temperatures were below 0°C, 93% of the 30-minute precipitation accumulations of >0.1 mm occurred at wind speeds of less than 2 m s^{-1}. Less than 0.5% exceeded 5 m s^{-1}. The average wind speed during precipitation events at AB5 in 2003 was 0.8 m s^{-1}. This average typically decreases with elevation. Preliminary wind-correction curves for the Geonor accumulating precipitation gauge (Campbell and Smith 2005) suggest that wind adjustments are likely small for speeds below 2 m s^{-1}. However, wind bias could potentially be a significant source of error and this should be revisited and more validation work is required to produce precise corrections of high resolution (automated) precipitation observations.

Several FOPEX sites were installed in June 2001 but not all of them were fully operational until October 2001. Sites AB2 and AB5 were removed in June 2004 and AB0 was destroyed by the flooding of Clearwater River in June 2005. Analysis in this chapter is focused on observations made during four hydrologic periods or water years (WY, defined as the period between 1 October and 30 September) between October 2001 and September 2005. The 2001–04 WY were used to develop the relationships between precipitation and elevation while the 2004/05 WY was used as an independent test of a simple precipitation–elevation model.

3.2 Quality Control and Analysis

Prior to analysis, the data underwent a quality control process. For precipitation, this involved the visual inspection of the monthly precipitation data for each site. The vibrating wire sensor used in the Geonor gauge produced some noise in the observations of bucket weight. This noise was manually filtered to produce a clean trace of 30-minute precipitation estimates, accumulated by month. Supplementary precipitation information obtained by other instrumentation (tipping-bucket rain gauge in summer and sonic

snow depth sensor in winter) was also used to filter the noise. Although random noise could produce inaccuracies during precipitation events, the error was not in excess of ± 0.2 mm per event. The sensor has a high resolution and can detect precipitation accumulations as small as 0.1 mm. As noted, no adjustments were made to correct gauge catch error caused by wind. Evaporation errors were considered negligible and wetting loss is not a concern as it is with manual precipitation observations. Gauge capping during large snowfall events could be a source of non-systematic error but this occurrence usually affects the timing rather than the quantity of the observed event (a snow cap will eventually fall into the collector bucket and be measured by the sensor).

Linear regression analysis was used to determine the change in precipitation with elevation for each month during the observation period. Previous studies in other locations have shown that such linear relationships are not uncommon (Burns 1953; Hanson et al. 1980; Houghton 1979; Lull and Ellison 1950). The slope of the linear monthly precipitation–elevation relationship is termed the precipitation lapse rate (PLR), expressed as mm of precipitation per 1000 m elevation change. The PLR is positive if precipitation increases with elevation. A relationship between the monthly PLRs and precipitation at AB1 was then used to develop a simple model to estimate precipitation at all elevations along the transect.

4 Results

4.1 Monthly Precipitation–Elevation Relationships

A linear precipitation–elevation relationship was derived for the period October 2001 to September 2004 to obtain a slope, intercept, and Pearson correlation coefficient for each month. The correlation coefficient for the monthly precipitation–elevation relationships (r_{PE}) averaged 0.58 but the range was large (-0.81 to 0.98). The slope (PLR) was also quite variable, ranging from -20.7 mm/1000m to 120.2 mm/1000m with an average of 21.8 mm/1000m. The overall correlation between precipitation and elevation was stronger when monthly precipitation in the region, as indicated by observations at AB1, exceeded 70% of the long term average (Fig. 5). As the threshold percentage decreased from 70% (i.e., r_{PE} values for months with less precipitation are included in the average), the average r_{PE} decreases from 0.70 to a minimum of 0.56. Raising the threshold from 70% to 100% preserves a high average (r_{PE} greater than 0.67) but the sample

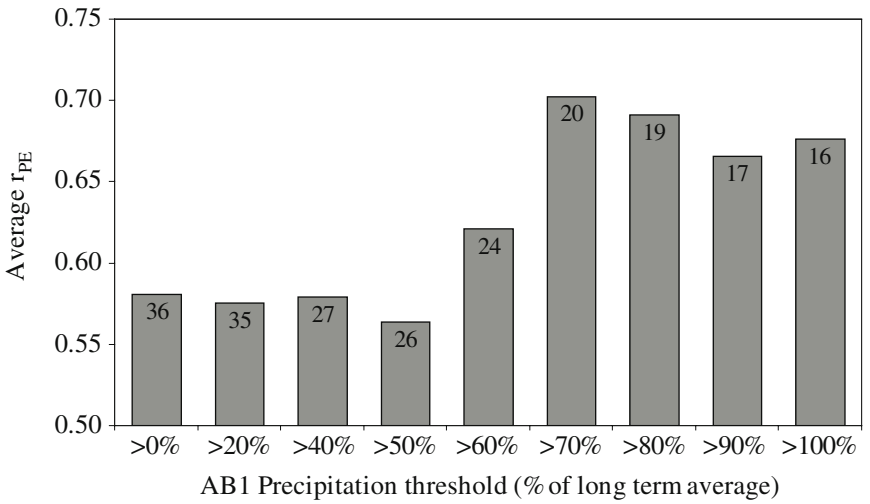

Fig. 5. Change in the average correlation coefficient (r_{PE}) for monthly precipitation-elevation relationships as months with low precipitation are sequentially excluded from the correlation analysis (e.g., when only months with precipitation greater than 70% of the normal amount are included, the r_{PE} value is 0.70). Sample size is shown inside the bars

size is reduced. The 70% threshold is therefore considered to be an optimum combination of high r_{PE} and maximum sample size.

Table 2 provides a summary of the calculated PLR and correlation coefficient r_{PE} divided into two subsets based on the 70% threshold. When monthly precipitation exceeded 70% of the long term mean, the PLR averaged 32.1 mm/1000m, and the average r_{PE} was 0.70 with 16 of 20 months (80%) showing an r_{PE} value greater than 0.80. When monthly precipitation was below 70% of the long term mean, the average PLR was 9.0 mm/1000m, but average r_{PE} was reduced to 0.43 and the distribution of r_{PE} changed substantially, with only 5 of 16 months (31%) having a value greater than 0.80.

When the entire set of monthly precipitation was divided into a warm (May to September) and a cold season (October to April), the average r_{PE} were 0.62 and 0.53 and the average PLR were 20.2 and 24.2 mm/1000m for these respective seasons. However, when these months were further subdivided based on the 70% precipitation threshold, the average r_{PE} for cold months with precipitation greater than the 70% threshold increased to 0.82. The average PLR for this subset was 32.4 mm/1000m. For warm months, the strength of the correlation was not increased by using the 70% threshold, but the average PLR rose to 31.8 mm/1000m when months with

lower precipitation were excluded. The implication of this analysis is that precipitation–elevation relationships in the FOPEX transect are strongest during the cold season when its monthly precipitation exceeds 70% of the long term average.

Table 2. Summary of regression analysis for monthly precipitation vs. elevation for the period of October-2001 through September-2004

AB1 Precipitation >70% Normal			AB1 Precipitation <70% Normal		
Month	Slope (PLR) [mm/1000 m]	r_{PE}	Month	Slope (PLR) [mm/1000 m]	r_{PE}
Nov-01	-0.8	-0.33	Oct-01	26.0	0.98
Jan-02	14.6	0.91	Dec-01	4.8	0.73
Feb-02	19.6	0.84	Jun-02	15.0	0.71
Mar-02	27.6	0.96	Jul-02	-20.7	-0.78
Apr-02	60.3	0.96	Nov-02	0.5	0.24
May-02	52.8	0.93	Dec-02	-0.1	-0.02
Aug-02	46.1	0.84	Jan-03	-13.4	-0.81
Sept-02	44.5	0.93	May-03	9.8	0.53
Oct-02	34.9	0.95	Jun-03	16.5	0.56
Feb-03	16.4	0.97	Jul-03	18.7	0.95
Mar-03	15.9	0.95	Aug-03	8.1	0.85
Apr-03	120.2	0.97	Dec-03	1.8	0.76
Sept-03	29.3	0.87	Jan-04	-1.9	-0.28
Oct-03	45.5	0.94	Feb-04	2.4	0.50
Nov-03	11.4	0.83	Apr-04	15.1	0.98
Mar-04	23.2	0.92	Jun-04	61.3	0.97
May-04	77.5	0.98			
Jul-04	26.8	0.50			
Aug-04	-18.2	-0.71			
Sept-04	-4.8	-0.17			
Average	32.1	0.70	Average	9.0	0.43

A linear regression analysis was used to examine the relationship between monthly precipitation at AB1 and the PLR for the period October 2001 to September 2004 inclusive (Fig. 6a). The correlation coefficient, r_{PLR}, was 0.56. Unlike the monthly precipitation–elevation relationship, this correlation did not become stronger by simply using the 70% threshold. In fact, r_{PLR} was reduced to less than 0.50 when the data were thus divided. However, the correlation was strengthened by binning the monthly precipitation into seasons, with $r_{PLR} = 0.94$ for the cold months (Fig. 6b) but no apparent correlation for the warm months (Fig. 6c). The r_{PLR} for cold months increased further to 0.96 when months with precipitation be-

low the 70% threshold were eliminated. It should be noted that the high precipitation event of 160 mm (April 2003) shown in Fig. 6a and b had only a small effect on the overall relationship. When precipitation was below the 70% threshold during the cold months (not shown), r_{PLR} decreased to 0.44. For the warm months, the strength of the correlation increased when the 70% threshold was used but the relationship became negative (r_{PLR} = -0.44) possibly due to more convective precipitation at low elevations.

From the above linear regression analysis, precipitation–elevation relationships were strongest when precipitation was not significantly below normal and during cold months. When these conditions are met and monthly precipitation at AB1 is known, accumulated precipitation can be estimated at any elevation along the transect with a high degree of confidence. By constraining the regression so that the intercept passes through the origin, precipitation is found to increase by a factor of 74% per 1000 m change in elevation. This scaling factor decreased to 46% per 1000 m when precipitation was less than 70% of normal but can be used with less confidence due to weaker monthly precipitation–elevation relationships. Warm season precipitation is best described by using the average PLR of 32 and 16 mm/1000m for months that are, respectively, above and below the 70% threshold.

4.2 Precipitation–Elevation Model

A simple model was developed to estimate monthly and seasonal precipitation in the FOPEX region based on the linear regression analysis:

$$P_E = P_{AB1} + \left[\alpha + \beta(P_{AB1})\right]\left(E - E_{AB1}\right)/1000 \qquad (1)$$

where P is monthly precipitation (mm) at any elevation E (m) in the transect, P_{AB1} is monthly precipitation (mm) at AB1, E_{AB1} is the elevation of AB1 (1280 m), and α = -4.97 and β = 0.81 are empirical coefficients.

Precipitation at AB0, AB3, and AB4 were modeled for the 2004–05 WY using precipitation observed at AB1 and validated by concurrent measurements at these sites. Unfortunately, AB0 was destroyed by the Clearwater River flood in June 2005 and validation data for this site were available only to the end of April 2005.

The monthly biases in the model at AB0, AB3, and AB4 were variable and often relatively large (Fig. 7). The absolute monthly error varied from 18 mm (AB4, Oct. 2004) to -60 mm (AB3, Jun. 2005) and relative month-

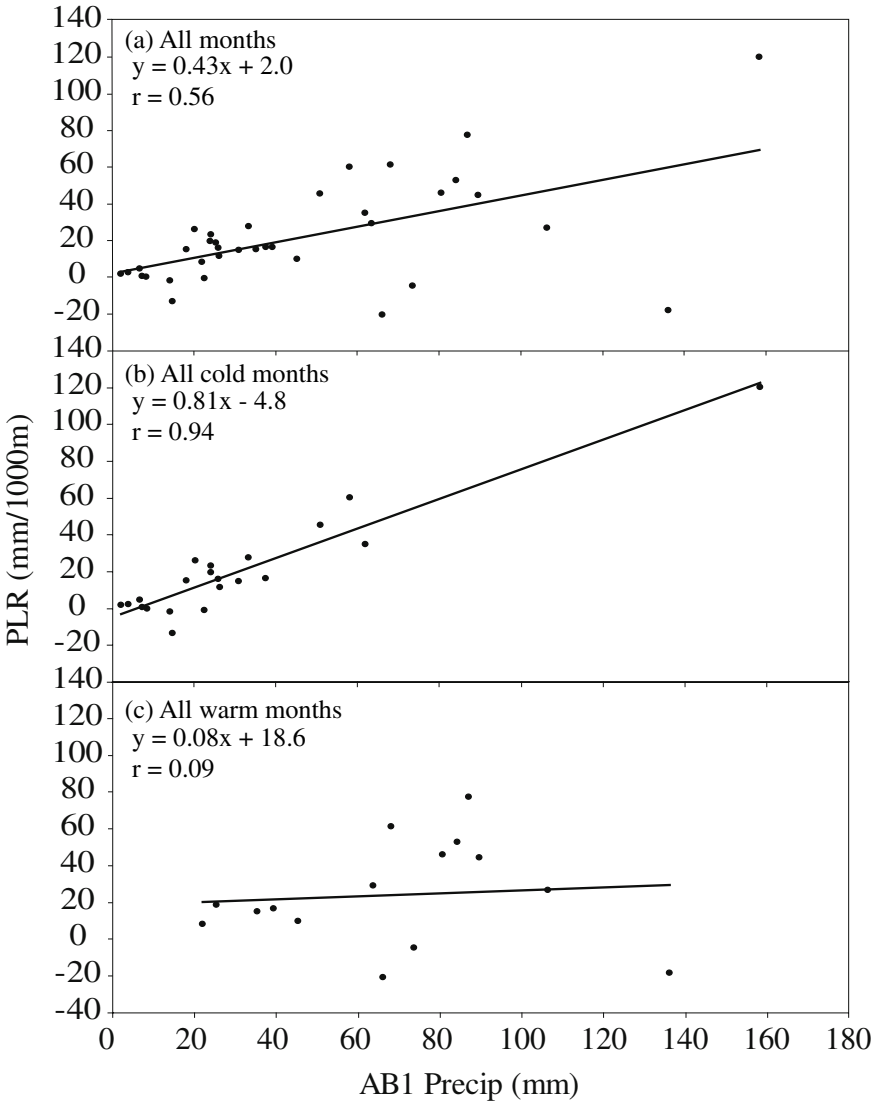

Fig. 6. Relationships between monthly precipitation lapse rates (PLR) and monthly precipitation at AB1 for (a) all months (October 2001 to September 2004), (b) all cold months (October–April) and (c) all warm months (May–September)

ly error varied from 80% (AB0, Apr. 2005) to -46% (AB4, Apr. 2005). However, when accumulated by season, modeled precipitation was remarkably similar to observed (Fig. 8) for all sites and seasons with relative

errors between 5% and -13%. When accumulated over the 2004–05 WY, the model underestimated precipitation at AB3 and AB4 by 7% and 1% respectively. This is considered to be well within the limits of instrument error.

5 Discussion

Analysis of monthly accumulated precipitation observed at the FOPEX sites between October 2001 and September 2004 illustrates the variability in the relationship between precipitation and elevation in this region. During some periods, the relationship was remarkably linear, as when the precipitation was greater than 70% of the long term average. The linear relationship breaks down when precipitation was substantially less than the long term average. This is a significant feature but the cause can only be hypothesized as being a result of synoptic storm type and the frequency of upslope events. During wetter months, especially in late autumn and early spring, more upslope flow events may have strengthened the precipitation–elevation relationships on these lee slopes. This needs to be investigated further, especially at short time scales.

Analysis has also shown that when certain climate conditions are met, the magnitude of the PLR was dependent on the relative amount of precipitation in the region. The change in precipitation with altitude tended to increase as higher precipitation was observed at the low elevations. This phenomenon occurred during the colder months of October through April and was strongest when precipitation was greater than 70% of the long term average. When these conditions occurred, precipitation increased by 74% per 1000 m of elevation change. Regression analysis yielded an r_{PLR} of 0.96, and an average r_{PE} of 0.85, suggesting a high level of confidence for the estimated precipitation. These strong relationships may be attributed to more frequent upsloping and the resulting influence that these lee slopes have on precipitation augmentation. During cold months with precipitation below the 70% threshold, the scaling factor was reduced to 46% with an r_{PLR} and an average r_{PE} of 0.39 and 0.34 respectively. This significantly reduces the confidence for the precipitation estimated by the linear regression. Again, the cause is only speculative but may be attributed to the dominance of lighter precipitation events that are not enhanced by upslope flow and therefore not influenced by elevation. The relationship between PLR and precipitation weakened even further during the warmer

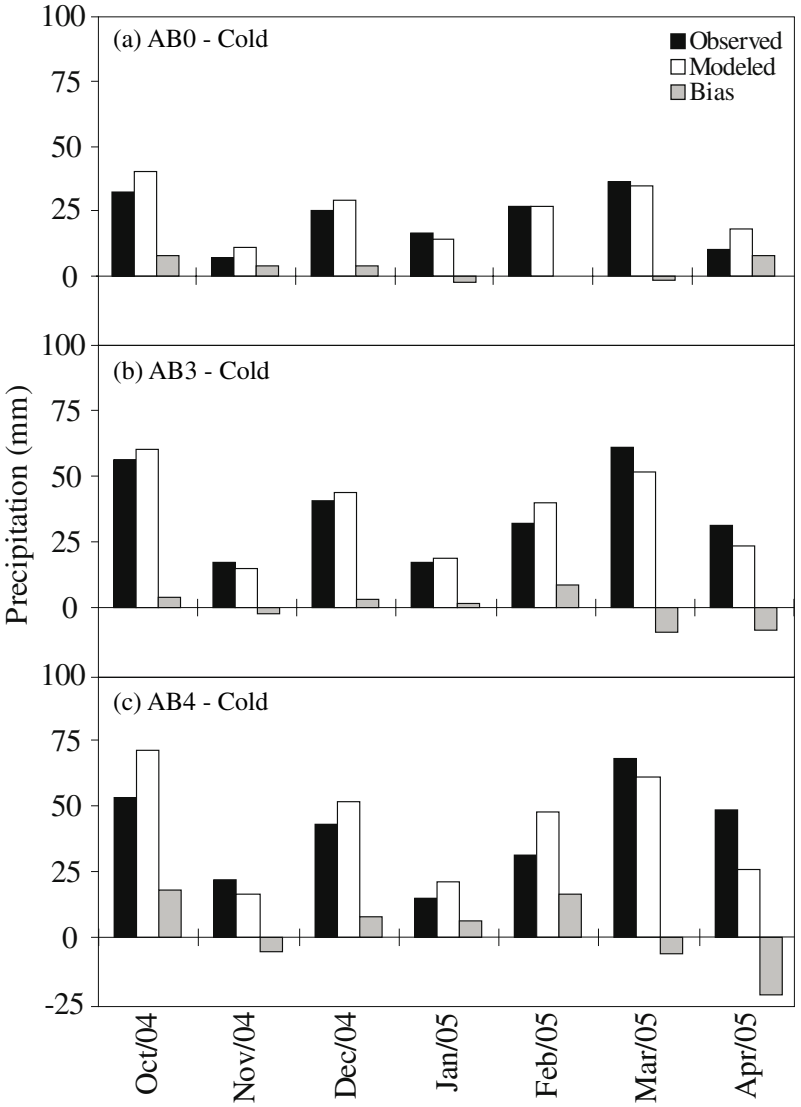

Fig. 7. Monthly observed and modeled precipitation and model bias (modeled minus observed) for (a) AB0 cold months, (b) AB3 cold months, (c) AB4 cold months, (d) AB3 warm months, and (e) AB4 warm months

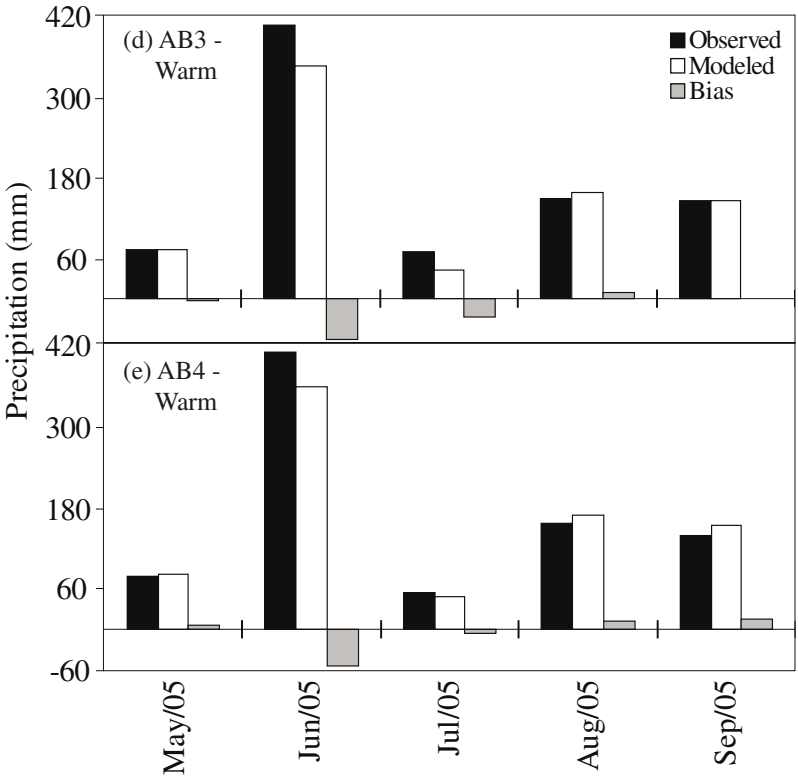

Fig. 7. (cont.)

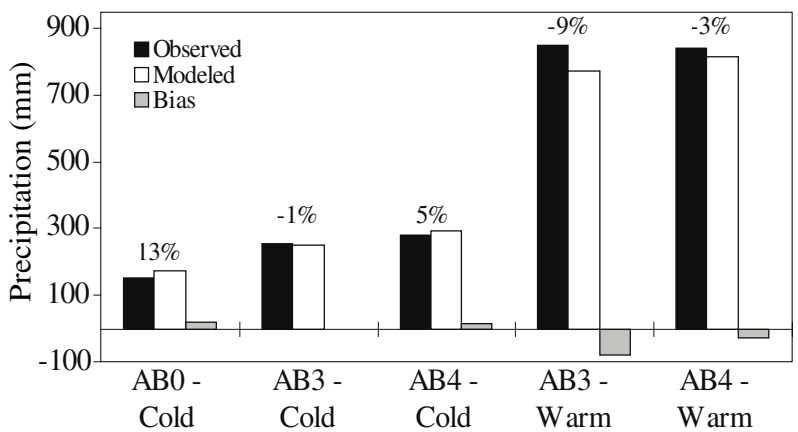

Fig. 8. Seasonal accumulated observed and modeled precipitation and model bias (modeled minus observed) for the 2004/2005 WY. Relative errors are shown above the bars

months, likely due to the higher spatial (and topographic) variability in convective precipitation between late spring and early fall.

The simple model presented worked surprisingly well in the validation period of October 2004 to September 2005, for the estimation of seasonal and annual precipitation. The expectation was that winter precipitation can be modeled with a low relative bias while summer precipitation would have a large relative bias. This distinction was not evident in the modeled results. It was also expected that the model bias would be higher for months with precipitation less than 70% of the long term average but this is not apparent. No relationship between model bias and site elevation could be discerned. The model performed quite well even during the intense precipitation events in June 2005 and produced an underestimate of only 15% and 13% for AB3 and AB4 respectively. Overall, the model performance was better than expected for this one-year validation period, especially considering that precipitation gauge errors could reach 10%. A longer validation period is needed.

The FOPEX project has been scaled back from six to three sites, but the remaining will continue to operation for several more years to provide opportunities to further develop and test the model. More work is required to classify storm types to better understand these precipitation–elevation relationships and to better explain the outliers. Although synoptic forcing of precipitation may be similar in other regions in lee of the Rocky Mountains, the effect of slope steepness, length, and exposure may be quite different and should be assessed. Thus, the relationships presented should be applied with caution in other lee regions.

Acknowledgements

The author thanks the following people for their assistance over the course of this project: Bruce Cole, Dell Bayne and Natasha Neumann (Climate Research Branch, Saskatoon); Drew Lebjac and Masaki Hayashi (Univ. of Calgary), Karl Runions and David Graham (Alberta Environment); Dennis Frisky (Rocky Mountain House) and the many co-op students involved in the project: Allison Theede, Erin Thompson, Lisa Christmas, Jodi Axelson, Dusty Guedo, Steve Hermanson, Courtney Campbell, and Brad Klaver. Gratitude is also extended to management of the Climate Research Branch for their continued support.

References

Alter JC (1937) Shielded storage precipitation gauges. Mon Weather Rev 65:262–265

Barry RG (1981) Mountain weather and climate. Methuen, London

Burns JI (1953) Small-scale topographic effects on precipitation distribution in San Dimas Experimental Forest. Eos T Am Geophys Un 34:761–768

Campbell C, Smith CD (2005) The Bratt's Lake Precipitation Intercomparison Project: estimating the systematic errors in measuring precipitation using the Geonor accumulating precipitation gauge. CMOS Bulletin SCMO 33:47–51

Colton DE (1976) Numerical simulations of orographically induced precipitation distributions for use in hydrological analysis. J Appl Meteorol 15:1241–1251

Côté J, Gravel S, Méthot A, Patoine A, Roch M, Staniforth A (1998) The operational CMC/MRB Global Environmental Multiscale (GEM) Model. Part I: design considerations and formulation. Mon Weather Rev 126:1373–1395

Daly C, Neilson RP, Phillips DL (1994) A statistical–topographical model for mapping climatological precipitation over mountainous terrain. J Appl Meteorol 33:140–157

Goodison BE, Louie PYT, Yang D (1998) WMO solid precipitation measurement intercomparison. WMO no. 872

Hanson CL, Morris RP, Engleman RL, Coon DL, Johnson CW (1980) Spatial and seasonal precipitation distribution in Southwest Idaho. Agricultural Reviews and Manuals, ARM-W-13, USDA

Honch RW, Strong GS (1990) Mesoscale dynamics associated with convection during LIMEX-85. 16th Conf. Severe Local Storms, Kananaskis Park, Alta., American Meteorological Society, Boston, pp 681–686

Houghton JG (1979) A model for orographic precipitation in the North-Central Great Basin. Mon Weather Rev 107:1462–1475

Kite GW, Haberlandt U (1999) Atmospheric model data for macroscale hydrology. J Hydrol 217:169–338

Lull HW, Ellison L (1950) Precipitation in relation to altitude in Central Utah. Ecology 31:479–484

Raddatz RL, Khandekar ML (1977) Numerical simulations of cold easterly circulations over the Canadian Western Plains using a mesoscale boundary-layer model. Bound-Lay Meteorol 11:307–327

Raddatz RL, Khandekar ML (1979) Upslope enhanced extreme rainfall events over the Canadian Western Plains: a mesoscale numerical simulation. Mon Weather Rev 107:650–661

Reinelt ER (1970) On the role of orography in the precipitation regime of Alberta. The Albertan Geographer 6:45–58

Sinclair MR (1994) A diagnostic model for estimating orographic precipitation. J Appl Meteorol 33:1163–1175

Smith SB, Yau MK (1993a) The causes of severe convective outbreaks in Alberta. Part I: a comparison of a severe outbreak with two nonsevere events. Mon Weather Rev 121:1099–1125

Smith SB, Yau MK (1993b) The causes of severe convective outbreaks in Alberta. Part II: conceptual model and statistical analysis. Mon Weather Rev 121:1126–1133

Soulis ED, Seglenieks FR (2007) The MAGS integrated modeling system. (Vol. II, this book)

Strong GS (2003) Review of prairie thunderstorms. CMOS Bulletin SCMO 31:11–27

Stong GS, Smith CD (2001) Assessment and prediction of prairie severe thunderstorm weather phenomena. Emergency Preparedness Canada

Szeto K (2007) Cold-season temperature variability in the Mackenzie Basin. (Vol. I, this book)

Voisin N, Leighton HG, Soulis ED, Feng J (2002) Sensitivity of the Mackenzie River Basin hydrology to solar radiation uncertainties. Proc 59th Eastern Snow Conference, Stowe, Vermont, pp 135–144

Chapter 11

On Predicting Maximum Snowfall

Max L. Dupilka and Gerhard W. Reuter

Abstract Using the principle of conserving water substance, the maximum snowfall amount is related to the saturated vapor mixing ratio at cloud base and cloud top levels. The inherent uncertainties of the input data allow for numerical approximations that lead to a linear relationship between maximum snowfall and cloud base temperature. To test the validity of this relationship, an analysis was made of the correlation of 24 hour accumulated snowfall measurements with temperature observations from upwind soundings. The data set covered all of Alberta (except the mountainous west) for October 1990 to April 1993. The result suggests that the snow amount depends roughly linearly on the 850 hPa temperature with a correlation coefficient of 0.62. The snowfall–temperature relationship can be used to complement the Quantitative Precipitation Forecast (QPF) available from operational NWP models.

1 Introduction

A major task of the Prairie and Northern Region Weather Office of Environment Canada is to predict snowfall amounts and provide timely warnings of heavy snowfall. Heavy snowfall warnings should be issued for an event when the snow accumulations are expected to be 10 cm or greater within a 24 hour period. Major snowfall events in Alberta are usually associated with lee cyclogenesis that is forced when a baroclinic wave disturbance moves over the Rocky Mountains. Numerical Weather Prediction (NWP) models are skilful to resolve and track these large-scale baroclinic disturbances and the resulting lee cyclogenesis. During the last two decades improvements in model grid resolution, physical parameterization, and initialization have led to useful guidance concerning the occurrence of snow storms. However, model predictions of snowfall accumulations are often inaccurate, particularly for heavy snowfall (Aktary and Reuter 1993). The operational forecaster could benefit from techniques, complementary to NWP guidance, to assist in deciding whether the 24 hour accumulation of snow will exceed 10 cm.

The amount of snow falling from synoptic-scale weather systems depends largely on the amount of vapor available for condensation or deposition. Studies of severe summer thunderstorms in Alberta have also shown that the

amount of water vapor in a column is associated with the potential for tornado formation (Dupilka and Reuter 2006). Local sources of atmospheric moisture within Alberta are limited during the cold months (when most lakes are ice covered), suggesting that heavy snowfall depends on transport of vapor from elsewhere. Major Alberta snowstorms fit well with the classical cyclone model with its warm and cold conveyer belt circulation. This conceptual model postulates that much of the precipitation comes from conversion of moisture transported within the warm conveyor belt. During ascent in the warm sector deposition occurs resulting in a broad shield of cloud and precipitation. From satellite and radar observation of Alberta cyclones, it is known that the instantaneous rate of precipitation field tends to be organized in banded formations parallel to the warm surface front (Reuter and Beaubien 1996).

We propose a two-step approach when deciding whether to issue a heavy snowfall warning for a particular region within Alberta. The first step is to decide if, indeed, there will be snowfall for the area concerned. This decision on snow occurrence is generally based on numerical guidance from NWP models. Once it is established that there will be snow, the second step consists of estimating the amount of snowfall accumulation for the event. It is in the second step that this paper offers some guidance in providing an estimate for the maximum snowfall based on available moisture from upwind sources. The emphasis is on establishing what temperature value at cloud base is needed to yield snowfall amounts equal to or larger than 10 cm. The purpose of this study is to provide a tool to forecast the amount of snowfall accumulation based on thermodynamic estimates.

2 Study Area and Observations

Our analysis includes 259 snowfall events that occurred in Alberta during three consecutive cold seasons: the October to April periods of 1990–91, 1991–92, and 1992–93. These do not include snowfall cases in the Rocky Mountains. Steep topography tends to locally enhance the snowfall due to forced orographic lifting and such orographic effects are beyond the scope of our investigation. Figure 1 shows the location of the 21 Environment Canada weather reporting stations used in our analysis (YOJ, YSM, YPY, YPE, YMM, YQU, YZH, YZU, YOD, YET, YXD, YLL, WRM, YQF, WCT, YYC, YBW, ZPC, YQL, YXH, and WGM). At each location, snowfall accumulation is measured manually once daily. These measurements are included in the weather (SA) reports for snowfall amounts exceeding 1 cm. To-

tal snowfall for 24 hour period is reported and the measurements are given to the nearest centimeter. In most cases, the duration of snowfalls lasted less than 12 hours, and there were no cases of uninterrupted snowfall (no snow for an hour or more) that continued for more than 24 hours. Mixed precipitation (rain and/or snow) cases were excluded. The choice of 1990 to 1993 as the analysis period was to coincide with a special forecasting project designed to examine correlations between snowfall measurements and other observations. There was enhanced quality control over the snowfall measurements from remote sites. The period also coincided with the studies of precipitation organization by slantwise convection (Reuter and Aktary 1995). Furthermore, the winters of 1990–91 and 1992–93 were close to the 30-year climatology in terms of the number of days with snowfall and the daily snowfall amounts for central Alberta. For specific case studies of snowfall events within this period we refer to Aktary and Reuter (1993) and Reuter and Beaubien (1996).

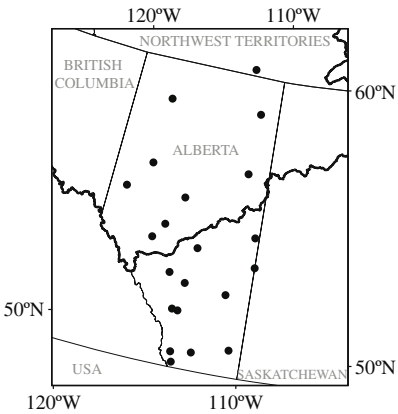

Fig. 1. Provincial boundary of Alberta in relation to the southern Mackenzie River Basin, with the location of snowfall reporting sites (black circles)

3 Method and Data Set

During ascent, vapor will condense into water, or deposit on ice. Assuming that all of the condensed water precipitates as rain (or snow), the mass of precipitation per unit area (i.e., time-integrated precipitation flux) can be estimated by

$$P = \int_{z_0}^{z_1} \left(\rho q_s(z_0, T_0) - \rho q_s(z) \right) dz \qquad (1)$$

where P denotes the snow mass per unit area (kg m^{-2}), z_0 and z_1 are the heights of cloud base and cloud top, T_0 denotes cloud base temperature, ρ is air density, and q_s denotes saturated water vapor mixing ratio. A basic as-

sumption of Eq. (1) is that height-integrated horizontal moisture flux convergence is very small and can thus be neglected. This assumption is invalid for convective precipitation produced in cumulus clouds that have significant horizontal convergence near cloud base. Usually the synoptic cloud systems producing heavy snowfall over Alberta are transitory and moving eastwards so that it is reasonable to assume that the horizontal moisture fluxes into a particular vertical column are small when integrated over 24 hours. Essentially, we make the assumption that the maximum accumulated snowfall over 24 hours is not controlled by horizontal moisture convergence, which differs from the assumption that the instantaneous snowfall rate depends on the short-lived moisture convergence. Using the hydrostatic balance, a linear assumption for the saturated mixing ratio, and approximating the integral by triangulation, we can express P as a linear function of the cloud base temperature

$$P = aT_0 + b \tag{2}$$

where $a = 1.4\left(1 - p_1/p_0\right)$ and $b = 18.9\left(1 - p_1/p_0\right) - 5\,q_{s1}\left(p_0 - p_1\right)$, with p_0 and p_1 denoting pressure (in mb = hPa) at cloud base and cloud top, respectively and q_{s1} is the vapor mixing ratio at cloud top. Snowfall measurements are recorded in depth rather than mass per unit area. To convert P into snow depth (S, in cm) we have

$$S = \left(\rho_{snow}\right)^{-1} P = \left(\rho_{snow}\right)^{-1}\left(a\,T_0 + b\right) \tag{3}$$

where ρ_{snow} denotes the density of 24 hour accumulation of new snow on the ground. It depends on the crystal characteristics and surface temperature, with typical values ranging from 80 kg m^{-3} for dry powdery snow to 200 kg m^{-3} for wet snow (Roebber et al. 2003).

For each of the 259 cases of snowfall we identified the upper air station upwind of the snow reporting site. Specifically, the 850 hPa weather charts were used to backtrack the airmass that produced the maximum snowfall. The distance of transport on the 850 hPa isobaric surface was estimated to be consistent with a 12 hour time interval. For example, if the 850 hPa map suggested southerly flow, we used the upper air sounding from Great Falls, Montana (47°N, 111°W). Other upper air stations used were Stony Plain from Alberta; Port Hardy, Prince George and Vernon in British Columbia; Quillayute and Spokane in Washington; Salem and Medford in Oregon; Great Falls and Glasgow in Montana; Whitehorse in Yukon, and Fort Smith in the Northwest Territories. The backtracking of moisture sources along 850 hPa isobaric surfaces has some uncertainties and there were cases where it was difficult to identify uniquely the "optimal" upwind sounding. For those cases,

satellite images were consulted to identify suitable air mass trajectories. Having identified the appropriate upper sounding site we used the observed 850 hPa temperature to the nearest °C. Typically, events of heavy snowfall were associated with southerly or westerly air flows while northerly flows were generally drier with lower snowfall.

4 Results

Figure 2a is a plot of the 24-hourly maximum snowfall (S, in cm) against the 850 hPa temperature (T_0, in °C) measured by balloon sounding upwind from the snowfall. Alberta snowfall occurred in air masses with T_0 values ranging from -18°C to +8°C. There were no cases of heavy snowfall (i.e., $S \geq 10$ cm) for $T_0 \leq$ -8°C. For a given T_0 value there was a clear tendency of higher snowfall to be associated with warmer T_0. The optimal linear regression expression is calculated as

$$S = 0.9T_0 + 9.7 \tag{4}$$

with a correlation coefficient of 0.62, which is statistically significant. This suggests that T_0 affects the snowfall, and a linear dependence of S on T_0 (derived by conserving water mass) fits the observations. The solid straight line in Fig. 2a represents the theoretical prediction of

$$S = 0.74T_0 + 9.7 \tag{5}$$

based on ρ_{snow} = 1 kg m^{-2} cm^{-1}, p_1 = 400 hPa, q_{s1} = 0.0002 kg/kg. The coefficients in Eq. (5) could be changed if different assumptions are made about snow densities and cloud top conditions. In addition, the cloud base pressure of p_0 = 850 hPa could differ in the observed events. The predicted snowfall is sensitive to the particular choices of snow density and cloud depth, an issue that is discussed in Dupilka and Reuter (2004). Despite all these uncertainties, the prediction line given by Eq. (5) provides a basis for describing the observed (S, T_0) data points scatter.

Bearing in mind that the weather service has the mandate to provide heavy snowfall warnings, we tallied the number of cases with $S \geq 10$ cm for a given T_0 value. Figure 2b shows that for $T_0 \leq$ -1°C the frequency of heavy snow is less than 0.3, for 0°C $\leq T_0$ 1°C the frequency is about 0.4, and for $T_0 \geq$ 2°C the frequency exceeds 0.5. We infer from these historic data that the conditional probability of heavy snowfall (i.e., $S \geq 10$ cm) exceeds 50% when the upwind 850 hPa temperature is $\geq$ 2°C. The condition to be satisfied is, of

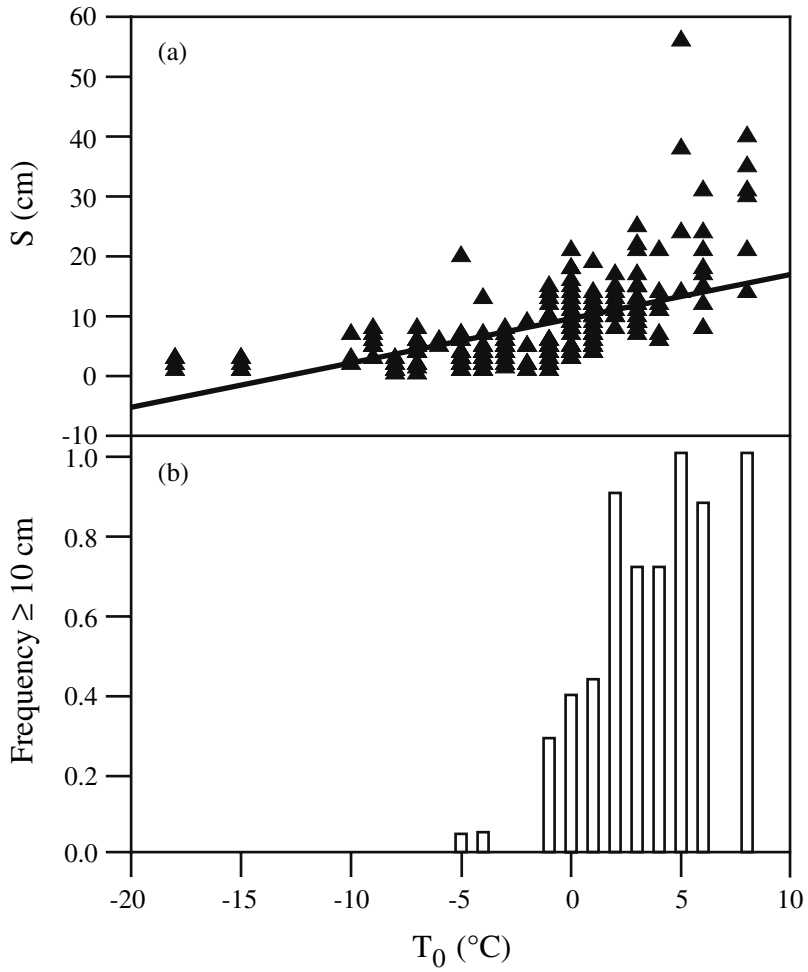

Fig. 2. Snowfall observations compared with 850 hPa temperature values from upwind site. (a) Maximum 24 hour snowfall S plotted against temperature T_0 at 850 hPa. Triangles denote observations and solid line shows theoretical prediction based on Eq. (5); (b) Frequency of cases when $S \geq 10$ cm plotted against T_0 at 850 hPa

course, that only cases of actual snowfall are considered. The decision of whether it will snow has to be determined a priori, for example by examining the prognostic weather charts.

In order to justify the development of a new technique, it must add value above and beyond what is available from Numerical Weather Prediction (NWP) output that is currently available to the forecaster. In other words, we must compare the snowfall–temperature model with the model Quantitative

Precipitation Forecasts (QPF). Dupilka and Reuter (2004) compared predicted snowfall amounts (P) based on the 850 hPa temperature using Eq. (5) against forecast QPF values produced by numerical weather prediction models. They found the model 24 hour maximum snowfall amounts tended to be lower than the observed snowfall amounts; the temperature based predictions for heavy snowfall amounts generally provided greater skill than the model forecasts.

5 Discussion and Conclusions

Operational forecasters are faced with two major issues when predicting snowfall for Alberta. Firstly, they must predict where it will snow; and secondly, they must predict whether the 24 hour snowfall for a given location will meet or exceed a critical amount (often 10 cm). Numerical weather prediction models offer reliable guidance for point 1 but the modeled accumulation often underestimates the observed amount of snowfall. Our analysis of historical data suggests that the 24 hour snowfall accumulation (S) increases linearly with increasing temperature at 850 hPa recorded at an upwind sounding (T_0), with the best regression line being $S = 0.9\ T_0 + 9.7$ and a correlation coefficient of 0.62. This empirical relationship agrees well with our theory based on conserving water substance. Assuming that the air at 850 hPa represents the cloud base conditions of the snow event, the water balance yields a linear relationship. The coefficients for different cloud top levels are consistent with the observations.

It is intriguing that the amount of maximum snowfall is correlated to the 850 hPa temperature of the upwind air mass in a simple linear fashion. Many of the synoptic-scale weather systems that produce heavy snowfall pass over the Continental Divide of the Rocky Mountains with altitudes higher than the 850 hPa pressure level. There tends to be significant orographic moisture removal when the moist air is forced upslope, resulting in precipitation over British Columbia. Therefore, the 850 hPa temperature value recorded at a Pacific coast sounding may not always quantify adequately the moisture available for sublimation in central Alberta.

The NWP model predictions of 24 hour maximum snowfall amounts were compared with the observations, and with the snowfall–temperature relationship. It was found that the simple snowfall–temperature method can complement the use of NWP model guidance for deciding whether to issue a snowfall warning for Alberta, i.e., predicting the likelihood of 24-hourly maximum snowfall $\geq$10 cm. Even so, we emphasize that the snowfall–temperature rela-

tionship should not be used as a "stand-alone" method, but should be used in conjunction with the NWP predictions.

In the analysis presented, the value of T_0 was obtained by identifying the upwind sounding. Instead, one could use the predicted 850 hPa temperature from the NWP model prognostic chart. As long as the model-predicted temperature field at 850 hPa is accurate, the criterion for issuing heavy snowfall could be easily implemented. One possible refinement is to examine the forecasted soundings at model grid points. Based on the prognostic sounding one might compute the appropriate cloud base level and estimates of the maximum snowfall based on predicted cloud base level rather than the assumed 850 hPa cloud base conditions. However, such refinements may not provide a better estimation of the snowfall accumulation because of the inherent uncertainties of such factors as snow density and cloud base height. Also, entrainment into the cloud would affect the water budget in the clouds and this cannot be easily included. In view of the severe time constraints in operational forecasting, a simple approach of identifying critical thermodynamic conditions necessary for heavy snowfall may be the most useful. The results presented here are based on three winters for Alberta. It would be useful to expand this dataset to cover more winter seasons and other geographical regions such as the Canadian Arctic.

References

Aktary N, Reuter GW (1993) Observations of a snowband in a symmetrically unstable flow over Alberta. Contrib Atmos Phys 66:25–282

Dupilka ML, Reuter GW (2006) Forecasting tornadic thunderstorm potential in Alberta using environmental sounding data. Part II: helicity, precipitable water, and storm convergence. Weather Forecast 21:336–346

Dupilka ML, Reuter GW (2004) On predicting maximum snowfall amounts in Alberta. Atmos Ocean 42:281–292

Reuter GW, Aktary N (1995) Convective and symmetric instabilities and their effect on precipitation: seasonal variations in Central Alberta during 1990 and 1991. Mon Weather Rev 123:153–162

Reuter GW, Beaubien R (1996) Radar observations of snow formation in a warm pre-frontal snowband. Atmos Ocean 34:605–626

Roebber PJ, Bruening SL, Schultz DM, Cortinas JV Jr. (2003) Improving snowfall forecasting by diagnosing snow density. Weather Forecast 18:264–287

Chapter 12

Estimating Snow Water Equivalent in Northern Regions from Satellite Passive Microwave Data

Chris Derksen, Anne Walker and Peter Toose

Abstract With all-weather imaging, a wide swath width, and sensitivity to volume scatter of the snowpack, satellite-derived passive microwave data are well suited to snow cover applications, though the development and validation of these techniques at high latitudes lags behind their operational use across southern Canada. This review presents key results from recent field initiatives conducted to address weaknesses in contemporary SWE retrieval algorithm performance at high latitudes. Of particular relevance is the recent progress made in (1) understanding the impact of sub-grid cell land cover variability (2) validating algorithm performance over large regions of the northern boreal forest, (3) northern boreal forest algorithm development using the improved spatial resolution and additional frequencies of data available with the 2002 launch of the Advanced Microwave Scanning Radiometer (AMSR-E), and (4) early efforts to develop a tundra specific SWE retrieval scheme. Significant advances will contribute to ongoing and future climatological, hydrological, and numerical modeling studies of high latitude energy and water cycles.

1 Introduction

Information on terrestrial snow water equivalent (SWE) can be retrieved from satellite passive microwave data because of the frequency-dependent scattering influence of snow crystals. While many pioneering SWE algorithm developments have derived single equations that are applied at the hemispheric scale (Chang et al. 1987, 1991; Rott et al. 1991; Schanda et al. 1983), a regional land cover based approach is needed to minimize uncertainty across the dominant landscape regions of Canada. Initial efforts (Goodison 1989; Goodison et al. 1986) focussed on the open prairie environment because of its generally homogeneous snow cover uncomplicated by the presence of overlying vegetation. At the outset of the Mackenzie GEWEX Study (MAGS) in 1995, it was apparent that the capability to retrieve SWE across Canadian landscapes needed to be improved because the dominant factors that complicate passive microwave retrievals of SWE

are all present in the Mackenzie River Basin (MRB): heterogeneous forest cover, sub-grid cell resolution lakes, deep snow cover, and topographic effects on snow distribution and catchment.

Coincident to the early years of MAGS, algorithm development for the non-mountainous boreal forest regions of western Canada was initiated as a component of the multi-disciplinary Boreal Ecosystem-Atmosphere Study (BOREAS). Through the analysis of high resolution airborne datasets (Chang et al. 1997) algorithms for three general classes of forest cover (deciduous, coniferous, sparse) were developed (Goita et al. 1997, 2003). This represented a significant enhancement to the operational passive microwave SWE retrieval capability in western Canada, although the accuracy of SWE estimates across the MRB remained an issue because of uncertainty in algorithm transferability to this region (Walker and Silis 2002). The spatial resolution and measurement frequencies of satellite passive microwave sensors have evolved over time (Table 1), changes that have provided new opportunities to enhance SWE estimates. In recent years, efforts have focused on addressing limitations of the BOREAS-era algorithms, with an emphasis on field programs to address three fundamental challenges:

1. resolving the integration of multiple land and snow cover conditions within the footprint of 25 km resolution passive microwave data.
2. determining the uncertainty associated with applying SWE retrieval algorithms developed for the closed canopy southern boreal forest to the open canopy northern boreal forest.
3. developing specific SWE retrieval algorithms optimized for northern boreal and tundra environments, both of which have yielded sparse observations.

This review describes the field campaigns conducted to address these research questions, and summarizes the advancements in passive microwave remote sensing of high latitude snow cover achieved in the context of the MAGS program.

2 Study Area/Field Campaign Overview

2.1 Prince Albert, Saskatchewan

New multi-scale research datasets were acquired at a mixed boreal forest site in Saskatchewan (Fig. 1), Canada, during February 2003 to investigate the impact of spatially heterogeneous landscape and snowpack properties on passive microwave SWE retrievals. Environment Canada (EC)

Table 1. Overview of the satellite passive microwave time series

	Scanning Multichannel Microwave Radiometer (SMMR)	Special Sensor Microwave/ Imager (SSM/I)	Advanced Microwave Scanning Radiometer (AMSR-E)
Time series	1978–1987	1987–present	2002–present
Frequencies in GHz (Footprint dimensions in km)	6.6 (148x95)		6.9 (76x44)
	10.7 (91x59)		10.7 (49x28)
	18.0 (55x41)	19.4 (69x43)	18.7 (28x16)
	21.0 (46x30)	22.2 (60x40)	23.8 (31x18)
	37.0 (27x18)	37.0 (37x29)	36.5 (14x8)
		85.5 (15x13)	89.0 (6x4)
Swath width [km]	780	1400	1445

microwave radiometers (6.9, 19, 37, and 85 GHz) were flown on the National Research Council (NRC) Twin Otter aircraft along a grid of flight lines covering a 25 by 25 km study area. Spaceborne Special Sensor Microwave/Imager (SSM/I) brightness temperatures were acquired in near real time as part of normal EC operations over this region. An intensive, coincident ground sampling program characterized in situ snow depth, density, water equivalent and stratigraphy for all representative land covers in the study area in order to isolate the variability in snow cover parameters that occur within and between forest stands and land cover types, yet within a single SSM/I grid cell. Micrometeorological measurements from seven sites within the study area were acquired to aid the interpretation of the passive microwave brightness temperatures by providing key variables such as soil moisture, and soil, snow, air, and tree temperature. Forest inventory data were obtained from the Canadian Forest Service and the pulp and paper industry, while land cover information was derived from Landsat TM imagery. Collectively, these datasets allowed a detailed study on the impact of sub-grid scale vegetation and snow cover properties on large footprint passive microwave SWE retrievals.

2.2 Northern Boreal Forest Regional Snow Surveys

Dedicated snow survey campaigns were conducted during the 2004 and 2005 winter seasons in order to characterize snow cover conditions across approximately 500 km of northern boreal forest and open tundra near the time of seasonal peak SWE. Measurement transects were established during March in northern Manitoba between the communities of Thompson

and Gillam, accessible on a winter-maintained gravel road, and between Gillam and Churchill, accessible only by helicopter (Fig. 1). Points were surveyed every 10 km between Thompson and Gillam, and at approximately 15 km intervals between Gillam and Churchill. At each site, depth, SWE, and bulk density samples were acquired to characterize local scale, within-site variability. Density profiles were obtained from 10 cm wedge samples extracted from the face of a snow pit. Snow stratigraphy information (grain size estimates, identification of stratigraphic layers and lenses) was also obtained at each site, through subjective characterization of the snow pit profile.

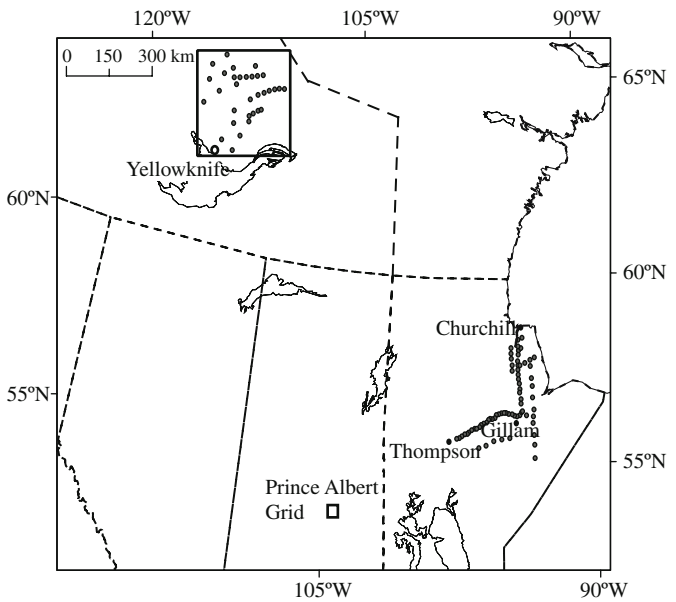

Fig. 1. Location map of field campaigns. Black boxes denote areas of aircraft sampling; circles denote regional ground measurement sites. Background is SSM/I derived SWE, 1 April 2005

Additional northern boreal measurements sites were sampled in the Northwest Territories during April 2005 (Fig. 1). Sites were accessed by helicopter and fixed wing aircraft, and the measurement protocol employed in Manitoba was repeated. While separated in space and time, the northern Manitoba and Northwest Territories (NWT) datasets provide a comprehensive perspective on northern boreal snow cover extending from the Hudson Bay Lowlands northwestward to the boreal Shield north of

Great Slave Lake, a region with an extremely poor historical conventional measurement record.

2.3 Daring Lake, NWT

Snow surveys conducted during late winter of 2003 and 2004 in the upper Coppermine River basin in the NWT indicated significant SWE underestimation when the EC open prairie algorithm was utilized in the open tundra. Two primary factors account for this bias. First, wind redistribution of snow across the tundra results in high snow density, and high SWE storage in spatially constrained drift areas within spaceborne passive microwave grid cells. Second, lake ice poses a challenge due to its unique microwave emission characteristics compared to terrestrial surfaces. In the arctic tundra, small water bodies constitute a significant portion of the surface, yet fractional lake ice area is presently not accounted for in any passive microwave algorithms.

Surface snow measurements and airborne and satellite passive microwave remote sensing datasets were acquired in the NWT during April 2005 to address the science questions necessary to develop a tundra specific SWE retrieval algorithm (Fig. 1). The NRC Twin Otter aircraft was again deployed with 6.9, 19, 37, and 89 GHz radiometers. Airborne experiments were designed to address a number of specific issues related to brightness temperature scaling, and the changing nature of brightness temperature spatial variability in mixed lake/land environments. Ground-based microwave radiometers identical to those on board the Twin Otter aircraft were also deployed. Ground measurements of snow cover properties were acquired in conjunction with the airborne datasets at both fixed intervals along flight lines, and at specifically defined points of interest.

3 Results

3.1 Sub-grid Variability

Retrieval validation of remotely sensed geophysical parameters typically focuses on the comparison of gridded satellite values with a ‘ground-truth’ dataset in order to determine first order agreement between measurements (Derksen et al. 2003). While this type of assessment provides an important perspective (see Section 3.2) the large grid cell resolutions of passive microwave data demand that relationships between local scale variability in

snow cover properties and the coarse scale satellite derived retrievals of snow cover parameters be examined in order to define the representativeness of the large footprint satellite measurements. Specific research datasets are required to investigate these issues because the distribution of conventional observing networks is insufficiently dense.

The in situ, multi-scale passive microwave and land cover data acquired during the Prince Albert 2003 campaign showed that within-grid cell SWE variability is significant, and driven by landscape controls on snow depth (Derksen et al. 2005a). After stratification based on land cover class, statistical testing of the snow survey data showed that snow density could be treated as homogeneous within the study area, while the highly variable in situ SWE measurements were normally distributed (Fig. 2a) and controlled by variations in snow depth. The box plots embedded in Fig. 2b illustrate the degree of within and between site SWE variability contained inside a single satellite passive microwave grid cell. Integrated SWE retrievals were produced from SSM/I data for the entire study area in order to determine how the spaceborne retrievals compared to the statistical distribution of in situ measurements. The SSM/I SWE retrievals were relatively stable across the five-day study period, ranging from 51 to 67 mm. Most importantly, the satellite SWE estimates fell in the center of the normally distributed in situ measurements, thus providing a reasonable estimate of mean SWE within the study area (Fig. 2a). Given the within-grid cell variability characterized by the snow survey data, this finding certainly represents the 'best case' scenario when comparing SWE data at such fundamentally different scales.

Landscape scale SWE variability cannot be captured with spaceborne passive microwave SWE retrievals given the disconnect between the scales of measurement (25 km grid cells) and the scales of snow catchment processes. The airborne passive microwave datasets acquired for the study, however, provided SWE retrievals more commensurate with the scale of SWE variability: approximately 100 to 200 m resolution footprints. A land cover class was assigned to each airborne brightness temperature measurement using a Landsat land cover classification. SWE was determined using the most appropriate of the four existing EC land cover sensitive algorithms: open, coniferous, deciduous, or sparse forest. Relative frequency histograms constructed for each land cover class illustrated that the full range of measured in situ SWE values were captured by the airborne data because the retrievals were sensitive to along flight line variations in vegetation. The airborne SWE retrievals however, were too low in coniferous forest stands (Fig. 2c) and too high in open fens and clear-cuts (Fig. 2d). Given the reasonable agreement at the satellite scale (Fig. 2a) these results

suggest that the degree of patchy openness within a grid cell is essential for producing sufficiently high satellite SWE retrievals in forested areas.

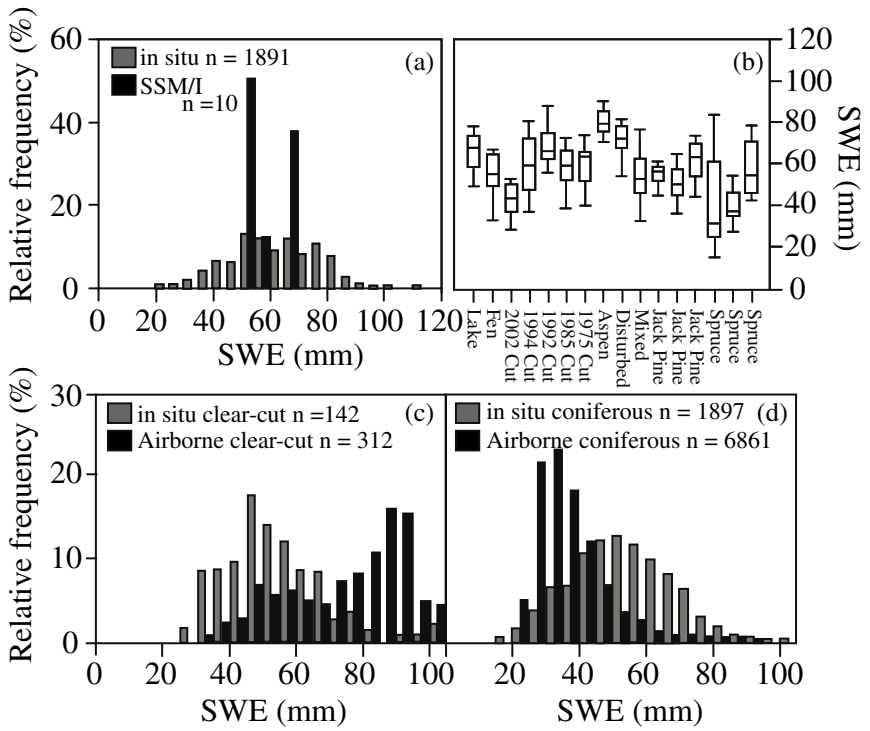

Fig. 2. (a) Relative frequency distribution of in situ SWE measurements and SSM/I SWE retrievals for a single grid cell. (b) Box plot illustrates the variability in ground measured SWE. Relative frequency distributions of high resolution (~100 m) airborne SWE retrievals and ground measurements are shown for (c) open and (d) and forested areas

Problematic to the interpretation of land cover class as a controlling influence on satellite retrievals is that forest structure is not considered. For instance, a coniferous stand with an open versus closed canopy will have very different microwave emission properties and snow catchment characteristics, which will not be apparent from information in land cover classification datasets. The forest inventory data acquired for this study represented an important step in moving beyond the consideration of land cover class, to the forest structure. The airborne SWE retrievals and in situ measurements were segmented into forest inventory classes based on canopy closure and stem density. Figure 3 shows that while no relationship

was observed for stem density, both SWE datasets were negatively correlated with the degree of canopy closure. While decreased surface SWE can be expected as the degree of canopy closure increases (through processes such as interception and sublimation loss) the exceptionally strong correlation between airborne brightness temperature and canopy closure (r^2 = 0.80) underscores the issue of consistent SWE underestimation from spaceborne passive microwave data in areas of closed canopy forest. Although forest inventory data are not as readily available as land cover class, information of this nature are required to identify and resolve the physical factors controlling SWE retrieval uncertainty at the stand level in mixed forest environments (Toose et al. 2005).

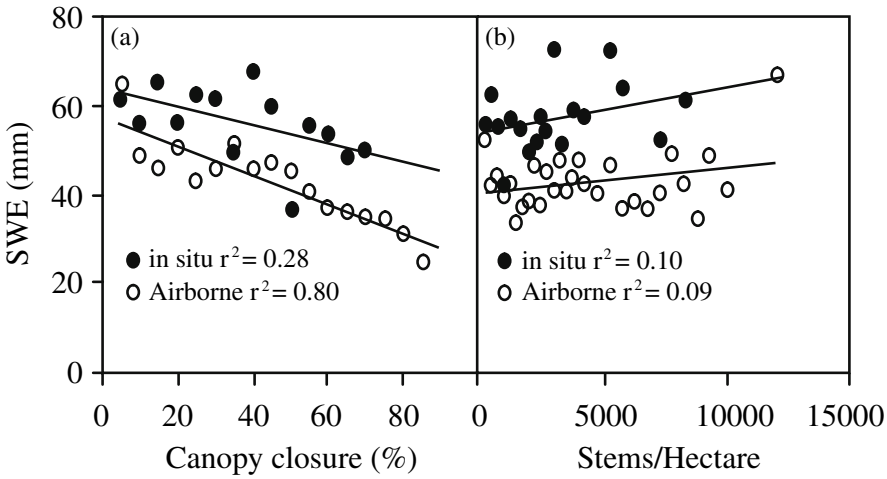

Fig. 3. Relationships between SWE and (a) canopy closure, and (b) stem density

3.2 Northern Boreal SWE Retrievals

Parallel to the Prince Albert field campaign, a study was conducted to improve understanding of the accuracy of passive microwave SWE retrievals at a regional scale, particularly across areas with a poor conventional observing network. One primary region of concern was a zone of interannually consistent high SWE retrievals co-located with the northern boreal forest, with lower SWE retrievals across both the comparatively dense boreal forest to the south, and the open tundra to the north. A similar SWE pattern across this region was found in a SWE reanalysis dataset (Brown et al. 2003) and simulated SWE fields from the Canadian Regional Climate

Model (Derksen and MacKay 2006; Derksen et al. 2007), but remained unvalidated because of a lack of independent SWE datasets. Northern Manitoba provided an excellent opportunity to acquire regional SWE ground-truth data because of relatively easy logistical access, and open and closed canopy forest and open tundra land cover are in relatively close proximity.

The boreal environment between Thompson and Gillam is a homogeneous closed conifer forest. North of Gillam, the northern boreal forest transitions to open tundra. This is an irregular and discontinuous boundary, composed of open conifer forest and a mosaic of tree islands and open tundra. Standing vegetation becomes extremely sparse approximately 150 km north of Gillam. This vegetation gradient corresponds to an interannually consistent pattern of lower passive microwave SWE retrievals near Thompson to approximately 50% higher retrievals north of Gillam (Derksen et al. 2005b). A lack of validation datasets across this SWE gradient limited the understanding of how the boreal forest algorithms developed with BOREAS data from central Saskatchewan (Goita et al. 2003) could be applied across the northern boreal forest, subsequently influencing the confidence with which this dataset could be applied to climatologic, hydrologic, and numerical modeling studies.

An intercomparison of the in situ and SSM/I derived SWE datasets for the March 2004 and 2005 surveys is shown in Fig. 4. Ground measurements sites were binned into the EASE-Grid cell in which they were located for comparison with the satellite retrievals. The lowest ground measured SWE was near Thompson, with a general increase measured along the transect east towards Gillam – a gradient that agrees closely with the SSM/I retrievals (Fig. 4) though the SSM/I estimates are systematically low, especially during 2005 when snow was generally deeper across the region (Fig. 4b). The highest ground measured SWE values were colocated with the zone of high SSM/I SWE retrievals north of Gillam (Fig. 4c), but underestimation was notably significant again in 2005.

It is evident from Figs. 4b and 4c that the current EC coniferous algorithm captures the gradient in SWE distribution, but the magnitude of SWE retrievals could be improved for the northern boreal environment, particularly in high snow years. This is expected since the algorithm was derived using BOREAS data from the southern boreal forest near Prince Albert during a winter season with anomalously low snow depth (Chang et al. 1997; Goita et al. 2003). The specific challenges in SWE retrieval across this region are related largely to the presence of a deep snowpack (up to 1 m) which limits the effectiveness of conventional algorithms that

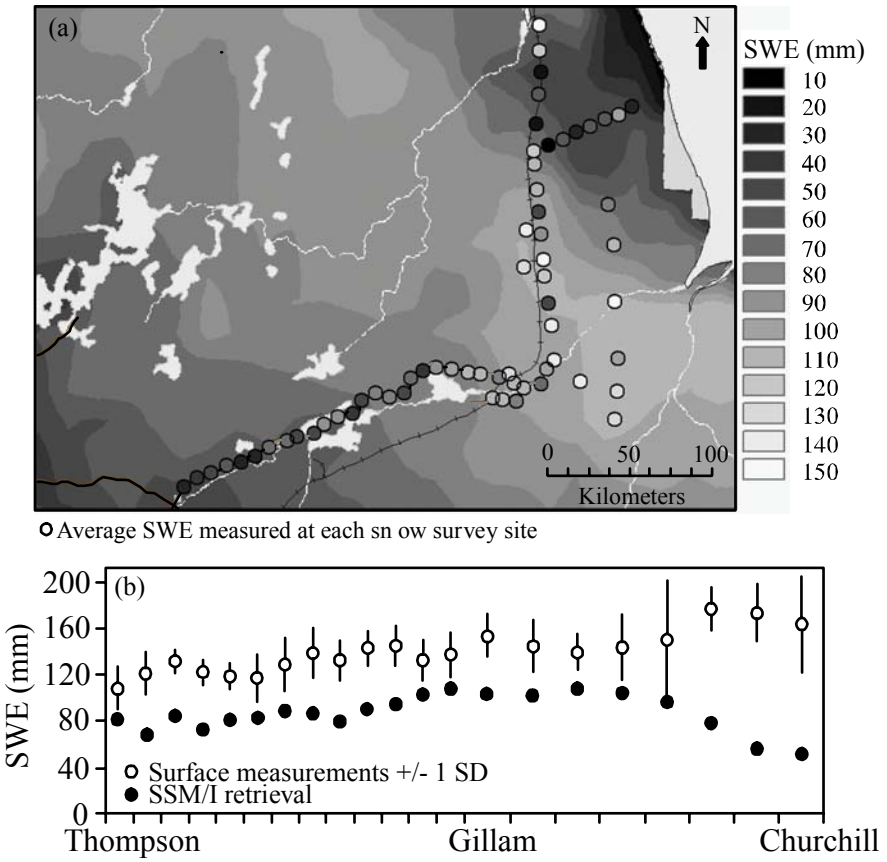

Fig. 4. (Top) Comparison of surface measured SWE (circles) and SSM/I SWE retrievals, March 2004. Comparison of March 2005 data are shown for transects between (bottom) Thompson and Gillam, and Gillam and Churchill

rely on the scattering difference between 19 and 37 GHz frequencies. While the open forest canopy of the northern boreal zone allows the surface snow scattering signal to be detected from space, there is a volume scattering threshold at 37 GHz that limits the maximum SWE retrieval to approximately 120–140 mm (Armstrong et al. 1993; De Seve et al. 1997). Additionally, the 19 GHz brightness temperatures are used as a reference 'background' measurement insensitive to the volume scatter of the snowpack. With deep snowpacks, however, a scattering signal at 19 GHz can be evident when SWE exceeds approximately 80 mm. The new microwave frequencies available since 2002 from the Advanced Microwave Scanning Radiometer (AMSR-E; 6.9 and 10.7 GHz) will contribute to new algo-

rithm development for the northern boreal zone by providing low-frequency brightness temperatures truly insensitive to volume scatter from deep snowpacks.

The potential enhancements provided by AMSR-E data are illustrated in Fig. 5 for the 2005 NWT snow survey sites. The linear response of the 19 GHz brightness temperature to increasing SWE is evident in Fig. 5a. This response reduces the 37–19 GHz brightness temperature difference that is the foundation of the EC coniferous forest algorithm, contributing strongly to low SWE retrievals. In contrast, the 10 GHz brightness temperatures are not sensitive to even the deepest snowpacks measured during the 2005 NWT survey (Fig. 5b). Replacing the old BOREAS derived coefficients with new values calculated from the 2005 NWT ground data and AMSR-E 37-10 GHz brightness temperature difference produced SWE retrievals that agreed more closely with ground measurements (Fig. 5c). The bias characteristics of these new retrievals are still linearly related to SWE magnitude, but to a lesser extent than the original EC algorithm scheme, and consistent SWE underestimation is less pronounced (Fig. 5d). An intercomparison of AMSR-E brightness temperatures from generally shallow snow (2004) versus deep snow (2005) suggested that the difference between 19 and 10 GHz measurements can be used to discriminate shallow from deep snow conditions (not shown).

The improved retrievals shown in Fig. 5 were derived and validated using only a single year of data, and as such represent only a proof of concept that the new ground datasets from across the northern boreal forest, combined with the new frequencies of microwave data available from AMSR-E will lead to improved SWE retrievals across the northern boreal forest and boreal-tundra transition. This will improve snow cover monitoring capabilities across a vast, conventionally observation poor zone extending from the Hudson Bay Lowlands through the MRB. Adjustments to the coefficients used in SSM/I derived retrievals will improve the historical record of SWE estimates.

3.3 Towards Tundra-specific SWE Retrievals

The distribution and magnitude of winter season water equivalent stored in the snowpack across the Canadian tundra is presently unknown. Quantifying this storage, and the degree of interannual variability, is essential because the tundra snowpack is a persistent landscape feature and a key parameter in water, energy, and biogeochemical cycling. Currently, no operational passive microwave algorithms exist for the spatially expansive

high latitude regions north of the boreal tree line. The airborne passive microwave data acquired during the April 2005 NWT campaign will allow the fundamental science issues behind tundra algorithm development to be addressed. This includes determination of scaling linkages between topography, snow catchment/retention, and brightness temperatures and consideration of fractional lake ice cover. During this campaign, airborne passive microwave data were acquired across a network of flight lines that spanned the boreal tree line, including the acquisition of airborne data in converging patterns (approximately 4 km^2) centered on sites where detailed surface snow cover measurements (SWE, depth, density, stratigraphy, grain size) were acquired.

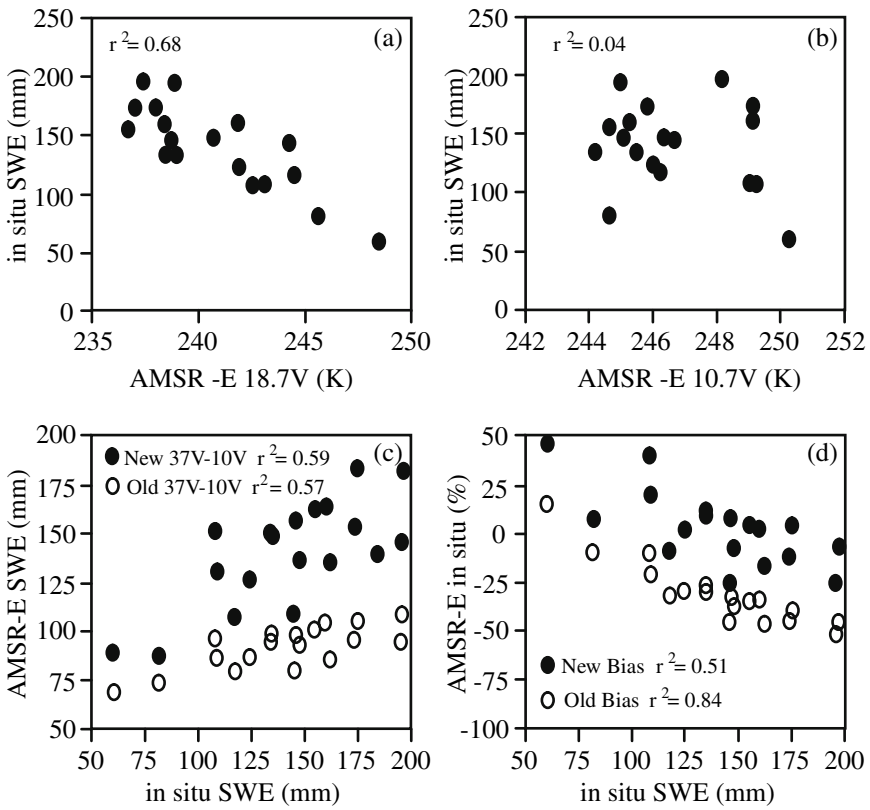

Fig. 5. Relationships between in situ SWE and (a) AMSR-E 18.7 GHz, and (b) AMSR-E 10.7 GHz brightness temperatures for Northwest Territories sites. AMSR-E SWE retrievals using 10.7 and 18.7 GHz data are shown in (c) with retrieval bias shown in (d)

Figure 6 illustrates data from one of these tundra sites. The statistical distributions of airborne brightness temperatures at 6.9 and 37 GHz were bimodal due to strong (up to 50 Kelvin) differences in response over lake versus land surfaces, which dominated the variability that could be attributed to land cover characteristics and snowpack physical properties (i.e., grain size). The 19 GHz measurements showed little sensitivity to changing surface characteristics at all scales. The airborne brightness temperatures (approximately 100 m resolution) for each 4 km^2 pattern were aggregated at 250 m, 500 m, and 1000 m radii from the center location where snowpack measurements were made. These multi-scale measurements illustrated two important issues. First, there is a strong dependence between 6.9V brightness temperature and fractional lake cover (determined from Landsat imagery) at both boreal and tundra sites (Fig. 7a). This result suggests that fractional lake cover estimates at the satellite scale can potentially be produced from AMSR-E 6.9 GHz data. Validating these satellite lake fraction estimates is presently a challenge, however, because the Landsat derived estimates produced for this study isolated an approximate level of 30–35% lake cover across the study region. This differs significantly from an existing lake fraction dataset (10–20% lake cover) produced from the National Topographic Data Base by the Canada Centre for Remote Sensing.

Secondly, the relationship between 37V brightness temperature and lake cover fraction is reversed across the open tundra compared to the northern boreal forest (Fig. 7b). Over forested sites, 37 GHz data responded to the transition from lake to terrestrial surfaces with lower brightness temperatures over lakes relative to land. While the 19 GHz data showed little sensitivity to lakes, the response at 37 GHz was strongly positively correlated to that at 6.9 GHz. Conversely, at tundra sites the 37 GHz brightness temperatures were higher over lakes than over terrestrial surfaces, the inverse response was observed at 6.9 GHz. When all airborne measurements were considered the correlation between 6.9V and 37V measurements was 0.70 at forested sites and -0.79 at tundra sites. This difference in response to lake ice at 37 GHz will have a dramatic effect on SWE retrievals because the increase in brightness temperature at 37 GHz across lake rich areas will decrease the 37-19 GHz (or 37-10) difference, and therefore decrease SWE estimates.

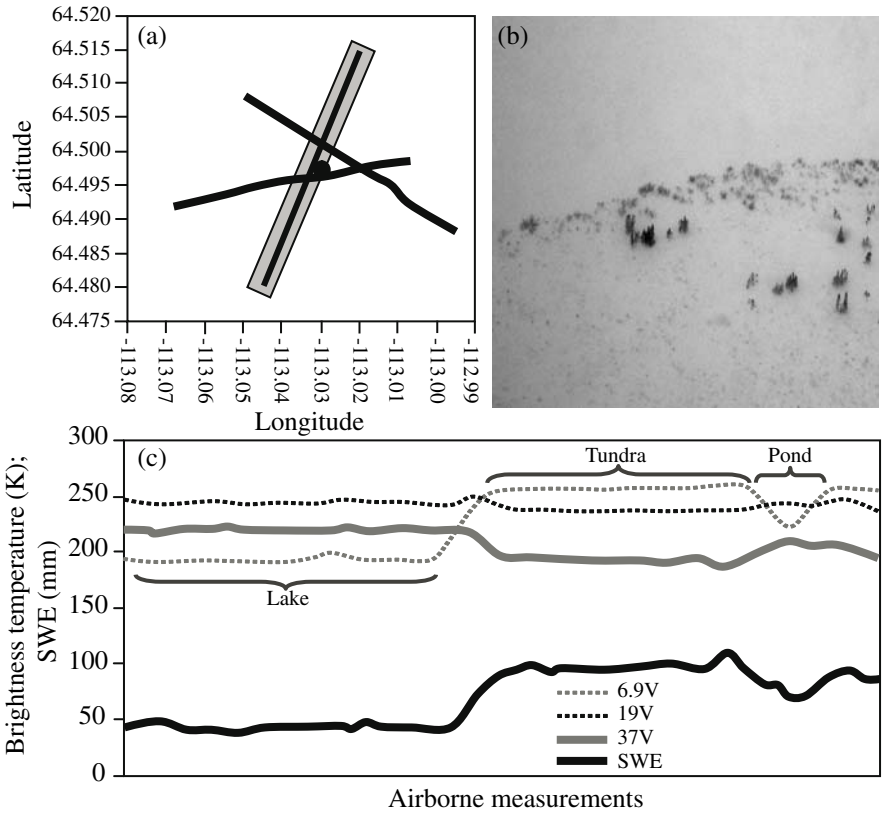

Fig. 6. (a) Ground survey transects and flight track (shaded) over a ground measurement site (marked by diamond). (b) Oblique site photo of Winter Lake showing tundra and lake. (c) Single transect of airborne brightness temperatures and SWE retrievals using the existing MSC open environments algorithm

4 Discussion and Conclusion

Notable progress has been made in improving our understanding of contemporary passive microwave SWE algorithm performance, and developing improved retrieval techniques across high latitude regions. At the within grid cell scale, the sensitivity of high resolution airborne brightness temperatures to land cover and snowpack variability has been defined to a new level of detail (Derksen et al. 2005a). Progress is being made on linking SWE retrieval uncertainty to more physically relevant forest structure parameters such as canopy closure, as opposed to simple land cover

(Toose et al. 2005). Given the large dimensions of satellite passive microwave data, it is important to establish that SWE retrievals fall into the center of the distribution of in situ SWE measurements, providing a reasonable estimate of mean grid cell SWE (Derksen et al. 2005a, 2005b). No insight can be gained on within-footprint SWE variability from satellite data alone, but there is potential for providing bulk grid cell passive microwave SWE retrievals, as well as supplementary information on within-grid cell variability if land cover and some in situ observations are available.

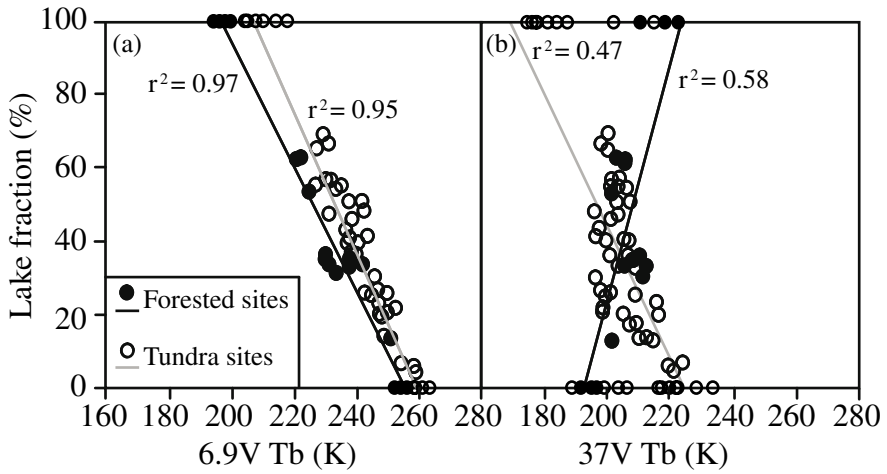

Fig. 7. Relationship between lake fraction and airborne brightness temperatures at (a) 6.9V and (b) 37V

Regional algorithm evaluation has occurred across vast, observation poor regions of the northern boreal forest, leading to a more mature understanding of the transferability of southern boreal retrieval algorithms. Long transects of field measurements have confirmed an interannually consistent zone of high SWE values aligned with the northern boreal forest across western Canada (Derksen et al. 2005b), a finding that has important implications for climatological studies (Derksen and MacKay 2006). The low frequency brightness temperatures available from the AMSR-E sensor show strong potential for modifying the existing EC algorithm suite for the deep snow conditions common across the northern boreal forest.

Tundra specific SWE retrieval algorithms are being pursued for the first time, with emphasis being placed on the many unique elements of the tundra snowpack. These include sub-pixel scale features like high density snow layers, spatially constrained areas of deep snow, and lake cover frac-

tion. Scaling challenges are clear: deep snow drifts on topographically sheltered areas are a major feature as they represent a significant volume of stored water. Deep snow drifts greater than 5 m can be found just meters from wind-scoured, nearly snow-free plateaus. From a landscape weighted perspective, however, these deep drifts occupy only a small percentage of a grid cell area (5–10%), and contribute minimally to overall brightness temperature at the scale of satellite passive microwave observations (Rees et al. 2005).

Freshwater lakes occupy between 20 and 40 percent of the tundra landscape, but are presently not accounted for in any passive microwave snow cover retrieval algorithm. Statistics from detailed in situ snow surveys conducted in Northern Manitoba (Derksen et al. 2005b) and the Alaskan North Slope (Sturm and Liston 2003) show that the snowpack on lakes is physically unique and relatively homogeneous in comparison to adjacent terrestrial surfaces. Current passive microwave satellite data are too coarse in resolution for determining microwave emission from freshwater ice on all but the very largest lakes. This underscores the need to develop the capability to consider the influence of sub-grid scale lakes on SWE retrieval algorithms. It is known that significant within grid cell lake cover leads to systematic underestimation of SWE (Duguay et al. 2005), although analysis in the Hudson Bay Lowlands showed that within-grid cell fractional lake and pond cover has a temporally inconsistent influence on SWE underestimation in tundra areas (Derksen et al. 2005b).

One region of undeveloped SWE retrieval capability remains the mountains. MacKay et al. (2003) showed that passive microwave SWE estimates above 800 m elevation in the MRB were strongly biased and not suitable for research applications. Even with the improved spatial resolution of AMSR-E, regions of complex topography cannot be resolved with current satellite passive microwave technology. Very deep mountain snowpacks also preclude the use of traditional brightness temperature difference algorithms. In the absence of technological advances in remote sensing technology, dense networks of elevation-sensitive in situ measurements, and dedicated field campaigns, operational SWE estimates for mountainous regions will remain elusive.

The momentum gained during the MAGS program will carry forward in the form of new algorithm development, validation, and field studies. Production of new historical SWE time series will result in improved understanding of the sources and magnitude of uncertainty.

Acknowledgements

Funding and in-kind support from the Canadian Foundation for Climate and Atmospheric Science (CFCAS), the EC Cryosphere System in Canada program (CRYSYS), National Research Council Flight Research Laboratory, Manitoba Hydro, Northwest Territories Power Corporation, and Indian and Northern Affairs, Yellowknife, is gratefully acknowledged. Thanks to personnel from the Climate Processes Section of the Climate Research Division (A. Silis) and Department of Geography, Wilfrid Laurier University (M. English, A. Rees) for leading the planning and execution of this field work. The EASE-Grid passive microwave data were obtained from the EOSDIS National Snow and Ice Data Center Distributed Active Archive Center (NSIDC DAAC), University of Colorado, Boulder.

References

Armstrong R, Chang A, Rango A, Josberger E (1993) Snow depths and grain-size relationships with relevance for passive microwave studies. Ann Glaciol 17:171–176

Brown R, Brasnett B, Robinson D (2003) Gridded North American monthly snow depth and snow water equivalent for GCM evaluation. Atmos Ocean 41:1–14

Chang A, Foster J, Hall D (1987) Nimbus-7 SMMR derived global snow cover parameters. Ann Glaciol 9:39–44

Chang A, Foster J, Hall D, Goodison B, Walker A, Metcalfe J, Harby A (1997) Snow parameters derived from microwave measurements during the BOREAS winter field campaign. J Geophys Res 102(D24):29,663–29,671

Chang A, Foster J, Rango A (1991) Utilization of surface cover composition to improve the microwave determination of snow water equivalent in a mountain basin. Int J Remote Sens 12:2311–2319

De Seve D, Bernier M, Fortin J-P, Walker A (1997) Preliminary analysis of snow microwave radiometry using the SSM/I passive-microwave data: the case of La Grande River watershed (Quebec). Ann Glaciol 25:353–361

Derksen C, Brown R, MacKay M (2007) Mackenzie Basin snow cover variability and trends from conventional data, satellite remote sensing, and Canadian Regional Climate Model simulations. (Vol. I, this book)

Derksen C, MacKay M (2006) The Canadian boreal snow water equivalent band. Atmos Ocean 44:305–320

Derksen C, Walker A, Goodison B (2003) A comparison of 18 winter seasons of in situ and passive microwave derived snow water equivalent estimates in Western Canada. Remote Sens Environ 88:271–282

Derksen C, Walker A, Goodison B (2005b) Evaluation of passive microwave snow water equivalent retrievals across the boreal forest/tundra transition of western Canada. Remote Sens Environ 96(3/4):315–327

Derksen C, Walker A, Goodison B, Strapp JW (2005a) Integrating in situ and multi-scale passive microwave data for estimation of sub-grid scale snow water equivalent distribution and variability. IEEE T Geosci Remote Sens 43:960–972

Duguay C, Green J, Derksen C, English M, Rees A, Sturm M, Walker A (2005a) Preliminary assessment of the impact of lakes on passive microwave snow retrieval algorithms in the Arctic. Proc 62nd Eastern Snow Conference, Waterloo, Ontario, June 2005, pp 223–228

Goita K, Walker A, Goodison B (2003) Algorithm development for the estimation of snow water equivalent in the boreal forest using passive microwave data. Int J Remote Sens 24:1097–1102

Goita K, Walker A, Goodison B, Chang A (1997) Estimation of snow water equivalent in the boreal forest using passive microwave data. CD-ROM, Proc Geomatics in the Era of Radarsat, Ottawa, Ontario, May, 1997

Goodison B (1989) Determination of areal snow water equivalent on the Canadian Prairies using passive microwave satellite data. Proc IGARSS 1989, Vancouver, 3:1243–1246

Goodison B, Rubinstein I, Thirkettle F, Langham E (1986) Determination of snow water equivalent on the Canadian Prairies using microwave radiometry. Modelling snowmelt induced processes, Proc Budapest Symposium, July 1986. IAHS Publication 155, pp 163–173

MacKay M, Seglenieks F, Verseghy D, Soulis E, Snelgrove K, Walker A, Szeto K (2003) Modeling Mackenzie Basin surface water balance during CAGES with the Canadian Regional Climate Model. J Hydrometeorol 4:748–767

Rees A, English M, Derksen C, Walker A (2005) Assessing snowpack water equivalent distribution in an open tundra environment using various scales of passive microwave data. Proc 62nd Eastern Snow Conference, Waterloo, Ontario, June 2005, pp 229–233

Rott H, Nagler T, Aschbacher J (1991) Algorithm development for monitoring the global snow cover by spaceborne microwave radiometry. Proc 11th EARSel Symposium, Graz, Austria, July, 1991, pp 58–69

Schanda E, Matzler C, Kunzi K (1983) Microwave remote sensing of snow cover. Int J Remote Sens 4:149–158

Sturm M, Liston G (2003) Snow cover on lakes of the Arctic Coastal Plain of Alaska, U.S.A. J Glaciol 49:370–380

Toose P, Derksen C, Walker A, LeDrew E (2005) Investigating relationships between forest structure and in situ and airborne passive microwave snow water equivalent in a boreal forest environment. Proc 62nd Eastern Snow Conference, Waterloo, Ontario, June 2005, pp 41–47

Walker A, Silis A (2002) Snow cover variations over the Mackenzie River Basin from SSM/I passive microwave satellite data. Ann Glaciol 34:8–14

Chapter 13

Mackenzie Basin Snow Cover: Variability and Trends from Conventional Data, Satellite Remote Sensing, and Canadian Regional Climate Model Simulations

Chris Derksen, Ross Brown and Murray MacKay

Abstract Variability and trends in Mackenzie River Basin (MRB) snow cover were investigated using in situ snow depth observations, NOAA snow extent charts, and satellite retrievals coupled with Canadian regional climate model (CRCM) simulations. Most stations with long conventional snow depth records showed significant decreases in spring snow cover duration and earlier snow disappearance, but no significant trends for snow cover onset in the autumn. These results are consistent with air temperature trends over the region. Within the MRB, the NOAA dataset show an east-west gradient with earlier snow melt concentrated in the mountains west of the Mackenzie River, and little change or slight increases in spring snow cover in the northeast. Southern MRB showed cyclical behavior in snow cover, linked to the Pacific-North American and Pacific Decadal Oscillation modes of atmospheric variability.

Spaceborne passive microwave datasets revealed a zone across the northern fringe of the boreal forest with high winter season snow water equivalent (SWE) of >100 mm; and the presence of this zone was confirmed by ground snow surveys. A series of CRCM simulations were conducted to identify feedbacks between the atmosphere and land surface for a domain focused on the northern boreal forest. The patterns of accumulated SWE correspond closely with the mean monthly patterns of 850 hPa frontogenesis forcing, suggesting that lower tropospheric frontal activity was responsible for the snowfall events that led to the deposition of the northern boreal SWE band.

1 Introduction

Snow covers the entire Mackenzie River Basin (MRB) for periods ranging from 3–4 months in the southern prairie sector to 6–9 months in the north and western mountains. Characterizing and understanding the spatial and temporal variability of snow cover (areal extent, albedo, density and SWE) is essential for closing the energy and water budgets and for climate moni-

toring (Cao et al. 2002; Serreze et al. 2002; Szeto et al. 2007). This is a challenging task as all the available data sources have limitations (Table 1). A number of studies have reported widespread trends toward earlier spring snow melt and a reduction of spring snow cover over the latter period of the 20th century, consistent with global warming (e.g., Brown 2000; Dye 2002; Groisman et al. 1994) while Schaefer et al. (2004) suggests a large fraction of the spring snow cover response over Europe can be explained by trends in the winter Arctic Oscillation (AO).

In addition to temporal variability, there are large spatial variations in snow distribution within the MRB. One notable example is the presence of an interannually consistent band of high snow water equivalent (SWE) values located along the northern fringe of the boreal forest of western Canada (Derksen and MacKay 2006; Derksen et al. 2005, 2007). While the snowpack water storage along this belt exceeds that found in the denser forest to the south and the open tundra to the north, the within- and between-season SWE variability across the northern boreal forest is exceptionally low relative to its adjacent biomes.

Given the importance of snow cover as a key variable for climatologic, hydrologic, and numerical modeling applications across the MRB, the main objectives of this study were:

1. to utilize in situ snow measurements and the time series of satellite-derived weekly snow extent charts produced by NOAA to characterize historical snow cover variability (1945–2004), and to assess the role played by the dominant modes of Northern Hemisphere (NH) atmospheric circulation in influencing snow cover variability in the MRB.
2. to utilize CRCM simulations to identify atmospheric and land cover mechanisms that influence SWE magnitude and distribution across the northern boreal forest. Progress in this area will improve understanding of the interplay between atmospheric and land cover processes that influence the magnitude and distribution of SWE in the MRB.

2 Data

2.1 Daily Snow Depth Observations

Regular daily ruler measurements of the depth of snow on the ground have been made at most Canadian synoptic stations since the mid-1950s. This program was extended to climatological stations in the early 1980s, doub-

Table 1. Summary of data sources for studying snow cover variability in Canada

Data source	Measurement	Temporal coverage	Spatial coverage	Comments
Snow depth observations	Daily manual measurements of snow depth with ruler; ultrasonic sensors on some automatic stations	Most synoptic stations since ~1955; climate stations from ~1980. Few stations have data prior to 1950	Sparse network north of ~55°N. Network biased to lower elevations; biased to coastal areas in the Arctic Archipelago	Measurements taken at open, exposed locations that may not be representative of the dominant land cover; arbitrary measurement and reporting of snow depths for patchy snow conditions
Snow surveys	Manual survey of snow depth and SWE along 5 to10 point transect using snow tube	Weekly or bi-weekly but often only in the 2nd half of the snow year to capture the peak SWE. Few sites have data series longer than ~30 years in length	Southern bias. Survey lines are designed to be representative of snow conditions within a catchment	Changing vegetation can affect the homogeneity of long term measurements
Snow pillows	Point measurement of SWE based on the mass of snow on the pillow; usually linked to real-time telemetry	High resolution information during snow year but few pillows have records longer than ~20 years	Usually in remote or mountain locations where access makes regular snow survey impractical; are point measurements which may not be representative (but efforts usually made to select pillow locations that are representative)	"Bridging" of snow over the pillow from hard snow or ice layers can affect measurements
NOAA weekly snow charts	Digitized weekly charts of snow cover derived from visual interpretation of visible satellite imagery	Weekly, 1966-1999 Derived from daily IMS product after May 1999	Northern Hemisphere on 190.5 km polar stereographic grid	50% snow cover threshold defines "snow" or "snow-free" grid cells. Changes in satellite resolution and charting procedures during the period of record

Table 1. (cont.)

Data source	Measurement	Temporal coverage	Spatial coverage	Comments
IMS daily snow charts	Mainly derived from visible satellite data (AVHRR; GOES; MODIS)	Daily, 2002-present	Northern Hemisphere on 23.8 km polar stereographic grid. 4km resolution beginning Feb. 2004	50% snow cover threshold defines "snow" or "snow-free" grid cells
Passive microwave	SWE retrievals derived from the influence of snowpack volume scattering on brightness temperatures	Scanning Multichannel Microwave Radiometer (SMMR) 1978-1987 Special Sensor Microwave/Imager (SSM/I) 1987-present. Advanced Microwave Scanning Radiometer (AMSR-E) 2002-present Daily repeat coverage at high latitudes (>60), better than weekly coverage at mid-latitudes	Resampling produces 25 km grid cells	Uncertainty related to overlying vegetation, snowpack heterogeneity (grain size, crusts, lenses, wetness), complex terrain, and large grid cell dimensions
QSCAT	Backscatter thresholds used to identify melt onset and duration	QuikSCAT scatterometer data available from 2000-present. Daily coverage	Effective resolution of 5 km	Short time series. See comments for passive m/w. Found to provide realistic maps of snow cover melt dates over northern Canada

ling the number of stations in the network to over 2000. The network is biased to southern latitudes and to low elevations, with most stations located in open locations or airports (Brown and Braaten 1998). Daily and weekly measurements of snow depth were made from the early 1900s at some stations and these data (as well as missing data from some Arctic sites) were rescued and included in the Canadian Snow CD (MSC 2000) through the Cryosphere System in Canada (CRYSYS) project. This process also included data filling and reconstruction of snow depth information from daily climate stations (Brown and Braaten 1998).

The Canadian daily snow depth observing network experienced a marked decline in the 1990s due to automation (without including snow depth sensors), changes in observing practices, and the closure of some manned stations. This resulted in a ~20–30% reduction in the total snow depth network but more importantly, a more than 50% reduction in the network of stations with long records suitable for monitoring variability and change in snow cover. A total of 25 stations (Table 2) were identified in the MRB with potential for investigation of snow cover variability. These stations are clustered in several sub-regions (e.g., Mackenzie Delta, Mackenzie Valley, Great Slave Lake, and the northern prairies), and large areas in the eastern and western parts of the Basin have little or no data. The start and end dates shown in Table 2 include periods with snow depth reconstructed Brown and Braaten (1998), using a degree-day melt index model driven by daily temperature and snowfall data calibrated to optimize the simulation of snow cover duration.

2.2 Snow Survey Data

Weekly and bi-weekly snow survey data from the national compilation included on the Canadian Snow CD (MSC 2000) were used to investigate interannual variability in SWE. To facilitate the SWE comparison, the snow course data were interpolated to a 1º latitude–longitude grid using an inverse-distance weighting scheme with a 75 km search radius. To avoid biasing grid averages, observations obtained at elevations that differ from the mean grid-point elevation by more than ±400 m were rejected. The gridding was carried out for snow seasons covering the period 1950/51–1998/99 and included bi-weekly SWE estimates from daily snow depth observations using interpolated snow density information (Braaten 1997). The snow course sites tend to be concentrated along the mountainous regions in the west of the MRB in contrast to the daily snow depth network which follows the main centers of population.

Table 2. Climate stations in the MRB with potential for investigating historical snow cover variability. A station had to have at least 30 years of complete daily snow depth data in the 1961–2000 period to be considered

ID	Name	Lat [°]	Long [°]	Elev [m]	Start [YYYY MM]	Finish [YYYY MM]	No. rec
3060321	ATHABASCA 2	54.82	-113.53	626	195208	200307	512
3061200	CAMPSIE	54.13	-114.68	671	191008	200307	1039
3062242	EDSON A	53.58	-116.47	927	191608	200307	934
3062440	ENTRANCE	53.37	-117.70	991	191708	200307	776
3062693	FORT MCMURRAY A	56.65	-111.22	369	194112	200307	721
3070560	BEAVERLODGE CDA	55.20	-119.40	745	191308	200307	1024
3072920	GRANDE PRAIRIE A	55.18	-118.88	669	194208	200307	732
3075040	PEACE RIVER A	56.23	-117.43	571	194408	200307	571
2100950	SHINGLE POINT A	68.95	-137.22	49	195708	200208	417
2101200	WATSON LAKE A	60.12	-128.82	687	193908	200307	740
2200100	AKLAVIK A	68.22	-135.00	6	192608	200307	554
2201400	FORT GOOD HOPE A	66.23	-128.65	82	193501	200307	673
2201700	TULITA A	64.92	-125.57	101	190408	200307	655
2202000	FORT RESOLUTION A	61.18	-113.68	160	193108	200307	677
2202200	FORT SMITH A	60.02	-111.97	205	194404	200307	702
2202400	HAY RIVER A	60.83	-115.78	166	194408	200307	699
2202570	INUVIK A	68.30	-133.48	68	195804	200307	517
2202800	NORMAN WELLS A	65.28	-126.80	74	194308	200307	719
2204000	WRIGLEY A	63.22	-123.43	150	194308	200305	576
2204100	YELLOWKNIFE A	62.47	-114.43	206	194208	200307	725
2204200	YELLOWKNIFE HYDRO	62.67	-114.25	159	194308	200006	524
1183000	FORT ST JOHN A	56.23	-120.73	695	194203	200307	737
1183090	GERMANSEN LANDING	55.78	-124.70	763	195108	200210	590
1192340	DEASE LAKE	58.43	-130.02	807	194508	200211	669
1192940	FORT NELSON A	58.83	-122.60	382	193808	200307	772

2.3 NOAA Weekly Snow Cover

NOAA weekly satellite snow cover data have been used extensively to document snow cover variability and change over the NH from the late-1960s (e.g., Brown 2000; Dye 2002; Frei and Robinson 1999). The data are described in Robinson et al. (1993) and consist of digitized weekly charts of snow cover derived from visual interpretation of visible satellite imagery by trained meteorologists. Until May 1999, the charts were digitized on a 190.5 km polar stereographic (PS) grid with a 50% snow cover threshold defining "snow" or "snow-free" grid cells. This NOAA product was discontinued at the end of May 1999 with the introduction of the daily Interactive Multi-Sensor (IMS) snow cover product (Ramsay 1998), which was provided on a higher resolution ~25 km polar stereographic grid. A pseudo-weekly product has been derived from the IMS daily product by taking each Sunday map as representative of the previous week. This has resulted in some inconsistencies in snow cover time series in mountain and coastal areas related to the higher resolution of the IMS grid and differences in the interpretation and application of the 50% snow cover fraction threshold (Brasnett 1999; Robinson personal communication). These changes have minimal effect on this investigation as our study area lies east of the Cordillera.

The weekly data used in this study were obtained from Dr. David Robinson of Rutgers University and contain the corrections recommended by Robinson et al. (1991). The NOAA weekly snow cover dataset has experienced a number of changes in satellite sensors and procedures since it was initiated in 1966 that could affect the homogeneity of the data series. The most notable changes were the introduction of higher resolution VHRR satellite series in 1972 and the switch to the higher resolution IMS product in May 1999. This latter change resulted in an abrupt end to snow cover time series at some coastal locations due to inconsistencies in the land/sea mask. These points were identified and removed prior to the analysis. In addition, Wang et al. (2005) found evidence of possible procedural differences in the interpretation of patchy snow that occurred in the late-1980s and early 1990s. The regime shift detection method of Rodionov (2004) was applied to investigate the presence of discontinuities in the data series but the results were inconclusive.

2.4 Satellite Passive Microwave SWE Retrievals

The Climate Research Division of Environment Canada has an ongoing program to develop SWE retrieval capabilities from spaceborne passive microwave brightness temperatures for major Canadian landscape regions. Overviews of algorithm development in open and forested environments can be found in Goodison and Walker (1995) and Goita et al. (2003) respectively. Algorithm evaluation studies can be found in Walker and Silis (2002) and Derksen et al. (2003) while applications of the SWE time series are documented in Derksen et al. (2000, 2004).

Scanning Multichannel Microwave Radiometer (SMMR; 1978–1987) and Special Sensor Microwave/Imager (SSM/I; 1987–present) data are available in a common 25 km gridded format (the Equal Area Scalable Earth Grid – EASE-Grid; see Armstrong and Brodzik 1995; Armstrong et al. 1994; Knowles et al. 2002). The sensors have slightly different spatial, temporal, and radiometric characteristics, so the standardization coefficients of Derksen and Walker (2003) were used to ensure a homogeneous cross-platform brightness temperature data record. Monthly-averaged (DJFM) patterns of SWE were derived for 1978/79 through 2003/04. This seasonal focus was selected to include only those months when the snow is largely deep and dry – conditions that optimize SWE retrieval algorithm performance (Walker and Goodison 1993).

The monthly SWE composites characterize a well-defined zone of high SWE retrievals (>100 mm) across the northern boreal forest of Canada (Fig. 1 in Derksen et al. 2007), producing a band that is evident in December and becomes more pronounced through the winter season. A similar pattern emerged from an independent SWE reanalysis of conventional data by Brown et al. (2003). This band is a prominent snow cover feature within the MRB, with high SWE centers-of-action located in the Slave, Bear, and Peel sub-basins. SWE coefficient of variation values were computed for the passive microwave dataset to determine the amount of interannual variability contained within each monthly composite. In contrast to the highly variable SWE across the prairies to the south and the tundra to the north, the northern boreal snow band is highly invariant throughout the satellite data record.

Dedicated snow survey campaigns were conducted during the 2004 and 2005 winter seasons to characterize snow cover conditions across approximately 500 km of northern boreal forest and open tundra environments near the timing of seasonal peak SWE (March). Details of these surveys are provided in Derksen et al. (2007).

2.5 Regional Climate Model Simulations

MacKay et al. (2007) analysed a seven year simulation (1997–2004) using the CRCM over western Canada, with an emphasis on prairie and boreal snowpack sublimation in central Canada (MacKay et al. 2006). In this study we examined the same simulation but focused on the accumulation of SWE over the northern boreal forest, particularly for the three year period of 1999–2001. Sensitivity experiments were also performed using hypothetical situations in which the surface vegetation and topography were altered.

3 Results

3.1 Historical Variability: Snow Cover

The MRB has not been exempt from recent trends toward earlier snow cover depletion (Bamzai 2003; Dye 2002). Figure 1 shows trends in snow cover duration in the fall (August–January) and spring (February–July) periods since 1966, derived from the NOAA snow chart data record. The number of days with snow cover in these two periods is strongly correlated with the dates of snow cover onset and disappearance. The fall results (Fig. 1a) suggest little change or slight advances in the start date of snow cover. However, the spring results (Fig. 1b) show a strong east-west gradient across the basin with earlier melt concentrated in the mountainous regions west of the Mackenzie River, and little change or a slight increase in spring snow cover along the northeastern basin boundary. These changes are consistent with fall and spring air temperature trends over the basin (Figs. 1c and 1d). Interestingly, the area of increased spring snow duration coincides with the high SWE zone detected in the passive microwave record.

Regression analysis of annual snow cover statistics from 14 stations in the MRB with at least 50 years of data in the 1945–2004 period (Table 3) revealed statistically significant reductions in spring snow cover duration at 12 of the 14 stations, with the largest decreases observed over the southern portion of the Basin (e.g., 0.72 days yr^{-1} at Beaverlodge CDA). The decrease in spring snow cover was also associated with statistically significant reductions in the end date of continuous snow cover of 0.2 to 0.5 days yr^{-1} at 8 sites. The spring season results contrast with fall snow cover duration and the first date of continuous snow where most of the stations showed no change. However, those stations exhibiting changes were all

associated with less snow cover. The contrast in the snow cover response between the fall and spring seasonal responses is consistent with temperature trends over the MRB which show extensive warming in April and a slight cooling in November (Figs. 1c and 1d). These results are similar to spring and fall temperature trends over the 1950–98 period reported by Zhang et al. (2000).

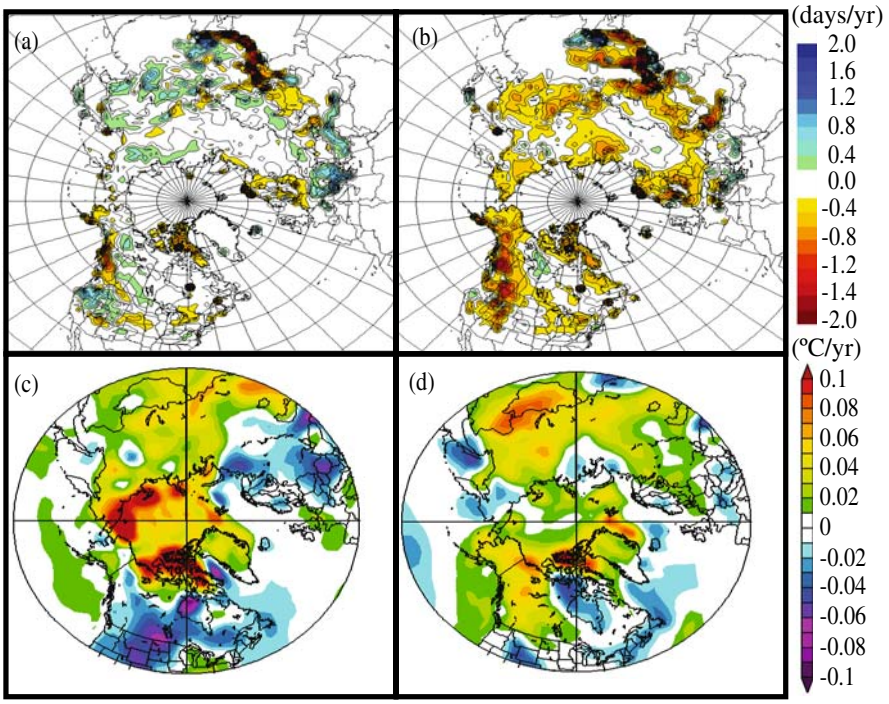

Fig. 1. Observed change (days yr^{-1}) in snow cover duration in (a) the fall and (b) spring halves of the snow year (August–July) from the NOAA weekly satellite product from 1966 to 2004. Trend (°C yr^{-1}) in (c) November, and (d) April NCEP surface air temperature over 1948–2003. Source: NOAA-CIRES Climate Diagnostic Center www.cdc.noaa.gov/Correlation/

Five of the 14 stations showed significant reductions in maximum snow depth with the largest reduction (-0.97 cm yr^{-1}) at Norman Wells. Only Dease Lake showed statistically significant increases in snow depth. The reductions in maximum depth are consistent with the findings of Déry and Wood (2005) of declining precipitation and river discharge in northern Canada between 1964 and 2000.

Table 3. Summary of linear regression analysis of annual snow cover variables over the 60-year period 1945–2004. *Italic* values denote statistical significance (95%)

Stn ID	First date	End date	Fall SCD	Spring SCD	Annual SCD	Max depth	Date of max	Mean depth	SD depth	Median depth
1183000	*0.34*	*-0.37*	*-0.60*	*-0.36*	*-0.96*	-0.21	-0.06	-0.12	-0.07	-0.09
1192340	-0.09	*-0.23*	0.03	*-0.24*	-0.21	0.17	*-0.88*	*0.20*	0.02	*0.29*
1192940	0.07	-0.09	-0.19	-0.09	*-0.28*	-0.21	-0.27	0.00	-0.07	-0.03
2101200	-0.04	*-0.20*	-0.18	*-0.33*	*-0.51*	*-0.30*	-0.26	-0.08	*-0.13*	0.02
2201400	0.39	0.00	*-0.45*	-0.09	-0.54	0.02	-0.40	-0.01	0.00	-0.03
2202200	-0.04	-0.13	-0.04	*-0.13*	-0.17	-0.05	-0.03	-0.07	-0.05	-0.11
2202400	-0.04	*-0.19*	-0.05	*-0.19*	*-0.24*	*-0.38*	-0.15	-0.18	*-0.12*	-0.20
2202800	0.00	*-0.37*	-0.09	*-0.30*	*-0.39*	*-0.97*	*-0.82*	*-0.61*	*-0.30*	*-0.67*
2204100	0.08	-0.12	-0.08	*-0.15*	*-0.23*	-0.19	0.12	*-0.15*	*-0.07*	*-0.16*
3061200	-0.04	*-0.41*	0.10	*-0.34*	-0.24	-0.22	-0.21	-0.08	-0.07	-0.07
3062242	0.03	-0.28	0.13	*-0.44*	-0.31	-0.01	-0.61	0.03	0.00	0.04
3062693	-0.15	*-0.50*	-0.12	*-0.32*	*-0.45*	*-0.29*	-0.39	*-0.20*	*-0.10*	*-0.22*
3070560	0.49	-0.24	*-0.58*	*-0.72*	*-1.29*	-0.22	-0.58	-0.14	-0.07	-0.14
3072920	0.14	*-0.42*	*-0.43*	*-0.30*	*-0.74*	*-0.35*	0.07	-0.13	*-0.11*	-0.09

The large reduction in spring snow cover duration shown over the Western Cordillera is associated with well-documented declines in spring snowpack (Mote 2003) and significant shifts towards earlier spring runoff (Cayan et al. 2001) that are consistent with global warming (Stewart et al. 2005). However, McCabe and Clark (2005) showed that the shift to earlier spring runoff in the western United States was not a gradual trend but an abrupt step-change that occurred during the mid-1980s. They concluded that the shift was more likely a regional response to natural climate variability than global warming. This finding underscores the need to carefully document and understand interannual variability before attributing changes to global warming (Woo et al. 2006). To pursue the investigation further, in situ data were used to extend the satellite snow cover record over the MRB following the methodology of Brown (2000) which is described in detail in Brown (2006). This regional analysis of the spring snow cover (Fig. 2a) shows evidence of a gradual decrease from the late-1960s to the early-1980s, to stabilize at a new lower mean. However, the interannual variability in spring snow cover appears to have increased noticeably after 1976 in response to a shift in the Pacific Decadal Oscillation to a warm mode. Fall snow cover duration showed no trend (Fig. 2b), but there was a period with noticeably less snow (later start to the snow season) in the late-1970s. A late start to the snow cover season has significant water resource implications since it shortens the period of snow accumulation, leading to less runoff from spring snowmelt.

3.2 Historical Variability: Snow Depth and SWE

Figure 3a provides a comparison of regionally-averaged March SWE over southern MRB derived from the gridded snow course data with regionally-averaged maximum snow depth estimated from 8 stations. March was selected as this month has the high average SWE and the March series displayed the highest correlation with values from the Brown et al. (2003) gridded SWE dataset ($r = 0.88$) over the 1979–97 period. Correlation of the SWE and maximum snow depth annual series for the 1950–98 period are statistically significant ($r = 0.70$). Both SWE and snow depth were above average from 1960 to 1975 but were slightly below average in the 1980s, followed by an increase in the 1990s. These data therefore showed a hint of an approximately 30 year cycle.

For northern MRB, defined as 65–70^{o}N, 110–135^{o}W, the gridded SWE datasets offer sufficient data to generate a regionally-averaged SWE series. The April series was selected for analysis as this month has the highest

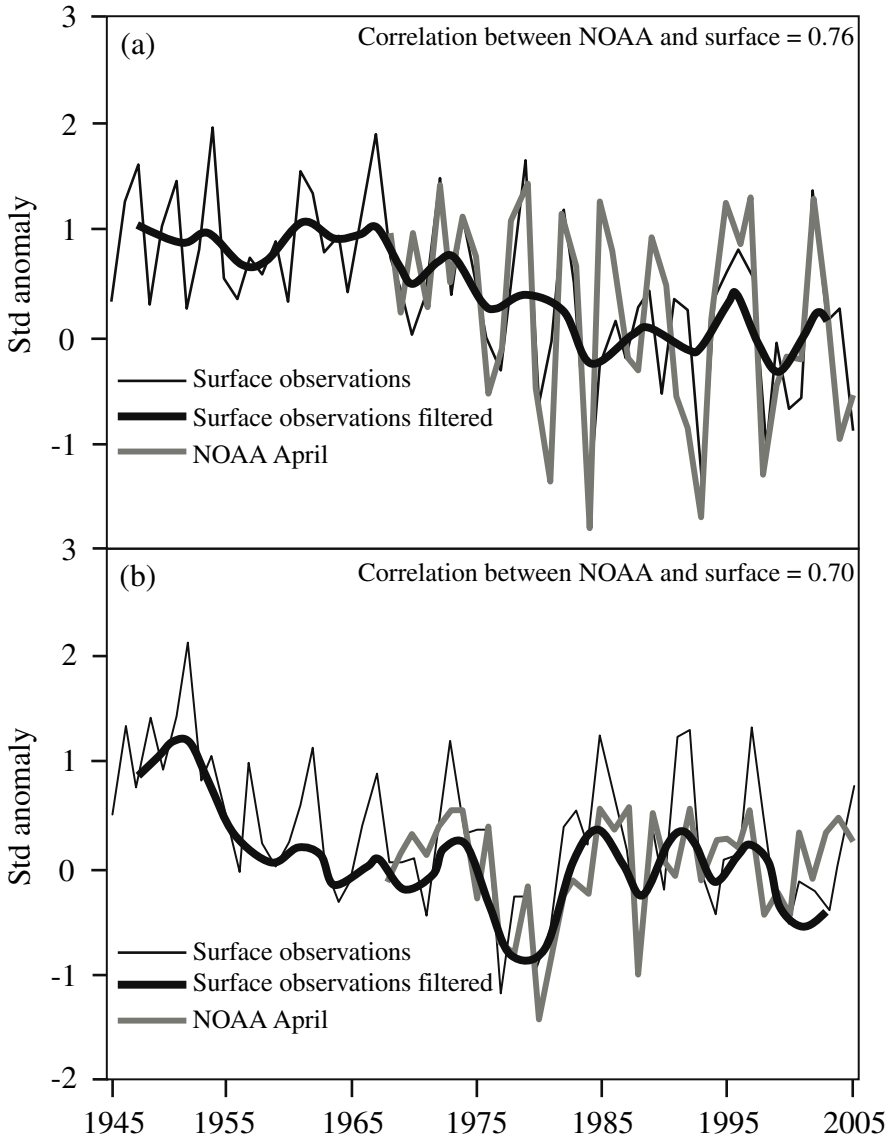

Fig. 2. Historical variability in (a) spring and (b) fall snow cover duration from regionally-averaged station data compared to NOAA SCE variability in April and November

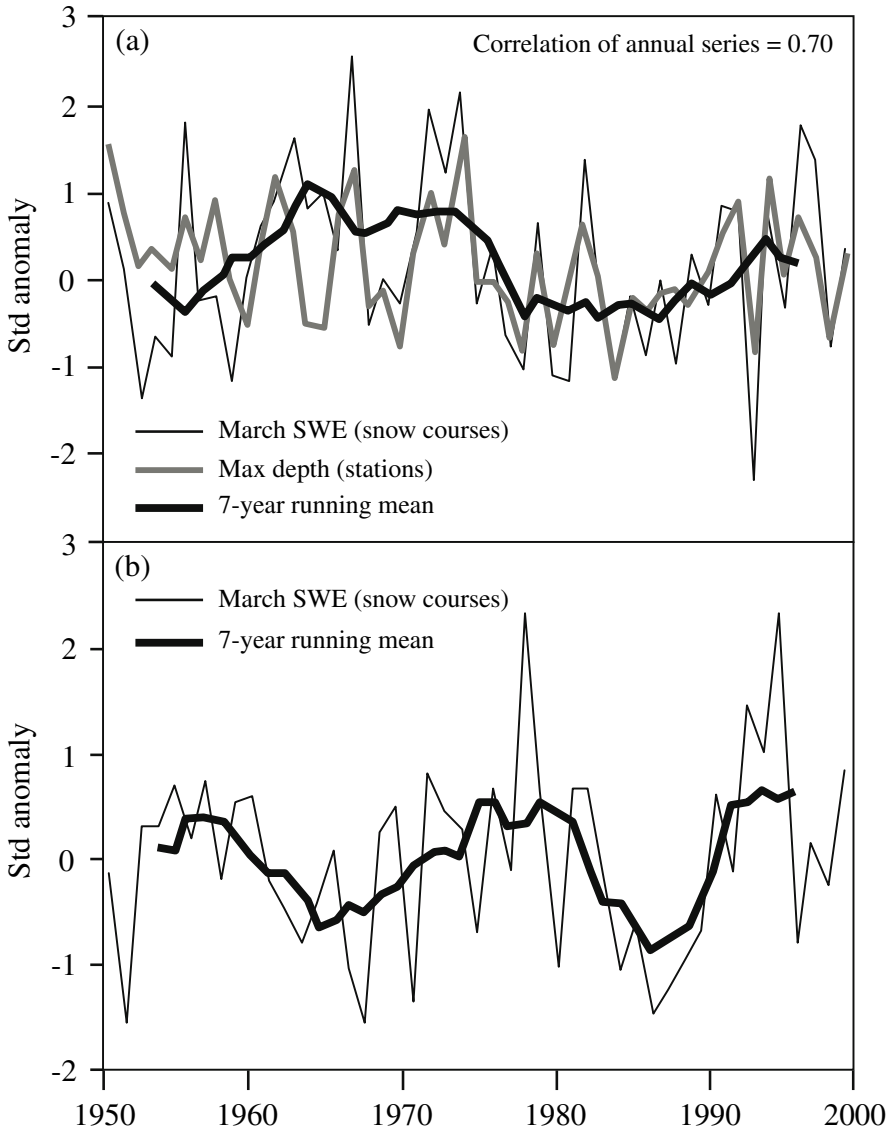

Fig. 3. (a) Comparison of annual maximum snow depth series derived from daily snow depth observations with March mean SWE derived from snow course data. (b) Annual mean April SWE over the northern Mackenzie Basin from snow course observations. All series were standardized with respect to a 1980–99 reference period (1980–98 for March SWE). Solid line presents the 7-yr running mean

mean SWE and the series displayed the highest correlation with values from the Brown et al. (2003) gridded SWE dataset (r = 0.82) over the 1979–97 period. The results (Fig. 3b) are quite different from the southern region (the two series are not correlated) and there is some evidence of an approximately 20 year cycle in the April SWE series. There were no significant correlations between April SWE and mean river flow of the Arctic Red River or of the Mackenzie River at the village of Arctic Red River.

3.3 Links to Atmospheric Circulation

Correlation analysis was employed to assess the role that the dominant modes of NH atmospheric circulation play in the variability of the snow cover in MRB. A composite analysis of the highest and lowest snow years was used to provide additional insight into the atmospheric patterns responsible for extreme conditions. Detail of the composite analysis is described in Brown (2006).

Using indices for NH winter atmospheric circulation obtainable from the NOAA Climate Prediction Center:

http://www.cpc.ncep.noaa.gov/data/teledoc/telecontents.shtml

correlations with regionally-averaged fall and spring snow cover characteristics revealed that the Pacific-North American (PNA) pattern in winter had the strongest influence on interannual variability in snow cover in southern MRB. The PNA was significantly correlated with spring snow cover duration in April (r = -0.55), fall snow cover in October (r = -0.51) and maximum SWE and snow depth in November (r = -0.54 and -0.53 respectively). These findings are supported by results of previous studies that documented a strong link between the PNA and snow cover over western North America (NA) in the fall, winter and spring seasons (Brown and Goodison 1996; Gutlzer and Rosen 1992). Note that the correlations to SWE and depth occur at the start of the snow season, confirming the importance of the start date of the snow accumulation season on the maximum snow accumulation.

The PNA pattern refers to the relative amplitudes of the ridge over western NA and the troughs over the central north Pacific and eastern NA (Leathers et al. 1991). The positive mode of the PNA is associated with a stronger Aleutian Low and a stronger ridge over central Canada. This pattern promotes more meridional flow over NA with Pacific storms diverted toward the northeast. The effect on precipitation is further compounded over the Rockies by the large-scale subsidence and compressional heating associated with the enhanced ridge which generates warmer, drier air east

of the main divide. The positive phase of the PNA pattern has a double effect on snow accumulation in the MRB by reducing the amount of time snow can accumulate as well as decreasing precipitation over the snow accumulation season. This is highlighted in Fig. 4 which shows the correlation structure of the PNA pattern on November and April mean monthly surface air temperatures, and on winter (DJFM) precipitation rate. The negative PNA pattern is associated with a weaker Aleutian Low and a weakening of the ridge over central Canada that favors the expansion of polar air over the continental interior of NA and increased winter precipitation from Pacific storms that are no longer diverted toward the northeast.

A composite analysis was performed for November and April air temperature (Fig. 5) and 500 hPa geopotential height (Fig. 6) using such temperature and pressure data selected from the 5 years with the shortest and longest fall and spring snow cover durations. In three of the composite plots, the PNA regional temperature response is clearly visible. The exception is the low spring snow cover (early snow melt) composite where the warming is spread over much of the NH high latitudes other than central Russia. Stewart et al. (2005) also found that early spring runoff years in the western US responded to a warming trend that cut across different phases of the PDO and is consistent with hemispheric temperature data which show an elevated spring warming trend across mid- and high latitudes (Jones and Moberg 2003).

Leathers and Palecki (1992) indicated a shift in the PNA pattern in 1957 to more meridional flow. This, however, was not corroborated with the PNA series from the NOAA Climate Prediction Center which showed a significant shift in 1976, corresponding with a deeper and eastward-shifted Aleutian low-pressure system that advected warmer and moister air into Alaska, and colder air over the North Pacific during the winters until 1988 (Trenberth 1990).

3.4 Passive Microwave SWE Retrievals and CRCM Simulations

Uncertainty in high latitude retrieval accuracy, however, necessitated an assessment of the passive microwave SWE data using long snow survey transects. A ground survey in Manitoba and the Northwest Territories for 2003/04 (Derksen et al. 2005, 2007) confirmed lower SWE over the southern boreal forest (~ 70 mm) and higher SWE in the northern boreal forest (~ 120 mm), with the highest values co-located in both the ground measur-

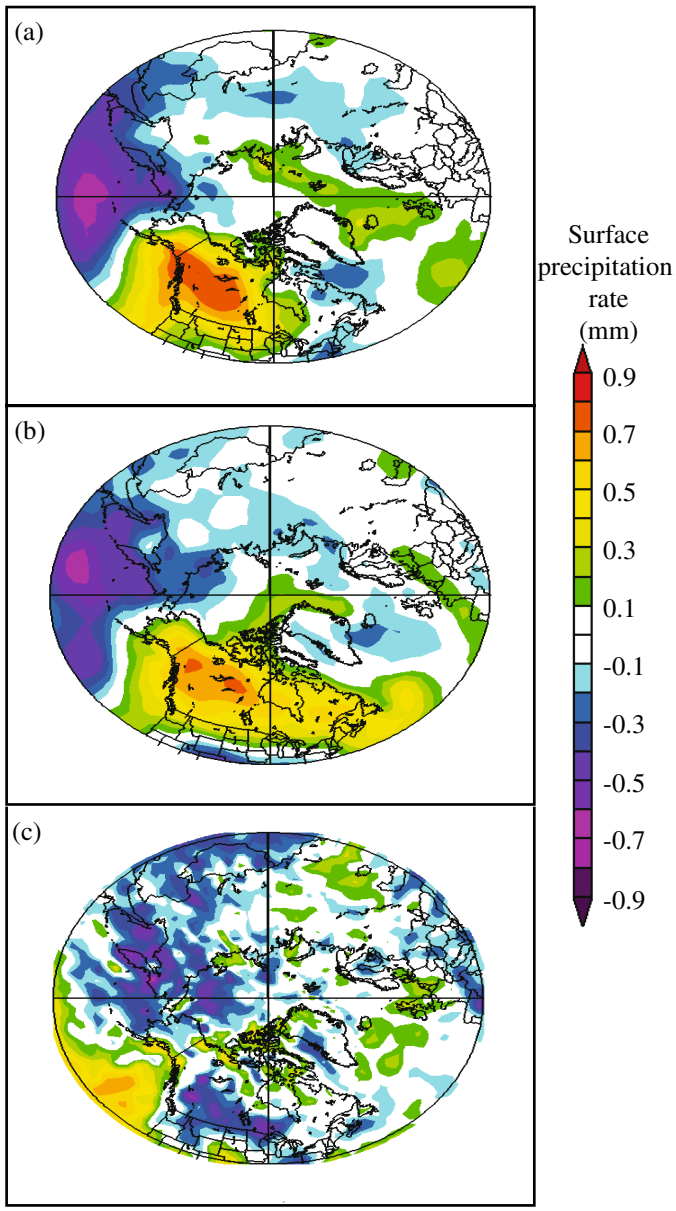

Fig. 4. Correlation of the PNA pattern in (a) November and (b) April with NCEP monthly air temperatures, and (c) with December-March precipitation rate, over the period 1948 to 2003. Source: NOAA-CIRES Climate Diagnostic Center (www.cdc.noaa.gov/Correlation/)

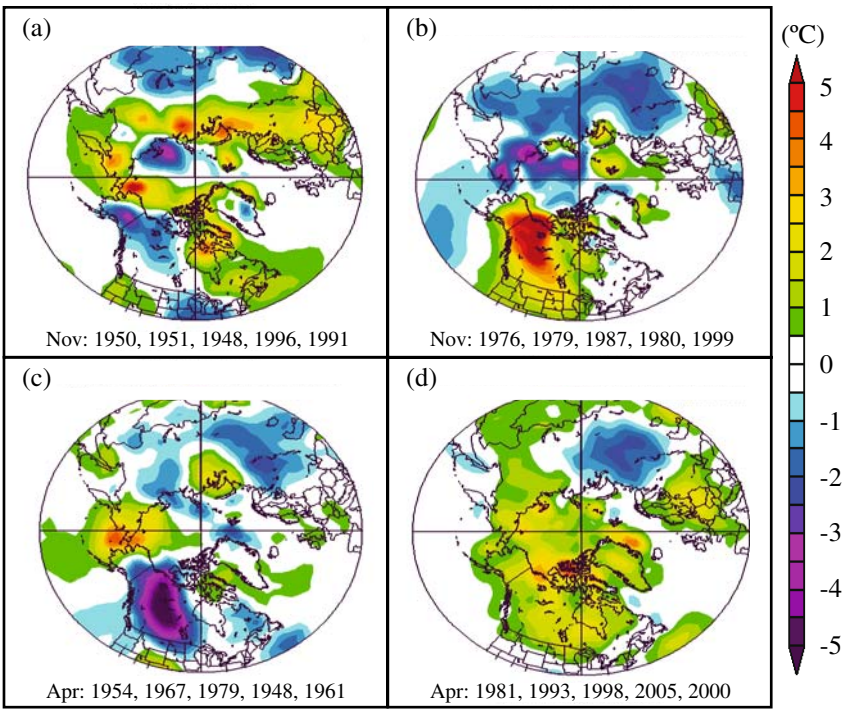

Fig. 5. Results of composite analyses: November mean air temperature for 5 years with (a) the earliest start and (b) the latest start of a snow cover in the fall; April mean air temperature for 5 years with (c) the earliest and (d) the latest loss of a snow cover in the spring in the southern Mackenzie Basin over the 1948–2004 period. Source: NOAA-CIRES Climate Diagnostic Center (www.cdc.noaa.gov/Correlation/)

ed and the satellite derived datasets just south of the forest-tundra treeline. Frequency histograms showed that a high percentage of satellite retrievals (November: 93%; March: 63%) fell within ±20 mm of the median ground measurement. The SWE gradient across the boreal forest was confirmed again for the comparatively heavy snow season of 2004/05. The maximum SWE values in the core of the high SWE band approached 200 mm, so passive microwave underestimation was more notable, though sufficient confidence could be placed in the passive microwave derived SWE patterns.

CRCM simulations were performed to seek linkage of the high SWE band with atmosphere circulation and land conditions (Derksen and MacKay 2006). The mean monthly CRCM simulated SWE pattern for October to January was consistent throughout the simulation period (1997-2004;

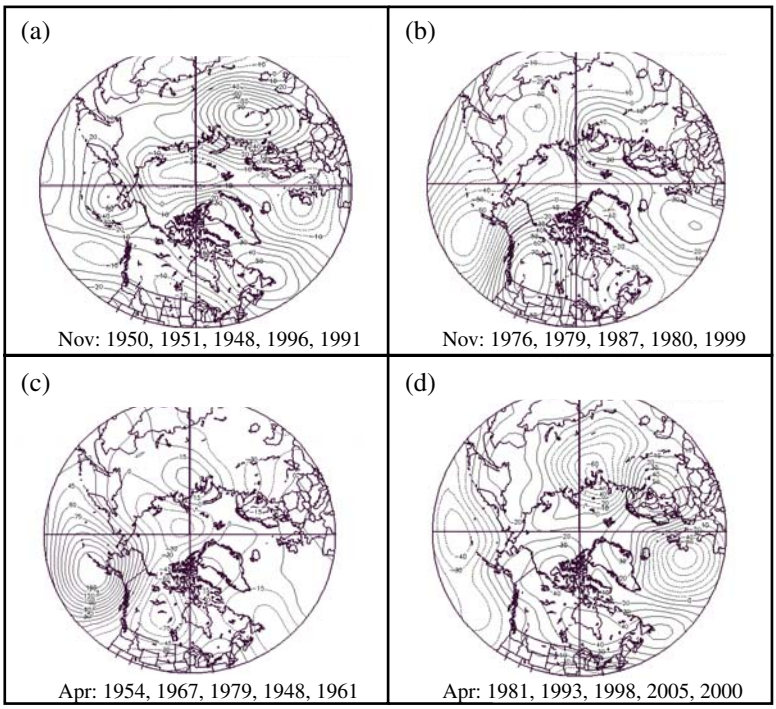

Fig. 6. Results of composite analysis for NCEP 500 hPa (hPa=mb) geopotential height for November and April for the 5 years with the longest and shortest fall and spring snow cover durations in the southern Mackenzie Basin over the 1948–2004 period. Source: NOAA-CIRES Climate Diagnostic Center (www.cdc.noaa.gov/Correlation/)

not shown). The simulations showed that the high SWE band begins to appear in October and is well established by January on average. The early season initiation of this was not detectable with the passive microwave dataset due to issues of detecting thin snow cover on warm ground. Maximum simulated SWE values also followed the northern edge of the boreal forest. Uniform snowfall over the entire region could result in this banded structure if sublimation losses were relatively high in the denser forest to the south and the tundra to the north. This was not the case, however, as the mean October (1999–2001) SWE accumulation (Fig. 7a) as the pattern of accumulated snowfall (Fig. 7b) closely followed that of accumulated SWE, though some melt did occur along the southern edge of the snowpack (Fig. 7c). Sublimation from the ground (Fig. 7d) and total evaporation and sublimation off the canopy (Fig. 7e) are both generally quite weak in this model (in fact large regions experience condensation). Note also

that blowing snow transport which may be important locally, is not represented in the CRCM. It is clear that the simulated boreal SWE band is a result of the simulated accumulation pattern. Results are similar for November (not shown) but December and January accumulation patterns are essentially uniform across the region, suggesting that the boreal snow band feature is usually established during October and November.

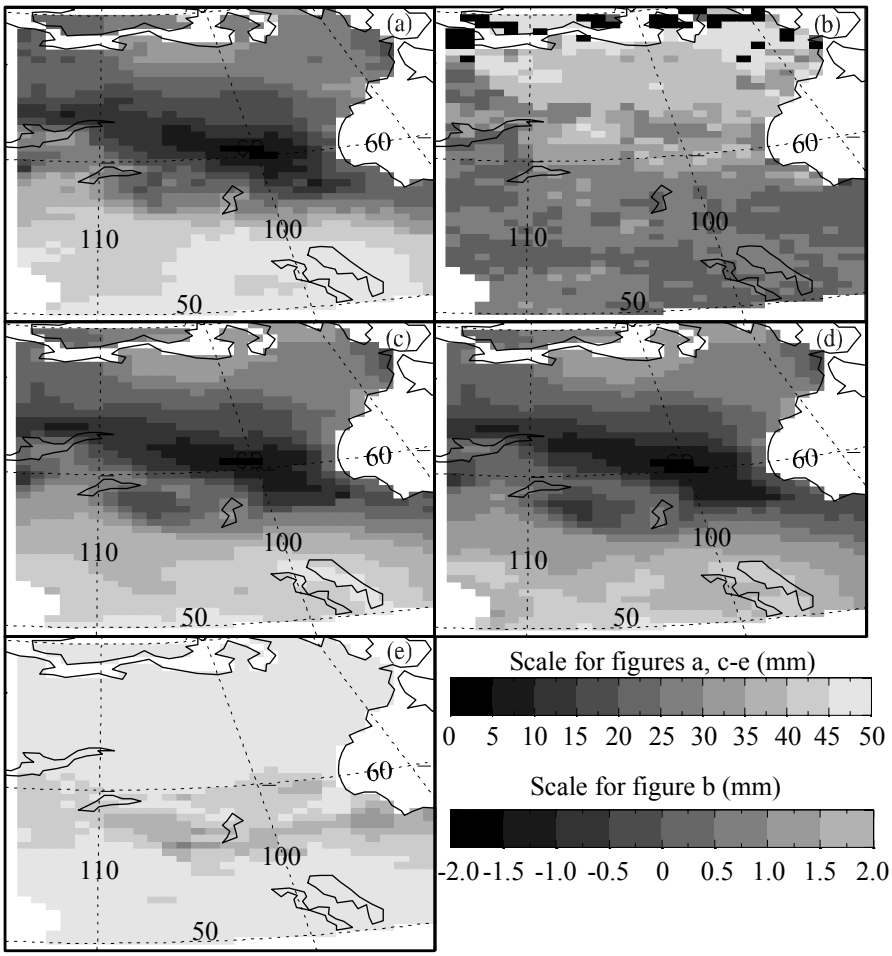

Fig. 7. Mean monthly snowpack water budget for October 1999–2001: (a) accumulated SWE; (b) accumulated snowfall; (c) accumulated snowmelt runoff; (d) accumulated sublimation from ground; (e) accumulated vapor flux (sublimation and evaporation) from canopy

Preferential snowfall over the northern boreal forest may correspond with a preferential zone of frontogenesis. To explore this hypothesis a mean frontogenesis forcing diagnostic was computed (Derksen and MacKay 2006) based on the conventional diagnostic used in the analysis of weather systems (e.g., Miller 1948; Petterssen 1936). For quasi-geostrophic flows, Hoskins and Pedder (1980) define this in terms of the vector Q, the rate of change of potential temperature gradient following the geostrophic flow. A monthly mean frontogenesis function was computed based on 6-hourly snapshots from the simulation. Negative values of the frontogenesis function were excluded from the averaging process as they tend to smear out the signal in the monthly averages. It is also possible to have quasigeostrophic frontogenesis but insufficient moisture to produce precipitation at the surface. Such cases were handled by excluding grid cells with less than 4 mm (water equivalent) of snowfall in the past 6 hours (results were not particularly sensitive to the value of this threshold).

The frontogenesis forcing evaluated at 850 hPa (Figs 8b and 8d) exhibited the same spatial pattern as the SWE accumulation (1999–2001) for October (Fig. 8a) and November (Fig. 8b), with the most intense 850 hPa frontogenesis occurring over areas of maximum SWE accumulation. This shows clearly that the snow accumulation pattern is associated with lower tropospheric frontal activity. To determine whether the treeline plays a role in establishing the region of preferred frontogenesis, the simulation was repeated with all vegetation designated as short grass to eliminate the abrupt changes in roughness, canopy interception and albedo caused by the treeline. The change in surface vegetation had a dramatic impact on summer precipitation (not shown), but the patterns of SWE accumulation and frontogenesis forcing remained qualitatively similar to those of our control simulation. Surface vegetation therefore plays a very small role in the establishment of these patterns, as was found in Lynch et al. (2001) for a study over Alaska.

On the other hand, Lynch et al. (2001) noted that topography played a significant role in their frontal frequency analysis. We performed a second sensitivity experiment where the surface elevation was scaled by a factor of 0.01, which rendered the highest elevations in the Rocky Mountains to no more than 30 m. Removing topography had a more dramatic impact on the accumulated SWE patterns, by both enhancing the magnitude and expanding the band zonally (in fact, almost to the Pacific Ocean). Complete results and discussion of these sensitivity experiments with altered surface vegetation and topography are provided in Derksen and MacKay (2006).

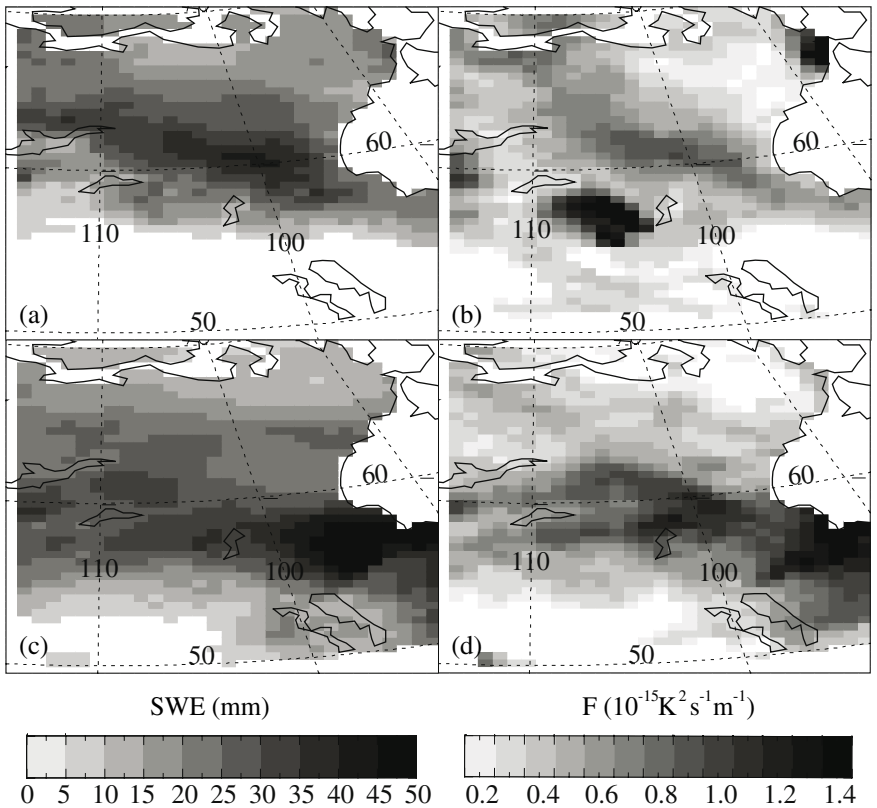

Fig. 8. (a, c) Mean monthly SWE accumulations; (b, d) mean monthly frontogenesis forcing for: (a, b) October; (c, d) November. Averages are computed for 1999–2001

4 Discussion and Conclusions

Based on historical conventional datasets, 12 of 14 stations with long periods of daily snow depth observations in the MRB show significant decreases in spring snow cover duration (and earlier snow cover disappearance) on the order of 0.3–0.5 days yr^{-1} since 1945. In contrast, there are few changes in fall snow cover or date of snow cover onset. The results are consistent with air temperature trends over the region which show a pronounced spring warming but a slight fall cooling. Trends in spring snow cover duration from NOAA snow extent charts (1966–2004) show a strong east-west gradient across the Basin with earlier snow melt concentrated in

the mountains west of Mackenzie River, but little change or slight increases in spring snow cover in the northeast.

The PNA pattern is significantly correlated with snow cover, snow depth and SWE variability in the MRB and contributes to the observed 3–5 year variability, especially in the spring. The PDO (Mantua et al. 1997) has a strong influence on the climate of northwestern North America, and is considered to be an important factor in the observed decadal-scale variability of spring snow cover. While the mechanisms linking the PNA and PDO remain unclear (Straus and Shukla 2002), they are strongly correlated over the 1950–2004 period ($r = 0.74$ for January) and they have similar influences on temperature and precipitation over northwestern NA. The well-documented shift in the circulation over NA in 1976 is linked to the PDO, and is detected in the MRB spring snow cover series. Analysis of spring snow cover data from Beaverlodge CDA from 1916 suggests that spring snow cover variability in the southern MRB is related to the state of the PDO: cool (warm) phases of the PDO are associated with lower (higher) variability.

Within the satellite passive microwave time series, an interannually consistent zone of high SWE was identified across the northern boreal forest. Ground snow surveys showed that the SWE gradient along the southern margin of the high SWE band is well captured by the satellite SWE retrieval, algorithm development is need to increase the magnitude of the SWE retrievals within the core of the band itself (for further discussion, see Derksen et al. 2007).

The occurrence of this SWE band was further analyzed through a series of regional climate model experiments. Simulated SWE was found to be consistent with the pattern of passive microwave SWE retrievals. Water budget computations showed the simulated SWE accumulation pattern to be a function of the regional precipitation pattern, and not the result of surface processes such as melt or evaporation/sublimation. Mean monthly patterns of 850 hPa frontogenesis forcing correspond closely to the patterns of accumulated SWE. The trajectory of this frontal activity follows a principal lower tropospheric (850 hPa) storm track identified in 22 years of ECMWF operational analyses by Hoskins and Hodges (2002). These results suggest that the lower tropospheric frontal activity in late fall and early winter is responsible for a spatially defined and temporally (within and between seasons) invariant SWE pattern, including the formation of the band of high SWE along the northern forest margin. The consistency of this SWE band through the period of passive microwave observations indicates that frontal activity in the lee of the northern Rockies has remained consistent through the time series, even through a period of pro-

nounced winter season warming through this region (Jones and Moberg 2003). Sensitivity experiment with changing the land cover from forest to grassland produces little effect on the SWE pattern, but removing the orographic influence greatly enhances the magnitude and zonal extent of the SWE band.

Acknowledgements

Thanks to Kathy Smith of the NOAA-CIRES Climate Diagnostics Center for her work in developing and maintaining the online analysis and plotting tools for the NCEP reanalysis dataset. The EASE-Grid brightness temperature data were obtained from the EOSDIS National Snow and Ice Data Center Distributed Active Archive Center (NSIDC DAAC), University of Colorado at Boulder. Key datasets were also provided by Dr. David Robinson (Rutgers U.). Thanks to Dr. Petr Štěpánek of the Czech Hydrometeorological Institute for making the climate analysis package *AnClim* available to the research community. Dr. Sergei Rodionov, NOAA/PMEL, is also acknowledged for making his regime shift detection method available online and for his material on climate variability in the Pacific Northwest.

References

Armstrong R, Brodzik M (1995) An earth-gridded SSM/I data set for cryospheric studies and global change monitoring. Adv Space Res 16:10,155–10,163

Armstrong R, Knowles K, Brodzik M, Hardman M (1994, updated 2003) DMSP SSM/I Pathfinder daily EASE-Grid brightness temperatures. National Snow and Ice Data Center, Digital media and CD-ROM

Bamzai A (2003) Relationship between snow cover variability and Arctic oscillation index on a hierarchy of time scales. Int J Climatol 23:131–142

Braaten R (1997) The Canadian snow water equivalent dataset. Unpublished contract report prepared for Atmospheric Environment Service (report contents comprise the SWE documentation included on the Canadian Snow Data CD-ROM, MSC, 2000)

Brasnett B (1999) A global analysis of snow depth for numerical weather prediction. J Appl Meteorol 38:726–740

Brown R (2000) Northern Hemisphere snow cover variability and change, 1915–1997. J Climate 13:2339–2355

Brown R (2006) Snow cover variability and trends in the Mackenzie Basin, 1945–2005. In: di Cenzo P (ed) Final report of the Mackenzie GEWEX Study

(MAGS): Proc 11th Annual Scientific Meeting, November 22–25, 2005, Ottawa, Ontario, Canada, pp 319–337
Brown R, Braaten R (1998) Spatial and temporal variability of Canadian monthly snow depths, 1946–1995. Atmos Ocean 36:37–54
Brown R, Brasnett B, Robinson D (2003) Gridded North American monthly snow depth and snow water equivalent for GCM evaluation. Atmos Ocean 41:1–14
Brown R, Goodison B (1996). Interannual variability in reconstructed Canadian snow cover, 1915–1992. J Climate 9:1299–1318
Cao Z, Wang M, Proctor B, Strong G, Stewart R, Ritchie H, Burnford J (2002) On the physical processes associated with the water budget and discharge of the Mackenzie Basin during the 1994/95 water year. Atmos Ocean 40:125–143
Cayan D, Kammerdiener S, Dettinger M, Caprio J, Peterson D (2001) Changes in the onset of spring in the western United States. B Am Meteorol Soc 82:399–415
Derksen C, Brown R, Walker A (2004) Merging conventional (1915–92) and passive microwave (1978–2002) estimates of snow extent and water equivalent over central North America. J Hydrometeorol 5:850–861
Derksen C, LeDrew E, Goodison B (2000) Temporal and spatial variability of North American Prairie snow cover (1988 to 1995) inferred from passive microwave derived snow water equivalent (SWE) imagery. Water Resour Res 36:255–266
Derksen C, MacKay M (2006) The Canadian boreal snow water equivalent band. Atmos Ocean 44:305–320
Derksen C, Walker A (2003) Identification of systematic bias in the cross-platform (SMMR and SSM/I) EASE-Grid brightness temperature time series. IEEE T Geosci Remote Sens 41:910–915
Derksen C, Walker A, Goodison B (2003) A comparison of 18 winter seasons of in situ and passive microwave derived snow water equivalent estimates in Western Canada. Remote Sens Environ 88:271–282
Derksen C, Walker A, Goodison B (2005) Evaluation of passive microwave snow water equivalent retrievals across the boreal forest/tundra transition of western Canada. Remote Sens Environ 96(3/4):315–327
Derksen C, Walker A, Toose P (2007) Estimating snow water equivalent in northern regions from satellite passive microwave data. (Vol. I, this book)
Déry S, Wood E (2005) Decreasing river discharge in northern Canada. Geophys Res Lett 32:doi:10.1029/2005GL022845
Dye D (2002) Variability and trends in the annual snow-cover cycle in Northern Hemisphere land areas, 1972–2000. Hydrol Process 16:3065–3077
Frei A, Robinson D (1999) Northern Hemisphere snow extent: regional variability 1972–1994. Int J Climatol 19:1535–1560
Goita K, Walker A, Goodison B (2003) Algorithm development for the estimation of snow water equivalent in the boreal forest using passive microwave data. Int J Remote Sens 24:1097–1102
Goodison B, Walker A (1995) Canadian development and use of snow cover information from passive microwave satellite data. In: Choudhury B, Kerr Y,

Njoku E, Pampaloni P (eds) Passive microwave remote sensing of land–atmosphere interactions. VSP BV, Utrecht, Netherlands, pp 245–262
Groisman P, Karl T, Knight W (1994) Observed impact of snow cover on the heat balance and the rise of continental spring temperatures. Science 263:198–200
Gutzler D, Rosen R (1992) Interannual variability of wintertime snow cover across the Northern Hemisphere. J Climate 5:1441–1447
Hoskins B, Hodges K (2002) New perspectives on the Northern Hemisphere winter storm tracks. J Atmos Sci 59:1041–1061
Hoskins B, Pedder M (1980) The diagnosis of middle latitude synoptic development. Q J Roy Meteor Soc 106:707–719
Jones PD, Moberg A (2003) Hemispheric and large-scale surface air temperature variations: an extensive revision and an update to 2001. J Climate 16:206–233
Knowles K, Njoku E, Armstrong R, Brodzik M (2002) Nimbus-7 SMMR Pathfinder daily EASE-Grid brightness temperatures. National Snow and Ice Data Center, Digital media and CD-ROM
Leathers D, Yarnal B, Palecki M (1991) The Pacific/North American teleconnection pattern and United States climate. Part I: regional temperature and precipitation associations. J Climate 4:517–528
Leathers D, Palecki M (1992) The Pacific/North American teleconnection pattern and United States climate. Part II: temporal characteristics and index specification. J Climate 5:707–716
Lynch A, Slater A, Serreze M (2001) The Alaskan Arctic frontal zone: forcing by orography, coastal contrast and the boreal forest. J Climate 14:4351–4362
MacKay M, Bartlett P, Chan E, Derksen C, Guo S, Leighton H (2006) On the problem of regional scale sublimation over boreal and agricultural landscapes. Atmos Ocean 44:289–304
MacKay K, Bartlett P, Chan E, Verseghy D, Soulis R, Seglenieks F (2007) The MAGS regional climate modeling system: CRCM-MAGS. (Vol. I, this book)
Mantua N, Hare S, Zhang Y, Wallace J, Francis R (1997) A Pacific interdecadal climate oscillation with impacts on salmon production. B Am Meteorol Soc 78:1069–1079
McCabe G, Clark M (2005) Trends and variability in snowmelt runoff in the western United States. J Hydrometeorol 6:476–482
MSC (2000) Meteorological Service of Canada, Canadian snow data CD-ROM. CRYSYS project, Climate Processes and Earth Observation Division, Meteorological Service of Canada, Downsview, Ontario
Miller J (1948) On the concept of frontogenesis. J Meteorol 5:169–171
Mote P (2003) Trends in snow water equivalent in the Pacific Northwest and their climatic causes. Geophys Res Lett 30:1601–1604
Petterssen S (1936) Contribution to the theory of frontogenesis. Geofys Publ 11:1–27
Ramsay B (1998) The interactive multisensor snow and ice mapping system. Hydrol Process 12:1537–1546
Robinson D, Dewey K, Heim R (1993) Global snow cover monitoring: an update. B Am Meteorol Soc 74:1689–1696

Robinson D, Keimig F, Dewey K (1991) Recent variations in Northern Hemisphere snow cover. Proc 15th NOAA Annual Climate Diagnostics Workshop, Asheville, North Carolina, October 29 to November 2, 1990. Asheville, NC, National Oceanic and Atmospheric Administration, pp 219–224

Rodionov S (2004) A sequential algorithm for testing climate regime shifts. Geophys Res Lett 31:doi:10.1029/2004GL019448

Schaefer K, Denning A, Leonard O (2004) The winter arctic oscillation and the timing of snowmelt in Europe. Geophys Res Lett 31:doi:10.1029/2004GL021035

Serreze M, Bromwich D, Clark M, Etringer A, Zhang T, Lammers R (2002) Large-scale hydro-climatology of the terrestrial Arctic drainage system. J Geophys Res 108(D2):8160–8188

Stewart I, Cayan D, Dettinger M (2005) Changes towards earlier streamflow timing across western North America. J Climate 18:1136–1155

Straus D, Shukla J (2002) Does ENSO force the PNA? J Climate 15:2340–2358

Szeto K, Tran H, MacKay MD, Crawford R, Stewart RE (2007) Assessing water and energy budgets for the Mackenzie River Basin. (Vol. I, this book)

Trenberth K (1990) Recent observed interdecadal climate changes in the Northern Hemisphere. B Am Meteorol Soc 71:988–993

Walker A, Goodison B (1993) Discrimination of a wet snow cover using passive microwave satellite data. Ann Glaciol 17:307–311

Walker A, Silis A (2002) Snow cover variations over the Mackenzie River Basin from SSM/I passive microwave satellite data. Ann Glaciol 34:8–14

Wang L, Sharp M, Brown R, Derksen C, Rivard B (2005) Evaluation of spring snow covered area depletion in the Canadian Arctic from NOAA snow charts. Remote Sens Environ 95:453–463

Woo MK, Thorne R, Szeto K (2006) Reinterpretation of streamflow trends based on shifts in large-scale atmospheric circulation. Hydrol Process 20:3995–4003

Zhang X, Vincent L, Hogg W, Nitsoo A (2000) Temperature and precipitation trends in Canada during the 20th century. Atmos Ocean 38:395–42

Chapter 14

Recent Studies on the Climatology and Modeling of Blowing Snow in the Mackenzie River Basin

Stephen J. Déry and M.K. Yau

Abstract This chapter presents a multi-scale analysis of the contribution of blowing snow to the hydrometeorology of the Mackenzie River Basin (MRB). A climatology of adverse wintertime weather events demonstrates that blowing snow events are rare within the forested sections of the MRB but become more frequent in the northern parts of the Basin covered by tundra, which experience the largest impacts of blowing snow transport and sublimation due to large-scale processes. A parameterization for blowing snow sublimation based on the PIEKTUK-D model and the European Centre for Medium-Range Weather Forecasts (ECMWF) Reanalysis (ERA-15) data is used to determine that the combined processes of surface and blowing snow sublimation deplete 29 mm yr^{-1} snow water equivalent, or about 7% of the watershed's annual precipitation. This study provides only a first-order estimate of the contribution of surface sublimation and blowing snow to the MRB surface mass balance because of limitations with the dataset and some uncertainties in the blowing snow process.

1 Introduction

Canada is renowned for its long, frigid winters which promote the accumulation of snow that is ubiquitous and even affects the lifestyle during the cold season. Despite their favorable aesthetic and cultural aspects, winter and snow also have negative impacts on Canadians. For instance, intense cold and associated high windchills remain Canada's most devastating natural hazard as about 100 people perish annually from exposure to extreme coldness (Phillips 1990). Severe winter weather such as blizzards, snowdrifting, or freezing rain storms can seriously disrupt the daily activities of millions of Canadians (Kind 1981). A spectacular example is the 1998 'Ice Storm' in Eastern Canada that caused over a billion dollars of damage and was responsible for the deaths of dozens of people (Szeto et al. 1999).

Despite their significant societal impacts, processes responsible for the formation and evolution of winter storms and the seasonal snowpack are

not fully understood. One region in Canada subject to much ongoing investigation is the Mackenzie River Basin (MRB) which is snow-covered for a substantial part of the year (up to 250 days on the Arctic tundra according to Phillips 1990). Some of the processes influencing surface mass balance of the Basin are potentially linked to the transport of wind-driven snow during blizzards and other high wind events (Stewart et al. 1998). Drifting and blowing snow occur when winds surpass a certain threshold value and then erode snow from exposed surfaces to relocate it to sheltered zones such as vegetated areas or depressions. A secondary process during advection is sublimation (phase change of ice to water vapor), providing an additional source of moisture while acting as a sink of sensible heat to the atmospheric boundary layer (ABL) (Déry and Taylor 1996).

Questions remain regarding the role played by blowing snow in the surface mass balance of high-latitude regions (Lawford 1994). This chapter presents a multi-scale analysis of the contribution of blowing snow to the surface mass balance of the MRB. For completeness, the contribution of surface sublimation from the snowpack is also investigated.

2 Background

2.1 Surface Mass Balance

The annual surface mass balance for a nival regime may be expressed as (King et al. 1996):

$$S = P - E - M - D - Q_s \tag{1}$$

where S is the change in storage or accumulation of snow at the surface, P is the precipitation rate, E is the evaporation rate that includes the surface sublimation rate Q_{surf}, and M is the divergence of water after melt and runoff. The two terms associated with blowing snow are represented by D and Q_s, the horizontal divergence and sublimation of blowing snow, respectively. Note that E, Q_{surf}, and Q_s are all defined here as positive quantities when representing an upward flux of water vapor from the surface to the atmosphere. All terms in Eq. (1) are expressed in units of mm yr^{-1} snow water equivalent (SWE) unless stated otherwise.

For the MRB, precipitation and evaporation estimates vary considerably, in part due to the lack of observations in the basin, most notably in the Mackenzie Mountains. Current estimates have the annual ($P - E$) averaged for the MRB to be at 180 mm yr^{-1} (Stewart et al. 1998). Although

much attention has been given to the influx and efflux of atmospheric water vapor in the MRB domain (Bjornsson et al. 1995; Lackmann and Gyakum 1996; Lackmann et al. 1998; Misra et al. 2000; Smirnov and Moore 1999), none of these authors attempted to evaluate the impact of blowing snow on the surface mass balance of the MRB as a whole. Walsh et al. (1994) and Betts and Viterbo (2000) examined the role of surface sublimation in the MRB, but they came to contradictory conclusions, with the former finding significant deposition during wintertime, and the latter strong sublimation. The lack of accurate (if any) information on the role of blowing snow and surface sublimation in the water balance of cold regions including the MRB warrants this study.

2.2 Surface Sublimation

Surface sublimation represents the continual exchange of water between the air (in the vapor phase) to or from the ice- or snowpack (in the solid phase). Following van den Broeke (1997), Q_{surf} is estimated from

$$Q_{surf} = \rho' u_* q_* \tag{2}$$

where u_* (m s^{-1}) is the friction velocity and ρ' (negative) is a conversion factor to units of mm yr^{-1} SWE. Assuming neutral stability near the surface and a logarithmic variation of wind speed with height, u_* can be obtained from (Garratt 1992):

$$u_* = \kappa U / \ln[(z+z_0)/z_0] \tag{3}$$

in which U (m s^{-1}) is the wind speed at a height z (m) above the surface, κ (= 0.4) depicts the von Kármán constant and z_0 (m) represents the aerodynamic roughness length for momentum. Similarly, the humidity scale q_* (kg kg^{-1}) is deduced from a logarithmic moisture profile by assuming saturation with respect to ice near the surface such that (Garratt 1992):

$$q_* = \kappa q_{si}[RH_i(z)\text{-}1] / \ln[(z+z_q)/z_q] \tag{4}$$

in which q_{si} (kg kg^{-1}) represents the saturation mixing ratio with respect to ice near the surface and z_q (m), taken here as equal to z_0, denotes the roughness length for moisture over snow. Surface sublimation therefore depends critically on the gradients of both humidity and wind speed near the surface. Note that when the relative humidity with respect to ice $RH_i >$ 1.0 and q_* becomes positive, deposition to the surface (or negative sublimation) is said to occur. For simplicity, we assume in this study that all surfaces are generally flat and homogeneous. Note however that interac-

tions between vegetation canopies and snow can lead to significant variations in surface sublimation rates compared to open areas (Pomeroy and Dion 1996; Pomeroy et al. 2007).

2.3 Blowing Snow Transport

Blowing and drifting snow occur when wind speeds exceed a certain threshold value and initiate the transport of snow that was formerly at the surface. Precipitating snow may also induce blowing snow, making the source of blown snow somewhat difficult to resolve in many instances. Two substantive processes are involved during blowing and drifting snow: saltation and suspension. Saltation is snow particles bouncing along the surface at heights of a few centimeters providing then a source for snow suspension (Pomeroy et al. 1997). Suspension occurs when snow particles are entrained by turbulent motions within the ABL. In this mode, particles may rise to 100 m or more above the surface (King and Turner 1997).

Although blowing snow usually refers to suspended snow that reduces visibility at eye level and drifting snow refers to snow transport below that height, we do not distinguish between them and consider both to be blowing snow. The 10-m wind speed threshold (U_t) for initiation of transport is usually about 5 to 10 m s^{-1} (King and Turner 1997), depending on such environmental factors as temperature and moisture conditions of the snowpack and the age of the snow (Schmidt 1980). Here we follow Li and Pomeroy (1997) who found a dependence on the 2-m air temperature T_a (°C) for U_t (m s^{-1}) as

$$U_t = U_{t0} + 0.0033(T_a + 27.27)^2 \tag{5}$$

where the minimum value of the threshold 10-m wind speed, U_{t0}, is equal to 6.98 m s^{-1} and is reached at about T_a = -27°C. This parabolic equation predicts higher resistance to transport at very low temperatures and near the freezing point. Near 0°C, the snow tends to be wet, and the imbedded water leads to higher cohesion of the snowpack. On the other hand, at very low temperatures, cohesion associated with strengthening elastic and frictional forces again reduces the capacity of the wind to displace snow from the surface. The intermediate range -25°C < T_a < -10°C is defined by Li and Pomeroy (1997) as the cold cohesive regime in which wind transport of dry snow is generally most favorable.

A number of empirical relationships describing the transport of blowing snow in terms of the wind speed can be found in the literature, as summarized by both Giovinetto et al. (1992) and Pomeroy and Gray (1995). Since

the results of Pomeroy and Gray (1995) are based on measurements conducted in the Canadian Prairies that extend into the southern sections of the MRB, we follow their results which express Q_t (kg m^{-1} s^{-1}) as:

$$Q_t = BU_{10}{}^{C} \tag{6}$$

where U_{10} is the 10-m wind speed (m s^{-1}), $B = 2.2 \times 10^{-6}$ kg m$^{-5.04}$ s$^{-3.04}$, and $C = 4.04$. Once the blowing snow transport rate is known, its net contribution to the surface mass balance is found by

$$D = -\rho' / \rho \nabla \cdot Q_t \tag{7}$$

with ρ (kg m^{-3}) being the air density. Note that by definition, positive values of D indicate horizontal divergence of mass through wind redistribution, and hence a sink in the mass balance equation. Given that D is inversely proportional to the fetch for blowing snow, however, this term decreases in importance for constant values of Q_t and for increasing fetches for snow transport.

2.4 Blowing Snow Sublimation

Blowing snow occurs when loose particles of snow at the surface are entrained by winds exceeding a certain threshold for transport. As particles become suspended in a sub-saturated (with respect to ice) ABL, they sublimate at relatively fast rates despite exhibiting certain self-limiting properties (Déry et al. 1998; Déry and Yau 1999a, 2001a; Gordon and Taylor 2007). The modeling of blowing snow has recently attracted much interest in the hydrometeorological community given its possible twofold impact (i.e., terms D and Q_s in Eq. 1) to the water budget of snow-covered regions (e.g., Bintanja 1998; Déry and Yau 2001b; Essery et al. 1999; Xiao et al. 2000). However, these models cannot be applied directly to long-term, global datasets as they are computationally restrictive. Therefore, to estimate blowing snow sublimation, we use a parameterization for Q_s derived by Déry and Yau (2001a) based on the development of a double-moment blowing snow model (PIEKTUK-D). The authors found that the relationship

$$\begin{aligned} Q_s = (&a_0 + a_1\xi + a_2\xi^2 + a_3\xi^3 + a_4U_{10} + a_5\xi U_{10} + a_6\xi^2 U_{10} \\ &+ a_7 U_{10}{}^2 + a_8\xi U_{10}{}^2 + a_9 U_{10}{}^3)/U' \end{aligned} \tag{8}$$

provided good estimates ($R^2 = 0.95$) of Q_s (here in units of mm d^{-1} SWE) at a Canadian Arctic location. Equation (8) shows that the rate of blowing

snow sublimation depends on the 10-m wind speed U_{10} (m s^{-1}) and the 2-m air temperature and humidity through a thermodynamic term ξ (-1 × 10^{-12} m^2 s^{-1}) given by:

$$\xi = (RH_i - 1)[2\,\rho_{ice}(F_k + F_d)]^{-1} \tag{9}$$

where ρ_{ice} (kg m^{-3}) denotes the density of ice, and F_k and F_d (m s kg^{-1}) represent the conductivity and diffusion terms (both temperature dependent) associated with the sublimation process (Rogers and Yau 1989). Equation (8) is normalized by a factor U' (dimensionless) to remove a dependence on the saltation mixing ratio. Values for the coefficients $a_0 - a_9$ and U' are provided by Déry and Yau (2001a).

3 Methods

Since observations of adverse wintertime processes are scarce and conducted under very harsh conditions, we compile a climatology of these events using gridded reanalysis data. Thus a 15-year (from 1979 to 1993 inclusive) climatology of significant cold-season "events" for the MRB and the globe is inferred from 6-hourly European Centre for Medium-Range Weather Forecasts (ECMWF) Re-Analysis (ERA-15) data on a 2.5° latitude × 2.5° longitude grid (Gibson et al. 1997). The presence of snow is determined from the snow depth parameter of the ERA-15 data that is based on station observations; sea ice coverage is provided by the Canadian Meteorological Centre (CMC) at the same resolution as the former.

In this work, the definition of a blowing snow event is any day when the surface was snow-covered land or sea ice (in concentration of 50% or more), the temperature was below 0°C, and the threshold velocity for transport was exceeded, as determined from Eq. (5), at any grid point. The ERA-15 data are available four times daily (0000, 0600, 1200, and 1800 UTC). A blowing snow event is considered to have occurred if the criteria for such an event are satisfied at any one of the four times. However, for all grid points we limit the number of events to a maximum of one per day. This allows a comparison of our results with observations, since significant cold-season processes are often recorded only on a daily basis, i.e., a day with or without such an event.

Once a surface sublimation or a blowing snow event has been detected, Q_{surf}, Q_s, and Q_t are computed following the equations given in the previous section. These rates are assumed constant for the 6-hourly periods of the ERA-15 data. However, we ensure that the mass eroded through any of

these processes does not exceed that present at the surface as deduced from the ERA-15 data. Note that we compute RH_i only when air temperatures are below the freezing point. In the event that RH_i is > 1.0, we set Q_s to zero despite the inference of a blowing snow event. Once the data have been compiled for the 15 years that span the ERA-15 data, we present our results using a polar stereographic projection.

4 Results

4.1 Climatology of Blowing Snow Events in the MRB

Although most of the MRB is forested, the northeastern and northern sections of the Basin lie within the tundra and the southern Basin is in the Canadian prairies (Woo et al. 2007). The tundra region is conducive to frequent blowing snow events (≥ 10 per year) which decline rapidly in number within the boreal forest, where fewer than five episodes occur annually (Fig. 1). The number of occurrence increases southward as the boreal forest gives way to the open prairies. Compared with Phillips (1990), we underestimate the frequency of blowing snow events in the forested regions of the MRB, where the ERA-15 displays a negative wind speed bias (Déry and Yau 1999b).

4.2 Contribution of Blowing Snow to the Mass Balance of MRB

Of the three processes examined in this study, only surface sublimation contributes significantly to the overall water budget of the MRB (Fig. 2a). Blowing snow sublimation reaches no more than a few millimeters per year SWE along the Arctic coast and remains negligible throughout most of the Basin (Fig. 2b). Minimal values of the blowing snow transport and divergence rates also prevail within the boreal forest in association with the reduced wind speeds there (Fig. 3). Thus, we find that all three terms combine to erode 28.8 mm yr^{-1} SWE from the MRB, equivalent to 7% of the annual precipitation input into the Basin (Fig. 4). Note also that this value is comparable with the sublimation rates reported at four individual meteorological stations within the MRB (Déry and Yau 2002). In the summer, both surface and blowing snow sublimation approach zero as the Basin remains nearly void of snow (Fig.5). Peak values of blowing snow (surface) sublimation are achieved during the month of January (April).

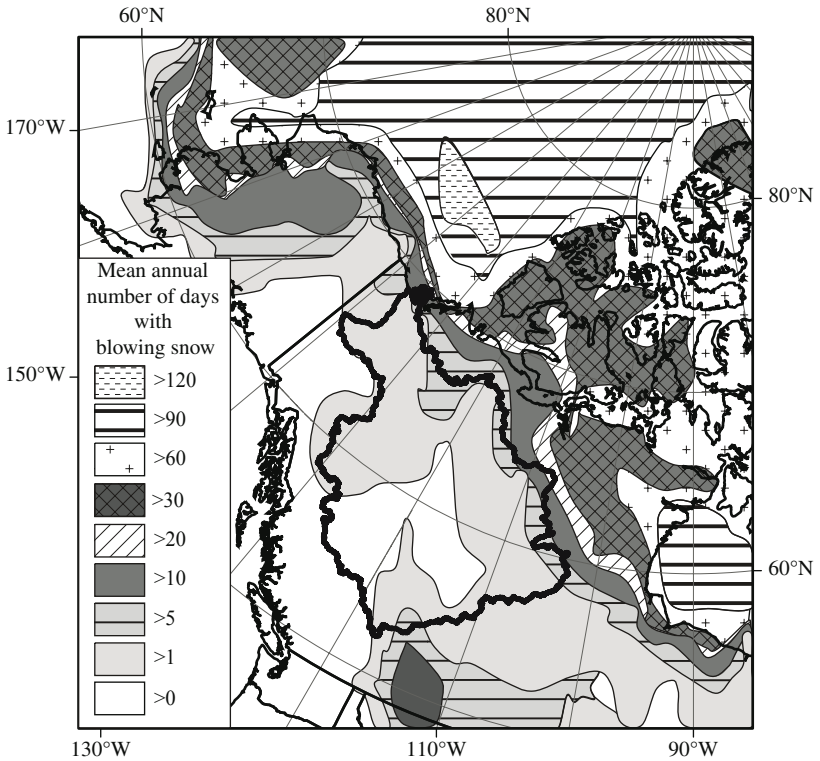

Fig. 1. Mean annual number of days with blowing snow events in Western Canada and Alaska for 1979–93. Boundary of Mackenzie River Basin is denoted by the thick line

An example of the zonally-averaged surface and blowing snow sublimation rates for 1979–93 is displayed in Fig.6. Note that the surface sublimation rates exhibit a seasonal cycle, with maximum values occurring in late spring and early fall and with lesser contributions during winter. Rare episodes of blowing snow sublimation are associated with strong wind events. During summer, there is no sublimation as snow is absent.

For the MRB as a whole, Déry and Yau (1999b) demonstrated that the divergence and sublimation of blowing snow may not contribute significantly to the large-scale surface mass balance since blowing snow events are rare in the largely forested Basin. On the other hand, significant surface sublimation is shown to occur across the entire Basin. This is at variance with the results of Walsh et al. (1994) who utilized 18 years of rawinsonde

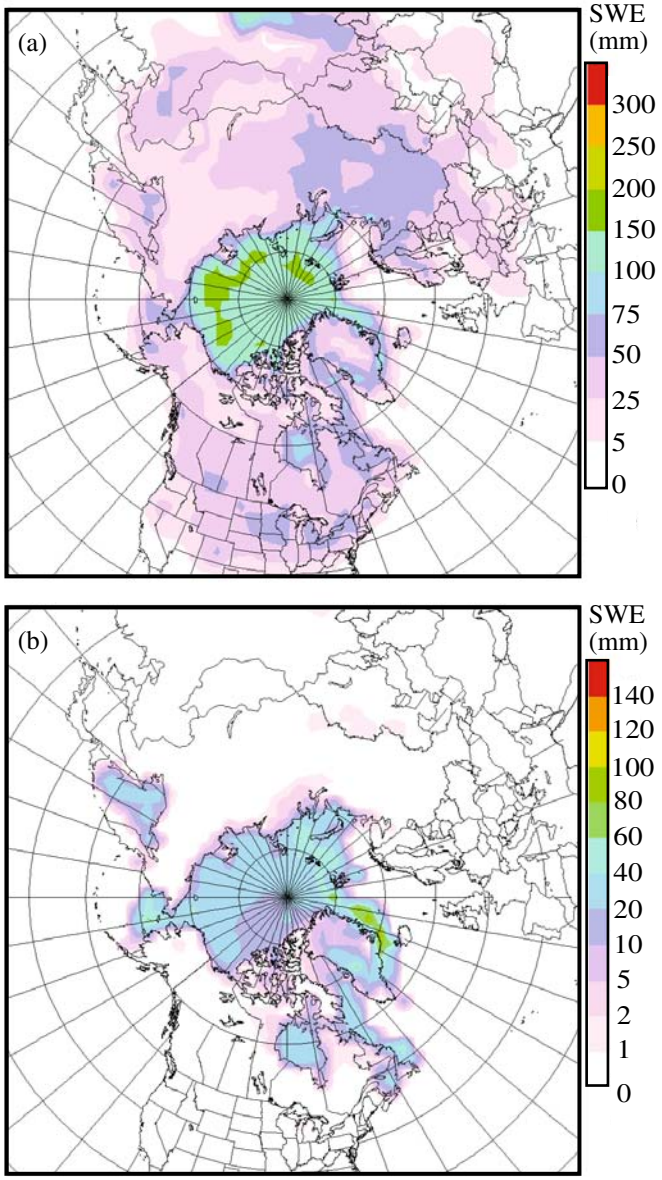

Fig.2. Mean annual (a) surface and (b) blowing snow sublimation rate (mm SWE) for the period 1979–93 in Northern Hemisphere

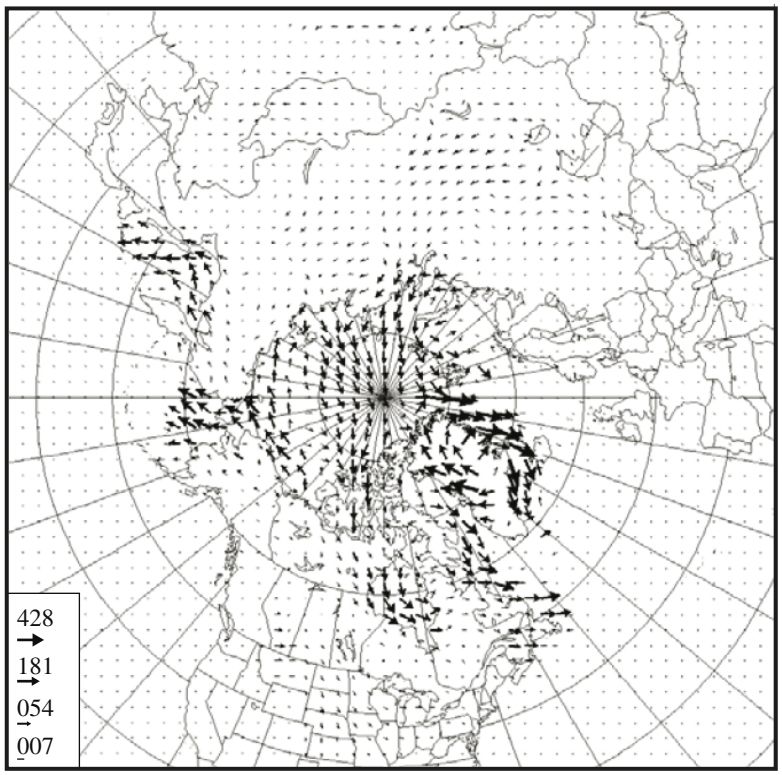

Fig. 3. Mean annual blowing snow mass transport vectors (Mg m^{-1}) for the period 1979–93 in Northern Hemisphere

data to obtain as a residual the evaporation over the MRB. They found negative monthly values of surface sublimation (i.e., deposition) approaching in some cases -10 mm SWE between October and April, and an annual total of about -45 mm SWE. In contrast, our estimates of surface sublimation for the same Basin are somewhat less than those of Betts and Viterbo (2000) who found the evaporation from the snow surface to average 92 mm yr^{-1} SWE over two years using the ECMWF forecast model. However, the authors noted a large positive bias (of about 60%) in the evaporation rate arising in the ECMWF model such that this value should in fact be closer to 37 mm yr^{-1} SWE. We determine that blowing snow and surface sublimation erode ≈ 29 mm yr^{-1} SWE over the entire MRB, a value more in line with the results of Betts and Viterbo (2000) than those of Walsh et al. (1994).

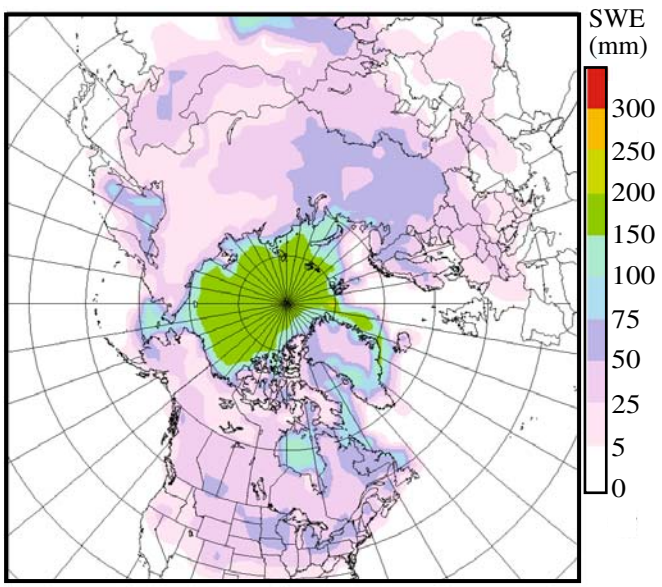

Fig. 4. Mean annual total surface sublimation, blowing snow sublimation, and divergence rates (mm SWE) for the period 1979–93 in Northern Hemisphere

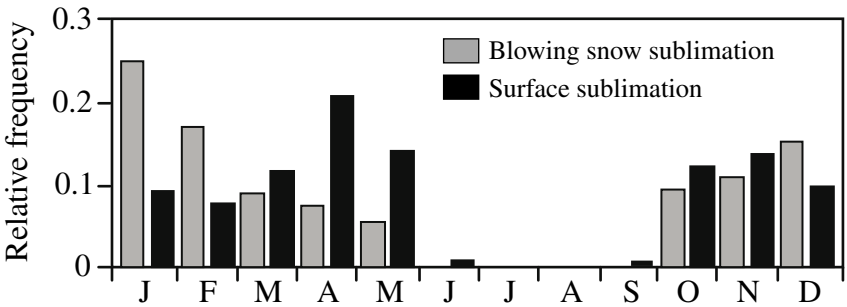

Fig. 5. Relative monthly contributions to the annual surface and blowing snow sublimation rates over the Mackenzie River Basin, 1979–93

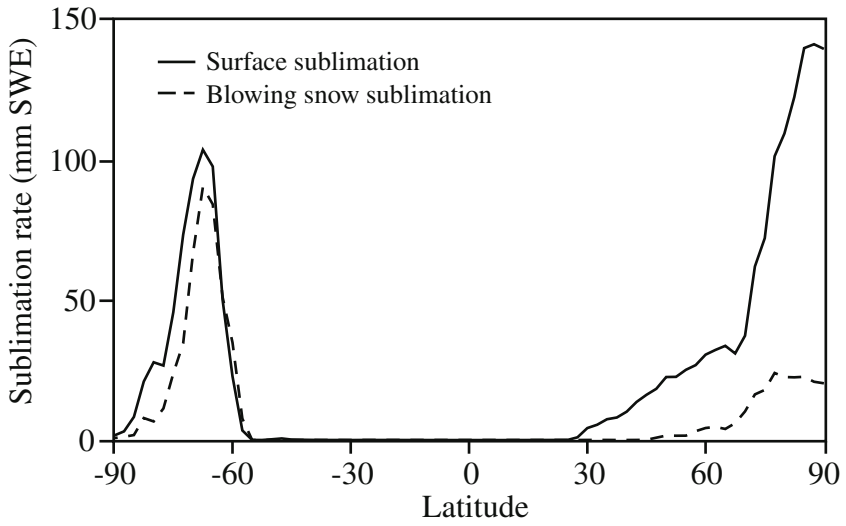

Fig. 6. Zonally-averaged surface and blowing snow sublimation rates (mm SWE) for 1979–93

5 Discussion

We have demonstrated that the ERA-15 dataset provides useful information for the detection of blowing snow and surface sublimation events and their impact on the large-scale surface mass balance. Nevertheless, some uncertainties exist in our results. The major factors of concern and their possible effects (listed in parentheses) are:

- the simple expression used to estimate wind speeds at which snow transport initiates or terminates (reductions or increases in Q_s, Q_t, and D)
- the usage of the blowing snow parameterizations at the scales of the ERA-15 dataset and that are not constrained by direct observations (changes to all blowing snow fluxes)
- the application of a parameterization for blowing snow sublimation based on the unsteady PIEKTUK-D model that generates relatively low sublimation rates of blowing snow compared to other snowdrift models, such as the Prairie Blowing Snow Model (Pomeroy et al. 1993), in part due to the appearance of negative thermodynamic feedbacks on the phase change process (a reduction of Q_s)

- the neglect of blowing snow in the ECMWF operational model and, hence, of the thermodynamic feedbacks associated with blowing snow sublimation in the ERA-15 dataset (an increase in Q_s and Q_{surf})
- the exclusion of surface sublimation during blowing snow events (a decrease in Q_{surf})
- the assumption of homogeneous surfaces and the neglect of blowing snow interception by vegetation (an increase in Q_t)
- the omission of surface sublimation from a forest canopy and when air temperatures exceed the freezing point (a decrease in Q_{surf})
- the sensitivity of surface and blowing snow sublimation rates to the ambient humidity (underestimation or overestimation of Q_s and Q_{surf}, depending on the accuracy of RH_i values)
- the assumption of neutral stability in the ABL (changes to Q_{surf})
- the uncertainty in the effects of entrainment and/or advection of dry air on sublimation processes (an underestimation of Q_s and Q_{surf}).

This study presents the first comprehensive attempt at establishing the large-scale impact of blowing snow and surface sublimation on the large-scale surface mass balance. As such, it provides possibly the best assessment yet of the significance of each of the relevant variables. However, we note that large uncertainties remain in closing the water budget at high latitudes, and more research is required to ascertain (or to improve) the results presented. A priority for future work, therefore, is the determination of scaling relations between station-based and large-scale gridded data.

6 Conclusion

A surface mass balance study of the MRB was conducted using the ERA-15 data for the years 1979–93 inclusive at a horizontal resolution of 2.5°. Emphasis was placed on surface sublimation, blowing snow sublimation and divergence. The results of the water budget computation indicate that this Basin loses mass on the order of 29 mm yr^{-1} SWE through these processes, disposing ≈7% of the total annual precipitation over the MRB. However, the importance of blowing snow sublimation and divergence varies widely within the Basin, with the greatest effects over the Arctic tundra.

As demonstrated by our underlying assumptions, the results provide only a first-order estimate of the contributions of these terms to the MRB surface mass balance. Blowing snow transport, for instance, is known to displace locally significant amounts of mass into large snowdrifts whereas

other areas become nearly devoid of snow (e.g., Sturm et al. 2001; Woo et al. 1983). Nonetheless, as we approach a full closure of high latitude water budgets, this contribution is a first step in establishing the large-scale climatological impacts of surface sublimation, blowing snow sublimation and divergence on the MRB surface mass balance.

References

Betts AK, Viterbo P (2000) Hydrology of seven sub-basins of the Mackenzie River from the ECMWF model. J Hydrometeorol 1:47–60

Bintanja R (1998) The contribution of snowdrift sublimation to the surface mass balance of Antarctica. Ann Glaciol 27:251–259

Bjornsson H, Mysak LA, Brown RD (1995) On the interannual variability of precipitation and runoff in the Mackenzie drainage basin. Clim Dynam 12:67–76

Déry SJ, Taylor PA (1996) Some aspects of the interaction of blowing snow with the atmospheric boundary layer. Hydrol Process 10:1345–1358

Déry SJ, Taylor PA, Xiao J (1998) The thermodynamic effects of sublimating, blowing snow in the atmospheric boundary layer. Bound-Lay Meteorol 89: 251-283.

Déry SJ, Yau MK (1999a) A bulk blowing snow model. Bound-Lay Meteorol 93:237–251

Déry SJ, Yau MK (1999b) A climatology of adverse winter-type weather events. J Geophys Res 104:16,657–16,672

Déry SJ, Yau MK (2001a) Simulation of blowing snow in the Canadian Arctic using a double-moment model. Bound-Lay Meteorol 99:297–316

Déry SJ, Yau MK (2001b) Simulation of an Arctic ground blizzard using a coupled blowing snow-atmosphere model. J Hydrometeorol 2:579–598

Déry SJ, Yau MK (2002) Large-scale mass balance effects of blowing snow and surface sublimation. J Geophys Res 107:4679, doi: 10.1029/2001JD001251

Essery R, Li L, Pomeroy JW (1999) A distributed model of blowing snow over complex terrain. Hydrol Process 13:2423–2438

Garratt JR (1992) The atmospheric boundary layer. Cambridge University Press, Cambridge

Gibson JK, Kallberg P, Uppala S, Hernandez A, Nomura A, Serrano E (1997) ERA description. ECMWF re-analysis project report series 1

Giovinetto MB, Bromwich DH, Wendler G (1992) Atmospheric net transport of water vapor and latent heat across 70°S. J Geophys Res 97:917–930

Gordon M, Taylor PA (2007) On blowing snow and sublimation in the Mackenzie River Basin. (Vol. I, this book)

Kind RJ (1981) Snowdrifting. In: Gray DM, Male DH (eds) Handbook of snow: principles, processes, management and use. Pergamon Press, pp 338–359

King JC, Anderson PS, Smith MC, Mobbs SD (1996) The surface energy and mass balance at Halley, Antarctica during winter. J Geophys Res 101:19,119–19,128

King JC, Turner J (1997) Antarctic meteorology and climatology. Cambridge University Press, Cambridge

Lackmann GM, Gyakum JR (1996) The synoptic- and planetary-scale signatures of precipitating systems over the Mackenzie River Basin. Atmos Ocean 34:647–674

Lackmann GM, Gyakum JR, Benoit R (1998) Moisture transport diagnosis of a wintertime precipitation event in the Mackenzie River Basin. Mon Weather Rev 126:668–691

Lawford RG (1994) Knowns and unknowns in the hydroclimatology of the Mackenzie River Basin. In: Cohen SJ (ed) Mackenzie Basin Impact Study (MBIS), interim report No. 2, Yellowknife, NWT, pp 173–195

Li L, Pomeroy JW (1997) Estimates of threshold wind speeds for snow transport using meteorological data. J Appl Meteorol 36:205–213

Misra V, Yau MK, Badrinath N (2000) Atmospheric water species budget in mesoscale simulations of lee cyclones over the Mackenzie River Basin. Tellus 52A:140–161

Phillips D (1990) Climates of Canada. Environment Canada

Pomeroy JW, Dion K (1996) Winter radiation extinction and reflection in a boreal pine canopy: measurements and modelling. Hydrol Process 10:1491–1608

Pomeroy JW, Gray DM (1995) Snowcover accumulation, relocation and measurement. NHRI Sci Rep 7, Environment Canada, Saskatoon

Pomeroy JW, Gray DM, Landine PG (1993) The Prairie Blowing Snow Model: characteristics, validation, operation. J Hydrol 144:165–192

Pomeroy JW, Gray DM, Marsh P (2007) Studies on snow redistribution by wind and forest, snow-covered area depletion and frozen soil infiltration in Northern and Western Canada. (Vol. II, this book)

Pomeroy JW, Marsh P, Gray DM (1997) Application of a distributed blowing snow model to the Arctic. Hydrol Process 11:1451–1464

Rogers RR, Yau MK (1989) A short course in cloud physics, 3rd edn. Pergamon Press

Schmidt RA (1980) Threshold wind-speeds and elastic impact in snow transport. J Glaciol 26:453–467

Smirnov VV, Moore GWK (1999) Spatial and temporal structure of atmospheric water vapor transport in the Mackenzie River Basin. J Climate 12:681–696

Stewart RE, Leighton HG, Marsh P, Moore GWK, Rouse WR, Soulis SD, Strong GS, Crawford RW, Kochtubajda B (1998) The Mackenzie GEWEX Study: the water and energy cycles of a major North American river basin. B Am Meteorol Soc 79:2665–2683

Sturm M, Liston GE, Benson CS, Holmgren J (2001) Characteristics and growth of a snowdrift in Arctic Alaska, U.S.A. Arct Antarct Alp Res 33:319–329

Szeto KK, Tremblay A, Guan H, Hudak DR, Stewart RE, Cao Z (1999) The mesoscale dynamics of freezing rain storms over Eastern Canada. J Atmos Sci 56:1261–1281

van den Broeke MR (1997) Spatial and temporal variation of sublimation on Antarctica: results of a high-resolution general circulation model. J Geophys Res 102:29,765–29,777

Walsh JE, Zhou X, Portis D, Serreze MC (1994) Atmospheric contribution to hydrologic variations in the Arctic. Atmos Ocean 32:733–755

Woo MK, Heron R, Marsh P, Steer P (1983) Comparison of weather station snowfall with winter snow accumulation in High Arctic basins. Atmos Ocean 21:312–325

Woo MK, Rouse WR, Stewart RE, Stone JMR (2007) The Mackenzie GEWEX Study: a contribution to cold region atmospheric and hydrologic sciences. (Vol. I, this book)

Xiao J, Bintanja R, Déry SJ, Mann GW, Taylor PA (2000) An intercomparison among four models of blowing snow. Bound-Lay Meteorol 97:109–135

List of Symbols

$a_0 - a_9$ empirical coefficients
B empirical coefficient [= 2.2×10^{-6} kg $m^{-5.04}$ $s^{-3.04}$]
C empirical coefficient [dimensionless]
D horizontal divergence of mass through wind redistribution [mm yr^{-1} SWE; or m s^{-1} SWE]
E evaporation rate [mm yr^{-1} SWE]
F_k, F_d conductivity and diffusion terms [m s kg^{-1}]
M divergence of water after melt and runoff [mm yr^{-1} SWE]
P precipitation rate [mm yr^{-1} SWE]
Q_t rate of blowing snow transport [kg m^{-1} s^{-1}]
Q_{surf} surface sublimation rate [mm yr^{-1} SWE]
Q_s sublimation of blowing snow [mm yr^{-1} SWE; or mm d^{-1} SWE]
q_{si} saturation mixing ratio with respect to ice near the surface [kg kg^{-1}]
q_* humidity scale [kg kg^{-1}]
RH relative humidity [kg kg^{-1}]
S change in storage or accumulation of snow at the surface [mm yr^{-1} SWE]
T_a air temperature [°C]
U wind speed at a height z [m] above the surface [m s^{-1}]
U_t 10-m wind speed threshold for initiation of snow transport [m s^{-1}]
U_{t0} minimum value of the threshold 10-m wind speed [m s^{-1}]
U' factor to remove dependence on the saltation mixing ratio [dimensionless]
u_* friction velocity [m s^{-1}]
z_0 aerodynamic roughness length for momentum [m]
z_q aerodynamic roughness length for moisture over snow [m]
κ von Kármán constant [= 0.4]
ρ density of air [kg m^{-3})]
ρ_{ice} density of ice [kg m^{-3}]
ρ' factor for conversion [to unit of mm yr^{-1} SWE]
ξ a thermodynamic term [-1×10^{-12} m^2 s^{-1}]

Chapter 15

On Blowing Snow and Sublimation in the Mackenzie River Basin

Mark Gordon and Peter A. Taylor

Abstract A parameterization of the sublimation of blowing snow is used to calculate the amount of blowing snow sublimation at six locations within the Mackenzie River Basin. The parameterization predicts that, based on estimates for these locations, between 0.5 and 12% of the total precipitated snow within the Basin may be removed by blowing snow sublimation. However, comparison with observed blowing snow frequencies and assumptions made in the parameterization suggests that these amounts may overestimate the actual blowing snow sublimation.

1 Introduction

Blowing snow events are quite frequent in northern Canada. In a study of 15 weather stations in northern Canada and the Arctic, Hanesiak and Wang (2005) find the monthly blowing snow frequency to be as high as 12% in northern Mackenzie River Basin (MRB), though that frequency has been decreasing over the last four or five decades. In the northern hemisphere, Déry and Yau (1999) determine the average frequency of blowing snow events to be over 6% throughout the year. For the MRB, Déry and Yau (2007) found that the combined processes of surface and blowing snow sublimation deplete about 7% of the annual precipitation of the Basin.

As snow is carried in suspension it can undergo sublimation. The frequent occurrence of blowing snow suggests a potentially large transfer of moisture from the surface to the atmosphere. The removal of snow through sublimation can accelerate the melting of sea and lake ice and affect local humidity and temperature. A model of Pomeroy and Li (2000) predicts one half of transported snow is sublimated in the arctic regions. The Prairie Blowing Snow Model (PBSM) (Pomeroy et al. 1993) estimates sublimation losses between 44% and 73% of the annual snowfall. Using the Variable Infiltration Capacity model at Trail Valley Creek, Northwest Territories, Bowling et al. (2004) estimated blowing snow sublimation losses as

high as 60% of the annual snowfall. The PIEKTUK model (Déry et al. 1998) predicts a thermodynamic feedback, where the air becomes saturated with respect to ice, and the sublimation rate decreases. This yields sublimation rates up to 65% less than calculated by the PBSM.

A simple blowing snow sublimation parameterization has been developed (Gordon et al. 2006) based on the results of the PIEKTUK and PBSM models, and other parameterizations (Bintanja 1998; Pomeroy et al. 1991; Schmidt 1982). Gordon et al. test the parameterization using the Canadian Land Surface Scheme (CLASS) (Verseghy 1991) with data from three Canadian locations. In this chapter, this parameterization is applied to blowing snow sublimation at several sites in the MRB.

2 Data Locations

A blowing snow sublimation parameterization (Gordon et al. 2006) is used within the general framework of CLASS to estimate the amount of blowing snow sublimation at six locations, chosen to represent various parts of the MRB (Table 1). Data collected at these locations include hourly measurements of wind speed at a height of 10 m; temperature, relative humidity, and pressure at a height of 2 m; and daily observations of precipitation (amount and type) and snow depth.

The data sets contain a varying degree of missing data (Fig. 1). At Tuktoyaktuk where observations were made every six hours rather than hourly, the missing data is spread evenly throughout the year. For the other stations, the majority of the missing data is during the winter months, when the frequency of blowing snow events is highest. This introduces a bias in the calculations.

Table 1. List of stations in the Mackenzie River Basin (from north to south) used with blowing snow sublimation parameterization, with period of data and percentage of missing data

Climate ID	Station name	Start year	End year	Missing data [%]	Latitude [°N]	Longitude [°W]
2203912	Tuktoyaktuk	1958	2004	76.8	69.42	133.02
2202570	Inuvik	1960	2004	20.3	68.30	133.47
2202800	Norman Wells	1955	2004	6.5	65.27	126.80
2204100	Yellowknife	1955	2004	6.9	62.45	114.43
2202101	Fort Simpson	1963	2004	2.0	61.75	121.23
3062693	Fort McMurray	1955	2004	12.6	56.65	111.22

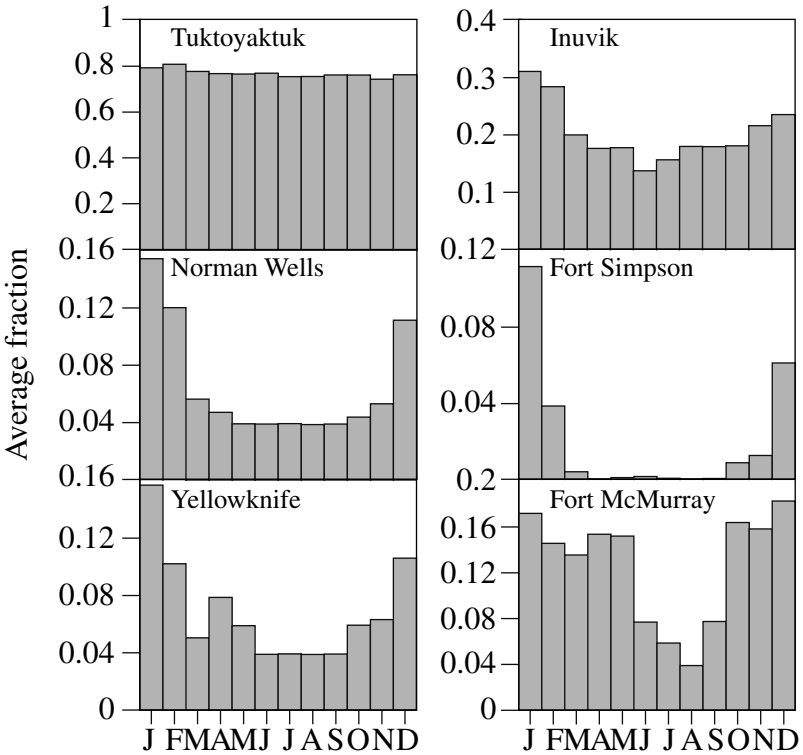

Fig. 1. Yearly frequency of missing data by month for each station

3 Methods

A threshold wind speed at which blowing snow occurs over flat homogeneous terrain without protruding vegetation is calculated as (Li and Pomeroy 1997)

$$U_t = U_{t*} + 0.0033\left(T_a - 245.88\right)^2 \tag{1}$$

where U_{t*} = 6.98 m s^{-1} is the minimum threshold wind speed and T_a (K) is the air temperature. The wind speed is at a height of 10 m and the temperature is at a height of 2 m. Using the criteria of Déry and Yau (1999), blowing snow is presumed to occur if the wind speed exceeds the threshold value, the temperature is below 0^{o}C, and there is snow on the ground. These criteria ignore physical properties of the snow pack, such as snow

ageing, wind hardening, or hardening due to melt and refreezing, which would decrease the amount of blowing snow and blowing snow sublimation. The effects of redistribution due to snow transport are also ignored. It is simply assumed that the net flux of blowing snow through the location is zero.

The parameterized blowing snow sublimation rate from Gordon et al. (2006) is

$$Q_s = A\left(T_o / T_a\right)^{\gamma} U_{t*} \rho_a q_{si} \left(1 - Rh_i\right)\left(U / U_{t*}\right)^{B}, \text{ for } U \geq U_t \tag{2}$$

where ρ_a is the air density and Rh_i is the relative humidity with respect to ice, both measured at a height of 2 m, q_{si} is the saturation specific humidity, and constants T_o = 273.14 K, A = 0.0018, B = 3.6, and γ = 4. For simplicity, the threshold wind speed U_t of Eq. (1) is used to determine when a blowing snow event occurs, while the minimum threshold wind speed U_{t*} is used in Eq. (2) to determine the blowing snow sublimation rate. Over a range of temperature, wind speed, and relative humidity, Eq. (2) predicts a sublimation rate up to an order of magnitude less than the predicted sublimation rate of PBSM (Pomeroy et al. 1993), up to two orders of magnitude greater than the predicted sublimation rate of Bintanja (1998), and generally equal to or greater than the predicted sublimation rate of PIEKTUK (Déry and Yau 2001). This parameterization has been tested using three land locations (Gordon et al. 2006), and two ice-surface locations (Gordon 2007).

During a blowing snow event, blowing snow sublimation is subtracted from the snow pack according to the parameterization of Eq. (4). If the air is supersaturated with respect to ice (Rh_i > 100%), a negative blowing snow sublimation rate results. In this case, the sublimation rate is set to zero. When the snow depth z_s is less than 0.1 m, a heterogeneous distribution of snow is assumed (after Verseghy 1991). The fraction of surface covered with snow, 0.1 m deep, is calculated as $f_s = z_s/0.1$, and the remaining grid square fraction ($1 - f_s$) is modeled as a grass surface. In this case, the blowing snow sublimation rate Q_s is reduced to $f_s Q_s$. If the total calculated sublimation exceeds the snow pack amount, the snow pack is removed.

4 Results

Table 2 lists the average temperature, wind speed at 10 m, and relative humidity for the six locations in the MRB. These values are not corrected

for the missing data bias shown in Fig. 1. Since a number of stations were missing more data in the winter months, the true average temperature at these locations would likely be slightly lower. As there is only a difference of a few percent, the bias is not corrected. Frozen precipitation is corrected according to Goodison et al. (1998). The yearly snow amount (mm SWE) shown in Table 2 is corrected for missing data, assuming that the average value for the missing data is equal to the average amount for the recorded data. However, it is not corrected for seasonal bias, and hence, may underestimate the actual average yearly snow amount.

Table 2. Average values of temperature (T), wind speed (U) at a height of 10 m, relative humidity with respect to water (Rh), yearly snow amount, maximum snow depth, estimated frequency of blowing snow (B.S.), and amount of blowing snow sublimation at six locations in the Mackenzie River Basin; and Goose Bay shown for comparison. Locations are listed with increasing wind speed

Station	T [°C]	U [m s^{-1}]	Rh [%]	Yearly snow [mm SWE]	Max. snow [m]	Freq. B.S. [%]	Freq. B.S. (T_a<0) [%]	B.S. subl. [mm SWE]	Frac.of snowfall [%]
Fort Simpson	2.5	2.5	73	145	0.63	0.9	1.8	0.7	0.5
Fort McMurray	1.1	2.7	70	119	0.41	0.2	0.6	0.5	0.4
Inuvik	7.5	2.8	71	146	0.65	1.0	1.6	1.5	1.0
Goose Bay	0.3	3.0	71	518	1.14	4.1	8.9	17.7	3.3
Norman Wells	4.7	3.2	69	138	0.61	4.0	7.3	11.2	8.1
Yellowknife	4.1	4.1	68	127	0.47	3.2	6.0	6.7	5.2
Tuktoyaktuk	9.0	4.6	80	74	0.38	8.6	13.3	4.8	6.4

The frequency of blowing snow is calculated for all locations according to the criteria listed in Section 3. The frequency is shown for each location in Table 2 as a percentage of all data, and as a percentage of data for T_a < 0°C. This gives an indication of the frequency of winds that could cause blowing snow, both throughout the year and during the cold season. The blowing snow sublimation parameterization is used to calculate the amount of blowing snow for each location, using the same criteria and steps described in Section 3, including the tile system based on recorded snow depth assuming a grass cover. The yearly average blowing snow sublimation amount is presented in Table 2. It is also expressed as a fraction of the total snowfall. Although some of the SWE amount is biased due to missing data in the winter, the fraction of total snowfall is not biased, as snowfall data are only used when other meteorological data are available.

Déry and Yau (2002) also calculated blowing snow amount using observations at four locations during 1993. They use the same criteria for a blowing snow event (Déry and Yau 1999), but calculate the blowing snow sublimation rate using a ten-term parameterization which is a best fit to the results of PIEKTUK over a range of wind speed, temperature, and relative humidity. Their results at Fort McMurray and Yellowknife are similar to the average amounts calculated in this study. However, the blowing snow sublimation amount calculated by Déry and Yau is 21% the average amount calculated in this study for Inuvik, and it is 27% the average amount calculated in this study for Norman Wells. This is due in part to lower average wind speeds during 1993 (2.4 m s^{-1} at Inuvik, and 2.6 m s^{-1} at Norman Wells). Déry and Yau (2007) present a range of snow budget results over the MRB based on ERA-40 reanalysis data for the period 1979–93 on a 2.5° latitude × 2.5° longitude grid. They estimate relatively low annual blowing snow sublimation rates (average value of 0.23 mm SWE) over the Basin, although there are higher values (2–10 mm SWE per year) in a narrow coastal zone. They state that "blowing snow sublimation reaches values of no more than a few mm per year SWE along the Arctic coastline and remains negligible throughout most of the basin". In contrast, they predict average surface sublimation rates (i.e., ablation from a non-mobile surface) as 28.54 mm SWE per year. As discussed in Section 3, the parameterization of Gordon et al. gives a generally higher sublimation rate than the parameterization of Déry and Yau, especially at high wind speeds and temperatures near 0°C. Also in relation to Déry and Yau (2007) we note that local winds at open, airport sites may well be higher than areal averages. The highly non-linear Eq. (2) will lead to low areally-averaged sublimation rate estimates from areally averaged winds.

5 Discussion

The study locations are divided into two categories according to average wind speed: light winds (less than 3 m s^{-1}) and moderate winds (between 3 and 5 m s^{-1}). According to the criteria of Déry and Yau, blowing snow occurs at the light wind locations (Inuvik, Fort Simpson, and Fort McMurray) for 1% or less of the year. At the moderate wind locations (Tuktoyaktuk, Normal Wells, and Yellowknife) blowing snow occurs between approximately 3 and 9% of the year. As a comparison, a winter study of blowing snow on the sea-ice in Franklin Bay (Savelyev et al. 2006) found an average wind speed of 5.3 m s^{-1}. The calculated frequency

of blowing snow at this location is 27%. However, this is only for the months of January though May, and is not representative of the entire year. The frequency of blowing snow events estimated using Déry and Yau's criteria (Eq. 4) is compared to observed frequency obtained by Hanesiak and Wang (2005) using climate records from the last four or five decades at several Arctic locations (Table 3). Also shown for comparison is the frequency of blowing snow at each location using the criteria of Szeto and Stewart (1997). These criteria require that there be more than 1 mm of snow on the ground, $T_a < -2.5^{o}$C, and $U > 9$ m s^{-1}. The observed frequencies of Hanesiak and Wang and the criteria of Szeto and Stewart are both based on the meteorological definition of blowing snow, which is a reduction in visibility to less than 9.7 km (6 miles) at a height of 2 m (Environment Canada 1990). However, the criteria used by Déry and Yau also include drifting snow, which occurs at heights of less than 2 m. Using measurements at Franklin Bay, Savelyev et al. (2006) demonstrate a relation between blowing snow particle number density and visibility. Using this relation, the authors find that visibility is less than 9.7 km for 27 % of the time, which is identical to the frequency of blowing snow calculated using the criteria of Déry and Yau. However, for the locations shown in Table 3, the observed frequency is significantly lower than the calculated frequency of Déry and Yau. The frequencies calculated by Szeto and Stewart are closer to observations, but still overestimate the observed frequencies for two of the four locations studied by Hanesiak and Wang. Changing the criteria for blowing snow to match observations would reduce the frequency of blowing snow events. This would result in a reduction of the total amount of modeled blowing snow sublimation.

Table 3. The frequency of blowing snow at each location, calculated using the criteria of Déry and Yau (1999), and Szeto and Stewart (1997), compared to the observed frequency of blowing snow (Hanesiak and Wang 2005)

Station	Déry and Yau	Szeto and Stewart	Hanesiak and Wang
Fort Simpson	0.9	0.2	0.4
Fort McMurray	0.2	0.03	n/a
Inuvik	1.0	0.2	0.6
Goose Bay	4.1	1.9	n/a
Norman Wells	4.0	1.6	1.2
Yellowknife	3.2	0.9	0.4
Tuktoyaktuk	8.6	4.1	n/a
Resolute	19.7	15.2	8.8
Av. of all stations	5.2	3.0	2.3

According to the categorization based on annual average wind speed, the light wind locations lose between 0.7 and 2.0 mm SWE to blowing snow sublimation. This only accounts for between 0.6 and 1.3% of the total snowfall each year. The snow pack at the moderate wind locations is reduced by between approximately 6 and 16 mm SWE due to blowing snow sublimation. This is between 7 and 12% of the annual snowfall. Although the average wind speeds are lower, more blowing snow is sublimated at Norman Wells compared to Yellowknife and Tuktoyaktuk. Tuktoyaktuk has a comparatively high average relative humidity, which reduces the amount of blowing snow sublimation. Normal Wells has larger blowing snow sublimation than Yellowknife because of a different distribution of wind speed that results in a higher frequency of blowing snow. For comparison, at the Franklin Bay location, the parameterization predicts that 4% of the snowfall is lost to blowing snow sublimation in the 120 day winter record. This relatively small amount is due to a high relative humidity (average of 75 % with respect to water) and very low temperatures (average of -26 ^{o}C) at Franklin Bay, compared to averages of 77 % and -21^{o}C at Tuktoyaktuk during the same 120 day period.

The parameterized blowing snow sublimation rate of Gordon et al. (2006) is based on the assumption of a homogeneous, flat terrain without protruding vegetation. At the more southern locations there may be trees and other tall vegetation. Hence, the amount of blowing snow sublimation reported will likely overestimate the true amount. The overestimation of blowing snow frequency compared to observations, also suggests that the blowing snow sublimation is overestimated. However, the bias of missing data during winter suggests that the blowing snow sublimation amount (but not the fraction of snowfall lost to blowing snow sublimation) is slightly underestimated. While the extent of these model errors is unclear, it is suggested that the blowing snow sublimation amounts reported here are representative of an upper limit of the blowing snow sublimation amount that actually occurs each year.

An uncertainty remains with respect to the mountainous part of the MRB. There, the wind speed has a high spatial variability, leading to significant redistribution of snow cover. While no estimates are made of blowing snow sublimation losses in these areas, one can speculate that redistribution will transfer snow from exposed high wind speed areas into valleys with lower wind speeds and that the overall average blowing snow sublimation rates may be low.

6 Conclusion

A parameterization of the sublimation of blowing snow (Gordon et al. 2006) is used to estimate the amount of blowing snow sublimation at six locations within the Mackenzie River Basin. These results demonstrate the potential for significant loss of the winter moisture budget in some areas of the Basin. For locations with light average yearly wind speeds (less than 3 m s^{-1}), the calculated frequency of blowing snow is 1% or less, and the fraction of annual snowfall lost to blowing snow sublimation is less than 1.5%. For moderate average yearly wind speeds (between 3 and 5 m s^{-1}), the frequency of blowing snow increases to between 3 and 9%, and the fraction of snowfall lost to blowing snow increases to between approximately 7 and 12%. The idealized conditions and airport weather station data used to determine the blowing snow sublimation rate, as well as comparisons of predicted blowing snow frequency to observed blowing snow frequency, suggest that the blowing snow sublimation amounts presented may be an overestimation. Further modifications to the blowing snow sublimation parameterization and the blowing snow criteria will attempt to improve these estimations.

Acknowledgements

Data used in this study were made available by Meteorological Service of Canada (MSC). Funding for this and related blowing snow work was provided by the Natural Sciences and Engineering Research Council of Canada (NSERC), and the Canadian Foundation for Climate and Atmospheric Sciences (CFCAS).

References

Bintanja R (1998) The contribution of snowdrift sublimation to the surface mass balance of Antarctica. Ann Glaciol 27:251–259

Bowling LC, Pomeroy JW, Lettenmaier DP (2004) Parameterization of blowing snow sublimation in a macroscale hydrology model. J Hydrometeorol 5:745–762

Déry S, Taylor PA, Xiao J (1998) The thermodynamic effects of sublimating, blowing snow in the atmospheric boundary layer. Bound-Lay Meteorol 89:251–283

Déry S, Yau MK (1999) A climatology of adverse winter-type weather events. J Geophys Res 104(D14):16657–16672

Déry S, Yau MK (2001) Simulation of blowing snow in the Canadian Arctic using a double-moment model. Bound-Lay Meteorol 99:297–316

Déry S, Yau MK (2002) Large-scale mass balance effects of blowing snow and surface sublimation. J Geophys Res 107(D23):4679, doi:10.1029/2001JD001251

Déry S, Yau MK (2007) Recent studies on the climatology and modeling of blowing snow in the Mackenzie River Basin. (Vol. I, this book)

Environment Canada (1990) Manual of surface weather observations (MANOBS). User's manual. (Available from Meteorological Services of Canada, 4905 Dufferin St, Downsview, ON M3H 574, Canada)

Goodison BE, Louie PYT, Yang D (1998) WMO solid precipitation measurement intercomparison, Final Report, WMO/TD-No 872, WMO, Geneva

Gordon M, Simon K, Taylor PA (2006) On snow depth predictions with the Canadian land surface scheme including a parameterization of blowing snow sublimation. Atmos Ocean 44:239–255

Gordon M (2007) Drifting and blowing snow: measurements and modelling. Ph.D. thesis, York University, Toronto, Canada

Hanesiak JM, Wang XLL (2005) Adverse-weather trends in the Canadian Arctic. J Climate 18:3140–3156

Li L, Pomeroy JW (1997) Probability of occurrence of blowing snow. J Geophys Res 102(D18):21955–21964

Pomeroy JW, Gray DM, Landine PG (1991) Modelling the transport and sublimation of blowing snow on the prairies. Proc 48th Eastern snow conference, pp 175–188

Pomeroy JW, Gray DM, Landine PG (1993) The prairie blowing snow model: characteristics, validation, operation. J Hydrol 144:165–192

Pomeroy JW, Li L (2000) Prairie and Arctic areal snow cover mass balance using a blowing snow model. J Geophys Res 105(D21):26619–26634

Savelyev SA, Gordon M, Hanesiak J, Papakyriakou T, Taylor PA (2006) Blowing snow studies in CASES (Canadian Arctic Shelf Exchange Study) 2004. Hydrol Process 20:817–827

Schmidt RA (1982) Vertical profiles of wind speed, snow concentration, and humidity in blowing snow. Bound-Lay Meteorol 23:223–246

Szeto KK, Stewart RE (1997) Cloud model simulations of surface weather elements associated with warm frontal regions of winter storms. Atmos Res 44:243–269

Verseghy DL (1991) CLASS – A Canadian land surface scheme for GCMs. I. Soil model. Int J Climatol 11:111–133

Chapter 16

Assessing Water and Energy Budgets for the Mackenzie River Basin

Kit K. Szeto, Hang Tran, Murray MacKay, Robert Crawford and Ronald E. Stewart

Abstract This study represents the first attempt at developing a comprehensive climatology of atmospheric and surface water and energy budgets for the Mackenzie River Basin (MRB), using various observed, remotely-sensed, reanalyzed, and modeled datasets. In particular, datasets included the National Centers for Environmental Prediction - Global Reanalysis 2 (NCEP-R2), the European Centre for Medium-Range Weather Forecasts 40-yr Global Reanalysis (ERA-40), the NCEP North American Regional Reanalysis (NARR) and the Canadian Meteorological Centre (CMC) operational regional analysis as well as results from the Canadian Regional Climate Model (CRCM) simulations. Apart from the development of state-of-the-art budget estimates for the MRB, the relative merits of current models, data assimilation systems, and global blended datasets in representing aspects of the water and energy cycle of this northern and data-sparse region were also assessed. The regional water budget for the Basin is closed within 10% of the observed runoff using the moisture flux convergence from ERA-40, NARR, CMC or CRCM. The sources and the levels of uncertainty in assessing the budgets are discussed. While the water closure is notably better than the previous assessments, magnitudes of the residuals in balancing the budgets are often comparable to the budget terms themselves, and the spreads of budget estimates from the different datasets are also typically large, suggesting a need for substantial improvements to the models and observations.

1 Introduction

The climate system of a region operates through the exchange of water and energy between the region and its environment and through the internal cycling and conversion of these quantities within the system. As such, a detailed quantitative specification of the water and energy fluxes and reservoirs in a region is an important first step in improving the characterization, understanding, and prediction of its climate. This is one of the major objectives for the GEWEX (Global Energy and Water Cycle Experiment)

Continental Scale Experiments (CSEs, see Fig. 6 in Woo et al. 2007) in undertaking the Water and Energy Budget Studies (WEBS) (Lawford et al. 2004; Roads et al. 2003).

WEBS in GEWEX differ from previous water and energy budget studies (e.g., Berbery et al. 1999; Roads et al. 2002; Trenberth et al. 2001) mainly in the use of various observational, assimilated, and model data to arrive at quasi-independent estimates of a more-or-less common set of variables that characterize the water and energy cycle of the respective CSE regions. In synthesizing the WEBS results we want to assess our ability to (1) observe basic climate variables, (2) simulate and assimilate those observations with current models, and (3) develop budgets from observations, models, and blended datasets such as reanalysis data. We also need to clarify levels of uncertainty in the budget components and their sources, and to recommend future research and data collection to address the problems.

To date, GCIP (GEWEX Continental-scale International Project; now known as GAPP or GEWEX Americas Prediction Project) in the United States and MAGS (Mackenzie GEWEX Study) in Canada have completed their WEBS (Roads et al. 2003; Szeto et al. 2007a) though less comprehensive studies that focused on particular aspects or specific components of the water and energy cycle have been conducted in several CSEs (e.g., Betts et al. 2003; Heise 1996; Morengo et al. 2006; Roads and Betts 2000; Strong et al. 2002; Xu and Haginoya 2001). This chapter presents a synopsis of the WEBS for the Mackenzie River Basin (MRB), including a description of the budget equations and datasets, an account of the budgets and discussion of the budget results.

2 Water and Energy Budget Equations

Many forms of the water and energy conservation equations can be used to describe water and energy balance in a climate system. In this study, we will limit the analysis to the two-dimensional (vertically-integrated) horizontal variations of key water and energy processes in the atmosphere–land surface subsystem and adopt the set of budget equations from Roads et al. (2002, 2003):

Atmospheric Water:

$$\frac{\partial Q}{\partial t} = E - P + MC + RESQ' \tag{1}$$

Surface Water:

$$\frac{\partial W}{\partial t} = P - E - N + RESW' \tag{2}$$

Atmospheric Temperature:

$$C_p \frac{\partial \{T\}}{\partial t} = QR + LP + SH + HC + REST' \tag{3}$$

Surface Temperature:

$$C_v \frac{\partial \{Ts\}}{\partial t} = QRS - LE - SH + RESG' \tag{4}$$

Definitions of the variables are given in the list of symbols and {} denotes vertical integrals over either the atmospheric column or soil column. Derivation of these equations and computational details of the convergence terms can be found in Roads et al. (2002, 2003). As in these reports, the water and energy fluxes are scaled appropriately to provide values in mm d^{-1} and K d^{-1}, respectively. It is convenient to combine the residual forcing with the tendency term (e.g., *RESQ = RESQ' - ∂Q/∂t*) in assessing the budget balance. This should have little effects on the values of the mean annual residuals since the long-term change in water and energy storages in the atmosphere and surface can be assumed to be negligible. Szeto et al. (2007a) provide further details of the budget calculations.

3 Datasets

A complete water and energy budget assessment for a region would require the evaluation of individual terms in Eqs. (2) to (4) over a range of spatial-temporal scales. In this first study, we restrict the analyses to basin-scale water and energy budgets on monthly and longer time intervals. A lack of extensive and detailed observations for the MRB necessitates heavy reliance on assimilated, modeled, and remotely-sensed datasets. As the quality of such datasets depends critically on the performance of the models or retrieval algorithms used in their development, it is essential to validate the derived budgets with available observations. To facilitate the intercomparison of budgets evaluated from the different datasets, analyses were performed over a five year period from June 1997 to May 2002

which is largely determined by the maximum overlap of availability period of the datasets (Tables 1 and 2).

Table 1. Summary of regional (R) and global (G) observations and remote-sensing data used in MAGS WEBS. The number of data points used in budget computations is given for each datasets

Parameter	Source	Resolution	Coverage period	Data points
Precipitable water	Rawinsondes (R)	sites	various–current	8
Precipitable water	GVAP/NVAP (G)	1 deg	1988–1999	294
Snow	SSMI (R)	25 km	1978–2003 (Dec.–Mar.)	3021
Surface air temperature	CANGRID (R)	50 km	1895–2003 Dec.	748
Atmospheric enthalpy	Rawinsondes (R)	sites	various–current	8
Precipitation	CANGRID (R)	50 km	1985–2003 Dec.	748
	CMAP (G)	2.5 deg	1979–2003 Sep.	44
	GPCP (G)	2.5 deg	1979–2003 Dec.	44
Discharge	WSC (R)	sites	1972–current (Arctic Red River)	1
Radiative fluxes	ISCCP FD (G)	280 km	1983 Jul.–2001 Jun.	24
Cloud amount	Surface obs. (R)	sites	various-current	7

Table 2. Summary of global (G) and regional (R) analysis and model datasets used in MAGS WEBS. Resolution of the operational CMC GEM model changed from 35 to 24 km in Sept. 1998. The number of data points used in budget computations is given for each datasets

Dataset	Resolution	Coverage period	Data points
CRCM (R)	51 km	1997 Apr.–2004 Dec.	736
CMC (R)	35/24 km	1997 Mar.–Current	1541/3259
NARR (R)	32 km	1979 Jan.–Current	1839
NCEP-R2 (G)	2.5 deg	1979 Jan.–Current	44
ERA-40 (G)	2.5 deg	1957 Sep.–2002 Aug.	44

3.1 Assimilated and Modeled Datasets

The global reanalysis datasets used in this study include the National Centers for Environmental Prediction – Global Reanalysis 2 (NCEP-R2) (Kanamitsu et al. 2002; Kistler et al. 2001) and the European Centre for Medium-Range Weather Forecasts 40-year Global Reanalysis (ERA-40) (Kållberg et al. 2004; Uppala et al. 2005;). Regional (re-)analysis data are obtained from both the NCEP North American Regional Reanalysis (NARR) (Mesinger et al. 2006) and the Canadian Meteorological Centre (CMC) Global Environmental Multiscale Model (GEM) operational analysis and forecast archive (Côté et al. 1998a, b). To assess the performance of modern climate models in simulating water and energy cycling in the region, results from a simulation of the Canadian Regional Climate Model (CRCM) (MacKay et al. 2007) are also used in this study. The simulation was performed in "climate mode" from April, 1997 and onward at a horizontal resolution of 51 km. Lateral boundary and initial (atmospheric) conditions are specified from the CMC GEM global analysis. Other aspects of the model and simulation can be found in MacKay et al. (2003, 2007).

3.2 Global Observations

The global datasets used in this study include satellite cloud and radiative products and blended satellite and in-situ or model global precipitation and water vapor datasets. Radiative fluxes are obtained from the International Satellite Cloud Climatology Project (ISCCP) (Rossow and Schiffer 1991) FD dataset (Zhang et al. 2004). For global blended precipitation datasets, both the GEWEX-sponsored Global Precipitation Climatology Project (GPCP) (Adler et al. 2003) and NCEP global precipitation climatology and NCEP Climate Prediction Center (CPC) Merged Analysis of Precipitation (CMAP) (Xie and Arkin 1997) datasets are employed in the study. The blended global water vapor climatology dataset from the NASA Water Vapor Project (NVAP) (Randel et al. 1996) is used to compare with estimates of vertically-integrated water vapor from other datasets.

3.3 Regional and In Situ Observations

Data from four regular rawinsonde sites within the MRB, and from four other sites nearby are used in the study. Launches are conducted every 12

hours. Also available are data from 10 principal surface synoptic and 43 automatic stations within the Basin. Hourly cloud fraction information for 7 sites is available since 1950. Streamflow is gauged at approximately 80 sites in the MRB by the Water Survey of Canada (WSC). The furthest downstream measurements, at Arctic Red River, are available on a daily time scale since 1973.

A gridded, monthly climate dataset of precipitation and screen temperature for Canada, known as CANGRID, is used for comparison with the model outputs. Briefly, this dataset is based on operational climate station data that have been homogenized and adjusted for all known measurement errors (Mekis and Hogg 1999; Vincent and Gullett 1999). Regional snow water equivalent (*SWE*) estimates derived from SSM/I passive microwave satellite data (Derksen et al. 2007) are used to compare against model and analyzed snowcover in the region.

4 Results and Discussions

4.1 The MRB Water and Energy Cycle

Like other major high-latitude continental basins, the MRB acts as a sink region for heat and water in the global climate system. During the boreal cold season (Nov.–Feb.) when the mean N–S global temperature contrast is strong and the atmosphere is dynamically active, a large amount of heat is transported into the MRB from the warm southern and oceanic regions (*HC* in Fig. 1a). As much of the basin receives little or no solar radiation during these months, there is a net radiation deficit at the surface (*QRS* in Fig. 1c) that chills the surface. Some of the heat transported into the Basin is lost to the cold underlying surface via sensible heat transfer (*SH* in Figs. 1a and 1c), thus cooling the lowest levels of the atmosphere. As a result, surface-based temperature inversions are created over much of the region (Cao et al. 2007), effectively decoupling the surface and the atmosphere and limiting their exchanges of heat and moisture (*E*, *LE*, and *SH* during the cold season in Figs. 1b and 1c). Because of the blocking effects of the Cordillera on the westerly moisture flux, net moisture flux convergence into the Basin is typically small throughout the year (*MC* in Fig. 1b). Winter precipitation (and the associated condensational heating *LP*) is relatively low and comes solely from synoptic systems that pass through or develop within the Basin. Consequently, the atmospheric heat convergence is largely balanced by thermal radiation loss to space (*QR* in Fig. 1a). As surface evaporation is extremely weak, winter precipitation is largely bal-

anced by the large-scale moisture flux convergence into the Basin. Winter precipitation comes almost exclusively as snowfall which accumulates with little melting so that much of the Basin is snow-covered by the end of winter. The effect is reflected in the negative *RESW* during the winter (Fig. 1d) when $RESW=RESW'-\partial W/\partial t$ is largely determined by the positive tendency term associated with the growing snow mass. Expectedly, runoff is extremely low under such conditions (Fig. 1d).

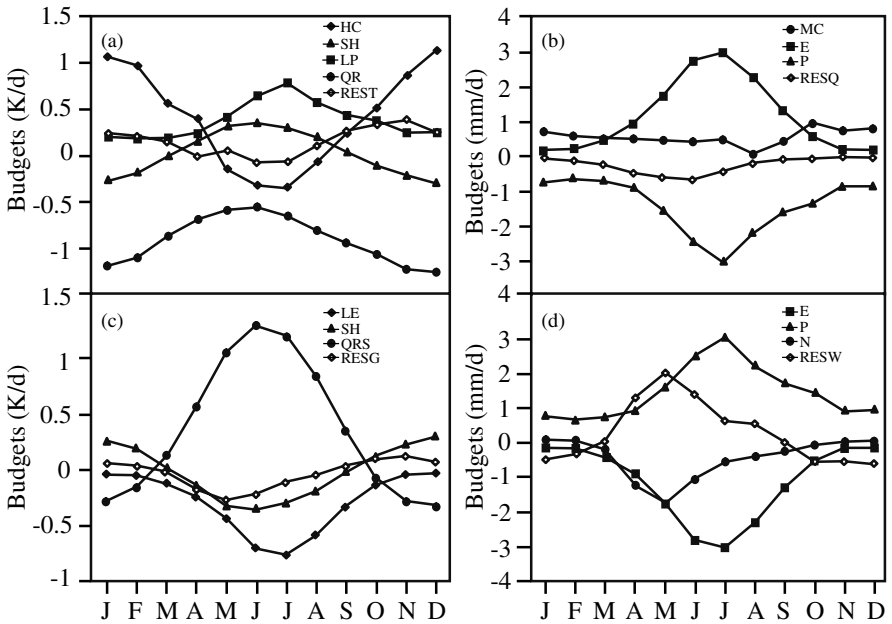

Fig. 1. Annual cycle of ensemble (NCEP-R2, ERA-40, NARR, CMC, and CRCM) mean basin-average budgets for (a) atmospheric energy, (b) atmospheric water, (c) surface energy, and (d) surface water. Note that NARR budgets are not included in calculations of HC and REST

Spring arrives with an increase in solar insolation (*QRS* in April–May, Fig. 1c) but much of the energy is used in snowmelt. The prevalence of frozen ground during this period limits meltwater infiltration (Pomeroy et al. 2007). Much of the meltwater stays on the ground or can only recharge the top soil layer, giving rise to surface saturation and generates substantial runoff (Woo and Rouse 2007). Long daylight hours in the summer are experienced in most parts of the Basin (*QRS* in Jun.–Aug., Fig. 1c). As most surfaces are covered with vegetation, wet soil, or surface water bodies, evaporation consumes much of the solar input and induces large latent heat

flux at the surface (*E* and *LE* in Jun.–Aug., Figs. 1b and c). A small portion of the solar radiation is used to warm the surface, which in turn warms the lower atmosphere via sensible heat transfer (*SH* in Figs. 1a and 1c). The surface sensible and latent heat fluxes destabilize the atmosphere and consequently, despite the northern location, a considerable portion (typically between a third and half of the total summer rainfall in the ERA-40 data) of the warm season precipitation comes from moisture convection. The large amounts of evaporation and precipitation and their strong phase coherence (Fig. 1b) show that moisture recycling plays an important role in governing the warm-season water cycle (Szeto 2002; Szeto et al. 2007c). Despite the rainfall contribution, summer runoff declines steadily after the spring snowmelt freshet (Woo and Thorne 2003). The Basin on the whole remains as a moisture sink despite large summer evaporation. Strong surface heat flux and condensation heating in the atmosphere (*SH* and *LP* in Fig. 1a) transform MRB into a heat source region (i.e., *HC* is negative) for the large-scale airflow.

Solar input decreases rapidly during the autumn months of September and October and the net basin surface radiation heating becomes negative in October. As the surface water and energy processes enter their dormant cold-season states, the atmospheric moisture and energy convergence into the Basin increases as the large-scale thermal and moisture gradients intensify. In particular, the moisture flux convergence reaches a maximum during October when the moisture contrast between MRB and the upstream region is enhanced and the synoptic processes again become active over the North Pacific.

4.2 Synopsis of Budget Assessment Results

Szeto and Crawford (2006) have compiled the budget results, and Szeto et al. (2007a) provide detailed discussions. The following sections assess the representativeness of the budgets, their variability due to usage of different datasets, and the self-consistency of the budget components within each dataset. Intercomparisons of current results with previous estimates will also be made. Because the evaluations of many budget terms are based on (re-)analysis data, it is convenient to discuss the results with reference to the degree by which the analysis variables are affected by observations. We adopt the convention used in describing the NCEP analysis variables (e.g., Kistler et al. 2001). Here, type-A variables are those that are strongly influenced by observations, type-B variables are those affected by both the

model performance and observations, and type-C variables are pure forecast variables with no correction from observations.

4.2.1 Representativeness of the Five-Year Study Period

Key basin-average budget parameters computed for the current (1997–2002) and longer-term (1979–99) periods are given in Table 3. Despite the occurrence of the record-breaking 1997–98 El Niño event, the 5- and 20-y climatologies remain similar. In particular, both the observed and modeled 5-y and 20-y mean precipitation show very little difference. The 5-y and 20-y mean basin evaporation also exhibit little difference for the ERA-40 data and a slight (5%) increase in the NCEP-R2 estimate. Both the WSC discharge measurements and the NCEP-R2 runoff show little difference between the periods, but the 5-y mean runoff from the ERA-40 reanalysis shows an 8% decrease when compared to the longer-term mean. Both the observed and analyzed surface air temperatures show that during the 5-y study period, the basin was 0.6–0.7°C warmer than during the previous 20 years, on average. In summary, the 5-y period chosen for the study, while exhibiting some abnormalities in its mean hydroclimatic state, can be considered representative of the longer-term climate in regard to many of the water and energy fluxes.

Table 3. Inter-comparison of 1979–99 (20y) and 1997–2002 (5y) climatologies of precipitation (*P*), evaporation (*E*), runoff (*N*), and screen temperature (*T2m*) for different datasets

	P [mm d^{-1}]		*E* [mm d^{-1}]		*N* [mm d^{-1}]		*T2m* [K]	
	20y	5y	20y	5y	20y	5y	20y	5y
CANGRID	1.28	1.23					269.4	270.1
WSC					-0.49	-0.49		
ERA-40	1.41	1.43	-0.99	-0.98	-0.52	-0.48	271.2	271.8
NCEP-R2	1.77	1.75	-1.67	-1.75	-1.01	-1.02	269.8	270.5

4.2.2 Water Storages

Although surface snow (*S*) and soil water content (*M*) are combined in evaluating the surface water budgets (Eq. 2), these two water storage variables will be discussed separately. While satellite data permit estimates of top-soil wetness (Leconte et al. 2007), regular in situ measurements of soil moisture are scarce. As such, *M* is typically a type-C variable in analysis datasets. Since the soil layer depths vary substantially among the different

models, the depth-to-bedrock information for the region from Soil Landscape of Canada (http://sis.agr.gc.ca/cansis/nsdb/slc/intro.html) was used to normalize the depth of the model soil layers in the calculation of their total soil moisture content. With this normalization, the range of annual basin-average M still varies from about 230 mm for CMC to about 324 mm for NCEP-R2. Due to the vast differences in the soil model configurations, it is more useful to inter-compare the spatial and temporal variability of M in the different models rather than their annual averages (some of these results can be found in Szeto and Crawford, 2006).

Compared to soil water, snow mass is much better observed in the Basin. Snow depth is measured routinely at various locations and there are also remote-sensing snowcover estimates from satellite (e.g., SSM/I). Although the same snow depth measurements are used by the forecast centers to derive snow water equivalent (*SWE*) information, the analysis procedure can vary substantially between the centers, and hence the large variability exhibited in their annual estimates for the region. The annual basin *SWE* varies with values less than 40 mm in the NCEP-R2 and NARR estimates to almost 50 mm in ERA-40 and exceeding 70 mm in the CRCM (Table 4). The high bias of *SWE* in the CRCM can be related to the cold bias in the model surface and lower troposphere during the cold season (Szeto et al. 2007a) which causes too early a start in snow accumulation and a delay in snowmelt. Since snow mass is a type-B variable while precipitation is a type-C variable in the analysis datasets considered here, the bias of *SWE* in each dataset usually does not correlate well with their corresponding cold season precipitation bias. For example, although the ERA-40 cold season precipitation is biased low, its *SWE* is biased high, while the reverse is true for *SWE* and precipitation from the CMC analysis.

The vertically-integrated atmospheric moisture content or precipitable water (Q) gives a measure of the storage of water in the atmosphere. Although Q is only a type-B analysis variable, the difference of annual Q among the various estimates is relatively small (Table 4). In particular, the Q from analyzed datasets agrees reasonably well with estimates from both the global NVAP (1988–99 climatology) and the regional rawinsonde datasets. The high bias of annual Q from the rawinsonde measurements can be related to the larger proportion of sites located in the warmer southern regions.

Although cloud amount is not one of the explicit variables in the budget equations and it typically only constitutes a small part of the atmospheric water storage, it is included in the assessment because of its critical role in affecting the water and energy cycle of the MRB (Hudak et al. 2007; Szeto et al. 2007b). Cloud amount is a type-C variable in the analysis datasets

Table 4. Summary of annual basin-average water and energy budgets for the MRB. All water storage terms (Q, M, SWE) are in mm, T2m in K, enthalpy H in 10^9 J km^{-2}, moisture fluxes (P, E, MC, N) in mm d^{-1}, energy fluxes in K d^{-1} and cloud fraction is given in percent. Global Q observation is the 1988–99 NVAP climatology and the two values of global precipitation are from CMAP (first) and GPCP (second), respectively. The coefficient of variation (CV, in %) is the ratio of the standard deviation to the absolute value of the mean estimate

Data\Para	Q	M	SWE	T2m	H	P	E	MC	N	HC	SH	RESQ	REST
NCEP	9.39	324.3	30.6	270.5	2.31	1.75	-1.75	0.69	-1.02	0.36	-0.27	-0.69	0.32
ERA-40	8.80	289.7	49.5	271.3	2.31	1.38	-0.99	0.46	-0.48	0.36	0.10	-0.33	0.23
NARR	9.43	301.1	23.0	271.2	2.15	1.23	-1.05	0.46	-0.48		0.13	-0.28	
CMC	8.97	229.2	37.2	270.3	2.32	1.34	-1.07	0.53	-0.27	0.33	0.10	-0.26	0.12
CRCM	9.30	261.3	71.0	267.5	2.32	1.39	-0.74	0.54	-0.66	0.52	0.05	0.12	-0.05
Reg Obs	10.00		34.2	270.3	2.39	1.28			-0.49				
Globl Obs	9.14					1.00/1.07							
Average	9.29	281.1	40.9	270.2	2.30	1.31	-1.12	0.53	-0.57	0.39	0.02	-0.29	0.16
Std Dev	0.39	36.8	17.1	1.4	0.03	0.23	0.38	0.09	0.26	0.09	0.16		
CV	4.2	13.1	41.8	0.5	1.3	17.6	33.9	17.0	45.6	23.1	800.0	89.7	87.5

Data \ Parameter	LP	QRS	QR	TOA SWD	TOA SWU	TOA LWU	BOA SWD	BOA LWU	BOA SWU	BOA LWD	Cloud cover	RESW	RESG
NCEP	0.33	0.37	-0.87	2.15	0.75	1.91	1.28	2.79	0.34	2.21	48.4	1.02	-0.18
ERA-40	0.27	0.39	-0.98	2.14	0.78	1.95	1.05	2.84	0.20	2.38	67.3	0.31	0.04
NARR	0.23	0.38	-0.86		0.76	1.82	1.26	2.84	0.38	2.34	56.1	0.30	0.06
CMC	0.25	0.37	-0.91	2.10	0.74	1.90	1.13	2.78	0.24	2.26	55.7	-0.27	0.01
CRCM	0.26	0.27	-0.89	2.10	0.93	1.79	1.04	2.62	0.26	2.11	60.3	-0.06	0.02
Reg Obs	0.24										65.0		
Globl Obs	0.19	0.39	-0.99	2.11	0.78	1.88	1.10	2.83	0.21	2.38	67.1		
Average	0.25	0.36	-0.92	2.12	0.78	1.88	1.14	2.78	0.27	2.28	60.0	0.26	-0.01
Std Dev	0.04	0.05	0.06	0.02	0.07	0.06	0.10	0.08	0.07	0.11	7.0	0.49	0.10
CV	16.0	13.9	6.5	0.9	9.0	3.2	8.8	2.9	25.9	4.8	11.7	188.5	1000.0

and it is also generally agreed to be one of the more poorly predicted variables in current models. Annual basin-average cloud cover is lowest in NCEP-R2 with mean basin-average below 50%, followed by both CMC and NARR with mean cloud coverage of 56% (Table 4). Annual estimates from the ERA-40, ISCCP, or the CRCM are all within 10% of the observed values of 65%, with the CRCM values biased to the low side, especially during the cold seasons.

4.2.3 Energy Storages

Although thermodynamic surface energy is given by C_vTs, the screen temperature (*T2m*) is discussed here instead of the surface temperature (*Ts*) because these two variables are very closely related. In addition, there are extensive observations for surface air temperatures but few measurements of *Ts*. Consequently, *T2m* is a type-B variable while *Ts* is type-C in the assimilated datasets. In terms of annual basin-average (Table 4), the CMC and NCEP-R2 *T2m* values are the closest to the CANGRID regional observations while the NARR and ERA-40 estimates showed moderate warm biases ($\leq$ 1 K). Note that the good agreement of the annual average of the estimates could be misleading because of compensating biases of different signs in different seasons. For example, NCEP-R2 showed relatively large warm (>3 K) bias during winter and weak (< 1K) cold bias during the rest of the year (Szeto et al. 2007a). Significant winter warm biases over the southern Basin, also noted in the longer-term surface budgets presented in Betts et al. (2003), are found in ERA-40 (Szeto et al. 2007a). Quite significant warm biases are found over the southeastern Basin in the NARR data during JJA. Strong cold biases are found in the CRCM data with the largest bias occurring in the fall and winter (>4K for SON) and less so during the summer (<1K). Szeto (2007) offers an explanation of this cold bias in the CRCM.

In a hydrostatically-balanced atmosphere, the vertical integral of its (mass-weighted) internal and potential energy is equal to its vertically-integrated C_pT (or equivalently, the atmospheric enthalpy or heat content, *H*). Since atmospheric temperature is well observed and it is a type-A variable in all analysis datasets, there is little difference in *H* among the various estimates (Table 4). It is of interest to note that the basin average *H* from the CRCM is very close to others despite the strong cold bias in its lower model troposphere. As in the annual *Q* estimates from rawinsonde measurements, high bias of the observed *H* is related to the larger number of southern rawinsonde sites used in the study (Szeto et al. 2007a). On the

other hand, the relatively low *H* estimate from NARR is due to the lack of archived temperature data at levels higher than 100 hPa.

4.2.4 Water Fluxes

As a high-latitude continental basin, the MRB is naturally a moisture sink region in the global water balance on the annual time scale, with large-scale moisture flux convergence (*MC*) playing a major role in producing the precipitation. For example, based on data from the 45 year ERA-40 archive, the correlation coefficient between daily basin-average *MC* and precipitation is about 0.7 and 0.5 during the month of July and January, respectively. *MC* estimates from all datasets exhibit a similarly weak seasonal variation, with maximum convergence occurring in October and minimum in August (Fig. 2a). Both NCEP-R2 and the CRCM have a high bias of net moisture flux convergence during the cold season which probably indicates an under-prediction of topographic precipitation over the coastal regions in the two datasets when compared to CMC, NARR, and ERA-40. Despite large evaporation, MRB as a whole remains a moisture sink during the summer in most datasets. Exceptions are found in the CRCM and NARR budgets, both of which suggest that the Basin becomes a moisture source for the large-scale circulation in August (Fig. 2a).

The annual *MC* is highest in NCEP-R2 (0.69 mm d^{-1}) and lowest in ERA-40 and NARR (0.46 mm d^{-1}). Previous estimates of annual *MC* by Walsh et al. (1994) (0.67 mm d^{-1}), Roads et al. (2002) (0.67 mm d^{-1} estimated by using the same NCEP-R2 data but for 1988–99), and Strong et al. (2002) (0.73 mm d^{-1}) are all closer to the NCEP estimate. It is arguable that *MC* estimates from the CMC, NARR, and ERA-40 analyses might be closer to the "truth" because of (1) the higher resolutions and generally more sophisticated model physics employed in these models, and (2) the differences between their *MC* estimates and the observed discharge are the smallest. Although the annual *MC* estimated from NARR and the CRCM are close to those from the CMC and ERA-40, it is actually a result of compensating relative biases during different seasons (relative high bias in the cold season and low bias in the summer, Fig. 2a).

Precipitation (*P*) and evapotranspiration (*E*) are the two processes that couple the atmospheric and surface branches of the water cycle. Despite the relatively abundant observations for precipitation, it is a type-C variable in most of the analysis datasets used in this study. NARR is the only exception which assimilates precipitation observations in its analysis by using observed precipitation to constrain its atmospheric latent heating.

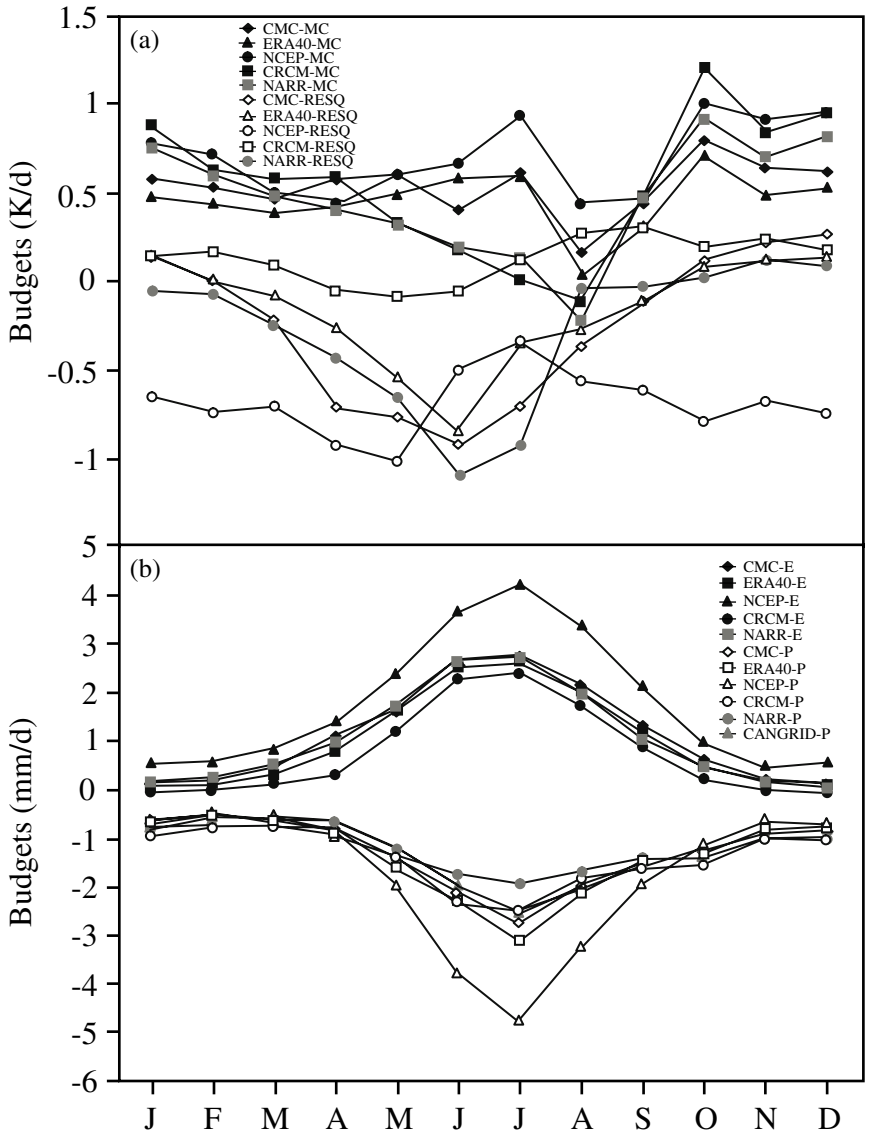

Fig. 2. Annual cycle of MRB atmospheric water budgets for NCEP-R2, ERA-40, NARR, CMC, and CRCM: (a) MC and RESQ, (b) P and E. Also included in (b) is the P from the CANGRID dataset

While differences are expected among the various estimates, the precipitation estimated from different datasets, except the NCEP-R2 and the global blended datasets, agrees relatively well in terms of their monthly and an-

nual means (Table 4 and Fig. 2b). The NCEP-R2 precipitation is substantially higher while both the CMAP and GPCP global blended precipitation are considerably lower than those from the other datasets. The high bias in the NCEP *P* occurs mainly in the summer (Fig. 2b) when most precipitation is of convective origin. Neglecting the global satellite and NCEP estimates, the mean annual precipitation for the Basin ranges from 449 mm (NARR) to 507 mm (CRCM), which are much larger than the values given in Stewart et al. (1998) (~410 mm) or Louie et al. (2002) (~421 mm). Discussions on the spatial-temporal variability of *P* and their related processes are presented in Szeto et al. (2007a, b, and c).

E is generally poorly observed and is purely a forecast variable in the analysis datasets. It is weak during DJF, with a basin-average that varies from ~0.1 mm d^{-1} in ERA-40 and CMC to about 0.5 mm d^{-1} for NCEP-R2. A surface sublimation rate of 29 mm y^{-1} estimated by Déry and Yau (2007) for the MRB is comparable to the ERA-40 value of ~33 mm y^{-1} (totaled between Oct. and Mar.). The CRCM differs from others in that it is characterized by general weak surface condensation during the winter that only occurs over the extreme northern basin in the other datasets. This enhanced deposition in the CRCM during the cold season might be a contributing factor to the high *SWE* bias in the CRCM previously noted. The relative low (high) biases that characterize *E* in the CRCM (NCEP-R2) prevail throughout all seasons and they consequently give the lowest (highest) values for the annual *E* estimate. Previous estimate of *E* for the MRB conducted by Louie et al. (2002) using the empirical model of Morton (1983) yielded an annual basin-average *E* of about 0.76 mm d^{-1} which is comparable to the CRCM value but substantially lower than the others.

Runoff (*N*) is an important component in the surface water budget. In the CMC analysis, runoff is simply computed as *P–E*. In other models used in this study, *N* is only crudely simulated even though sophisticated surface modules are included in the CRCM, NCEP-R2, NARR, and the ERA-40 models. In the cold region, most river flow follows a nival regime in which spring melt generates high flows that are orders of magnitude larger than the winter discharge (Woo et al. 2007). All datasets (except CMC) exhibit such a runoff pattern to some degree (Fig. 3), but none of them replicates faithfully the phase and magnitude of the observed discharge. Such discrepancies with measured discharge are expected because of the large basin size and the absence of streamflow routing in the models. Both the annual and peak runoff in NARR and ERA-40 are comparable to the observed streamflow; yet similar to the findings of Betts et al. (2003), maximum runoff in ERA-40 occurs two months earlier than the observed peak and a month before those produced in the other model datasets. Early run-

off in ERA-40 can be related to its cold season warm biases, hence early snowmelt over the southern Basin. Both the peak and annual model runoff from the CRCM is higher than the observed, as expected from the high bias in its model snowcover (Table 4). Although NCEP-R2 exhibits low bias in its snowcover, its spring and summer runoff is the highest among the estimates due to a significant over-prediction of warm-season precipitation.

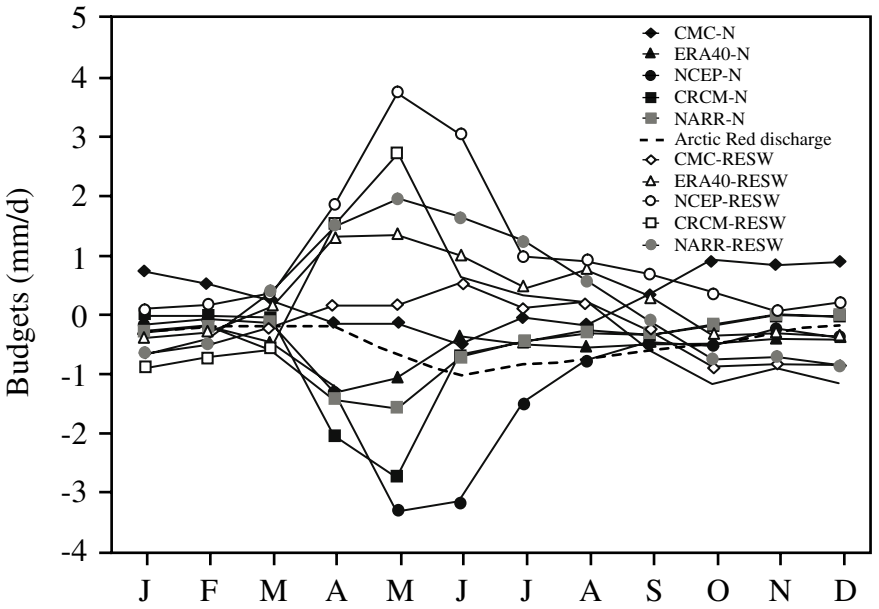

Fig. 3. Annual cycle of MRB surface water budgets for NCEP-R2, ERA-40, NARR, CMC, and CRCM: N and RESW. Also shown is the mean discharge from the Mackenzie River at Arctic Red for the same period. Corresponding P and E budgets are given in Fig. 2b

If surface water storage change is negligible over the study period then Eq. (2) implies $E \sim P–N$. Applying the observed discharge and CANGRID precipitation (Table 4) to the relationship yields an annual basin-average E of about 0.8 mm d^{-1}. Hence, on the annual and basin-scales, the E estimate from CRCM might be closer to the "truth" than those from the analysis datasets.

4.2.5 Energy Fluxes

In contrast to the *MC*, the dry static energy convergence (*HC*) into the Basin is characterized by strong seasonal variations in all datasets (Fig. 4a). As expected, *HC* is strongest during the winter when the pole-to-equator and continental–oceanic temperature contrasts are the greatest. Estimates of *HC* from all datasets suggest that the Basin is a heat source for the summer circulation (i.e., $HC<0$). The annual basin-average *HC* agrees reasonably well among the analysis datasets (within 0.03 K d^{-1} or 10% of each other, Table 4), though the CRCM result is biased high among the estimates, mainly between May and November when the CRCM depicts the Basin as a much weaker heat source region than indicated by the other models). The current estimates of *HC* are lower than the 0.51 K d^{-1} estimated by Roads et al. (2002) for 1988–99 using the same NCEP-R2 dataset, suggesting a possible recent decrease in the mean convergence of dry static energy into the Basin.

Sensible heat (*SH*) is heat energy transferred between the surface and air. Not being part of routine observations, it is a pure forecast variable in all the assimilated datasets. All datasets agree that there is downward transfer of sensible heat into the surface during the cold season when the surface is substantially colder than the overlying air (Fig. 4b). While the magnitude of the basin-average cold-season *SH* is similar among the CMC, NARR, ERA-40, and CRCM results, the NCEP-R2 SH is substantially larger than the others. For the basin as a whole, upward (positive) sensible heat flux occurs between March and September for all datasets except NCEP-R2, which exhibits negative basin-average *SH* apart from the months of June and July. The weaker upward *SH* in the CRCM during the spring is consistent with its low bias in *Ts* and high bias in *SWE*. The lower than average *SH* in the NCEP-R2 analysis is reflected in its negative annual *SH* while all four other annual estimates are positive (Table 4).

Radiative transfer plays a critical role in affecting water and energy balance in the MRB due to its strong coupling to other hydrometeorological processes. With very few ground-based measurements, most information on radiative fluxes comes from either satellite measurements or model data (Guo et al. 2007). Although radiative fluxes are type-C variables in the analyses, the variability among their estimates (e.g., measured by using the coefficient of variation CV = the ratio of standard deviation to sample mean of the estimates) is typically smaller than those for other flux variables (Table 4) and much of the revealed variability can be related to the variability of cloud cover in the different datasets.

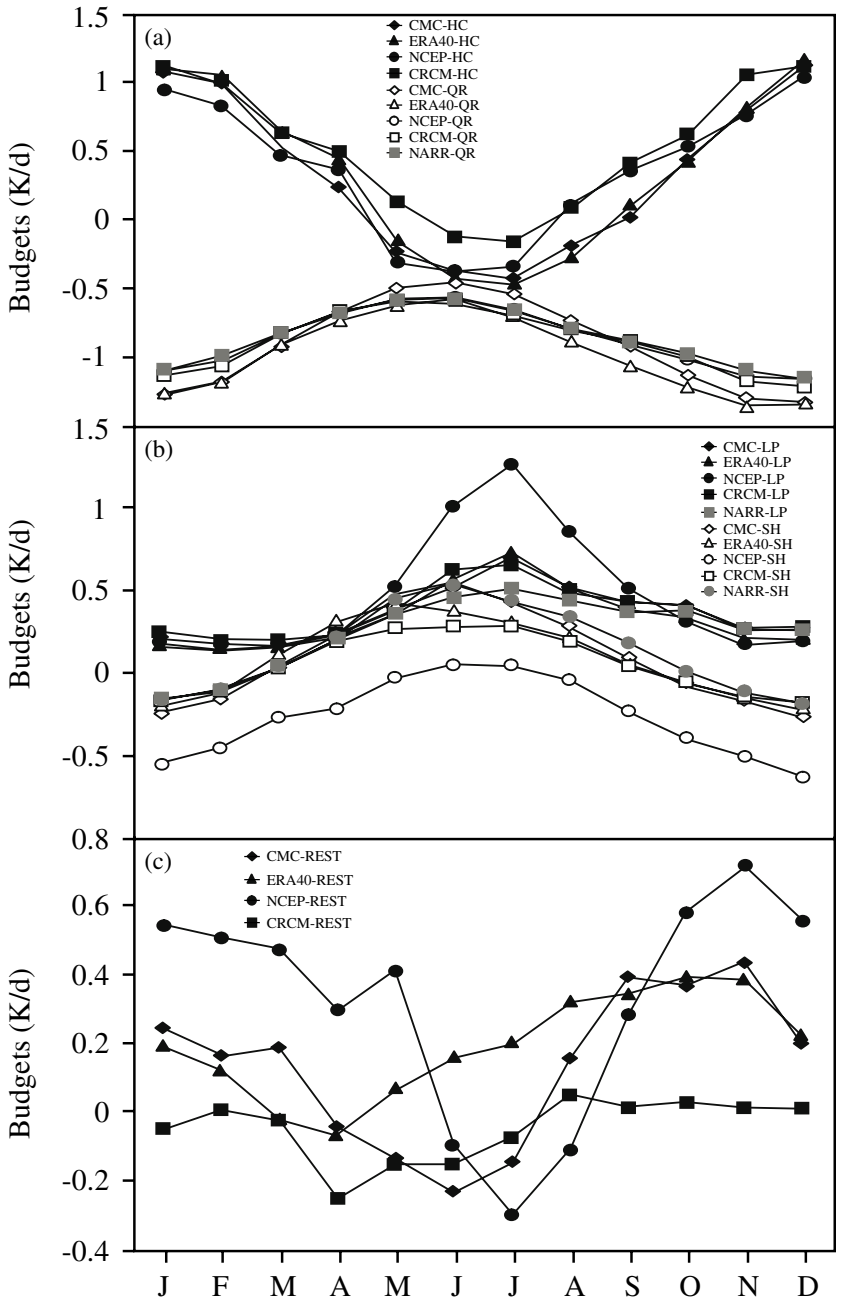

Fig. 4. Annual cycle of MRB atmospheric energy budgets for NCEP-R2, ERA-40, NARR, CMC, and CRCM: (a) HC and QR, (b) LP and SH, and (c) REST

Radiative transfer plays a critical role in affecting water and energy balance in the MRB due to its strong coupling to other hydrometeorological processes. With very few ground-based measurements, most information on radiative fluxes comes from either satellite measurements or model data (Guo et al. 2007). Although radiative fluxes are type-C variables in the analyses, the variability among their estimates (e.g., measured by using the coefficient of variation CV = the ratio of standard deviation to sample mean of the estimates) is typically smaller than those for other flux variables (Table 4) and much of the revealed variability can be related to the variability of cloud cover in the different datasets.

Although all models use fairly standard values in specifying top-of-the-atmosphere (TOA) incoming shortwave radiation (TOA_*SWD*), they produce substantially different estimates of the shortwave radiation that reaches the surface (BOA_*SWD*) (Table 4). In particular, the high bias of BOA_*SWD* in the NCEP-R2 and NARR data can be related to the lower model cloud cover in these datasets. The high surface upward shortwave flux (BOA_*SWU*) in NCEP-R2 and NARR can be related directly to their high BOA_*SWD* despite their lower than average *SWE* (hence lower than average mean surface albedo during the spring). Top-of-the-atmosphere *SWU* (TOA_*SWU*), however, is highest in the CRCM, likely a result of the enhanced mean TOA albedo from the above average cloud cover and more extensive and longer duration of snowcover in the model.

Relatively lower variability is found in the estimates for both the BOA and TOA longwave fluxes. Both the downward and upward longwave fluxes at the surface, as well as the outgoing longwave flux at TOA (TOA_*LWU*) from the CRCM are slightly lower than others, presumably a result of the cold bias in its model surface and lower-atmosphere. On the other hand, the slightly above average BOA longwave fluxes in NARR and ERA-40 can be related to the warm bias identified for these datasets.

Although all the datasets exhibit similar seasonal variability of net atmospheric radiative cooling *QR* and surface radiative heating *QRS* (Figs. 4a and 5a), there is substantial seasonal dependence in their relative biases. In particular, *QR* is strongest in ERA-40 and weakest in CMC during the summer; and weaker in the RCM, NARR, and NCEP-R2 during the cold season. For basin-average *QRS*, surface cooling (heating) is the strongest in NCEP-R2 during the winter (summer), presumably also related to the reduced cloudiness in the model. Annual *QRS* is the lowest in the CRCM, mainly as a result of the lower than average *QRS* simulated in the model during the warm season, particularly between May and September (Fig. 5a). Further discussion of cloud-radiative feedbacks in the MRB can be

found in Szeto et al. (2007b), and Guo et al. (2007) provided detailed validation of radiation budgets in the CRCM using satellite measurements.

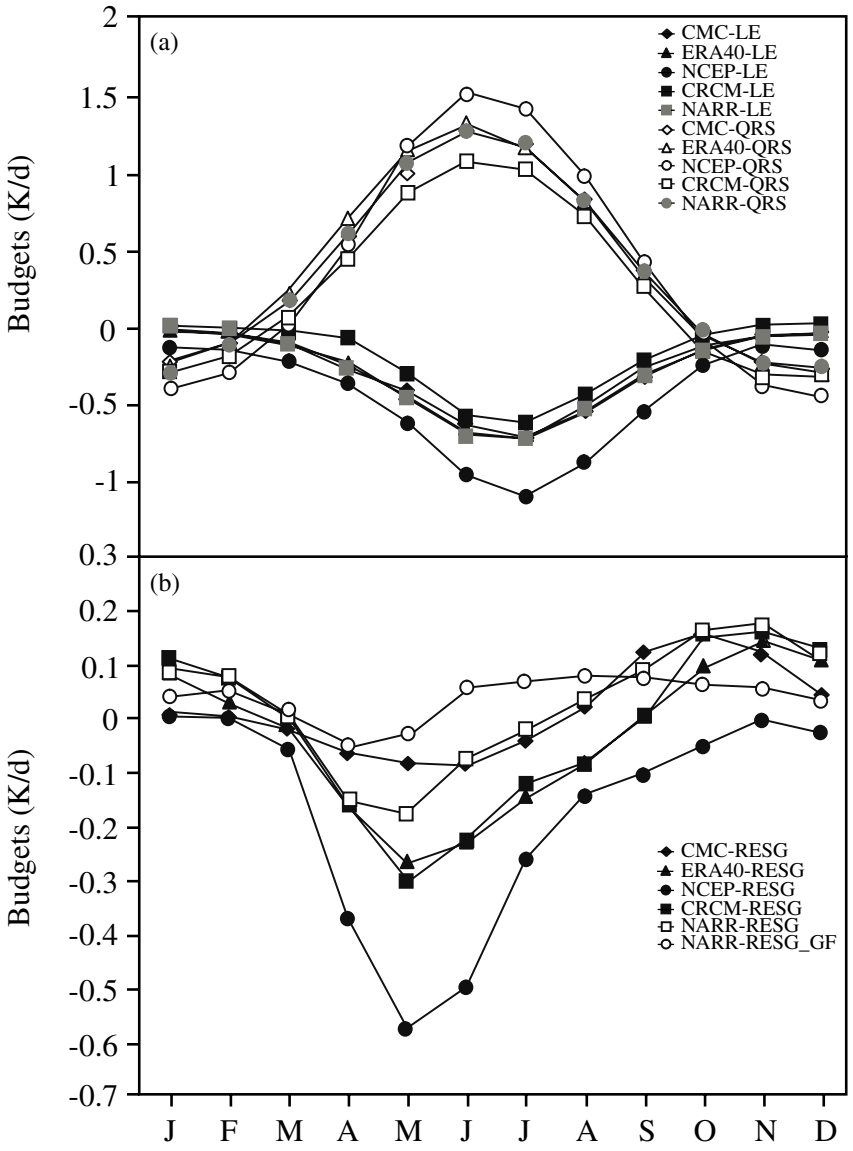

Fig. 5. Annual cycle of MRB surface energy budgets for NCEP-R2, ERA-40, NARR, CMC, and CRCM: (a) LE and QRS and (b) RESG. Also included in (b) is the NARR budget residual when ground heat flux is included in its surface energy budget (NARR-RESG_GF)

4.3 Budget Closure and Error Analysis

Completeness and accuracy of the water and energy information can be assessed through comparing the budget estimates with available observations and examining the degree to which the budgets can be closed at various spatial-temporal scales. WEBS parameters derived from strongly "corrected" variables in the analysis datasets (e.g., atmospheric enthalpy, screen temperatures, and precipitable water) compare best to the observed values. Among the forecasted fluxes that can be compared against observations, precipitation has a better match with observations than does annual runoff. When no measurement is available for validation of the modeled fluxes, the spread of the budget estimates from different datasets will indicate the uncertainties in their evaluations. In this regard, parameters derived from strongly-correlated analysis variables show less variability than that of the purely forecasted flux variables (e.g., in evapotranspiration, runoff, and sensible heat flux), with the exceptions being precipitation and radiative fluxes.

Precipitation in the MRB is the end result of many strongly-coupled hydrometeorological processes. The fact that precipitation, including its spatial and temporal (at least on monthly and longer time scales) variability, can be simulated successfully in many models is a good indicator that these processes are well represented in the models. On the other hand, wide discrepancies between modeled and observed snowcover and runoff suggest that the cold region surface and runoff processes in the models should be much improved.

The residuals in the closure of the budgets provide a convenient indication of how well the budgets are balanced. Ideally, the purely-modeled water and energy budgets from a single model should be perfectly balance; but budget imbalance can result from non-conservative numerical schemes employed in the model or from errors introduced in off-line computations using archived model outputs. The budget residuals for the CRCM are in general smaller than those for the analysis datasets. Larger residuals related to the analysis datasets are due to the nudging of the forecast variables with observations during an analysis cycle and the neglect or misrepresentation of important processes in modeling the water and energy cycles. The residuals for the annual atmospheric water budgets (*RESQ*) range from ~50% of the assessed MC (for CRCM) to >50% for CMC and 100% for NCEP-R2; and for the atmospheric energy budgets, the residuals (REST) generally reach magnitudes comparable to the budget terms themselves. Residuals are usually smaller in the surface budget balances. This suggests that much of the inaccuracy in closing the atmospheric budgets

may be due to numerical errors introduced through data interpolation from model grids to the archiving grids, and are then propagated into the computation of the convergence terms. In this regard, it is encouraging that most of the off-line *MC* estimates compare favorably with the NARR MC calculated in-line with the model computation, in either their mean values or seasonal variability (Table 4 and Fig. 2a).

There are characteristic seasonal dependencies in the residuals that vary among the datasets (Figs. 2a, 3, 4c, and 5c). A general atmospheric energy deficit is shown in the models ($REST > 0$) when compared to observations during the cool and cold seasons (see Szeto 2007 for a discussion on possible causes). In addition, strong atmospheric moisture surplus ($RESQ < 0$) is found in CMC, NARR, and ERA-40 during the warm season and in NCEP-R2 throughout the year (Fig. 2a). Part of the seasonal variations of *RESW* (Fig. 3) can be accounted for by the seasonal accumulation and melting of surface snow in the models, and deficits in predicted total surface water during snowmelt period have been noted in the NCEP-R2 (Roads et al. 202) and ERA-40 budgets (Betts et al. 2003), the latter being related to the warm bias and early modeled melt.

Assuming negligible long-term changes in the atmospheric and surface water storage (i.e., $MC \sim P–E \sim N$), water budget closure is traditionally assessed by the balance between the average atmospheric moisture flux convergence and observed runoff. With this definition, the regional water budget for the MRB is closed within 6, 8 and 10 % of the observed runoff using the moisture flux convergence from ERA-40/NARR, CMC, and CRCM, respectively. These are better than the closure of ~26% obtained with the previous generation CMC analysis dataset (Strong et al. 2002), possibly reflecting the recent advances in the modeling of atmospheric water cycling processes for the region. However, the absolute magnitude of the residuals is still large and further improvement in the current models is needed to significantly enhance the water and energy budget assessments for the MRB.

5 Concluding Remarks

As a first attempt at developing a comprehensive assessment of water and energy budgets for the MRB, this study also evaluates the capability of current models and data assimilation systems in simulating aspects of the water and energy cycle of this northern and data-sparse region. Although the CRCM simulation was performed in ”climate mode”, it simulated suc-

cessfully the climate for the MRB when compared with observations and analysis data. All of its budget biases can be partially attributed to the strong cold bias in its low-level tropospheric temperatures, especially during the cold season. Despite considerable differences in model resolutions and physics employed in the different data assimilation systems, the water and energy budgets derived from these datasets for the MRB are similar and compare well with the available observations. It is noted, however, that NARR under-predicts summer orographic rainfall even this system assimilates observed precipitation into its analysis. The NCEP-R2 reanalysis, used in many previous hydrometeorologic studies of the MRB, yields the largest deviation from the ensemble mean budgets. In general, it compares poorly with available observations and presents a significantly more intense warm-season water cycle than the other datasets. These findings suggest that NCEP-R2 fluxes should be used with caution for hydrometeorologic and climate change studies for the Basin.

This study quantifies the merits and deficiencies of global satellite or blended datasets in representing the water and energy budgets for northern and mountainous environments such as the MRB. The results show that (1) the annual basin average precipitable water estimates from the NVAP dataset compare extremely well with those estimated from the analysis datasets, (2) both the CMAP and GPCP precipitation exhibit low biases which worsen during the summer, and (3) the ISCCP FD radiative fluxes compare closely with estimates from other datasets, notably the ERA-40.

The regional water budget for the MRB is closed within 6, 8 and 10 % of the observed runoff by using the moisture flux convergence from ERA-40/NARR, CMC, and CRCM, respectively. While the performance is notably better than those of the previous studies, the magnitudes of the residuals are often as large as the budget terms and this points to the need for further improvement to the models and observations in order to improve the closure of the water and energy budgets for this northern region.

The climate of the MRB is governed by complex interactions among the atmospheric and surface features and processes that occur over a wide range of spatial-temporal scales. A number of these processes are not represented (e.g., organic soil processes and fluxes from the northern lakes), or are only crudely represented (e.g., ground frost processes, orographic precipitation, and sublimation from canopy-top) in current climate models. These limitations will negatively affect the model simulation of the various components of the water and energy budgets. Knowledge on these processes gained through MAGS and their future incorporation into numerical models will certainly enhance our predictive capability for northern basins. Results from this study will serve as a reference climatology to gauge the

progress in budget estimates using improved models and newly available remotely sensed data.

Acknowledgments

K.K. Szeto acknowledges insightful discussions with John Roads and his comments on an early version of the manuscript. Alex Wong, Patrick Lui, Niranchala Nithyanandan and Billy Szeto are acknowledged for their assistance in the WEBS calculations, data gathering and processing. This study was supported by Environment Canada and funded by the Panel on Energy Research and Development (PERD).

References

Adler RF, Huffman GJ, Chang A, Ferraro R, Xie P-P, Janowiak J, Rudolf B, Schneider U, Curtis S, Bolvin D, Gruber A, Susskind J, Arkin P, Nelkin E (2003) The version-2 Global Precipitation Climatology Project (GPCP) monthly precipitation analysis (1979–present). J Hydrometeorol 4:1147–1167

Berbery EH, Mitchell K, Benjamin S, Smirnova T, Ritchie H, Hogue R, Radeva E (1999) Assessment of land surface energy budgets from regional and global models. J Geophys Res 104(D16):19329–19348

Betts AK, Ball JH, Viterbo P (2003) Evaluation of the ERA-40 surface water budget and surface temperature for the Mackenzie River Basin . J Hydrometeorol 4:1194–1211

Cao Z, Stewart RE, Hogg WD (2007) Extreme winter warming over the Mackenzie Basin: observations and causes. (Vol. I, this book)

Côté J, Desmarais J-G, Gravel S, Méthot A, Patoine A, Roch M, Staniforth A (1998b) The operational CMC-MRB global environmental multiscale (GEM) model: Part II – Results. Mon Weather Rev 126:1397–1418

Côté J, Gravel S, Méthot A, Patoine A, Roch M, Staniforth A (1998a) The operational CMC-MRB global environmental multiscale (GEM) model: Part I – design considerations and formulation. Mon Weather Rev 126:1373–1395

Derksen C, Walker A, Toose P (2007) Estimating snow water equivalent in northern regions from satellite passive microwave data. (Vol. I, this book)

Déry SJ, Yau MK (2007) Recent studies on the climatology and modeling of blowing snow in the Mackenzie River Basin (Vol. I, this book)

Guo S, Leighton HG, Feng J, MacKay M (2007) Comparison of solar radiation budgets in the Mackenzie River Basin from satellite observations and a regional climate model. (Vol. I, this book)

Heise E (1996) An investigation of water and energy budgets for the BALTEX region based on short-range numerical weather predictions. Tellus 48A:693–707

Hudak D, Stewart R, Rodriguez P, Kochtubajda B (2007) On the cloud and precipitating systems over the Mackenzie Basin (Vol. I, this book)

Kållberg P, Simmons A, Uppala S, Fuentes M (2004) The ERA-40 archive. ERA-40 project report series 17

Kanamitsu M, Ebisuzaki W, Woollen J, Yang S-K, Hnilo JJ, Fiorino M, Potter GL (2002) NCEP–DOE AMIP-II reanalysis (R-2). B Am Meteorol Soc 83:1631–1643

Kistler R, Kalnay E, Collins W, Saha S, White G, Woollen J, Chelliah M, Ebisuzaki W, Kanamitsu M, Kousky V, van den Dool H, Jenne R, Fiorino M (2001) The NCEP-NCAR 50-year reanalysis: monthly means CD-ROM and documentation. B Am Meteorol Soc 82:247–267

Lawford R, Stewart R, Roads J, Isemer H-J, Manton M, Marengo J, Yasunari T, Benedict S, Koike T, Williams S (2004) Advancing global- and continental-scale hydrometeorology: contributions of GEWEX Hydrometeorology Panel. B Am Meteorol Soc 85:1917–1930

Leconte R, Temimi M, Chaouch N, Brissette F, Toussaint T (2007) On the use of satellite passive microwave data for estimating surface soil wetness in the Mackenzie River Basin. (Vol. II, this book)

Louie PYT, Hogg WD, MacKay MD, Zhang X, Hopkinson RF (2002) The water balance climatology of the Mackenzie Basin with reference to the 1994/95 water year. Atmos Ocean 40:159–180

MacKay M, Barlett P, Chan E, Verseghy D, Soulis ED, Seglenieks FR (2007) The MAGS regional climate modeling system: CRCM-MAGS. (Vol. I, this book)

MacKay MD, Seglenieks F, Verseghy D, Soulis ED, Snelgrove KR, Walker A, Szeto K (2003) Modeling Mackenzie Basin surface water balance during CAGES with the Canadian Regional Climate Model. J Hydrometeorol 4:748–767

Mekis E, Hogg WD (1999) Rehabilitation and analysis of Canadian daily precipitation time series. Atmos Ocean 37:53–85

Mesinger F, DiMego G, Kalnay E, Mitchell K, Shafran PC, Ebisuzaki W, Jovic D, Woollen J, Rogers E, Berbery EH, Ek MB, Fan Y, Grumbine R, Higgins W, Li H, Lin G, Manikin G, Parrish D, Shi W (2006) North American regional reanalysis. B Am Meteorol Soc 87:343–360

Morengo J, Alves LM, Camargo H (2006) Assessments of water and energy budgets in the Amazon Basin. GEWEX news 16(2):10–11

Morton FI (1983) Areal estimates of evapotranspiration and their significance to the science and practice of hydrology. J Hydrol 66:1–76

Pomeroy JW, Gray DM, Marsh P (2007) Studies on snow redistribution by wind and forest, snow-covered area depletion, and frozen soil infiltration in northern and western Canada. (Vol. II, this book)

Randel DL, Vonder Haar TH, Ringerud MA, Stephens GL, Greenwald TJ, Combs CL (1996) A new global water vapor dataset. B Am Meteorol Soc 77:1233–1246

Roads J, Kanamitsu M, Stewart RE (2002) Continental-scale experiment water and energy budgets in the NCEP-DOE reanalysis II. J Hydrometeorol 3:227–248

Roads JO, Lawford R, Bainto E, Berbery E, Chen S, Fekete B, Gallo K, Grundstein A, Higgins W, Kanamitsu M, Krajewski W, Lakshmi V, Leathers D, Lettenmaier D, Luo L, Maurer E, Meyers T, Miller D, Mitchell K, Mote T, Pinker R, Reichler T, Robinson D, Robock A, Smith J, Srinivasan G, Verdin K, Vinnikov K, Vonder Haar T, Vörösmarty C, Williams S, Yarosh E (2003) GCIP Water and Energy Budget Synthesis (WEBS). J Geophys Res 108:doi:10.1029/2002JD002583

Roads J, Betts A (2000) NCEP–NCAR and ECMWF reanalysis surface water and energy budgets for the Mississippi River Basin. J Hydrometeorol 1:88–94

Rossow WB, Schiffer RA (1991) ISCCP cloud data products. B Am Meteorol Soc 72:2–20

Stewart RE, Leighton HG, Marsh P, Moore GWK, Ritchie H, Rouse WR, Soulis ED, Strong GS, Crawford RW, Kochtubajda B (1998) The Mackenzie GEWEX Study: the water and energy cycles of a major North American River basin. B Am Meteorol Soc 79:2665–2683

Strong GS, Proctor B, Wang M, Soulis ED, Smith CD, Seglenieks F, Snelgrove K (2002) Closing the Mackenzie Basin water balance, wateryears 1994–95 through 1996–97. Atmos Ocean 40:113–124

Szeto KK (2002) Moisture recycling over the Mackenzie Basin. Atmos Ocean 40:181–197

Szeto KK (2007) Cold-season temperature variability in the Mackenzie Basin. (Vol. I, this book)

Szeto KK, Crawford R (2006) The MAGS WEBS CD-ROM. Available from K. Szeto (kit.szeto@ec.gc.ca) or B. Crawford (Robert.crawford@ec.gc.ca)

Szeto KK, Tran H, MacKay M, Crawford R, Stewart RE (2007a) The MAGS water and energy budget study. J Hydrometeorol (in press)

Szeto KK, Stewart RE, Yau MK, Gyakum J (2007b) The Mackenzie climate system: a synthesis of MAGS atmospheric research. (Vol. I, this book)

Szeto KK, Liu J, Wong A (2007c) Precipitation recycling in the Mackenzie and three other major river basins. (Vol. I, this book).

Trenberth KE, Caron JM, Stepaniak DP (2001) The atmospheric energy budget and implications for surface fluxes and ocean heat transports. Clim Dynam 17:259–276

Uppala SM, Kållberg PW, Simmons AJ, Andrae U, da Costa Bechtold V, Fiorino M, Gibson JK, Haseler J, Hernandez A, Kelly GA, Li X, Onogi K, Saarinen S, Sokka N, Allan RP, Andersson E, Arpe K, Balmaseda MA, Beljaars ACM, van de Berg L, Bidlot J, Bormann N, Caires S, Chevallier F, Dethof A, Dragosavac M, Fisher M, Fuentes M, Hagemann S, Hólm E, Hoskins BJ, Isaksen L, Janssen PAEM, Jenne R, McNally AP, Mahfouf J-F, Morcrette J-J, Rayner

NA, Saunders RW, Simon P, Sterl A, Trenberth KE, Untch A, Vasiljevic D, Viterbo P, Woollen J (2005) The ERA-40 reanalysis. Q J Roy Meteor Soc 131:2961–3012

Vincent LA, Gullett DW (1999) Canadian historical and homogeneous temperature datasets for climate change analyses. Int J Climatol 19:1375–1388

Walsh JE, Zhou X, Serreze MC (1994) Atmospheric contribution to hydrologic variations in the Arctic. Atmos Ocean 32:733–755

Woo MK, Rouse WR (2007) MAGS contribution to hydrologic and surface process research. (Vol. II, this book)

Woo MK, Rouse WR, Stewart RE, Stone JMR (2007) The Mackenzie GEWEX Study: a contribution to cold region atmospheric and hydrologic sciences. (Vol. I, this book)

Woo MK, Thorne R (2003) Streamflow in the Mackenzie Basin, Canada. Arctic 56:328–340

Xie P, Arkin P (1997) Global precipitation: a 17-year monthly analysis based on gauge observations, satellite estimates, and numerical model outputs. B Am Meteorol Soc 78:2539–2558

Xu J, Haginoya S (2001) An estimation of heat and water balances in the Tibetan plateau. J Meteorol Soc Jpn 79:485–504

Zhang Y-C, Rossow WB, Lacis AA, Mishchenko MI, Oinas V (2004) Calculation of radiative fluxes from the surface to top-of-atmosphere based on ISCCP and other global datasets: refinements of the radiative transfer model and the input data. J Geophys Res 109:doi 10.1029/2003JD004457 (1-27+1-25)

List of symbols

BOA	bottom of atmosphere
Cp	heat capacity at constant pressure for dry air
Cv	heat capacity of the surface
E	evapotranspiration
H	atmospheric enthalpy
HC	dry static energy convergence
LE	surface latent heat flux
LP	latent heat of condensation
LWD	long-wave (down)
LWU	long-wave (up)
M	soil moisture (liquid + frozen), vertically-integrated over soil column
MC	moisture flux convergence
N	runoff
P	precipitation
Q	atmospheric precipitable water
QR	atmospheric radiative heating
QRS	surface radiative heating
RESG'	surface residual temperature forcing
RESQ'	atmospheric residual water forcing
REST'	atmospheric residual temperature forcing
RESW'	surface residual water forcing
RESG	*RESG'* minus surface residual temperature tendency
RESQ	*RESQ'* minus atmospheric residual water tendency
REST	*REST'* minus atmospheric residual temperature tendency
RESW	*RESW'* minus surface residual water tendency
S	snow mass
SH	surface sensible heat flux
SWD	short-wave (down)
SWE	snow water equivalent
SWU	short-wave (up)
T	atmospheric temperature
Ts	surface temperature
T2m	air temperature at 2m above surface
TOA	top of atmosphere
W	total surface water (M+S)

Chapter 17

Characteristics of the Moisture Flux Convergence over the Mackenzie River Basin for the 1990–2000 Water-years

Mark Schuster

Abstract Moisture flux convergence into the Mackenzie River Basin was examined for the 1990–2000 period using the National Centers for Environmental Prediction (NCEP) reanalysis data, and the European Center for Medium-Range Weather Forecasting (ERA-40) data. Moisture flux convergence was calculated along with other moisture terms for each water-year, as well as the vertical profile of moisture flux convergence. There was significant yearly variation in the amount of convergence over the Basin, with the 1994–95 water-year being among the lowest. The level of largest moisture flux convergence was usually at 700 hPa; but for some years, the maximum was at 850 hPa, which implies an overall greater moisture flux convergence. The 1994–95 water-year was studied in detail as it was the year of record low discharge for the Mackenzie River. It had the second smallest yearly moisture flux convergence value according to the NCEP data, with the highest flux convergence at 700 hPa. Results from this study were in general agreement with those of two previous studies by Liu et al. and by and Strong et al.

1 Introduction

One goal of the Mackenzie Global Energy and Water Cycle Experiment (GEWEX) Study (MAGS) is to gain knowledge on the transport of water vapor into and out of the Mackenzie River Basin (MRB). Previous investigations have focused on the moisture budget of the MRB for various water years (defined as the period October to September) including 1994–95 (Liu et al. 2002), and 1994–95 to 1996–97 (Strong et al. 2002). The objective of this study is to examine moisture flux convergence (MFC) into the MRB for each water-year during the 1990–2000 period and compare results to the previous studies. A detailed analysis of the 1994–95 water-year was conducted as this was a year of record-low discharge for the Mackenzie River that merits a thorough study. Comparisons were made between the MFC of this and the other water-years. Differences between the results obtained using two sets of reanalysis data were also addressed.

2 Method and Data

The basic water balance equation for a column is

$$\partial W / \partial t + \nabla \cdot \overline{Q} = E - P \tag{1}$$

where W is the vertically integrated water content per unit area, E is evapotranspiration, P is precipitation, ∇ is the horizontal divergence operator and $\overline{Q}$ is the vertically integrated moisture flux given by

$$\overline{Q} = -\frac{1}{g}\int_{psurf}^{ptop} q\overline{V}\,dp \tag{2}$$

where q is the specific humidity in kg kg^{-1}, g is the gravitational constant of 9.8 m s^{-2}, dp is the change in pressure, and $\overline{V}$ is the horizontal wind vector

$$\overline{V} = u\bar{i} + v\bar{j} \tag{3}$$

with u and v being the eastward and northward wind components respectively. The horizontal divergence of the moisture flux is the variable of interest in this study.

Two sets of data are used in the analysis: the National Centers for Environmental Prediction (NCEP) reanalysis data, and the European Centre for Medium-Range Weather Forecasting (ECMWF) data. The NCEP pressure level data were obtained twice daily, at 00 and 12Z. Only four of the many available atmospheric variables are used, including the specific humidity q, u and v winds, and the surface pressure *psurf*. The variables u, v, and q are located on a 144x73 horizontal grid with a resolution of 2.5 x 2.5 degrees of latitude by longitude, and on 8 levels in the vertical: 1000, 925, 850, 700, 600, 500, 400 and 300 hPa. Water vapor above the 300 hPa level is negligible, and thus all levels above this are ignored. Surface pressure *psurf* is also available on the 144 x 73 horizontal grid. The ECMWF-40 (ERA-40) data are available on the same grid and at the same levels in the vertical. As no surface pressure is available from this dataset, the surface pressure values from the NCEP data was applied in conjunction with the ERA-40 data.

Two methods were used to calculate MFC, and both yielded consistent results. Their difference lies in the ordering of integration. The results from integrating first in the vertical are presented in this chapter. Computa-

tion of MFC into the entire MRB requires the evaluation of the $\nabla \cdot \overline{Q}$ term using Gauss' Divergence theorem, given by

$$\iint \nabla \cdot \overline{Q} dS = \oint \overline{Q} \cdot \overline{n} dl \tag{4}$$

where $\overline{n}$ is a unit vector normal to the domain boundaries and *dl* is the length of the line segment. The right side is an integral performed around the entire domain of the MRB. The boundary chosen for the MRB is quite coarse, at a grid spacing of 2.5° x 2.5°, but this produces a boundary identical to that used by Liu et al. (2002). Particular attention has to be paid when choosing the boundary, especially in the mountainous area in the southwest. Evaluating the right hand side of Eq. (4) around the chosen boundary of the MRB and then dividing by the area of the Basin will give the desired result.

The complex terrain of the MRB, especially in the mountainous southwest (Woo et al. 2007), presents a problem to performing the vertical integrals around the Basin, as the surface pressure does not necessarily correspond to 1000 hPa, which is the lowest pressure level available in the datasets. Some 1000 hPa points along the boundary of the MRB actually lie below ground level. Thus, $q\overline{V}$ values were linearly interpolated to the surface pressure before performing the vertical integration. Note that mm is usually the preferred unit for MFC, but cm is used here to be consistent with Liu et al. (2002).

3.1 The Period 1990–2000

During the 10-year study period, the total annual MFC exhibits considerable interannual variability (Table 1). Convergence values obtained using NCEP data ranged from a low of 14.3 cm (1997–98) to a high of 25.7 cm (1995–96), with a 10-year average value of 22.7 cm; while using ERA-40 data, the corresponding values were 6.5 cm (1997–98) and 23.2 cm (1995–96), with a 10-year average of 17.6 cm. The 1994–95 water-year had the second lowest reading of 14.6 cm with the NCEP data and the fifth lowest reading of 15.6 cm with the ERA-40 data. Both datasets showed similar trends throughout the period, though the NCEP data consistently produced larger values for MFC. There did not appear to be any pattern to the MFC from year to year, as peak values occurred in various months. The monthly $\partial W / \partial t$ term was very small, ranging between ± 1.0 cm month^{-1}. Given

that the $\partial W / \partial t$ term is small, *P-E* should closely follow the MFC. Figure 1 shows the monthly variation of the terms in Eq. (1).

Table 1. Yearly moisture flux convergence into the MRB using NCEP and ERA-40 data

	Moisture flux convergence [cm]	
Water-year	NCEP	ERA-40
1990–91	21.4	19.2
1991–92	24.6	17.2
1992–93	16.4	11.6
1993–94	17.7	13.3
1994–95	14.6	15.6
1995–96	25.7	23.2
1996–97	25.5	20.8
1997–98	14.3	6.5
1998–99	19.4	13.8
1999–2000	22.7	17.6
Average	20.2	15.9

The vertical profile of the net moisture flux was investigated by calculating the amount of moisture entering the MRB at several pressure levels on a monthly basis. At the upper pressure levels, the amount of moisture entering above the Basin becomes expectedly smaller as there is less moisture higher in the atmosphere. On the other hand, the topography of the MRB is very complex and parts of the Basin frequently have a surface pressure that is less than 1000 hPa. Figure 2 provides an example of the average surface pressure distribution for the 1994–95 water-year, indicating low pressures on the mountainous southwestern side of the Basin. Thus, the 1000 hPa level will make very little contribution, as it will lie below the surface along most of the boundary. The 925 hPa level is the most interesting: along the mountains in the southwest, surface pressures are often lower than 925 hPa but on the eastern side of the Basin, this is not necessarily so. Since moisture advection tends to go from west to east, very little moisture can enter MRB at 925 hPa on the western side as this level is likely underground. However, much moisture at 925 hPa can be advected out through the eastern boundary and therefore the MFC at this level is a large negative quantity (i.e., moisture flux divergence).

Figure 3 shows that during the ten-year period, the 700 hPa level was most often the level of most significant MFC using the NCEP data. In some years, the greatest contributing level was at 850 hPa, and these were the years of larger MFC. This makes sense intuitively since there is less

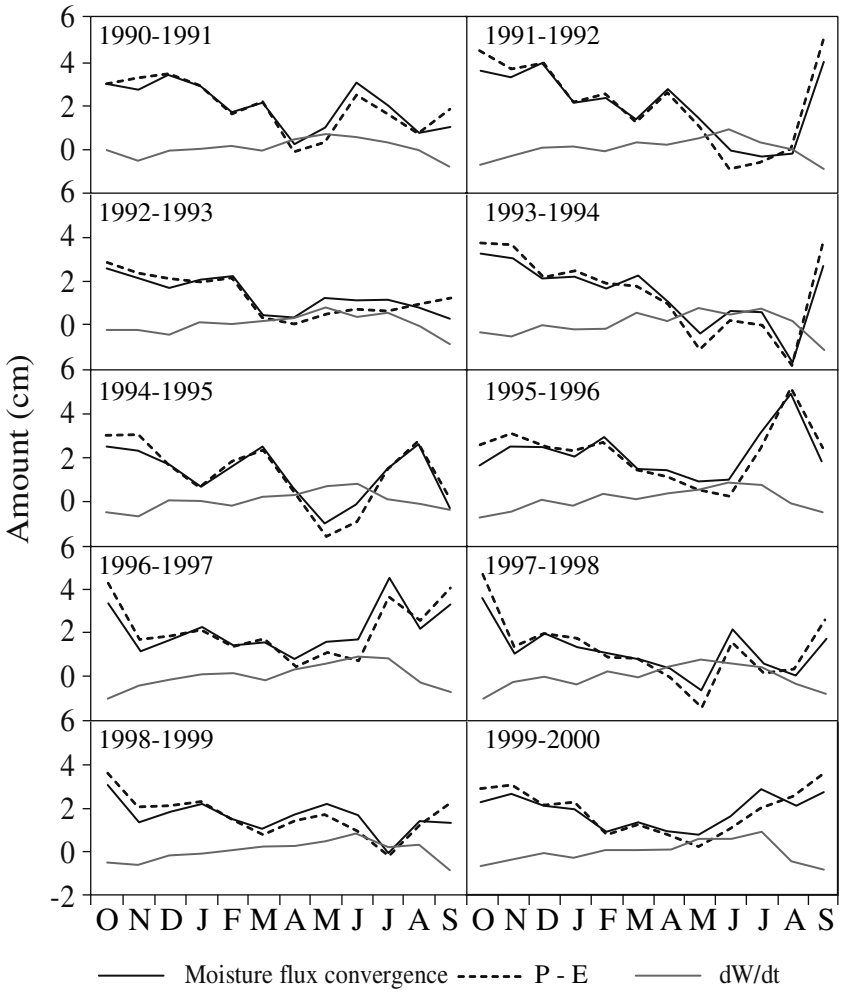

Fig. 1. Time series of $\partial W / \partial t$, $P - E$, and moisture flux convergence into the Mackenzie River Basin (MRB)

moisture higher up in the atmosphere. Thus, having the 850 hPa level as the greatest contributing level would mean a larger MFC than if it were at 700 hPa, assuming that the wind fields are identical. However, using the ERA-40 data yielded a very different MFC at the 850 hPa level, with much lower convergence values than obtained with the NCEP data. For all other levels, the ERA-40 data agree quite well with the NCEP data. Due to the low values at 850 hPa, 700 hPa was always the level of greatest contribution of MFC for the ten-year period. Low values at 850 hPa also explains

why the monthly MFC calculated with this dataset was always lower than that obtained using NCEP data.

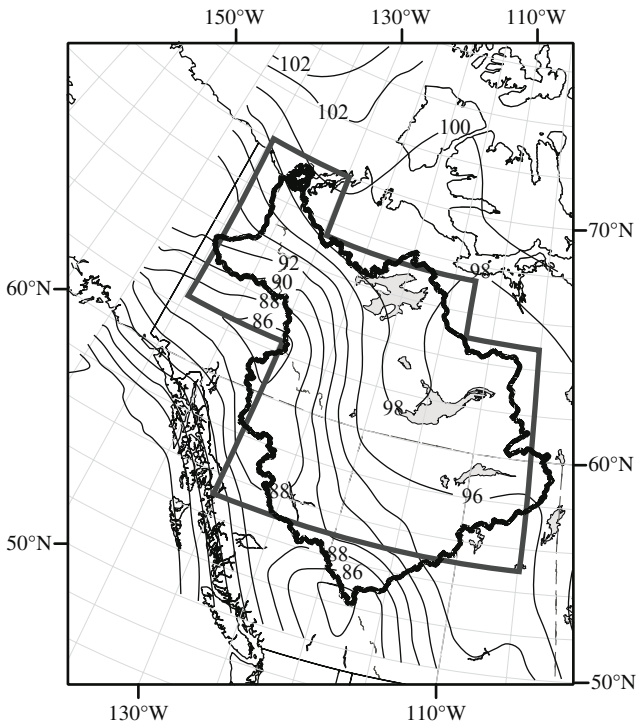

Fig. 2. Average surface pressure (Pa) over the MRB for the 1994–95 water-year. Heavy solid line depicts the MRB boundary used in this study

3.2 The 1994–95 Water-year

The Mackenzie River experienced its record low discharge in the 1994–95 water-year which stands out also as one with a very low MFC during the 10-year study period. The moisture flux convergence was positive in all months except May, June, and September, while the $\partial W / \partial t$ term was near zero for most months (Fig. 1). This latter term was calculated as the difference in W value between consecutive months. Due to its small value, $P - E$ closely followed the MFC. The water content W decreased in October–November 1994 and this combined with a positive MFC suggests that precipitation exceeded evaporation (Eq. 1). In the next several months, the water content stayed relatively constant. The water content increased in the

spring and due to the very low MFC (in some cases negative), such an increase is attributed to evaporation over the Basin, as implied from Eq. (1). Starting in July, the water content was relatively constant, and the MFC became larger, suggesting that precipitation was exceeding evaporation.

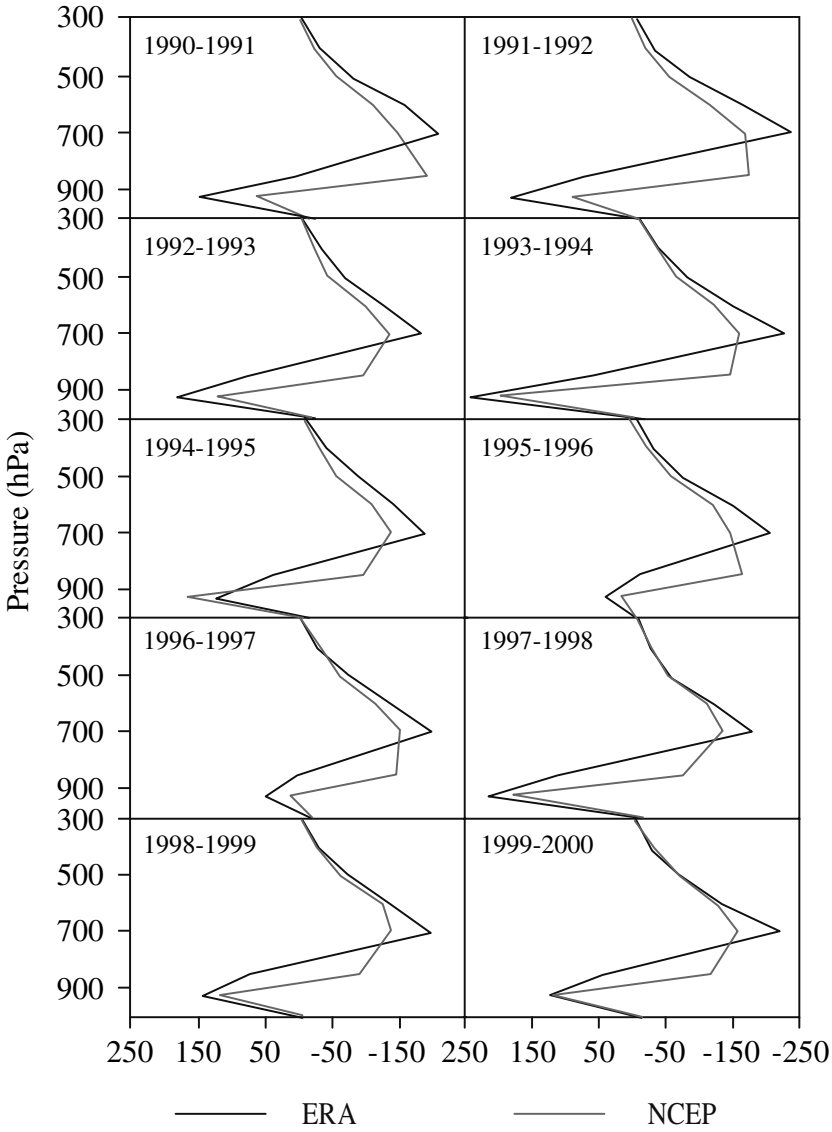

Fig. 3. Vertical structure of moisture flux convergence into the MRB, averaged for 1990–2000 (x-axis values in 10^8 kg Pa^{-1})

The vertical structure for the 1994–95 water-year was calculated for each month using the NCEP data (Fig. 4). The 700 hPa level was the level of greatest MFC for most months, while some months had 850 hPa as the greatest contributing level (e.g., during the summer months with larger MFC over the MRB). May was the month with the least MFC and its greatest contributing level was 600 hPa. Nearly every month had negative convergence values at 925 hPa, for reasons given in Sect. 3.1.

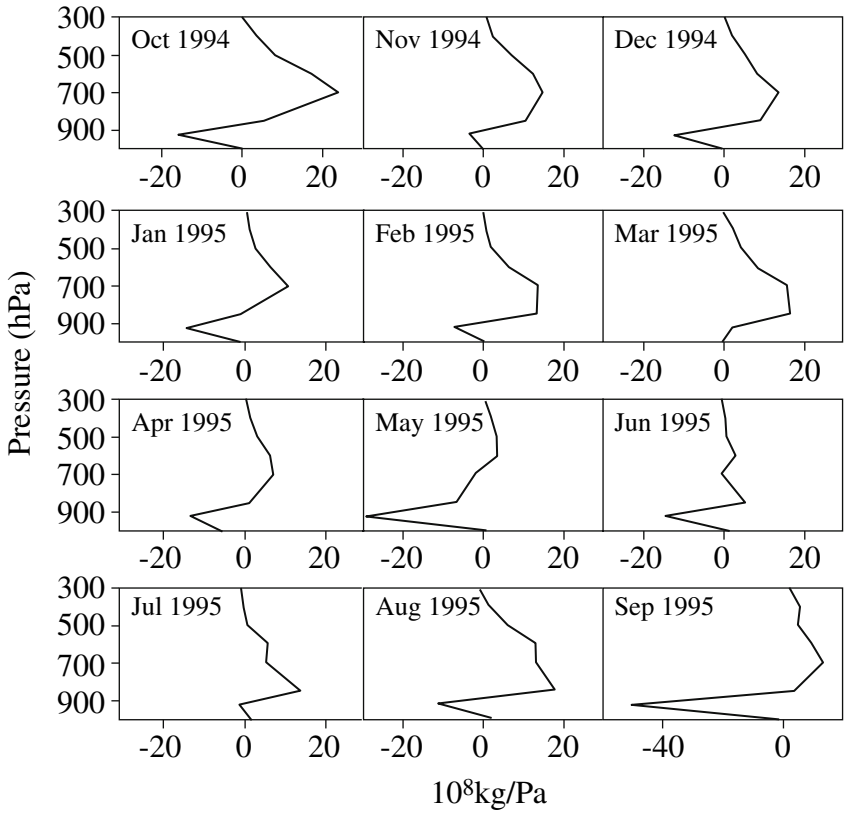

Fig. 4. Vertical structure of moisture flux convergence into the MRB for 1994–95 (x-axis values 10^8 kg Pa^{-1})

The moisture flux convergence was calculated for every 12 hours to obtain the monthly values. Figure 5 is a boxplot showing the maxima and minima 12-hour convergence values based on the NCEP data for each month, represented by the ends of the lines coming from the box. The middle horizontal lines in the boxes show the medians, while the upper

and lower bounds of the box indicate the 25th and the 75th percentiles. The boxes have a range that is much smaller than that of the extending lines, indicating that 50% of the monthly 12-hour convergence values do not vary much from the monthly median, while outlying values can be substantially different. For example, in October 1994, the minimum MFC for a 12-hour period was -0.3 cm, while the maximum was 0.41 cm. Half of the convergence values however were confined between -0.02 cm and 0.08 cm, which is a much smaller range than that between the maximum and minimum. This pattern occurred every month.

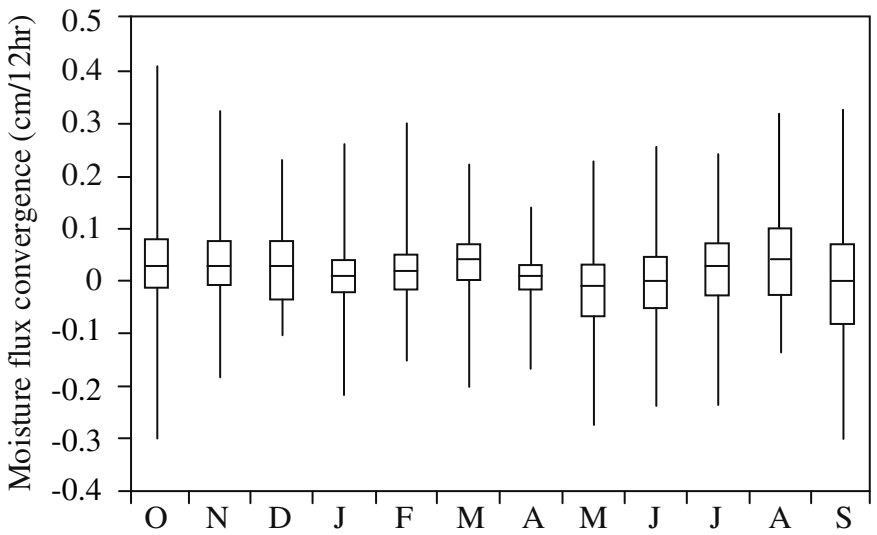

Fig. 5. Boxplot of 12-hour moisture flux convergence into the MRB for 1994–95. Line within box represents the median value, while the lower and upper bounds of the box represent the 25th and 75th percentiles. Extending lines represent maximum and minimum values

3.3 Comparison with Other Studies

Results from this study were compared with those from two previous studies (Fig. 6). Liu et al. (2002) presents MFC results based on NCEP reanalysis data for the 1994–95 water-year. The difference in methodology between our study and that of Liu et al. led to in differences in the MFC, especially for the summer months of 1995. The vertical profile of MFC depicted by Liu et al. was similar to ours in general, but there were large

discrepancies for the 1000 hPa and 925 hPa levels, again attributable to the methodological differences between studies.

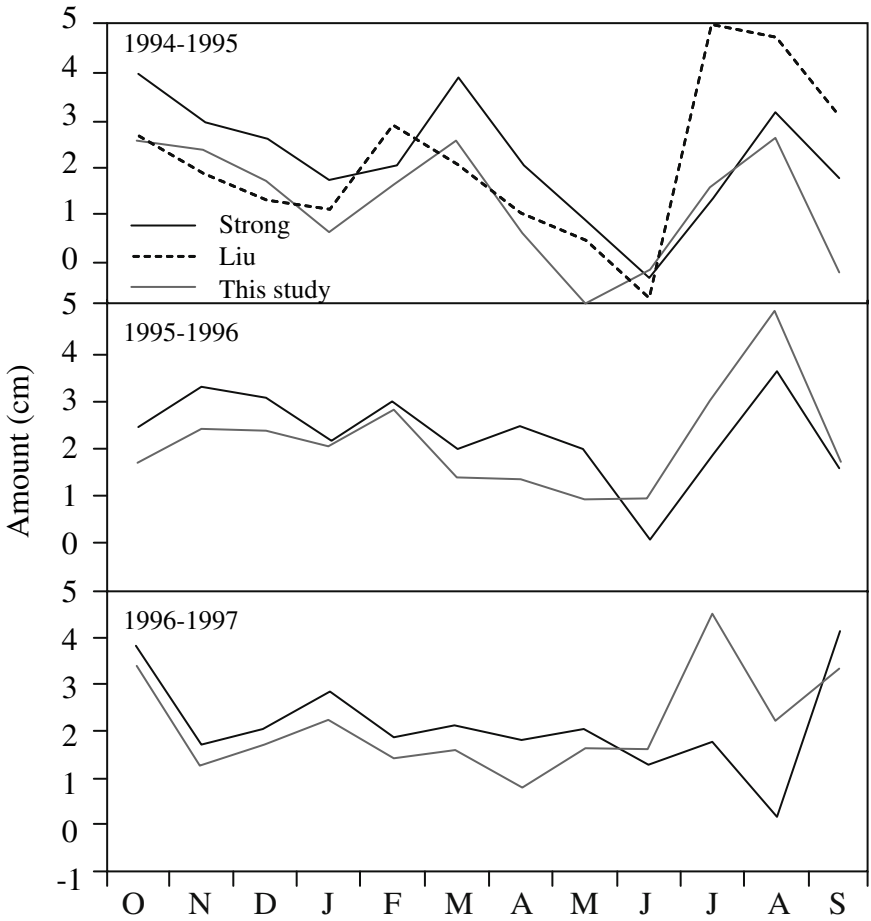

Fig. 6. Comparison with results by Liu et al. (2002) and Strong et al. (2002) for 1994–95, 1995–96 and 1996–97 water-years. Comparison with Liu only available for 1994–95 water-year

Strong et al. (2002) studied MFC for the water-years 1994–95, 1995–96, and 1996–97, using Run-0 gridded analysis data from the Canadian Regional Finite Element Model (same as SEF, see Ritchie and Delage 2007) and its replacement, the Global Environmental Multiscale Model. Output data from these two models are at a resolution of approximately 35 km and 25 km respectively, both of which are finer than the 2.5 degree

resolution of the present study. Consequently, the chosen boundaries of the MRB are different between studies. Even so, Strong et al.'s finding compare favorably with the results of our study which uses the NCEP data. There is good agreement for the months of maximum and minimum MFC, as well as in the overall trend (Fig. 6). However, our values of MFC tend to be lower than those from both Strong et al. and from Liu et al.

4 Conclusion

The NCEP reanalysis data and the ERA-40 data were used to compute the moisture flux convergence over the MRB for the period 1990–2000, with particular attention paid to the 1994–95 water-year. Identical trends were obtained from the two datasets, but the flux convergence values differ. Differences in moisture flux convergence over the Basin between the two models arose mainly at the 850 hPa level where large variations in the flux convergence occurred. There was better agreement at the other pressure levels.

Within the 10-year study period, 1997–98 was the water-year with the least moisture flux convergence into the MRB, based on both the NCEP and ERA-40 datasets, and 1994–95 had the second lowest value based on NCEP and the fourth lowest value based on ERA-40 data. The vertical structure of the moisture flux convergence indicated that generally most moisture enters the Basin at 700 hPa, while for years with the highest flux convergence values, this occurs at 850 hPa. The most important level for 1994–95 water-year was at 700 hPa, likely due to the warm and dry conditions that prevailed across the Basin in that year.

This analysis yielded results that are in general agreement with those from two previous studies. However, Liu et al. (2002) used a slightly different method for computing the moisture flux convergence, resulting in different values especially for the summer months. Although a different dataset was used in Strong et al. (2002), there was closer agreement with the results from the present study.

Acknowledgements

This study used NCEP Reanalysis data available from the NOAA-CIRES Climate Diagnostics Center, Boulder (http://www.cdc.noaa.gov/), and the ERA-40 data (http://data.ecmwf.int/dat a/). Many thanks to Jinliang Liu

and Geoff Strong for their input and discussion related to the comparisons with their earlier results. This work was part of an M.Sc. project conducted under the supervision of Peter Taylor of York University.

References

Liu J, Cho HR, Stewart RE (2002) Characteristics of the water vapour transport over the Mackenzie River Basin during the 1994–95 water-year. Atmos Ocean 40:101–111

Ritchie H, Delage Y (2007) The impact of CLASS in MAGS monthly ensemble predictions. (Vol. I, this book)

Strong G.S, Proctor B, Wang M, Soulis ED, Smith CD, Seglenieks F, Snelgrove K (2002) Closing the Mackenzie Basin water budget, water years 1994–95 to 1996–97. Atmos Ocean 40:113–124

Woo MK, Rouse WR, Stewart RE, Stone JMR (2007) The Mackenzie GEWEX Study: a contribution to cold region atmospheric and hydrologic sciences. (Vol. I, this book)

Chapter 18

The Influence of Lakes on the Regional Energy and Water Balance of the Central Mackenzie River Basin

Wayne R. Rouse, Jacqueline Binyamin, Peter D. Blanken, Normand Bussières, Claude R. Duguay, Claire J. Oswald, William M. Schertzer and Christopher Spence

Abstract The goal of this study is to define the role of lakes in the energy and water cycling of the lake-rich central Mackenzie River Basin and discuss the impacts of climate variability on the regional terrestrial water balance. This is pursued by synthesizing the results of measured data on a regional scale. Our results indicate that lake-rich regions are high energy landscapes in the thaw season. Lakes have larger net radiation and much larger water vapor fluxes and smaller sensible heat fluxes than their terrestrial surroundings. Energy exchange with the atmosphere is dominated by the annual evaporative heat flux. The presence of large lakes in a region substantially decreases the interannual variability in evaporation totals. A hypothetical region with no lakes shows a positive annual terrestrial water balance for wet and average precipitation years and only a small negative water balance for the driest years. The existing lake-rich region has a positive annual water balance only in the wettest years. Comparisons of the region with all small, all medium or all large lake scenarios indicates increased regional evaporation of 8% and 10% respectively for the latter two scenarios. Basin evaporation is a significant source for precipitation within the Mackenzie River Basin during the summer. It is hypothesized that fall and early winter evaporation from medium and large lakes enhances downwind snowfall. In response to climate warming, lake-rich high latitude basins will witness substantially increased annual evaporation.

1 Introduction

Lakes of various sizes, shapes, and depths occupy extensive areas in the Mackenzie River Basin (MRB). For the whole MRB, the estimated lake coverage approaches 11% (Rouse et al. 2005, 2007) with about 32,370 lakes occupying the central Basin. This chapter examines the role of lakes and evaluates the functioning of lakes of different sizes in the energy and water cycles.

The central MRB features typical Canadian Shield terrain, with uplands of exposed bedrock and valleys with wetlands, and many lakes that range from small to very large size (Fig. 1 in Spence and Woo 2007). Small, shallow lakes, though numerous, comprise only a small percentage of the total lake area (Table 1 in Rouse et al. 2007). Their winter ice cover is a function of air temperature and particularly of lake snow depth (Duguay et al. 2003). Lake ice thickness ranges from approximately 1 m for moderate snow covers to 2 m where there is very thin or no snow cover. This is enough to freeze shallow lakes to the bottom. In the central and lower MRB, the ice-cover lasts from about 6.5 to 8.5 months (Rouse et al. 2007). The onset of thaw normally coincides with long daylight periods in spring. The thermal and moisture cycles, and the energy flux of MRB lakes during the open water season, are described in detail in Rouse et al. (2007).

The magnitude and timing of regional evaporative and sensible heat inputs to the atmosphere is strongly influenced by the number and size of lakes. This makes them important to the regional climatic, meteorological, and hydrologic processes. In this study the role of different-size lakes in the regional radiation balance and water vapor and heat exchanges with the atmosphere is characterized and quantified. The energy and water balances for the region with no lakes can then be compared to those for a region with lakes. The chapter terminates with a discussion of the likely influence of lakes in high latitude watersheds under climate change.

2 Study Area

The study region is a 50,000 km^2 sector of mainly Canadian Shield that includes the northern half of the main basin of Great Slave Lake and extends northward to near the southern shore of Great Bear Lake (Fig. 1). It is bounded in the east-west direction by longitudes 112° and 116° W. Within this sector, upland terrain and Great Slave Lake comprise the largest surface areas, with the remainder fairly equally divided between wetlands,

small lakes, and medium size lakes (Table 1). The lake sites (Fig. 1) include three small, one medium, and one large lake, each providing three

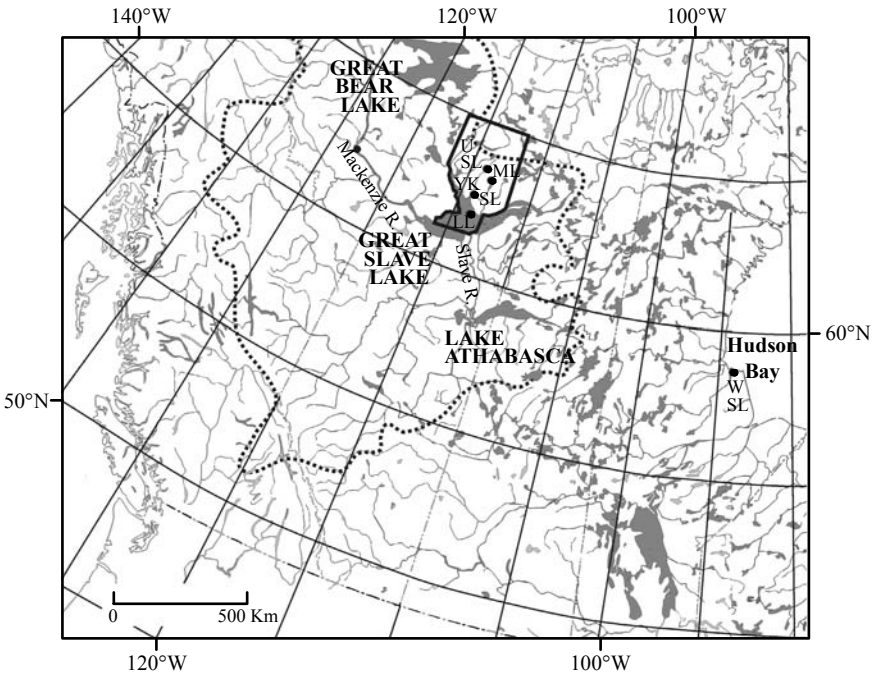

Fig. 1. Location map showing boundaries of the Mackenzie River Basin (dotted), the study area (solid) and the measurement sites within the study area and in the Hudson Bay Lowland. YK is the city of Yellowknife. U is upland; W is wetland; SL are small lakes; ML is medium lake; LL is large lake. Only the larger lakes are indicated on the map

Table 1. Regional coverage of surface units for the study region (adapted from Rouse et al. 2005)

Surface type	Area [km^2]	% Landscape
Uplands	27,269	55
Wetlands	4,067	8
Small lakes	3,706	7
Medium lakes	5,632	11
Large lakes	9,326	19
Total	50,000	100

years of data. The medium size lake is Sleepy Dragon Lake and the large one is Great Slave Lake (Fig. 1 in Oswald et al. 2007). In this paper, these size and name designations are used interchangeably.

Two terrestrial sites are used in this study (Table 1). One is upland, bedrock-dominated terrain of the Canadian Shield located roughly in the center of the study region (Spence and Rouse 2002) and the other is wetland fen terrain located in the northern Hudson Bay Lowland (Eaton et al. 2001). Two years of energy balance data are available from the upland site. It has a surface cover typical of the subarctic Canadian Shield (Spence and Rouse 2002), with stands of black spruce, mixed stands of spruce and aspen, peat wetlands, and exposed bedrock. There is a significant understory vegetation dominated by dwarf birch, Labrador tea, blueberry, and other shrubs. At this site, wetlands occur in small isolated pockets surrounded by forest. They include sphagnum moss mats overlying organic soils. They are not sufficiently large to allow accurate flux measurements to be undertaken. In contrast, the site in the Hudson Bay Lowland is extensively covered by wetlands, featuring hummocky organic terrain with peat underlain by continuous permafrost. The dominant vascular vegetation consists of sedges, with an abundant nonvascular representation of mosses. Six years of data from are available from this site (Eaton et al. 2001).

3 Methods

3.1 Surface Energy Balance

Details on the theoretical framework for this study are contained in Rouse et al. (2005) and are only generally outlined here. The one-dimensional surface energy balance is given by

$$Q^* = Q_E + Q_H + Q_S \tag{1}$$

where Q^* is net radiation, Q_E is the latent heat flux (evaporative heat flux), Q_H is the sensible heat flux, and Q_S is the heat storage in the subsurface. Net radiation is fundamental to evaluating surface differences in the energy balance of different surface types. Most of the heat entering a lake is through the absorption of solar radiation. Solar radiation can penetrate deeply which results in low surface albedo. Clear-water lakes warm deeply with absorbed solar energy driven deeper by forced and free convective mixing. The surface convective heat exchanges with the atmosphere, Q_E and Q_H, are driven primarily by eddy diffusivities and the vertical temperature and vapor pressure gradients.

In this study, net radiation was measured directly or calculated from component fluxes of the radiation balance. The heat storage in lakes was determined using calorimetric techniques. The latent and sensible fluxes were determined using the Bowen ratio (Q_H/Q_E) energy balance (BREB) approach or eddy covariance methods (Blanken et al. 2000; Eaton et al. 2001; Oswald and Rouse 2004; Rouse et al. 2005; Spence and Rouse 2002). The BREB approach derives from the surface energy balance and flux-gradient relationships for latent and sensible heat. Eddy covariance is a direct measurement of the latent and sensible heat fluxes from the eddy covariance of vertical wind speed and water vapor density and vertical wind speed and temperature respectively.

Larger lakes differ from land surfaces because, on a daily and even a weekly basis, the surface fluxes often do not correspond in magnitude to the solar or net radiation regimes. Due to their large heat storage capacity, larger lakes can lose heat and water vapor almost as readily at night as during the day, and more readily in late summer and fall than in spring and early-summer (Rouse et al. 2003, 2007). They are very responsive to the characteristics of the overlying air. If a warm, relatively calm and sunny period is followed by a cold, dry air mass and cloudy, windy conditions, the convective and latent heat fluxes can increase rapidly, even if there is no direct solar input. This arises because the vertical gradients of temperature and vapor pressure grow large, and both buoyant and mechanical convection are large (Blanken et al. 2003).

3.2 Representing Lake Sizes

Lake size categories are defined in Rouse et al. (2007, Table 1). Small and medium size lakes are abundant in the central MRB. Large lakes, though fewer, are important in terms of total surface area and water volume. It is necessary to address the representativeness of the experimental lakes of the total lake assemblage. Small lakes are well represented by the available data, but only one lake is chosen for each of the medium size and large lake classes. No data are available for the many lakes in the medium size category that are substantially larger than Sleepy Dragon. We investigated whether these lakes are best represented by the energy balance established for Sleepy Dragon or the energy balance established for Great Slave Lake (Oswald and Rouse 2004; Schertzer et al. 2003). A comparison of surface temperatures (Bussières and Schertzer 2003) indicates that their temporal cycles more closely correspond to those of Sleepy Dragon, and even to those of the small lakes, than to the cycle of Great Slave Lake. On this ba-

sis it is concluded that the energy balance of Sleepy Dragon best represents those lakes of the medium lake size category (Rouse et al 2005).

3.3 Accuracy and Data Integrity

For the upland site, Q^* was measured continuously from a tower, and periodically over different upland surface with net radiometers. Q_S was estimated from the Fourier heat flow equation with the vertical temperature gradient determined from thermistor strings and the heat conduction based on measurements of the mineral, organic and water components of the ground. Q_H was measured directly with a vertical propeller anemometer coupled with an unshielded thermocouple. Corrections to the Q_H measurement are detailed in Spence and Rouse (2002). Q_E was derived as a residual. At the wetland, Q^* was measured with a net radiometer, Q_S was determined using a combination of heat flux transducer measurements and calorimetric calculations, while Q_E and Q_H were derived from BREB calculations (Eaton et al. 2001). At the small and medium size lake sites, Q^* was measured with net radiometers and Q_S was determined calorimetrically. The vertical temperature gradients in the lakes were measured using either thermistor or thermocouple strings depending on the lake. The atmospheric vertical temperature and humidity gradients for BREB determinations were obtained at three heights using shielded air temperature and relative humidity sensors. Instruments were mounted on floating platforms for two of the small lakes, a tower mounted and guyed in the center of one of the small lakes and a small rock outcrop for the medium lake (Boudreau and Rouse 1995; Oswald et al. 2007). Q^* for the large lake was either measured using a net radiometer or was derived from the component fluxes. Thermistor strings were employed to measure lake temperatures, and Q_S calculations were made calorimetrically. Q_E and Q_H were measured directly by eddy covariance (Rouse et al. 2005).

Fetch and footprint are important to the representativeness and accuracy in measurement. At the upland, considerable care was taken in matching the radiation and eddy covariance footprints so they represent the upland landscape (Spence and Rouse 2002). The wetland site is remarkably uniform over many kilometers and the upwind fetch is unlimited in all directions (Eaton et al. 2001). For the small and medium size lakes, the height of the instruments above the homogeneous lake surface did not exceed 1% of the fetch in any direction. The measurements are considered representative of a fully adjusted boundary layer (Boudreau and Rouse 1995; Oswald and Rouse 2004). The large lake eddy covariance measurements had

unlimited fetch and minimal influence from the Inner Whaleback Islands (Blanken et al. 2000).

Root-mean-square errors (in %) in the calculation of Q_E and Q_H (first and second terms within each brackets) are as follows: upland (±21, ±16), wetland (±15, ±15), small lakes (±18, ±18), medium lake (±20, ±20), and large lake (±12, ±10). Usually measurements could not be made during the formation and breakup of lake ice. For these periods, quadratic polynomials were used to extend the seasonal data back to the beginning of the ice-free period in spring and forward to the onset of freezing in the fall. Quadratic polynomials generated the most stable results for comparison of a large number of satellite (AVHRR) data time series. Anchoring of these polynomials at either end of the season was aided by lake temperatures from thermistors operating throughout the year, by observation of the end and beginning of freeze, and for the large lake, observations from passive microwave satellite data (Walker et al. 2000).

4 Results

4.1 Regional Energy Balance

In general, uplands, wetlands, and small lakes have the shortest snow free periods. Although they become snow and ice-free earliest in the spring, their freeze-back occurs much earlier in fall than the medium size and large lakes. During the snow free season, lakes of all sizes have larger Q^* than upland and wetland because of their lower albedo. The upland has the least Q^* primarily due to its relatively high surface albedo (Rouse et al. 2005). Small lakes show the largest Q^*. After the small lakes freeze, the medium size and large lakes remain ice-free into the very short days of early winter. During that period they experience substantial negative Q^* because they absorb little solar radiation but experience large net long-wave radiation loss from their warm surface waters.

Seasonal latent heat flux, Q_E, increases sequentially from upland, through wetland, small lakes, medium size lake, to large lake (Fig. 2). Q_E for the large lake is 86, 34, 22 and 4% greater than for upland, wetland, small lakes, and medium size lake, respectively. The ratios of Q_E /Q^* indicate that medium size and large lakes are in a category of their own with about 80% of annual Q^* used in Q_E (Table 2). In contrast, the average sensible heat flux, Q_H, from upland, wetland, and small lakes is about two times greater than the average for the medium size and large lakes (Fig. 2).

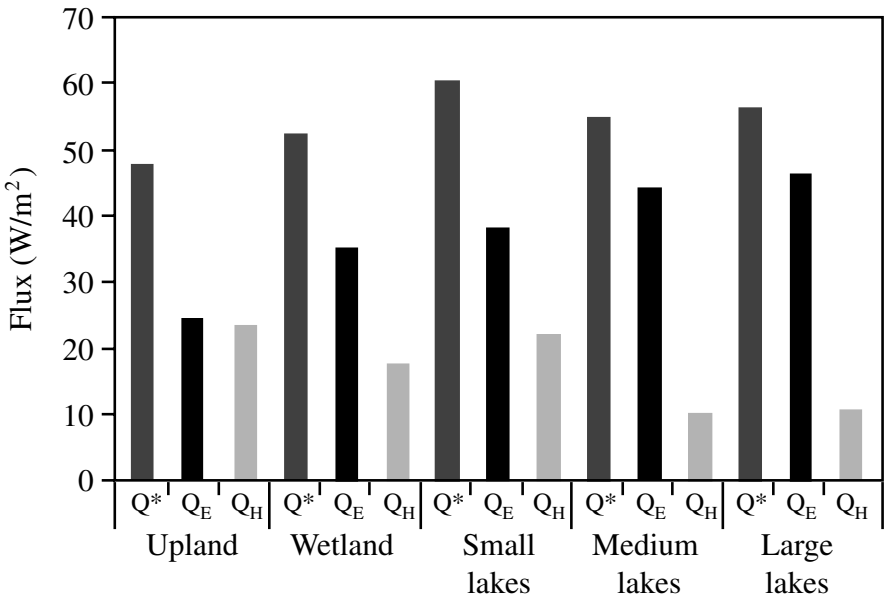

Fig. 2. Comparative 24-hour fluxes of net radiation (Q^*), latent heat flux (Q_E) and sensible heat flux (Q_H) averaged over the snow-free season

Table 2. Comparative surface energy balance components and ratios for the main surface types.

Surface type	Q^*	Q_E/Q^*	Q_H/Q^*	Q_H/Q_E
Upland	1094	0.51	0.49	0.96
Wetland	1199	0.66	0.34	0.52
Small lakes	1386	0.63	0.37	0.59
Medium lake	1259	0.80	0.20	0.25
Large lake	1290	0.81	0.19	0.23

Q^* net radiation, Q_E latent heat flux, Q_H sensible heat flux (all in W m^{-2}).

For the study region Q^* (with lakes) exceeds Q^* (no lakes) by 7% (Fig. 3). Q_E (with lakes) exceeds Q_E (no lakes) by 22% and Q_H (with lakes) is 18% less than Q_H (no lakes) (Table 3). For a region with no lakes, the Bowen ratio is 0.83, whereas for a region with lakes it is 0.58. The presence of lakes creates a higher energy landscape in which the annual latent heat flux to the atmosphere dominates the total convective heat flux to the atmosphere.

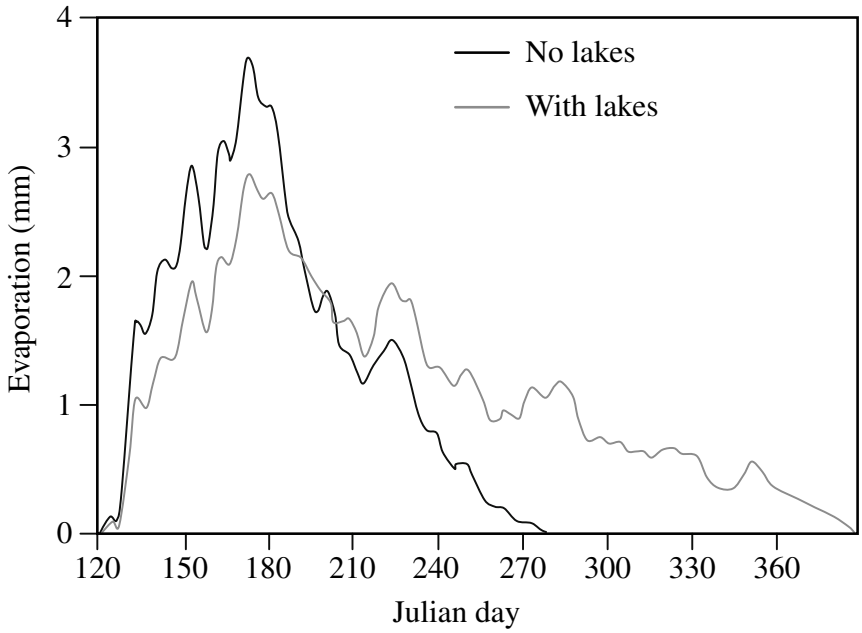

Fig. 3. Average evaporation patterns for a region with no lakes and a region with lakes

Table 3. Comparative regional energy balance with no lakes and with lakes, averaged over the season

	Q^* [W m^{-2}]	Q_E [W m^{-2}]	Q_H [W m^{-2}]
No lakes	47	25	22
With lakes	51	32	19

Q^* net radiation, Q_E latent heat flux, Q_H sensible heat flux.

4.2 Regional Evaporation

Measured annual evaporation from the five surface types varies substantially, even for the small number of years for each surface represented in this study (Table 4). Lakes have smaller inter-annual range in evaporation than the upland. The ratio of the highest to the lowest annual evaporation varied from 1.4 for the large lake to 1.6 for the small lakes, compared with 1.8 for the upland and 1.3 for wetland. The presence of lakes also strongly affects the seasonal pattern of evaporation (Fig. 3). Evaporation (no lakes) lasts for 5 months, starting in early May, peaking at the end of June, and

ceasing in early October. Evaporation (with lakes) starts and peaks at about the same time but does not cease until the end of the calendar year. This extends the evaporation period to 8 months. Compared with a region of no lakes, it is in the fall and early winter that all of the excess evaporation from a lake-dominated region occurs (Rouse et al. 2005).

Table 4. Comparative annual total evaporation [mm] for each of the surface types showing the year with the lowest, average, and highest evaporation totals

	Upland	Wetland	Small lakes	Medium lake	Large lake
Low	130	283	274	344	369
Average	227	314	346	406	422
High	238	356	434	484	506
High/Low	1.83	1.26	1.58	1.41	1.37

4.3 Regional Water Balance

For conditions of normal precipitation, the scenario of a region with no lakes always yields a positive water balance (Table 5), the magnitude of which varies with the magnitude of evaporation. However, with the same regional precipitation, a region with lakes exhibits a positive water balance only if the evaporation is small. With average or large evaporation, the water balance is negative (Table 5). The seasonal characteristics of the water balance indicate considerable difference for a regional scenario with no lakes and one with lakes. Both show a positive water balance from the beginning of the year to near the end of May (Fig. 4). This is fairly independent of precipitation regime. Subsequently, the water balance becomes negative, with the greatest deficits occurring around mid-August. During this period, water balance deficits are more than doubled during dry years

Table 5. Comparative annual water balances calculated for the region with no lakes and the region with lakes for different magnitudes of regional evaporation.

		No lakes		Lakes	
	P	*E*	*WB*	*E*	*WB*
Small	296	150	146	221	74
Average	272	238	34	298	-26
Large	302	253	49	339	-37

P precipitation (Yellowknife), *E* average regional evaporation , *WB*=*P*–*E* water balance

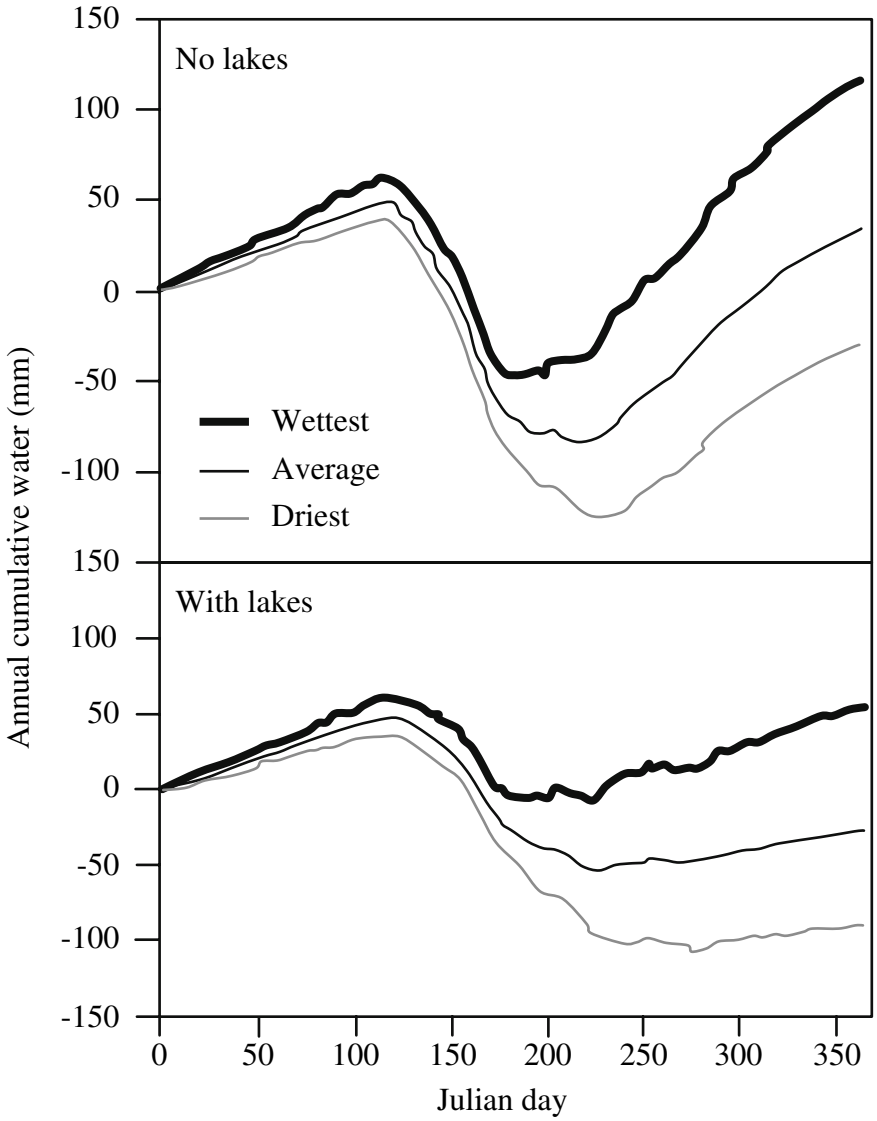

Fig. 4. Cumulative water balance for the wettest (quartile of years with highest precipitation) average (all years) and driest (quartile of years with lowest precipitation) conditions, for a region with no lakes and a region with lakes

(lower quartile of precipitation) as during wet years (upper quartile of precipitation). Negative water balances are greater in regions of no lakes than in those with lakes (Fig. 4). However, whereas the negative water balances

in lake-rich regions recover slowly or not at all by the end of the year, those in regions of no lakes recover more quickly. At the end of the year, regions with no lakes show a positive water balance for wet and average precipitation years and only a small negative water balance for the driest years. In contrast, the water balance in a lake-rich region becomes positive by the end of the year only for the wettest years, and remains negative for the scenarios of average and lower quartile precipitation.

4.4 Impact of Lake Size

The regional impact of lake size was evaluated by analyzing evaporation and the water balance from the region by assigning the 37% lakes portion (Table 1) to small lakes only, to medium size lakes only, or to large lakes only. Compared with an all small lakes scenario, scenarios of all medium size or all large lakes result in an increased regional evaporation of 8% and 10%, respectively. The influence on the seasonal pattern of the regional water balance is also noteworthy. Under conditions of average precipitation, the existing regional distribution of lakes (Table1) creates a negative regional water balance. In the scenario of all small lakes, this negative balance amplifies quickly between mid-June (DOY 166) and late August (DOY 234), but recovers through the fall and early winter to yield an annual water balance that is only marginally negative (Fig. 5). In the scenario of all medium size lakes, the negative water balance commences in late June (DOY 174) and reaches its trough in early October (DOY 278). It gradually lessens through the fall and early winter but remains negative to the end of the year. In the all large lakes scenario, the negative balance commences in late June (DOY 176), reaches its largest deficit in mid- to late August (DOY 235) and persists till the year ends.

5 Discussion

This study demonstrates that the number of lakes within a region, and their size distribution, significantly affect the regional atmospheric and hydrologic regimes. Large and medium-size lakes especially enhance the latent heat flux and suppress the sensible heat flux into the atmosphere. This agrees with evidence from Bonan (1995) and Nagarajan et al. (2004). Evaporation is a significant source for precipitation within the MRB during the summer (Walsh et al. 1994). Szeto (2002) and Szeto et al. (2007) found the highest recycling ratios (fraction of evaporation that is obtained

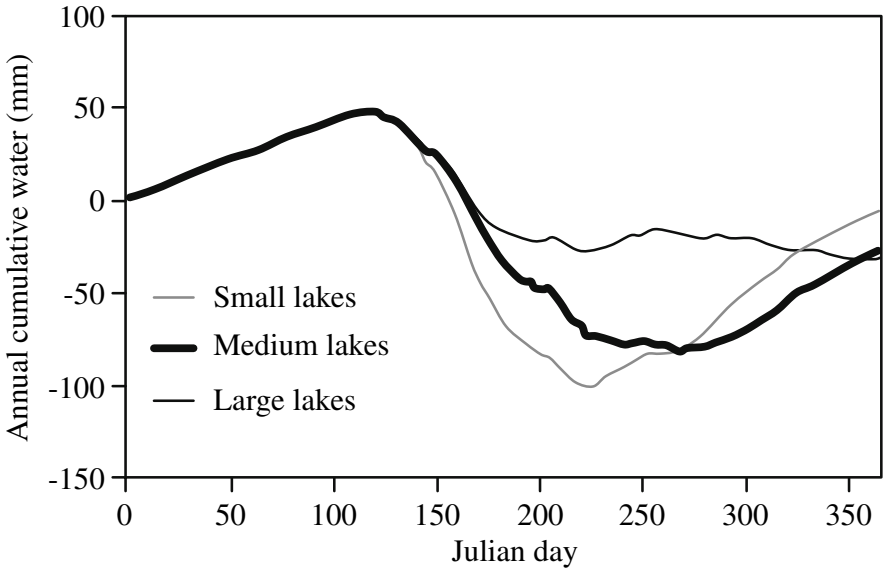

Fig. 5. Cumulative regional water balance if the precipitation is average and the lake portion of total area (37%) is all small lakes, all medium lakes, or all large lakes

from precipitation within a basin) over the eastern part of the Basin in the warm season, and attributed this, in part, to large evaporation from the extensive lake and wetland systems.

It is well documented that in late fall and in winter the Laurentian Great Lakes produce enhanced downwind snowfall. Conditions for these lakes (late-season evaporation, frozen upland surfaces with substantial relief that contributes to low level condensation) are similar to those for Great Slave Lake and other deep large and medium size lakes in the MRB. We hypothesize, therefore, that downwind snowfall will be similarly enhanced for the northern lakes. No major studies have yet been pursued on this phenomenon in the MRB, though there is some evidence from passive microwave satellite data that the larger lakes contribute to enhanced downwind snow water equivalent.

We further hypothesize that, in lake-rich high latitude basins, enhanced precipitation due to enhanced evaporation raises an interesting hydrologic duality. Enhanced evaporation from a lake-rich river basin will yield less runoff than from a basin with no lakes, yet on an annual basis, this may be partly compensated for by increased precipitation. However, this does not negate the findings presented in Fig. 5 since the water balance calculations already use the augmented precipitation as inputs.

We can speculate on the response of lake-rich high latitude basins to climate change. In some respects this study already includes some effects of climate warming since central MRB already undergoes some of the most rapid warming that has taken place in recent times (Stewart et al. 1998). In high latitudes especially, higher temperatures can greatly increase evaporation from lakes of all sizes (Blanken et al. 2000; Rouse et al. 2000, 2003). Unless the magnitude of this evaporation is matched by increased precipitation, the water balance will become increasingly negative with a resulting negative impact on river discharge. In the case of climate cooling the opposite applies. Both evaporation and precipitation exert the major influences on the basin water balance. This poses important questions about the annual and seasonal lake-enhanced evaporation-precipitation linkages and basin recycling and how they are likely to respond to climate change. These linkages need addressing by regional climate models and weather prediction models that incorporate lake model subroutines (Rouse et al. 2007).

6 Conclusions

Lakes of all sizes have larger net radiation than their terrestrial surroundings. Seasonal latent heat fluxes and evaporation increase sequentially from upland, through wetland, small lakes, medium to large lakes. The average sensible heat flux from upland, wetland, and small lakes is almost three times greater than for medium size and large lakes. The annual latent heat flux to the atmosphere dominates the total surface to atmosphere convective heat flux. Additionally, lakes extend the evaporation season from 5 months (no lakes) to eight months (with lakes). When the region with lakes is compared to one without lakes, net radiation is 7% larger, latent heat flux is 22% larger, but sensible heat flux is 18% less. Regions with no lakes show a positive annual water balance for wet and average precipitation years and only a small negative water balance for the driest years. In contrast, the annual water balance of a lake-rich region is positive only for the wettest years. The seasonal water balance cycle is also strongly affected by lakes. Lake size influences the regional water balance: compared to all small lake scenarios, all medium size and all large lake scenarios show increased regional evaporation of 8% and 10%, respectively. Evaporation is a significant source for precipitation within the MRB during the summer. It is hypothesized that fall and early winter evaporation from medium size and large lakes will enhance downwind snowfall. The response

of lake-rich high latitude basins to climate warming will entail an enhanced annual regional evaporation. Unless matched by increased precipitation, the terrestrial water balance will become increasingly negative with a resulting decrease in river discharge.

Acknowledgements

Financial support for this project was provided by individual NSERC research grants, a research grant from NASA, USA, and Student Northern Training Grants from the Canada Department of Indian and Northern Affairs. Logistical and equipment support during measurement campaigns was provided by the Great Slave Lake Branch of the Canadian Coast Guard; Environment Canada; Institute of Hydrology, Wallingford, U.K.; Royal Canadian Mounted Police Marine Unit, Yellowknife, NT; and Churchill Northern Studies Centre, Churchill, MN. Lake ice information was provided by Anne Walker. Bob Kochtubajda facilitated obtaining appropriate meteorological data and other aspects of this study. We thank many graduate students and technical support staff involved in the various field campaigns.

References

Blanken PD, Rouse WR, Culf AD, Spence C, Boudreau LD, Jasper JN, Kotchtubajda B, Schertzer WM, Marsh P, Verseghy D (2000) Eddy covariance measurements of evaporation from Great Slave Lake, Northwest Territories, Canada. Water Resour Res 36:1069–1078

Blanken PD, Rouse WR, Schertzer WM (2003) The enhancement of evaporation from a large northern lake by the entrainment of warm, dry air. J Hydrometeorol 4:680–693

Bonan GB (1995) Sensitivity of a GCM simulation to inclusion of inland water sources. J Climate 8:2691–2704

Boudreau LD, Rouse WR (1995) The role of individual terrain units in the water balance of wetland tundra. Climate Res 5:31–47

Bussières N, Schertzer WM (2003) The evolution of AVHRR-derived water temperatures over lakes in the Mackenzie Basin and hydrometeorological applications. J Hydrometeorol 4:660–672

Duguay CR, Flato GM, Jeffries MO, Ménard P, Morris K, Rouse WR (2003) Ice cover variability on shallow lakes at high latitudes: model simulations and observations. Hydrol Process 17:3465–3483

Eaton AK, Rouse WR, Lafleur PM, Marsh P, Blanken PD (2001) Surface energy balance of the western and central Canadian subarctic: variations in the energy balance among five major terrain types. J Climate 14:3692–3703

Nagarajan B, Yau MK, Schuepp PH (2004) The effects of small water bodies on the atmospheric heat and water budgets over the Mackenzie River Basin. Hydrol Process 18:913–938

Oswald CJ, Rouse WR (2004) Thermal characteristics and energy balance of various-size Canadian Shield lakes in the Mackenzie River Basin. J Hydrometeorol 5:129–144

Oswald CJ, Rouse WR, Binyamin J (2007) Modeling lake energy fluxes in the Mackenzie River Basin using bulk aerodynamic mass transfer theory. (Vol. II, this book)

Rouse WR, Blanken PD, Schertzer WM, Spence C (2000) The role of lakes in the surface climate of cold regions. In: Stewart R, Ohata T (eds) Proc GAME-MAGS Int workshop, research report IHAS no 7, Instit Hydrospheric-Atmospheric Sci, Nagoya, Japan, pp 77–81

Rouse WR, Oswald CJ, Spence C, Schertzer WM, Blanken PD (2002) Cold region lakes and landscape evaporation. In: diCenzo P, Martz LW (eds) Proc 2nd GAME-MAGS Joint int workshop, Publ by GEWEX-MAGS Secretariat, pp 37–42 (Available from MAGS Secretariat, NWRI, Saskatoon, SK, S7N 3H5, Canada)

Rouse WR, Oswald CJ, Binyamin J, Blanken PD, Schertzer WM, Spence C (2003) Interannual and seasonal variability of the surface energy balance and temperature of Central Great Slave Lake. J Hydrometeorol 4:720–730

Rouse WR, Oswald CJ, Binyamin J, Spence C, Schertzer WM, Blanken PD, Bussières N, Duguay C (2005) The role of northern lakes in a regional energy balance. J Hydrometeorol 6:291–305

Rouse WR, Blanken PD, Duguay CR, Oswald CJ, Schertzer WM (2007) Climate-lake interactions. (Vol. II, this book)

Schertzer WM, Rouse WR, Blanken PD, Walker AE (2003) Over-lake meteorology, thermal response, heat content and estimate of the bulk heat exchange of Great Slave Lake during CAGES (1998–1999). J Hydrometeorol 4:649–659

Spence C, Rouse WR (2002) The energy budget of Canadian Shield subarctic terrain and its impact on hillslope hydrology. J Hydrometeorol 3:208–218

Spence C, Woo MK (2007) Hydrology of the northwestern subarctic Canadian Shield. (Vol. II, this book)

Szeto KK (2002) Moisture recylcling over the Mackenzie Basin. Atmos Ocean 40:181–187

Szeto KK, Liu J, Wong A (2007) Precipitation recycling in the Mackenzie and three other major river basins. (Vol. I, this book)

Stewart RE, Leighton HG, Marsh P, Moore GWK, Ritchie H, Rouse WR, Soulis ED, Strong GS, Crawford RW, Kochtubajda B (1998) The Mackenzie GEWEX Study: the water and energy cycles of a major North American river basin. B Am Meteorol Soc 79:2665–2683

Walker A, Silis A, Metcalf JR, Davey MR, Brown RD, Goodison BE (2000) Snow cover and lake ice determination in the MAGS region using passive microwave satellite and conventional data. In: Strong GS, Wilkinson YML (eds) Proc 5th Sci workshop Mackenzie GEWEX Study, Edmonton, AB, Canada, pp 39–42 (Available from MAGS Secretariat, NWRI, Saskatoon, SK, S7N 3H5, Canada)

Walsh JE, Zhou X, Serreze D, Serreze MC (1994). Atmospheric contributions to hydrologic variations in the Arctic. Atmos Ocean 32:733–755

Chapter 19

Mapping of Surface Albedo over Mackenzie River Basin from Satellite Observations

Alexander P. Trishchenko, Konstantin V. Khlopenkov, Calin Ungureanu, Rasim Latifovic, Yi Luo and William B. Park

Abstract This chapter presents the approach and results of mapping surface albedo and bi-directional reflectance distribution function (BRDF) properties over the Mackenzie River Basin (MRB). Satellite observations from three types of sensors were used: (1) the Advanced Very High Resolution Radiometer (AVHRR) sensor onboard the NOAA platforms, (2) the VEGETATION (VGT) sensor onboard the SPOT platforms, and (3) the Moderate Resolution Imaging Spectroradiometer (MODIS) sensor onboard the TERRA platform. The data collected using these sensors span the period of 1985 to 2004. Seasonal and interannual variability of spectral and broadband albedo over the MRB was analyzed. Broadband albedo averaged over the region changed from 0.11±0.03 in summer to 0.4-0.55 in winter. No substantial long-term systematic trends in surface albedo could be detected over the study period, mainly due to large interannual variability, uncertainties in sensors properties, atmospheric correction, and retrieval procedure.

1 Introduction

Albedo is defined as a ratio of reflected upward hemispheric solar flux (termed the surface radiant exitance M) to downward solar flux (termed the surface irradiance E). Surface albedo is an important property of the Earth climate system, as it influences the radiation budget of the surface, serves as an indicator of vegetation phenological processes, and affects the surface hydrologic and energy cycles. The accurate parameterization and representation of surface albedo in Global and Regional Climate Models (GCM and RCM) is important for the overall reliability of model prediction. The validation of model results against observations is a crucial indicator of model strength and weakness. However, ground point albedo measurements are scarce and represent only very small areas. Satellite observations are therefore indispensable for characterizing spatial and temporal variations in albedo (Luo et al. 2005; Wang et al. 2006). Since albedo is

a ratio of hemispherical quantities, it cannot be inferred directly from satellite observations obtained from scanning radiometers. Instead, it is obtained by constructing the bi-directional reflectance distribution function (BRDF) (Nicodemus 1970) of the surface from a series of satellite observations, which is then integrated over angles to derive albedo. Frequently, the BRDF is expressed as a combination of kernel functions. Weights for each kernel are derived by fitting a set of atmospherically-corrected clear-sky satellite observations for a particular point or land cover type (Luo et al. 2005).

The main objective of this work was to produce time series of surface albedo and BRDF parameters over the entire Mackenzie River Basin (MRB) from historical and current satellite sensors that cover the complete annual cycle. Since the MRB region contains a diversity of land cover types, the surface properties over the region are highly variable, and can change substantially between seasons due to the variability of snow cover and vegetation phenology. For the period 1985 to 2004 we produced surface albedo at 1-km spatial resolution every 10 days from historical satellite sensors such as the Advanced Very High Resolution Radiometer (AVHRR) onboard the NOAA satellites and the VEGETATION (VGT) sensor onboard the SPOT platforms. For the period 2000-04 we produced surface albedo at 1-km spatial resolution every 16 days using the MODIS product MOD43B1/MYD43B1 from TERRA/AQUA spacecraft. This work was a component of a Natural Resources Canada (NRCan) project conducted at the Canada Centre for Remote Sensing (CCRS) that focused on producing national-scale satellite data products in the framework of the scientific program "Reducing Canada's Vulnerability to Climate Change" (http://ess.nrcan.gc.ca/2002_2006/rcvcc/index_e.php).

2 Study Area

The study area covers the entire Mackenzie River Basin, extending from 52ºN to 69ºN where the Mackenzie Delta reaches the Beaufort Sea. Figure 1a shows the distribution of land cover types in the region, extracted from datasets described by Latifovic and Pouliot (2005). Surface elevation extracted from the GTOPO30 database is shown in Fig. 1b (http://edcdaac.usgs.gov/gtopo30/gtopo30.html). The eastern part of the basin is a low-lying area containing three major lakes: Athabasca, Great Slave and Great Bear Lakes. The western sector covers part of the Western Cordillera.

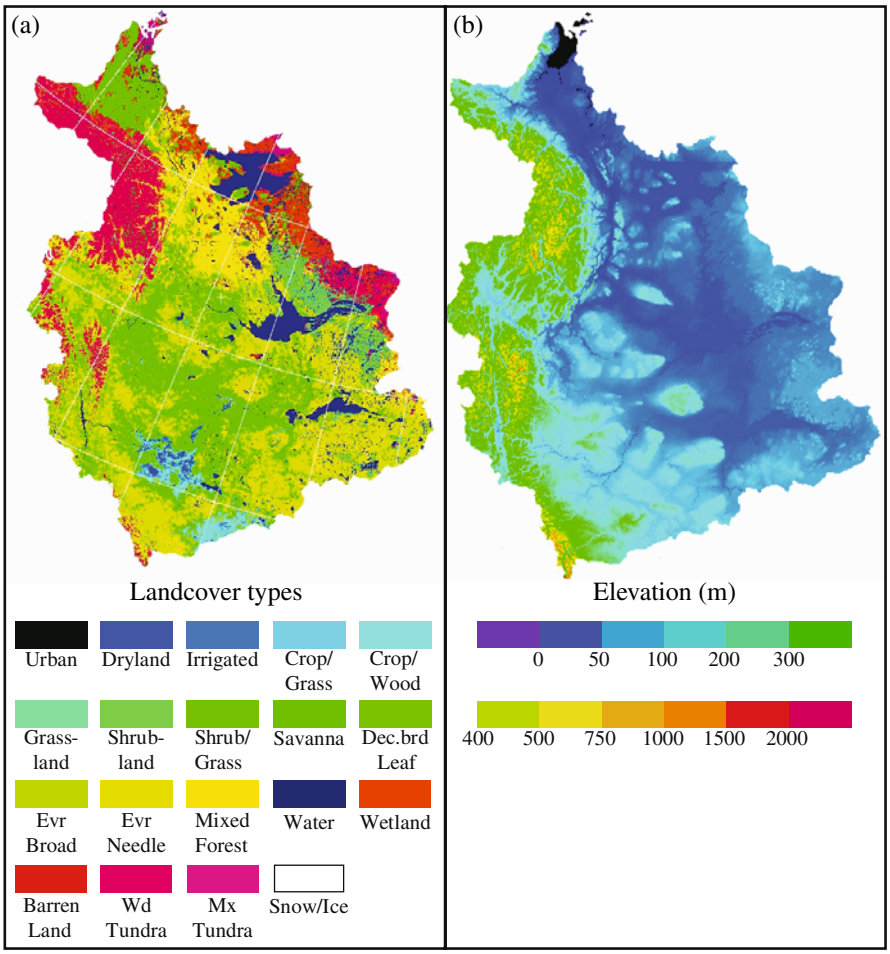

Fig. 1. (a) Distribution of land cover types (mid-summer conditions) in the Mackenzie River Basin (extracted from datasets described by Latifovic and Pouliot 2005); (b) Surface elevation of the Basin (extracted from GTOPO30 database http://edcdaac.usgs.gov/gtopo30/gtopo30.html)

3 Methods

3.1 Definitions

Albedo varies with wavelength and can be a spectral (for monochromatic or very narrow spectral bands) or broadband (for finite spectral intervals or the entire solar domain) quantity. Albedo is an integrated product of the downward radiance field $L^{\downarrow}_{\lambda}(t, \theta_i, \phi_i)$ and the bi-directional reflectance distribution function $f_{\lambda}(t, \theta_r, \phi_r, \theta_i, \phi_i)$, where λ denotes a wavelength, t is the time to account for temporal changes in surface properties and radiance field. The BRDF determines the reflective properties of an image pixel for the radiative energy at wavelength λ incident upon the surface from direction (θ_i, ϕ_i) and reflected at angle (θ_r, ϕ_r) with relative azimuth $\Delta\phi = \phi_r - \phi_i$ between the direction of incidence and reflection (Nicodemus 1970). In general, it is assumed that the BRDF depends on the relative azimuth angle, i.e.,

$$f_{\lambda}(\theta_r, \phi_r, \theta_i, \phi_i) = f_{\lambda}(\theta_r, \theta_i, \Delta\phi = \phi_r - \phi_r,) \tag{1}$$

The spectral monochromatic albedo α_{λ}, also called bihemispherical reflectance (Nicodemus 1970), is obtained as ratio of two quantities, the surface radiant exitance $M_{\lambda}(\theta_0)$ and the surface irradiance $E_{\lambda}(\theta_0)$, and depends on the solar zenith angle (SZA) θ_0

$$\alpha_{\lambda}(\theta_0) = M_{\lambda}(\theta_0) / E_{\lambda}(\theta_0) \tag{2}$$

For clear-sky conditions, the downward solar radiance field can be considered approximately as a collimated beam. In such a case, albedo is called the *direct albedo* and can be expressed as

$$\alpha_{\lambda}(\theta_0) = \int_{2\pi} f_{\lambda}(\theta_r, \theta_0, \Delta\phi)\mu_r \, d\omega_r \tag{3}$$

where $\mu_{(i,r,0)} = \cos\theta_{(i,r,0)}$, and $d\omega_{(r,i)} = d\cos\theta_{(r,i)} d\phi_{(r,i)}$.

Under overcast conditions, when surface downward solar flux is approximated by an isotropic field, albedo is called the *diffuse albedo* and can be expressed as

$$\overline{\alpha}_{\lambda} = 2\int_0^1 \mu \, d\mu \; \alpha_{\lambda}(\theta) \tag{4}$$

Usually the BRDF is parameterized as a combination of kernel functions (Strahler et al. 1999)

$$f_\lambda(\theta_r,\theta_0,\phi)=\sum_k f_k(\lambda)F_k(\theta_r,\theta_0,\phi) \tag{5}$$

Then, for the monochromatic case, one can derive the following expressions for the direct and diffuse albedo

$$\alpha_\lambda(\theta_0)=\sum_k f_k(\lambda)h_k(\theta_0) \tag{6}$$

$$\overline{\alpha}_\lambda=\sum_k f_k(\lambda)\overline{h}_k \tag{7}$$

where

$$\begin{aligned} h_k(\theta_0)&=\int_{2\pi} F_k(\theta,\theta_0,\phi)\mu\,d\mu\,d\phi \\ \overline{h}_k&=\int_0^1 h_k(\theta)\mu\,d\mu \end{aligned} \tag{8}$$

A popular and convenient choice of kernel functions widely used for BRDF parameterization is the Ross-Thick-Li-Sparse (RTLS) parameterization employed in MODIS data processing (Strahler et al. 1999; Wanner et al. 1995). This model is reciprocal (i.e., symmetrical relative to incoming and outgoing directions) and contains three kernels

$$f_\lambda(\theta_r,\theta_i,\phi)=f_0(\lambda)+f_1(\lambda)F_1(\theta_r,\theta_i,\phi)+f_2(\lambda)F_2(\theta_r,\theta_i,\phi) \tag{9}$$

Function F_1 in Eq. (9) is the Ross-Thick kernel. It represents volumetric scattering from a dense leaf canopy based on a single-scattering approximation of radiative transfer theory (Ross 1981; Roujean et al. 1992). Function F_2 is the Li-Sparse kernel which is derived from the geometric-optical mutual shadowing model, and assumes a sparse ensemble of surface objects (Li and Strahler 1992). Parameters $f_0(\lambda)$, $f_1(\lambda)$, and $f_2(\lambda)$ are related to the isotropic, volumetric, and geometric components, respectively. Expressions for these kernel functions can be found in Strahler et al. 1999).

For finite spectral intervals, the surface albedo for direct and diffuse cases are given by

$$\alpha_{\Delta\lambda}(\theta_0) = \sum_k h_k(\theta_0) w_k(\theta_0) \tag{10}$$

$$\overline{\alpha}_{\Delta\lambda} = \sum_k \overline{h}_k \overline{w}_k \tag{11}$$

where

$$w_k(\theta_0) = \frac{\int_{\lambda_1}^{\lambda_2} d\lambda \; f_k(\lambda) E_\lambda^0(\theta_0)}{\int_{\lambda_1}^{\lambda_2} d\lambda \, E_\lambda^0(\theta_0)}, \quad \overline{w}_k = 2\frac{\int_{\lambda_1}^{\lambda_2} d\lambda f_k(\lambda) L_\lambda^0}{\int_{\lambda_1}^{\lambda_2} d\lambda \, L_\lambda^0} \tag{12}$$

Eqs. (10–12) emphasize the dependence of wideband and broadband albedo on the spectral distribution of direct $E_\lambda^0(\theta_0)$ and diffuse L_λ^0 downward fields, when the BRDF varies with wavelength. An example of spectral weighting coefficients for several spectral bands for average illumination conditions can be found in Strahler et al. (1999).

3.2 Clear-sky Composites and BRDF-fitting: AVHRR and VGT

The BRDF parameters were derived from satellite clear-sky composites. The clear-sky composites from historical AVHRR observations since 1985 were produced using the Earth Observation Data Manager (EODM) described by Latifovic et al. (2005). The identification of clear-sky pixels was based on the SPARC (Separation of Pixels using Aggregated Rating over Canada) cloud detection scheme (Khlopenkov and Trishchenko 2007). This scheme generates a mask of clear-sky, cloud, snow/ice and cloud shadow flags for each image pixel, and a special score that determines the probability of pixel cloud contamination. The higher the degree of cloud contamination, the larger is the score (aggregated rating) obtained; the smaller the aggregated rating, the better the clear-sky conditions appear for a particular pixel.

Each AVHRR sensor provides information about surface reflectivity in three spectral channels: channel 1 (visible red (VIS): 0.58-0.68 μm), channel 2 (near-infrared (NIR): 0.725-1.10 μm), and channel 3 (shortwave infrared (SWIR): 3.55-3.93 μm). The latest AVHRR-3 instruments onboard NOAA-15, 16, 17, and 18 have an additional channel, 3A, that covers the wavelength range 1.58-1.64 μm in the shortwave infrared part of the spec-

trum. However, only one channel in SWIR region is operational at any time. After introducing channel 3A, the original channel 3 was renamed as 3B.

The EODM system was also used to produce surface products from VGT sensors onboard SPOT-4 and SPOT-5. We acquired the S-10 VGT data product that contains atmospherically corrected 10-day clear-sky composites from the SPOT VITO archive (http://www.vgt.vito.be). The VGT sensor has four spectral channels: channel 1 (0.43-0.47 μm, blue), channel 2 (0.61-0.68 μm, red), channel 3 (0.78-0.89 μm, NIR), and channel 4 (1.58-1.75 μm, SWIR). Data from VGT sensors are available since 1998.

A land-cover-based method has been proposed to generate the BRDF for AVHRR data (Cihlar et al. 2004). A similar method has been employed for VGT data. This method uses kernels Eq. (9) with parameters depending on the Normalized Difference Vegetation Index (NDVI). An additional term with correction for the hotspot effect was also introduced (Chen and Cihlar 1997).

3.3 BRDF and Albedo from MODIS

Pre-processed MODIS MOD43B1 data available from the NASA Distributed Active Archive Center (DAAC) were used to generate surface albedo product over the entire MRB. Original MOD43B1 data of version 4 were used in this study. They are available as a set of granules (1200x1200 pixels) in EOS hierarchical data format (HDF) and Sinusoidal projection (SIN). We processed all available granules that covered the Canadian landmass and assembled them into one large image in Lat-Long projection. These images were then re-projected onto the Lambert Conformal Conic (LCC) projection. The parameters of the LCC projection are described in Latifovic et al. (2005). To minimize re-projection errors, the procedure was applied to super-sampled data using a 3x3 matrix for each pixel with subsequent weighted averaging to preserve the 1 km pixel spatial resolution. Data over the MRB study area were then extracted from the Canada-wide LCC images.

Occasionally, entire granules or pixels within granules were missing due to the presence of clouds or the failure of the standard MODIS BRDF fitting procedure to retrieve all parameters. This often led to incomplete coverage and large gaps in the BRDF maps. Overall, nearly 20% of pixels were missing over Canada in the standard MODIS product, with the most affected areas including Canada's northern regions and the Arctic Cordil-

lera. Such missing data and the irregular location of data gaps created substantial problems for the effective application of data. Because spatially and temporally complete data products are required for research and applications, simple, robust, and efficient methods of spatio-temporal interpolation were devised to fill the data gaps. These methods involved extracting a temporal sequence of all values for a particular pixel. Single gaps were filled by linear temporal interpolation. If data gaps could not be filled using this method, they were instead filled using spatial bi-linear interpolation. The procedure was applied iteratively two or three times until all data gaps were filled. To distinguish between original and reconstructed data, a special quality bit was created in the 32-bit quality mask.

An example of MODIS spectral albedo over the region where gaps were filled as described above is shown for the winter (Fig. 2) and summer (Fig. 3) periods. Albedo for seven spectral bands and one broadband shortwave (SW) channel are presented. The black area over Great Slave Lake corresponds to deep water and does not contain valid data points.

4 Long-term Trends and Annual Cycle of Albedo

Long-term seasonal variations in surface albedo from AVHRR channels 1 (visible, red) and 2 (near infrared), as well as an estimate of SW broadband albedo from these two channels, are presented in Fig. 4a-c. Data from AVHRR onboard NOAA-9, 11, 14, 16, and 17 were employed to produce these data records. The SW broadband albedo was determined using the approach proposed by Csiszar and Gutman 1999). For the summer period, the albedo for the visible channel varies around 0.05±0.02; the AVHRR NIR albedo is in the range of 0.18±0.13; and the SW broadband albedo estimated from AVHRR data is in the range of 0.11±0.03. Although the absolute magnitudes of these variations are small, their relative magnitudes are large compared to their mean values. Large uncertainty arises from cloud/haze/smoke contamination, aerosol variability, and the atmospheric correction procedure, as well as differences in spectral response function between various AVHRR sensors and uncertainties in BRDF shape (Trishchenko et al. 2002).

In winter time, year-to-year absolute variability is much higher. Winter peak values of SW broadband albedo averaged over the region can be as low as 0.4 and as high as 0.55 (i.e., absolute difference can reach 0.15). A similar difference is found for the visible and NIR channels. The observed

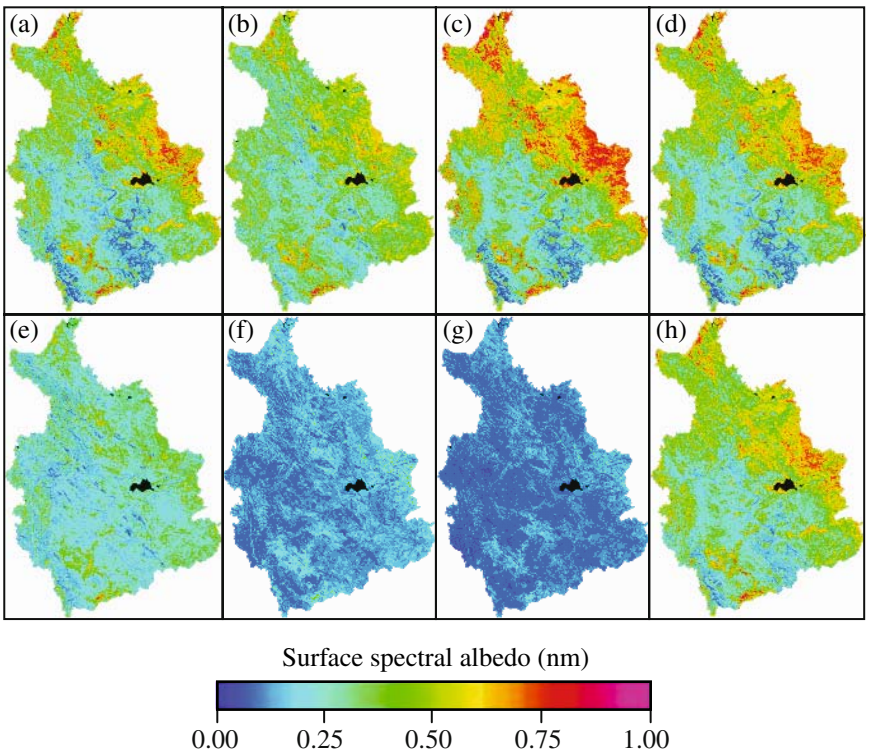

Fig. 2. Example of Mackenzie River Basin surface spectral albedo for seven MODIS land channels (1-7) and synthetic broadband channel for winter condition, January 17-31, 2003: (a) Ch.1 620-670 nm, (b) Ch.2 841-876 nm, (c) Ch.3 459-479 nm, (d) Ch.4 545-565 nm, (e) Ch.5 1230-1250 nm, (f) Ch.6 1628-1652 nm, (g) Ch.7 2105–2155 nm, (h) Broadband SW. Black area within the study region corresponds to deep water and does not contain valid data points

variability is explained by snow cover and snow depth variation across the region. Uncertainties due to cloud screening, BRDF shape, and atmospheric corrections are also contributing factors.

Five years of basin-averaged MODIS spectral albedo data are plotted in Fig. 5a-c. The strongest seasonal cycle exists for the channels with wavelengths less than 1μm (blue, green, VIS (red), and NIR). Channels with wavelengths greater then 1μm show relatively smaller amplitude in the seasonal cycle. Albedo for SWIR channels 1.6μm and 2.1μm varies in an opposite way to all other channels, being larger for the snow-free season and smaller for the snow-cover season.

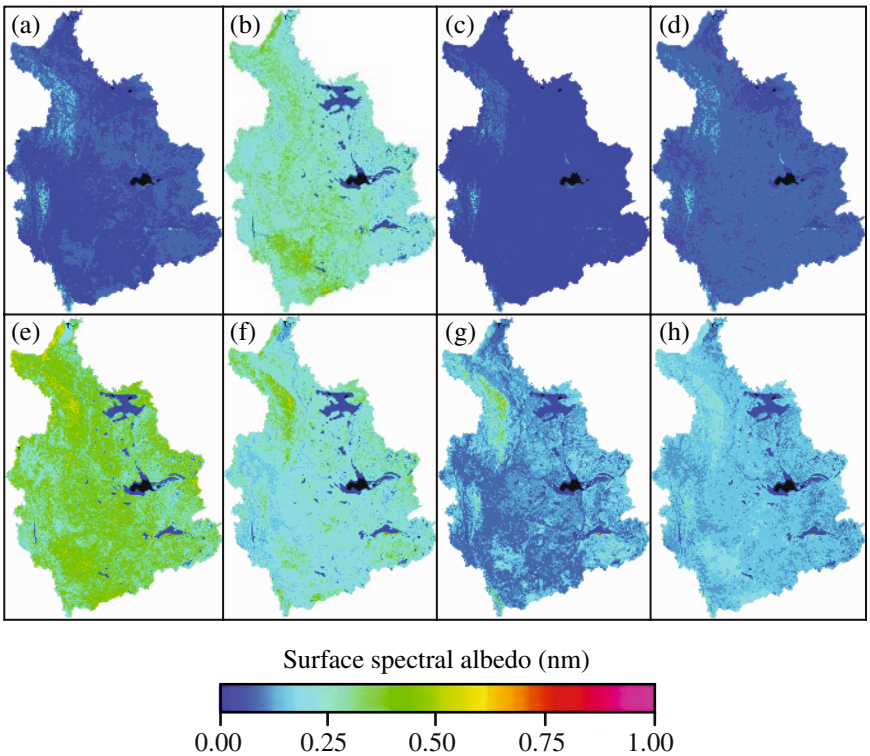

Fig. 3. Same as in Figure 2, but for July 12–27, 2003

The annual averages for the entire region for AVHRR and MODIS spectral channels and SW broadband albedo are listed in Table 1. These averages are reasonably consistent between sensors, especially for visible (red) and SW broadband wavelengths. The difference in SW broadband albedo is approximately 0.02, with MODIS values being greater than those from AVHRR. Albedo for similar spectral channels (red and NIR) available from MODIS and AVHRR for the period 2000-04 are plotted in Fig. 6 a-b. Results for the visible channels are consistent between sensors, although a systematic difference is observed for NIR channels. The MODIS NIR albedo is 0.34 and the AVHRR NIR albedo is 0.28. This bias occurs in all months. The major factor that causes this bias is the difference in spectral response functions between MODIS and AVHRR NIR channels, as described by Trishchenko et al. (2002). A good relationship exists between the SW albedo from these two sensors for both the winter and summer seasons of 2000-04 (Fig. 6c). Minor differences between these sensors during the winter are probably due to cloud contamination.

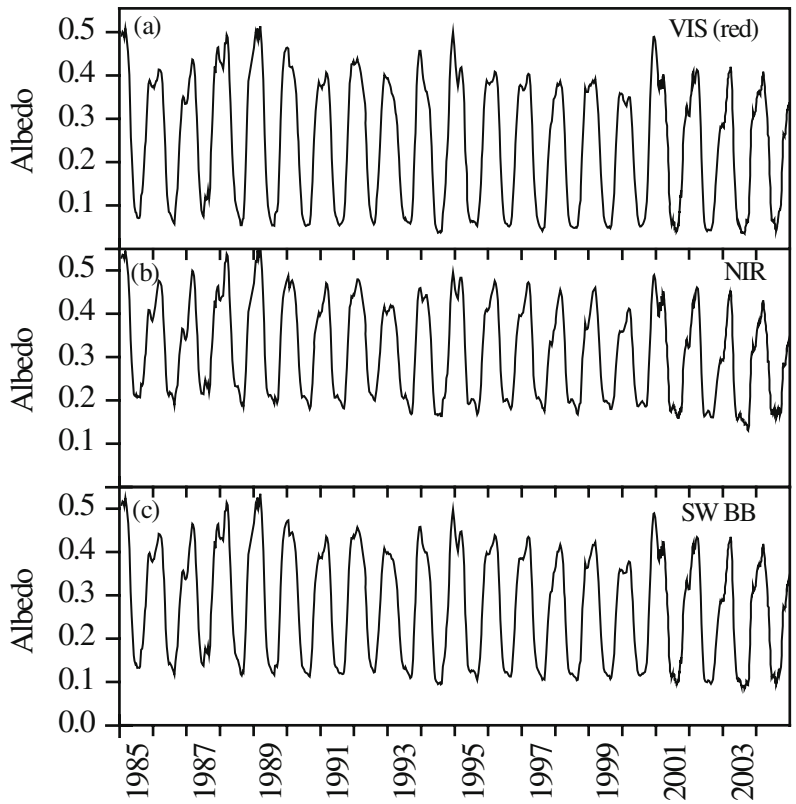

Fig. 4. Long-term variations of average surface albedo over the Mackenzie River Basin derived from AVHHR: (a) channel 1 – visible, red, (b) channel 2 – near-infrared (NIR), and (c) estimated SW broadband albedo

5 Conclusions and Discussion

For the first time, this work presents results on mapping surface albedo over the Mackenzie River Basin over a 20 year period (1985–2004) using data from more than a dozen satellite sensors at 1-km spatial resolution and at 10- to 16-day intervals. The principal sources of satellite data were from the AVHRR/NOAA instruments. Data from the MODIS sensor were extensively used from 2000 to 2004. Data from VGT/SPOT sensors were also assembled, but these results are not presented here.

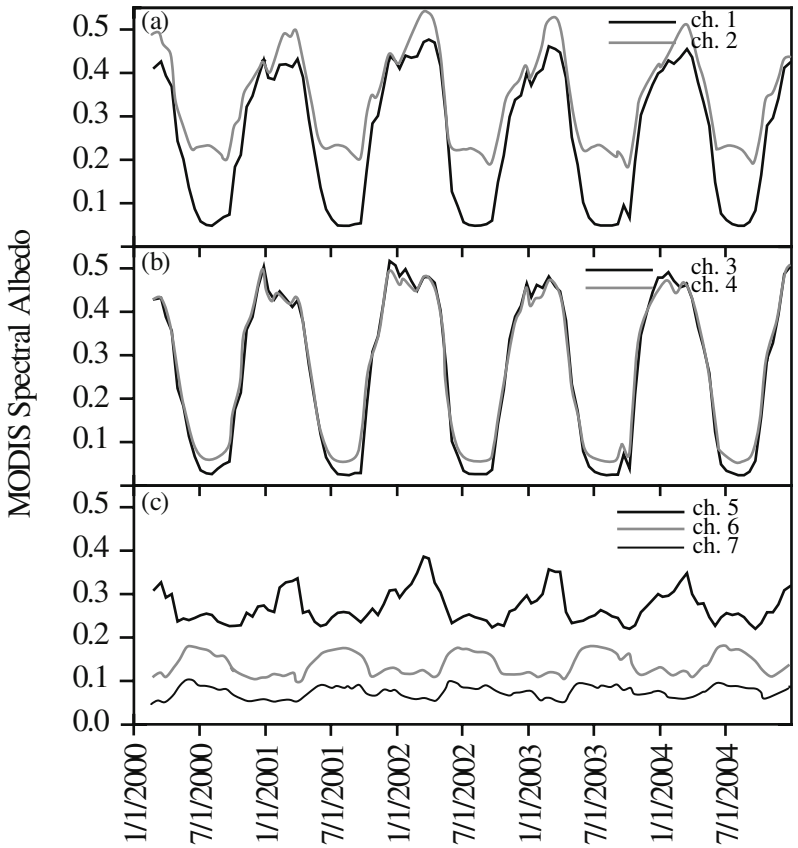

Fig. 5. Seasonal variations of MODIS spectral albedo from 2000 to 2004 averaged over the Mackenzie region

Table 1. Basin-averaged annual mean albedo for AVHRR and MODIS, 2000-04

Spectral band	AVHRR	MODIS	Δ (MODIS-VHRR)
1. Visible	0.22 ± 0.14	0.25 ± 0.16	0.03
2. NIR (0.8 μm)	0.28 ± 0.11	0.34 ± 0.11	0.06
3. Blue	-	0.26 ± .018	-
4. Green	-	0.27 ± 0.17	-
5. NIR (1.2 μm)	-	0.27 ± 0.04	-
6. SWIR (1.6 μm)	-	0.14 ± 0.03	-
7. SWIR (2.1 μm)	-	0.08 ± 0.01	-
SW BB	0.25 ± 0.13	0.27 ± 0.12	0.02

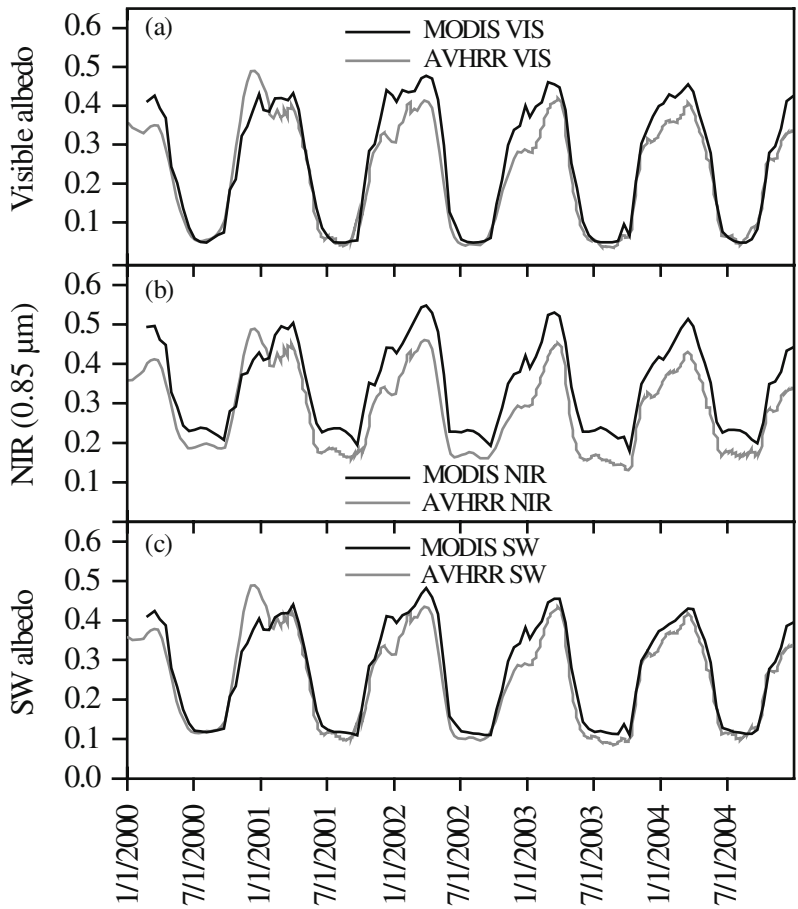

Fig. 6. Average albedo over the Mackenzie River Basin from AVHRR and MODIS data: (a) Channel 1 – visible albedo, (b) Channel 2 – NIR albedo, and (c) SW broadband albedo

The seasonal and interannual variability of spectral and broadband albedo over the study region were analyzed. Broadband albedo changes from 0.11±0.03 in the summer to 0.4-0.55 during winter. Visible (red) and SW broadband albedo derived from AVHRR and MODIS sensors are consistent (within 5% to 10% relative difference). However, systematic bias is observed between NIR channels, and this is due to differences in spectral response functions (Trishchenko et al. 2002). It is difficult to estimate the magnitude of long-term systematic trends in average surface albedo over the region because of the large interannual variability and uncertainties in

sensors properties, atmospheric correction, and the retrieval procedure. One major obstacle in deriving reliable information on surface albedo is cloud contamination, which complicated our analysis and reduced the number of available clear-sky surface observations. The generated datasets (albedo and the parameters of the BRDF) are available from the NRCan public archives at ftp://ftp.ccrs.nrcan.gc.ca/ad/CCRS_MAGS and http://geogratis.cgdi.gc.ca/frames.html. These data represent a valuable source of information for climate applications and model validation.

Acknowledgements

This work was conducted at the Canada Centre for Remote Sensing (CCRS), Earth Sciences Sector of the Department of Natural Resources Canada as part of Project J28 of the Program "Reducing Canada's Vulnerability to Climate Change". This work was partially supported by the Canadian Space Agency under the Government Related Initiative Program (GRIP) grant to CCRS. The authors thank Andrew Davidson and Darren Pouliot for their help with editing the manuscript.

References

Chen JM, Cihlar J (1997) A hotspot function in a simple bidirectional reflectance model for satellite applications. J Geophys Res 102:25907–25913

Cihlar J, Latifovic R, Chen JM, Trishchenko AP, Du Y, Fedosejevs G, Guindon B (2004) Systematic corrections of AVHRR image composites for temporal studies. Remote Sens Environ 89:217–233

Csiszar I, Gutman G (1999) Mapping global land surface albedo from NOAA AVHRR. J Geophys Res 104:6215–6228

Khlopenkov KV, Trishchenko AP (2007) SPARC: new cloud, snow, and cloud shadow detection scheme for historical 1-km AVHHR data over Canada. J Atmos Ocean Tech 24: 322-343

Latifovic R, Pouliot D (2005) Multi-temporal landcover mapping for Canada: methodology and product. Can J Remote Sens 31:347–363

Latifovic R, Trishchenko AP, Chen J, Park W, Khlopenkov KV, Fernandes R, Pouliot D, Ungureanu C, Luo Y, Wang S, Davidson A, Cihlar J (2005) Generating historical AVHRR 1-km baseline satellite data records over Canada suitable for climate change studies. Can J Remote Sens 31:324–346

Li X, Strahler AH (1992) Geometric-optical bidirectional reflectance modeling of the discrete crown vegetation canopy: effect of crown shape and mutual shadowing. IEEE T Geosci Remote 30:276–292

Luo Y, Trishchenko AP, Latifovic R, Li Z (2005) Surface bidirectional reflectance and albedo properties derived using a land cover-based approach with Moderate Resolution Imaging Spectroradiometer observations. J Geophys Res 110: D01106, doi:10.1029/2004JD004741

Nicodemus EF (1970) Reflectance nomenclature and directional reflectance and emissivity. Appl Optics 9:1474–1475

Ross J (1981) The radiation regime and architecture of plant stands. Dr W Junk Publishers

Roujean J-L, Leroy M, Deschamps P-Y (1992) A bidirectional reflectance model of the Earth's surface for the correction of remote sensing data. J Geophys Res 97:20455–20468

Strahler AH, Muller J-P, Team MS (1999) MODIS BRDF/albedo product: algorithm theoretical basis document, version 5.0

Trishchenko AP, Cihlar J, Li Z (2002) Effects of spectral response function on the surface reflectance and NDVI measured with moderate resolution sensors. Remote Sens Environ 81:1–18

Wang S, Trishchenko AP, Khlopenkov KV, Davidson A (2006) Comparison of IPCC AR4 climate model simulations of surface albedo with satellite products over northern Latitudes. J Geophys Res 111:D21108, doi:10.1029/2005-JD006728

Wanner W, Li X, Strahler AH (1995) On the derivation of kernels for kernel-driven models of bi-directional reflectance. J Geophys Res 100:21077–21090

Chapter 20

Comparison of Solar Radiation Budgets in the Mackenzie River Basin from Satellite Observations and a Regional Climate Model

Song Guo, Henry G. Leighton, Jian Feng and Murray MacKay

Abstract The reflected solar fluxes and the emitted outgoing longwave (LW) fluxes at the top of atmosphere (TOA) and the net surface solar fluxes from the Canadian Regional Climate Model (CRCM) are compared with those from satellite observations. Both broadband and narrowband satellite data are used in the evaluation of the CRCM results. It is found that the CRCM overestimated shortwave fluxes at the TOA and underestimated the surface absorbed solar fluxes. A systematic underestimate by the CRCM of the outgoing LW fluxes at the TOA is found during the winter season. Differences between the simulated clouds and cloud fields deduced from the satellite measurements persisted throughout the various phases of the project. The model–satellite differences improved with the improvement of the surface characteristics in the model.

1 Introduction

One major objective of the Mackenzie GEWEX Study (MAGS) is to understand the energy and hydrologic systems within Mackenzie River Basin (MRB) and their impacts on the regional climate system. The Canadian Regional Climate Model (CRCM) is a key component in the modeling strategy to study the energy and hydrological processes within MRB and their impacts on the regional climate system (MacKay et al. 2007). Due to the limited surface observation sites within the MRB, satellite observations are invaluable in the evaluation of the CRCM outputs.

Satellite observations can provide direct assessment of the modeling results through radiative budget comparison (Barker and Li 1995; Barker et al. 1994; Berbery et al. 1999; Feng et al. 2002, 2003; Li et al. 1997; Roads et al. 2003). At high latitudes, such as much of the MRB, geostationary satellites provide only an oblique view of the scene. Polar orbiting satellites, on the other hand, are particularly useful due to convergence of their

orbits at high latitudes. Radiation fluxes absorbed and emitted at the surface are important linkages between atmospheric and surface processes. The reflected solar fluxes at the top of atmosphere (TOA) that are deduced from satellite observations can provide an indirect way of deriving the absorbed surface solar fluxes (Li et al. 1993a; Pinker et al. 1995). Pinker and Laszlo (1992) relied on detailed radiative transfer calculations and known atmospheric vertical structures (e.g. cloud and aerosol vertical distributions) to deduce downward solar irradiance at the surface. The surface absorbed fluxes are then determined using an independent surface albedo (Pinker et al. 1995). Two parameterization approaches are used in the CERES SSF (Single Scanner Footprint) dataset. One is developed for cirrus cloud (Fu and Liou 1993) and the other is developed for all-sky conditions (Li et al. 1993a). The Li et al. (1993a) algorithm has been shown to agree remarkably well with tower observations (Li et al. 1993b).

The outgoing longwave (LW) radiation at the TOA (OLR) is also important in the model-satellite comparison as it can reveal errors in surface temperatures in the model and in the cloud properties (cloud thickness and cloud height). Therefore, both the reflected solar fluxes at the TOA and the OLR as well as the net surface solar fluxes from model simulations can be compared with satellite observations to evaluate the model results.

Both the satellite observations from the broadband sensors Scanner for Radiation Budgets (ScaRaB) and Clouds and the Earth's Radiant Energy System (CERES) and the narrowband Advanced Very High Resolution Radiometer (AVHRR) are used in comparisons with the CRCM results to evaluate the model performance. A new narrowband to broadband (NTB) conversion algorithm is developed to convert the AVHRR narrowband radiance to broadband radiance (Feng and Leighton 2005; Feng et al. 2002) in order to carry out the comparison.

This chapter summarizes analyses of three different versions of the CRCM. The first simulation (June–September 1994) makes use of the standard CRCM (Caya and Laprise 1999). This system utilizes the physical parameterization package of the Canadian Centre for Climate Modeling and Analysis (CCCma) general circulation model GCMII (McFarlane et al. 1992). Radiation budgets for this system were analyzed by Feng et al. (2002). The second simulation examines the Canadian GEWEX Enhanced Study (CAGES) water year 1998–99. The model used in this experiment is described by MacKay et al. (2003). The dynamic component is unaltered but the physics package was upgraded to GCMIII, which includes an improved radiation code as well as the Canadian Land Surface Scheme – CLASS 2.7. The physics package is identical to that used in the GCM except that cloud onset is diagnosed following Lorant et al. (2002) to account

for the higher resolution of the CRCM. This simulation has been analyzed by Feng et al. (2003). The final simulation covers the period 1997–2003 and is evaluated against CERES data for 2000–03. The model in this case is identical to that described in MacKay et al. (2003) with improvements to the land surface characterization and initial soil conditions as outlined in MacKay et al. (2007).

The main objective of this project is to compare the radiation fields both at the TOA and at the surface from the CRCM with satellite observations and to interpret the differences. Besides being a tool for the evaluation of the CRCM, satellite observations can also provide radiation budgets both at the TOA and at the surface in the MRB.

2 Study Domain

Three different periods were used in the comparison of satellite observations with the CRCM simulations to evaluate the model results. The daytime reflected solar fluxes at the TOA and the net surface solar fluxes for June, July, August, and September 1994 were used in the first comparison with the CRCM results (Feng et al. 2002). Then the focus was on the 14-month CAGES period. The retrieved and derived results from the NOAA narrowband AVHRR sensor are mainly used for both the summer 1994 comparison and the 14-month CAGES period comparison as there were only limited satellite observations over the MRB from the broadband ScaRaB sensor. The launching of the NASA broadband CERES satellite sensors on board Terra and Aqua platforms in 1999 and 2002 makes the model–satellite comparison more direct as the CERES sensor is designed to measure solar-reflected and earth-emitted radiation at the TOA with a design objective of 1% uncertainty (Wielicki et al. 1996). Post-launch validation shows the design objective is achieved (Loeb et al. 2003b).

3 Methods

3.1 Narrowband to Broadband Conversion

ScaRaB was the only broadband sensor available to measure TOA fluxes directly during the summer of 1994 and the 14-month CAGES period. Due to the limited coverage of the MRB by ScaRab (FM-1) on board the Russian Meteor-3 satellite during the summer of 1994 and (FM-2) on board

the Russian Resurs satellite during the 14-month CAGES period, the NOAA AVHRR is used as the primary sensor to provide more extensive datasets of radiative budgets during these two comparison time periods.

Many NTB algorithms have been developed independently before and after this study (e.g., Hucek and Jacobowitz 1995; Laszlo et al. 1988; Li and Leighton 1992; Li and Trishchenko 1999; Valiente et al. 1995). Due to the differences in surface type and the influences from solar zenith angle and satellite viewing angle, a new NTB algorithm was developed specifically for the MRB region by Feng et al. (2002) using narrowband and broadband ScaRaB data. The NTB conversion is based on a linear relationship, $F_{bb} = aF_{nb} + b$, where F_{bb} and F_{nb} are broadband and narrowband radiative radiances, respectively. The regression coefficients a and b are derived based on surface type, cloud cover, cosine of solar zenith angle, and cosine of satellite viewing angle. Eight surface types are used for MRB region based on the Mackenzie Basin Impact Study (MBIS) land classification scheme (Yin et al. 1994). The mean differences and standard deviations of TOA fluxes from broadband ScaRaB measurements and the NTB conversion applied to ScaRaB narrowband in different month are investigated and the maximum monthly mean-difference for a certain surface type within the MRB for all passes is 3.5 W m^{-2} and the maximum standard deviation is 11.4 W m^{-2}, indicating the good consistency between the two methods (Feng et al. 2002). A narrowband to narrowband conversion algorithm (NTN) is also developed to convert the AVHRR visible channel (ch1) radiance to the SacRaB visible channel (ch1) radiance. With the use of both the NTB and the NTN algorithms, broadband radiances at the TOA can be deduced from AVHRR narrowband (visible channel) radiance.

The broadband fluxes deduced from AVHRR ch1 have been compared with ScaRaB broadband observations (Fig. 1). Data from nine pairs of collocated scenes with time differences of less than 15 minutes were available. The comparisons show that the mean TOA flux difference of the nine comparisons is -0.2 W m^{-2} and the standard deviation is 19.3 W m^{-2} (Feng et al. 2002), indicating that the AVHRR data may be used to deduce broadband fluxes. The net surface solar fluxes from the AVHRR were compared with surface solar radiation measurements at Inuvik and Great Slave Lake. The tower measurements were interpolated to match the time of satellite observations. Those results indicated that the monthly-mean differences of all the satellite passes for different sites are from -3.0 to 8.6 W m^{-2} for NOAA-12 and from -6.8 to 4.5 W m^{-2} for NOAA-14, confirming the reliability of the net surface solar fluxes from the AVHRR (Feng et al. 2003). The comparison of AVHRR deduced net surface fluxes and the

surface solar radiation measurements at Havikpak Creek (Fig. 2) also demonstrates good agreement of the two with the monthly-mean differences of all interpolated tower measurements and satellite observations of all the satellite passes -5.2 to -0.2 W m^{-2} (Feng et al. 2003). These comparisons suggest that the NTB algorithm is accurate and reliable enough to carry out any model–satellite comparison between AVHRR narrowband datasets and the CRCM results.

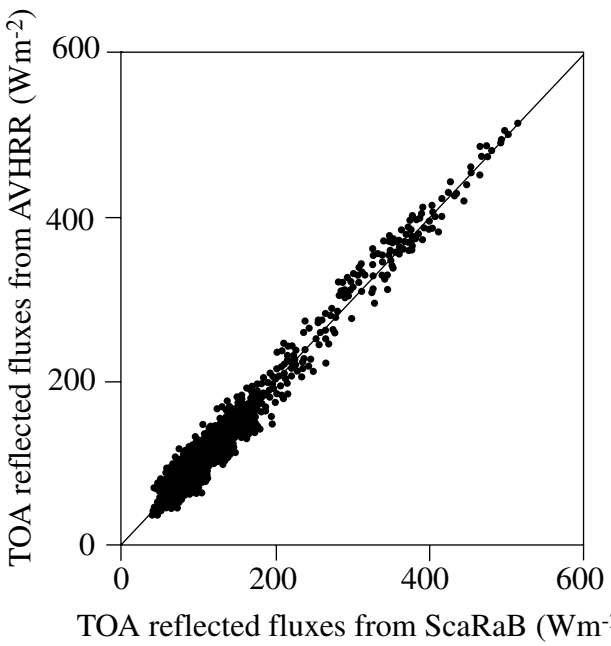

Fig. 1. Comparison of the reflected solar fluxes at the TOA from the AVHRR and the ScaRaB (excerpted from Feng et al. 2002)

Feng and Leighton (2005) also used ScaRaB broadband and narrowband data collected during 1994–95 to derive the NTB relationship for other surface types, such as desert, ocean, snow, land, and coastal (mixed land and ocean) surfaces. NTN conversion between the ScaRaB visible channel (narrowband) and the AVHRR visible channel (narrowband) radiances were calculated with the Moderate Resolution Transmittance (MODTRAN) code version 3.7 for different surface types and cloud cover. With the developed NTB and NTN relationships, broadband radiance at TOA can be derived from the AVHRR narrowband (visible channel) radiance. The derived conversion coefficients for different surface types were

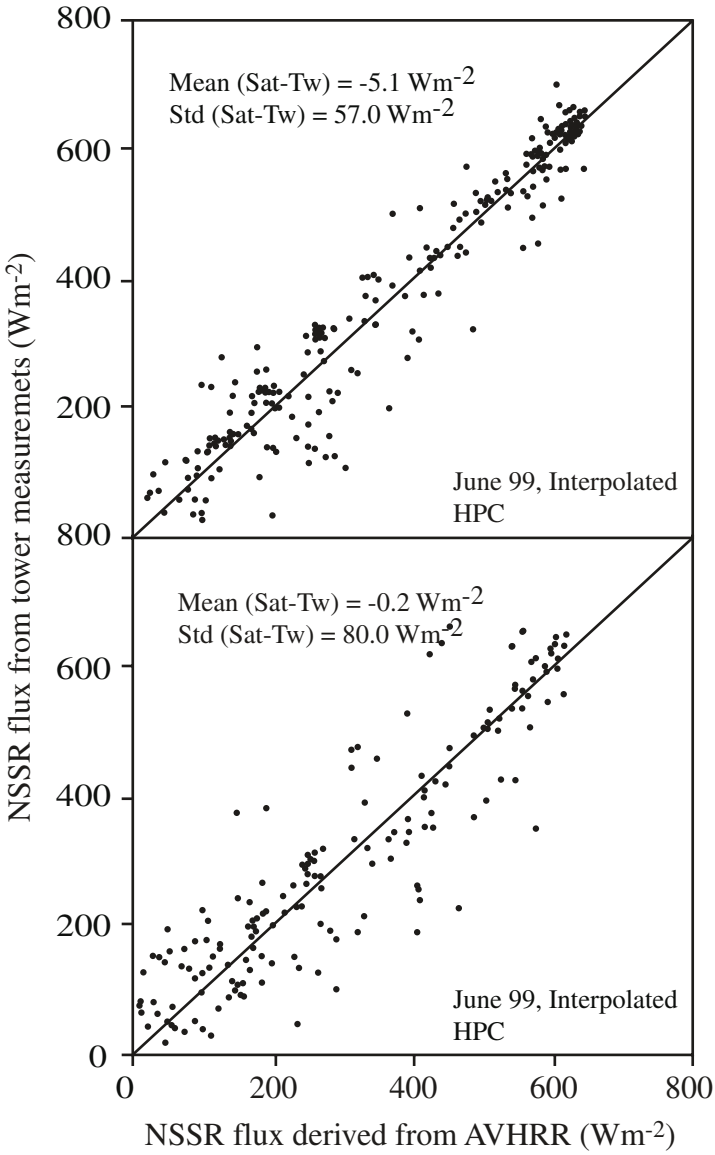

Fig. 2. Comparison of interpolated net surface solar fluxes from AVHRR with tower measurement at HPC for June and July 1999 (excerpted from Feng et al. 2003)

evaluated with other ScaRaB data which are not used for developing the algorithm and the second NTB model developed by Li and Trishchenko

(1999). The results indicated that the flux differences between ScaRaB broadband observations and narrowband derivations were of the order of 1 W m^{-2} with standard deviation of the order of 15 W m^{-2} (Feng and Leighton 2005). The reliability of all the NTB algorithms developed by Feng and Leighton (2005) for different surface types demonstrates the reliability and robustness of using narrowband AVHRR radiance in deriving broadband radiance and is an indirect proof of the reliability of using the AVHRR data in evaluation of the CRCM.

3.2 Data Matching in Model–satellite Comparison

The data-matching strategy is described in detail in Feng et al. (2002, 2003). The CRCM simulation for MRB region was run on a polar stereographic projection with a resolution of 51 km and a time step of 15 minutes (Feng et al. 2003). The 15-minute model outputs are averaged to the 1-hour outputs. More detailed description of the CRCM simulation is given by MacKay et al. (2003, 2006). In order to obtain values from satellite observations that are consistent with model outputs temporally, the satellite data are extrapolated to the model output time by using the ERBE directional model (Brooks et al. 1986). If the satellite observation time is within 0.5 h of the model output time, the extrapolated fluxes by the Brooks-model are used in the comparison directly. Otherwise, if there are two satellite observations within 1.5 h of the model output time, the two extrapolated fluxes from the Brooks-model at the two satellite observation times are interpolated to get the flux at the model output time. Finally, the temporally collocated satellite data are matched to the model data spatially by averaging the satellite data within each model grid box.

3.3 Radiative Fluxes Absorbed at the Surface

The absorbed surface solar fluxes are deduced from the reflected solar fluxes at the TOA by using the algorithm developed by Li et al. (1993a). The net surface flux is parameterized in terms of TOA reflected solar flux, solar zenith angle, and column water amount. The algorithm has been validated against surface measurements and results indicated that the differences between tower measurements and satellite retrieved surface absorbed fluxes are within 10 W m^{-2} (Li et al. 1993b). An estimated accuracy of 5 W m^{-2} has been found in the comparison of the surface fluxes deduced from the algorithm of Li et al. (1993a) with the global energy balance archive data (Li et al. 1995).

4 Results

4.1 Satellite–model Comparison during the 1994–95 Water Budget Year

The satellite-model comparison during the 1994–95 water budget year is described in detail in Feng et al. (2002). The monthly hourly-mean (12:00–24:00) basin-average reflected solar fluxes at the TOA and surface absorbed fluxes from both satellite observations (ScaRaB and AVHRR) and the CRCM simulations for June–September 1994 are compared. The reflected solar fluxes at the TOA from the CRCM simulations generally agree very well with those from satellite observations. Comparison of the monthly one-hour fluxes from the CRCM simulations and satellite observations of reflected solar fluxes at the TOA and net surface solar fluxes in the MRB for June–September 1994 are shown in Fig. 3. The mean differences of the daily average (12:00–24:00 UTC) fluxes in June, July, August, and September are 0.8, -19.4, -5.5, and 2.6 W m^{-2}, respectively (Feng et al. 2002). The spatial distribution of the reflected solar fluxes at the TOA and net surface solar fluxes from both the AVHRR and the model have maximum values in the southern and western portions of the Basin, indicating higher cloud amounts in these regions. A systematic difference is found in the diurnal cycle of model–satellite differences. The monthly-mean model–satellite (CRCM minus satellite) differences of reflected solar fluxes at the TOA in the morning are 20 W m^{-2} for June, 30 W m^{-2} for July while the model–satellite differences in the afternoon are -20 W m^{-2} for June and -10 W m^{-2} for July (Feng et al. 2002). The model and satellite basin image comparison reveals that the net surface fluxes from the CRCM are always larger than those from satellite observations. For 1994, the monthly daily-mean (12:00–24:00 UTC) basin-averaged model–satellite differences of net surface reflected solar fluxes are 68.4 W m^{-2} for June, 40.0 W m^{-2} for July, 38.9 W m^{-2} for August, and 31.5 W m^{-2} for September, respectively (Fig. 4). Individual pixel flux difference may be larger than 100 W m^{-2}. It can also be concluded that the CRCM overestimates the net surface radiation budgets by 15.3%, 11.1%, 13.8%, and 14.6% for June, July, August, and September, respectively (Feng et al. 2002).

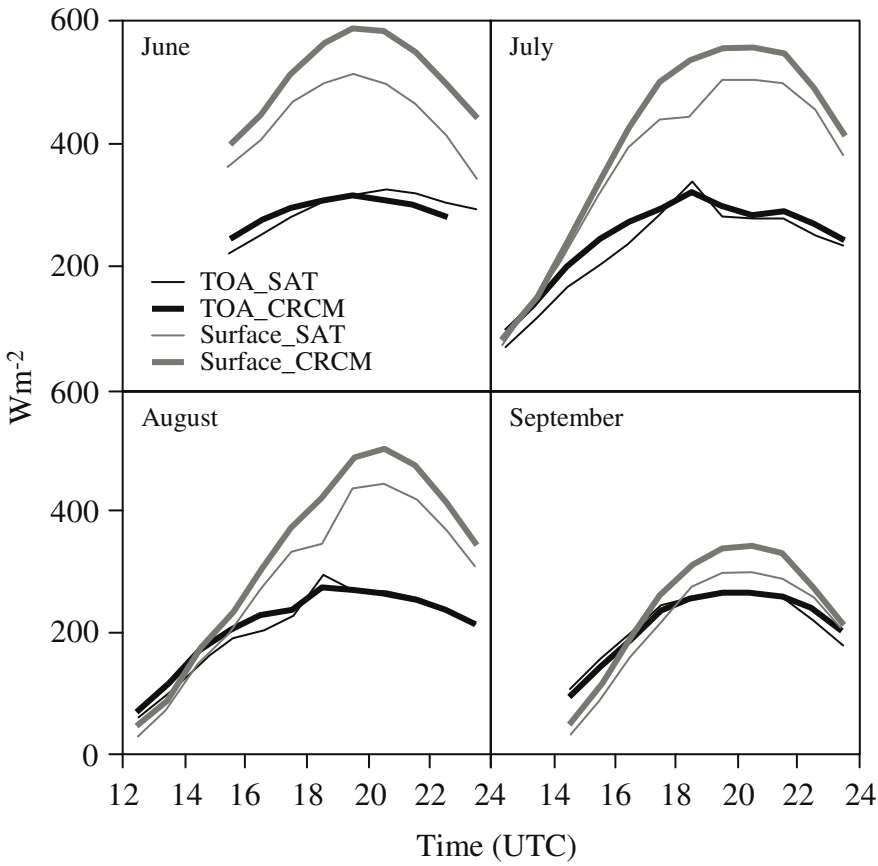

Fig. 3. Comparison of the monthly one-hour average fluxes from the CRCM simulations and satellite observations for the reflected solar fluxes at the TOA and the net surface solar fluxes in MRB in June–September 1994 (excerpted from Feng et al. 2002)

4.2 Satellite–model Comparison during the CAGES Period

The model–satellite comparison during the 14-month CAGES period is described in Feng et al. (2003). Comparisons of monthly-mean basin-average solar fluxes at the TOA and at the surface from the CRCM and AVHRR retrievals are shown in Fig. 5. The comparison is done between August 1998 and September 1999 except the winter months (November 1998 to February 1999) due to the small solar fluxes and short day-light

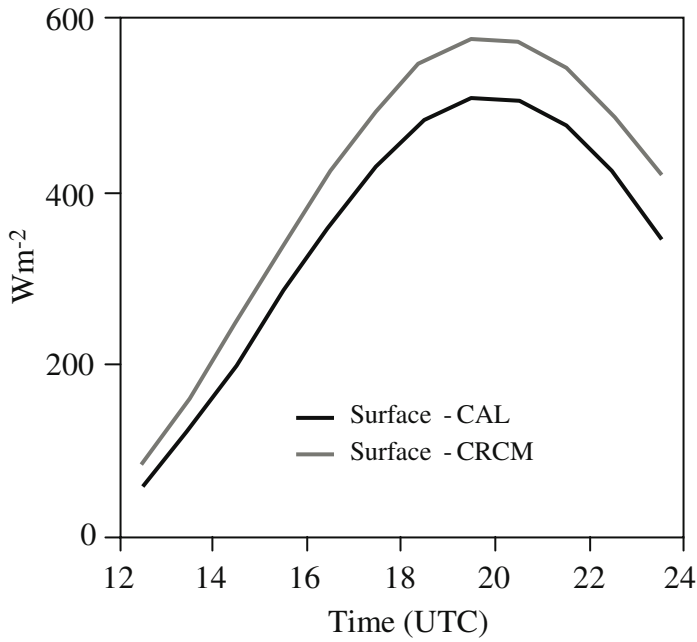

Fig. 4. Comparison of the net surface solar fluxes from the CRCM and from the AVHRR (derived from the algorithm of Li et al.) in June 1994 (excerpted from Feng et al. 2002)

4.2 Satellite–model Comparison during the CAGES Period

The model–satellite comparison during the 14-month CAGES period is described in Feng et al. (2003). Comparisons of monthly-mean basin-average solar fluxes at the TOA and at the surface from the CRCM and AVHRR retrievals are shown in Fig. 5. The comparison is done between August 1998 and September 1999 except the winter months (November 1998 to February 1999) due to the small solar fluxes and short day-light period. During the summer (June to September), the CRCM overestimated the reflected solar fluxes at the TOA by amounts from 16 to 44 W m^{-2} and underestimated the net surface solar fluxes by 14 to 56 W m^{-2} (monthly-mean basin-average) (Feng et al 2003). For October 1998 and March and April 1999, both reflected solar fluxes at the TOA and net surface solar fluxes from the CRCM simulations and AVHRR retrievals agree well (<1 W m^{-2} difference at the TOA and 7–11W m^{-2} at the surface). For May

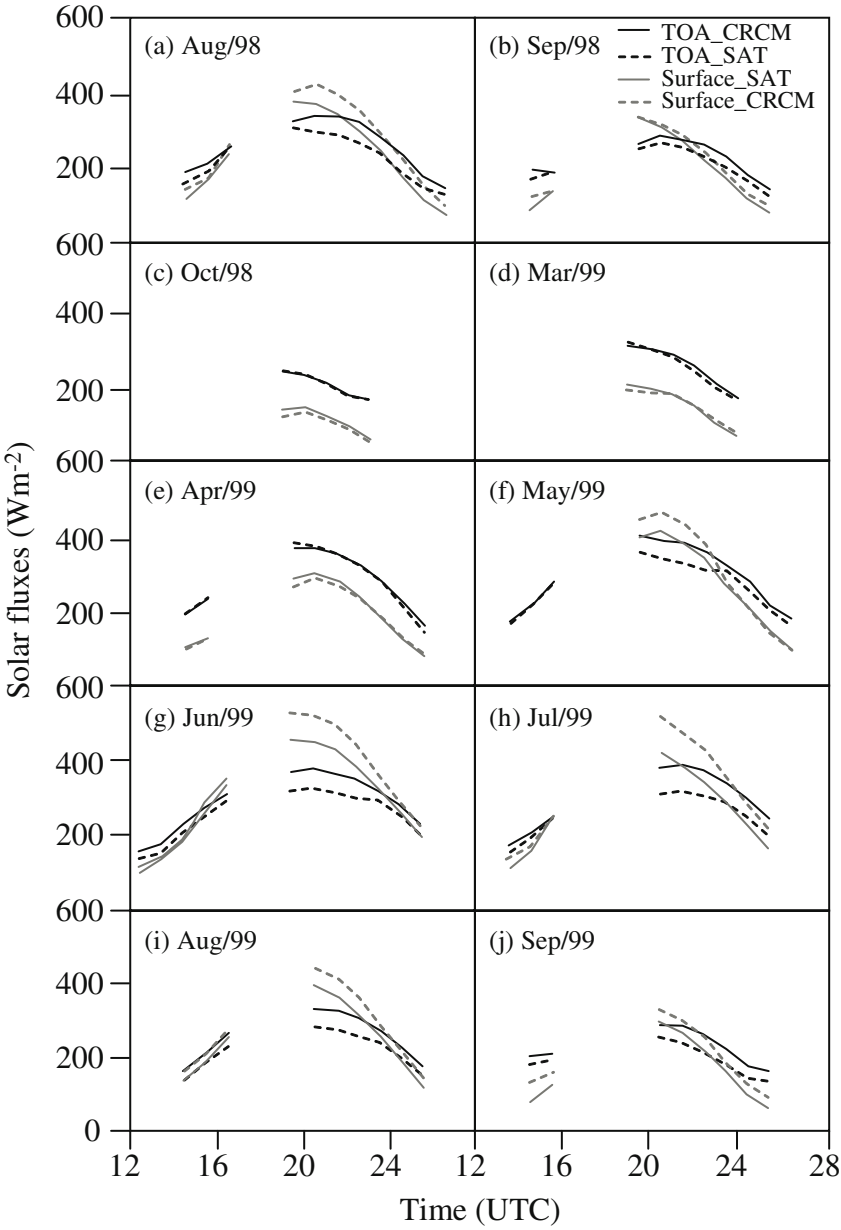

Fig. 5. Comparisons of monthly-mean basin-average solar fluxes at the TOA and at the surface at each 1-h period between the CRCM and the satellite retrievals (excerpted from Feng et al. 2003)

1999, both the TOA reflected fluxes and net surface solar fluxes from the CRCM and AVRHH are in agreement in the early morning and in late afternoon, but the differences exceed 50 W m^{-2} around noon (Feng et al. 2003). Figure 6 illustrates the clear-sky comparison of reflected solar fluxes at the TOA and net surface solar fluxes from the CRCM and the AVHRR retrievals. The results indicate that the CRCM underestimates the reflected solar fluxes at the TOA by 24 and 20 W m^{-2} and overestimates the net surface solar fluxes by 38 and 31 W m^{-2} in August 1998 and June 1999. For the other four months, the model–satellite differences for the reflected solar fluxes at the TOA are -2.6, -8.9, -3.4 and 6.5 W m^{-2} and for the net surface solar fluxes are between 7.6 and 15.6 Wm^{-2} (Feng et al. 2003).

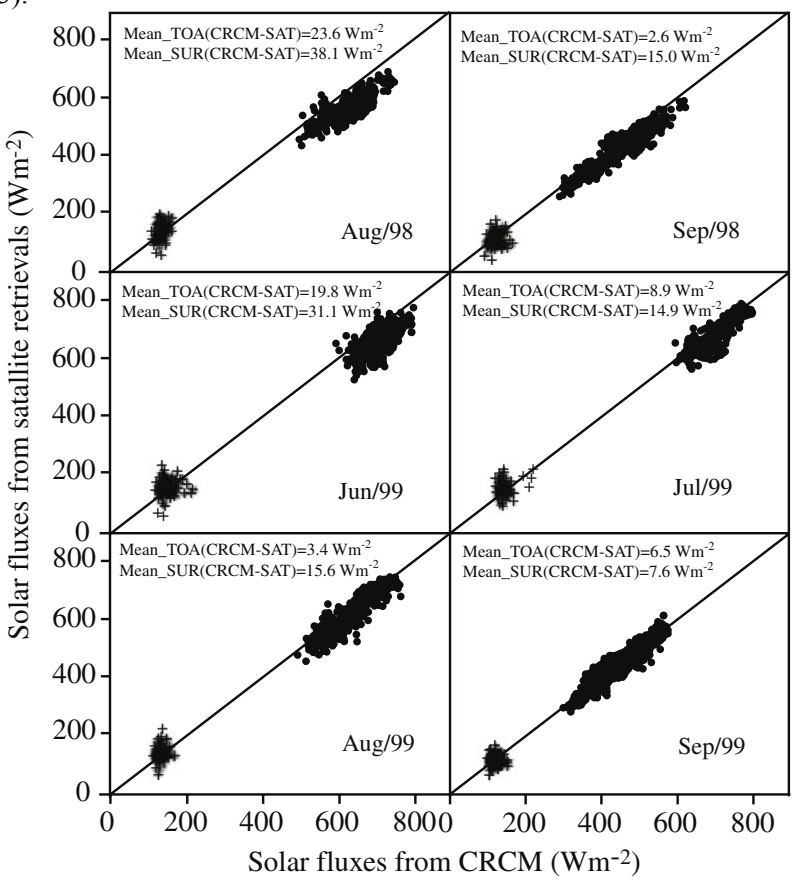

Fig. 6. Comparisons of reflected solar fluxes at the TOA (plus signs) and net surface solar fluxes (solid circles) under clear skies from the CRCM and the AVHRR retrievals (excerpted from Feng et al. 2003)

Both the CRCM simulation and AVHRR retrievals show high TOA albedo along the western border of the Basin, corresponding to greater cloud amounts over the mountains in that area (Feng et al. 2002,2003), and/or the presence of snow. Over the three Great Lakes in the MRB, the CRCM overestimated the reflected solar fluxes at the TOA significantly as the model does not consider lakes in its surface scheme. The CRCM overestimated the reflected solar fluxes at the TOA over most parts of MRB during the summer months except August and September of 1998. For the month of March and April 1999, a negative bias is found in the northern Basin and a positive bias is found in the southern Basin for the TOA reflected solar flux; the opposite sign of the biases results in smaller monthly-mean basin-average model–satellite difference (Feng et al. 2003).

As cloud cover information from the satellite is not reliable over snow covered surfaces, only the snow-free months of June to September are used in investigating the influence of clouds on model–satellite flux differences. The cloud fraction from the CRCM is consistently overestimated in the summer months (Fig. 7). The cloud fraction monthly-mean differences are between 0.15 and 0.32 for August and September in 1998 and June to September in 1999. The basin-average cloud fraction for these six months is 0.69 from the CRCM and 0.46 from the satellite retrievals (Feng et al. 2003). The overestimate of cloud fraction by the CRCM is consistent with its overestimation of the reflected solar fluxes at the TOA.

From a comparison of the mean differences of the reflected solar fluxes at the TOA from the CRCM and the satellite for clear-skies for the period of June to September 1999, positive biases are found mainly in the western part of the Basin and over the three lakes. This can be explained by the overestimate of surface albedo caused by presence of snow in the CRCM simulation in the western mountains and an overestimate of surface albedo over the three lakes which are not resolved by the model as water surfaces.

The CRCM underestimates the OLR by 6 to 12 W m^{-2} from November 1998 to March 1999 (Fig. 8), indicating an overestimation of cloud fraction, that the simulated cloud top is too high, or that the surface temperature is underestimated in the CRCM (Feng et al. 2003). MacKay et al. (2003) found a consistent underestimate of surface temperature throughout the entire MRB.

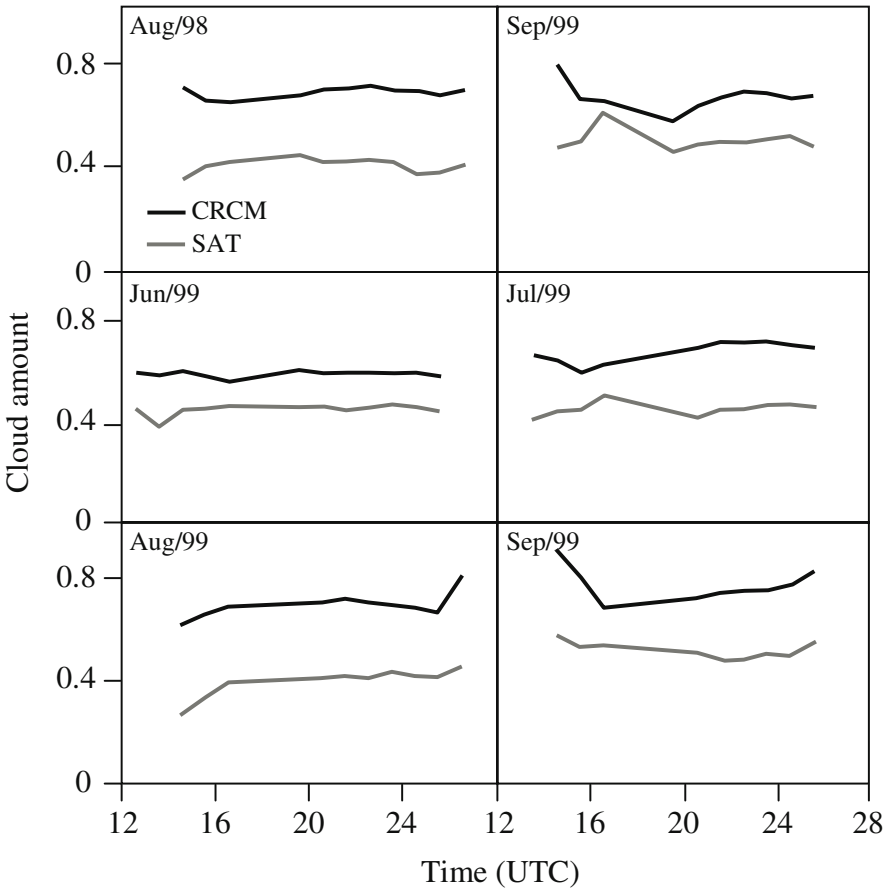

Fig. 7. Comparison of hourly basin-average cloud amount from the CRCM and the AVHRR retrievals for summer months (excerpted from Feng et al. 2003)

4.3 Long-term Satellite–model Comparison from CERES Observations and the CRCM Simulations

Long-term (March 2000 to Sept. 2003) monthly-mean basin-average model–satellite (CERES results subtracted from CRCM results) differences for the reflected solar fluxes at the TOA and the net surface solar fluxes at 19 UTC (12PM local time) are shown in Fig. 9. It is found that CRCM overestimated the monthly-mean basin-average reflected solar flux at the TOA by 25 W m^{-2} at 19 UTC (19 W m^{-2} between 18:00 UTC and 22:00 UTC) and underestimated the basin-average net surface solar sur-

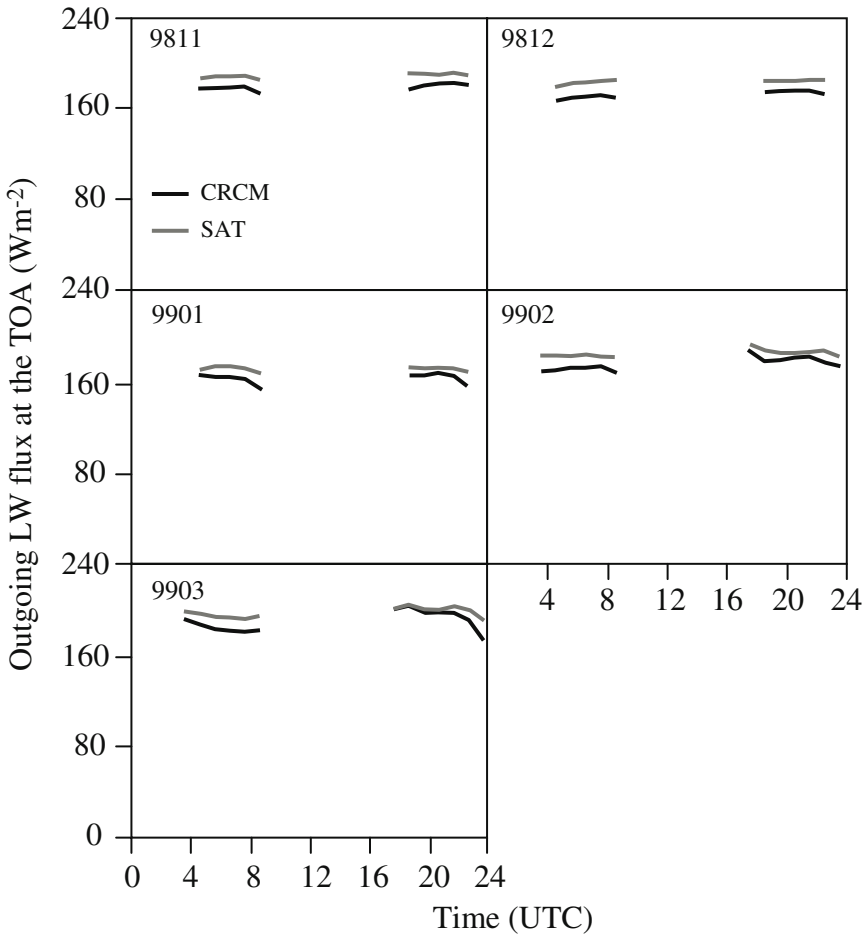

Fig. 8. Comparison of hourly OLR from the CRCM and satellite retrievals (excerpted from Feng et al. 2003)

face by 33 W m^{-2} at 19 UTC (26 W m^{-2} between 18:00 UTC and 22:00 UTC). The maximum differences occur in the summer (35 W m^{-2} at the TOA and -51 W m^{-2} at the surface, at 19 UTC). Both the overestimate of TOA reflected fluxes and underestimate of the net surface fluxes by CRCM indicate that either the surface albedo used in CRCM is too high or the cloud fraction is too large or the cloud is too thick. The monthly-mean basin-average OLR from the CRCM run agrees very well with the CERES 19 UTC observations at the TOA (Fig. 10), with a mean difference of -4 W m^{-2}. A consistent underestimate of the OLR by the CRCM (-8.8 W m^{-2}) is found during the winter season, indicating that either the cloud fraction or

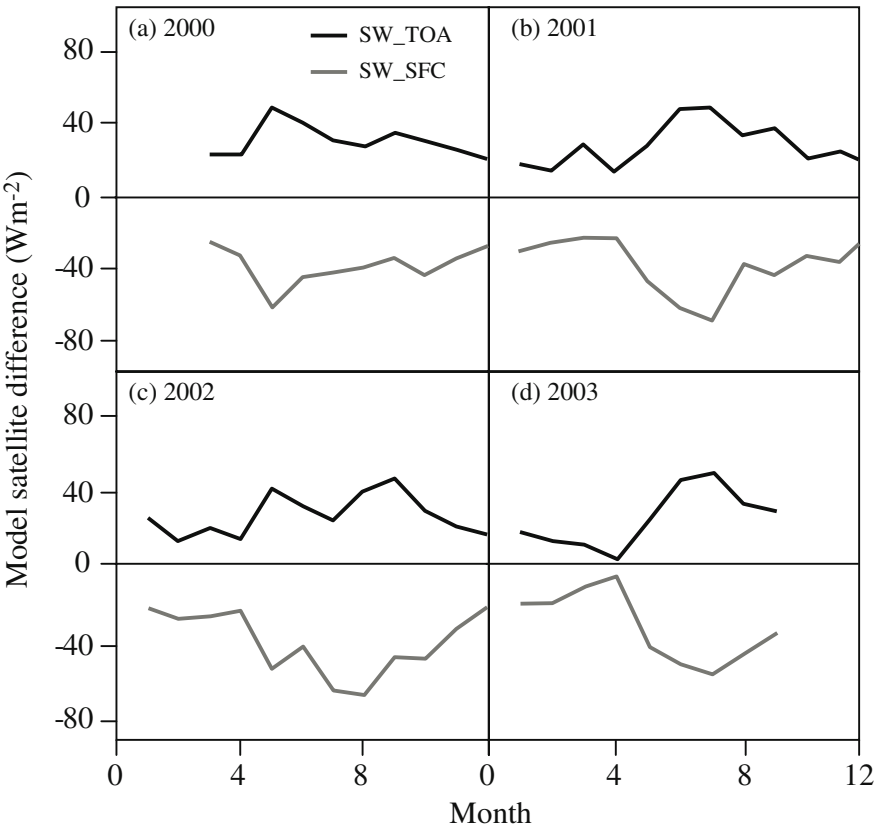

Fig. 9. Monthly-mean basin-average model-satellite (CRCM minus CERES) differences for the reflected solar fluxes at the TOA and net surface solar fluxes at 19 UTC in the year (a) 2000 (b) 2001 (c) 2002 (d) 2003

cloud thickness is overestimated or that the surface temperature is underestimated, or the cloud height is overestimated.

The model–satellite differences for both reflected solar fluxes at the TOA and net surface solar fluxes do not have a systematic seasonal trend except that the differences reach their maximum during the summer. The causes include the larger in-coming solar radiation and the greater wildfire aerosol interference during the summer months (Guo et al. 2007).

Larger model–satellite differences are found under cloudy conditions than clear-sky conditions, indicating that the cloud fields simulated in the CRCM could have larger impacts on radiation budgets. The larger cloud fraction simulated by the CRCM (Feng et al. 2003) is consistent with the overestimate of reflected solar fluxes at the TOA and the underestimate of

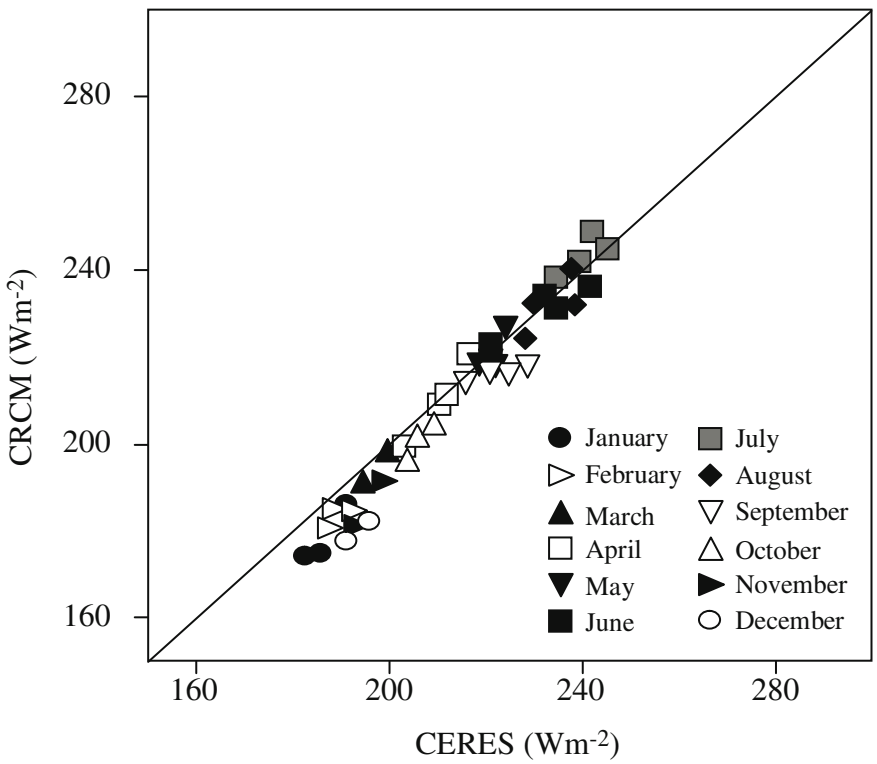

Fig. 10. Comparison of monthly-mean basin-average OLR at 19 UTC from CRCM simulations and CERES observations

net surface solar fluxes. The overestimate of cloud fraction is expected to result in an underestimate of OLR. In fact, there is no obvious bias in the OLR in the summer (Fig. 10). In the winter the underestimate of OLR may be due to a combination of a surface and a cloud top that is too cold (MacKay et al. 2006).

Surface type might also play an important role in the model–satellite differences. Larger biases are found for the three lakes as they are treated as land in the CRCM simulations. Slightly smaller model–satellite differences are found for monthly-mean basin-averaged night time OLR than those of daytime, indicating that the differences are mainly caused by the temperature differences of the night time and daytime.

5 Discussion and Conclusion

The CRCM was one of the key models used in the MAGS project to study the energy and hydrological processes within the MRB and their impacts on the regional climate system. The evaluation of the CRCM outputs through comparisons of radiation fields both at the TOA and at the surface with satellite observations is thus important in achieving the MAGS objectives. Surface radiation is one of the main linkages between atmospheric and surface processes. The net surface solar fluxes can been derived from the satellite-measured reflected solar fluxes at the TOA through the algorithm of Li et al. (1993a) which has been validated by both surface tower measurements (Li et al. 1993b) and other independent datasets (Li et al. 1995).

The reflected solar fluxes and OLR can be measured by broadband instruments such as CERES and ScaRaB. Furthermore, AVHRR visible channel radiances can be converted to broadband radiances by means of NTN and NTB algorithms for radiation budget studies. The AVHRR has the advantage of offering data for much longer periods than the broadband instruments (Feng and Leighton 2005; Feng et al. 2002, 2003) and the AVHRR data provides better daily coverage than that from broadband instruments because usually more than one AVHRR sensor was in orbit on a polar orbiting satellite.

The model–satellite solar radiative flux differences at both the TOA and at the surface are mainly controlled by the accuracy of the cloud fields simulated by the model. Errors in the model surface albedo are also responsible for differences between the model and satellite data. Additional uncertainty in the model–satellite data comparisons arises from inadequate treatment of the atmospheric aerosol, from satellite radiance measurements, from radiance to radiative flux through the angular distribution model (ADM), from narrowband to broadband (NTB) conversion, and from net surface solar flux derived through the algorithm of Li et al. (1993a).

For the summer of 1994, the model–satellite differences (monthly daily-average between12:00 to 24:00 UTC) of reflected solar fluxes at the TOA are 2.8, 8.8, 2.7 and 1.2% for June to September, respectively (Feng et al. 2002), corresponding to 0.82, -19.4, -5.5 and 2.6 W m^{-2}. The monthly daily-average (12:00-24:00 UTC) basin-mean differences of net surface solar fluxes from June to September are 68.4, 40.0, 38.9 and 31.5 W m^{-2}, respectively (Feng et al. 2002). Feng et al. (2002) noted that the radiation scheme used in the CRCM may produce too little atmospheric absorption

under clear-sky conditions, leading to excessive insolation over the land. Barker and Li (1995) showed that the adoption of more accurate water vapor transmittance functions and the inclusion of a background tropospheric aerosol in the physical parameterization package improved model radiation budgets both at the TOA and at the surface. However, even with these modifications in the CRCM, the model–satellite comparison during the 14-month CAGES period showed no significant improvement. This indicates that other factors such as the model cloud properties and the surface characteristics might play more important roles than the radiative transfer scheme itself. Feng et al. (2003) found that the CRCM overestimates the TOA reflected fluxes by 16 to 44 W m^{-2} (an average of 33 W m^{-2}) and underestimates the net surface solar radiation by 14 to 56 W m^{-2} during the snow-free summer months. The TOA reflected fluxes agree well with the satellite retrievals with a mean difference of 2.1 W m^{-2} in March and April, when the MRB is mostly covered by snow (Feng et al. 2003). Detailed comparison indicated that the CRCM underestimates TOA reflected fluxes in the northern part of the Basin and overestimates in the south. This is attributed by Feng et al. (2003) to errors in the spatial variations of the surface albedo for snow-covered surfaces. The OLR is underestimated by 6–12 W m^{-2} in the CRCM and is explained by its underestimation of surface temperature (Feng et al. 2003).

Under clear skies, basin-averaged monthly mean solar flux differences between the CRCM and satellite are about 6.5 W m^{-2} at the TOA and 15.3 W m^{-2} for the flux absorbed at the surface, values that are substantially smaller than for the all-sky comparisons. The major biases in the model–satellite differences for all skies are mainly due to the cloud simulation. It is found the cloud fraction is consistently overestimated by the CRCM in the summer (Fig. 7): the basin-average cloud fraction for these six months is 0.69 from the CRCM and is 0.46 from the satellite retrievals (Feng et al. 2003). The overestimate of cloud fraction by the CRCM is consistent with its overestimation of the reflected solar fluxes at the TOA.

No further improvement was made to the cloud scheme used in the CRCM for the March 2000 to September 2003 simulation, but a more sophisticated treatment of the surface scheme was introduced (MacKay et al. 2006). Comparisons for this period with data from CERES on the Terra and Aqua satellites showed that the basin-average TOA reflected solar flux is overestimated by 25 W m^{-2} at 19 UTC (19 W m^{-2} between 18 and 22 UTC) and the basin-average flux absorbed at the surface is underestimated by 33 W m^{-2} at 19 UTC (26 W m^{-2} between 18 and 22 UTC) by the CRCM. The model–satellite differences are slightly reduced compared to the model–satellite comparison results for the summer of the CAGES pe-

riod. This may be attributed partially to the modification of the land surface scheme, but the use of broadband data and an improved angular distribution model (Loeb 2003a) to convert CERES radiances to fluxes may also be important. The monthly-mean basin-average OLR from the CRCM run agrees well with the satellite observations with a mean difference of -4 W m^{-2}, but with a consistent underestimate of OLR by the CRCM (-8.8 W m^{-2}) during the winter. The larger winter biases are mainly due to the cloud fields simulated by the CRCM, but underestimation of the surface temperature may also contribute (MacKay et al. 2006).

6 Acknowledgements

The CERES data were obtained from the NASA Langley Research Center Atmospheric Sciences Data Center, the MODIS data were obtained through the Goddard Space Flight Center Data Center.

7 References

Barker HW, Li Z (1995) Improved simulation of clear-sky shortwave radiative transfer in the CCC GCM. J Climate 8:2213–2223

Barker HW, Li Z, Blanchet JP (1994) Radiative characteristics of the Canadian Climate Centre second-generation general circulation model. J Climate 7:1070–1091

Berbery EH, Mitchell KE, Benjamin S, Smirnova T, Richie H, Hogue R, Radeva E (1999) Assessment of land-surface energy budgets from regional and global models. J Geophys Res 104:19329–19348

Brooks DR, Harrison EF, Minnis P, Suttles JT (1986) Development of algorithms for understanding the temporal and spatial variability of the earth's radiation balance. Rev Geophys 24:422–438

Caya D, Laprise R (1999) A semi-implicit, semi-Lagrangian regional climate model: the Canadian RCM. Mon Weather Rev 127:341–362

Feng J, Leighton HG (2005) Broadband solar radiances from visible band measurements: a method based on ScaRaB observations and model simulations. Int J Remote Sens DOI:10.1080/01431160500181754

Feng J, Leighton HG, MacKay MD (2003) Radiation budgets in the Mackenzie River Basin: retrieval from satellite observations and an evaluation of the Canadian Regional Climate Model. J Hydrometeorol 4:731–747

Feng J, Leighton HG, MacKay MD, Bussières N, Hollmann R, Stuhlmann R (2002) A comparison of solar radiation budgets in the Mackenzie River Basin

from satellite measurements and a regional climate model. Atmos Ocean 40:221–232
Fu Q, Liou KN (1993) Parameterization of the radiative properties of cirrus clouds. J Atmos Sci 50:2008–2025
Guo Q, Leighton HG, Feng J, Trischenko A (2007) Wildfire aerosol and cloud radiative forcing in the Mackenzie River Basin from satellite observations. (Vol. I, this book)
Hucek R, Jacobowitz H (1995) Impact of scene dependence on AVHRR albedo models. J Atmos Ocean Tech 12:697–711
Laszlo I, Jacobowitz H, Gruber A (1988) The relative merits of narrowband channels for estimating broadband albedos. J Atmos Ocean Tech 5:757–773
Li Z, Charlock T, Whitlock C (1995) Assessment of the global monthly mean surface insolation estimated from satellite measurements using global energy balance archive data. J Climate 8:315–328
Li Z, Leighton HG (1992) Narrowband to broadband conversion with spatially autocorrelated reflectance measurements. J Appl Meteorol 31:653–670
Li Z, Leighton HG, Cess RD (1993b) Surface net solar radiation estimated from satellite measurements: comparison with tower observations. J Climate 6:1764–1772
Li Z, Leighton HG, Masuda K, Takashima T (1993a) Estimation of SW flux absorbed at the surface from TOA reflected flux. J Climate 6:317–330
Li Z, Moreau L, Arking A (1997) On solar energy disposition, a perspective from observation and modeling. B Am Meteorol Soc 78:53–70
Li Z, Trishchenko A (1999) A study towards an improved understanding of the relationship between visible and SW albedo measurements. J Atmos Ocean Tech 16:347–360
Loeb NG, Kato S, Loukachine K, Smith NM (2003a) Angular distribution models for top-of-atmosphere radiative flux estimation from the Cloud and Earth's Radiant Energy System instrument on the Tropical Rainfall Measuring Mission Satellite. Part I: methodology. J Appl Meteorol 42:1748–1769
Loeb NG, Loukachine K, Manalo-Smith N, Wielicki BA, Young DF (2003b) Angular distribution models for top-of-atmosphere radiative flux estimation from the Cloud and Earth's Radiant Energy System instrument on the Tropical Rainfall Measuring Mission Satellite. Part II: validation. J Appl Meteorol 42:1748–1769
Lorant V, McFarlane N, Laprise R (2002) A numerical study using the Canadian Regional Climate Model for the PIDCAP period. Boreal Environ Res 7**:**203–210
MacKay MD, Bartlett P, Chan E, Derksen C, Guo S, Leighton GH (2006) On the problem of regional scale sublimation over boreal and agricultural landscapes. Atmos Ocean 44:289–304
MacKay MD, Bartlett P, Chan E, Verseghy D, Soulis ED, Seglenieks FR (2007) The MAGS regional climate modeling system: CRCM-MAGS. (Vol. I, this book)

MacKay MD, Seglenieks F, Verseghy D, Soulis ED, Snelgrove KR, Walker A, Szeto K (2003) Modeling Mackenzie Basin surface water balance during CAGES with the Canadian Regional Climate Model. J Hydrometeorol 4:748–767

McFarlane NA, Boer GJ, Blanchet JP, Lazare M (1992) The Canadian Climate Centre second generation general circulation model and its equilibrium climate. J Climate 5:1013–1044

Pinker RT, Frouin R, Li Z (1995) A review of satellite methods to derive surface shortwave irradiance. Remote Sens Environ 51:108–124

Pinker RT, Laszlo I (1992) Modeling surface solar irradiance for satellite applications on global scale. J Appl Meteorol 31:194–211

Roads JO, Lawford R, Bainto E, Berbery E, Chen S, Fekete B, Gallo K, Grundstein A, Higgins W, Kanamitsu M, Krajewski W, Lakshmi V, Leathers D, Lettenmaier D, Luo L, Maurer E, Meyers T, Miller D, Mitchell K, Mote T, Pinker R, Reichler T, Robinson D, Robock A, Smith J, Srinivasan G, Verdin K, Vinnikov K, Vonder Haar T, Vörösmarty C, Williams S, Yarosh E (2003) GCIP Water and Energy Budget Synthesis (WEBS). J Geophys Res 108:doi:10.1029/2002JD002583

Valiente JA, Nunez M, Lopez-Baeza E, Moreno JF (1995) Narrow-band to broad-band conversion for Meteo-visible channel and broad-band albedo using both AVHRR-1 and –2 channels. Int J Remote Sens 16:1147–1166

Wielicki BA, Barkstrom BR, Harrison EF, Lee III BB, Louis Smith G, Cooper JE (1996) Clouds and the Earth's Radiant Energy System (CERES): an earth observing system experiment. B Am Meteorol Soc 77:853–868

Yin Y, Gong P, Cohen S (1994) An integrated data base for Mackenzie River Basin climate change impact assessment. Can J Remote Sens 20:426–434

Chapter 21

Wildfire Aerosol and Cloud Radiative Forcing in the Mackenzie River Basin from Satellite Observations

Song Guo, Henry G. Leighton, Jian Feng
and Alexander Trishchenko

Abstract Clouds and wildfire aerosols are both important in our understanding of the radiation budgets in the Mackenzie River Basin (MRB). The smoke aerosols produced by wildfires are predominately aerosols that can absorb incoming solar radiation in the atmosphere. Both the cloud and wildfire aerosol radiative forcing at the top of atmosphere (TOA) and at the surface in the MRB are investigated. Second-order polynomial relationships are found between forcing (ΔF) and aerosol optical thickness (τ) for the reflected solar fluxes at the TOA, the outgoing longwave (LW) fluxes at the TOA, and the net surface solar fluxes. The monthly-mean basin-average cloud shortwave forcing at the TOA and at the surface between June and September are between 150 and 200 W m^{-2} and -160 and -220 W m^{-2}, respectively, while the basin-averaged outgoing LW cloud forcing at the TOA is around -40 W m^{-2}. Overall, the cloud forcing could impact the shortwave and longwave radiation budgets by 30–50% both at the TOA and at the surface for the MRB region.

1 Introduction

The burning of forests and grasslands that frequently happens each summer in the western United States and Canada produces large amounts of smoke aerosol particles that are predominately radiation absorbing (Li and Liou 1998). These wildfires could have significant impacts on atmospheric radiation budgets and could influence the regional climate (Crutzen and Andreae 1990). The wildfires that occurred in British Columbia from mid-June to late July of 2004 represented one of the largest wildfire events in the last 10 years in Canada (Pfister et al. 2005). They had a major influence on the Mackenzie River Basin (MRB) which is located downwind of these fires. Intense wildfires such as these and others that occurred in

Alaska were mainly related to the unusually warm and dry weather conditions (Pfister et al. 2005).

Wildfire smoke aerosols can affect solar radiation budgets both directly and indirectly. Direct effects include cooling at the ground surface resulting from the scattering and absorption of incoming solar radiation by the aerosol. Indirectly, aerosols affect radiation budgets through their influence on cloud properties. Solar fluxes absorbed at the surface have been derived from satellite measurements of reflected solar radiation at the TOA by means of the Li and Leighton algorithm (Li et al. 1993a). Masuda et al. (1995) added several correction terms to this algorithm including a term for an absorbing aerosol, which is a function of its optical thickness, the cosine of solar zenith angle, and the normalized outgoing TOA fluxes. Through comparison with surface tower measurements, Feng and Leighton (2003) demonstrated that the inclusion of the modification for smoke aerosols could reduce the bias of the derived net surface solar radiative (NSSR) flux.

Clouds are also important in the solar radiation budget. The key variables controlling the solar radiation budget include the amount, vertical distribution, and optical properties of clouds, atmospheric aerosol, and some absorbing gases as well as the earth surface characteristics (Li 2004). Clouds remain the major source of uncertainty in our understanding of incoming solar radiation partitioning (Arking 1991; Cess et al. 1996; Li et al. 1997). They can reflect the incoming short wavelength (SW) radiation, thus cooling the earth surface; and can also reduce the longwave (LW) cooling of the atmosphere below the cloud base and increase the LW cooling above the cloud top.

Satellite observations have proven to be effective in estimating wildfire aerosol radiative forcing (WARF) and cloud radiative forcing (CRF) both at the TOA and at the surface over a large area. Forest fire or biomass burning aerosol radiative forcing has previously been studied using satellite data by Christopher et al. (1998, 2000), Li and Liou (1998) and Zhang et al. (2005). A narrowband sensor (MODIS) and a broadband sensor (CERES) are on-board the same satellite platforms (Terra and Aqua). The MODIS instrument has 36 channels and has been used to retrieve aerosol optical depth and particle size information (Tanré et al. 1997). The validation indicates that MODIS can provide more accurate retrievals of aerosol optical thickness (AOT) than the previous sensors such as the AVHRR (Chu et al. 2002; Remer et al. 2002). On the basis of surface measurements, Remer et al. (2002) concluded that the uncertainty in aerosol optical thickness at 0.55 μm ($\tau_{0.55}$) is $\pm 0.03 \pm 0.05\tau$. The Clouds and Earth's Radiant Energy System (CERES) was designed to monitor SW and LW

radiative energy fluxes at the TOA (Wielicki et al. 1996). The CERES sensor was designed to measure solar-reflected and earth-emitted radiation at the TOA with a design objective of 1% uncertainty (Wielicki et al. 1996) and the validation shows the design objective has been achieved (Loeb et al. 2003b).

The objectives of this study are to investigate the relationships between the wildfire aerosol radiative forcing (ΔF) and aerosol optical thickness (τ), and to examine the wildfire aerosol and cloud impact on the radiative budgets both at the TOA and at the surface in the MRB. Satellite observations provided the primary information source for this study.

2 Research Domain

Satellite images show that a series of wildfires started in northern British Columbia around June 14, 2004, and lasted for about one and half months, with most intensive fires occurring between June 20 and July 10 (Canadian Wildland Fire Information System website: http://cwfis.cfs.nrcan.gc.ca/en/index_e.php).

On the basis of the MODIS cloud mask data, three mainly cloud-free days (June 23–25) were selected to investigate the relationship between wildfire aerosol radiative forcing (ΔF) and aerosol optical thickness at 0.55 μm ($\tau_{0.55}$), and the maximum wildfire aerosol impacts on the radiation budgets both at the TOA and at the surface of the MRB. Since cloud forcing is much less important over high albedo surfaces (such as snow) we use only snow-free pixels from June to September during the four year (2000–03) period.

3 Methods

3.1 Effects of Absorbing Aerosols on the Determination of the Surface Solar Radiation

Five tower flux sites from the Boreal Ecosystems Atmosphere Study (BOREAS) and six optical depth observation sites described by Markham and Schafer (1998) were selected to compare with the net surface solar fluxes from the Scanner for Radiation Budget (ScaRaB) observations. Such measurements of the radiative fluxes are accurate to within 2% (Gu and Smith 1997). The optical depth data indicated a strong influence of

forest fires at the tower sites. The ScaRaB sensor onboard the Meteor-3 satellite (Kandel et al. 1998) has a broadband channel to directly measure the reflected solar radiation and outgoing LW radiation at the TOA. Water vapor amounts are interpolated from NCEP Reanalysis data (Kalnay et al. 1996). ScaRaB pixels are treated as spatially matched at a tower when the center of the pixel is within 0.25^{o} latitude and longitude of the tower. The tower measurements are interpolated to temporally match the satellite measurements. Feng and Leighton (2003) provide a more detail description of the method.

For comparing clear-sky NSSR fluxes as well as cloud radiative forcing ratios (the ratio between cloud radiative forcing at the surface and at the TOA) derived from satellite observations with those based on tower measurements, it is important that clear-sky conditions be determined. Clear-sky pixels are identified according to the ScaRaB classification (Kandel et al. 1998). The clear-sky values are determined from the regression lines through all the nominally clear-sky data points plotted as functions of θ_0 for both the TOA and the surface.

3.2 Wildfire Aerosol Direct Radiative Forcing

The "Clear Scenes Only" algorithm described in Ackerman et al. (1998) is used on the MODIS cloud mask products to identify clear-sky pixels. The MODIS cloud mask products are generated by using 14 of the 36 MODIS spectral channels to maximize cloud detection accuracy and reliability and to mitigate previous difficulties.

The aerosol cloud forcing (ΔF) both at the TOA and at the surface is defined as the differences between aerosol fluxes under cloud-free aerosol-laden conditions ($F_{a,clr}$) and clear-sky aerosol-free fluxes (F_{clr}). The radiative fluxes at the TOA are based on CERES ES-8 data (Wielicki et al. 1996) and at the surface are derived from fluxes at the TOA by using the algorithm of Masuda et al. (1995). In this study, the calculated surface absorbed flux for each pixel is determined on the basis of the aerosol optical thickness (AOT) in that pixel. The AOT values are obtained from MODIS MOD04 data. Both the AOT (10 km resolution) and cloud-mask data (1 km resolution) from MODIS are averaged to spatially match CERES footprint (20 km resolution at nadir). The clear-sky pixels are determined by the procedure described above for those pixels when $\tau_{0.55}$ is less than 0.05. The data used for the selection of clear-sky aerosol-free pixels are from the period June 21 to June 27 in the years 2000 to 2004. The selected F_{clr} is used for wildfire aerosol forcing calculation only when the solar zenith an-

gle and satellite viewing angle are within 0.5^o of the selected $F_{a,clr}$. The $F_{a,clr}$ values are selected when $\tau_{0.55}$ is larger than 0.1. The precipitable water amount used to determine the net solar flux at the surface is obtained from Canadian Regional Climate Model (MacKay et al. 2003).

3.3 Cloud Radiative Forcing

Cloud radiative forcing (CRF) is defined as the difference in the radiative fluxes observed under all-sky condition (F_{all}) and under clear-sky condition (F_{clr}). Only data obtained between 19–20 UTC (12:00–13:00 local time) are used in order to minimize the solar zenith angle effects. The F_{clr} values in CRF calculation are first selected by using the clear-sky scene identification from CERES ES-8 products, and then finalized by the procedure described in Section 3.2 through using the MODIS cloud mask products. The clear-sky fluxes (F_{clr}) are assembled from all clear-sky pixels within the same seven-day period in each of the four years, 2000–03. Both the weekly clear-sky fluxes and daily all-sky fluxes are averaged over every $0.25^o \times 0.25^o$ latitude-longitude bin. Because of the significant increase in pixel size and large uncertainty from the CERES angular distribution model (ADM) at larger solar zenith angles and satellite viewing angles (Loeb et al. 2003a), only the CERES pixels that have viewing zenith angles and solar zenith angles less than 60° are used. The CRF fluxes are obtained by subtracting the weekly clear-sky fluxes (F_{cls}) of a $0.25^o \times 0.25^o$ bin from the bin-averaged daily all-sky fluxes (F_{clr}).

The absorbed surface solar fluxes are estimated from reflected solar fluxes at the TOA using the algorithm of Li et al. (1993a) which parameterizes net surface solar radiation in terms of the reflected solar fluxes at the TOA, solar zenith angle, and precipitable water amount. The parameterization is independent of cloud optical thickness and therefore can be used under different sky conditions. The algorithm has been validated by surface measurements and has an estimated accuracy of 5 W m^{-2} when compared with the global energy balance archive data (Li et al. 1995a).

4 Results

4.1 Effects of Absorbing Aerosols on the Determination of Surface Solar Radiation

A correction procedure was applied to the data to remove the effects of mismatches between the footprints of the instruments mounted on the towers and ScaRaB, the deficiencies in the algorithm, and errors in the tower and satellite measurements. More details of the work are given in Feng and Leighton (2003). After this adjustment, differences between NSSR fluxes from ScarRaB and from the towers were calculated for all data with an optical depth $\tau > 0.15$. For these data, the mean optical depth is $\bar{\tau} = 0.38$, and the mean difference between the fluxes from the ScaRaB and the towers is 21.7 W m^{-2} with a standard deviation of 35.2 W m^{-2} (Fig. 1a). The remaining differences between the fluxes from ScaRaB and the towers are attributed to aerosol absorption not adequately accounted for in the Li et al. (1993a) algorithm. When the algorithm of Masuda et al. (1995), which contains an absorbing aerosol correction term, was applied to the data, the mean difference between the ScaRaB and tower data was reduced to -4.7 W m^{-2} with a standard deviation of 35.2 W m^{-2} (Fig. 1b). This improved agreement suggests that the Masuda correction for absorbing aerosols is a useful refinement to the Li et al. (1993) algorithm.

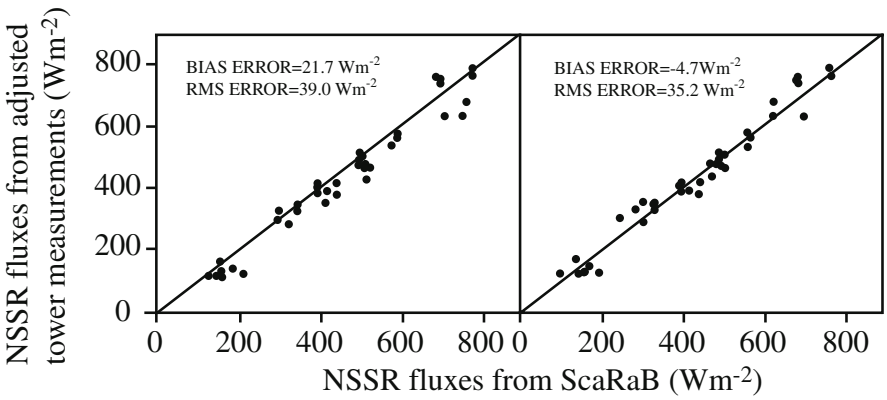

Fig. 1. Comparisons of NSSR fluxes derived from ScaRaB with those from tower measurements under clear skies at five sites in the BOREAS study region in the summer of 1994, for measurements when aerosol optical thickness was greater than 0.15 (a) with the algorithm of Li et al. (1993a) applied, and (b) with the algorithm of Masuda et al. (1995) applied (excerpted from Feng and Leighton 2003)

The TOA reflected solar fluxes and the net surface solar fluxes from tower measurements and satellite observations indicate that the radiative forcing is larger at the surface than at the TOA due to the presence of absorbing aerosols (Feng and Leighton 2003). These aerosols can reflect the incoming solar radiation to decrease the net solar flux at the TOA, but can also absorb solar radiation in the atmosphere to enhance the net solar flux at the TOA. The net effect on the TOA reflected solar fluxes depends on the surface albedo and the properties of the absorbing aerosol. At the surface both effects decrease the net solar radiation. Thus, the net effect is smaller at the TOA than at the surface. The resulting CRF ratios are found to be between 1.08 and 1.18. A potential source of uncertainty in the determination of the cloud forcing ratio is the mismatch in the fields of view between satellite and tower. Using the tower-measured surface albedo to calibrate the albedo from SacRaB yields only a 1% change in the mean value of the ratio for the five sites, indicating that mismatches in the fields of view have little impact. The use of the algorithm of Masuda et al. (1995) with the absorbing aerosol correction term gives CRF ratios that match the theoretical prediction.

4.2 Wildfire Aerosol Forcing from Satellite Observations

The MODIS and CERES data for 20:37 UTC (13:37 local time), June 25, 2004, were used to study the wildfire aerosol radiative forcing over northern British Columbia and the western part of the MRB. The region was mostly clear except for the clouds in two small areas (Fig. 2a), one just outside the MRB where the aerosol thicknesses were large due to the wildfire, and the other inside the MRB in an area where the optical thicknesses were small. Missing values of aerosol optical thickness are due to the presence of cloud. The reflected solar and LW radiative forcing at the TOA and the net surface solar radiative forcing are shown in Figs. 2b, 2c, and 2d, respectively. The aerosol optical thicknesses were as large as 4.3 (Fig. 2a) while the reflected solar radiative forcings at the TOA were as large as 100 W m^{-2} and the net surface solar radiative forcings were as low as -190 W m^{-2}. The LW forcing at the TOA was much smaller and the highest forcing was about -18 W m^{-2}. The difference between solar radiative forcing at the TOA and at the surface was due to the strongly absorbing nature of the wildfire aerosols. Up to ~100 W m^{-2} of incoming radiation was absorbed by the aerosol in the atmosphere for heavily aerosol-loaded pixels. High optical thickness regions (τ>2) existed outside and inside the western

MRB (Fig. 2a). Clearly, all regions of strong forcing (Figs. 2b, 2c, and 2d) were associated with high optical thickness regions.

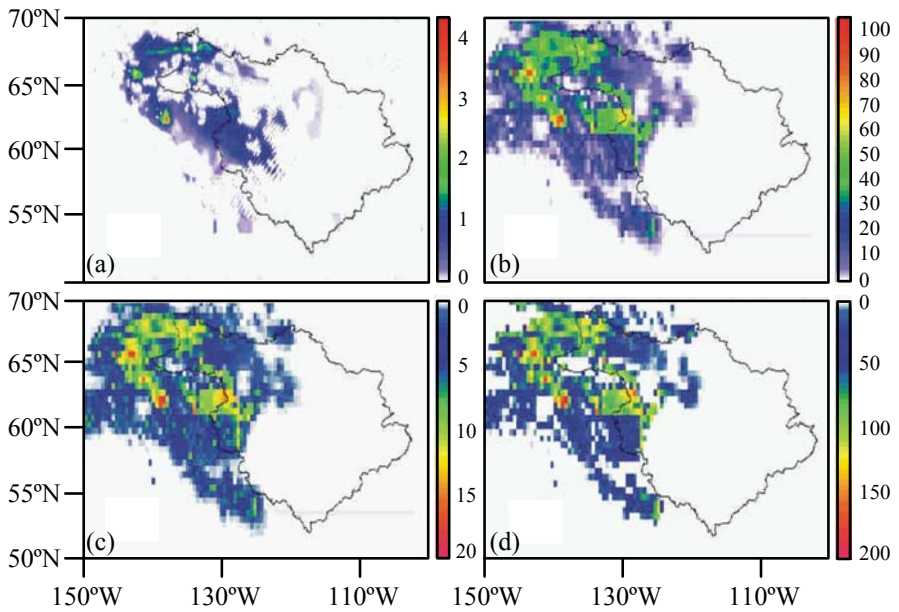

Fig. 2. 20:37 UTC 06/25/2004 images of (a) aerosol optical thickness from MODIS MOD04 data, (b) short-wave radiative forcing at the TOA from CERES ES-8 data, (c) long-wave radiative forcing at the TOA from CERES ES-8 data, and (d) short-wave radiative forcing at the surface from CERES ES-8 data

Two other clear-sky cases (20:49 UTC, 06/23/2004; 21:45 UTC, 06/24/2004) were also examined. It is found that the reflected solar radiative forcing at the TOA (ΔF_{SW_TOA}) increases with the increase of aerosol optical thickness (τ) and the net surface solar radiative forcing (ΔF_{SW_SFR}) and LW forcing at the TOA decrease with the increase of aerosol optical thickness (τ) (Fig. 3). A second-order polynomial provides the best fit to the ΔF–τ relationship when the data points from all three cases are combined. The relationships for the reflected solar radiative forcing at the TOA, the outgoing LW forcing at the TOA, and the net surface solar radiative forcing are, respectively:

$\Delta F_{SW\_TOA} = -2.9303\ \tau^2 + 36.091\ \tau + 3.818$ with $R^2 = 0.95$,

$\Delta F_{LW\_TOA} = 0.3598\ \tau^2 - 5.8454\ \tau - 2.2076$ with $R^2 = 0.94$,

$\Delta F_{SW\_SFR} = 6.765\ \tau^2 - 72.821\tau - 11.109$ with $R^2 = 0.94$.

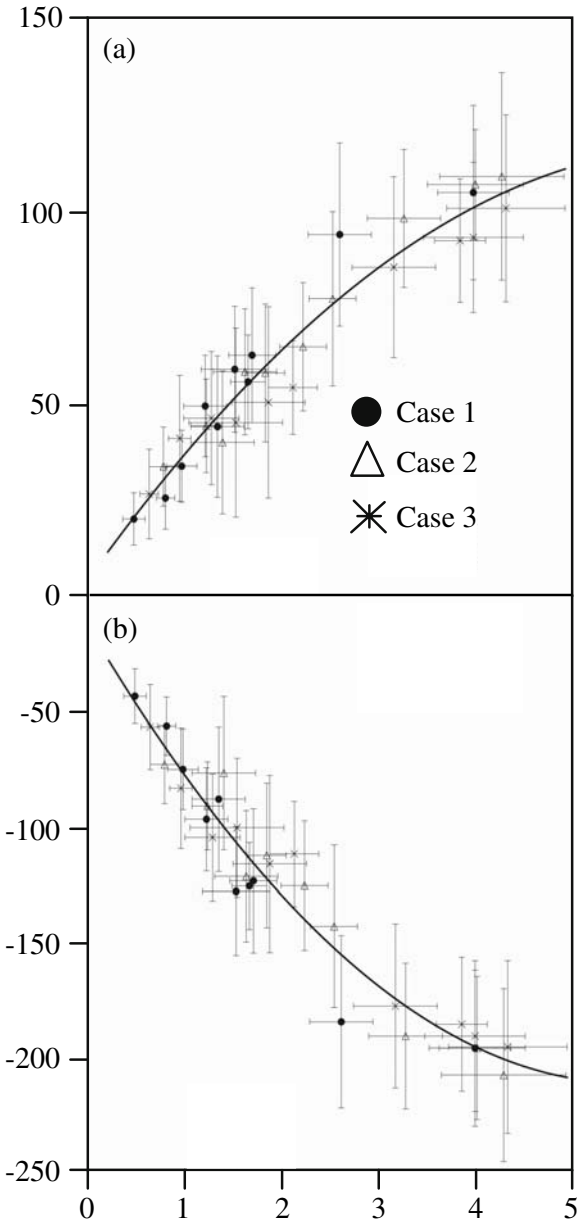

Fig. 3. (a) Short-wave radiative forcing at the TOA vs aerosol optical thickness, (b) short-wave radiative forcing at the surface vs aerosol optical thickness (case 1: 20:49 UTC 06/23/2004; case 2: 21:45 UTC 06/24/2004; case 3: 20:37 UTC 06/25/2004)

4.3 Cloud Radiative Forcing for the Mackenzie River Basin from Satellite Observations

Over a study period of June to September, the monthly-mean basin-average CRF decreases steadily from ~200 W m^{-2} to ~150 W m^{-2} for the reflected solar fluxes at the TOA and the magnitude decreases from about -220 to about -160 W m^{-2} for the net surface solar CRF (Fig. 4). The net monthly-mean basin-average outgoing LW CRF values are steady at around -40 W m^{-2}. The changes in the monthly-mean basin-average CRF values are mainly due to the seasonal decline in incoming solar radiation from June to September. The July monthly-mean CRF images for the reflected solar CRF at the TOA, the outgoing LW CRF at the TOA, and the net surface solar CRF in the years 2000 to 2003 are displayed in Figs. 5, 6, and 7, respectively. Significant inter-annual variation can be seen in Figs. 5 to 7 and the monthly-mean values change by up to about 50 W m^{-2} (Fig. 4). Overall, high CRF values tend to occur in the western mountain area and the eastern taiga Shield area; low CRF values are found mainly in the upper-middle part of the MRB. All the other parts of the MRB have values close to the basin average. Under clear-sky conditions, the monthly-mean basin-average TOA reflected solar fluxes and net surface solar fluxes during the summer months are 150–200 W m^{-2} (TOA) and 500–750 W m^{-2} (surface), and under all-sky conditions they are 250–450 W m^{-2} and 300–500 W m^{-2}, respectively. These values show that cloud radiative forcing can impact the total radiation budgets by about 30–50% both at the TOA and at the surface.

5 Discussion and Conclusion

The NSSR fluxes derived from ScaRaB are compared with the measurements at five towers and the results indicate that neglecting the effect of absorbing aerosols can cause a bias of 21 W m^{-2} in the satellite retrieval of the NSSR (Feng and Leighton 2003).

The Cloud Radiative Forcing Ratio (CRFR) has been used in the debate regarding the existence of a "cloud absorption anomaly" (Cess et al. 1995; Li et al. 1995b*;* Li and Trishchenko 2001; Ramanathan et al. 1995). CRFR, as predicted by theoretical models, is usually less than 1.25 (Li and Moreau 1996). The existence of larger CRFR (> 1.25), called the "cloud absorption anomaly", has been suggested by some studies (Cess et al. 1995, 1999; Ramanathan et al. 1995; Valero et al. 1997; Zender et al. 1997) but opposed by others (Li 2004; Li et al. 1995b, 1999). Feng and

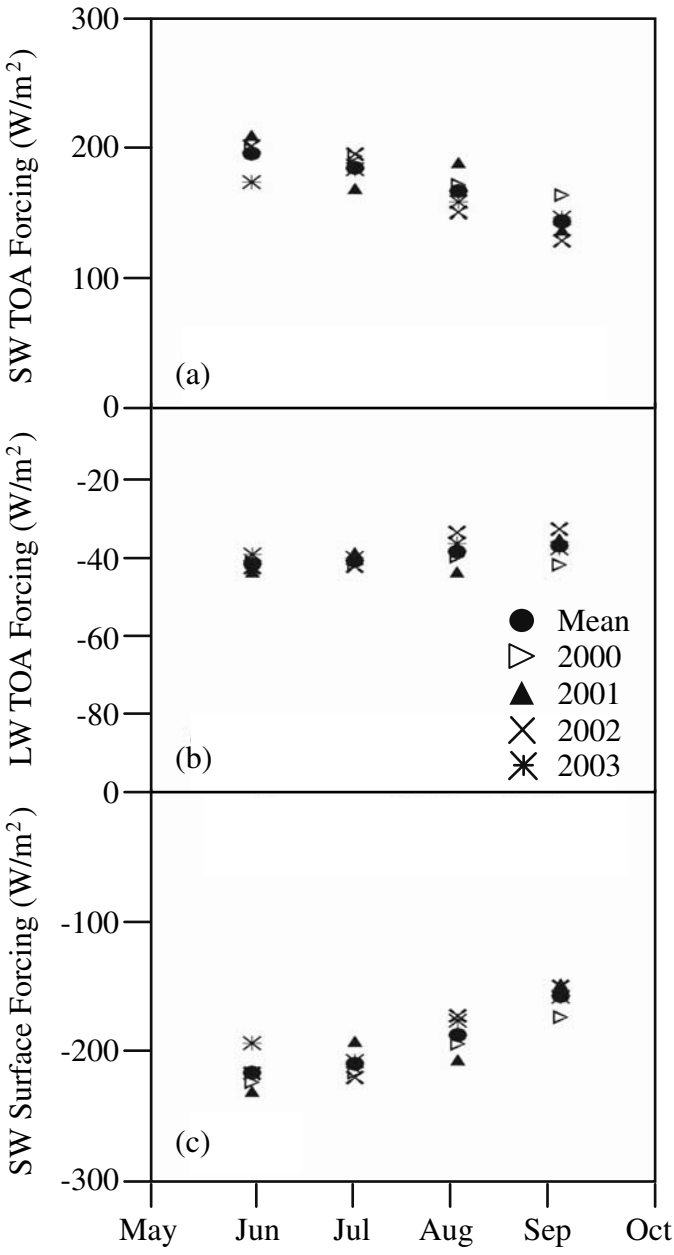

Fig. 4. Monthly-mean basin-average cloud radiative forcing (CRF) in the years 2000–03 (mean is the average value of the four years): (a) TOA reflected solar fluxes, (b) outgoing long-wave fluxes at the TOA, and (c) net surface solar fluxes

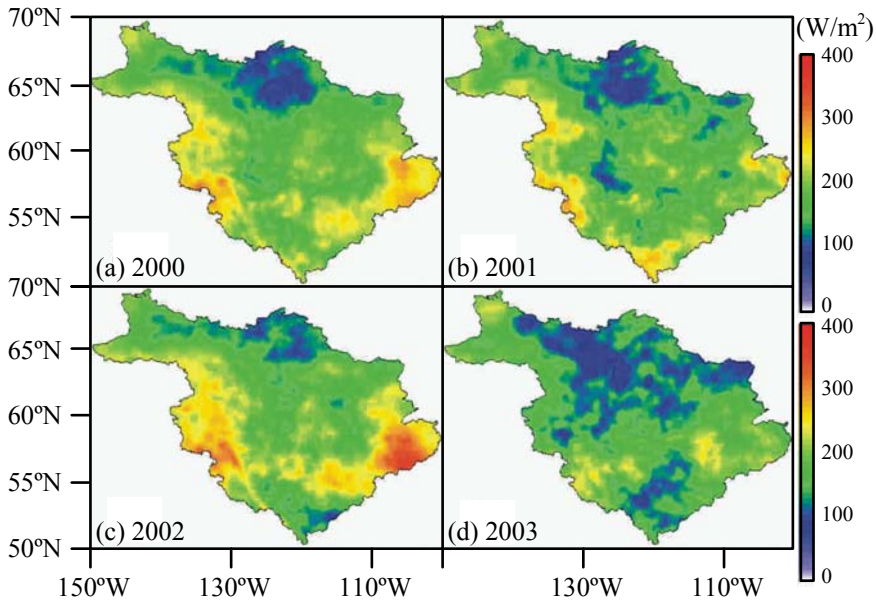

Fig. 5. July (monthly-mean) cloud radiative forcing for the TOA reflected solar fluxes in (a) 2000, (b) 2001, (c) 2002, and (d) 2003

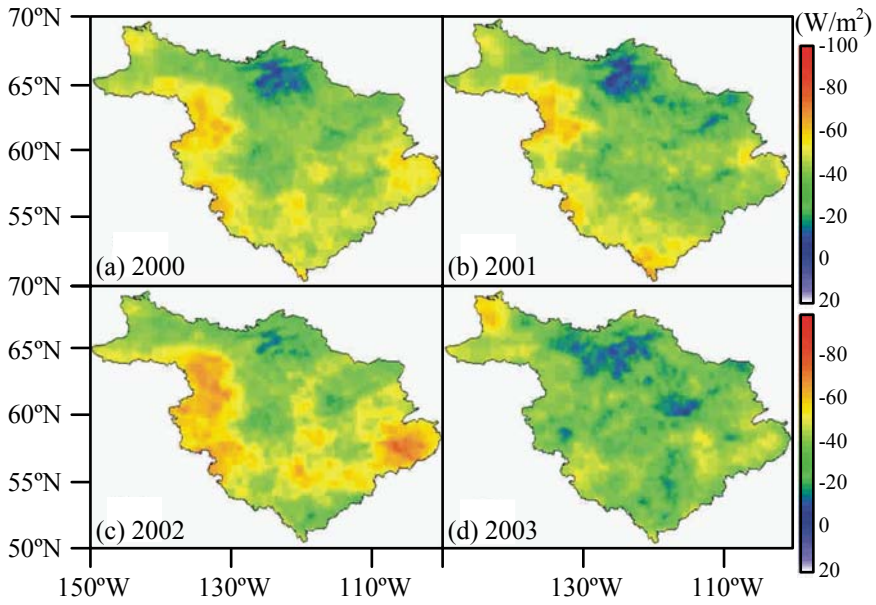

Fig. 6. July (monthly-mean) cloud radiative forcing for the outgoing long-wave fluxes at the TOA in (a) 2000, (b) 2001, (c) 2002, and (d) 2003

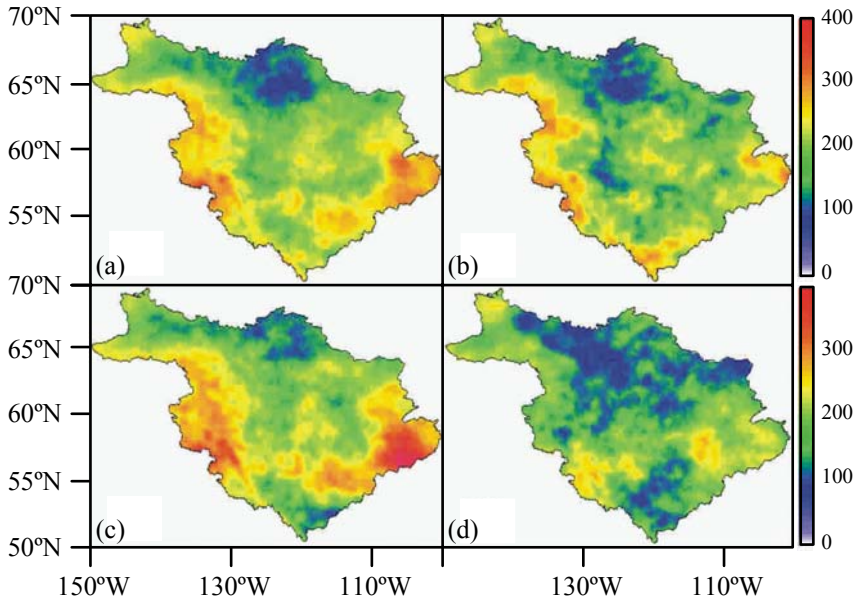

Fig. 7. July (monthly-mean) cloud radiative forcing for the net surface solar fluxes in (a) 2000, (b) 2001, (c) 2002, and (d) 2003

Leighton (2003) demonstrated that the application of the algorithm of Masuda et al. (1995) with an absorbing aerosol term yields a value of CRFR between 1.08 and 1.18, thus opposing the idea of such an anomaly.

The second-order polynomial ΔF–τ relationships obtained by this study are similar to the second-order polynomial ΔF–τ relationship for aerosol radiative forcing over the ocean obtained by Christopher and Zhang (2002) and Zhang et al. (2005). The relationship is more linear when τ is less than 1.5 and more curvilinear when τ is larger than 2.5. The methodology introduced in this paper can be easily applied to other aerosol radiative forcing studies, such as sandstorm aerosol, sea-salt aerosol, and large volcanic aerosol, by using CERES and MODIS data.

A study of the monthly-mean cloud radiative forcing for MRB during the summer months indicates that clouds could impact the total radiation budgets by about 30–50% both at the TOA and at the surface. As CRF can be directly derived both at the TOA and at the surface using satellite data, it has proven to be a useful tool in diagnosing and evaluating climate models (Barker et al. 1994; Cess et al. 1997; Li et al. 1997).

Acknowledgements

The CERES data were obtained from the NASA Langley Research Center Atmospheric Sciences Data Center, the MODIS data were obtained through the Goddard Space Flight Center Data Center. We thank Dr. Murray D. MacKay for providing output from the Canadian Regional Climate Model.

References

Ackerman SA, Strabala KI, Menzel WP, Frey RA, Moeller CC, Gumley LE (1998) Discriminating clear sky from clouds with MODIS. J Geophys Res 103:32141–32157

Arking A (1991) The radiative effects of clouds and their impacts on climate. B Am Meteorol Soc 72:795–813

Barker HW, Li Z, Blanchet JP (1994) Radiative characteristics of the Canadian Climate Center second-generation general circulation model. J Climate 7:1070–1091

Cess RD, Zhang MH, Minnis P, Corsetti L, Dutton EG, Forgan BW, Garber DP, Gates WL, Hack JJ, Harrison EF, Jing X, Kiehi JT, Long CN, Morcrette JJ, Potter JL, Ramanathan V, Subasilar B, Whitlock CH, Young DF, Zhou Y (1995) Absorption of solar radiation by clouds: observations versus models. Science 267:496–499

Cess RD, Zhang MH, Ingram WJ, Potter GL, Alekseev V, Barker HW, Cohen-Solal E, Colman RA, Dazlich DA, Del Genio AD, Dix MR, Dymnikov V, Esch M, Fowler LD, Fraser JR, Galin V, Gates WL, Hack JJ, Kiehl JT, Treut KLe, Lo KK-W, McAvaney BJ, Meleshko VP, Morcrette J-J, Randall DA, Roeckner E, Royer J-F, Schelsinger ME, Sporyshev PV, Timbal B, Volodin EM, Taylor KE, Wang W, Wetherald RT (1996) Cloud feedback in atmospheric general circulation models: an update. J Geophys Res 101:12791–12794, doi:10.1029/96JD00822

Cess RD, Zhang MH, Potter GL, Alekseev G, Barker HW, Bony S, Colman RA, Dazlich DA, DelGenio AD, Deque M, Dix MR, Dymnikov V, Esch M, Fowler LD, Fraser JR, Galin V, Gates WL, Hack JJ, Ingram WJ, Kiehl JT, Kim Y, LeTreut H, Liang XZ, McAvaney BJ, Meleshko VP, Morcrette JJ, Randall DA, Roeckner E, Schlesinger ME, Sporyshev PV, Taylor KE, Timbal B., Volodin EM, Wang W, Wang WC, Wetherald RT (1997) Comparison of the seasonal change in cloud-radiative forcing from atmospheric general circulation models and satellite observations. J Geophys Res 102:16593–16603

Cess RD, Zhang M, Valero FPJ, Pope SK, Bucholtz A, Bush B, Zender CS, Vitko J (1999) Absorption of solar radiation by the cloudy atmosphere: further in-

terpretations of collocated aircraft measurements. J Geophys Res 104:2059–2066

Christopher SA, Chou J, Zhang J, Li X, Welch RM (2000) Shortwave direct radiative forcing of biomass burning aerosols estimated from VIRS and CERES. Geophys Res Lett 27:2197–2000

Christopher SA, Wang M, Berendes TA, Welch RM, and Yang SK (1998) The 1985 biomass burning season in South America: satellite remote sensing of fires, smoke, and regional radiative energy budgets. J Appl Meteorol 37:661–678

Christopher SA, Zhang J (2002) Shortwave aerosol radiative forcing from MODIS and CERES observations over the oceans. Geophys Res Lett 29, doi:10.1029/2002GL014803

Chu DA, Kaufman YJ, Ichoku C, Remer LA, Tanré D, Holben BN (2002) Validation of MODIS aerosol optical depth retrieval over land. Geophys Res Lett 29, doi:10.1029/2001GL013205

Crutzen PJ, Andreae MO (1990) Biomass burning in the tropics: impacts on atmospheric chemistry and biogeochemical cycles. Science 250:1669–1678

Feng J, Leighton HG (2003) Effects of absorbing aerosols on the determination of the surface solar radiation. J Geophys Res 108, doi:10.1029/2002JD002852

Gu J, Smith EA (1997) High-resolution estimates of total solar and PAR surface fluxes over large-scale BOREAS study area from GEOS measurements. J Geophys Res 102(D24):29,685–29,706

Kalnay E, Kanamitsu M, Kistler R, Collins W, Deaven D, Gandin L, Iredell M, Saha S, White G, Woolen J, Zhu Y, Chelliah M, Ebisuzaki W, Higgins W, Janowiak J, Mo KC, Ropelewski C, Wang J, Leetma A, Reynolds R, Jenne R, Joseph D (1996) The NCEP/NCAR 40-year reanalysis project. B Am Meteorol Soc 77:437–471

Kandel R, Viollier M, Raberanto P, Duvel JP, Pakhomov LA, Golovko VA, Trishchenko AP, Mueller J, Raschke E, Stuhlmann R (1998) The ScaRaB earth radiation budget dataset. B Am Meteorol Soc 79:765–783

Li Z (2004) On the solar radiation budget and cloud absorption anomaly debate. In Zhu X (ed) Observation, theory, and modeling of the atmospheric variability. World Scientific Pub. Co., pp 437–456 (Also available from: http://www.atmos.umd.edu/~zli/PDF_papers/a05_li_z_final.pdf)

Li Z, Leighton HG, Masuda K, Takashima T (1993a) Estimation of SW flux absorbed at the surface from TOA reflected flux. J Climate 6:317–330

Li Z, Leighton HG, Cess RD (1993b) Surface net solar radiation estimated from satellite measurements: comparisons with tower observations, J Climate 6:1764–1772

Li Z, Charlock T, Whitlock C (1995a) Assessment of the global monthly mean surface insolation estimated from satellite measurements using global energy balance archive data. J Climate 8:315–328

Li Z, Barker HW, Moreau L (1995b) The variable effect of clouds on atmospheric absorption of solar radiation. Nature 376:486–490

Li Z, Liou KN (1998) The direct radiative effect of smoke aerosols on atmospheric absorption of visible sunlight. Tellus B 50:543–554

Li Z, Moreau L (1996) Alteration of atmospheric solar absorption by clouds: simulation and observation. J Appl Meteorol 35:653–670

Li Z, Moreau L, Arking A (1997) On solar energy disposition: a perspective from observation and modeling. B Am Meteorol Soc 78:53–70

Li Z, Trishchenko A (2001) Quantifying uncertainties in determining SW cloud radiative forcing and cloud absorption due to variability in atmospheric conditions. J Atmos Sci 58:376–389

Li Z, Trishchenko A, Barker HW, Stephens GL, Partain PT (1999) Analysis of Atmospheric Radiation Measurement (ARM) program's Enhanced Shortwave Experiment (ARESE) multiple data sets for studying cloud absorption. J Geophys Res 104:19,127–19,134

Loeb NG, Kato S, Loukachine K, Smith NM (2003a) Angular distribution models for top-of-atmosphere radiative flux estimation from the cloud and Earth's radiant energy system instrument on the Tropical Rainfall Measuring Mission Satellite. Part I: methodology. J Appl Meteorol 42:1748–1769

Loeb NG, Loukachine K, Manalo-Smith N, Wielicki BA, Young DF (2003b) Angular distribution models for top-of-atmosphere radiative flux estimation from the cloud and Earth's radiant energy system instrument on the Tropical Rainfall Measuring Mission Satellite. Part II: validation. J Appl Meteorol 42:1748–1769

MacKay MD, Seglenieks F, Verseghy D, Soulis ED, Snelgrove KR, Walker A, Szeto KK (2003) Modeling Mackenzie Basin surface water balance during CAGES with the Canadian Regional Climate Model. J Hydrometeorol 4:748–767

Markham BL, Schafer JS (1998) BORES RSS-11 Ground network of sunphotometer measurements dataset, http://www-eosdis.ornl.gov/, Oak Ridge Natl. Lab. Distributed Active Arch. Cent., Oak Ridge, Tenn.

Masuda K, Leighton HG, Li Z (1995) A new parameterization for the determination of solar flux absorbed at the surface from satellite measurements. J Climate 8:1615–1629

Pfister G, Hess PG, Emmons LK, Lamarque J-F, Wiedinmyer C, Edwards DP, Pétron G, Gille JC, Sachse GW (2005) Quantifying CO emissions from the 2004 Alaskan wildfires using MOPITT CO data. Geophys Res Lett 32, doi:10.1029/2005GL022995

Ramanathan V, Subasilar B, Zhang GJ, Conant W, Cess RD, Kiehl JT, Grassl H, Shi L (1995) Warm pool heat budget and shortwave cloud forcing: a missing physics. Science 267:499–503

Remer LA, Tanre D, Kaufman YJ, Ichoku C, Mattoo S, Levy R, Chu DA, Holben BN, Dubovik O, Smirnov A, Martins JV, Li R-R, Ahmad Z (2002) Validation of MODIS aerosol retrieval over ocean. Geophys Res Lett 29, doi:10.1029/2001GL013204

Tanré D., Kaufman YJ, Herman M, Matto S (1997) Remote sensing of aerosol properties over oceans using the MODIS/EOS spectral radiance. J Geophys Res 102:16971–16988

Valero FPJ, Cess RD, Zhang S,Pope K, Bucholtz A, Bush B, Vitko J. (1997) Absorption of solar radiation by the cloudy atmosphere: interpretations of collocated aircraft measurements. J Geophys Res 102:29,917–29,928

Wielicki BA, Barkstrom BR, Harrison EF, Lee III BB, Louis Smith G, Cooper JE (1996) Clouds and the Earth's Radiant Energy System (CERES): an earth observing system experiment. B Am Meteorol Soc. 77:853–868

Zender CS, Bush B, Pope SK, Bucholtz A, Collins WD, Kiehl JT, Valero FPJ, Vitko J (1997) Atmospheric absorption during the Atmospheric Radiation Measurement (ARM) Enhanced Shortwave Experiment (ARESE). J Geophys Res 102:29,901–29,916

Zhang J, Christopher SA, Remer LA, Kaufman YJ (2005) Shortwave aerosol cloud-free radiative forcing from Terra, II: global and seasonal distributions. J Geophys Res 24, doi:10.1029/2004jd005009

Chapter 22

The Nature and Impacts of Thunderstorms in a Northern Climate

Bohdan Kochtubajda, Michael D. Flannigan, John R. Gyakum, Ronald E. Stewart, William R. Burrows, Andrew M. Way, Evan Richardson and Ian Stirling

Abstract. Thunderstorms and associated lightning play an important role in the cycling of water and energy during the warm season, over the boreal and subarctic ecosystems of northern Canada, including the Mackenzie Basin. A variety of observational data sets and model-derived products have been used to characterize these storms, to examine their impacts on the forests of the Basin and on polar bear habitat in western Hudson Bay, and to assess predictive applications of lightning information.

The convective storm season and resultant lightning activity are characterized as short but intense with a strong peak in cloud-to-ground (C-G) flashes during June and July. The maximum area of lightning activity varies in space and in time, and there is evidence that smoke from fires enhances the probability of positive C-G flashes. Although fire occurrence in the Basin peaks in July, much of the burned area occurs in June. Fires have also significantly changed vegetation and permafrost conditions, resulting in a decrease in the stability of polar bear maternity den sites, the collapse of dens and deterioration of the surrounding habitat in western Hudson Bay. A tree-structured regression method for constructing statistical probability forecast models successfully predicts the probability of lightning in 3-h projection intervals out to 45–48 h.

Introduction

Lightning from cumulonimbus clouds (CBs) is one of the most spectacular displays in the atmosphere that has fascinated man since early days, and is a common type of severe weather that significantly affects people directly. The magical thunderbird is believed by many indigenous peoples of the Americas to bring lightning. Thunder and the great winds are attributed to the flapping wings, and lightning is made when the thunderbird opens and shuts its eyes. Thus, in stormy weather, he flies through the skies flapping his wings and opening and closing his eyes (Clark 1973). Inuit elders re-

port that from oral history and traditional knowledge, it is forbidden to burn a feather of a ptarmigan because the associated smoke brings thunder (MacDonald J, pers commun 2003). During Alexander Mackenzie's historic journey from Fort Chipeywan to the Arctic Ocean in 1789, the occurrence of thunderstorms and lightning was entered in his journal, and on one occasion he described the devastation following a lightning-ignited fire (Mackenzie c2001).

Technological advances for lightning detection have shown that lightning is far more common than most people think. Satellite observations reveal that thunderstorms produce an average of 44 lightning flashes (intracloud (IC) and cloud-to-ground (C-G) combined) every second around the world (Christian et al. 2003). In Canada, over 21 million combined IC and C-G flashes have been detected by the Canadian Lightning Detection Network from 1998 to 2000 (Burrows et al. 2002). Analysis of media reports, vital statistics, hospital admission and emergency visitation records, and fire loss data, shows that on average about 9–10 lightning-related fatalities and 92–164 injuries occur annually (Mills et al. 2006). Lightning caused about 30% of the 8,000 forest fires in Canada in the 1990s, but these lightning-induced fires accounted for about 85% of the 2.8 million ha annual area burned (Stocks et al. 2002). However, the percentage of lightning-caused fires varies regionally and through time. Epp and Lanoville (1996) report that C-G lightning flashes typically start approximately 80% of the forest fires in the Northwest Territories (NWT). Lightning sensors installed at various locations throughout the forested area are an important part of the NWT forest fire management program (Ward and Mawdsley 2000).

Forest fires are influenced by four factors: fuels, ignition sources, weather/climate and humans (Flannigan and Wotton 2001). In Canada, weather/climate is the critical natural factor influencing forest fires (Gillett et al. 2004). Not only does it affect the ignition of fires through lightning, but it also influences fire behavior. Strong winds, high temperatures and low humidity enhance the rate of fire growth. Atmospheric instability is an indirect factor in fire growth. For example, in an unstable atmosphere, smoke column circulations can be strengthened which in turn will strengthen winds and intensify the fire.

The lightning mechanism discharges regions of excess electrical charge developed in thunderstorms. The lifecycle of thunderstorms has several distinct stages: (1) the growth or "cumulus" stage when air currents are continuously rising (updrafts) throughout the cloud and ice crystals and water droplets form and grow, (2) the "mature" stage when updraft and downdraft currents cause ice particles, graupel and water droplets in the

cloud to collide with each other to produce excess electric charges and dramatic lightning activity, and (3) the "dissipating" stage when the air currents sinks continuously, precipitation is less intense and the cloud erodes. There are two key types of lightning discharges: flashes between the cloud and the earth (cloud-to-ground discharges) and flashes within the cloud (intra-cloud discharges). Discharges can also occur from the cloud to the sky or between clouds but these are not as frequent (Uman 2001).

The objectives of this study were to improve understanding of thunderstorm and lightning processes through an examination of their spatial and temporal distributions, to examine their impacts on ecosystems in the Mackenzie River Basin (MRB) and elsewhere, and to develop predictive applications of lightning information. Complementary studies include Flannigan et al. (2007) which examined the changes in fire activity with respect to climate change.

2 Study Area

The MRB covers about 1.8 million km^2 and encompasses six provincial, territorial, and federal fire management jurisdictions in Canada. The landscape is diverse and comprises many eco-climatic zones (Ecological Stratification Working Group 1995). The focus of this work is the forested region of the NWT, an area covering about 615,000 km^2, or 18%, of the Territory. Black spruce (*Picea mariana*), lodge pole pine (*Pinus contorta*), jack pines (*Pinus banksiana*), and trembling aspen (*Populus tremuloides)* are the common tree species (Rowe 1972). The climate within the forested area of the NWT is relatively uniform. Winters are long and cold. Summer average monthly maximum temperatures are about 20°C, though daily temperatures can reach well above 30°C. Annual precipitation totals vary from 200 mm in the northeast to 500 mm in the southwest (Woo et al. 2007), with most of this precipitation falling during the summer months.

3 Data and Methods

Observational data used in this study included the archived lightning strike data from the Northwest Territories government (1994–99); fire data for the period 1984–99 from the Canadian Forest Service's national Large Fire Database (Stocks et al. 2002), and the territorial fire database; and sounding data (1961–2002) from the Environment Canada upper air digital ar-

chive. Data from the Global Environmental Multiscale (GEM) weather prediction model (Côté et al. 1998) at the Canadian Meteorological Centre and from the Canadian Lightning Detection Network (CLDN) were used in the development of a lightning prediction model (Burrows et al. 2005).

The study period 1994–99 was selected because the area burned in the MRB showed great variability and the territorial lightning network operating in the region was most reliable and relatively stable. Daily lightning strike statistics for the MBR were determined from the lightning detection network operating in the NWT (Fig. 1). The network has undergone a few configuration changes during the study period, including the reactivation of one station in the Inuvik region and the relocation of three stations in the North Slave, South Slave and Sahtu regions. The uncertainties in the

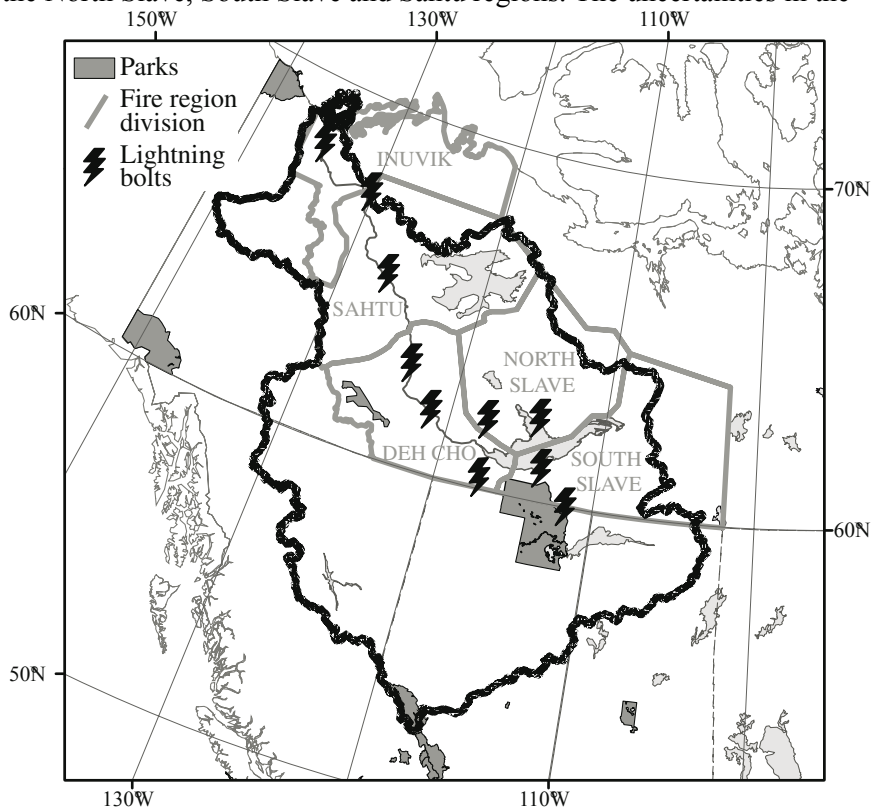

Fig. 1. Mackenzie Rive Basin (thick outline) showing the NWT fire regions and the configuration of the lightning detection network in 1999 (after Kochtubajda et al. 2006)

location accuracy of the lightning data and the detection efficiency of the network are described in Kochtubajda et al. (2002). In this study, the data were not corrected for detection efficiency. Fires larger than 200 ha comprise the Large Fire Database; although small in number, large fires account for approximately 97% of the total area burned (Stocks et al. 2002).

4 Results and Discussion

4.1 Enhanced Understanding of Convective and Lightning Processes

Traditionally, thunderstorm studies have utilized information gathered at weather observing stations. Conducting spatial studies of thunderstorm activity in the North therefore presents some challenges due to the sparse network of surface stations. However, due to the widespread, continuous coverage of lightning detection networks, information obtained from this network can be used to determine typical and unusual lightning patterns and to improve an understanding of the processes responsible for them. This type of climatology also provides additional information to increase the reliability of lightning prediction models.

The temporal evolution of lightning for the period 1994–99 is illustrated in Fig. 2a. The lightning season is characterized as short but intense, peaking in July and diminishing by August. Convective activity is rare in September. The start of the lightning season is influenced by the timing of snowmelt, whereas the southward passage of the Arctic cold front in late summer usually ends the convective season. The diurnal variations of lightning during this period (Fig. 2b) show that the majority of flashes occur in the late-afternoon, peaking near 1800 local time. This indicates that airmass daytime heating generated thunderstorms (Kochtubajda et al. 2002) produce most of the lightning, as opposed to longer-lived convective complexes that last through the night.

Positive lightning flashes (lightning discharges transferring positive charge to the earth) typically account for about 10% of all the C-G flashes around the world (Latham and Williams 2001). During the study period, positive flashes over the NWT comprised approximately 12% of all the ground flashes (Fig. 2c). Lightning activity during the 1995 fire season, however, was very unusual. The thunderstorms produced a relatively low amount of lightning but a large percentage of positive flashes (about 25%). Surface weather observations and satellite imagery suggest that the smoke

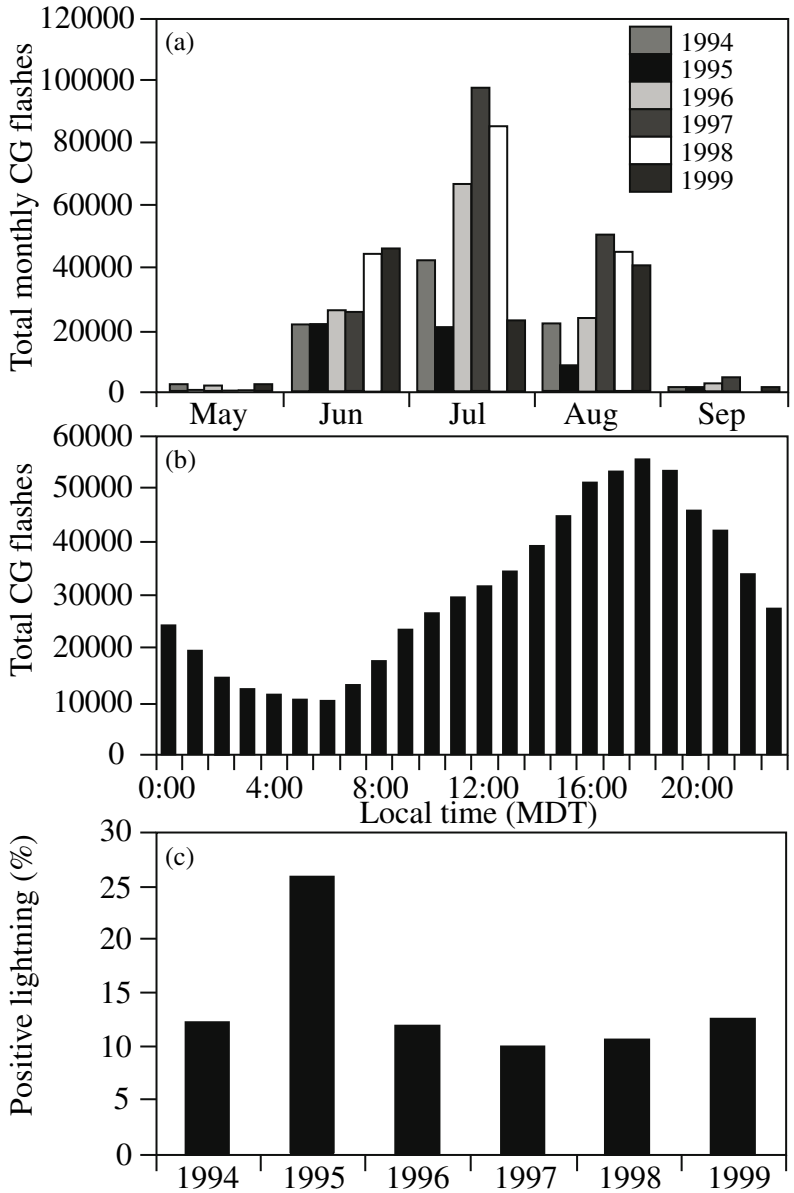

Fig. 2. Selected cloud-to-ground lightning characteristics in the NWT, 1994–1999: (a) monthly distribution of lightning flashes, (b) diurnal distribution of lightning flashes, and (c) annual fraction of positive lightning flashes (after Kochtubajda et al. 2006)

from existing forest fires may have contributed to the enhanced positive lightning activity (Kochtubajda et al. 2002).

4.2 Impacts of lightning

4.2.1 Impact on the Boreal Forest of the Basin

Fires in the boreal ecosystem of the NWT leave a patchwork of burnt trees and blackened earth (Fig. 1 in Flannigan et al. 2007). From this scorched landscape, new plants and trees emerge. Fires are also beneficial to the control of diseases and insects as well as maintaining biological diversity. On the other hand, fires can threaten human life, property and valuable commercial resources. The intensity of forest fires varies. Some fires can burn just the undergrowth or smoulder beneath the ground, whereas others are very destructive and consume large areas of forest.

During the 1994–99 fire seasons, a total of 1,695 lightning-initiated fires burned approximately 8.3 Mha, or 13.5% of the available forest. A fraction of these fires (22%) were larger than 200 ha, but these accounted for more than 98% of the total area consumed. The spatial distribution of fires (Fig. 3) shows that most of the territory has been impacted at some time. The areas burned in 1994 and 1995, over 3 Mha and about 2.8 Mha, respectively, were unusual. In fact, 1994–95 was the worst 2-year period on record for area burned in Canada (Simard 1997). Area-burned statistics are influenced by a number of factors including the weather, forest extent, topography, the composition of the landscape, fire suppression policies and priorities, organizational size and efficiency, and fire site accessibility. The Percent Annual Area Burned (PAAB) can be used to represent the frequency of large fires over a defined area such as an ecozone or ecoregion (Stocks et al. 2002). A PAAB of 2.21% over the forested area of the NWT was calculated for the 1994–99 study period. In the combined areas of the Taiga Plains and Taiga Shield West ecozones, Stocks et al. (2002) show that over the 39 years of record, an average of 0.7 % of the land area burns annually. Our study period thus reflects an unusually active period of fire.

The temporal evolution of fire occurrence and area burned by lightning (Fig. 4) shows an unusual pattern. Lightning-initiated fire occurrences peak during July, while much of the burned area occurs in June. Information from the Large Fire Database in Canada for 1959–99 (Stocks et al. 2002) also shows that most of the area burned occurs in June (~40%) with July being slightly lower (33%). There are several possible reasons why this pattern occurs. For example, there is a minimum in the foliar moisture content of conifer needles in the spring that may give rise to increased fire

activity (Van Wagner 1967), June is normally drier than July, and winds are typically stronger in June (Phillips 1990).

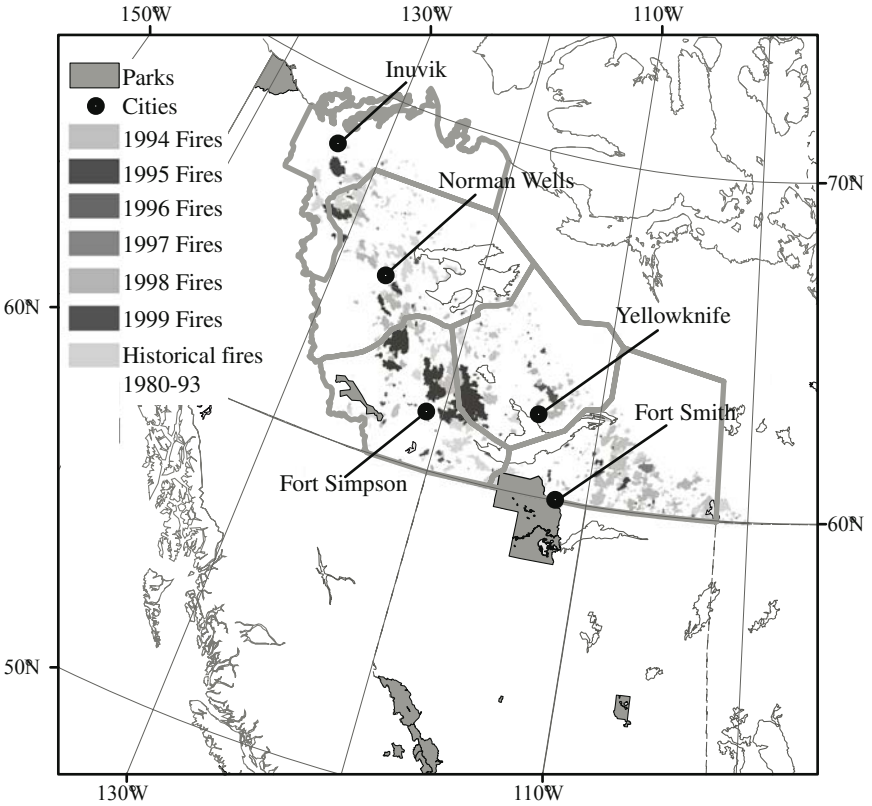

Fig. 3. Forest fire history in the NWT, 1980–1999 (after Kochtubajda et al. 2006)

4.2.2 Impact on the Polar Bear Habitat of Western Hudson Bay

A better understanding of the short-term and long-term threats of habitat loss due to forest fires is important in the development of habitat management strategies. A recent study (Richardson et al. 2005) illustrates the interactions and impacts of forest fires on polar bear maternity denning habitat near the western Hudson Bay coastline.

The maternity denning habitat, which the western Hudson Bay polar bear *(Ursus maritimus)* population depends on for survival, is located in Wapusk National Park, Manitoba, in the coastal lowlands of the Hudson Plain ecozone (Fig. 5). It is also one of the three largest polar bear denning areas in the world. Polar bears give birth to altricial young, which need to

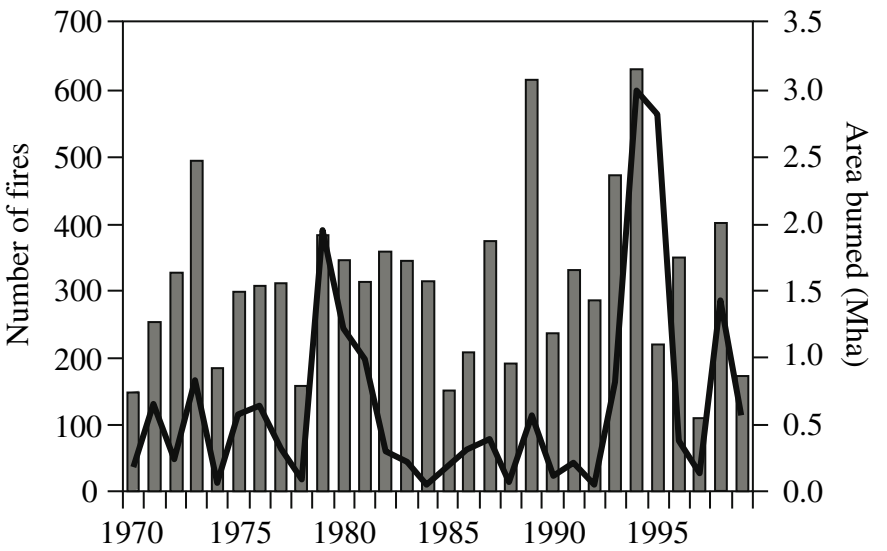

Fig. 4. Monthly fire occurrence and area burned statistics for 1970–1999 (after Kochtubajda et al. 2006)

be protected from the environment inside a den and nursed by their mothers for 3–4 months through mid-winter before they are large enough to be able to survive on the sea ice. Thus, the reliable availability of suitable denning habitat in which to give birth (from about mid-November through mid-December) is critical to successful reproduction and survival of polar bears throughout their range. In northern latitudes, polar bears rely on snow dens as reproductive sites. However, in western Hudson Bay adequate snowdrifts do not form in time in most years so the bears dig earthen dens into the permafrost along riparian banks where there is an overstory of small spruce trees (Fig. 6a). The roots of small spruce trees provide support to the ceilings of the den structures and prevent collapse.

Several large fires burned through parts of denning area in Wapusk National Park between 1998 and 2003, disturbing extensive areas of polar bear habitat. During this period, 33 fires burned a total of 944 km^2 of the study area. Lightning was determined to be the primary ignition source of the fires. The temporal evolution of lightning for this period (Fig. 7) illustrates the short convective season and annual variability. During the fire season the majority of lightning flashes were attributed to one or two storm days. The frequency of fires and area burned was highly variable. The most destructive season was in 1999 when 18 fires burned a total area of 683 km^2, while no fires were observed in 2001 and 2002. These large fires

burned through parts of the denning area resulting in the collapse of dens sites and the elimination of crucial habitat (Fig. 6b). The denning habitat in the study area was estimated to be 1210 km^2 in 1996. Over the six year period, approximately 5.5 % (or 67 km^2) of the denning habitat was lost, with the greatest loss occurring in 1999 when 46 km^2 of habitat was destroyed.

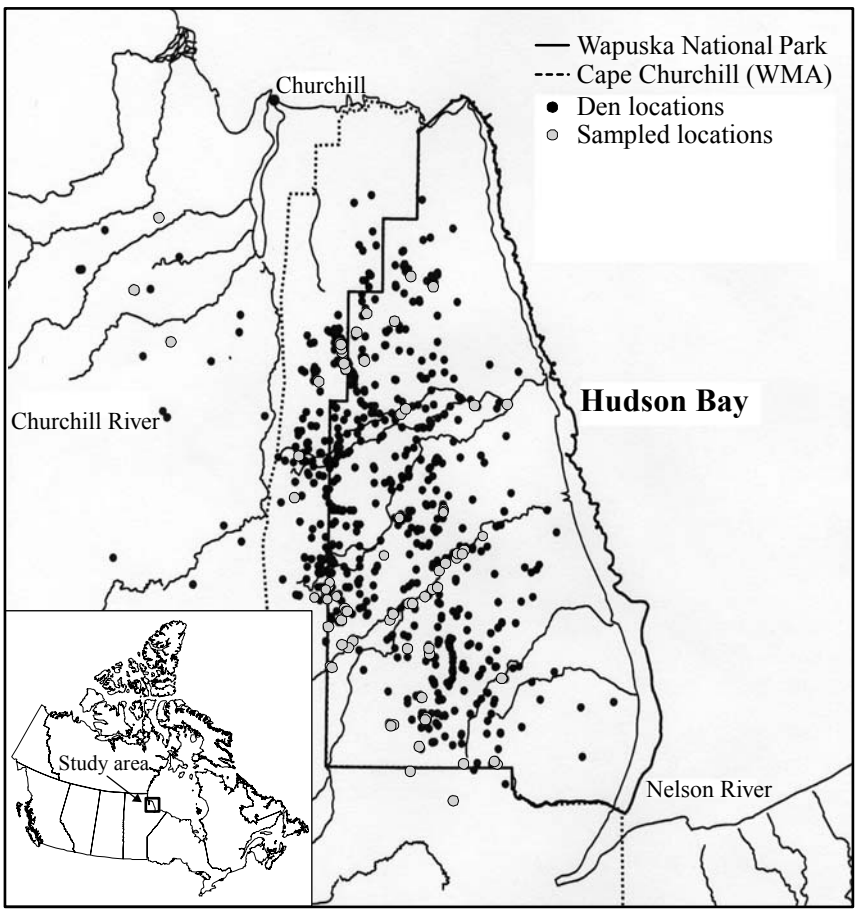

Fig. 5. Polar bear study area in western Hudson Bay showing the distribution of den locations

Projected climate changes toward longer, warmer and drier seasons are expected to increase the frequency and intensity of forest fires (Flannigan et al. 2005, 2007) and may limit the availability of suitable denning habitat in the future. The future loss of denning habitat as a result of fire in the Wapusk National Park presents an interesting management dilemma. His-

torically, fire has been viewed as a natural disturbance and has been left to simply burn out. Managers will have to weigh the benefits of fire as a natural disturbance and evaluate where fire suppression would be appropriate in order to preserve some of the most important denning habitats in the long-term.

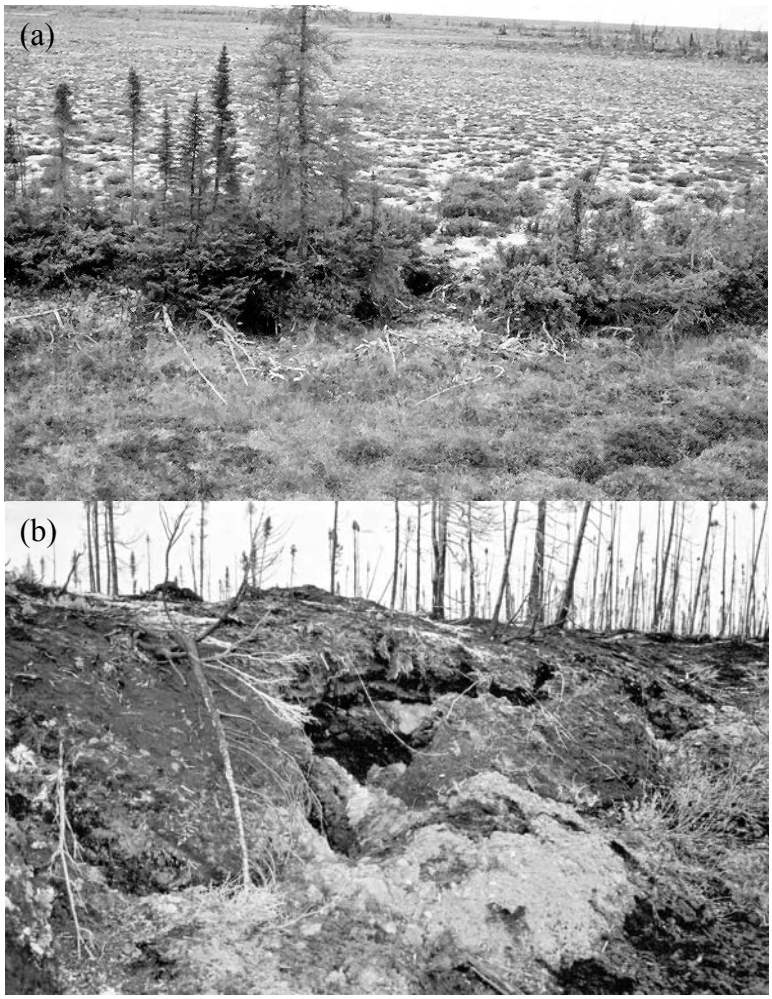

Fig. 6. Polar bear maternity den habitat in Wapusk National Park: (a) a typical den, and (b) removal of vegetation and collapse of a den as a result of fire

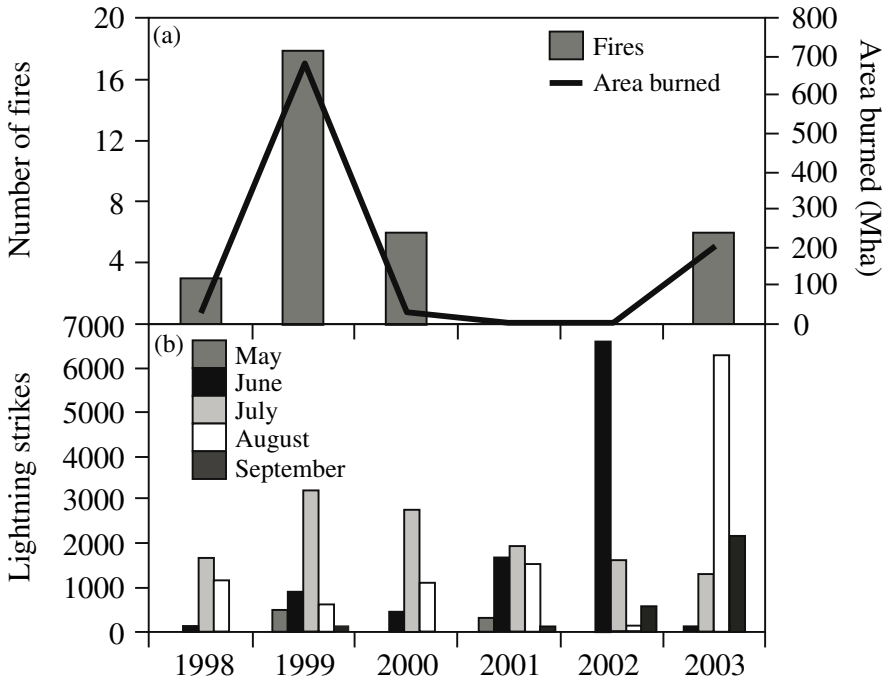

Fig. 7. History of lightning flashes and fire in the denning habitat, 1998–2003: (a) number of fire and area burned, (b) total lightning strikes in the denning area

4.3 Lightning Applications

4.3.1 Lightning Prediction

The general mandate of the provincial and territorial fire agencies focuses on pre-suppression activities and marshalling equipment and manpower resources to limit forest fire outbreaks. A variety of fire detection sources are utilized, including fire lookouts, aerial patrols, helicopters with fire fighters onboard, ground patrols, infrared scanners, and reports from the general public and resource industries. The agencies incorporate lightning data and observations from surface weather networks into their operations to evaluate ignition risk. Predictions of lightning-initiated forest fires can also assist forest protection agencies in preparing for outbreaks of multiple ignitions, fine-tuning detection flight routes, and locating holdover fires. A need also exists for better short-term predictions of lightning in public and aviation forecasts.

In response to these needs, dynamical-statistical models were constructed over the last several years to predict the probability of lightning occurrence in three-hour intervals, projected to 48 hours (Burrows et al. 2005). The original models were updated to include additional predictors and to expand coverage to all of Canada and the United States including Alaska, and to run year round (Burrows 2007).

The models ingest a variety of variables (predictors) derived from output of the GEM weather prediction model (Côté et al. 1998) at the Canadian Meteorological Centre (CMC). Two predictands are fitted by tree-structured regression (Brieman et al. 1984): (1) time-area coverage, which is similar to a probability of lightning occurrence, and (2) time-area average of the number of flashes counted at grid points where lightning occurs, i.e., flash rate. Here "time" refers to a three-hour period spanned by the 4 hourly GEM outputs at t, t+1, t+2, t+3, and "area" refers to a 9x9 grid centered on a grid point. This gives a data cloud of 324 points at every grid point with which to calculate smoothed predictands and predictors. The time-area coverage predictand is the fraction of the 324 points where lightning occurred. The flash rate predictand is calculated as the average flash count at only those of the 324 points where lightning occurred. Grid point separation is 15 km.

Predictor candidates (Table 1) are drawn from important environmental predictors identified from knowledge of physical processes and from several previous studies (e.g., Price 2000; Reap and MacGorman 1989) and from output of the deep and shallow convection parameterisations in GEM (Kain and Fritsch 1993; Kuo 1974). The basic predictor set (Table 1) was expanded by calculating various statistics for each predictor over the entire 324 point data cloud such as averages, maxima, fraction of points exceeding various threshold values, and so on (Burrows 2007). Smoothing of predictands and predictors was because the raw flash count at grid points rarely coincides exactly with predictors. Only predictors with correlation coefficients of 0.2 or more with the predictand were retained; and of these, if any in a group were correlated more than 0.9 with others in the group, only the predictor correlated highest with the predictand was kept. This reduced the total number of predictors in models to 50 or fewer. Only seven days of data, one from each month April to September 2005, were needed for training the models because the entire area of the northern USA and Canada where lightning is detected by the NALDN was used, and on any given day there are a large range of meteorological situations. Trees found by tree-structured regression had several hundred nodes in all cases, thus the output predictands are quasi-continuous spatially. Estimates by ten-fold cross-validation of the training data shows that when the models are

applied to independent data they can be expected to explain approximately 85–90% of the variance of the time-area coverage predictand and 80–85% of the variance of the flash rate predictand.

Table 1. Predictor selections for updated lightning forecast models (Burrows 2007)

Environment
Showalter index of convection
Lifted index of convection
Net convective available potential energy (CAPE – convective inhibition)
Lifted parcel cloud top, allowing entrainment
Precipitable water, surface to top of atmosphere
Precipitable water, 700 hPa to top of atmosphere
Severe weather threat index (SWEAT)
Mean sea level pressure
Boundary layer helicity
CMC severe storm index
Three-hour change of 500-1000 hPa thickness
Maximumwet bulb potential temperature Θ_w in the lowest 50 hPa
700 hPa vertical motion
Wind speed shear, surface to 700 hPa
GEM Convection parameterization
Deep convection precipitation rate
Shallow convection precipitation rate
Accumulated 3-hr implicit precipitation
Deep convection cloud depth (top–base)
Deep convection cloud base
Deep convection maximum vertical velocity
Deep convection CAPE
Vertical integral of cloud-ice mixing fraction in deep convection

Figure 8 shows the 24–27 hr FL01 flash rate forecast valid for 0000–0300 UTC 16 July 2006, and the 27-hr forecast mean sea level pressure valid 0300 UTC for the same day. FL01 is the time-area average number of flashes per 3-hours where the corresponding time-area coverage is 0.01 or greater. Lightning is forecast to occur over a large portion of the MRB north of Great Slave Lake. This forecast is verified by the lightning observed by the NALDN for the same three-hour period, smoothed in the same manner as the flash rate predictand was calculated (Fig. 9). The forecast for areas east of Great Bear Lake and at the northern edge of the Basin could not be verified because they lie beyond the limit of NALDN detection. In general, there is agreement in the overall shape and position of ob-

served lightning although details differ. The dynamical-statistical models described are currently used in operational weather forecast environments.

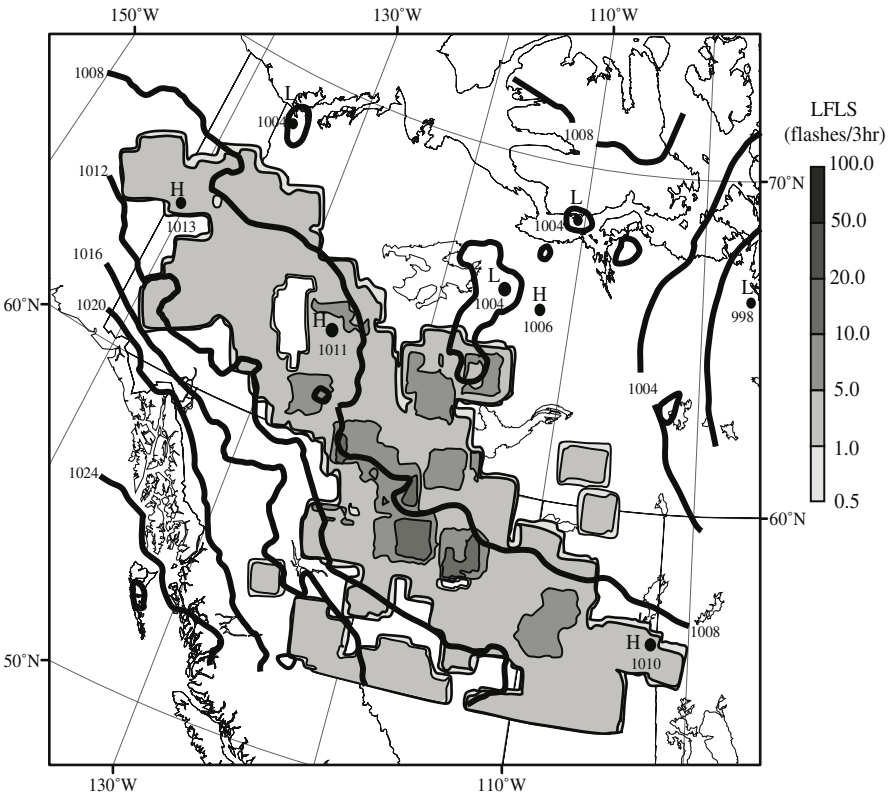

Fig. 8. 27-hr flash rate forecast filtered at each grid point by time-area coverage 0.01 or greater, valid for 0000-0300 UTC 16 July 2006; and mean sea level pressure [hPa] valid 0300 UTC 16 July 2006

4.3.2 Convective Precipitation Production and C-G Lightning

Accurate estimates of precipitation are important to characterize the moisture conditions in fire occurrence prediction models (Anderson 2002). Distances between weather stations vary and can be quite large, in some cases requiring interpolations to estimate precipitation. Convective precipitation and lightning are two physically related phenomena of thunderstorms. Several studies have calculated rain yields over various temporal and spatial scales and for different climatic regimes (e.g., Ezcurra et al. 2002;

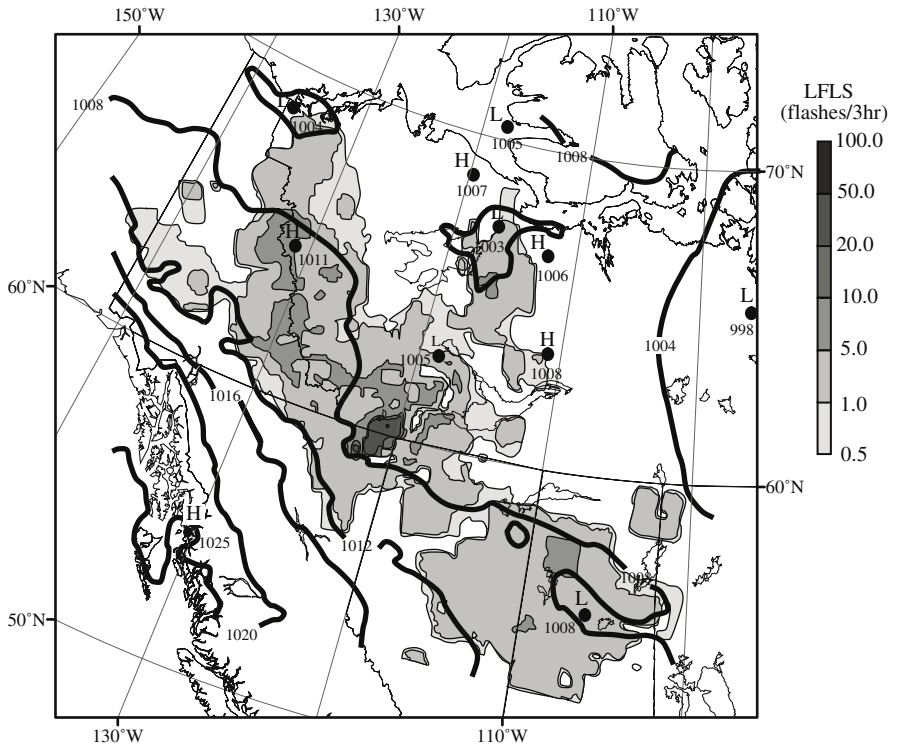

Fig. 9. Lightning flashes detected 0000-0300 UTC 16 July 2006 and MSL pressure [hPa], valid 0300 UTC 16 July 2006. Lightning flashes are calculated as the time-area average of the flash count at grid points where lightning occurred

Peterson and Rutledge 1998) but few such studies have been carried out over Canada.

The relationship between cloud-to-ground (C-G) lightning and convective rainfall over different eco-climatic regions of Canada was analyzed. Fifty four weather stations were selected to cover the cordilleran zone of the Pacific coast, the grasslands zone of the Prairies, the boreal, sub-arctic, and the temperate zones of the eastern Canada. The study period comprised the months of June to August from 1999 to 2003. The components of rain yield (viz., C-G lightning flashes and rainfall) were obtained from the Canadian Lightning Detection Network, and the daily rainfall measurements reported at each of the stations on confirmed thunderstorm days from the Meteorological Service of Canada surface weather archive. All C-G lighting strikes detected within a 20-km radius of each station were used in the calculation of the rain yield. The same rain depth was assumed over the entire 20-km radius, and the rain yield was determined by taking

the ratio of the volume of precipitation to the total number of C-G flashes. Depending on the recorded precipitation amount, thunderstorm days were classified as wet (rainfall greater than 3 mm) or dry (rainfall from trace amount to < 3 mm). The observations show that the storms producing the highest lightning frequencies are associated with those yielding the highest rainfall (Fig. 10). The rain yield characteristics for dry and wet thunderstorms across various eco-climate regimes (Table 2) reflect the complexity of thunderstorm characteristics and structure across Canada.

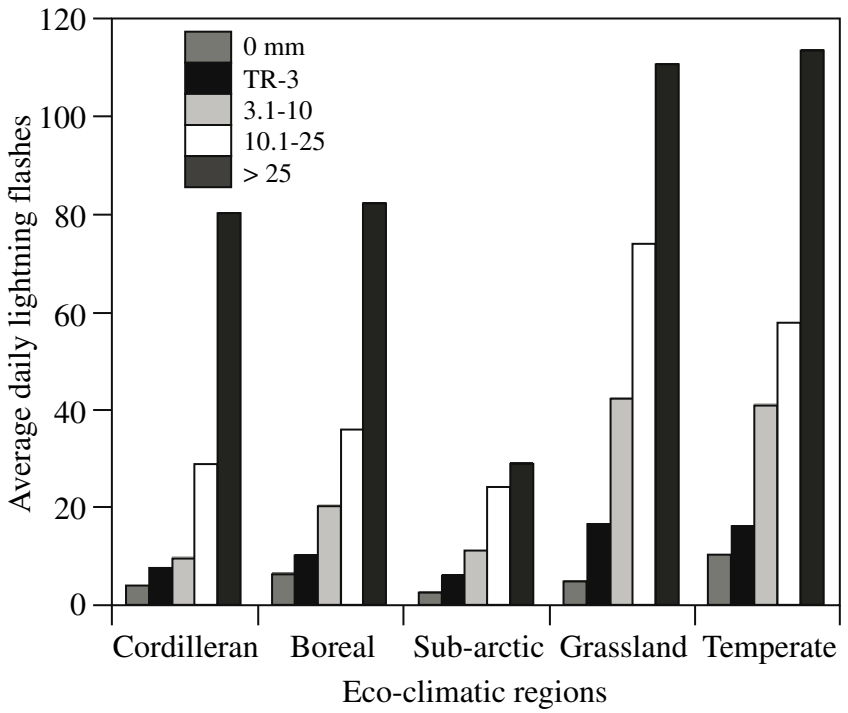

Fig. 10. Average daily lightning flashes stratified by precipitation range and eco-zone

Table 2. Summary of the rain yield characteristics for dry (Trace to 3 mm) and wet (> 3.1 mm) thunderstorms across various eco-climate regimes in Canada

Rain yield [10^4 m^3/fl]	Boreal	Cordilleran	Grassland	Subarctic	Temperate
Dry thunderstorms	1.8	1.7	0.1	6.3	0.5
Wet thunderstorms	14.0	196.0	4.3	39.0	3.7

5 Conclusion

The North experiences a large amount of lightning activity due to its geographic alignment, large scale air flows, and diurnal heating cycle. The short but intense period of lightning is driven by highly variable, daytime-heating generated thunderstorms. On occasion, such as during 1994 and 1995, the intertwined nature of convective storms and their lightning as well as surface conditions and forest fires can combine to produce extraordinary impacts such as widespread burning. Lightning-initiated fires have significantly changed vegetation and permafrost conditions. This has led to a decrease in the stability of polar bear maternity den sites in western Hudson Bay.

A tree-structured regression method for constructing statistical probability forecast models has been shown to successfully predict the probability of lightning in 3-h projection intervals out to 45–48 h. The potential also exists to use lightning information to improve the inter-station estimates of rainfall from thunderstorms.

An improved characterization of the convective storm season and associated lightning climatology over the MRB provide critical information on the occurrence, impacts and predictability of lightning and the lightning-caused forest fires. Experience gained from this research can be applied to other circumpolar boreal regions.

Acknowledgements

Funding support for this project was provided by the Prairie and Northern Region and Climate Research Branch of Environment Canada, the Northern Ecosystem Initiative, and by the Natural Sciences and Engineering Research Council of Canada. The authors thank the many people who have contributed and supported these initiatives. Special thanks are extended to Rick Lanoville of the Government of the Northwest Territories, Forest Management Division in Fort Smith who provided the lightning data

References

Anderson K (2002) A model to predict lightning-caused fire occurrences. Int J Wildland Fire 11:163–172

Brieman L, Friedman JH, Olshen RA, Stone CJ (1984) Classification and regression trees. Chapman & Hall/CRC Press, Boca Raton, FL (www.crcpress.com)

Burrows WR (2007) Dynamical-statistical models for lightning prediction to 48-hr over Canada and the United States. Proc 5th Conf artificial intelligence and its applications to environmental science. San Antonio, TX, Jan. 2007, Am Meteorol Soc, 23 pp

Burrows WR, King P, Lewis PJ, Kochtubajda B, Snyder B, and Turcotte V (2002) Lightning occurrence patterns over Canada and adjacent United States from lightning detection network observations. Atmos Ocean 40:59–81

Burrows WR, Price C, Wilson LJ (2005) Warm season lightning probability prediction for Canada and the northern United States. Weather Forecast 20:971–988

Christian HJ, Blakeslee RJ, Boccippio DJ, Boeck WJ, Buechler DE, Driscoll KT, Goodman SJ, Hall JM, Koshak WJ, Mach DM, Stewart MF (2003) Global frequency and distribution of lightning as observed from space by the optical transient detector. J Geophys Res, doi:10.1029/2002JD002347

Clark EE (1973) Indian legends from the northern Rockies. University of Oklahoma Press, Norman, OK.

Côté J, Gravel S, Méthot A, Patoine A, Roch M, Staniforth A (1998) The operational CMC-MRB global environmental multiscale (GEM) model, Part I: design considerations and formulation. Mon Weather Rev 126:1373–1395

Ecological Stratification Working Group (1995) A national ecological framework for Canada. Agric and Agri-food Can and Environ Can, Ottawa

Epp H, Lanoville R (1996) Satellite data and geographic information systems for fire and resource management in the Canadian Arctic. Geocarto Internat 11:97–103

Ezcurra A, Areitio J, Herrero I (2002) Relationships between cloud-to-ground lightning and surface rainfall during 1992–1996 in the Spanish Basque country area. Atmos Res 61:239–250

Flannigan MD, Kochtubajda B, Logan KA (2007) Forest fires and climate change in the Northwest Territories. (Vol. I, this book)

Flannigan MD, Logan KA, Amiro BD, Skinner WR, Stocks BJ (2005) Future area burned in Canada. Climatic Change 72:1–16

Flannigan MD, Wotton BM (2001) Climate, weather and area burned. In: Johnson EA, Miyanishi K (eds) Forest fires: behaviour and ecological effects. Academic Press, San Diego, pp 335–357

Gillett NP, Weaver AJ, Zwiers FW, Flannigan MD (2004) Detecting the effect of climate change on Canadian forest fires. Geophys Res Lett 31, L18211, doi:10.1029/2004GL020876

Kain JS, Fritsch JM (1993) Convective parameterization for mesoscale models: the Kain-Fritsch scheme. The representation of cumulus convection in numerical models. Meteorol Monogr 27, Am Meteorol Soc, pp 165–170

Kochtubajda B, Stewart RE, Gyakum JR, Flannigan MD (2002) Summer convection and lightning over the Mackenzie River Basin and their impacts during 1994 and 1995. Atmos Ocean 40:199–220

Kuo HL (1974). Further studies on the parameterization of the influence of cumulus convection on large scale flow. J Atmos Sci 31:1232–1240

Latham D, Williams E (2001) Lightning and forest fires. In: Johnson EA, Miyanishi K (eds) Forest fires: behaviour and ecological effects. Academic Press, San Diego, pp 375–418

Mackenzie A (c2001) The journals of Alexander Mackenzie: Voyages from Montreal, on the river St. Laurence, through the continent of North America, to the Frozen and Pacific oceans; in the years 1789 and 1793. With a preliminary account of the rise, progress, and present state of the fur trade of that country. The Narrative Press, Santa Barbara, California

Mills B, Unrau D, Parkinson C, Jones B, Yessis J, Spring K (2006) Striking back: an assessment of lightning-related fatality and injury risk in Canada. Final tech report prepared for the Canadian lightning detection network, September. Adaptation and impacts research division, Environ Can, Waterloo, Ontario

Peterson WA, Rutledge SA (1998) On the relationship between cloud-to-ground lightning and convective rainfall. J Geophys Res 103(12):14025–14040

Phillips D (1990) The climates of Canada. Can Gov Publ Centre, Supply and Services Canada. Ottawa, ON.

Price C (2000) Evidence for a link between global lightning activity and upper tropospheric water vapour. Nature 406:290–293

Reap RM, MacGorman DR (1989) Cloud-to-ground lightning: climatological characteristics and relationships to model fields, radar observations, and severe local storms. Mon Weather Rev 117:518–535

Richardson E, Stirling I, Kochtubajda B (2005) The effects of forest fires on polar bear maternity denning habitat in western Hudson Bay. Polar Biology doi:10.1007/s00300-006-0193-7

Rowe JS (1972) Forest regions of Canada. Dept of Fisheries and the Environment, Canadian Forestry Service, pub no 1300

Simard AJ (1997) National workshop on wildland fire activity in Canada. Science Branch, Canadian Forestry Service, Natural Resources Canada, Ottawa, Ontario, Inf rep ST-X-13

Stocks BJ, Mason JA, Todd JB, Bosch EM, Wotton BM, Amiro BD, Flannigan MD, Hirsch KG, Logan KA, Martell DL, Skinner WR (2002) Large forest fires in Canada, 1959–1997. J Geophys Res, doi:10.1029/2001JD000484

Uman MA (2001) The lightning discharge. Dover Publ Inc, Mineola, New York

Van Wagner CE (1967) Seasonal variation in moisture content of eastern Canadian tree foliage and the possible effect on crown fires. Can Dept For Rural Develop Forest, Br Publ 1204

Ward PC, Mawdsley W (2000) Fire management in the boreal forest of Canada. In: Kasischke ES, Stocks BJ (eds) Fire, climate change and carbon cycling in the boreal forest. Springer-Verlag, New York, pp 66–84

Woo MK, Rouse WR, Stewart RE, Stone J (2007) The Mackenzie GEWEX Study: a contribution to cold region atmospheric and hydrologic sciences. (Vol. I, this book)

Chapter 23

Forest Fires and Climate Change in the Northwest Territories

Michael D. Flannigan, Bohdan Kochtubajda
and Kimberley A. Logan

Abstract Fire is the major stand-renewing disturbance in the circumboreal forest. Weather and climate are the most important factors influencing fire activity and these factors are changing due to human-caused climate change. Under a future warmer climate, we expect more severe fire weather, more area burned, more ignitions and a longer fire season, although there will be large spatial and temporal variation in the fire activity response to climate change. Results indicate increases of 25 to 300% in area burned and a lengthening of the fire season by 30 to 50 days over a large portion of the Northwest Territories, Canada. This field of research allows better understanding of the interactions and feedbacks between fire, climate, vegetation and humans, and identification of vulnerable regions. Projections of fire activity for this century can be used to explore options for mitigation and adaptation.

1 Introduction

Forest fire is the dominant disturbance that shapes and maintains many of Canada's forests (Fig. 1). During the 1990s an annual average of close to 8,000 forest fires burned about 2.8 million ha in Canada. They were typically crown fires (Fig. 2) that were responsible for renewal of stands (Stocks et al. 2002; Weber and Stocks 1998). Fire activity is strongly influenced by four factors: weather/climate, fuels, ignition agents and humans (Flannigan and Wotton 2001; Johnson 1992; Swetnam 1993). Climate and the associated weather are dynamic and our climate experiences recent warming due to increases of radiatively active gases (carbon dioxide, methane etc.) as a result of human activities (IPCC 2001). This altered climate as modelled by General Circulation Models (GCMs) may have a profound impact on fire activity in Canada and elsewhere. This is particularly important for northern areas like the Northwest Territories (NWT),

Fig. 1. Fire in the boreal forest has left swaths of burnt areas as shown by the dark patches in the photograph. (Photo: W. DeGroot, Canadian Forest Service)

Fig. 2. Wildfire in the boreal forest, often started by lightning activities. (Photo: W. DeGroot, Canadian Forest Service)

Canada, as rapid and significant changes are expected at higher latitudes (ACIA 2005).

In Canada, weather/climate is the most important natural factor influencing forest fires (Flannigan and Wotton 2001; Gillett et al. 2004; Hely et al., 2001). Weather determines fuel moisture, causes lightning ignitions, and contributes to fire growth through wind action. However, the long term average of area burned across a landscape is determined by a complex set of variables including the size of the sample area, the period under consideration, the extent of the forest, the topography, fragmentation of the landscape (rivers, lakes, roads, agricultural land), fuel characteristics, season, latitude, fire suppression policies and priorities, fire control, organizational size and efficiency, fire site accessibility, ignitions (people and lightning), and simultaneous fires, as well as the weather.

The objective of this study is to explore the changes in fire weather, fire season and fire activity with respect to climate change. The potential impacts of these changes in the fire regime on the forests and communities of the Northwest Territories will also be discussed.

2 Study Area

The forested region of the NWT covers approximately 615,000 km^2 (or 18% of the territory) and is largely made up of black spruce (*Picea mariana*), lodge pole pine (*Pinus contorta*), jack pine (*Pinus banksiana*) and trembling aspen (*Populus tremuloides)* tree species. Numerous small lakes and marsh areas characterize the landscape. The regional climate is influenced by several factors including latitude, amount of incoming solar radiation, topography, and the character of its weather systems. Although incoming solar energy, which arrives at low angles, limits the amount of surface warming, increased length of day balances this limitation in the summer. In Yellowknife, for example, daily sunlight lasts about 20 h in June, while at Inuvik the sun does not set in midsummer. Summer average monthly maximum temperatures are about 20°C, but daily temperatures can reach well above 30°C. Annual precipitation totals over the NWT vary from 200 mm in the northeast to 500 mm in the southwest, with at least half of this precipitation falling during the summer.

3 Data and Methods

Area burned data taken from the large fire database for the 1959-1997 period (Stocks et al. 2002) included start date, location, cause and final size of the fire. Area burned was sorted into half month periods, monthly periods and seasons for May to September by modified ecoregions and ecozones (Ecological Stratification Working Group 1996; Fig. 3). Note that April was not included in this study as less than 2% of Canada's area burned occurs in April (Stocks et al. 2002).

Fig. 3. Ecozones of Canada used in this study, modified from Ecological Stratification Working Group (1996). Triangles denote the location of meteorological stations (after Flannigan et al. 2005)

Meteorological data for the same period as the fire data were obtained from Environment Canada. Variables included temperature, relative humidity, wind speed and 24-h precipitation at 1200 LST each day from April 15 to September 30. Stations were selected manually based on their long-running representativeness within each ecogroup or ecozone. If no stations were available then nearby stations were assigned, resulting in some stations being used for more than one region. In the case of an ec-

ogroup or ecozone containing more than one station, the station values were averaged. The 1200 LST observations of temperature, relative humidity, wind speed and 24-h precipitation are the inputs required to calculate the components of the Canadian Forest Fire Weather Index (FWI) System (Van Wagner 1987). The FWI System is a weather-based system that models fuel moisture using a dynamic bookkeeping method that tracks the drying and wetting of distinct fuel layers in the forest floor. There are three moisture codes that represent the moisture content of fine fuels (Fine Fuel Moisture Content, FFMC), loosely compacted organic material (Duff Moisture Code, DMC) and a deep layer of compact organic material (Drought Code, DC). The drying time-lags for these three fuel layers are 2/3 of a day, 15 days and 52 days respectively for the FFMC, DMC and DC under normal conditions (temperature 21.1°C, relative humidity 45%).These moisture indexes are combined to create a generalized index of the availability of fuel for consumption (Build Up Index, BUI) and the FFMC is combined with wind to estimate the potential spread rate of a fire (Initial Spread Index, ISI). The BUI and ISI are combined to create the FWI which is an estimate of the potential intensity of a spreading fire. The Daily Severity Rating (DSR) is a simple exponential function of the FWI intended to increase the weight of higher values of FWI in order to compensate for the exponential increase in area burned with fire diameter (Van Wagner 1970; Williams 1959). Means and extremes of the meteorological variables and FWI System components were calculated for half month, month and season periods. Extremes of the variables were used because much of the area burned occurs during extreme fire weather conditions.

The last meteorological variable used was the North American upper air database consisting of 500 hPa height anomalies obtained from Environment Canada for 1959–97 (Skinner et al. 2001). These data were available as half-monthly and monthly anomalies in a grid with a spatial resolution of 5^{o} latitude by 10^{o} longitude for our study area. The data for gridpoints covering Canada were interpolated using a thin-plate cubic-spline technique (Flannigan and Wotton 1989) to the weather station locations and averaged if necessary in the same way as the other variables. The position and strength of the 500 hPa flow is related to fire activity (Newark 1975; Skinner et al. 1999, 2001). All the variables used in this study are displayed in Table 1.

Daily data were collected from both the Canadian (CCCma) and the Hadley GCM for two time periods. For the Canadian model 1975–95 was considered to correspond to a $1xCO_2$ scenario, while 1975–90 was the $1xCO_2$ scenario for the Hadley model. The Canadian model used was the First Generation Coupled GCM (CGCM1). This model included both

Table 1. Meteorological and FWI system variables

ANOM	mean 500 hPa height anomaly [m]
BUI	mean buildup index
BUIX	maximum buildup index
DC	mean drought code
DCX	maximum drought code
DMC	mean duff moisture code
DMCX	maximum duff moisture code
DSR	mean daily severity rating
DSRX	maximum daily severity rating
FFMC	mean fine fuel moisture code
FFMCX	maximum fine fuel moisture code
FWI	mean fire weather index
FWIX	maximum fire weather index
ISI	mean initial spread index
ISIX	maximum initial spread index
PREC	mean precipitation [mm]
TPREC	total precipitation [mm]
RH	mean relative humidity [%]
RHN	minimum relative humidity [%]
RHX	maximum relative humidity [%]
TEMP	mean temperature [°C]
TEMPX	maximum temperature [°C]
WIND	mean windspeed [km h^{-1}]
WINDX	maximum windspeed [km h^{-1}]

greenhouse gas and sulfate aerosol forcing contributing to a 1% increase in CO_2 per year. The time period 2080–2100 roughly corresponds to an equivalent $3xCO_2$ scenario when including the net radiative effect of all the greenhouse gases. The grid spacing is approximately 3.75° longitude by 3.75° latitude. The Hadley model, HadCM3GGa1, contained only greenhouse gas forcing and output from 2080–99 as its equivalent $3xCO_2$ scenario. The grid for the Hadley Model had slightly better resolution at 3.75^o longitude by 2.5^o latitude. The modelled variables examined from both models were maximum temperature, precipitation, wind speed, and humidity. Only daily noon values were used in the analysis. Noon temperature was estimated as the maximum daily temperature minus 2.0°C. In examining the amount of daily precipitation for the $1xCO_2$ scenarios in the models, it was noted that the GCM grid cells contain more moisture than was observed by point measurements at the weather stations. This effect has been noted in other studies on rainfall event frequencies (Mearns et al. 1995; Osborn and Hulme 1997; Skelly and Henderson-Sellers 1996) and

various calibrations have been proposed. We calculated daily rainfall amount frequencies for representative areas in eastern and western Canada and compared them with observed frequencies from weather stations. The frequency of duration of rain-free periods was also examined. We attempted to reduce the unrealistic incidence of small frequent daily precipitation by calibrating the modeled precipitation with a daily correction factor (Mearns et al. 1995) for the current time period of each model. The correction factor took the form of a constant amount subtracted from the daily precipitation value. Frequencies were recalculated and compared with the observations again. These comparisons were repeated using several different correction factors from 0 to 2.5 mm daily until the modeled frequencies were as close to observed as possible. For the Canadian model a correction of 2.0 mm per day worked best. For the Hadley model a correction of 1.5 mm per day was most appropriate. These corrections were applied to daily precipitation outputs from the $1xCO_2$ scenarios and $3xCO_2$ scenarios. Additional information on these GCMs can be found in Flato et al. (2000) and Gordon et al. (2000).

From the FWI System, the seasonal severity rating (SSR) (Van Wagner 1970) was calculated. SSR is a seasonal average (May–August) representing the fire control difficulty. SSR was calculated for each time period and model. Ratios were determined for the $3xCO_2$ to $1xCO_2$ scenarios of mean SSR. A temperature-duration criterion was used to determine the start and the end of the fire season. Fire season length was calculated by considering the start of the season to be the point at which there were 3 consecutive days with an average maximum daily temperature above 3.5°C. The end of the season was considered to be the first occurrence of that average temperature dropping below 3.5°C after August 1.

Using SAS version 8.02 (SAS 2000) a linear forward stepwise regression was performed for each spatial unit, ecogroup or ecozone and for each time period, half month, month or season with area burned as the predictand and the variables listed in Table 1 as the predictors. Terms were accepted only if they met the 0.05 significance level; terms were removed when they failed to meet the 0.15 significance level.

4 Results and Discussion

Figure 4 shows the ratio in $3xCO_2$ to $1xCO_2$ mean seasonal SSR; both models suggest significant increases in SSR over the Mackenzie Basin (1.19 for the CCCma model and 1.44 for the Hadley model averaged over

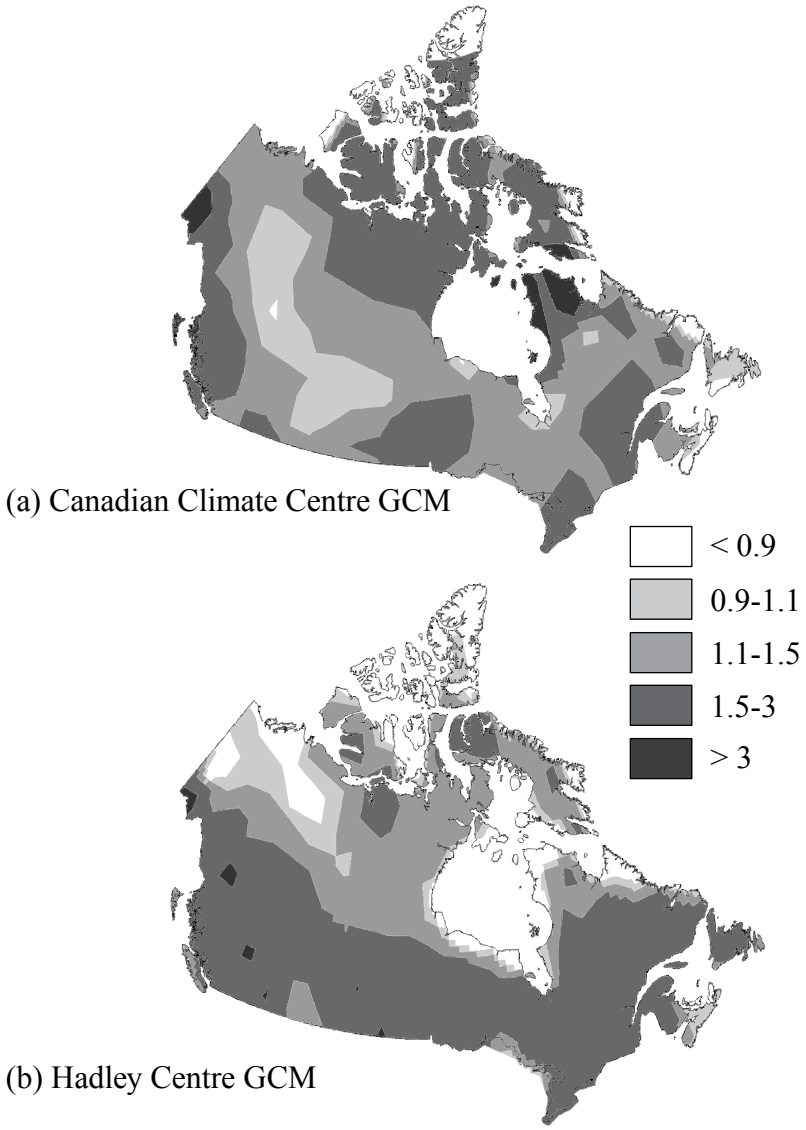

Fig. 4. Projected changes in the ratio of $3xCO_2$ to$1xCO_2$ mean seasonal fire severity from (a) the Canadian Climate Centre and (b) and Hadley Centre GCMs

the basin) but the models differ in the details. The CCCma model suggests little change in SSR over the southern Mackenzie region of the NWT with significant increases in northwestern NWT. On the other hand, the Hadley model suggests significant increases in the southern NWT and northern

Alberta and BC but decreasing SSR is expected over north-western NWT. This suggests considerable regional variation in the response to climate change, some of which arises from model differences in their large scale scenario patterns. As well, due to the coarse spatial resolution of the GCM (approx. 400 km) confidence in the results over complex, mountainous terrain is low over part of our study domain.

Table 2 shows the results from the forward stepwise regression of monthly area burned in ecozones across Canada. The variance explained ranges from 36 to 64% and all regressions were highly significant ($p<0.0001$). Using different time periods (half month and season) and modified ecoregions and ecozones showed similar results (not shown) though not quite as high as those presented in Table 2. Therefore we opted to use monthly ecozone area burned in tandem with GCM outputs to generate future area burned values. Temperature, mean or maximum, was selected by the regressions in every ecozone except ecozones 62, 9 and 14. Extremes of meteorological variables and FWI System indexes are important as much of the area burned often occurs during a few critical days of rapid fire growth that coincide with severe fire weather (hot, windy and dry) (Flannigan and Wotton 2001). For the Northwest Territories (ecozones 4 and 5) mean and maximum temperature were the most important variables in the regression (Table 2). Mean or maximum values of fuel moisture codes (FFMC, DMC and DC) were selected 8 times and were selected by regression in every ecozone except ecozones 4 and 11.

Table 2. Ecozone monthly area-burned explained variance and variables selected, in order of importance, by stepwise regression

Modified ecozone	Significant variables	Variance explained [%]	No. of samples	Prob.
4	*TEMP,DSR*	56	195	< 0.0001
5	*TEMPX,DMCX*	64	195	< 0.0001
61	*FFMCX*, *TEMP,* DMCX	60	195	< 0.0001
62	*DMC*	42	195	< 0.0001
9	*ISI*, *FFMCX*, *DMC*,*TPREC*	50	195	< 0.0001
11	*TEMP*, *DSR*	36	195	< 0.0001
12	*TEMP*, *FFMCX*	36	195	< 0.0001
14	*FWI*, *RHX*, *DC*	42	195	< 0.0001

Figure 5 shows the ratio of $3xCO_2/1xCO_2$ area burned predictions using the two GCM models. Both models suggest significant increases in area burned in a $3xCO_2$ climate. Increases in area burned of 25–300% are predicted with the Canadian GCM while increases 50–300% are predicted

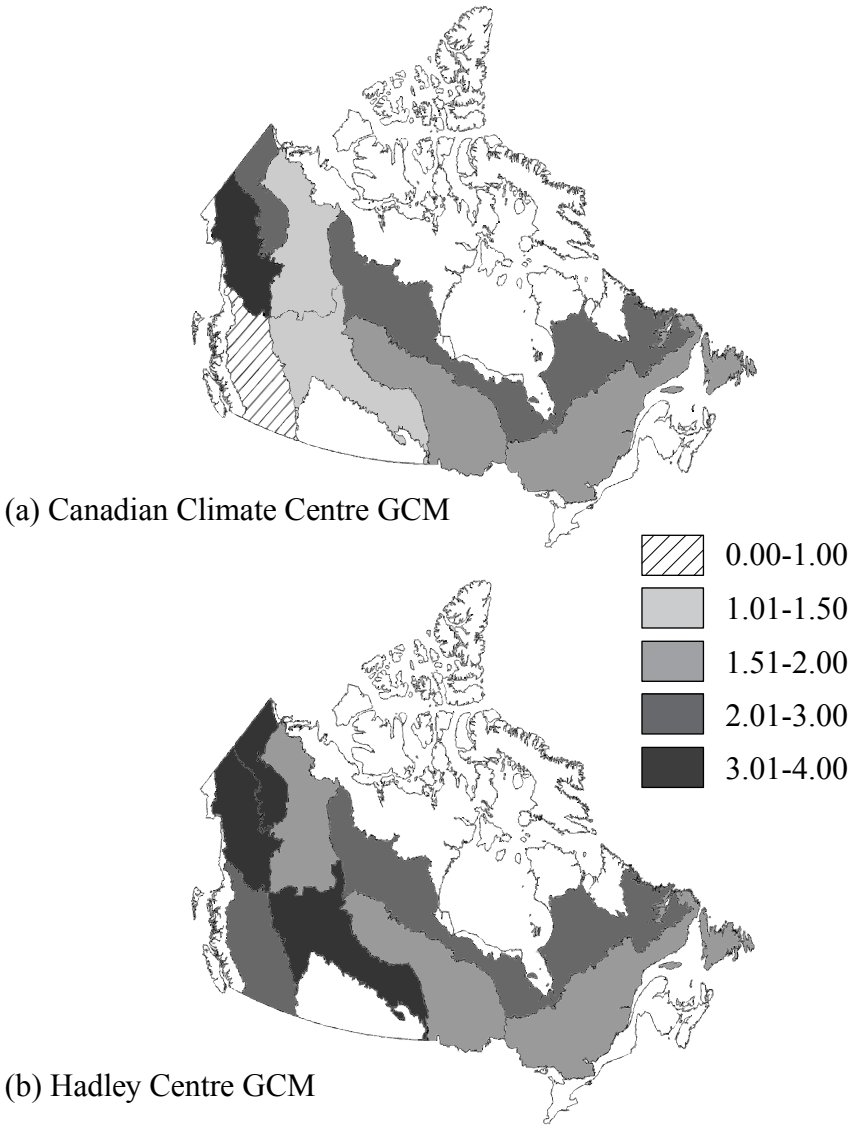

Fig. 5. Ratio of $3xCO_2/1xCO_2$ area burned by Ecozone using (a) the Canadian and (b) Hadley GCMs, respectively (after Flannigan et al. 2005)

with the Hadley Model. These results suggest a significant increase in area burned in the Northwest Territories that could have important implications on forests, forestry activities, community protection and carbon budgets. Direct emissions of carbon from forest fires on average over the last 40

years are equivalent to 20% of fossil fuel emissions in Canada (Amiro et al. 2001). Fire management agencies in Canada already spend half a billion dollars a year on direct suppression costs; if area burned does increase as suggested by this study these suppression costs could rise significantly. Additionally, fire management agencies operate with a narrow margin between success and failure, a disproportionate number of fires may escape initial attack under a warmer climate, resulting in an increase in area burned much greater than the corresponding increase in fire weather severity (Stocks 1993). Lastly, the interplay between climate change and area burned could overshadow the direct effects of global warming on plant species distribution and migration (Weber and Flannigan 1997). Thus, fire could be viewed as an agent of change in Canadian forests (Stocks 1993).

In this study, we did not explicitly address any changes in the number of ignitions but we would expect an increase in lightning-caused ignitions in Canada as well due to more thunderstorms (Price and Rind 1994) and more receptive fuels (Wotton et al. 2003). Recent results for people-caused ignitions in Ontario suggest increases of 18% and 50% for 2050 and 2100, respectively (Wotton et al. 2003). Also, in this initial assessment, we assume that the future vegetation mosaic will have similar fuel characteristics to the present situation. This is probably a reasonable assumption as many forested regions in Canada were able to sustain significantly more fire activity in the past as determined by fire history studies (Flannigan et al. 1998, 2005). Future studies will include changes to fuel types in a changing climate with particular emphasis on the feedbacks caused by a changing fire regime. Changes in fire season length that are anticipated with climate change are not included in this present study. Wotton and Flannigan (1993) found that the fire season length in Canada increased by an average of 22% or 30 days using the Canadian GCM $2xCO_2$ scenario. Lastly, future human activities could impact on the area burned numbers. Humans start forest fires but they also try to suppress most of the fires. People can fragment the forest with agricultural, urban development and transportation corridors. Given all these factors that are not included in this preliminary study we feel that overall our numbers may be conservative.

Changes in fire season length from $3xCO_2$ to $1xCO_2$ from the CCCMa and Hadley GCMs over our region of interest were calculated. Both models indicate an extension of 30 to 50 days in the fire season length over much of the Mackenzie basin (Kochtubajda et al. 2006). These estimates may be conservative because the fire season length analysis was constrained by our criteria and time period. It is possible that in some situations we ended the fire season prematurely if, for example, there was a cold snap early in September but the rest of the month was relatively

warm. According to our temperature-duration criteria, the fire season would have ended though in reality the season may have continued. Furthermore, there are a few areas of Canada that have fire seasons that begin before April 1 or end after September 30. Any such changes in season length would not be reflected in this study.

As the southern edge of the boreal forest may shift rapidly northward due to drought, disease and especially fire; the northern edge will shift northward only slowly due to soil and nutrient constraints, with an end result that the forested area in the Mackenzie Basin may shrink. Decreased forested area in the basin would have impacts on the hydrology and climate of the region through various feedbacks like reduced surface vegetation cover and changed albedo (Bonan 2002). All these factors suggest that the northern forests and communities may be even more susceptible to forest fires in the future with the possibility of some significant and rapid changes.

Results from the fire and climate change research allow us to ascertain which regions are potentially vulnerable to a climate change altered fire regime. This would encourage the development of plans and options to mitigate or adapt to the possible changes. One tool that could be used from a fire suppression perspective is a level of protection analysis model (McAlpine and Hirsch 1999) which determines how many fires will escape initial attack based on fuels, weather and available suppression resources. Simulations can be used to explore the impact of changing climate and changing resource levels on escaped fires.

Lastly, feedbacks and interactions between fire and humans, climate, the atmosphere and ecosystems need to be understood. Lavorel et al. (2007) proposed an integrated fire research framework to address fire and climate change issues. In addition to fire, other disturbances (e.g., insects, disease, wind and human activities) should be considered along with interactions between disturbances and there is the potential for synergies between disturbances. For example, fire is more likely during the first decade following a severe spruce budworm outbreak (Fleming et al. 2002). Additionally, there is an interaction with fire-generated smoke that may impact regional and probably even global radiation budgets (Guo et al. 2007; Simmonds et al. 2005). In the short term, smoke can have a positive feedback on weather and fire activity by promoting lightning ignitions (Kochtubajda et al. 2002; Lyons et al. 1998) and reducing local precipitation (Rosenfeld 1999). The feedbacks of carbon losses from global fire have the potential to be a major factor in our changing climate. There is the possibility of a positive feedback, whereby a warmer and drier climate will create conditions conducive to more fire. This in turn will increase carbon emissions

from fires, which would feed the warming (Kurz et al. 1995). Although this scenario is possible, we believe that the boreal forests may present some limit to large fire occurrence and increasing area burned since very young forests tend to be less susceptible to fire and could create more landscape fragmentation. We do not yet have a quantitative estimate of these feedbacks, an area of needed research combining fire and climate science with landscape dynamics. A fundamental question pertains to the ecological amplitude of our forests in their adjustment and adaptation to fire. Many of our forests have evolved with some level of fire, but we still need to ask how much fire they need, and how much fire they can tolerate.

References

Amiro BD, Todd JB, Wotton BM, Logan KA, Flannigan M, Stocks BJ, Mason JA, Skinner WR, Martell DL, Hirsch KG (2001) Direct carbon emissions from Canadian forest fires, 1959 to 1999. Can J Forest Res 31:512–525

ACIA (2005). Arctic climate impact assessment. Scientific report. Cambridge University Press, Cambridge

Bonan GB (2002) Ecological climatology: Concepts and applications. Cambridge University Press, Cambridge

Ecological Stratification Working Group (1996) A national ecological framework for Canada. Agr. and Agri-food Can. and Environ Can., Ottawa

Flannigan MD, Bergeron Y, Engelmark O, Wotton BM (1998) Future wildfire in circumboreal forests in relation to global warming. J Veg Sci 9:469–476

Flannigan MD, Logan KA, Amiro BD, Skinner WR, Stocks BJ (2005) Future area burned in Canada. Climatic Change 72:116

Flannigan MD, Wotton BM (1989) A study of interpolation methods for forest fire danger rating in Canada. Can J Forest Res 19:1059–1066

Flannigan MD, Wotton BM (2001) Climate, weather and area burned. In: Johnson EA, Miyanishi K (eds) Forest fires: Behavior & ecological effects. Academic Press, pp 335–357

Flato GM, Boer GJ, Lee WG, McFarlane NA, Ramsden D, Reader MC, Weaver AJ (2000) The Canadian centre for climate modelling and analysis global coupled model and its climate. Clim Dynam 16:451–467

Fleming RA, Candau J-N, McAlpine RS (2002) Landscape-scale analysis of interactions between insect defoliation and forest fire in central Canada. Climatic Change 55:251–272

Gillett NP, Weaver AJ, Zwiers FW, Flannigan MD (2004) Detecting the effect of climate change on Canadian forest fires. Geophys Res Lett 31:L18211, doi:10.1029/2004GL020876

Gordon C, Cooper C, Senior CA, Banks H, Gregory JM, Johns TC, Mitchell JFB, Wood RA (2000) The simulation of SST, sea ice extents and ocean heat

transports in a version of the Hadley Centre coupled model without flux adjustments. Clim Dynam 16:147–168
Guo S, Leighton HG, Feng J, Trishchenko A (2007) Wildfire aerosol and cloud radiative forcing in the Mackenzie River Basin from satellite observation. (Vol. I, this book)
Hely C, Flannigan MD, Bergeron Y, McRae D (2001) Role of vegetation and weather on fire behavior in the Canadian mixedwood boreal forest using two fire behavior prediction systems. Can J Forest Res 31:430–441
IPCC (2001) Intergovernmental panel on climate change. Climate change 2001: the scientific basis. Cambridge University Press, Cambridge
Johnson EA (1992) Fire and vegetation dynamics: studies from the North American boreal forest. Cambridge University Press, Cambridge
Kochtubajda B, Flannigan MD, Gyakum JR, Stewart RE, Logan KA, Nguyen T-V (2006) Lightning and fires in the Northwest Territories and responses to future climate change. Arctic 59:211–221
Kochtubajda B, Stewart RE, Gyakum JR, Flannigan MD (2002) Summer convection and lightning over the Mackenzie River Basin and their impacts during 1994 and 1995. Atmos Ocean 40:199–220
Kurz WA, Apps MJ, Stocks BJ, Volney WJA (1994) Global climate change: disturbance regimes and biospheric feedbacks of temperate and boreal forests. In: G.Woodwell (ed) Biotic feedbacks in the global climate system: will the warming speed the warming? Oxford University Press, Oxford, UK, pp 119–133
Lavorel S, Flannigan MD, Lambin EF, Scholes MC (2007) Vulnerability of land systems to fire: interactions between humans, climate, the atmosphere and ecosystems. Mitigation and Adaptation Strategies for Global Change 12:33–53
Lyons WA, Nelson TE, Williams ER, Cramer JA, Turner TR (1998) Enhanced positive cloud-to-ground lightning in thunderstorms ingesting smoke from fires. Science 282:77–80
McAlpine RS, Hirsch KG (1999) An overview of LEOPARDS: the level of protection analysis system. Forest Chron 75:615–621
Mearns LO, Giorgi F, McDaniel L, Shields C (1995) Analysis of daily variability of precipitation in a nested regional climate model – comparison with observations and doubled CO_2 results. Global Planet Change 10:55–78
Newark MJ (1975) The relationship between forest fire occurrence and 500 mb ridging. Atmos 13:26–33
Osborn TJ, Hulme M (1997) Development of a relationship between station and grid-box rainday frequencies for climate model evaluation. J Clim 10:1885–1908
Price C, Rind D (1994). The impact of a $2xCO_2$ climate on lightning-caused fires. J Clim 7:1484–1494
Rosenfeld D (1999) TRMM observed first direct evidence of smoke from forest fires inhibiting rainfall. Geophys Res Lett 26:3105–3108

SAS Institute Inc (2000) SAS OnlineDoc®, Version 8, SAS Institude Inc., Cary, NC.

Simmonds PG, Manning AJ, Derwent RG, Ciais P, Ramonet M, Kazan V, Ryall D (2005) A burning question: can recent growth rate anomalies in the greenhouse gases be attributed to large-scale biomass burning events. Atmos Environ 39:2513–2517

Skelly WC, Henderson-Sellers A (1996) Grid box or grid point: what type of data do GCMs deliver to climate impacts researchers? Int J Climatol 16:1079–1086

Skinner WR, Flannigan MD, Stocks BJ, Martell DM, Wotton BM, Todd JB, Mason JA, Logan KA, Bosch EM (2001) A 500 mb synoptic wildland fire climatology from large Canadian forest fires, 1959–1996. Theor Appl Climatol 71:157–169

Skinner WR, Stocks BJ, Martell DL, Bonsal B, Shabbar A. (1999) The association between circulation anomalies in the mid-troposphere and area burned by wildland fire in Canada. Theor Appl Climatol 63:89–105

Stocks BJ (1993) Global warming and forest fires in Canada. Forest Chron 69:290–293

Stocks BJ, Mason JA, Todd JB, Bosch EM, Wotton BM, Amiro BD, Flannigan MD, Hirsch KG, Logan KA, Martell DL, Skinner WR (2002) Large forest fires in Canada, 1959–1997. J Geophys Res 107:8149, doi:10.1029/2001JD000484

Swetnam TW (1993) Fire history and climate change in giant sequoia groves. Science 262:885–889

Van Wagner CE (1970) Conversion of Williams severity rating for use with the fire weather index. Can. Dept. Fish and Forest, Petawawa Forest Exp. Stn., Inf rep PS-X-21

Van Wagner CE (1987) The development and structure of the Canadian forest fire weather index system. Can Forest Serv, forest tech rep 35, Ottawa, Canada

Weber MG, Flannigan MD (1997) Canadian boreal forest ecosystem structure and function in a changing climate: impacts on fire regimes. Environ Rev 5:145–166

Weber MG, Stocks BJ (1998) Forest fires and sustainability in the boreal forests of Canada. Ambio 27:545–550

Williams DE (1959) Fire season severity rating. Can. Dept. Northern Affairs and Nat. Res., Div tech note 73, Ottawa, Canada

Wotton BM, Flannigan MD (1993) Length of the fire season in a changing climate. Forest Chron 69:187–192

Wotton BM, Martell DL, Logan KA (2003) Climate change and people-caused forest fire occurrence in Ontario. Climatic Change 60:275–295

Chapter 24

The Impact of CLASS in MAGS Monthly Ensemble Predictions

Harold Ritchie and Yves Delage

This chapter is dedicated to the memory of Yves Delage, a long-term supporter and investigator in MAGS, who after struggling with cancer, passed away on August 4, 2005

Abstract Canadian global spectral forecast model (SEF) predictions of surface water and energy fluxes over the Mackenzie River Basin were analyzed using nine-member ensemble forecasts of one month duration for the four seasons of the year. The sensitivity to initial conditions was measured by the degree to which the individual forecasts in the ensembles vary one from another. The greatest sensitivity was found for the net accumulation of precipitation minus evaporation.

The impact of the Canadian Land-Surface Scheme (CLASS) on the predictability of the fluxes was examined by connecting the model successively to the force-restore land surface scheme and to CLASS. Overall, the replacement of the force-restore scheme with CLASS in SEF has a beneficial effect on the predicted energy and water budgets for the Mackenzie Basin. Preliminary results also indicate that better initialization of CLASS predictive variables could significantly affect its performance, especially in the snow-free periods.

1 Introduction

One major MAGS objective of the Mackenzie GEWEX Study (MAGS) is to understand and model the high-latitude water and energy cycles on monthly and longer time scales. The plan for achieving the goals of MAGS during its first phase included using the operational weather prediction models to estimate atmospheric and surface state variable fields over the Mackenzie River Basin (MRB), before simulating them with regional climate models. Both the climate and weather prediction models were coupled to hydrologic models and enhanced land surface schemes, suitably adapted for northern conditions (Rouse et al. 2003; Stewart et al. 1998).

The Canadian Meteorological Centre (CMC) global numerical weather prediction (NWP) system has been calibrated and verified to produce very good operational medium-range (up to 10 days) forecasts. At the time when we did the experiments in this study, the system was based on the Canadian global spectral model (SEF) (Ritchie 1991; Ritchie and Beaudoin 1994) running on a grid with a spatial resolution of about 100 km. (The SEF model was replaced by the Global Environmental Multiscale or GEM model in October 1998) The spectral model was also used for operational monthly forecasts at CMC, running at a lower resolution, and as one of the models providing guidance for operational seasonal forecasts. Consequently the SEF NWP system, used in this project, is suitable for assessing the monthly energy and water budgets over the MRB.

One key issue is understanding and quantifying the degree to which the climate system is sensitive to fluctuations and errors in the initial conditions provided by large-scale analyses (Stewart et al. 1998). These analyses, being a product of the global data-assimilation and forecast system at CMC, are used as initial forcing and a driving platform for MAGS simulations with both the weather prediction and the regional climate models. The main research domain of this project was to use ensemble forecasts to quantify the uncertainty in monthly water and energy budgets over the MRB caused by uncertainties in the analyses from which the models are run.

2 Methods

It has long been accepted that running an ensemble of numerical forecasts from slightly perturbed initial conditions can enhance the skill of the forecast by means of ensemble averaging (Houtekamer et al. 1996; Toth and Kalnay 1997). Besides providing a better estimate of possible future states, the ensemble approach also offers the possibility of estimating the forecast spread, which can be used as an indicator of expected skill (predictability). The basic tool used in this project was the operational CMC ensemble system which was designed to produce a variety of possible analyses to represent the atmosphere at a given moment, with each analysis respecting the likely errors due to uncertainties in the observations, analysis techniques, and assimilating numerical model. The ensemble system also maximizes the rate of growth of the errors in the forecasts made from its analyses, so that the ensemble of forecasts encompasses all the likely possibilities. As used in this study, each ensemble set consists of an unperturbed, or "con-

trol" member based on the standard operational forecasting system, as well as eight perturbed global analyses for the same date. The method of producing the perturbed analyses here consists of running independent assimilation cycles that use perturbed sets of observations and are driven by eight different models (Houtekamer and Lefaivre 1997; Houtekamer et al. 1996; Lefaivre et al. 1997). All observations (i.e., radiosondes, satems, satobs, synops, ships, acars/amdars, humsat) used to feed the analysis are randomly perturbed in agreement with their error statistics. The models, though based on the same Canadian spectral model (Ritchie 1991) with a horizontal resolution of T95 and a horizontal diffusion in ∇^8, have different switches activated, hence reflecting the uncertainty in the models used in NWP. In addition, some physical parameters are set with random values (horizontal diffusion, minimal roughness length over sea, and time filter). Perturbations are also introduced in the surface forcing through perturbations of the fields for sea surface temperature, albedo, and roughness length. As explained in Houtekamer et al. (1996), this method for generation of perturbed analyses attempts to produce a set of representative error fields at the initial time of a forecast.

Water and energy budget terms were calculated over the Mackenzie and Mississippi basins for each forecast in the ensemble, and the ensemble means and standard deviations were used to assess the most probable forecast state (mean) and the uncertainty (standard deviation) in the budget terms.

3 Results

Before assessing the predictability issue, a baseline study was completed (Ek and Ritchie 1996). Two ensemble forecasts of one month duration were produced, one for a spring case and the other for a summer case, and budgets were examined over the MRB. For comparison, the calculations were also repeated for the Mississippi basin and over all of North America. The greatest sensitivity was found for the net accumulation of precipitation minus evaporation (often referred to as water excess). The spring ensemble was done at a coarser horizontal resolution (T47), and the results were similar. The forecast uncertainty (ensemble standard deviation) of the area-averages over the basin appear to be unaffected by this change, though the ensemble mean values were sensitive to the change in resolution. It was found that the ensemble standard deviation makes a significant, abrupt increase towards the end of the second week into the forecasts, which agrees

with other studies of the duration of deterministic predictability with current NWP systems.

A subsequent study (Radeva and Ritchie 2001) assessed the impact of the more sophisticated Canadian Land-Surface Scheme (CLASS) (Delage and Verseghy 1995) on the predictability of the fluxes, using the operational configuration of the global model with the force-restore land surface scheme as a baseline for comparison. This model was connected successively to the current operational force-restore land surface scheme, and then to CLASS. It generated nine-member ensemble simulations of one month duration from analyses perturbed with the Monte-Carlo method, for spring, summer, fall, and winter cases. The means of the ensemble forecasts were compared with monthly accumulations of surface energy and water fields constructed from 12-hour forecasts of the operational regional forecast model as well as with satellite-derived observations of precipitation. Overall, the replacement of the force-restore scheme with CLASS in the CMC global forecasting system has a beneficial effect on the predicted MAGS energy and water budgets. The model with the CLASS scheme produces a slight increase in sensitivity to initial conditions. Compared with the budgets constructed from the short-term predictions of the CMC regional forecasting system, the budgets forecast with CLASS performed better than the outputs from the model with the operational force-restore scheme (Radeva and Ritchie 2001). This is illustrated by Figs. 1 and 2 which present 31-day accumulations of energy and water fluxes for a spring and summer case, respectively. For the spring case (Fig. 1a), the CLASS accumulated net radiative flux agrees better with its counterpart from the short-term forecasts, as do the sensible and ground heat fluxes, with the latent heat flux being slightly poorer. For the summer case (Fig. 2a), all components of the energy budget produced by CLASS compare significantly better with their counterparts from the short-term forecasts. CLASS also leads to a better agreement for precipitation, evaporation, and resultant water excess in the summer (Fig. 2b) but not in the spring (Fig. 1b). In verifying predicted precipitation over the MRB by comparing with satellite rainfall estimates (RAINSAT) for the summer case, it was found that SEF with CLASS produced better estimates than both SEF with force-restore and the counterpart from the short-term forecasts (Radeva and Ritchie 2001).

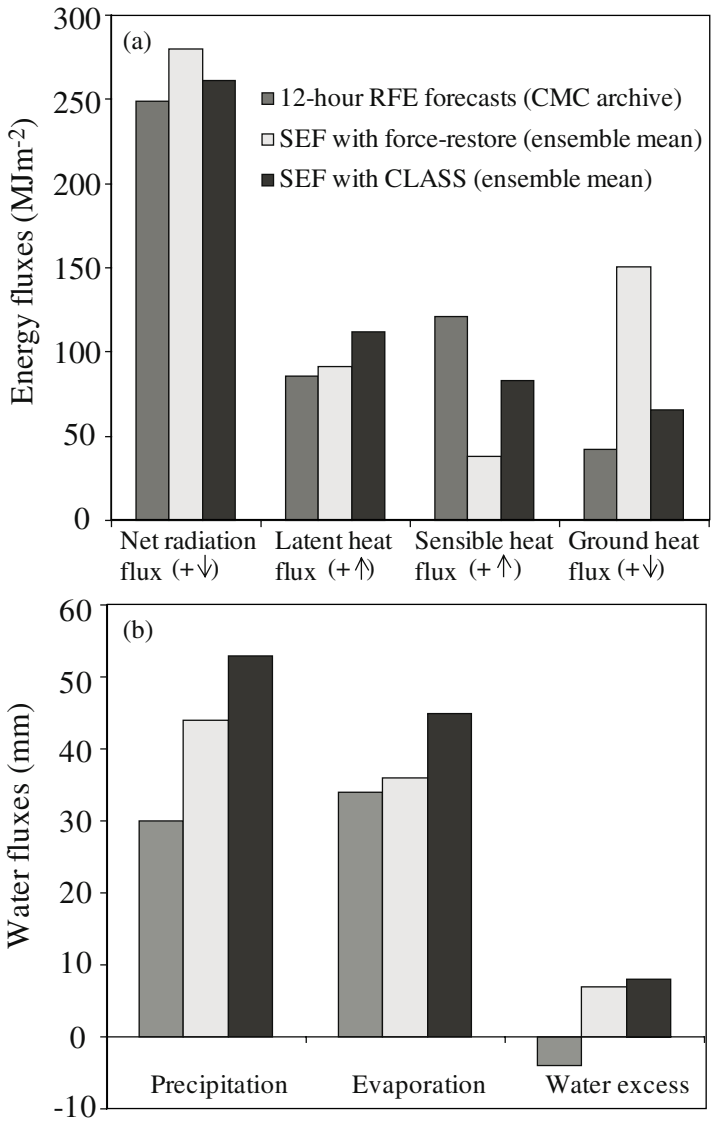

Fig. 1. 31-day accumulations of (a) energy, and (b) water fluxes at surface, valid at 00Z 16 May 1996. Area-averages over the MAGS region. Fluxes from the short-term predictions of the CMC regional forecasting system are labeled as "12-hour RFE forecasts (CMC archive)", those produced by the ensemble forecasts of the global model with the force-restore land surface scheme are labeled as "SEF with force-restore (ensemble mean)", and those from the ensemble forecasts of the global model with CLASS are labeled as "SEF with CLASS (ensemble mean)". (after Radeva and Ritchie 2001)

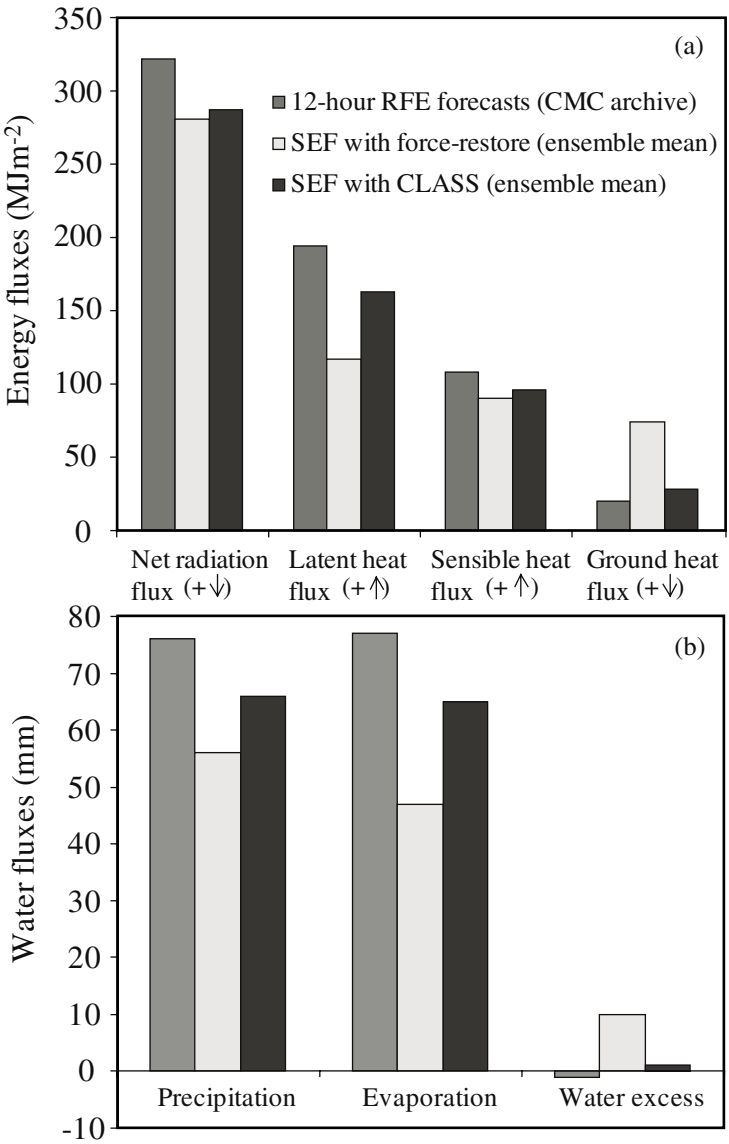

Fig. 2. Same as Fig. 1 but for the summer case. Accumulations valid at 00Z 11 August 1996. (after Radeva and Ritchie 2001)

Subsequent work, as yet unpublished, focused on the sensitivity of the ensemble budgets to the initial soil moisture. First we quantified the CLASS sensitivity to initial soil moisture using two different climatologies, the ECMWF's (Louis 1981) and Mintz and Walker's (1993), as ini-

tial conditions. We then verified MRB water and energy monthly budgets against data from the CMC GEWEX archive (Radeva and Hogue 1998). To this end, we added accumulations, between 0 and 12 integration hours, of water and energy surface fluxes, produced by the then operational regional forecast model at a horizontal resolution of 35 km and archived, starting at the initial time of our ensemble spring and summer predictions and covering their whole 31-day integration period.

Table 1 summarizes the statistics of the spring and summer ensemble predictions performed using SEF with the force-restore scheme and CLASS. In view of the scarcity of observations over the MRB, it is reassuring that most of the area-averaged energy and water budget fields are only moderately sensitive to errors in the initial conditions. This is particularly true for the net all-wave radiation and the evaporation, whose ensemble standard deviations stay below 6% of the ensemble mean values after one month of integration in all four cases. The sensible heat flux and the precipitation show larger spread as their ensemble standard deviations represent 16% or less of the respective mean monthly accumulations. The most divergent of all is the water excess, as it is computed as a small residual of two comparable fields. Besides, it is a distillation of all the model physics, thereby incorporating errors in all the initial fields that were perturbed.

Table 1. Ensemble mean / Standard deviation of 31-days accumulations of net all-wave radiation (NR), sensible heat flux (SH), ground heat flux (GF), precipitation (PR), evaporation (EV), and water excess (WE), averaged over the Mackenzie River Basin (after Radeva and Ritchie 2001)

	Spring case		Summer case	
Field [units]	SEF + force-restore	SEF + CLASS	SEF + force-restore	SEF + CLASS
NR [MJ m^{-2}]	280 / 5	261 / 9	281 / 4	287 / 7
SH [MJ m^{-2}]	38 / 6	83 / 9	90 / 5	96 / 9
GF [MJ m^{-2}]	151 / 13	66 / 6	74 / 10	28 / 3
PR [mm]	44 / 5	53 / 8	56 / 3	66 / 7
EV [mm]	36 / 2	45 / 1	47 / 2	65 / 3
WE [mm]	7 / 4	8 / 7	10 / 3	1 / 5

Comparison of the ensemble statistics of the SEF forecast with the force-restore scheme and with CLASS reveals that both schemes yield uncertainties of the same order of magnitude, due to the initial conditions, in the monthly ensemble forecasts of energy and water accumulations over the MRB. Water budgets produced by SEF in conjunction with CLASS in

the summer ensemble simulation compare better with their counterparts from the GEWEX archive than the ones based on the force-restore scheme. This holds also for the surface energy fluxes for both spring and summer cases (not shown). However, one must be cautious in interpreting the above results, as the 12-hourly regional model forecasts of surface fluxes could be contaminated by model artifacts. In fall and winter cases, the ensemble standard deviations of the forecast monthly accumulations are similar to or lower than the ones in the spring and summer case, but their ratio to the corresponding ensemble means is high (especially in the case of winter sensible heat flux) due to the smaller values of the means (not shown).

The effect of the soil moisture initialization on the predicted surface fluxes is most pronounced in the summer case. A difference of 0.14 between the MRB-averaged volumetric soil moisture contents of the two climatologies used as initial conditions, leads to differences of 21 MJ m^{-2} in monthly accumulated sensible heat flux and 7 mm in monthly accumulated evaporation. This sensitivity to the initial soil moisture highlights the importance of establishing accurate values of this field. The goal can best be met by a proper land data assimilation system, so we started preliminary testing on designing a CLASS-based land-surface data assimilation system. We produced the soil-related and snow-related CLASS initial fields in a spin-up integration beginning at 00Z 15 March 1996 and running for one month without re-initialization. Then we used these balanced CLASS-generated fields to initialize a one-month spring simulation (hereafter called SPIN-UP) and compared the resulting surface fluxes with their counterparts from the integration fed with climatology/analysis values (hereafter CLIM). The comparison between simulations SPIN-UP and CLIM showed little difference in MAGS-averaged monthly accumulations of water and energy budgets. However, the fluxes over the snow-free Mississippi Basin area, produced by SPIN-UP, verify better against the GEWEX archive then the ones of CLIM.

As a consequence of this sensitivity it is expected that realistic initial conditions for these fields are necessary in order to produce realistic water and energy budgets in the subsequent simulations. With the current state of available data and data assimilation methods, CLASS initial fields produced by a 3DVAR atmospheric data assimilation system with CLASS being included in the assimilating model are expected to produce more realistic results than the former integrations in which CLASS was fed by analysis/climatological values.

Data assimilation of land surface variables is the most complete description of actual surface and near surface conditions on an extended domain,

which is a valuable contribution from atmospheric modeling. Towards achieving this goal, we started investigating the impact on the energy and water budgets of errors introduced by the model forecast in the data assimilation technique. Model spin up is a particular concern because the forecast model takes some time to adjust to its initial conditions and will not give climatologically correct quantities during the first hours of integration, since data assimilation cycles are currently made with short forecasts of six hours. The known underforecast of both precipitation and cloudiness should contribute to reducing the amount of soil water, the latter by increasing evapotranspiration via an increase in solar flux. We attempted to quantify these errors by running several forecast cycles for the same one-month period as above (summer 1996). The cycles are different from the previous experiment in that the energy and water budgets for that month are produced not by a single one-month integration, but by a series of short forecasts, each feeding its surface variables from the previous integration, as in data assimilation mode. The different cycles differ in that the length of the forecasts is varied, in order to provide a quantitative measure of the spin up and of its impact. These experiments were also made with a more recent version of the spectral model and of CLASS. In addition, the budgets were carefully analyzed to verify consistency.

With CLASS included in the assimilating model, the CLASS fields (the soil moisture and temperature are considered to be especially important) adjust in response to the meteorological data assimilated throughout the cycle. This work was undertaken in a step-wise fashion starting by inserting the forecast model used by Radeva and Ritchie (2001) as the driving model in a 6-hour intermittent data assimilation cycle using the 3-dimensional variational data assimilation method (3DVAR). The coding was prepared for this insertion and we performed a preliminary examination for our summer 1996 case. As a control run we have the integration performed when a forecast is initiated from standard climatology/analyses as in Radeva and Ritchie (2001). As experimental runs, we performed one-month 3DVAR data assimilation cycles with CLASS included in the assimilating model over the one month period prior to the initial time for the desired forecast (hereafter 3DVAR). The water and energy budgets over the subsequent one-month forecasts were then compared with each other and with the corresponding budgets calculated from the MAGS CMC archive (Radeva and Hogue 1998) to evaluate the impact of this CLASS land data assimilation system on the MAGS water and energy budgets in our global prediction system. Preliminary results based on the subsequent one-month integrations suggest that this indirect assimilation of meteorological data into the CLASS fields improves the MRB water budgets as compared

against available observations. This may be attributed to the slightly more realistic evaporation during the integration.

4 Discussion

The above results indicate that the modeled water and energy budgets over the MAGS region are sensitive to the initial state of the CLASS fields used in the simulations. CLASS initial fields produced by a 3DVAR atmospheric data assimilation system with CLASS being included in the assimilating model are expected to produce more realistic results than the former integrations in which CLASS was fed by analysis/climatological values. With this motivation, a project was envisaged, with Yves Delage as Principal Investigator, to complete a full land-surface data assimilation system with the GEM model, including CLASS as a sub-model over the North American continent. Although curtailment of funding prevented completion of the entire project, considerable achievements were accomplished through related work relevant to this objective.

A prototype land data assimilation system based on the off-line version of the CLASS scheme was developed and tested using the interactive CLASS scheme working inside the SEF model as a control run. The meteorological fields generated by the SEF model were supplied to the stand-alone version of CLASS whose outputs agreed with the control run to within computer truncation error. This framework was then generalized for the GEM model and ISBA (Interactions Sol-Biosphère-Atmosphère) land surface scheme currently used operationally at the CMC. Experiments were performed to compare the outputs of the surface model at a resolution of 3 km with those of a 30 km run over the entire North America. This work highlighted the importance of forcing the surface model with cumulative radiative fluxes and precipitation in order to reproduce in the off-line model the results obtained during a full run of GEM/ISBA. It also involved, in collaboration with Diana Verseghy, preparing version 3.0 of CLASS and making it available to the MAGS community through GEM and the CMC/RPN library.

Comparison of the CLASS and ISBA land surface models was conducted by Carole Labadie and Émilie Mallet under the supervision of Yves Delage, over North America for 1 May 2002 to 31 March 2003:

http://collaboration.cmc.ec.gc.ca/science/rpn/publications/pdf/Mallet_Labadie_rapport_de_stage_xx_xx_03_author.pdf.

The two models were run at a resolution of 10 km in off-line mode (i.e., without feedback to the atmosphere). They were forced with the same series of 24-hour forecasts from the operational regional GEM (with ISBA as surface model). A maximum number of common parameters were given to the two models to minimize their differences. In this comparison the ISBA model is the operational model with some parameters modified and CLASS is the new version 3.0 without the mosaic capability and without the new sloping terrain runoff parameterization. Results indicate larger runoff in ISBA, except that due to snowmelt. With less runoff, more ground water is available in support of evapotranspiration. Snowmelt is slower in ISBA because it retains liquid water in the snow and allows larger sublimation than CLASS. This extra sublimation in ISBA (which takes more energy away from melt) is due to the unrealistic >0°C temperature in the snow. Over warm wet grounds, ISBA evaporates more than CLASS due to a larger roughness length over bare soil. Another important difference is in the freezing and melting of ground water. ISBA cannot model this phenomenon correctly because it does not conserve energy in the soil.

The intercomparison has prompted improvements to the ISBA land surface scheme currently used in the operational forecast system at CMC. CLASS is also being considered for future operational implementation. These MAGS collaborations have thus paved the way for future testing of MAGS-based models and algorithms outside the MRB. An extension that grew out of this land surface modeling is the development of MEC (Modèle Environnemental Communautaire) which can host several surface models (land surface, lake, hydrologic, river flow, etc), as well as atmosphere, ocean, ice, and other environmental models, together with the couplers used to combine them into an environmental modeling system. This framework makes the data flow and the computing environment easier to manage.

5 Conclusion

Coupling the global NWP system with CLASS shows low to moderate sensitivity to errors in the initial conditions when predicting summer and spring monthly energy and water budgets for the MAGS domain. The uncertainties in the fall and winter ensemble predictions of those budgets are commensurate with their spring and summer counterparts, but the predictability is lower due to the lower ensemble means. There is good agreement of MAGS monthly budgets produced by SEF with CLASS with those

based on the CMC GEWEX archive, especially for the summer case. In addition to the archive, direct observations of the fields of interest are needed to verify the simulated budgets.

Initial steps towards land surface data assimilation and other developments related to the CLASS and ISBA land surface schemes have led to valuable improvements to both. Such accomplishment is a tribute to the synergies among meteorologists, climate modelers, and hydrologists that have been fostered by MAGS.

Acknowledgements

The work during the first phase of MAGS as reported on in Section 3 was supported by Canadian GEWEX funding and by the Environment Canada Stagiaire Programme, enabling the activity by Nils Ek and Ekaterina Radeva at RPN. Technical assistance was provided by Christiane Beaudoin, James Caveen, Bernard Bilodeau, and Bernard Dugas of RPN, and Louis Lefaivre of CMC. Dr. Alexander Medvedev worked at Dalhousie University on developing a stand-alone version of the CLASS scheme for use in a land data assimilation system. Pierre Pellerin has been leading the development of the MEC system reported on in Section 4.

References

Delage Y, Verseghy D (1995) Testing the effects of a new land surface scheme and of initial soil moisture conditions in the Canadian global forecast model. Mon Weather Rev 123:3305–3317

Ek N, Ritchie H (1996) Forecasts of hydrological parameters over the Mackenzie River Basin: sensitivity to initial conditions, horizontal resolution, and forecast range. Atmos Ocean 34:675–710

Houtekamer PL, Lefaivre L (1997) Using ensemble forecasts for model validation. Mon Weather Rev 125:2416–2426

Houtekamer PL, Lefaivre L, Derome J, Ritchie H, Mitchell HL (1996) A system simulation approach to ensemble prediction. Mon Weather Rev 124:1225–1242

Lefaivre L, Houtekamer PL, Bergeron A, Verret R (1997) The CMC ensemble prediction system. Proc 6th ECMWF Workshop on meteorological operational systems, Reading, U.K., pp 31–44

Louis J-F (1981) ECMWF forecast model documentation manual, vol 1. European Centre for Medium-Range Weather Forecasts A1.21–A1.33

Mintz Y, Walker GK (1993) Global fields of soil moisture and land surface evapotranspiration derived from observed precipitation and surface air temperature. J Appl Meteorol 31:1305–1334

Radeva E, Hogue R (1998) CMC model archive and activities in support of GEWEX. Proc 4th Scientific workshop for MAGS, pp 143–144. Information also available at http://www.cmc.doe.ca/cmc/CMOI/htmls/Gewex_archa.html

Radeva E, Ritchie H (2001) Impact of the Canadian Land Surface Scheme on monthly ensemble predictions of water and energy budgets over the Mackenzie River Basin. Atmos Ocean 39:71–88

Ritchie H (1991) Application in the semi-Lagrangian method to a multi-level spectral primitive-equations model. Q J Roy Meteor Soc 117:91–106

Ritchie H, Beaudoin C (1994) Approximation and sensitivity experiments with a baroclinic semi-Lagrangian spectral model. Mon Weather Rev 122:2391–2399

Rouse WR, Blyth EM, Crawford RW, Gyakum JR, Janowicz JR, Kochtubajda B, Leighton HG, Marsh P, Martz L, Pietroniro A, Ritchie H, Schertzer WM, Soulis ED, Stewart RE, Strong GS, Woo MK (2003) Energy and water cycles in a high latitude, north-flowing river system: summary of results from the Mackenzie GEWEX – Phase 1. B Am Meteorol Soc 84:73–87

Stewart RE, Leighton HG, Marsh P, Moore GWK, Ritchie H, Rouse WR, Soulis ED, Strong GS, Crawford RW, Kochtubajda B (1998) The Mackenzie GEWEX study: The water and energy cycles of a major North American River basin**.** B Am Meteorol Soc 79:2665–683

Toth Z, Kalnay E (1997) Ensemble forecasting at NCEP and the breeding method. Mon Weather Rev 125:3297–3319

Chapter 25

The MAGS Regional Climate Modeling System: CRCM-MAGS

Murray MacKay, Paul Bartlett, Ed Chan, Diana Verseghy, E.D. Soulis and Frank R. Seglenieks

Abstract The Mackenzie GEWEX Study (MAGS) regional climate modeling system (denoted CRCM-MAGS) is a developmental version of the Canadian Regional Climate Model (CRCM) tailored for use over North America. It is composed of three major components: the dynamical kernel of the CRCM, the operational physical parameterization package of the Canadian Centre for Climate Modelling and Analysis (CCCma) atmospheric general circulation model (GCMIII), and a high resolution land surface database developed for MAGS. In addition, surface runoff can be routed offline using the WATFLOW hydrologic model and a drainage database constructed over North America for the CRCM-MAGS. Although closely related to the CRCM, the CRCM-MAGS differs in several major aspects. The Mackenzie Basin climate from a five year (plus 21 month spin up period) simulation was evaluated against surface observations. The model simulates a mean annual precipitation bias of about 13%, and a cold surface temperature bias of less than 1^{o}C in both summer and winter. These results suggest that the GCMIII physics package, developed for a relatively coarse resolution GCM, can be used successfully in a high resolution regional climate model with minimal modification, provided a realistic surface representation is included.

1 Introduction

Regional climate models (RCMs) are essential tools for understanding regional climate processes and feedbacks as they provide complete and physically self-consistent representations of reality. As such they can fill in gaps in observational programs, an especially useful attribute for studies of remote, sparsely populated areas such as the Mackenzie River Basin (MRB). RCMs are generally run in one of two modes, the difference being the nature of the lateral atmospheric boundary conditions that must be specified for any limited area model. In *climate regionalization* studies, the RCM downscales the results from a current or projected future climate simulation from a General Circulation Model (GCM). In this mode the

RCM dynamically interpolates coarse resolution GCM results to finer resolution over a limited area of interest. Such interpolation is an essential component of assessing the local effects of any global climate change scenario produced by a GCM.

The emphasis here, however, has been placed on model evaluation/development and climate process studies. In this mode of operation the RCM is driven by (or nested within) an operational data assimilation system rather than a GCM. These analyzed (or re-analyzed) fields are generally 0-hour forecasts from a numerical weather prediction model, and so this mode of driving the RCM is sometimes known as "perfect boundary condition" mode since the analysis is generally considered to be the best guess of the actual instantaneous state of the atmosphere. This contrasts with the GCM-mode in that the GCM generally does not capture the instantaneous state of the atmosphere at any given time; rather it reproduces only the average state of the atmosphere (or climatology).

This chapter describes the development and application of the regional climate modeling system used within MAGS, denoted as CRCM-MAGS, which is essentially a developmental version of the Canadian Regional Climate Model. The emphasis of regional climate modeling in MAGS has been largely on land surface (including subsurface) processes and the interaction between the land surface and the atmosphere. Most of the modeling effort has thus been directed at characterizing the heterogeneous landscape of western Canada, and understanding processes arising from this heterogeneity of direct relevance to the current regional climate.

2 Research Domain

The standard CRCM-MAGS modeling domain is indicated in Fig. 1. The grid projection is polar stereographic, with a nominal horizontal resolution of 51 km at 60^{o} north latitude. Parameters uniquely defining this grid are indicated in Table 1. The grid is 100x90 points with approximately 711 grid cells within the MRB. Also indicated in the figure is the 9-point lateral "sponge layer" commonly used in limited area models to gradually introduce the specified boundary conditions into the high resolution domain.

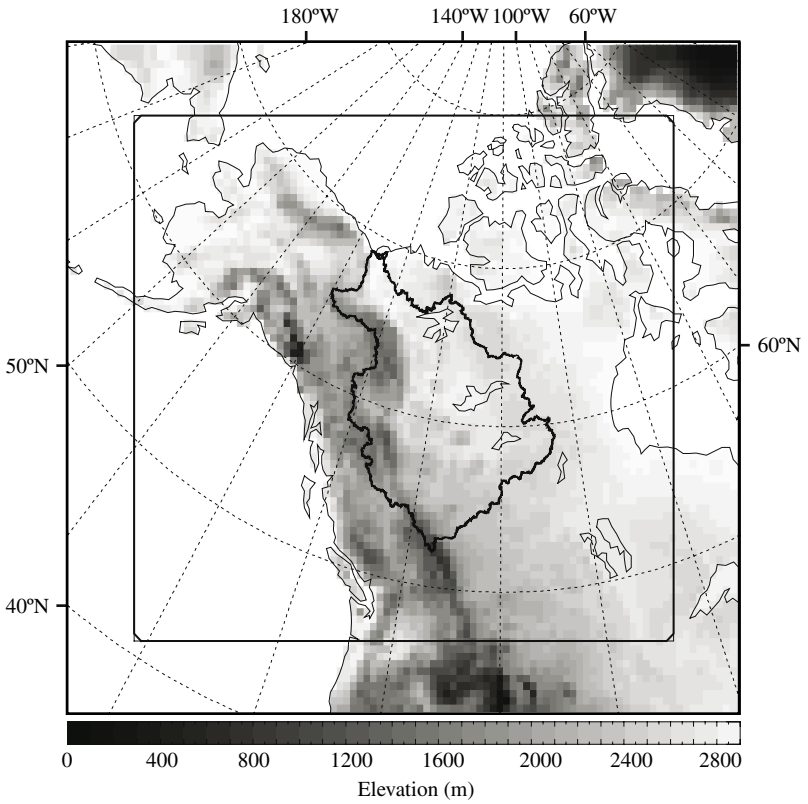

Fig. 1. Standard MAGS RCM domain. Elevation (shaded, contour interval 200 m), boundary of the Mackenzie River Basin (MRB) and the 9 point lateral sponge zone are also indicated

Table 1. Standard MAGS RCM grid parameters. This is a standard CMC grid: northern polar stereographic true (i.e., secant) at 60° N

NI=100	number of points in X-direction
NJ=90	number of points in Y-direction
CLAT=62.0984	center latitude (north)
CLON=124.7624	center longitude (west). The Y-axis of this grid lies along this meridian
D60=51000.0	resolution at 60 degrees north (m)
PI=65.6459	X-coordinate of north pole
PJ=101.3916	Y-coordinate of north pole
DGRW=19.6	rotation of grid from Greenwich

3 Model Development

The CRCM-MAGS is essentially a developmental version of the Canadian Regional Climate Model (CRCM) tailored for use over North America and especially western Canada. It consists of three major components: the dynamical kernel of the CRCM, the operational physical parameterization package of the Canadian Centre for Climate Modelling and Analysis (CCCma) atmospheric general circulation model (GCMIII), and a high resolution land surface database developed within MAGS specifically for this project. In addition, channel routing is accomplished offline through the University of Waterloo's WATFLOW system. The operational physics package of GCMIII – internal version gcm13d (McFarlane et al. 2005) is taken in its entirety, with minor modifications as discussed in Section 3.2. This package contains the Canadian Land Surface Scheme (CLASS) version 2.7, which does not include some improvements in hydrology developed under the MAGS program. The CRCM-MAGS, though closely related to the conventional CRCM, differs from it in several important ways. The physics parameterization package is taken from the CCCma operational GCM essentially unaltered, apart from minor cloud tuning. Such an approach is not guaranteed to work in general since the package as a whole was developed and tuned for a coarse resolution model. On the other hand, the CRCM makes use of certain process schemes (e.g., deep convection) developed for mesoscale models. The CRCM-MAGS also makes use of a detailed high resolution (1 km^2) land surface and soils database constructed for use by CLASS. This database currently covers only North America, and further work is needed to render the model globally portable. The CRCM normally makes use of a lower resolution land surface characterization, with initialization data generally coming from equilibrated GCM simulations. The importance of these differences in land surface characterization and initialization for CLASS has not been systematically studied but is currently under investigation.

3.1 Dynamics

The CRCM-MAGS is based on the dynamical kernel of the Canadian Regional Climate Model (CRCM-V3.5), originally developed at the Université du Québec à Montréal (Caya and Laprise 1999). This dynamical core is essentially that of the Mesoscale Compressible Community Model (MC2) which solves the fully elastic nonhydrostatic Euler equations by way of the efficient semi-implicit and semi-Lagrangian integration scheme

(Laprise et al. 1997; Tanguay et al. 1990). In this way a relatively long time step of 15 minutes can be employed with our standard 51 km resolution grid. The model uses 29 unevenly spaced levels in the vertical, 10 of which are below 850 hPa.

Lateral boundary conditions are provided by the operational data assimilation system of the Canadian Meteorological Centre: 6-hourly data are spatially interpolated onto the model grid and linearly interpolated in time. The specified boundary conditions are introduced into the model domain gradually, following the "sponge layer" approach of Davies (1976) and refined by Robert and Yakimiw (1986). In our simulations, a 9-point lateral sponge is used for horizontal winds.

3.2 Physical Parameterization

The GCMIII physical parameterization package incorporates version 2.7 of the Canadian Land Surface Scheme, CLASS (Verseghy 1991; Verseghy et al. 1993). The latest version (CLASS 3.~~1~~2) is being coupled to the system and results from the final coupled model will be presented elsewhere. Version 2.7, finalized in 1997, contains a number of additional features, mainly a new set of surface stability functions (Abdella and McFarlane 1996), modifications to allow inhomogeneity between soil layers, and the incorporation of variable soil permeable depth. Briefly, CLASS models the energy and moisture balances of the soil, vegetation and snow cover (if any) of the land surface. The soil is divided into three layers, of thickness 0.10 m, 0.25 m and 3.75 m. Separate prognostic values of temperature and of liquid and frozen soil moisture are carried for each layer. The vegetation and snow are treated as thermally and hydrologically separate from the soil, and energy and moisture exchanges are calculated based on physical principles.

Above the surface layer, turbulent transfer of scalar quantities in the atmospheric boundary layer (ABL) results from both local down-gradient processes as well as non-local counter-gradient processes associated with convection. Local down-gradient transfers are based on diffusivities that are functions of the vertical wind shear and the local gradient Richardson number. Non-local effects are accounted for by relaxing local values of the scalar quantity within the boundary layer to a vertically homogeneous reference state over a specified time period. This is to prevent the occurrence of a statically unstable ABL during periods of strong surface heating. Subgrid scale mixing of momentum is also based on eddy diffusivities in the

same way as heat and moisture, though there is no non-local mixing analogue in this case.

Radiation is handled in a manner similar to that in the previous physics package (GCMII), with some improvements, including additional solar and terrestrial bands and a more sophisticated treatment of the water vapor continuum. The impact of these improvements on, for example, simulated atmospheric absorption of shortwave radiation over the MRB is readily apparent in Guo et al. (2007). Moist convection is based on the mass flux formulation of Zhang and McFarlane (1995), and large scale (i.e., resolved) precipitation is described in Scinocca and McFarlane (2004). Cloud cover is still diagnosed based on relative humidity (as in GCMII), but in a more sophisticated way depending on the vertical gradient of potential temperature (relative to that on a local moist adiabat), rather than simply on height above the surface. As our simulations are at much higher horizontal resolution than is typical in the GCM, cloud onset thresholds have been adjusted following Lorant et al. (2002). In another departure from the standard GCMIII physics package as used by the CCCma GCM, we revert back to the previous gravity wave drag scheme of GCMII.

3.3 Surface Characterization

To take full advantage of the additional complexity that CLASS adds to our regional climate modeling system, considerable effort was expended on the production of gridded, high resolution, self consistent datasets of land cover, soils, and other geophysical information in a format suitable for land surface models. These data already exist in a variety of formats over a variety of regions. The impact of this high resolution land surface dataset on progressively higher resolution simulations of snowmelt in the boreal forest of western Canada was examined in MacKay et al. (2003b).

3.3.1 Land Cover Data

An assessment of various land cover datasets for the MRB was conducted by Pietroniro and Soulis (2001). According to this assessment, the Canadian Centre for Remote Sensing 1995 31-category 1-km resolution land cover for Canada (Cihlar et al. 1999) was found superior in representing the MRB land features to other datasets (Soulis and Seglenieks 2007). The CCRS land cover (Trischenko et al. 2007, Fig. 1) was thus chosen to represent this Basin and other Canadian regions for use in CLASS. The USGS North American land cover (e.g., Loveland et al. 1995) and the Olson

global ecosystem (Olson 1994a, b) classifications were used to provide data over non-Canadian locations.

All of these land cover datasets were available in their own geographical projection, and had to be re-projected onto the polar stereographic grid used by the model. Also, since each land cover classification differed in the number and types of classes, a series of further transformations was required. First, the USGS 27 categories and the Olson 94 categories were (subjectively) converted to the CCRS 31 categories. Examination of continuity at political borders indicated a number of problems related to the differences between the various schemes. Several a posteriori adjustments were made to improve matching of the USGS and Olson categories at the borders. Once all the land cover data had been converted to the CCRS-31, these were transformed into the 22 categories used by CLASS.

3.3.2 Soils Data

Soil texture profiles and depth-to-bedrock information are required by CLASS, and since there are no readily available gridded soil data suitable for this purpose, a 1-km gridded resolution soil dataset was developed. The gridded soil data were derived from SLC (Soil Landscapes of Canada, Centre for Land and Biological Resources Research, 1996) GIS coverage of digitized soil maps over Canadian regions and from the USGS soil data processed by CONUS-SOIL (Miller and White 1998) for the United States. Data processing includes the mapping of soil information on irregular map polygons to a 1-km resolution grid, the extraction of soil texture (sand and clay %) profile data from descriptive soil classifications, the mapping of soil texture profiles at each grid to standard CLASS soil layers, a consistency check for land-sea mask, water and ice points by using the CCRS vegetation data as the standard, and the smoothing of data across political boundaries. For consistency in the soil data across the US-Canadian border, procedures used in the preparation of the CONUS-SOIL dataset were employed to extract soil texture and depth-to-bedrock data from descriptive soil classifications, and to map the profiles to CLASS soil layers.

3.3.3 Other Surface Data

In addition to vegetation cover and soils data, our regional climate modeling system requires a variety of other geophysical and initialization data. Topography was taken from the 30 arc-second resolution GTOPO30 digital elevation model (Gesch et al. 1999), aggregated (simple average) onto

the model grid of each experiment (Fig. 1). Note that a significant fraction of the domain is occupied by ocean. In our simulations, SST and ice cover were specified from the monthly, one degree resolution Hadley Centre dataset HADISST1.1 (Rayner et al. 2003) linearly interpolated in time to the model time step. Ice mass, which is also required by the model, was as used in GCMII (McFarlane et al. 1992) to reconcile with the observed ice cover fraction.

Apart from fixed soil properties (texture, etc.), CLASS also requires initial values of soil moisture and temperature. Sufficiently unrealistic values might contaminate the simulation of surface climate for many years while the land surface model "spins up" to reach its own equilibrium. However, there is very little observed information, particularly of soil moisture, in our region of interest. Our strategy was to initialize our simulations in late spring without snow cover, and with soil moisture set to field capacity (based on the porosity of the soil), and allow the model to "spin up" for at least 1 or 2 annual cycles. Earlier simulations (e.g., MacKay et al. 2003a) in which soil moisture was initialized saturated produced a number of grid cells at high latitudes where the soil column took excessively long to reach equilibrium and this distorted the surface water balance.

Temperature in the first soil layer was initialized to the mean atmospheric temperature near the surface from operational analysis for the first day of the simulation. Initial temperature for the third (deepest) soil layer was taken from the annual average surface temperature of the Climatic Research Unit's half-degree monthly climate time series (New et al. 2000). The second soil layer was initialized as the average of the first and third layers.

3.4 Streamflow Routing

Runoff generated by CLASS is routed offline through the WATFLOW hydrologic model (Soulis and Seglenieks 2007), and the simulated streamflow compared to actual stream gauge measurements. This allows for evaluation of both the timing and volume of the generated runoff, and represents an important validation tool for simulations in traditionally data sparse areas such as the MRB. In CLASS 2.7, runoff is the combination of surface flow and baseflow, but in version 3.2 sub-surface (i.e., inter-) flow will also be included.

In order to run this hydrologic component, it is necessary to derive the drainage database (i.e., stream channel network, slopes, etc.) over the domain of interest. Using an established technique developed by the Hydrol-

ogy Lab at the University of Waterloo, the drainage database for North America was produced using the WATMAP system. The resulting stream channel network for the MRB at 20 km resolution is shown in Fig. 4.

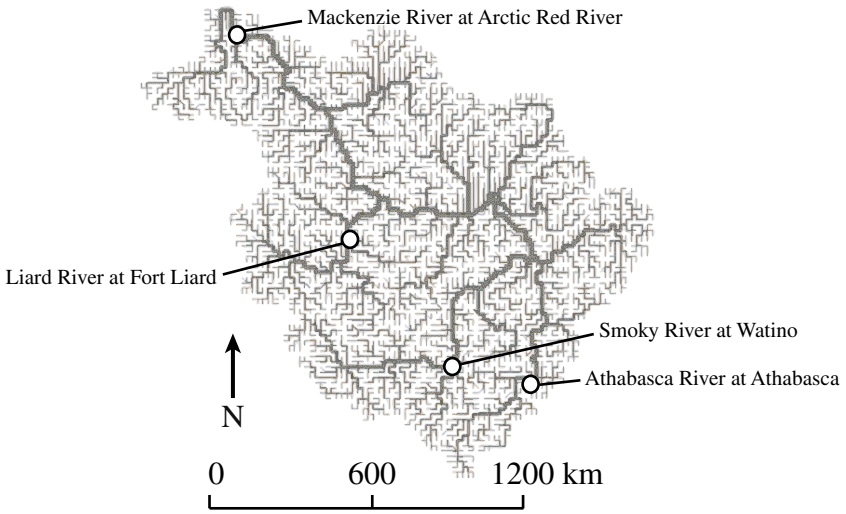

Fig. 2. Stream channel network for the MRB at 20 km resolution

4 Results

4.1 Surface Climate Evaluation

As in MacKay et al. (2003a), Environment Canada's CANGRID gridded monthly surface climate dataset was used to evaluate surface temperature and precipitation. This dataset was produced by combining a gridded climate normal based on the square-grid technique of Solomon et al. (1968), with a gridded climate anomaly (Zhang et al. 2000). Recently this technique has come under some criticism. Milewska et al. (2005) compared gridded climatologies generated over western Canada using different methodologies. They found that all four techniques examined produced very good results for temperature over the prairies (where station density is relatively high), but the precipitation generated by the square-grid technique was significantly different from the others. However, the station dataset used was not the same in each method. In particular, only the square-grid method made use of gauge data that had been adjusted for un-

dercatch, a significant problem for precipitation measurements in high latitudes (e.g., Goodison et al. 1998). As pointed out by Milewska et al., it was difficult to determine how much of the difference between the square-grid precipitation and the other gridded products was due to the use of adjusted station data. However, it is encouraging that the square-grid technique appeared to produce temperatures consistent with the other methods.

Figure 3 compares simulated precipitation over the MRB with that estimated by CANGRID for the five year period (1999–2003). The simulation was initialized on April 1 1997 and allowed to spin up for 21 months prior to the analysis. The mean annual precipitation simulated by the model was 507 mm compared with 450 mm from the observed climatology: a simulated bias of about 13%. Locally the bias could be larger, but the model did capture the general spatial pattern and mean monthly variation (Fig. 3c).

Figures 4 and 5 compare simulated maximum and minimum screen level temperatures respectively from the model and observed climatology. Again the overall patterns are consistent, though the model tends to be slightly cooler in the southern part of the Basin than the observations suggest in both cases. The simulated mean annual biases for T_{max} and T_{min} are -1.5^{o}C and -2.3^{o}C, respectively. In both cases the bias is generally small in spring and summer, and much larger during winter. However, some of this may be an artifact of how screen level temperature is diagnosed in the model. Laprise et al. (2003) pointed out that the simulated screen level temperature is determined based on the surface and lowest atmospheric level temperatures in a manner that performs poorly under conditions of atmospheric inversion. Such conditions are expected to occur frequently over the MRB during winter (Cao et al. 2007). To avoid this problem, MacKay et al. (2003a) suggest comparing the mean observed screen level temperature from CANGRID ($[T_{max} + T_{min}]/2$) with the mean simulated first layer soil temperature. As the first layer is only 10 cm deep, it is expected to follow the mean monthly air temperature quite closely, at least while not snow covered. In the presence of snow the soil can remain warmer than the overlying air, though in this case MacKay et al. propose the snow itself would follow the air temperature more closely (provided no phase change takes place).

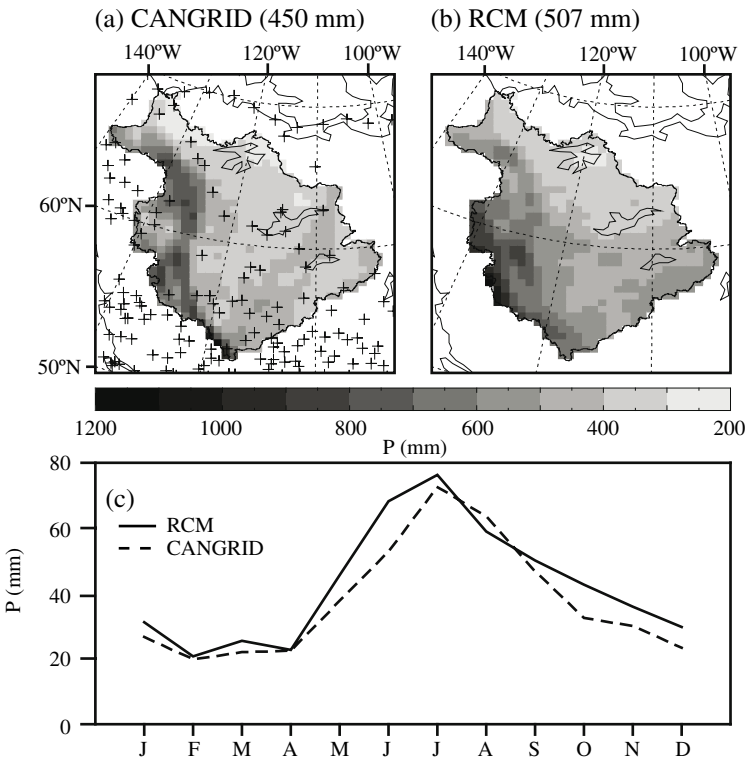

Fig. 3. Mean annual precipitation over the MRB for 1999–2003: (a) CANGRID; (b) RCM; (c) mean monthly totals. Also indicated in (a) are station locations used in producing CANGRID climatology

Figure 6 indicates both, suggesting that our simulation of temperature in general may be better than our standard diagnosis of model screen level temperature shows. The top panels compare the CANGRID mean screen level temperature for Dec–Feb (averaged over 1999–2003) with simulated snow temperature over the MRB. The middle panels compare the CANGRID data for Jun–Aug over the same period with simulated first soil layer temperature. In both cases there appears to be very good spatial agreement between observations and the simulation, with an overall simulated bias of -0.7°C in each case. The lower panel suggests that the comparison works well except during the shoulder months of March and November, where partial snow cover is likely common.

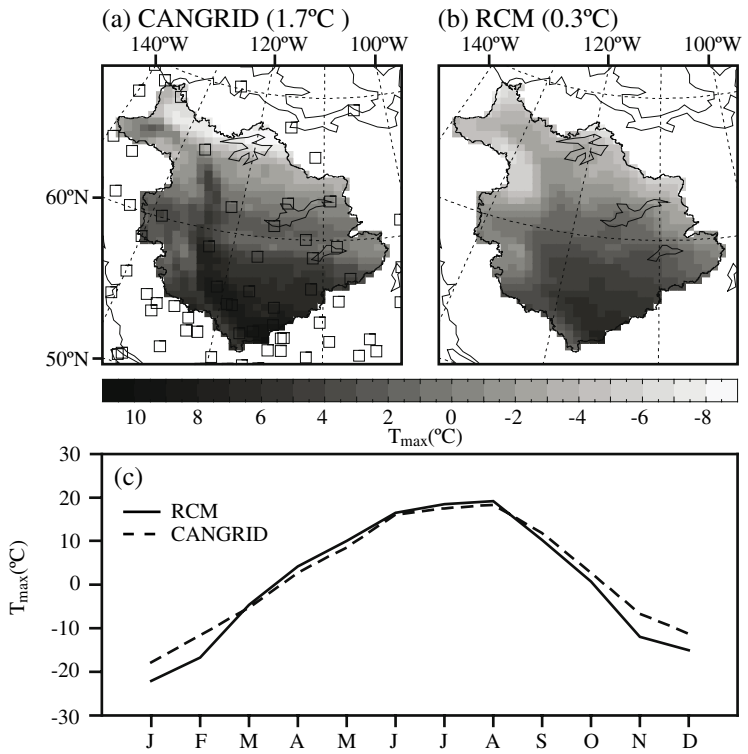

Fig. 4. As in Fig. 3 but for mean annual maximum screen level temperature

4.2 Clouds and Radiation

Guo et al. (2007) analyzed our simulated top of atmosphere (TOA) reflected shortwave and outgoing long-wave radiation vis-à-vis the Clouds and the Earth's Radiant Energy System (CERES) broadband sensor on board the Terra and Aqua satellite platforms. While they do note improvements over previous versions of the model used in MAGS, a systematic positive bias in reflected shortwave radiation persists (along with the concomitant negative bias in net surface solar radiation which was also analyzed). The reasons for this are currently under investigation but could include the simulation of excessive cloud cover or problems in cloud microphysics leading to errors in computed cloud albedo. Outgoing long-wave radiation (OLR) was generally found to be quite good, though there was a systematic low bias (-9 W m^{-2}) during winter. Again, the reasons for this are being investigated. Interestingly, MacKay et al. (2006) examined

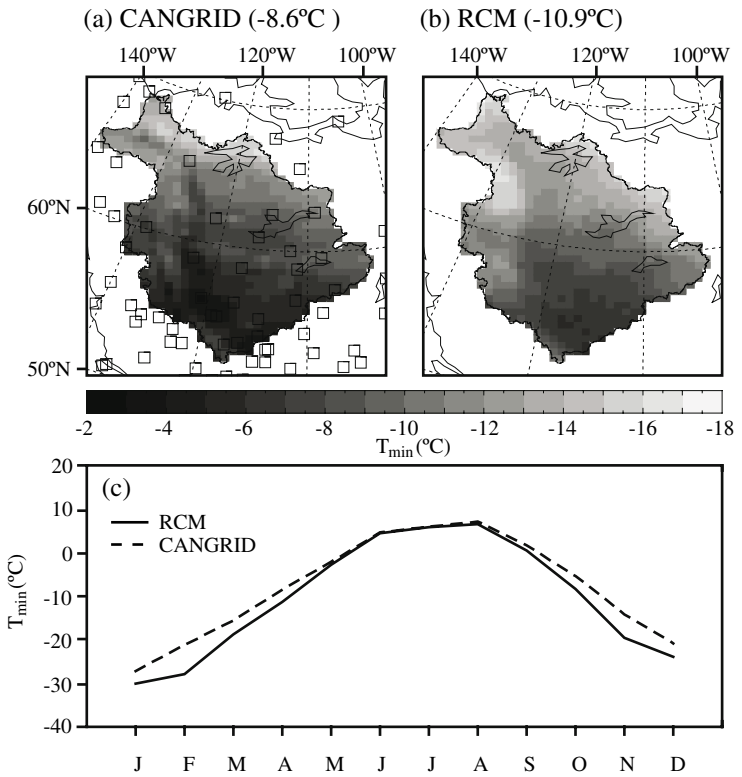

Fig. 5. As in Fig. 3 but for mean annual minimum screen level temperature

simulated and satellite derived OLR for both clear and overcast conditions over a patch of Canadian prairie from this (same) simulation. They found excellent agreement between simulated and observed results during clear sky conditions, but a systematic simulated bias of about -12 W m^{-2} for overcast conditions, again suggesting problems with the simulation of cloud. Downwelling long-wave radiation at the surface was also too weak (likely for the same reasons) and this had a negative impact on the surface energy balance, contributing to an excessive amount of night-time frost, and a snow temperature bias of approximately -2.5^{o}C.

4.3 Surface Water Balance

An obvious application to water resource management is the regional water balance. Based on the last five water years of this simulation for the

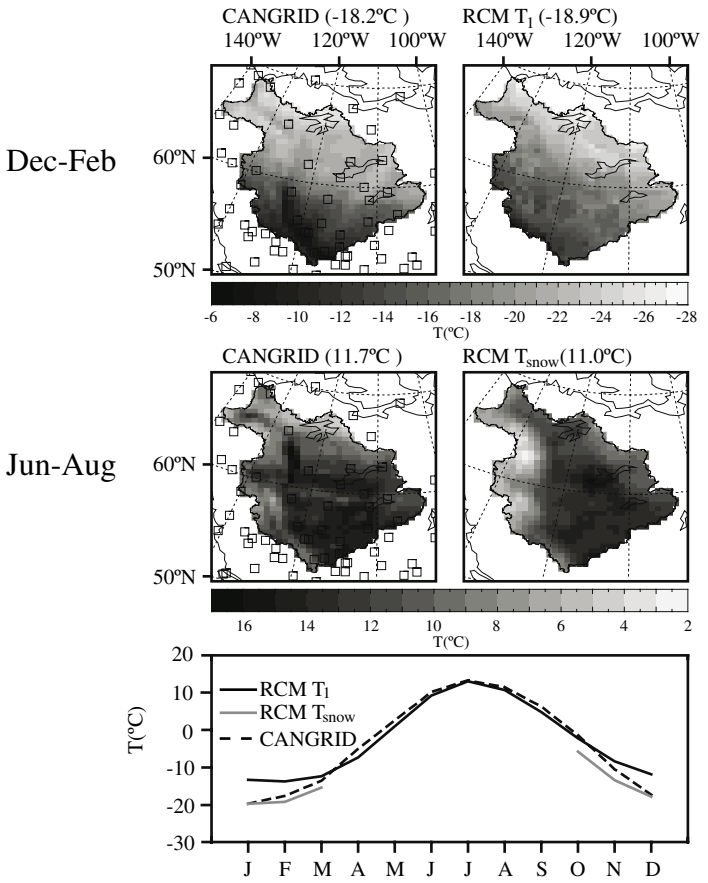

Fig. 6. Mean observed screen level temperature from CANGRID (left panels) and simulated snow (top right) and first soil layer (middle right) temperatures for Dec.–Feb. (top) and Jun.–Aug. (middle). Bottom panel shows mean monthly averages. All data are averaged over the MRB for 1999–2003

MRB (Fig. 7), precipitation minus evaporation (P–E) is on average 245 mm per year, the bulk of which exists over the mountainous western part of the Basin. This is a challenge as the region has a limited number of observations and is likely to be where the simulation is least reliable due to poor orographic representation. The change in soil moisture is small overall, averaging about 5 mm per year with some areas gaining and some losing water on average. Total surface runoff averages at 206 mm per year, most of which is generated in the mountains, and total runoff (the sum of surface runoff and deep drainage) is 240 mm per year.

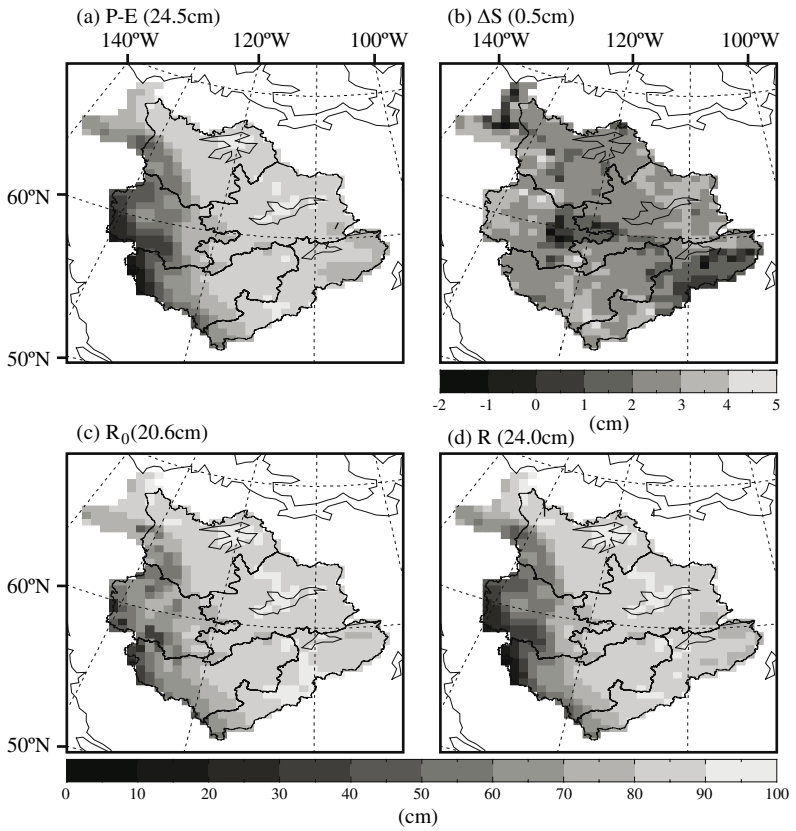

Fig. 7. Mean annual Mackenzie Basin surface water balance (cm) for 1998/99–2002/03: (a) P–E, (b) net soil moisture change, (c) surface runoff, (d) total runoff (surface runoff + baseflow)

5 Conclusion

This chapter summarizes the development and application of the CRCM-MAGS climate modeling system to the Mackenzie region. Analysis of the last five years of a seven year simulation suggests surface climate biases on the order of those found in other regional climate models operating over different regions of the world. Using a similar model (identical except for the land surface characterization), Lorant et al. (2002) found good results over the BALTEX region of northern Europe. That study, along with ours, suggests that a physics parameterization package developed specifically

for a GCM can be used with only minor modification in a higher resolution model. Of course problems remain: the radiation analysis of Guo et al. (2007) indicates systematic difficulties with the simulation of cloud in the model. A more recent study by Lorant et al. (2006) highlights the delicate interaction between the deep convective and stratiform precipitation schemes in this model, and the sensitivity of the former scheme to an assumed closure hypothesis. They found that adjusting key parameters in these schemes produced not only a change in the distributions of convective and stratiform precipitation but also to the radiative balance of the model through the production of cloud. Clearly, future work with this model must direct attention away from the surface where it has been largely focused during the MAGS program, and towards the simulation of clouds (especially radiative properties) and the associated precipitation.

Acknowledgements

The CRCM has been developed over the past decade under the leadership of Rene Laprise (Université du Québec à Montréal) and Daniel Caya (Ouranos Consortium) jointly with the Climate Research Branch of Environment Canada. The land surface database developed for the CRCM-MAGS benefited from the contributions of Normand Bussières and especially Kit Szeto, amongst others. Clouds and radiation analysis of our simulations throughout the MAGS period has been spearheaded by Henry Leighton, Jian Feng, and Song Guo.

References

Abdella K, McFarlane NA (1996) Parameterization of the surface-layer exchange coefficients for atmospheric models. Bound-Lay Meteorol 80:223–248

Cao Z, Stewart RE, Hogg WD (2007) Extreme winter warming over the Mackenzie Basin: observations and causes. (Vol. I, this book)

Caya D, Laprise R (1999) A semi-implicit, semi-Lagrangian regional climate model: the Canadian RCM. Mon Weather Rev 127:341–362

Centre for Land and Biological Resources Research (1996) Soil landscapes of Canada, v.2.2, Research Branch, Agriculture and Agri-Food Canada, Ottawa. (Available on-line at http://sis.agr.gc.ca/cansis/nsdb/slc/intro.html)

Cihlar J, Beaubien J, Latifovic R, Simard G (1999) Land cover of Canada 1995 Version 1.1, Digital data set documentation, Natural Resources Canada, Ottawa, Ontario

Davies HC (1976) A lateral boundary formulation for multi-level prediction models. Q J Roy Meteor Soc 102:405–418

Gesch DB, Verdin KL, Greenlee SK (1999) New land surface digital elevation model covers the Earth. Eos T Am Geophys Un 80:69–70

Goodison B, Louie PYT, Yang D (1998) WMO solid precipitation measurement intercomparison: final report. World Meteorological Organization Tech. Doc. WMO/TD-872

Guo S, Leighton H, Feng J, MacKay MD (2007) Comparison of solar radiation budgets in the Mackenzie River Basin from satellite observations and a regional climate model. (Vol. I, this book)

Laprise, RD, Caya D, Bergeron G, Giguère M (1997) The formulation of André Robert MC2 (Mesoscale Compressible Community) model. Atmos Ocean 35:195–220

Laprise RD, Caya D, Frigon A, Paquin D (2003) Current and perturbed climate as simulated by the second generation Canadian Regional Climate Model (CRCM-II) over northwestern North America. Clim Dynam 21:405–421

Lorant V, McFarlane N, Laprise R (2002) A numerical study using the Canadian Regional Climate Model for the PIDCAP period. Boreal Environ Res 7:203–120

Lorant, V, McFarlane N, Scinocca JF (2006) Variability of precipitation intensity: sensitivity to treatment of moist convection in an RCM and a GCM. Clim Dynam 26:183-200

Loveland TR, Merchant JW, Brown JF, Ohlen DO, Reed BC, Olson P, Hutchinson J (1995) Seasonal landcover regions of the United States. Ann Assoc Am Geogr 85:339–355

MacKay MD, Bartlett P, Chan E, Derksen C, Guo S, Leighton H (2006) On the problem of regional scale sublimation over boreal and agricultural landscapes. Atmos Ocean 44:289–304

MacKay MD, Szeto K, Verseghy D, Chan E, Bussières N (2003b) Mesoscale circulations and surface energy balance during snowmelt in a regional climate model. Nordic Hydrol 34:91–106

MacKay MD, Szeto K, Verseghy D, Seglenieks F, Soulis ED, Snelgrove KR, Walker A (2003a) Modeling Mackenzie Basin surface water balance during CAGES with the Canadian Regional Climate Model. J Hydrometeorol 4:748–767

McFarlane N, Boer G, Blanchet JP, Lazare M (1992) The Canadian Climate Centre second-generation general circulation model and its equilibrium climate. J Climate 5:1013–1044

McFarlane N, Scinocca JF, Lazare M, Harvey R, Verseghy D, Li J (2005) The CCCma third generation atmospheric general circulation model (AGCM3). CCCma Internal Report, available at http://www.cccma.bc.ec.gc.ca/

Milewska EJ, Hopkinson RF, Niitsoo A (2005) Evaluation of geo-referenced grids of 1961–1990 Canadian temperature and precipitation normals. Atmos Ocean 43:49–75

Miller DA, White RA (1998) A conterminous United States multi-layer soil characteristics data set for regional climate and hydrology modeling. Earth Interactions, 2 (Available on-line at http://EarthInteractions.org)

New M, Hulme M, Jones P (2000) Representing twentieth-century space-time climate variability. Part II: development of 1901–96 monthly grids of terrestrial surface climate. J Climate 13:2217–2238

Olson JS (1994a) Global ecosystem framework – definitions: USGS EROS Data Center Internal Report, Sioux Falls, SD

Olson JS (1994b) Global ecosystem framework – translation strategy: USGS EROS Data Center Internal Report, Sioux Falls, SD

Pietroniro A, Soulis ED (2001) Comparison of global land-cover databases in the Mackenzie Basin, Canada. Proc Remote Sensing and Hydrology 2000, Santa Fe, New Mexico, USA, April 2000, IAHS publication no. 267

Rayner NA, Parker DE, Horton EB, Folland CK, Alexander LV, Rowell DP, Kent EC, Kaplan A (2003) Global analyses of sea surface temperature, sea ice, and night marine air temperature since the late nineteenth century. J Geophys Res 108(D14), 4407, doi:10.1029/2002JD002670

Robert A, Yakimiw E (1986) Identification and elimination of an inflow boundary computational solution in limited area model integrations. Atmos Ocean 24:369–385

Scinocca J, McFarlane N (2004) Variability of modelled tropical precipitation. J Atmos Sci 61:1993–2015

Soulis ED, Seglenieks FR (2007) The MAGS integrated modeling system. (Vol. II, this book)

Solomon SI, Denouvilliez JP, Chart EJ, Wooley JA, Cadou CF (1968) The use of a square grid system for computer estimation of precipitation, temperature, and runoff. Water Resour Res 4:919–929

Tanguay M, Robert A, Laprise R (1990) A semi-implicit semi-Lagrangian fully compressible regional forecast model. Mon Weather Rev 118:1970–1980

Trishchenko AP, Khlopenkov KV, Ungureanu C, Latifovic R, Luo Y, Park WB (2007) Mapping of surface albeldo over Mackenzie River Basin from satellite observations. (Vol. I, this book)

Verseghy D (1991) CLASS – A Canadian land surface scheme for GCMs. I: soil model. Int J Climatol 11:111–133

Verseghy D, McFarlane N, Lazare M (1993) CLASS – a Canadian land surface scheme for GCMs. II: vegetation model and coupled runs. Int J Climatol 13:347–370

Zhang GJ, McFarlane NA (1995) Role of convective scale momentum transport in climate simulation. J Geophys Res 100:1417–1426

Zhang X, Vincent LA, Hogg WD, Niitsoo A (2000) Temperature and precipitation trends in Canada during the 20th century. Atmos Ocean 38:395–429

Chapter 26

Synopsis of Hydrologic Research under MAGS

Ming-ko Woo

This volume of the book gives detailed accounts of the principal atmospheric processes investigated under the Mackenzie GEWEX Study (MAGS). These processes are of paramount importance to the weather and climate of northwestern North America, the understanding of which is of direct relevance to all circumpolar cold regions. There are close links between the atmosphere, hydrosphere and cryosphere through the energy and water cycles, and many connections through forcings, feedbacks and storage mechanisms that lead to amplification or acceleration, and suppression or delay, of atmospheric and hydrologic events. Volume II of the book, entitled "Hydrologic Processes of a Cold Region: the Mackenzie GEWEX Study Experience" provides a comprehensive survey of the land surface and hydrologic processes that occur in the Mackenzie River Basin (MRB) and its adjoining areas. Under MAGS, new concepts, models and field methods have been developed that greatly improved understanding and representation of cold region hydrologic processes. These results are summarized in this synopsis of MAGS hydrologic research. All chapters that appear in Volume II are listed in the Appendix.

Volume II begins with a summary of atmospheric research results presented in Volume I. This is followed by Woo and Rouse (Chap. 2) which provide an overview of hydrologic process investigations and modeling studies conducted under MAGS. Snow, frost and ice exert considerable influence on the hydrology of cold regions. MAGS research contributed to advancement in the accumulation, sublimation and ablation aspects of the boreal forest and tundra snow cover; infiltration into and thawing of frozen soil; breakup of river ice and the associated floods. Additionally, there are several land surface features distinctive to the Basin, including lakes and wetlands, mountainous topography, Precambrian Shield and organic terrain. Hydrologic knowledge on these landscapes was gained through field research, conceptualization and modeling effort. Most of these studies were carried out at a local scale that allow understanding of the physical processes through intense field and modeling investigations.

On a regional scale, an application of satellite information at high resolution (1-km) over the MRB provides spatial images of land surface temperature, evapotranspiration, water temperature time series over lakes of size >100 km^2 and cloud top temperature (Bussières, Chap. 3). These satellite-derived products were compared with ground observations and with regional climate model outputs of low spatial resolution. Such information is useful for the analysis of water and energy budgets over large regions. Satellite-derived data from passive microwave measurements were used to obtain soil wetness and fractional water surface in the MRB (Leconte et al., Chap. 4). The approach accounts for the seasonal evolution of the vegetation state and the basin surface heterogeneity. When applied to the Peace-Athabasca-Delta area, this method improved the correlation between soil wetness and precipitation measured at a climate station.

MAGS made important contributions towards advancing knowledge on snow and frozen soil processes. Pomeroy et al. (Chap. 5) reported research results in regard to the transport and sublimation of blowing snow, interception and sublimation of snow in forest canopies, snow spatial distributions in complex environments, snowmelt in open environments and under forest canopies, advection of energy from bare ground to snow, snowcover depletion during melt, and heat and mass transfer during infiltration to unsaturated frozen mineral soils. These studies covered a range of northern environments including the arctic–taiga transition, the cordilleran subarctic, the southern boreal forest, and the northern prairie. At the tundra–forest transition zone, snowmelt and runoff processes were studied for over ten years (Marsh et al., Chap. 6), focusing on snow accumulation, spatial variability of energy fluxes, local scale advection of sensible heat from bare ground to snow patches, percolation and storage of meltwater in the snow, and hillslope runoff from snowmelt. Land surface and hydrologic models were tested that demonstrated an enhanced capability to simulate melt-related runoff.

Frozen ground, be it seasonally frozen soil or permafrost, is ubiquitous in the circumpolar region. To overcome the scarcity of data, Woo et al. (Chap. 7) empirically derived near-surface ground temperature to drive the Stefan's algorithm to compute active layer thaw in boreal and tundra environments. The results permit an evaluation of the probability distributions of maximum active layer thaw and such information has applications for hydrologic processes, terrestrial and aquatic ecosystems, and the integrity of northern infrastructure, including oil and gas pipelines.

Lakes cover an estimated 11% of the MRB and they are subjected to a wide range in air temperature from south to north, and to substantial differences in precipitation. Rouse et al. (Chap. 8) found that the ice-covered

period is shorter for the smaller and more southern lakes than for the large northern lakes. During the open water period, the seasonality of convective fluxes for small lakes is similar to the surrounding land surfaces, but for medium-sized and large lakes there is a substantial time lag. A very large lake like Great Slave Lake achieves greater heat storage, higher temperatures and greater evaporative and sensible heat fluxes during a warmer year than during an average year. Lakes of all sizes are strongly impacted by climate variability and change and this has large influences on the regional hydrologic regimes.

For calculating lake evaporation, bulk aerodynamic mass transfer method works well but is specific to size of the lake and its exposure to atmospheric forcing. Oswald et al. (Chap. 9) studied four lakes and found that the transfer coefficients were similar for the two smallest lakes, slightly smaller for the large lake (Great Slave) and erroneously high for the medium-sized lake. No strong relationships were found between the coefficient values and morphometric parameters, so that these coefficients cannot be transferred from one lake to another, unless the lakes are similar in size. Blanken et al. (Chap. 10) used eddy covariance method to measure the latent and sensible heat fluxes from Great Slave Lake, noting that both these fluxes were consistently small following ice breakup. Instead of exhibiting strong diurnal evaporation cycles, its thermal and evaporative behavior is dominated by synoptic systems that approach a three-day cycle. In terms of determining the sensitivity of the relationship between evaporation and its controls to various sampling intervals, altering the sampling interval from one to six hours in 1-hr steps had no significant effect on the coefficients used to predict the 24-hr evaporation totals.

Intensive year-round observations revealed that Great Slave Lake is dimictic and exhibits spatial and temporal variability in air temperature and wind speed that impacts water surface temperature and lake heat flux (Schertzer et al., Chap. 11). Storm events cause deep vertical mixing of lake water to affect its thermal stratification characteristic. Over a 16-yr observation period, there were large interannual variations in ice-free duration (174 to 213 days), maximum surface temperature (14 to 21.2^{o}C), annual heat content (2.13×10^{19} to 2.61×10^{19} J) and bulk heat exchange (from -338 to 267 W m^{-2}). Simulation of surface temperature using a 3-D hydrodynamic model demonstrated marked nearshore and offshore temperature differences.

The presence of lakes in a semi-arid Precambrian Shield setting causes seasonal severance of streamflow connection in many drainage systems. Rapid and substantial snowmelt runoff leads to a rise of lake levels above their outlet elevations to generate outflow but continued summer evapora-

tion draws down the lake storage, usually to the level where outflow would cease and the lake–stream network becomes disconnected (Woo and Mielko, Chap. 12). The principle of fill-and-spill of lakes should be considered in modeling Shield hydrology under semi-arid conditions, to take account of (1) antecedent storage in individual lakes, (2) their storage change calculated through water balance, and (3) the thresholds to be exceeded for outflows to occur. In general, the fill-and-spill concept applies to the semi-arid Shield hydrology (Spence and Woo, Chap. 13). In the heterogeneous Shield landscape comprising exposed bedrock uplands, soil mantled slopes, wetlands and lakes, the water budget of bedrock uplands is influenced by rock fractures, slope aspect, precipitation or snowmelt intensity, and storage capacity. Water transferred laterally from bedrock uplands maintains moisture storage and evaporation in the soil-filled valleys. Flow thresholds must be exceeded before runoff generated in headwaters can be transferred to basin outlets. The hydrologic connectivity is then controlled in part by the geometry and spatial distribution of landscape components.

Wetlands are common on the Interior Plains. Quinton and Hayashi (Chap. 14) studied the major water flux and storage processes within a wetland-dominated zone of the discontinuous permafrost region. They examined the dominant peatland types and their influence on basin runoff, the physical processes and how the hillslope processes relate to basin-scale runoff. The distinct hydrologic roles of flat bog, channel fen and peat plateau were recognized. A conceptual model contributes to resolving the storage and routing functions of wetlands-dominated basins underlain by discontinuous permafrost.

One subject of great concern in winter and spring hydrology of cold regions is the formation and breakup of rive ice (Hicks and Beltaos, Chap. 15). Frazil ice production and accumulation can obstruct water intakes to hydro-power plants and affect fish habitat. Ice breakup may be characterized by severe ice runs associated with ice jam formation and release, with potential impacts on infrastructure and a high risk of flooding. River ice research carried out under MAGS included investigations into the potential impacts of climate change on rivers in the MRB, the dynamic processes of ice jam formation and release, application of satellite remote sensing techniques for river ice characterization and the development of new models for ice jam flood forecasting. Mahabir et al. (Chap. 16) used Fuzzy Expert Systems to explore their potential for developing long lead time ice jam risk forecasts for the Athabasca River at Fort McMurray, Alberta, where serious ice jam events have been documented for over 100 years and where breakup has been monitored intensively for the past 25 years. The

System identified seven out of twenty two years that had the potential for high water levels, including all four years when high water levels actually occurred.

Andrishak and Hicks (Chap. 17) developed a one-dimensional hydrodynamic model that includes river ice formation and melting processes and used it to assess climate change impact on the ice regime of the Peace River in Alberta. This model employs an Eulerian frame of reference for both the flow hydrodynamics and the ice processes and uses the characteristic-dissipative-Galerkin finite element method to solve the primary equations. Under a higher air temperature scenario predicted by the CGCM2, the model generates future ice front profiles that suggest a shorter ice-covered season by the mid-twenty-first century. At the Town of Peace River, the average total reduction in ice cover duration is 28 days (31%) under the scenario applied. Baltaos et al. (Chap. 18) studied the climate impacts on ice-jam flooding in the Peace-Athabasca Delta, Alberta, which has experienced prolonged dry periods since the mid-1970s due to a reduction of ice-jam flooding in the lower Peace River. From archived hydrometric data and in situ observations, ice-jam flooding is shown to depend on freeze-up stage and spring flow; the former has increased as a result of flow regulation and the latter has decreased due to recent climatic trends. Under a projected future (2070–99) climate, the ice season may be reduced by 2–4 weeks, while future ice covers would be slightly thinner than they are at present. More importantly, a large part of the Peace River basin is expected to experience frequent and sustained mid-winter thaws, leaving a much depleted snowpack in the spring and leading to severe reduction in the frequency of ice-jam flooding.

The MRB has been experiencing a general air temperature rise in the past decades and this may have effects on the streamflow. Burn and Hesch (Chap. 19) analyzed the hydrologic regimes of three major rivers in the Basin: the Athabasca, Peace, and Liard. Monthly and annual trends were identified using the Mann-Kendall test with an approach that corrects for serial correlation. The global (or field) significance of the results for each watershed was evaluated using a bootstrap resampling technique. The results reveal more trends in some hydrologic variables than are expected to occur by chance. There are both similarities and differences between the trend characteristics for the three watersheds investigated.

The last section of Volume II, before the concluding chapter, is devoted to hydrologic modeling. Martz et al. (Chap. 20) discussed five approaches to up-scale flow data: simple averaging of Digital Elevation Model (DEM) elevation data to coarser resolution, drainage enforcement that minimizes impact on the DEM outside the drainage network area, subdivision of

drainage basins at various scales while the DEM resolution is held constant, vector averaging of sub-grid flow directions from a higher resolution DEM and a quasi-expert system approach based on the WATFLOOD (a hydrologic model) parameterization scheme. It was found that an objective approach based on vector addition is mathematically appropriate and effective in preserving the essential features of the sub-grid flow patterns. A quasi expert system approach developed by the automation of the WATFLOOD manual method of topographic parameterization is shown to be the superior approach to rescaling flow data for macro or regional scale hydrologic modeling.

Several land surface schemes and macro-scale hydrologic models have been used by the MAGS community. The Semi-distributed Land Use-based Runoff Processes (SLURP) model has been successfully applied to basins of various sizes, notably those in cold regions. Although the SLURP manual offers much information, users can benefit from additional information on certain procedures in order to operate the model successfully. Thorne et al. (Chap. 21) shared their experiences in operating this model, including the preparation of input data, initialization of variables, optimization of parameters, and validation of model results. They suggested that the lessons learned from the use of SLURP are equally applicable to other macroscale hydrologic models.

Kerkhoven and Gan (Chap. 22) applied stand-alone runs of the land surface model ISBA to the Athabasca River Basin, using meteorological forcings from the GEM and ERA-40 archives. The original ISBA produced unrealistic hydrographs. When its hydrologic scheme was modified by applying the Xinanjiang distribution to represent variation in soil water retention, the modified version (MISBA) improved the simulation of runoff. MISBA was then used to simulate flow under climate change scenario conditions. Although most scenarios predict increased precipitation, all simulations produced significantly decreased streamflow by the end of the century (2070–99), primarily due to a predicted reduction in the snow cover due to warmer winters.

CLASS is the land surface scheme commonly used in MAGS. Wen et al. (Chap. 23) tested the ability of CLASS to simulate soil moisture and sensible and latent heat fluxes at two tundra sites underlain by permafrost and which feature mineral earth hummocks with organic soil in the inter-hummock zones. Two versions of CLASS were used, one with and the other without an organic soil parameterization. Results from the peatland version showed significant improvement over the standard version though they both underestimated latent heat and overestimated sensible heat fluxes. CLASS used in this study is a one-dimensional column model and

cannot explicitly represent lateral flow. The observed soil moisture content remained almost constant, a condition that may be attributed to the depressed topography at both sites that collects lateral flow from adjacent hillslopes.

The MAGS integrated modeling system was developed to couple, with full feedback, selected atmospheric and hydrologic models, with the expectation that the imposed consistency will enhance the performance of both models and so mitigate the lack of data for northern basins. Soulis and Seglenieks (Chap. 24) present a new mesoscale distributed hydrologic model (WATCLASS), created using CLASS for vertical processes and the routing algorithms from WATFLOOD. Changes were made primarily to the soil water budget and included improvements in the between-layer transfer procedures, the addition of lateral flow, and the enhancement of the treatment of cold soil. Streamflow simulations using the WATCLASS model are compared to measured values for basins with areas that spread across several orders of magnitude, from the small MAGS research basins to the major tributaries of the Mackenzie. As well as streamflow, simulated internal state variables from WATCLASS were compared to measurements taken in the research basins. Finally, the water balance of the MRB is examined and the change in storage within the basin is compared to satellite data.

The concluding chapter (Woo, Chap. 25) is a retrospective on the Mackenzie GEWEX studies on the atmospheric–hydrologic system of the MRB which shares many traits special to the world cold regions. MAGS investigators used a variety of research methods (field investigations, remote sensing, data analyses and modeling) to characterize, understand and predict the cold climate phenomena. Research emphasized the atmospheric and hydrologic processes in the MRB which exhibit pronounced seasonality. In general, the atmospheric is most dynamic in the cold season and hydrologic activities are particularly vigorous in the snowmelt period. The Basin experiences large climate variability that may be linked to shifts in the direction and intensity of airflows. Climate warming signals are also being recognized and a number of studies examined the future warming effects on snow, frost, wildfire, river ice and streamflow.

We reiterated that MAGS was an integrative study of the atmospheric–hydrologic system, using the MRB as a natural laboratory for our field and modeling research. Volume I of this book concentrates on the atmosphere-related topics and Volume II provides complementary results on the hydrology-related aspects. Together, these two volumes present the total contribution of MAGS to cold region science.

Appendix

List of chapters in Volume II

Woo MK (Chapter 1) Synopsis of atmospheric research under MAGS

Woo MK, Rouse WR (Chapter 2) MAGS contribution to hydrologic and surface process research

Bussières N (Chapter 3) Analysis and application of 1- km resolution visible and infrared satellite data over the Mackenzie River Basin

Leconte R, Temimi M, Chaouch N, Brissette F, Toussaint T (Chapter 4) On the use of satellite passive microwave data for estimating surface soil wetness in the Mackenzie River Basin

Pomeroy JW, Gray DM, Marsh P (Chapter 5) Studies on snow redistribution by wind and forest, snow-covered area depletion and frozen soil infiltration in northern and western Canada

Marsh P, Pomeroy J, Pohl S, Quinton W, Onclin C, Russell M, Neumann N, Pietroniro A, Davison B, McCartney S (Chapter 6) Snowmelt processes and runoff at the Arctic treeline: ten years of MAGS research

Woo MK, Mollinga M, Smith SL (Chapter 7) Modeling maximum active layer thaw in boreal and tundra environments using limited data

Rouse WR, Blanken PD, Duguay CR, Oswald CJ, Schertzer WM (Chapter 8) Climate–lake interactions

Oswald CJ, Rouse WR, Binyamin J (Chapter 9) Modeling lake energy fluxes in the Mackenzie River Basin using bulk aerodynamic mass transfer theory

Blanken P, Rouse WR, Schertzer WM (Chapter 10) The time scales of evaporation from Great Slave Lake

Schertzer WM, Rouse WR, Blanken PD, Walker AE, Lam DCL, León L (Chapter 11) Interannual variability of the thermal components and bulk heat exchange of Great Slave Lake

Woo MK, Mielko C (Chapter 12) Flow connectivity of a lake–stream system in a semi-arid Precambrian Shield environment

Spence C, Woo MK (Chapter 13) Hydrology of the northwestern subarctic Canadian Shield

Quinton WL, Hayashi M (Chapter 14) Recent advances toward physically-based runoff modeling of the wetland-dominated central Mackenzie River Basin

Hicks F, Beltaos S (Chapter 15) River ice

Mahabir C, Robichaud C, Hicks F, Robinson Fayek A (Chapter 16) Regression and fuzzy logic based ice jam flood forecasting

Andrishak R, Hicks F (Chapter 17) Impact of climate change on the Peace River thermal ice regime

Beltaos S, Prowse T, Bonsal B, Carter T, MacKay R, Romolo L, Pietroniro A, Toth B (Chapter 18) Climate impacts on ice-jam floods in a regulated northern river

Burn DH, Hesch N (Chapter 19) Trends in Mackenzie River Basin streamflows

Subject Index

C

D

E

F

G

H

I

L

M

N

O

P

R

S

T

U

V

W

Z